



**Leading Edge Oscillatory Blowing:  
Influence on Subsonic Cavity Flow and  
Application in Synchronized Dynamic Store Separation**

THESIS

Matthew L. Wood, Captain, USMC  
AFIT-ENY-MS-18-J-083

**DEPARTMENT OF THE AIR FORCE  
AIR UNIVERSITY**

***AIR FORCE INSTITUTE OF TECHNOLOGY***

---

**Wright-Patterson Air Force Base, Ohio**

DISTRIBUTION STATEMENT A  
APPROVED FOR PUBLIC RELEASE; DISTRIBUTION UNLIMITED.

The views expressed in this document are those of the author and do not reflect the official policy or position of the United States Air Force, the United States Department of Defense or the United States Government. This material is declared a work of the U.S. Government and is not subject to copyright protection in the United States.

AFIT-ENY-MS-18-J-083

LEADING EDGE OSCILLATORY BLOWING:  
INFLUENCE ON SUBSONIC CAVITY FLOW AND  
APPLICATION IN SYNCHRONIZED DYNAMIC STORE SEPARATION

THESIS

Presented to the Faculty  
Department of Aeronautics and Astronautics  
Graduate School of Engineering and Management  
Air Force Institute of Technology  
Air University  
Air Education and Training Command  
in Partial Fulfillment of the Requirements for the  
Degree of Master of Science in Aeronautical Engineering

Matthew L. Wood, B.S.M.E.

Captain, USMC

June 1, 2018

DISTRIBUTION STATEMENT A  
APPROVED FOR PUBLIC RELEASE; DISTRIBUTION UNLIMITED.

AFIT-ENY-MS-18-J-083

LEADING EDGE OSCILLATORY BLOWING:  
INFLUENCE ON SUBSONIC CAVITY FLOW AND  
APPLICATION IN SYNCHRONIZED DYNAMIC STORE SEPARATION  
THESIS

Matthew L. Wood, B.S.M.E.  
Captain, USMC

Committee Membership:

Dr. M. F. Reeder  
Chair

Dr. D. L. Kunz  
Member

Maj D. S. Crowe, PhD  
Member



## Abstract

The objective of the research was twofold: first, investigate the effect of leading-edge flow control on subsonic ( $\text{Mach} < 0.13$ ) flow fields over a rectangular cavity ( $L/D = 4.465$ ), and second, develop the capability to synchronize store release with an oscillatory leading edge blowing device's position and identify any trends in forces and moments imparted on the store. The active flow control method utilized a linear motor oscillating at 5.0 Hz to provide leading edge blowing. Five different leading-edge devices were designed and characterized: a single channel slot and four fluidic diodes. The study used the AFIT low-speed wind tunnel in combination with a tri-axial velocity probe to gather time-accurate data for all three velocity components. Flow control methods were compared using measurements of growth in the shear layer, turbulence intensity, and spatial representation of secondary flows. Compared to the slot, the fluidic diode designs increased shear layer thickness and displaced it toward the freestream. A second linear motor was used to move the store from 0.75 inches below the cavity lip line to 2.25 inches above the lip line. Two initialization positions were tested: the oscillatory linear motor either fully retracted or fully extended. Synchronization between the motors was successfully accomplished using in-situ position readouts from the high-resolution digital encoders in each linear motor and visually with a high-speed digital camera. A dedicated data acquisition system incorporating a Nano-25 balance, collecting data at 1000 Hz, provided time-accurate measurements of the forces and moments acting on the store before, during, and after trajectory motion. The oscillatory blowing was observed to influence the normal force component within the shear layer prior to store motion. During trajectory motion, distinct and generally repeatable patterns in the normal forces during the store motion were observed for the two different initialization positions.

# Table of Contents

|  | Page |
|--|------|
| Abstract .....   | iv   |
| List of Figures .....  | viii |
| List of Tables .....   | xvi  |
| I. Introduction .....  | 1    |
| 1.1 Motivation .....   | 1    |
| 1.2 Problem Statement .....  | 3    |
| 1.3 Methodology .....  | 3    |
| 1.4 Limitations .....  | 4    |
| 1.5 Overview of Subsequent Chapters .....                              | 5    |
| II. Literature Review .....  | 6    |
| 2.1 Chapter Overview .....   | 6    |
| 2.2 Cavity Aeroacoustics .....   | 6    |
| 2.2.1 The Aeroacoustic Environment .....                               | 6    |
| 2.2.2 Classifications of Cavities .....                                | 14   |
| 2.2.3 Evaluating the Flow Field .....                                  | 15   |
| 2.3 Open Flow Phenomena .....  | 17   |
| 2.4 Store Effects .....  | 19   |
| 2.5 Flow Control .....   | 23   |
| 2.5.1 Passive Flow Control .....                                       | 24   |
| 2.5.2 Active Flow Control .....  | 33   |
| 2.6 Summary .....  | 38   |
| III. Methodology .....   | 40   |
| 3.1 AFIT Wind Tunnel .....   | 40   |
| 3.2 3-D Printers Used for Rapid Prototype Design .....                 | 43   |
| 3.3 Cavity and Mechanical Components .....                             | 45   |
| 3.3.1 Cavity .....   | 45   |
| 3.3.2 Linear Motor and Controllers .....                               | 46   |
| 3.3.3 Traverse and Tri-axial Probe .....                               | 52   |
| 3.3.4 Nano-25 Force/Torque Transducer .....                            | 58   |
| 3.4 Experimental Models: Piston and Sleeve Design .....                | 60   |
| 3.5 Experimental Models: Leading Edge Passive Control<br>Devices ..... | 62   |
| 3.6 Experimental Models: Leading Edge Blowing Devices .....            | 63   |
| 3.6.1 Leading Edge Blowing Device: Single Channel<br>‘Slot’ .....      | 64   |

|   | Page |
|---|------|
| 3.6.2 Leading Edge Blowing Device: Fluidic Diodes .....                         | 65   |
| 3.7 Experimental Model: Mission Store Model and Support                         |      |
| Sting .....   | 73   |
| 3.7.1 Mission Store Models .....  | 73   |
| 3.7.2 Support Sting .....   | 74   |
| 3.8 Overview of the Experimental Setups .....                                   | 76   |
| 3.9 Phase I .....   | 77   |
| 3.9.1 Test Profiles: Phase I .....  | 77   |
| 3.9.2 Forcing a Dominant Tone in the Cavity .....                               | 83   |
| 3.9.3 Post-Processing:Phase I .....   | 84   |
| 3.10 Phase II .....   | 88   |
| 3.10.1 Triggering the Trajectory Motion .....                                   | 88   |
| 3.10.2 Test Profiles: Phase II .....  | 91   |
| 3.10.3 Post-Processing: Phase II .....  | 92   |
| 3.11 Summary .....  | 98   |
| IV. Analysis and Results .....  | 100  |
| 4.1 Chapter Overview .....  | 100  |
| 4.2 Verification of Hot-Wire Suitability .....                                  | 101  |
| 4.3 Phase I: Linear Plots .....   | 111  |
| 4.3.1 Linear Plots: Slot vs. Diode 0.0 (50 mph) .....                           | 111  |
| 4.3.2 Linear Plots: Slot vs. Diode 0.0 (25 mph) .....                           | 117  |
| 4.3.3 Linear Plots: Slot vs. Diodes 0.0, 1.0, 1.0a, 2.0 .....                   | 123  |
| 4.4 Phase I: Raster Plots .....   | 129  |
| 4.4.1 Contour Plots: Baseline vs. Slot vs. Diode 1.0a .....                     | 129  |
| 4.4.2 Vorticity: Slot vs. Diode 1.0a .....                                      | 135  |
| 4.5 Forcing a Dominant Tone in the Cavity .....                                 | 137  |
| 4.6 Phase II .....  | 140  |
| 4.6.1 Verification of Store Release Timing .....                                | 140  |
| 4.6.2 Trajectory Analysis .....   | 144  |
| 4.6.3 Trajectory Analysis: $C_N$ for 10.0° AoA, 50 mph .....                    | 145  |
| 4.6.4 Trajectory Analysis: $C_N$ for 10.0° AoA, 100 mph .....                   | 151  |
| 4.6.5 Trajectory Analysis: Average $C_N$ Values for<br>10.0° AoA, 100 mph ..... | 155  |
| 4.7 Summary .....   | 157  |
| V. Conclusions and Recommendations .....  | 158  |
| 5.1 Summary of Results .....  | 158  |
| 5.2 Significance of Research .....  | 160  |
| 5.3 Recommendations for Future Testing .....                                    | 161  |
| Appendix A. Additional Experimental Data .....                                  | 163  |

|   | Page |
|---|------|
| Appendix B. Galil and MATLAB Code ..... | 245  |
| Appendix C. Drawings of Models .....    | 286  |
| Bibliography .....                      | 299  |

## List of Figures

| Figure |   | Page |
|--------|---|------|
| 1      | Typical Oscillation Cycle [24] .....  | 11   |
| 2      | An example of the pressure magnitudes as a function of distance from the leading edge data gathered from Heller and Bliss' analytical model [24] .....  | 12   |
| 3      | Matrix categorization of fluid-dynamic, fluid-resonant, and fluid-elastic types of cavity oscillations [43] .....   | 13   |
| 4      | Depictions of the different flow field types based upon the varying dimensions of $L/D$ [63] .....  | 15   |
| 5      | Cavity flow feedback loop [36] .....  | 17   |
| 6      | Illustration of the how the quasi-steady assumption of CTS neither captures the time-dependent forces of the unsteady shear layer or allow for accurate prediction of store separation. [9] ..... | 21   |
| 7      | The effect of release time on trajectory based upon a two dimensional CFD model [28] .....  | 22   |
| 8      | Classification of flow control [7] .....  | 24   |
| 9      | Leading edge spoiler configurations tested by Saddington et al. [46] .....  | 26   |
| 10     | Effect of leading edge spoilers on the sound pressure level (SPL) at $M_\infty = 0.71$ and $x/L = 0.9$ . FTS = Flat Top Spoiler, STS = Squaretooth Spoiler, SWS = Sawtooth Spoiler [46]. .....    | 27   |
| 11     | Effect of the shed vortices shed from a rod in a crossflow, referred to by McGrath and Shaw as a High Frequency Tone Generator, on the shear layer [34]. .....                                    | 29   |
| 12     | Typical configuration of a Helmholtz resonator in a flow field. $r$ = radius of the Helmholtz resonator opening and $L$ = opening neck length of the resonator. ....                              | 31   |
| 13     | Depictions of the two different injection nozzle configurations used by Sarno and Franke [47] .....   | 35   |

| Figure |   | Page |
|--------|---|------|
| 14     | Nikolai Tesla’s fluidic diode (valvular conduit) patented in 1920. (US Patent 1,329,559 [71] .....  | 38   |
| 15     | AFIT Wind Tunnel (Not to Scale) .....   | 40   |
| 16     | AFIT wind tunnel top access panel. Access panel without the inserts (top) and access panel with the inserts in place (bottom). ....   | 41   |
| 17     | AFIT Wind Tunnel test section with the traverse system placed on the top of the tunnel. ....  | 42   |
| 18     | Empty Weapons Cavity elevated on the support base .....   | 45   |
| 19     | Original cavity rear design. The left picture is a view from the inside of the cavity looking aft the center picture is a side profile view and the right picture is from behind the cavity looking forward.....  | 46   |
| 20     | New cavity rear design. Small channel at the floor of the cavity prevents bunching of the wiring by allowing the linear motor’s wiring to lie flush with the deck. The left picture is a view from the inside of the cavity looking aft the center picture is a side profile view and the right picture is from behind the cavity looking forward. .... | 46   |
| 21     | SRS-003-04-003-01 Linear Motor used for the experimental study .....  | 47   |
| 22     | Galil DMC-30012 single-axis motion controller .....   | 48   |
| 23     | Galil DMC-34020 dual-axis motion controller .....   | 49   |
| 24     | AFIT wind tunnel coordinate system compared to traverse coordinate system (Not to Scale).....   | 53   |
| 25     | DANTEC 55P91 Tri-axial probe. The alignment face is used to mount the alignment tool required for velocity and directional calibration .....  | 54   |
| 26     | Wind tunnel control room .....  | 55   |
| 27     | DANTEC 90H02 Calibration Unit. The pitch-yaw manipulator allows for calibration of the tri-axial probe. ....  | 56   |

| Figure |  | Page |
|--------|--|------|
| 28     | Tri-axial wire alignment tool. The left photo shows the alignment tool, and the right photo shows how to line up the probe when it is mounted to the pitch-yaw manipulator. ....   | 57   |
| 29     | Nano-25's designed reference frame. ....   | 59   |
| 30     | The left image is the Nano-25 reference frame when mounted to the sting. The right image is the body reference frame in agreement with AIAA standards after post-processing the Nano-25 reference frame. ....  | 60   |
| 31     | Piston for the leading edge blower ....  | 61   |
| 32     | Cylinder for the leading edge blower. ....   | 62   |
| 33     | Support mount for the piston-cylinder apparatus. ....  | 62   |
| 34     | Passive leading edge devices. Left: sawtooth spoiler, Center: triangular tab, Right: rectangular tab. ....   | 63   |
| 35     | Channel to connect the cylinder and leading edge device. The channel opens at the bottom of the leading edge device to simplify process for removal and replacement of leading edge devices during testing. ....   | 64   |
| 36     | Slot-Leading Edge Blower. ....   | 65   |
| 37     | Reference for terminology used in describing geometry of the Diodes. ....  | 66   |
| 38     | Internal view of the fluidic diode openings. The leftmost image is a side view of the entire fluidic diode for orientation. The center image shows the curve of outer channels with respect to flow direction. The right image shows the curve of central channel with respect to the flow direction. .... | 67   |
| 39     | Internal view of Diode 0.0. The view presented is from within the cavity looking towards the leading edge. ....  | 68   |
| 40     | Depicting the difference in the geometry of the openings at the top of Diode 0.0. Outer channels coming to an abrupt end (left) and central channel having proper curvature (right). ....  | 69   |

| Figure |   | Page |
|--------|---|------|
| 41     | Internal view of the Diode 1.0. The view presented is from within the cavity looking towards the leading edge. ....   | 70   |
| 42     | Pictures on the left is Diode v1.0a and on the right is the cover plate. The view presented is from within the cavity looking towards the leading edge. ....                                    | 71   |
| 43     | Internal view of the Diode 2.0. The view presented is from within the cavity looking towards the leading edge. ....   | 72   |
| 44     | Generic Missile (top) and Ogive-cylinder (bottom) models pictured alongside their access panels. ....   | 74   |
| 45     | The left two images are of the Nano-25 attachment piece and the right image is the sting-arm with the Nano-25 attachment piece mounted. ....  | 75   |
| 46     | Ogive-cylinder with the access panel open, showing the store and Nano-25 attached to the sting-arm using the 0.0° AoA(left). Cavity store and sting-arm secured to the base plate (right). .... | 76   |
| 47     | Fully assembled cavity used for Phase I. ....   | 78   |
| 48     | Linear profile used with the tri-axial probe, starting in the freestream and ending within the cavity. ....   | 79   |
| 49     | Raster profile used with the tri-axial probe. ....  | 79   |
| 50     | DANTEC 55P91 Tri-axial probe coordinate system [30] ....  | 84   |
| 51     | Fully assembled cavity used for Phase II with second linear motor, sting, and cavity store. ....  | 89   |
| 52     | MATLAB code prior to any visual alignment. Distance between the data cursors is used for alignment. ....  | 94   |
| 53     | MATLAB after visual alignment ....  | 95   |
| 54     | TARED data set shown after the tared data is subtracted from the test data ....   | 96   |
| 55     | Filter developed in MATLAB for the normal force data. The cut-off frequency and order were chosen based on best visual fit. [4] ....  | 97   |



| Figure |   | Page |
|--------|---|------|
| 56     | Mean and RMS values of velocity data collected from the linear profile for an empty cavity compared to a cavity with a leading edge sawtooth spoiler. ....  | 104  |
| 57     | Contour Plots of the streamwise mean velocity and turbulence intensity using data collected from the raster pattern for a baseline cavity compared (left) to a cavity with a leading edge Sawtooth spoiler (right). ....  | 106  |
| 58     | Contour Plots of the wall normal mean velocity and turbulence intensity using data collected from the raster pattern for a baseline cavity compared (left) to a cavity with a leading edge Sawtooth spoiler (right). ....   | 107  |
| 59     | Contour Plots of the floor normal mean velocity and turbulence intensity using data collected from the raster pattern for a baseline cavity compared (left) to a cavity with a leading edge Sawtooth spoiler (right). ....  | 108  |
| 60     | Streamwise vorticity plots using velocity data collected from the raster pattern for a rectangular tab(left) and a triangular tab(right). ....  | 110  |
| 61     | Mean streamwise velocity data collected from linear profiles at $x/L = 0.25, 0.55$ , and $0.85$ of the cavity at 50 mph. The data depicted shows the change at each position when the oscillating linear motor is off and on. ....  | 113  |
| 62     | Turbulence intensity values of the streamwise velocity data collected from linear profiles at $x/L = 0.25, 0.55$ , and $0.85$ of the cavity at 50 mph. The data depicted shows the change at each position when the oscillating linear motor is off and on. ....            | 114  |
| 63     | Mean and turbulence intensity values of the wall normal velocity data collected from linear profiles at $x/L = 0.25, 0.55$ , and $0.85$ of the cavity at 50 mph. The data depicted shows the change at each position when the oscillating linear motor is off and on. ....  | 115  |
| 64     | Mean and turbulence intensity values of the floor normal velocity data collected from linear profiles at $x/L = 0.25, 0.55$ , and $0.85$ of the cavity at 50 mph. The data depicted shows the change at each position when the oscillating linear motor is off and on. .... | 116  |

| Figure |  | Page |
|--------|--|------|
| 65     | Streamwise mean velocity data collected from linear profiles at $x/L = 0.25, 0.55$ , and $0.85$ of the cavity at 25 mph. The data depicted shows the change at each position when the oscillating linear motor is off and on. ....                                 | 119  |
| 66     | Turbulence intensity values of the streamwise velocity data collected from linear profiles at $x/L = 0.25, 0.55$ , and $0.85$ of the cavity at 25 mph. The data depicted shows the change at each position when the oscillating linear motor is off and on. ....   | 120  |
| 67     | Turbulence intensity values of the wall normal velocity data collected from linear profiles at $x/L = 0.25, 0.55$ , and $0.85$ of the cavity at 25 mph. The data depicted shows the change at each position when the oscillating linear motor is off and on. ....  | 121  |
| 68     | Turbulence intensity values of the floor normal velocity data collected from linear profiles at $x/L = 0.25, 0.55$ , and $0.85$ of the cavity at 25 mph. The data depicted shows the change at each position when the oscillating linear motor is off and on. .... | 122  |
| 69     | Mean and turbulence intensity values of the streamwise velocity data collected from linear profiles at $x/L = 0.55$ of the cavity at 50 mph. The data depicted compares the influence that each diode has on the shear layer. ....                                 | 126  |
| 70     | Turbulence intensity values of the wall normal velocity data collected from linear profiles at $x/L = 0.55$ of the cavity at 50 mph. The data depicted compares the influence that each diode has on the shear layer. ....   | 127  |
| 71     | Turbulence intensity values of the floor normal velocity data collected from linear profiles at $x/L = 0.55$ of the cavity at 50 mph. The data depicted compares the influence that each diode has on the shear layer. ....  | 128  |
| 72     | Streamwise mean velocity data collected from raster profiles at $x/L = 0.55$ of the cavity at 50 mph. The data depicted shows the change at each position when the oscillating linear motor is on. ....  | 131  |

| Figure |  | Page |
|--------|--|------|
| 73     | Turbulence intensity values of the streamwise velocity data collected from raster profiles at $x/L = 0.55$ of the cavity at 50 mph. The data depicted shows the change at each position when the oscillating linear motor is on. ....  | 132  |
| 74     | Turbulence intensity values of the wall normal velocity data collected from raster profiles at $x/L = 0.55$ of the cavity at 50 mph. The data depicted shows the change at each position when the oscillating linear motor is on. ....   | 133  |
| 75     | Turbulence intensity values of the floor normal velocity data collected from raster profiles at $x/L = 0.55$ of the cavity at 50 mph. The data depicted shows the change at each position when the oscillating linear motor is on. ....  | 134  |
| 76     | Vorticity plots generated from the v- and w-components of velocity data collected using a raster profiles at $x/L = 0.55$ with the motor on at 50 MPH ....   | 136  |
| 77     | Velocity vs. Time comparison with the Leading Edge Slot off and on at $z/D = 0.035$ . ....   | 138  |
| 78     | Energy Frequency Spectrum for the leading edge Slot at $x/L = 0.55$ and $z/D = 0.035$ with the motor off and motor on. ....  | 139  |
| 79     | Encoder position taken from the Galil Software for trajectory release in a 100 mph test when piston is fully retracted or fully extended. ....   | 142  |
| 80     | Images from high speed camera footage demonstrating motor synchronization. Timing between each image is 22 milliseconds, time-stamp is in the top right of each frame. Zero indicates when fully retracted or extended position has been reached and initiates motion of the store. .... | 143  |
| 81     | Comparison of the difference in detecting trends for the $0.0^\circ$ AoA and $10.0^\circ$ , with $V_\infty = 50\text{mph}$ . ....  | 146  |
| 82     | $C_N$ , Fully Retracted (Min Stroke), $10.0^\circ$ AoA, $V_\infty = 50\text{mph}$ . ....   | 149  |
| 83     | $C_N$ , Fully Extended (Max Stroke), $10.0^\circ$ AoA, $V_\infty = 50\text{mph}$ . ....  | 150  |

| Figure |   | Page |
|--------|---|------|
| 84     | $C_N$ , Fully Retracted (Min Stroke), $10.0^\circ$ AoA, $V_\infty = 100\text{mph}$ . . . . .              | 153  |
| 85     | $C_N$ , Fully Extended (Max Stroke), $10.0^\circ$ AoA, $V_\infty = 100\text{mph}$ . . . . .               | 154  |
| 86     | $C_N$ Averages, Fully Retracted vs Fully Extended, $10.0^\circ$ AoA, $V_\infty = 100\text{mph}$ . . . . . | 156  |

## List of Tables

| Table |   | Page |
|-------|---|------|
| 1     | Ultimaker 2+ and Ultimaker 3 Specifications [67][66] .....  | 43   |
| 2     | PLA Technical Data [65] .....   | 44   |
| 3     | Nano-25 Calibration Specifications [50] .....   | 58   |
| 4     | Nano-25 Single-Axis Overload [50] .....   | 58   |
| 5     | Linear profiles completed with the passive flow control<br>devices for tri-axial probe validation. ....                             | 81   |
| 6     | Linear profiles completed with the oscillating motor<br>inactive. ....  | 81   |
| 7     | Linear profiles completed with the oscillating motor<br>active. ....  | 81   |
| 8     | Raster patterns completed with the oscillating motor<br>inactive. ....  | 82   |
| 9     | Raster patterns completed with the oscillating motor<br>active. ....  | 82   |
| 10    | Summary of Phase II wind tunnel tests performed with<br>the generic missile store model. Each test was repeated<br>five times. .... | 92   |
| 11    | Calibration matrix for the Nano-25 provided by ATI for<br>converting voltage signals to force and torque<br>measurements. ....      | 92   |
| 12    | Reynolds numbers calculated using the store diameter .....  | 98   |
| 13    | Machs used in the experimental study. ....  | 98   |
| 14    | Integral length and time scales in the streamwise<br>direction at $z/D = 0.70$ .....  | 213  |
| 15    | Integral length and time scales in the streamwise<br>direction at $z/D = 0.385$ .....   | 214  |
| 16    | Integral length and time scales in the streamwise<br>direction at $z/D = 0.035$ .....   | 215  |

| Table |   | Page |
|-------|---|------|
| 17    | Integral length and time scales in the streamwise<br>direction at $z/D = -0.14$ ..... | 216  |

LEADING EDGE OSCILLATORY BLOWING:  
INFLUENCE ON SUBSONIC CAVITY FLOW AND  
APPLICATION IN SYNCHRONIZED DYNAMIC STORE SEPARATION

## I. Introduction

### 1.1 Motivation

Advances made in the capacity to wage war have increased exponentially in the last seventy-five years and, through it all, the United States has remained at the forefront of technological development. Marching hand-in-hand with the advance in aircraft has been the simultaneous advance in the capability to detect, acquire, and engage aircraft in a threat environment. To maintain the capacity for establishing air superiority in this evolving threat environment, the United States Air Force (USAF) has placed emphasis on the development of low observable air vehicles. One of the key methods for an aircraft to maintain a low observable profile, and improve aerodynamic characteristics, requires that the weapons loadout be moved to an internal weapons bay. The latest aircraft in the United States' inventory, such as the F-22, F-35, and P-8A, employ weapons delivery from a bomb bay [9].

With the increased prevalence of internal weapons carriage, the cavity aeroacoustic environment that results when the bay doors are open, causing the weapons bay to behave as a cavity in a flow field, has become a topic of particular interest. Weapons bay cavity flows are naturally unsteady due to a robust free shear layer instability that is coupled to, and driven by, a self-reinforced acoustic resonance phenomenon [9]. The combination of acoustic resonance and pressure fluctuations can lead to high

dynamic loads within the cavity. In aircraft bays, dynamic loads in excess of 160 dB are not uncommon and can lead to structural fatigue of the cavity and its contents [8]. Additionally, a weapons bay experiencing strong acoustic resonance will have an unsteady component of normal forces that change sign from instant-to-instant, from ‘into the bay’ to ‘out of the bay’ [9]. The highly oscillatory flow-field generated by cavity flows can adversely affect the safe departure and accurate delivery of munitions stored in the weapons bay, imposing a time-dependency on store release [8].

To overcome the severe acoustic environment of a weapons bay and enhance weapons separation characteristic, both passive and active flow control devices have been investigated. All modern USAF fighter and bomber aircraft with internal weapons bays, since the F-111, have used a leading-edge spoiler to reduce the severe acoustic environment present in a weapons bay. However, the USAF is currently investigating the effectiveness of leading edge blowing as an active flow control technique due to its adaptability across a wider range of flight conditions [22].

Prior research in the Air Force Institute of Technology low-speed wind tunnel has highlighted the importance of collecting time-accurate data for the characterization of dynamic loads during mission store release [50] [4]. This is because typical wind tunnel data is time-averaged and cannot detect the sensitivity to timing of mission store release. The goal of this experimental study was to assess various flow control devices’ capacity to influence the cavity flow field using time-accurate data gathered with a tri-axial velocity probe. Additionally, a method for overcoming the time-dependent nature of store release through synchronizing the release of a store with the cycle of a leading edge oscillatory blowing device was investigated. Time-accurate force and moment data were used to characterize the dynamic loads of store release.



## 1.2 Problem Statement

The goal of the current research is two-fold. First, time-accurate measurements with a tri-axial probe were used to characterize the effect that different leading edge oscillatory blowing devices would have on the cavity environment. The oscillatory blowing was accomplished using a piston and cylinder device driven by an oscillating linear motor. Second, synchronizing the position of an oscillatory motor with release of a store was successfully implemented as a proof-of-concept in an effort to overcome the time-critical nature of store release. This was investigated using select leading edge devices for dynamic testing in the AFIT low speed wind tunnel with the ultimate goal of producing time-accurate force and moment measurements. Mission store separation events were conducted for models at speeds ranging from 0 mph to 100 mph.

## 1.3 Methodology

This experimental study can be broken down into two major phases. In the first phase, the use of the tri-axial probe was validated by using passive flow control devices and comparing velocity data with the literature. The tri-axial probe was then used to characterize the effect that five different leading edge oscillatory blowing devices would have on the cavity environment. A linear motor programmed to oscillate at 5.0 Hertz was used to provide the oscillatory blowing. Post-processing procedures for Phase I included the use of mean and RMS data to develop linear profiles and contour plots of the u-, v-, and w-components. Additionally, the v- and w-components were used to generate streamwise vorticity plots. The raw, time-accurate, data was used to analyze the statistical properties and turbulent characteristics at different locations within the shear layer.

In the second phase, a second synchronized linear motor was integrated into the

experimental setup. A support sting was mounted to the second linear motor, to which a Nano-25 6-DOF force balance and mission store could be attached. The initial position of the store was 0.75 inches below the lip line of the cavity and the final position was 2.25 inches above the cavity lip line. The initialization of the store release was synchronized with position of the oscillating linear motor. Two different positions of the oscillatory motor were used to trigger the store trajectory and for a store at two fixed angles of attack:  $0.0^\circ$  and  $10.0^\circ$ . Initial force and torque data for a sample mission store trajectory out of the cavity were collected using a Nano-25. Post processing procedures for Phase II included the conversion of time-accurate voltage data to force and torque measurements in the x-, y-, and z- directions and the subsequent determination of force and moment coefficients. This proof-of-concept provides ample opportunity to explore store and flow control variations in future work.

#### 1.4 Limitations

The goal of Phase I was to assess the capacity for flow control devices to influence the cavity flow using a tri-axial velocity probe. The physical limitations of the the experimental setup are applicable to the traverse's range of motion, the linear motor's operating rate, and the linear motor's range of motion. The traverse used to manipulate the tri-axial probe's position within the wind tunnel's test section could only access the wind tunnel through small channels that had been pre-cut into the access panel on top of the test section, limiting the  $x/L$  positions of the cavity that could be evaluated. To maintain a one hundred percent duty cycle, the oscillation of the linear motor used to drive the leading edge blowing device was restricted to 5.0 Hz. During the store release tests of Phase II, the linear motors used in the experimental study only have a 3.0 inch range of motion, severely limiting the stores trajectory. Furthermore, a conservative approach with respect to testing led to relatively low

loading of the sensor and limited variations explored for cavity configuration. Thus, Phase II focuses on the development of the synchronized trigger and collection of baseline data for analysis.

## **1.5 Overview of Subsequent Chapters**

The organization of the remaining chapters is as follows. Chapter II provides a literature review of the cavity aeroacoustic environment, store effects, and previous research on passive and active flow control devices. Chapter III addresses the equipment and system developed and utilized in the experimental study for Phases I and II; validation of the tri-axial probe using passive flow control methods; experimental setup and methodology for acquiring data in both phases; and methods used in post-processing and analyzing the acquired data. Chapter IV provides experimental results for select tests of the leading edge devices and their effect on both the cavity environment and the trajectory of a mission store model. Chapter V contains conclusions reached on the effectiveness of the designed leading edge oscillatory blowing devices to influence the cavity environment and identification of generally repeatable patterns in the normal forces during store motion observed for the two different trajectory store initialization positions.

## II. Literature Review

### 2.1 Chapter Overview

This chapter serves as a review of the literature pertaining to the cavity environment and is broken into five sections. The second section is cavity aeroacoustics, and covers previous research conducted in the development and understanding of the phenomena associated with a cavity in a flow field. The third section specifically describes the phenomenon revolving around open-flow cavities. Open cavities are expounded upon since most of the weapons bays designed for United States aircraft fall into this category, making it pertinent to this research. The fourth section covers store effects within the cavity, and more relevantly, during release. The fifth section covers the various methods of flow control that have been explored in previous research. This includes passive and active control methods, specifically active control methods, in addition to the concept of fluidic diodes. Section six summarizes the literature review and briefly outlines the experimental setup.

### 2.2 Cavity Aeroacoustics

#### 2.2.1 The Aeroacoustic Environment.

Research focused on the harmful effects of the acoustic environment generated by subsonic and supersonic flow past rectangular cavities was first conducted in the 1950s by Karamcheti. Using Schlieren methodology and hot wire anemometers, Karamcheti was able to observe and measure the strong acoustic field generated by a cavity in a flow field. Measurements of frequency were made by varying the cavity length gradually while maintaining the flow at constant free stream Mach number,  $M_\infty$ , and stagnation temperature,  $T_o$ . The frequency,  $f$ , at a given free stream Mach number and stagnation temperature was found to be inversely proportional to the cavity

length,  $b$ , as seen in Equation 1. The measurement at each constant Mach number were plotted as  $f$  versus  $1/b$  and the slope of the line was defined as the constant of proportionality,  $\alpha$ , which is a constant  $= fb$  [31]. His observations indicated that there is a minimum cavity length required to generate acoustic noise. This minimum length was dependent upon: the boundary layer type, the size of the cavity, and the free stream velocity [31].

$$f = \alpha \frac{1}{b} \quad (1)$$

The most notable difference between the tones generated in laminar and turbulent cases was that while only a single dominant frequency was observed in the laminar case, the turbulent case generated two frequencies of nearly equal strength [31]. For both the laminar and turbulent cases, harmonic frequencies developed in the cavity in addition to the dominant frequency tones generated. Seeking to nondimensionalize his results, Karamcheti used the Strouhal number, Equation 2, with cavity length used as the scaling parameter. The Strouhal number is a dimensionless parameter derived by Czech physicist Vincenc Strouhal that relates the vortex shedding frequency of an oscillating flow mechanism, a characteristic dimension, and the free-stream velocity. Karamcheti's results showed that the intensity of the acoustic field grew with increased speed but decreased with an increase in cavity length. However, the ability to calculate the cavity frequency based upon the flow field conditions did not come about until nearly a decade later through the work of J.E. Rossiter.

$$S = \frac{f * L}{U} \quad (2)$$

Leveraging the observations of Karamcheti, Rossiter's study focused on the unsteady pressure fluctuations generated by a cavity. He concluded that the unsteady

pressures acting in and around a rectangular cavity may contain both random and periodic components. The forcing function for the frequency and magnitude of these pressure fluctuations is a property of the flow over the cavity and not the approaching boundary layer. Through his experimental study, Rossiter observed that dominant frequencies generated by the cavity 'jump' in an apparently arbitrary manner from one value to another as the speed of the flow field is increased, while the secondary frequencies lie on a 'family of curves' [44]. The dominant frequencies are included in the 'family of curves', and the 'jumps' in the dominant frequency that appeared arbitrary are actually the dominant frequency shifting from one family of curves to another. These observations formed the basis for Rossiter's empirical formula, Equation 5, which builds upon Karamcheti's equation; taking into account the behavior of the dominant frequencies as the speed of the flow field changes [44]. A development of Rossiter's equation for the calculation of cavity frequency, starting with the non-dimensional Strouhal number utilized by Karamcheti, is shown below.

$$S = \frac{fL}{U_\infty} \quad (3)$$

$$\frac{fL}{U_\infty} = \frac{m-n}{\frac{1}{K} + M_\infty} \quad (4)$$

$$f = \frac{m-n}{\frac{1}{K} + M_\infty} \frac{U_\infty}{L} \quad (5)$$

Rossiter's formula for the calculation of the cavity frequency,  $f$ , is based upon the parameters of the flow field, empirically determined constants, and the integer mode number,  $m$ . Rossiter used the work of Brown [5] to develop the mode number, which indicates the frequency ranges between jumps. In Equation 5, the  $L$  represents the cavity length,  $U_\infty$  is the freestream velocity, and  $M_\infty$  is the freestream Mach number.

$K$  is an empirical constant for the ratio of convective velocity of vortices to freestream velocity. The empirical constant,  $n$ , is the phase delay between acoustic wave and new vortex and will vary depending on  $L/D$  [62]. For a cavity with an  $L/D = 4.0$ , Rossiter empirically derived the values of  $n = 0.25$  and  $K = 0.57$  [44].

In 1971, Heller, Holmes, and Colvert conducted experiments in a supersonic wind-tunnel at Mach numbers ranging from 0.8 to 3.0 using a cavity varying in  $L/D$  from 4.0 to 7.0. Heller et al. measured fluctuating pressures using nine piezoelectric microphones located within the cavity and a tenth microphone that was mounted within a movable rod spanning the length of the cavity. This microphone could be traversed remotely and permitted a detailed study of the longitudinal distribution of unsteady pressures in the cavity [23]. Additionally, a thermocouple was mounted within the cavity to measure cavity temperature, allowing for a calculation of the speed of sound for the fluid within the cavity, as seen in Equation 6. In Equation 6,  $\lambda$  is the adiabatic exponent,  $a_c$  is the speed of sound in the cavity, and  $a_\infty$  is the free stream static speed of sound.  $T_c$  is the static temperature for the entire cavity while  $T_\infty$  and  $T_0$  are, respectively, the static and stagnation temperatures of the free stream flow [23]. Having the ability to estimate the speed of sound in the cavity would prove instrumental to the further refinement of Rossiter's equation.

$$a_c = a_\infty \left[ 1 + \left( \frac{T_c - T_\infty}{T_0 - T_\infty} \right) \left( \lambda - \frac{1}{2} \right)^{1/2} \right] \quad (6)$$

Through Heller et al.'s work, it was determined that Rossiter's equation, while having small error at low Mach numbers, shows an increasing level of error as Mach number is increased above 1.5. This outcome stems from Rossiter assumption that the speed of sound for the fluid in the cavity is equivalent to the free-stream speed of sound. At low Mach numbers this assumption introduces only a small error, but at high Mach numbers the error is greater [23]. Based on their observations, Heller et

al. improved the Rossiter formula to be applicable at higher Mach ranges, Equation 7 [23].

$$f = \frac{(m - n)}{\left[ \frac{1}{K} + \left( \frac{M_\infty}{1 + \frac{\gamma - 1}{2} M_\infty^2} \right)^{1/2} \right]} \frac{U_\infty}{L} \quad (7)$$

In forming this modified equation, the ratio of specific heats  $\gamma$  was introduced. Heller et al.'s modifications to Rossiter's formula proved effective in predicting the potential oscillation frequencies for a shallow cavity across a much larger range of Mach numbers [23]. However, determination of which oscillation frequencies will actually be observed in the cavities, and at what amplitude, is the subject of scrutiny for basic research and important applications.

In 1975, an experimental and analytical research program was conducted by Heller and Bliss to improve understanding of the physical mechanisms that control the pressure fluctuations in shallow rectangular cavities exposed to high speed flow. Additionally, Heller and Bliss sought to devise and evaluate devices capable of suppressing the pressure fluctuations [24]. Through water table visualization techniques, Heller and Bliss observed that the unsteady motion of the shear layer leads to the periodic addition and removal of mass at the trailing edge of the cavity [24]. The process received its name, the "pseudopiston" effect, because the mass addition and removal results from a periodic process internal to the cavity that can be likened to what would occur if the rear of the cavity were replaced with an oscillating piston. The "pseudopiston" effect creates a feedback loop in which waves, generated by the addition or removal of mass in the rear of the cavity, travel forward and reflect off the front of the cavity before traveling back towards the rear wall. The motion of the waves forward and aft generate an unsteady motion in the shear layer. This unsteady motion is responsible for the addition and removal of mass at the trailing edge of the cavity that originally



produced the cavity internal wave structure; thus the feedback loop is complete [24].

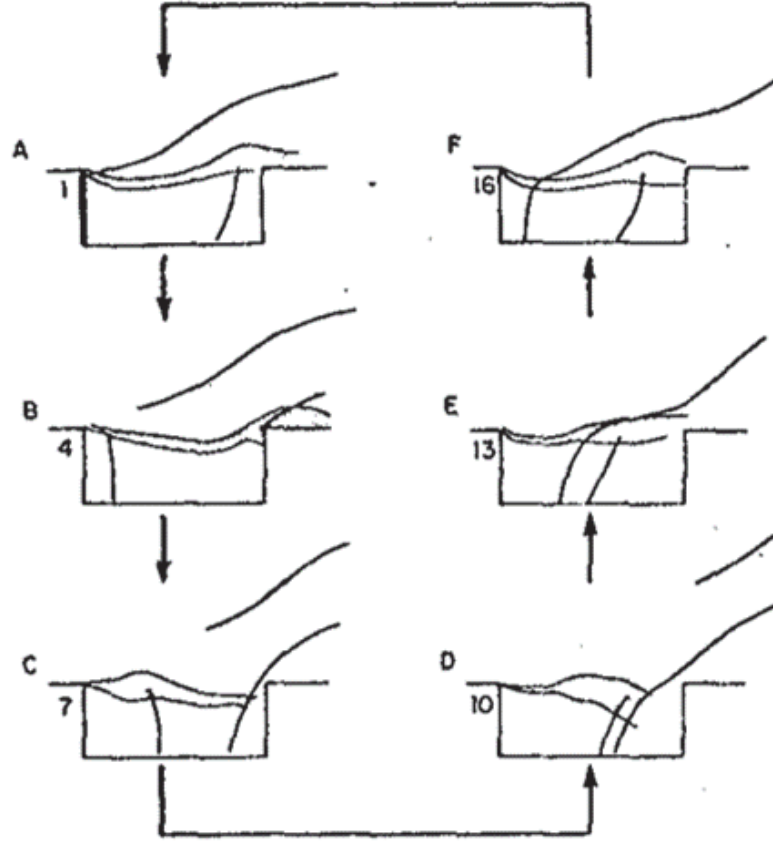


Figure 1. Typical Oscillation Cycle [24]

Figure 1 depicts the six-step oscillation cycle of a forward traveling wave and rearward traveling wave as presented by Heller and Bliss. The cycle shows how the mass addition, resulting from fluctuations of the shear layer at the aft of the cavity, generates forward traveling compression waves. In turn, these forward traveling waves reflect off of the front of the cavity and while traveling aft, cause fluctuations in the shear layer. The fluctuations in the shear layer result in the addition and removal of mass, which then generates another forward traveling compression wave; a cycle that continues to repeat itself [24].

Heller and Bliss utilized their observation of the pseudopiston effect to develop a simple analytical model for the internal wave structure of the cavity. At a given

freestream Mach number and corresponding frequency, the analytical model allowed for the accurate prediction of the location of peak pressure magnitudes within the cavity [24]. The peak magnitudes of the pressure were presented as a function of distance from the leading edge, Figure 2. Heller and Bliss suspected that the trailing edge locations identified are the point where the ratio of shear layer displacement to pseudopiston displacement is at a maximum [24]. The calculations were capable of being repeated at different frequencies, generating mode shapes for a different set of length to depth ratios. Heller and Bliss claimed that the mode shapes agreed qualitatively with those measured experimentally [24]. Unfortunately, an equation representing the model was never presented.

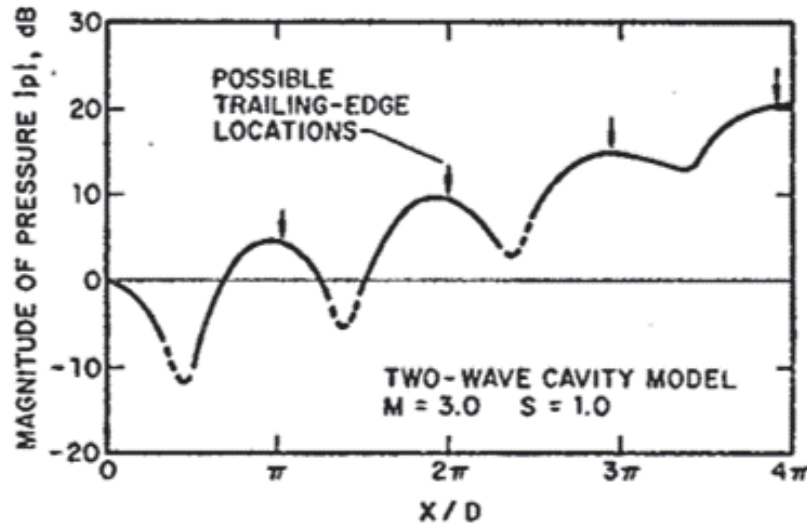


Figure 2. An example of the pressure magnitudes as a function of distance from the leading edge data gathered from Heller and Bliss' analytical model [24]

By 1978, nearly three decades of research and observations revolving around the oscillating shear layer and internal cavity pressure fluctuations had been conducted by engineers and scientists around the world. In an effort to classify the diverse types of self-sustaining cavity oscillations, Rockwell and Naudascher generated a framework, as seen in Figure 3. The framework, or matrix, makes an effort to categorize self-sustaining oscillations into three groups: (a) fluid dynamic, where oscillations

arise from inherent instability of the flow; (b) fluid resonant, where oscillations are influenced by resonant wave effects (standing waves); and (c) fluid elastic, where oscillations are coupled with the motion of a solid boundary [43].

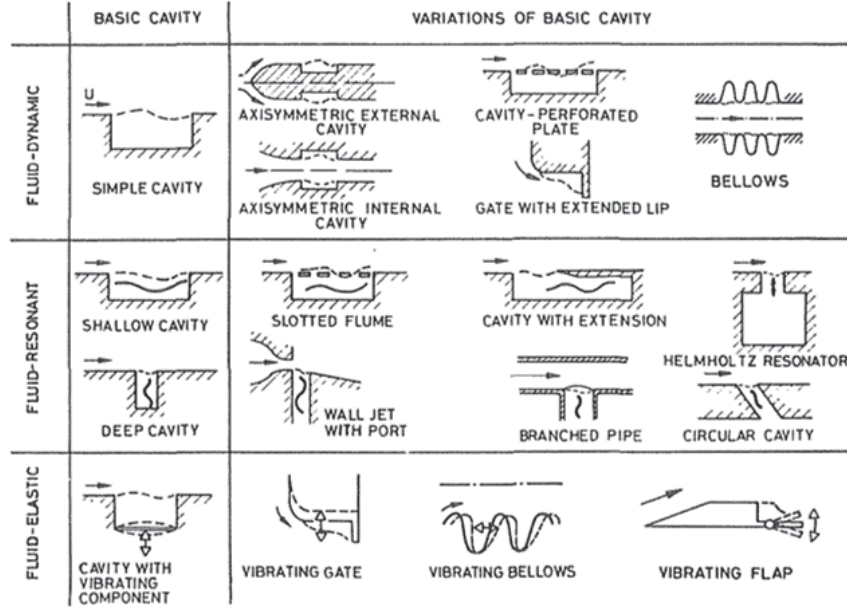


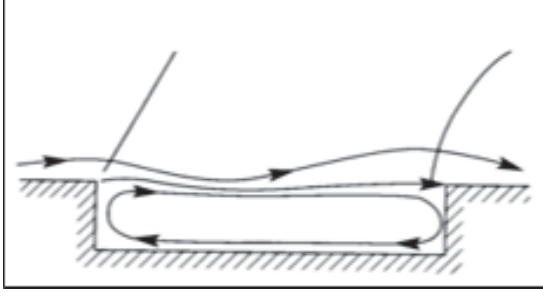
Figure 3. Matrix categorization of fluid-dynamic, fluid-resonant, and fluid-elastic types of cavity oscillations [43]

Rockwell and Naudascher understood that, in practice, the mechanisms influencing the oscillations can be fluid dynamic, fluid-resonant, and fluid-elastic in nature. However, their goal was to identify the dominant mechanism influencing the oscillations, so that Figure 3 could be used to facilitate a detailed analysis [43]. Additionally, at the time their framework was generated, there was a lack of understanding of the effects that a turbulent free shear layer would have on the generation of self-sustaining cavity oscillations. As a result, the quasi-two-dimensional nature of the flow, which governs the overall nature of the oscillation, received the most attention [43].

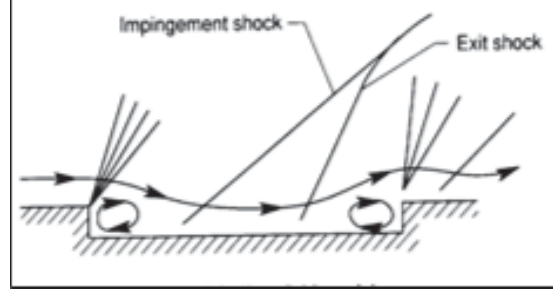
### 2.2.2 Classifications of Cavities.

Through the research conducted by Stallings and Wilcox, it was determined that the type of flow field appears to be largely a function of cavity length-to-depth ratio. There are two fundamentally different types of cavity flow fields which have been classified as open and closed cavity flow [57]. For  $L/D < 10.0$ , the cavity flow field is classified as an open cavity flow. In open cavities, the incoming boundary layer separates at the leading edge of the cavity, forming a shear layer that flows over, or bridges, the cavity. The shear layer interacts with the rear wall of the cavity, generating acoustic waves that travel upstream through the cavity, Figure 4a [72]. For  $L/D > 13.0$ , a closed cavity flow develops. In closed cavities, the shear layer expands over the leading edge of the cavity, impinges on the cavity floor, and exits ahead of the rear face, Figure 4b [57].

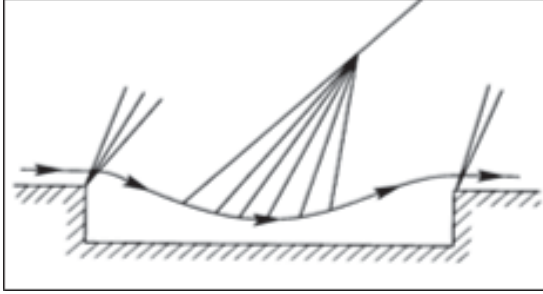
Additionally, at  $L/D$  of approximately 12.0 the cavity flow is on the verge of changing from closed cavity flow to open cavity flow, and is referred to as transitional cavity flow, Figures 4c and 4d [57]. Further studies conducted by Tracy, Plentovich, and Stallings determined that the switch from transitional to closed flow is highly dependent on Mach number and cavity configuration (length, width, and depth). The range of  $L/D$  over which transitional flow occurs at a given Mach number generally increases with increasing cavity width-to-depth ratios [63].



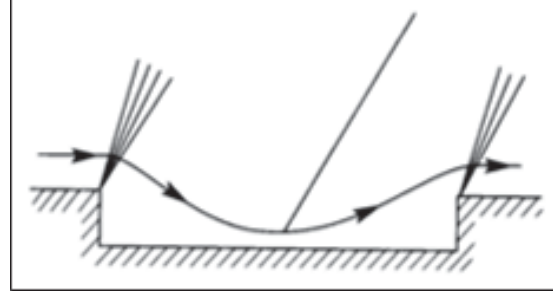
(a) Open cavity flow field at supersonic speeds,  $L/D < 10$



(b) Closed cavity flow field at supersonic speeds,  $L/D > 13$



(c) Transitional open cavity flow field at supersonic speeds  $10 < L/D < 13$



(d) Transitional closed cavity flow field at supersonic speeds  $10 < L/D < 13$

Figure 4. Depictions of the different flow field types based upon the varying dimensions of  $L/D$  [63]

### 2.2.3 Evaluating the Flow Field.

In recent years, with the advances in hot-wire anemometry and the advent of new technologies, such as, particle image velocimetry (PIV) and computational fluid dynamics (CFD), the ability to model and evaluate the flow using computationally demanding methods has brought new perspective to the aeroacoustic environment. PIV is a non-invasive optical technique that is characterized by the accurate, quantitative measurement of the fluid velocity vectors of multiple points simultaneously. In PIV, a high speed camera may be utilized to capture images of a flow field. A computational program is then used to calculate velocity and vorticity profiles by analyzing the relative change in the location of particles between two high speed camera image frames. The ability to visualize both the velocity and vorticity has allowed for a thorough analysis of the cavity flow field.

Computational Fluid Dynamics allows for the modeling and analysis of a system without having to run numerous experiments. CFD has become more prevalent in recent years because it provides a cheaper alternative to the high expense incurred by running repeated experiments. CFD seeks to match the physical occurrences observed in an experiment in order to further refine the computational methods. Therefore, it will never fully replace the need for experiments. Although, as a marked benefit, the drive to accurately model the physical occurrences within the cavity has led to deeper understanding of the core flow mechanics [62].

For several decades, constant temperature anemometry (CTA) has been a reliable method for analyzing the behavior of a flow field. A CTA probe consists of a thin wire stretched between two needle shaped prongs. Current is sent through the wire, which results in the heating of the wire. The resistance across the wire is constantly monitored and compared to a reference resistance, typically using a Wheatstone bridge circuit. When the wire is placed in a flow field, the flow of the fluid past the wire results in convective heat transfer from the heated wire to the surrounding fluid, causing a change in the wire's temperature and therefore the resistance of the wire [30]. Any deviations from the reference resistance results in an increase or decrease to the current sent through the wire. Using an energy balance equation, the changes in resistance allows for the calculation of velocity.

Advances in manufacturing capability, data acquisition rates, and computing power have greatly increased the capability of CTA probes [56]. The ability to manufacture and produce CTA probes using extremely thin wires, typically only a few micrometers in diameter, allows for a greater sensitivity to changes in the flow field. Modern CTA probes also come in a variety of configurations which can measure multiple velocity components using multiple wires, allowing for the measurement of turbulent quantities such as vorticity. The increase in data acquisition rate and com-

putational capability has also increased the ability to analyze a flow field by providing significantly improved frequency response, sampling rate, and data reduction. The versatility of CTA probes, and the advances in their capability, make them a valid and valuable tool for analyzing a cavity flow field.

### 2.3 Open Flow Phenomena

The latest generation of attack aircraft in the United States, such as the F-22, F-35, P-8A, and the Unmanned Combat Air System (UCAS), employ weapons delivery from bomb bays [9]. The dimensions of the bomb bay on each platform varies; however, they all have a length to depth ratio less than ten and are therefore categorized as open cavity. In order to gain a better understanding of the physical process occurring within a weapons bay, a brief discussion of open cavity phenomena is required.

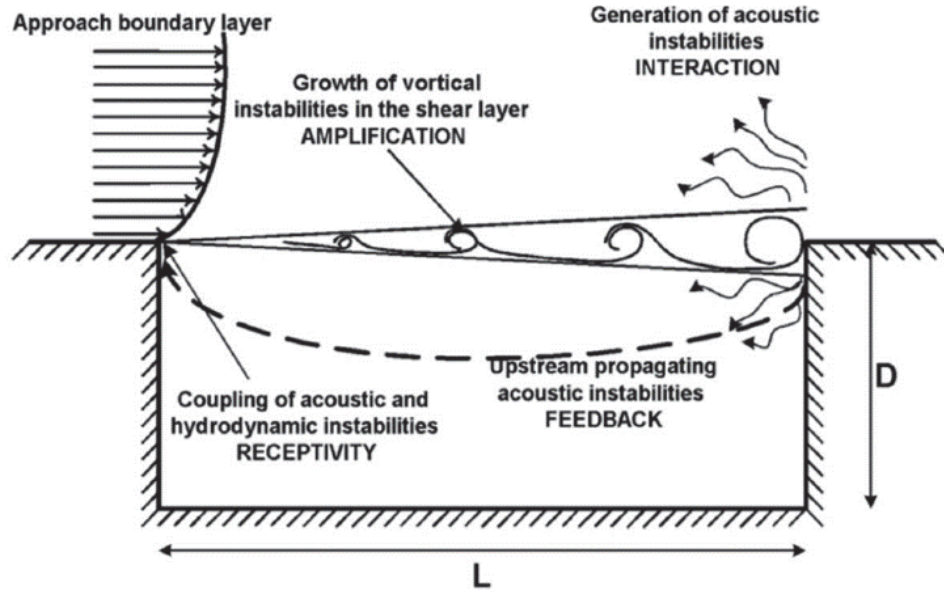


Figure 5. Cavity flow feedback loop [36]

In an open cavity flow field, the acoustic waves generated can perturb the shear layer, potentially leading to the creation of tones significantly larger in amplitude

than the broadband fluctuations [44]. The defining characteristic of an open cavity flow field is the shear layer's interaction with the rear wall, which creates cavity resonance. Panickar and Raman [36] summarized the mechanisms for cavity resonance in four steps: the amplification phase, the interaction phase, the feedback phase, and the receptivity phase. An illustration of the phases can be seen in Figure 5. The amplification phase is characterized by the growth of vortical instabilities in the free shear layer as they travel aft from the leading edge of the cavity. The growth continues until the free shear layer reaches the rear wall of the cavity and begins the interaction phase. During the interaction phase, the large vortical structures that have been generated during the amplification phase impinge on the trailing edge and produce periodic acoustic instabilities. The acoustic instabilities propagate upstream during the feedback phase. On reaching the upstream end of the cavity, the receptivity phase occurs, wherein the acoustic waves excite disturbances in the shear layer resulting in the shedding of new vortices [36], completing feedback loop.

This feedback mechanism of shear layer instabilities and acoustic waves creates a defined resonance consisting of high-amplitude tones as a function of the freestream conditions and cavity geometry [36]. These physical mechanisms should be familiar as they were the basis for the 'pseudopiston' analytical model developed by Heller et al. [24] covered in the previous subsection. In addition to the acoustic waves generated by the shear layer's interaction with the rear wall, pressure gradients develop that further impact the cavity environment. The pressure coefficients over the cavity floor are slightly positive and relatively uniform with the exception of a small adverse gradient occurring ahead of the rear face that is associated with the shear layer impinging on the outer edge of the rear face [57].



## 2.4 Store Effects

The combination of acoustic resonance and pressure fluctuations can lead to high dynamic loads within the cavity. In aircraft bays, dynamic loads in excess of 160 dB are not uncommon and can lead to structural fatigue of the cavity and its contents [8]. Driven by the desire for lower collateral damage, the push towards smaller and more advanced munitions has increased the impact that high dynamic loads within a cavity have on a weapons store [8]. The advanced electronics being developed in modern weapons are particularly susceptible to fatigue and failure. Additionally, and most applicable to this research, the highly oscillatory flow-field generated by cavity flows can adversely affect the safe departure and accurate delivery of munitions stored in the weapons bay [8].

Aircraft have been delivering weapons stores, mounted either externally or internally, for decades. While both means of weapons carriage have unsteady flow phenomenon associated with them, the impact that unsteady flow has on an externally mounted store is, by comparison, minimal [9]. This is largely due to the fact that external flow over an aircraft is designed to be non-separated and steady. As such, the flow field that the external store is immersed in is predominantly steady and the store separation trajectory can be predicted with reasonable accuracy [9].

Delivering ordnance from a weapons bay has been common practice for greater than seventy-five years and the unsteady flow associated with a weapons cavity is a known phenomenon that has been well documented and studied. It is only recent trends in store design that has driven further study of the unsteady flow associated with a weapons cavity. These trends include decreased store aerodynamic stability (to increase glide time), a tendency towards folded fins and wings for enhanced packing density, and the move towards smaller and lighter munitions; all of which may conspire to make future stores more sensitive to unsteady weapon bay aerodynamics [9].

Captive Trajectory System (CTS), where the store is placed on a sting and positioned in the flow field, has been used extensively to predict the separation trajectory of an external store. The force and moment measurements provided by CTS, which assume a quasi-steady flow, are time-averaged and have historically provided the right level of fidelity for external clearance problems [9]. Unfortunately, the unsteadiness associated with the flow field of a cavity results in the inability of CTS to reliably predict store trajectory from a weapons bay. As stated by Dr. Cenko in his 2008 paper, a weapons bay experiencing strong acoustic resonance will have an unsteady component of normal forces that change sign from instant to instant, from "into the bay" to "out of the bay" [9]. The constant change in the direction of the force introduces a time-dependent aspect of weapons release that cannot be accurately represented by CTS, as seen in Figure 6. In order to emphasize the potentially extreme behavior that a store can exhibit as a result of these unsteady forces, the example of pitch bifurcation is often used [9]. In the case of pitch bifurcation, when a store is released from within the cavity, the interaction with the shear layer could potentially result in the store either falling away from the aircraft or flying back up into the weapons bay and striking the aircraft, a clearly undesirable behavior. Accurate modeling of store separation, that takes into account the store's sensitivity to small perturbations in the shear layer, required a different approach than the time-averaged and quasi-steady assumptions of CTS.

The Combined Asymptotic and Numerical Analysis (CANs) model developed by Shalaev, Fedorov, and Malmuth in 2001 provides insight into the sensitivity of a store's trajectory to small perturbations present in the unsteady shear layer over a weapons cavity [27]. The CANs model is a theoretical model for a store separating from a weapons bay that divides the departure of the store from the aircraft into three distinct phases. The first phase occurs when the store is located within the cavity,

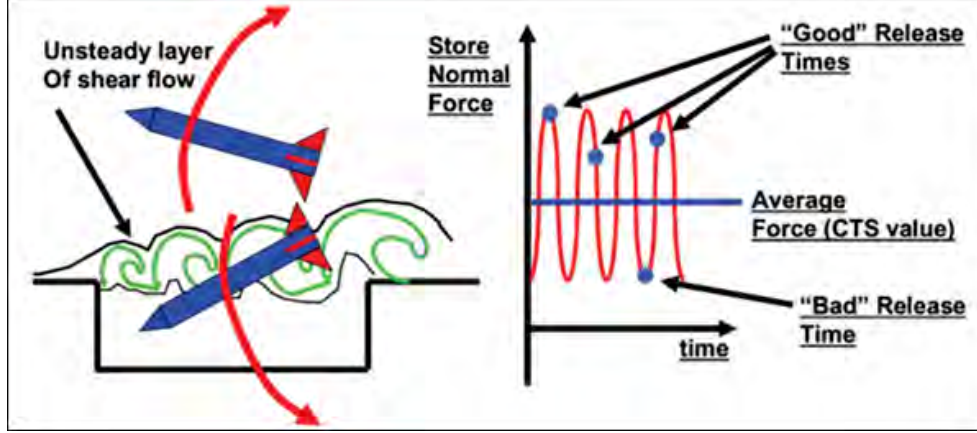


Figure 6. Illustration of the how the quasi-steady assumption of CTS neither captures the time-dependent forces of the unsteady shear layer or allow for accurate prediction of store separation. [9]

the second phase is when the store crosses the shear layer separating the cavity flow from the external flow, and the third phase is when the store is outside of the cavity [52]. The assumptions of slender body theory, asymptotic methods, and a steady inviscid shear layer were made in the development of the model. The assumption of an inviscid shear layer was made based on the observation that the unsteady motion of the shear layer are three orders of magnitude faster than the time-scale of the separating body [52]. The flow inside the cavity is not included in the model and was noted as being a potential cause of the divergence between predicted and experimental curves [9]. Although the model did not account for cavity flow, it provided theoretical evidence that the pitch behavior in phase three is strongly dependent on the entry condition of the store after it has passed through the shear layer during phase two. The aerodynamics associated with phase two, wherein the store pitch moment phase could vary from  $0^\circ$  to  $180^\circ$  depending on the relatively short transition time through the shear layer, determines the possibility for one of two trajectories outside of the cavity [52].

Having established the theoretical evidence of a store's sensitivity to the unsteady shear layer provided by Shalaev et al. we will now consider time-accurate CFD/6-

degree of freedom (DOF) models to further our understanding of the time-sensitive phenomenon associated with an unsteady shear layer. In 2006, a B-52 mishap occurred in which a GBU-12 released from the weapons bay experienced a dramatic pitch bifurcation, resulting in the tail of the aircraft being struck. During the mishap investigation that followed, the Air Force Seek Eagle Office (AFSEO) modeled four dynamic GBU-12 separations from a deep weapons bay using a fully viscous, time-accurate CFD model [19]. All initial conditions in the model were held constant, with the exception being time of release. Despite time of release being the only initial condition changed, each of the four simulations resulted in the store following a different path and ending in a different store orientation. The results of the the time-accurate model for the four releases, seen in Figure 7, further emphasizes the influence that unsteadiness in the shear layer can have on a store's trajectory.

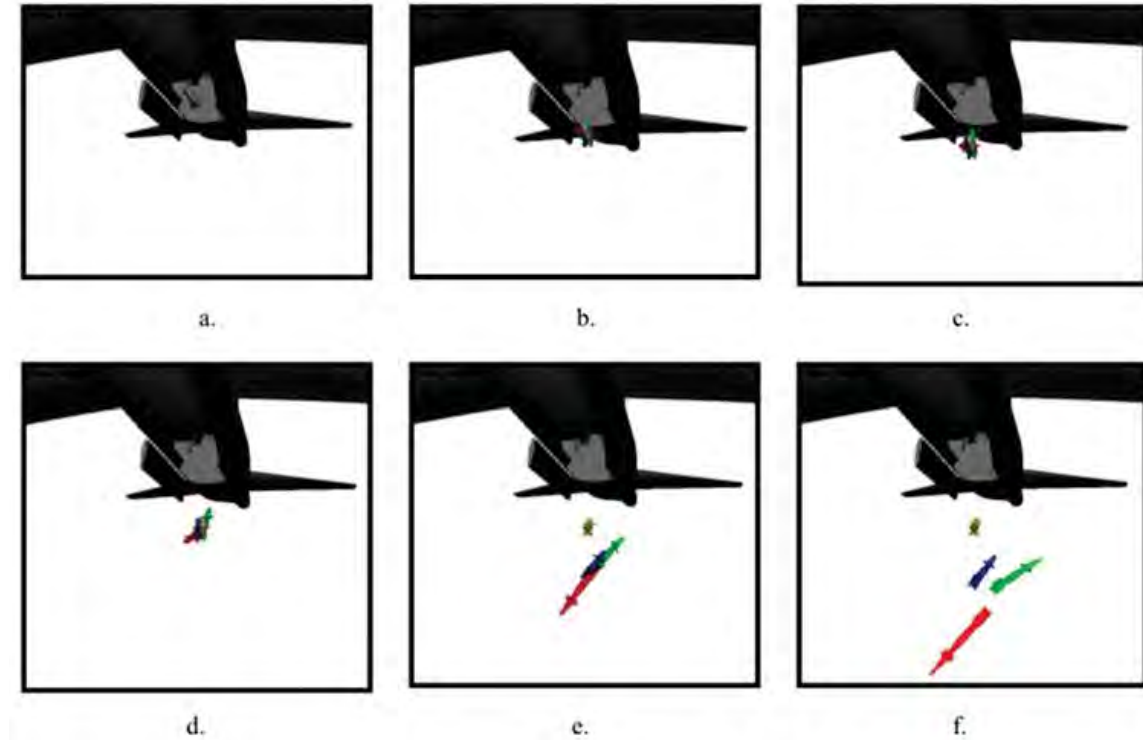


Figure 7. The effect of release time on trajectory based upon a two dimensional CFD model [28]

In 2012, Coley and Lofthouse conducted a CFD study using OVERFLOW 2.1 to investigate the relationship between the acoustic modes present in a cavity and the force and moment loading on a store released from a bay [10]. Modeling a cavity of  $L/D = 4.5$  and  $\text{Mach} = 0.95$ , three different configurations of store location in the cavity were compared to an empty cavity. The three configurations consisted of two cases with the store located in the shear layer and one instance with the store in the carriage position. For the cases observed by Coley and Lofthouse, it was found that the presence of the store in the cavity did not fundamentally alter the acoustic response that was observed in the cavity. Furthermore, the suppression of cavity vibrations due to the presence of a store in the shear layer were not observed [10]. This observation by Coley and Lofthouse implies that the characterization of an empty cavity can be used to analyze the separation of entire classes of stores, offering a potential simplification for store separation engineers. However, time-accurate prediction of the stores' trajectory after passing through the shear layer remains a challenge. Fortunately, the challenging environment of the cavity has generated significant research in the area of flow control.

## 2.5 Flow Control

For the purposes of this research, we are most concerned with the aspect of the multidisciplinary field of flow control that revolves around the desire to suppress the oscillations caused by flow over a cavity. Schmit and Semmelmayr [49] identified two major considerations when selecting the best control device for a given cavity: the state of the approaching boundary layer prior to separation and the separated turbulent shear layer. A multitude of control devices have been developed over the last three decades, all created for the express purpose of reducing cavity noise created by oscillations in the shear layer. Vakili and Gauthier [69] identified several shear

layer forcing parameters which allow growth and development of the shear layer to be controlled. The forcing methods identified include, but are not limited to: frequency forcing to directly affect the formation of shear layer instabilities, restructuring of the streamwise vortices through spoilers and leading edge blowing, and amplitude control [69].

The most common terminology used when classifying flow control devices is: passive and active control. Active control can be further divided into open-loop and closed-loop control. A further classification of closed-loop cavity control is quasi-static and dynamic feedback control [7], as seen in Figure 8. The following sections will serve to elaborate on the different flow control approaches as well as examine the effectiveness of different devices and actuators studied in recent years.

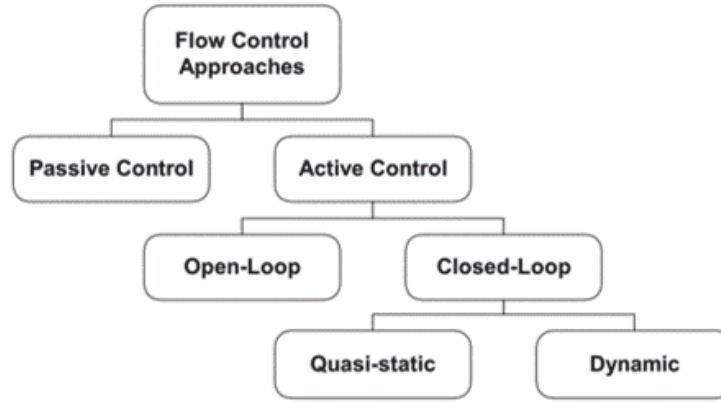


Figure 8. Classification of flow control [7]

### 2.5.1 Passive Flow Control.

Passive flow control devices generally attenuate the tones in a cavity by changing the characteristics of the shear layer's flow over the cavity [7]. In his 2003 review, Cattafasta identified three mechanisms by which passive actuators disrupt resonance in a cavity: 1) the shear layer's trajectory is changed and its reattachment point is shifted downstream from the cavity edge, 2) the change in the shear layer modifies

the stability characteristics so that the resonant modes are not amplified, and 3) the shear layers spanwise flow, and its corresponding Rossiter mode, is disrupted [7]. Passive actuators have been shown to reduce the amplitude of cavity tones and their lack of moving parts make them appealing. However, it is important to note that the major drawback to passive devices are that they often do not work well at off-design conditions and come with associated penalties such as drag [74]. While there are a multitude of passive actuator designs that have been explored in recent studies, the most applicable to this research are leading edge spoilers, rods, and Helmholtz resonator excitation.

#### **2.5.1.1 Leading Edge Spoilers.**

The leading edge spoiler influences the shear layer through inducing turbulence. The induced turbulence causes the shear layer to destabilize and thicken the boundary layer. Furthermore, a leading edge spoiler often changes the trajectory of the shear layer, shifting its reattachment point downstream.

In his 1966 paper [44], Rossiter observed the significant effect that changes to the thickness of the boundary have upon the cavity's acoustic environment. Based on these observations Rossiter tested three different spoilers and found that even a small spoiler (half the boundary layer height and only a quarter of the cavity width) has the potential to produce a large reduction in the magnitude of the periodic pressure fluctuations [44]. His findings also determined that the maximum tone suppression, with minimum drag penalties, occurs when the spoiler height is equal to the incoming boundary layer thickness [44]. Exploring the physical mechanisms that influence the observations made by Rossiter, Ukeiley et al. postulated that the mechanisms which are influenced by the lofting and thickening of the shear layer reduce both the fluctuating surface loads and the turbulent velocity profiles in the shear layer and the

cavity [15]. It is these changes to the shear layer and cavity flow field which result in the the acoustic suppression of the cavity.

In the last 40 years, numerous studies on the suppression capability of various spoiler configurations were conducted, including Heller and Bliss [24] and Kaufman and Clark [26]. These studies concluded that leading edge spoilers provide greater acoustic suppression then trailing edge spoilers due to the ability of leading edge spoilers to lift the upstream boundary layer [48]. Furthermore, in their 1983 study, Shaw et al. tested twelve different spoiler configurations and determined that the location, size, and orientation of the spoiler with reference to the flow are more important then the degree of turbulence created by a particular device [53]. In other words, a large spoiler with the potential to cause very high turbulence that is not placed in the optimal location and orientation will be outperformed by a smaller, well placed spoiler. Further research into leading edge spoilers tended towards optimizing geometry and size with respect to the boundary layer thickness and cavity dimensions.

In a 2016 study by Saddington et al., thirteen different passive control techniques were tested in a transonic wind tunnel. Of the thirteen devices, three different spoiler profiles were tested: flat top, sawtooth, and square tooth [46]. In accordance with Rossiter’s findings, the height of the spoilers were chosen to be equal to the incoming boundary layer thickness of 8.0 mm and, for consistency, the blockage ratios of the sawtooth and squaretooth spoilers were equal to one another. Figure 9 shows the experimental setup used by Saddington et al.

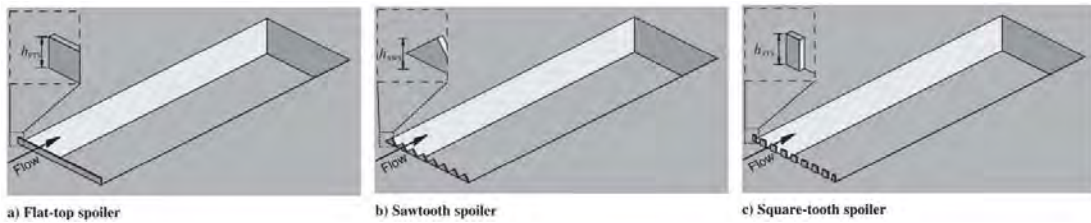


**Figure 9.** Leading edge spoiler configurations tested by Saddington et al. [46]



Using an integrated pressure device which allowed data from pressure tappings on the cavity floor to be collected, Saddington et al. were able to measure the Overall Sound Pressure Level (OASPL) reduction for the different passive control devices. From these measurements, a fast Fourier transform algorithm was used to determine amplitude of different frequency components [46]. When compared to the Rossiter tones of an empty cavity, as seen in Figure 10, the leading edge spoilers show significant reduction of the OASPL throughout the cavity. Of the thirteen passive devices evaluated in the study, the squaretooth and sawtooth leading edge spoilers showed the highest average reduction of OASPL along the centerline of 8.13 and 7.9 dB, respectively [46].

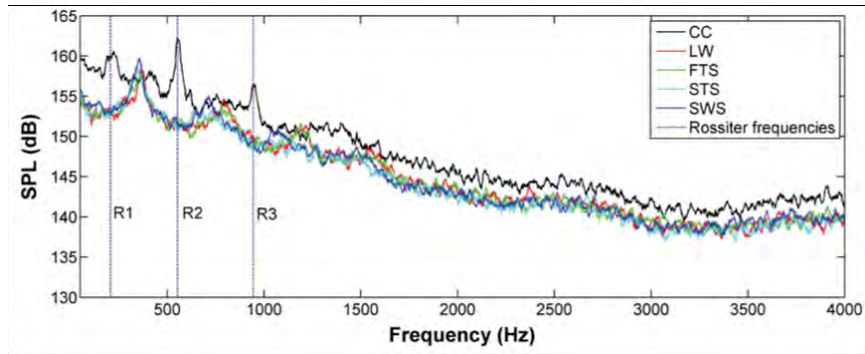


**Figure 10.** Effect of leading edge spoilers on the sound pressure level (SPL) at  $M_\infty = 0.71$  and  $x/L = 0.9$ . FTS = Flat Top Spoiler, STS = Squaretooth Spoiler, SWS = Sawtooth Spoiler [46].

While the simplicity and suppression capability of the leading edge spoiler is evident, they generally fail to provide adequate acoustic suppression at supersonic conditions [60]. The height of a spoiler can be increased above that of the incoming boundary layer, resulting in greater acoustic suppression. However, an increased drag penalty results, which becomes more significant as Mach number increases.

### 2.5.1.2 Rods in a Crossflow (High Frequency Forcing).

The motivation to find an alternative to the leading edge spoiler led to research of the rod in a crossflow. Interestingly, when compared to a leading edge spoiler, the work of Stanek et al. [58] showed that a rod in a crossflow has greatly improved suppression capabilities at supersonic speeds as well as improved suppression capabilities at subsonic speeds. The first use of a rod in a crossflow as a passive suppression device was suggested by McGrath and Shaw [34]. In their 1996 study, McGrath and Shaw wanted to determine what effect forcing the shear layer at frequencies an order of magnitude greater than the natural frequencies would have on suppression of the cavity's dominant tones. They chose to use a cylinder in the crossflow, based on the known phenomenon that flow over a cylinder can induce a wake of vortices at a frequency dependent on the diameter of the cylinder, and the velocity and density of the flow [34]. This phenomenon can be seen in Figure 11, and is discussed in greater detail in texts such as *Incompressible Flow* by Panton [38]. Placing a cylinder, with a diameter approximately half the thickness of the boundary layer at the leading edge of the cavity, McGrath and Shaw observed significant reduction in the peak tones of a cavity. The results from this study were inconclusive in determining the mechanism for suppression. However, Shaw suggested that either the rod displaces the boundary layer and breaks the acoustic feedback loop, or energy is extracted from the larger oscillating structures in the shear layer by the high frequency vortex shedding [34]. A direct comparison between the effectiveness of high frequency and low frequency forcing would be undertaken in 2000 by Stanek, Raman, Kibens, and Ross.

Stanek et al. [58] delineated two methods by which actuators can suppress the frequency of a cavity: low frequency forcing and high frequency forcing. This study compared low frequency active control methods to that of the high frequency forcing generated by a rod in a crossflow. When measuring the perturbations that are gener-

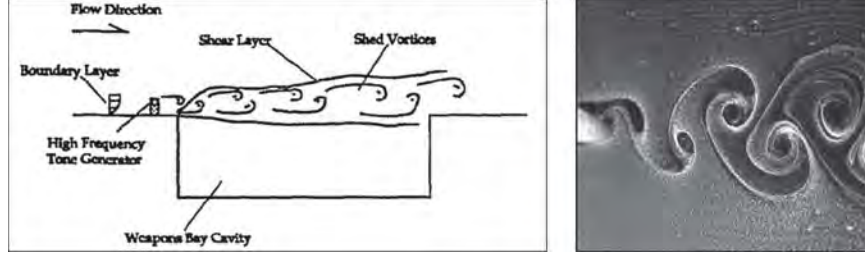


Figure 11. Effect of the shed vortices shed from a rod in a crossflow, referred to by McGrath and Shaw as a High Frequency Tone Generator, on the shear layer [34].

ated in the shear layer by a flow control device, Stanek et al. used the Rossiter tones (dominant tones) of the cavity as the reference point.

In low frequency (LF) acoustic suppression, the frequency generated by the flow control device is on the same order as the dominant mode. This is done in the hopes that by perturbing the shear layer traversing the bay at frequencies near the dominant mode, energy will be "drawn" away from the peak natural modes [58]. The result is a balance in suppression of the frequencies neighboring the dominant tone. While the LF techniques have moderate success at reducing the OASPL, typically on the order of 5.0-10.0 dB, significant energetic tones still remain after suppression [58]. Stanek et al. critiqued the use of low frequency active control as being less than optimal, given the fact that the OASPL reduction is on the same order as the much simpler leading edge spoiler, which has no moving parts [58].

In high frequency (HF) forcing, the frequency generated by the flow control device is orders of magnitude greater than the dominant mode. In essence, the high frequency forcing "drains" the energy out of all of the lower frequencies without causing an excessive spike to be produced at the forcing frequency [58]. Stanek et al. concluded that this is a result of the high frequency vortical structures shed from the rod destructively interfering with the lower frequency modes by accelerating the energy cascade in the inertial range [60]. The work by Smith et al. [55] compared numerous rod dimensions and locations with reference to the cavity leading edge in

order to determine an optimal configuration. It was found that while virtually any rod can function as a spoiler-like device, the most effective suppression occurs at rod diameters between 30.0 and 45.0% of the boundary layer thickness. Additionally, the top of the rod must be near the outer edge of the boundary layer, and located at the leading edge [55]. The suppression levels in subsonic and supersonic condition are approximately 13.0 and 20.0 dB respectively [60]. When compared to a spoiler with similar suppression effectiveness, a rod is likely to be lighter, smaller, and experience significantly lower loads; which makes the rod in a crossflow a valid alternative to traditional vertical spoilers [55].

### **2.5.1.3 Helmholtz Resonator Excitation.**

The effectiveness of suppressing cavity resonance by altering the characteristics of the upstream boundary layer using leading edge spoilers and rods has been thoroughly investigated. However, there have been alternate passive suppression techniques explored. One such technique is the use of Helmholtz resonators to reduce amplitude of the noise produced in the cavity [25]. Helmholtz resonance is the widely known phenomenon of air resonance in a cavity. The geometry of a Helmholtz resonator requires that a cavity cross section decrease to an opening which is small relative to the cavity dimension. A typical configuration can be seen in Figure 12. In the matrix developed by Rockwell and Naudascher [43], Helmholtz resonance falls into the category of fluid resonant oscillation, wherein the oscillations are influenced by resonant wave effects (standing waves). The desired effect is that the flow field, passing over the opening of the cavity, will cause a resonance that dampens the noise over a frequency domain of interest.

In a Helmholtz resonator, the air in the neck acts as a discrete mass which undergoes large oscillations at resonance, alternately compressing and expanding the

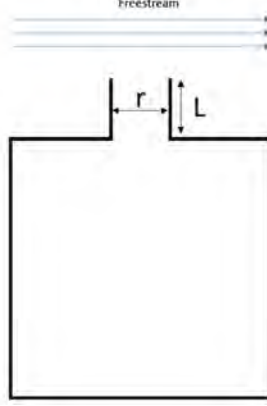


**Figure 12.** Typical configuration of a Helmholtz resonator in a flow field.  $r$  = radius of the Helmholtz resonator opening and  $L$  = opening neck length of the resonator.

volume of air in the cavity in a spring-like manner [35]. The oscillation of the mass and the volume of air in the cavity have a characteristic frequency. This frequency is known as the Helmholtz frequency and can be calculated, for a circular opening, according to Equation 8 [25]. In the equation,  $r$  is the radius of the Helmholtz resonator opening,  $L$  is the opening neck length of the resonator, and  $c$  is the speed of sound, and  $V$  is the Helmholtz resonator volume.

$$f_H = \frac{c}{2\pi} \sqrt{\frac{\pi r^2}{V(L + 1.7r)}} \quad (8)$$

In 1989, Panton investigated the effect of thirteen different orifice geometries in order to determine effective configurations for the tuning of the boundary layer and Helmholtz resonator [37]. All of the resonators had identical acoustic properties, the only variable was the orifice(opening and neck) geometries. The equation utilized by Panton [37] in his research was a modified version of Equation 8 that accounted for the various geometries. The resonators were evaluated in a low speed wind tunnel, with maximum speeds of 160 miles per hour. Panton found that the orifice sidewall shape has an important effect on the response of the resonator and the orifices slanted towards the upstream flow have increased response [37]. However, the responsiveness

of the Helmholtz resonators, and their ability to decrease peak cavity tones, were reduced at higher velocities. This was a result of the resonator de-tuning at higher velocities [37].

In 1996, Hsu et al. investigated the effectiveness of reducing the amplitude of the noise produced at the trailing edge of the cavity using syringes as Helmholtz resonators [25]. Because the mass impingement at the trailing edge and resultant feedback loop are a key component in the production of cavity tones, Hsu et al. believed that reducing the noise at the trailing edge would result in an overall reduction in the amplitude of the cavity tone. The ability to move the plunger of the syringes allowed for ease of tuning to a Helmholtz frequency calculated using Equation 8. Excellent results were obtained at low Mach numbers and it was also found that the total noise reduction increases linearly with the number of tuned resonators [25]. However, performance was reduced at high Mach numbers and at conditions for which the resonator was not specifically tuned.

In the studies conducted by Panton and Hsu et al., Helmholtz resonators effectively reduced tonal levels at low Mach numbers when configured for the predicted flow field conditions. However, the Helmholtz resonators evaluated in both studies, while effective in controlling cavity tones at design conditions, did not perform well in off-design conditions. The Helmholtz resonator used in both of these tests were passive control devices and, as noted by Cattafasta in his 2003 review [7], passive control devices prove effective at specific design conditions only. This inability to perform across a changing set of flight conditions is exactly the shortcoming that active control devices seek to overcome.

### **2.5.2 Active Flow Control.**

Active flow control devices suppress cavity oscillations by providing external energy to the flow field [7]. As previously mentioned, active flow control devices can be split into two main categories: open-loop and closed-loop. Closed-loop systems are defined by the application of a feedback loop, where the flow is directly sensed, or estimated, and the necessary changes to provide proper suppression at a new flight condition are sent to the actuator [7]. An open-loop actuator does not possess a feedback loop. The attractiveness of active loop control devices is the ability to provide suppression at more than a single design condition. The following sections will briefly discuss methods of open-loop active control that were found to be most applicable to this research.

#### **2.5.2.1 Open-Loop.**

Oscillating fences and flaps were explored as a method for open-loop active control by Sarno and Franke [47] as well as Shaw [54]. Sarno and Franke investigated the effect that static and pulsating fences oriented normal to the flow would have on the shear layer. Fences of various heights, measured with respect to the boundary layer height, were oscillated at frequencies ranging from 20.0 Hz to 220.0 Hz [47]. In their experiment, Sarno and Franke oscillated the fences at low excitation frequencies with the hope of reducing the amplitude of dominant modes through low frequency forcing. They achieved limited success in suppressing the first cavity mode with fence heights greater than 75.0% of the boundary layer thickness. However, the second mode was unaffected and it was found that the ability to suppress peak amplitudes did not necessarily improve at higher oscillation rates [47].

In 1998, inspired by the positive results from Sarno and Franke [47], Leonard Shaw investigated the effectiveness that an oscillating flap positioned at the leading

edge would have on cavity suppression. The flaps were designed to oscillate about a neutral angle at deflection angles ranging from 2.0 to 20.0° and at frequencies from 5.0 Hz to 100.0 Hz [54]. Shaw found the most effective suppression was observed when maximum excitation was introduced to the flow field; which occurred when the flap was set to achieve the largest deflection angle, 20.0°. Furthermore, this research found that maximum suppression of the tonal amplitude occurred when using the largest deflection angle at an excitation frequency of 5.0 Hz [54]. Based on the degree of oscillation required to achieve adequate suppression of cavity tones, Shaw conceded that a leading edge flap would be impractical to design on an operational aircraft. Alternatively, leading edge blowing has become an attractive method for active flow control, due largely in part to the removal of mechanical devices oscillating in the free stream.

In their 1994 papers, Vakili and Gauthier [69] as well as Sarno and Franke [47] investigated the effects of upstream mass injection on the attenuation of cavity oscillations. Vakili and Gauthier leveraged the work of Fernandez and Zukoski [17], to describe three categories of mass injection: weak mass injection, massive mass injection, and blow-off mass injection [69]. Weak mass injection is where the momentum of the injected flow is small, resulting in a slow growth of boundary layer thickness over a long distance with little impact on the external flow field. Massive mass injection is where the momentum of the injected flow is less than the external-flow momentum but larger than the skin friction, resulting in a lifting of the boundary layer and external flow above the injected fluid. Blow-off mass injection is where the momentum of the injected flow is comparable to the external flow [69]. Additionally, when characterizing the injection rates, Vakili and Gauthier defined a blowing parameter,  $B_c$ , which is the ratio of injected mass flow to external mass flow multiplied by the area ratio of total injection area to cavity area [69]. In the equation for the blowoff parameter,



Equation 9, the subscript  $w$  indicates the injected fluid and subscript  $e$  indicates the external, or freestream fluid. Using porous plates upstream of the cavity leading edge to increase the cavity shear layer thickness, Vakili and Gauthier were able to achieve significant suppression levels at a  $B_c$  of 4.0 percent [69].

$$B_c = \left( \frac{\rho_w V_w}{\rho_e V_e} \right) \left( \frac{A_{inj}}{A_{cavity}} \right) \quad (9)$$

Sarno and Franke [47] observed the effects of steady and pulsed flow injection at the cavity leading edge using a  $B_c$  of up to 7.0%. Compressed air was injected into the free-stream at the leading edge of the cavity using two different configuration of flow injection nozzles: parallel to the flow and at a  $45.0^\circ$  angle, as seen in Figure 13. The pulsed flow was injected at 50 psig and at frequencies varying from 0.0 to 80.0 Hz. With steady flow injection, Sarno and Franke found that the  $45.0^\circ$  injection nozzle was generally more effective at suppression then the parallel flow injection nozzle. In Sarno and Franke's research, pulsating the flow was found to have minimal effect on suppressing cavity pressure oscillation. These findings were contradictory to a great deal of the research on leading edge blowing that followed, which observed that pulsed injection attains higher levels of suppression then steady injection at low frequencies. These experimental studies include, but are not limited to, Shaw [54] and Lamp and Chokani [32].

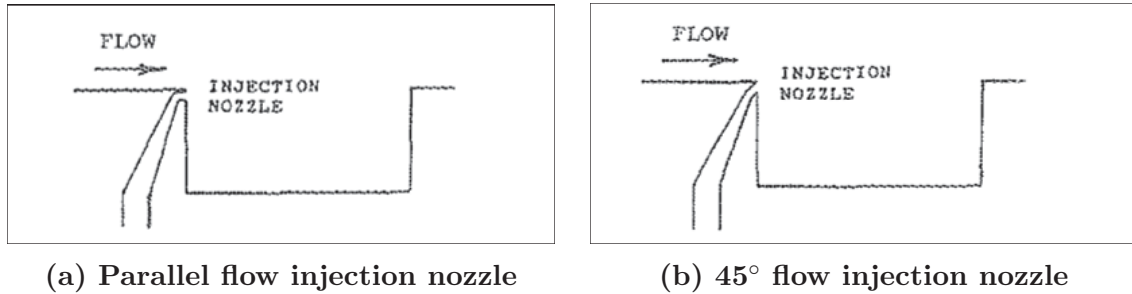


**Figure 13.** Depictions of the two different injection nozzle configurations used by Sarno and Franke [47]

Injecting pulsating air at a  $B_c$  of up to 4.5% through a rectangular slot positioned as close to leading edge as possible, Shaw observed that the suppression of the cavity is a function of both the pulsing frequency and the mass flow rate [54]. Shaw varied the frequency of the pulsing mass flow from 0.0 to 100.0 Hz. In line with his findings on the oscillating flap at the leading edge, Shaw concluded that varying the excitation frequency will dictate the mass flow requirements to achieve adequate levels of suppression. In other words, the larger the flap or level of mass flow, the lower the excitation frequency required; likewise, the smaller the flap or level of mass flow, the higher the excitation frequency required. Furthermore, Shaw evaluated three discharge angles: parallel to the flow,  $45.0^\circ$  to the flow, and  $90.0^\circ$  to the flow. The jet oriented  $90.0^\circ$  to the flow was found to be the most effective at suppressing cavity sound levels. Shaw concluded that this was a result of a greater transfer of momentum into the shear layer when the jet is oriented  $90.0^\circ$  to the flow [54].

In 1999, Lamp and Chokani [32] explored the effectiveness of reducing the amplitude of pressure fluctuations using a leading edge actuator designed for steady and oscillatory blowing. Their focus was to evaluate the capability of leading edge blowing devices to inject momentum into the shear layer. Lamp and Chokani expected that the momentum 'injected' into the boundary layer would increase its ability to withstand higher-pressure gradients, thus interrupting the feedback loop in the cavity [32]. The momentum coefficients were estimated based on jet velocities measured with a hot wire. Using an actuator capable of creating pulsed injection of up to 750.0 Hz, Lamp and Chokani were able to attain forcing frequencies that could span the first four dominant modes calculated for the cavity [32]. Their results showed that the tonal amplitudes can be significantly reduced through leading edge blowing. Oscillatory blowing proved more capable of interrupting the cavity's feedback loop, as long as the forcing frequency chosen is not a harmonic frequency of the cavity's

resonant modes [32]. If the forcing frequency chosen is a harmonic frequency of the cavity, then the oscillatory blowing will only serve to reinforce the tonal amplitudes [32].

Some of the additional research into open loop active control methods include the use of: plasma actuators by Yugulis et al. [72]; powered whistles by Ukeiley et al. [64]; leading edge microjets by Arunajatesan et al. [2], Zhuang [74]; and steady leading edge slot blowing was revisited using PIV to evaluate turbulence levels in the shear layer by George et al. [21]. The review by Cattafasta et al. [7] is an excellent source for an overview of research that has been conducted in the field of active control. The next developmental step, and the premise behind closed-loop control, is to take the active control methods that have proven successful and develop a feedback loop which allows them to adjust for changing flight conditions.

#### **2.5.2.2 Closed-Loop.**

Closed-loop actuators require a system that is composed of at least one flow state sensor and a feedback control algorithm [7]. Closed-loop actuators are classified into two types: Type A and Type B. The classification of the actuator is based upon the time-response of the feedback algorithm when compared to the time-scale of the cavity flow dynamics. Type A actuators are able to change on a time-scale that is proportional to that of the cavity. A Type B actuator changes on a time-scale that is large when compared to the time-scale of the cavity [7]. The equipment, processing power, and algorithms necessary for closed loop active control all lead to an increase in the complexity of closed-loop active control methods. This ultimately means that closed-loop systems are more expensive. The benefit to the complexity and cost, is that closed-loop active control devices offer the greatest adaptability to the constantly changing flow conditions that would be present in an aircraft's weapons bay [7]. The

focus of this paper’s research does not incorporate a closed-loop system. However, the refinement of proven open-loop systems to be utilized in a closed-loop, several of which can be found in Cattafesta’s 2003 review, deserved mention.

### 2.5.2.3 Fluidic Diodes.

A fluidic diode is a device that encourages flow in one direction while offering high resistance to flow in the opposite [71]. The first design and patent of a fluidic diode, referred to as a valvular conduit, was proposed by Nikolai Tesla in 1920 [61]. Tesla designed the fluidic diode, seen in Figure 14, as a replacement for costly and delicate check valves in machinery. More importantly, Tesla emphasized that while significant resistance would be present to a fluid under constant pressure, the resistance will be strongest when the fluid is pulsing [61]. The stated resistance to pulses is why fluidic diodes have been explored in this research as well as for use as pulmonary heart valve replacement [6] [33]. The device utilized in this research employs a linear motor driving a piston in order to produce oscillatory flow for a leading edge blowing device. A fluidic diode design was explored to encourage flow in the desired direction during the stroke of the motor driven piston.



Figure 14. Nikolai Tesla’s fluidic diode (valvular conduit) patented in 1920. (US Patent 1,329,559 [71])

## 2.6 Summary

This chapter provided a brief overview of the aeroacoustic environment and its effect on stores within a cavity as well as during release. A background of

previous research on passive and active control flow devices was provided, to include: leading edge fences, rods in a crossflow, leading edge tabs, Helmholtz resonators, and both steady and oscillatory blowing actuators. Finally, the concept of fluidic diodes was covered. Several of these devices were tested in the AFIT low-speed wind tunnel to determine their capacity to influence the flow field of various leading edge devices. Additionally, the use of oscillatory blowing to force a low-speed flow field such that effects analogous to a high-speed environment are emulated was investigated. These processes are further discussed in Chapter III.

### III. Methodology

#### 3.1 AFIT Wind Tunnel

The AFIT low speed wind tunnel is an open circuit design with a 44.0 inch wide by 31.0 inch tall test section. The dimensions of the wind tunnel can be seen in Figure 15. The tunnel is capable of achieving a maximum speed of 150 miles per hour (mph) and is controlled using a LabView Interface located in the tunnel control room. Two transparent Plexiglas doors allow access to the test section from either side of the tunnel and an additional panel allows access to the tunnel from above. The overhead panel is a 47.0 x 23.0 x 0.75 inch Plexiglas panel with cutouts, shown in Figure 16, that allows manipulation of the probe position within the tunnel by the traverse system, mounted on top of the tunnel as seen in Figure 17. When a channel is not being used during test runs they are sealed with custom inserts to minimize pressure losses.

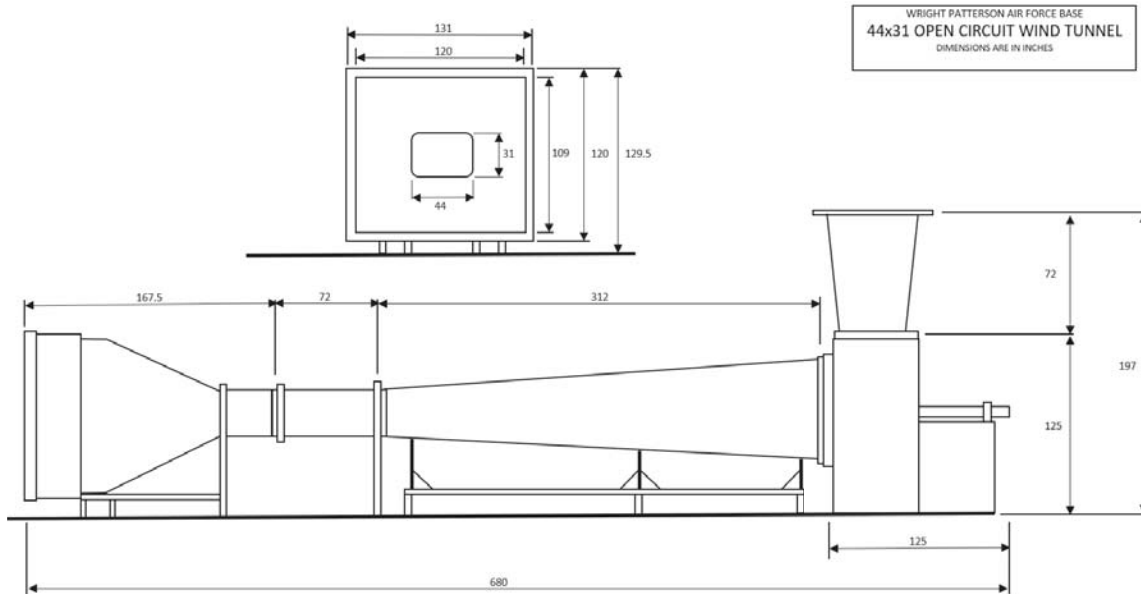


Figure 15. AFIT Wind Tunnel (Not to Scale)

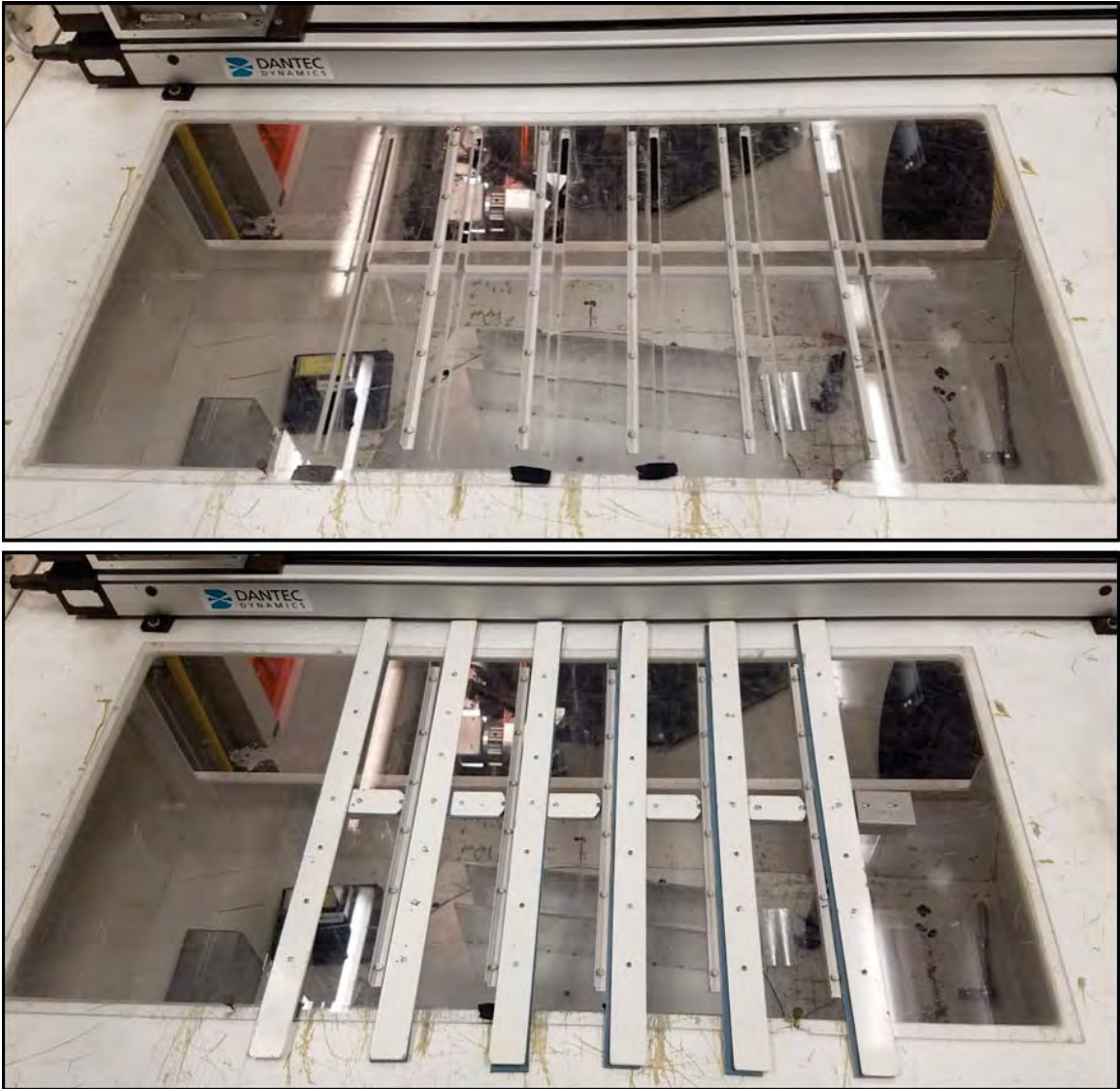


Figure 16. AFIT wind tunnel top access panel. Access panel without the inserts (top) and access panel with the inserts in place (bottom).





Figure 17. AFIT Wind Tunnel test section with the traverse system placed on the top of the tunnel.



### 3.2 3-D Printers Used for Rapid Prototype Design

Three dimensional printing was used extensively in fabricating pieces for the cavity and components of the leading edge actuators. The Ultimaker 2+ and Ultimaker 3 were used to facilitate rapid prototyping of leading edge devices. The Ultimaker 2+ uses fused deposition modeling (FDM) technology and a single-extrusion print head. The single extrusion print head comes with four swappable nozzles that range in diameter from 0.25 mm in diameter to 0.80 mm [67]. The Ultimaker 3 also uses FDM, but has a dual extrusion print head with an auto-nozzle lifting system that can change between three nozzles ranging in diameter from 0.25 mm to 0.80 mm [66]. The specification of the print nozzles available for each Ultimaker model and layer resolution can be found in Table 1. The greatest difference between the Ultimaker 2+ and the Ultimaker 3 is the ability of the Ultimaker 3 to construct a single design using two different materials. The 0.40 mm nozzle was used for all of the builds in this experimental study.

**Table 1. Ultimaker 2+ and Ultimaker 3 Specifications [67][66]**

| Specifications    | Ultimaker 2+                  | Ultimaker 3                   |
|-------------------|-------------------------------|-------------------------------|
| Filament Diameter | 2.85mm                        | 2.85mm                        |
| Layer Resolution  | 0.25 mm nozzle: 150-60 micron | 0.25 mm nozzle: 150-60 micron |
|                   | 0.40 mm nozzle: 200-20 micron | 0.40 mm nozzle: 200-20 micron |
|                   | 0.60 mm nozzle: 400-20 micron |                               |
|                   | 0.80 mm nozzle: 600-20 micron | 0.80 mm nozzle: 600-20 micron |
| XYZ Accuracy      | 12.5, 12.5, 5.0 micron        | 12.5, 12.5, 5.0 micron        |

The material used for the fabrication of all flow control device pieces was polylactic acid (PLA). PLA was chosen because of its high print speed and the capability to produce high resolution parts with good tensile strength and surface quality [65]. Further specification on the material can be seen in Table 2.

One version of the fluidic diode models using polyvinyl alcohol (PVA) as a support

material was attempted in the Ultimaker 3. PVA is a water-soluble support material that is ideal for printing complex models [68]. The intent was to use the PVA as a support material for the diodes possessing more intricate internal designs. However, there were complications that occurred while removing the water-soluble material. In the first attempt, after sitting in a water bath for 24 hours, the PVA still had not fully dissolved. In an effort to speed up the process, the three fluidic diode models were submerged in heated water. It was discovered after the fact that the primary printing material, PLA, is not suitable for applications where the printed part is exposed to temperatures higher than 50.0° Celsius [65]. Unfortunately, the three pieces were warped beyond use.

In the second attempt, the PVA dissolved after sitting in a water bath for 72 hours. However, there were imperfections that occurred during the actual printing process. The Ultimaker 3, switching between the two materials, dragged and deposited PVA throughout the layers of PLA. Because of this, gaps were left in the PLA after the PVA had dissolved, allowing for water intrusion to occur. Two of the pieces remained water logged, despite drilling holes in the base and placing them in a Terra Universal Desiccator Cabinet for 48 hours. As a result of the complications, a further refinement of the fluidic diode design was developed to avoid using PVA. The different designs of leading edge devices used in this study will be covered more thoroughly in Section 3.6. All printed models were designed using Solidworks CAD software.

**Table 2. PLA Technical Data [65]**

| Mechanical Properties   | Typical Value | Test Method         |
|-------------------------|---------------|---------------------|
| Tensile Modulus         | 2346.5 MPa    | ISO 527 (1 mm/min)  |
| Tensile Stress at Yield | 49.5 MPa      | ISO 527 (50 mm/min) |
| Tensile Stress at Break | 45.6 MPa      | ISO 527 (50 mm/min) |
| Flexural Strength       | 103.0 MPa     | ISO 178             |
| Flexural Modulus        | 3150.0 MPa    | ISO 178             |

### 3.3 Cavity and Mechanical Components

#### 3.3.1 Cavity.

The cavity model, seen in Figure 18, is 24 inches long,  $5\frac{3}{8}$  inches deep, and  $5\frac{3}{8}$  inches wide with a Length-to-Depth Ratio of 4.465. The cavity design is based on the SUU-41 pod that was utilized for the HAVE Weapons-cavity Acoustics Store Separation Pod (WASSP) test management project [40]. Previous work investigating store separation in the AFIT low speed wind tunnel by Andrew Bower utilized the same cavity model [4]. The cavity is attached to a base constructed of 80/20 aluminum. In addition to securing the cavity to the floor of the tunnel, the base also elevates the cavity 10.5 inches. Elevation of the cavity compensates for limitations on the range of the traverse system and allows the tri-axial velocity probe to be positioned deeper in the cavity.

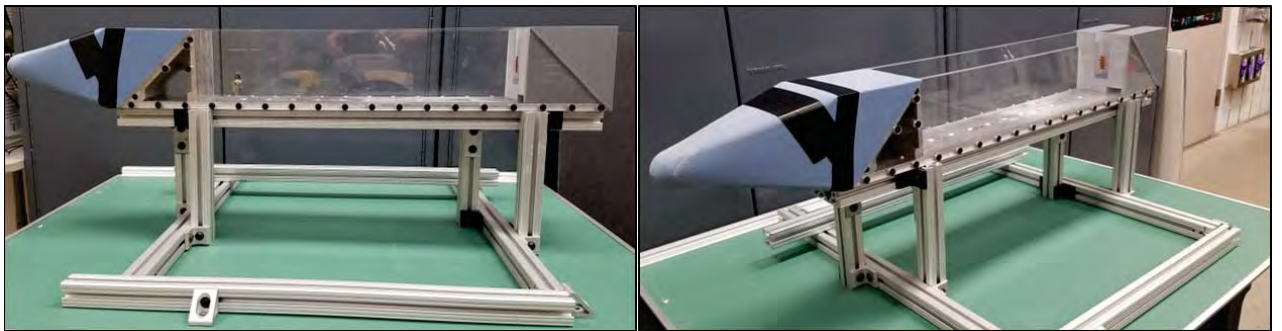
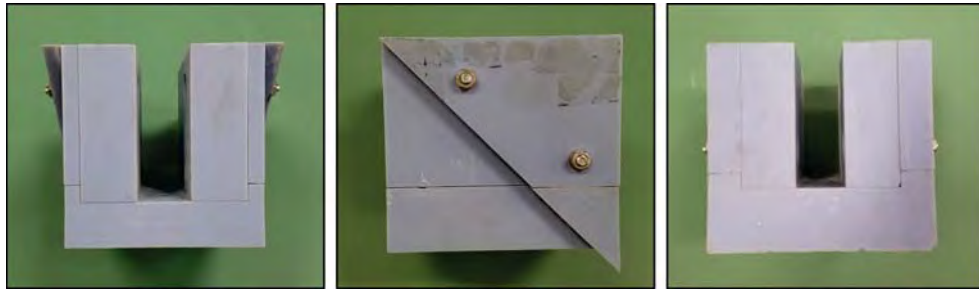


Figure 18. Empty Weapons Cavity elevated on the support base

The original design for the rear of the cavity, pictured in Figure 19, had an open face that could be covered with a removable insert, creating the aft cavity wall. This design did not facilitate the motion of the linear motor's wiring during operation. The new design, built with PLA using the Ultimaker 2+, has the same dimensions and features of the original, with the addition of 1.5 x 0.5 inch channel at the base of the cavity. The purpose of the channel is to mitigate the possibility that the wiring might catch, bunch up, and strike the probe within the cavity. Figure 20 depicts

images of the new design, and the CAD drawing with dimensions is located in the Appendix C.



**Figure 19. Original cavity rear design.** The left picture is a view from the inside of the cavity looking aft the center picture is a side profile view and the right picture is from behind the cavity looking forward.



**Figure 20. New cavity rear design.** Small channel at the floor of the cavity prevents bunching of the wiring by allowing the linear motor's wiring to lie flush with the deck. The left picture is a view from the inside of the cavity looking aft the center picture is a side profile view and the right picture is from behind the cavity looking forward.

### **3.3.2 Linear Motor and Controllers.**

#### **3.3.2.1 Linear Motor Design and Performance.**

The brushless linear motors used in the experimental study, pictured in Figure 21, were designed by H2W Technologies, Incorporated. The SRS-003-04-003-01 low profile single rail linear motor has a 5.3 x 5.3 inch base with four tapped holes that allow the linear motor to be secured to the cavity floor without impeding range of motion. The total stroke length of the linear motor is 3.0 inches (76.0 mm). The motor is capable of generating a continuous force of 2.7 pounds and a peak force of

10.7 pounds. The LM13 encoder installed on the linear motor is a contactless linear magnetic system with a resolution of 1.0 micrometer [42].

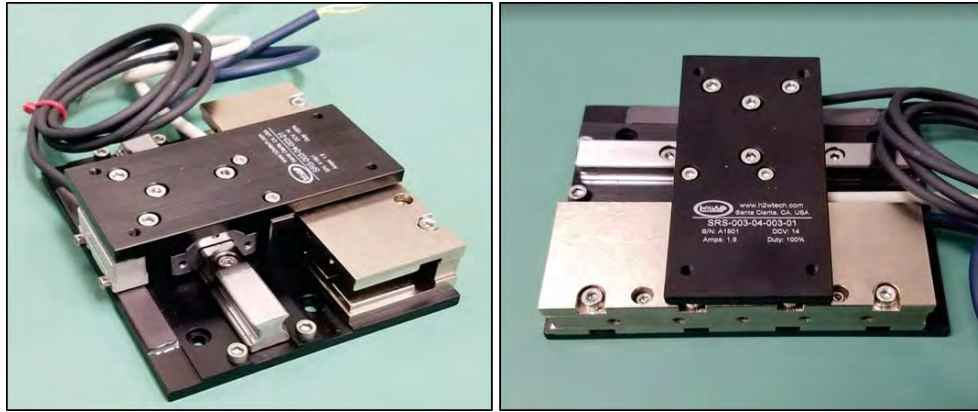


Figure 21. SRS-003-04-003-01 Linear Motor used for the experimental study

### 3.3.2.2 Controllers: DMC-30012 and DMC-4020.

The Galil DMC-30012, seen in Figure 22, was used during the first phase of the experimental study. It is capable of executing point-to-point positioning, jogging, and sinusoidal modes of motion. It also contains an amplifier that can drive motors at 20-80 VDC and up to 10 Amps continuous and 15 Amps peak [11]. The amplifier also provides protection against over-voltage, under-voltage, over-current, and short circuit protection [11]. Interface with the controller was accomplished using one of its two Ethernet ports. The main processor of the controller is RAM and Flash capable, allowing for the execution of not only ‘live’ commands from the host computer, but also the download of entire groups of commands for later execution [11].

The Galil DMC-4020, seen in Figure 23, was used during the second phase of the experimental study. The programmable motion control features and amplifier were comparable to the DMC-30012 and controller interface was also accomplished using an Ethernet port. The processor is capable of accepting encoder inputs up to 22.0 MHz and provide servo update rates of 16.0 kHz [20]. However, the most attractive feature



Figure 22. Galil DMC-30012 single-axis motion controller

of the DMC-4020 for use in the Phase II of the experimental study is its inherent capacity for multi-axis control, which dramatically simplified the synchronized motion of two linear motors.



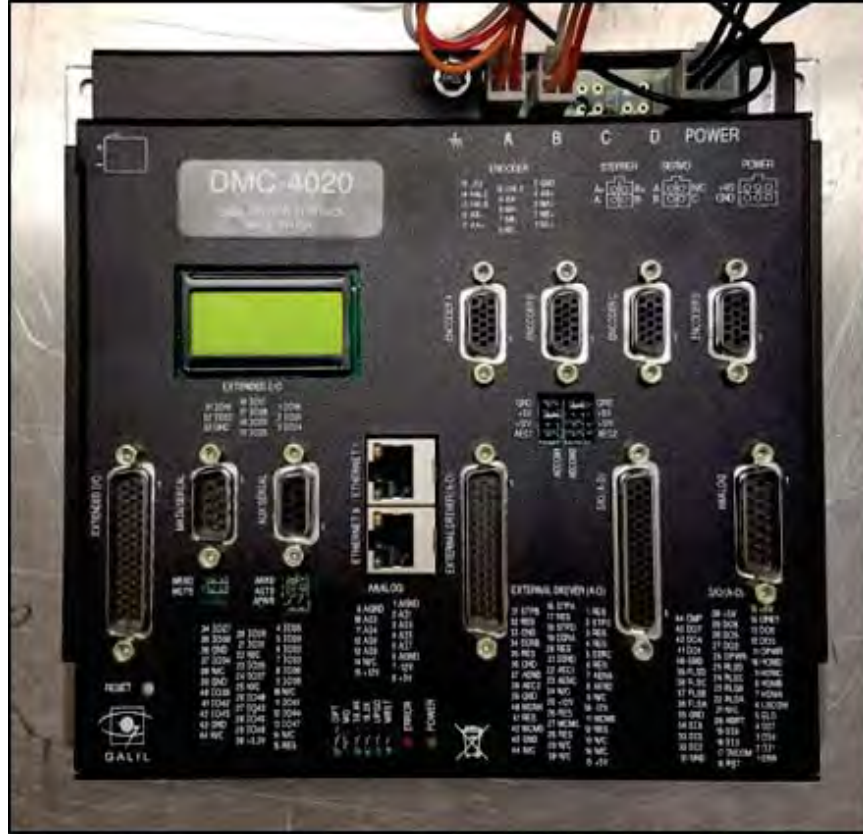


Figure 23. Galil DMC-34020 dual-axis motion controller

### 3.3.2.3 Linear Motor Programming and Operation.

Power to the Galil controller is provided by an Acopian linear regulated power supply with AC to DC single output. The Galil controller's amplifier converts a  $\pm 10$  Volt signal into current to drive the linear motor. When power is supplied to the system, a green light on the encoder of the linear motor and a green light labeled 'PWR' on the controller will illuminate.

Commands to the controllers were sent using two ASCII uppercase characters followed by an applicable argument [11]. The controller is capable of interpreting conditional statements (IF/ELSE/ENDIF) for positional based triggers and looping specific commands until a criteria is met. The Galil Design Kit (GDK) software package was purchased for communication with the controller. The GDK provides a

built-in tool set that includes a terminal, program editor, scope, as well as auto-tuner capabilities.

An initialization code, shown below, was required to set the operating parameters and required gains for motor control during program execution. The GDK auto-tuner and scope were used to refine the initialization codes proportional (KPA), derivative (KDA), and integral (KIA) gains, which control the corrective responses sent to the motor based on position error [11]. The filter transfer functions used to calculate the necessary gain settings can be found in the Galil Command Reference Manual [12]. One issue discovered with the controller was that if power is removed from the controller, or if the linear motor is moved without securing power to the motor (MO command in the terminal), operation of the motor would be inhibited until the position error was reset. To reset the position error, set the ERA equal to -1 in line 5 of the initialize program and run the program. Stop the program from the GDK, and then re-run the initialize program with  $ERA \geq 1000$ . This process often had to be conducted on initial start-up of the system.

#### INITIALIZATION CODE:

```
BA A;           'Designates sinusoidal commutations on the A axis
BMA=30720;      'Defines the length of the magnetic cycle in encoder counts
TLA=6.75;      'Sets the torque limit on the motor to prevent over current
TKA=9;         'Sets peak torque limit
ERA=1000;      'Position Error Limit
AUA=1;         'Sets the amplifier current loop gain
OEA=1;         'Commands controller to shut off the motor error limit exceeded
BZA=4;         'Sets current limit for sinusoidal commutation
MTA=1;         'Sets the motor type
KPA=53.6250;   'Proportional gain, outputs a control signal proportional error
KDA=400.625;   'Derivative gain, outputs a voltage based on ROC of error
KIA=2.5801;    'Integral gain, reduces position error at rest to zero
```

Once initialization of the controller and linear motor has been accomplished, the program developed for sinusoidal motion can be run using the program editor in the GDK. For convenience, the program developed for the oscillation of the linear mo-



tor is included below. The amplitude and frequency of the sinusoidal motion can be set in the program by changing the 'amp' and 'freq' variables under the program label of # SINE. To achieve maximum stroke length for the designed piston, an amplitude of 24736 counts was used. For the stroke length of 49.5 mm, a maximum frequency of 10.0 Hz was determined using the frequency calculator available on the H2WTechnology website. However, resistance to motion due to load from the piston assembly, and the resulting amperage increase, reduced the maximum frequency attainable. The frequency chosen for the experimental study was 5.0 Hz.

#### SINEWAVE CODE:

```
#home    'Program Label: Home Routine
SH A;    'Sets the coordinate axis
JG 25000;'Jog command
FI A;    'Find index
BG A;    'Begin motion
AM A;    'After motion
DP 0;    'set current position to 0
MG "Found Index"; 'Message sent to terminal
WT 500   'Wait 0.5 secs

#reposit 'Program Label: Reposition to center
SH A
PR -19532;'move to position
BG A;    'Begin Motion
AM A;    'After Motion
DP 0;    'Set current position to 0
MG "New Zero"; 'Message sent to terminal
WT 3000; 'Wait 3.0 seconds

#sine    'Program Label: Sine Wave Motion
SH A;    'turns on motor A
amp= 24736;'amplitude in counts
freq= 5;  'frequency in Hz
rate= freq*amp*6.2832; 'calculates correct speed
VS rate

#init    'Program Label: Initialize
go= 1    'sine wave on "A" axis
```

```

VM AN
  CR amp,0,360; 'one sine wave to get started
  BG S          'starts motion

#loop      'Program Label: Loop
CR amp,0,360; 'add one sine wave continuously

#wait      'Program Label: wait
  JP #loop,_LM>1; '_LM shows how many segments in buffer
  JP #wait,go=1; 'continue adding sine waves until go=0 is entered

#stop;      'Program Label: wait
  ST ;      'stops motion
  AM S;      'waits for motion to complete
  VE;        'ends vector mode
  CS S;      'clears all sine waves out of vector buffer
  MG "FINISHED"; 'Message sent to terminal
  EN;        'End Program

```

### 3.3.3 Traverse and Tri-axial Probe.

#### 3.3.3.1 Traverse System.

An ISEL lightweight three dimensional traverse system was installed on top of the test section of the wind tunnel, as seen in Figure 17. It is important to note that the wind tunnel and the traverse system do not share the same reference frame, and all movement of the traverse system through the Streamware-Pro software is with reference to the traverse's coordinate system. Figure 24, depicts the two coordinate systems with the subscript '*W*' denoting the wind tunnel reference frame, and the subscript '*T*' indicating the traverse system reference frame. While the wind tunnel's reference frame follows the right hand rule, the traverse system's does not. The traverse system is capable of providing maximum translation in the x-, y-, and z- directions of 1220 mm, 820 mm, and 820 mm, respectively and is accurate to within  $\pm 0.1$  mm. All motion of the traverse system is controlled from the work station in

the wind tunnel control room.

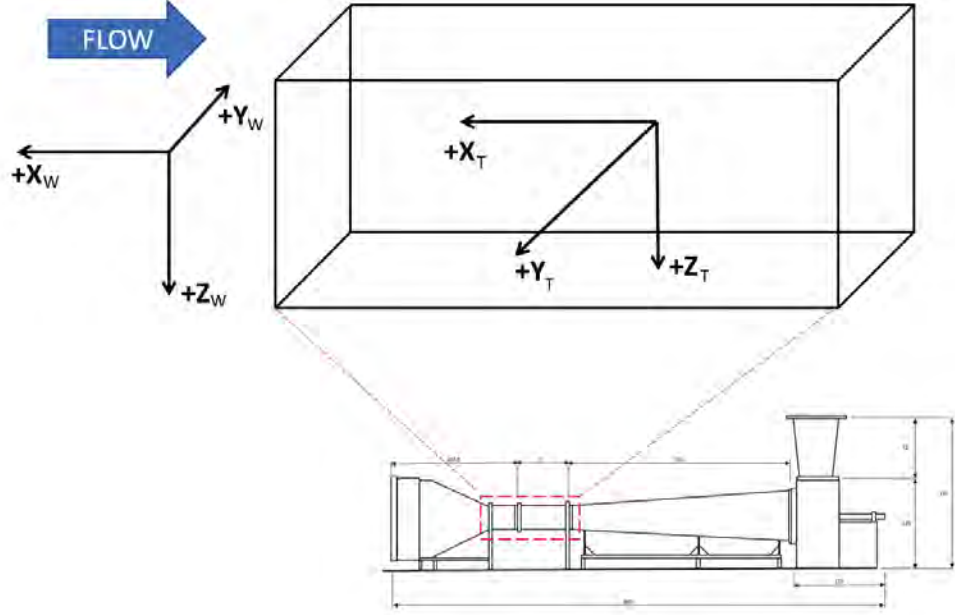


**Figure 24.** AFIT wind tunnel coordinate system compared to traverse coordinate system (Not to Scale).

### 3.3.3.2 Tri-axial Probe.

The DANTEC 55P91 gold plated wire tri-axial probe, seen in Figure 25, was selected to gather velocity data for the experimental study. The 55P91 is a straight type probe with three gold-plated wires, each having a diameter of 5.0 micrometers, a sensor length of 1.25 mm, and an overall length of 3.5 mm. The three sensors are arranged in a tri-axial array with mutually orthogonal spacing. The 55P91 is designed for two dimensional flows where the angle between the velocity vector and the probe axis stays inside a cone of  $70.4^\circ$  [14]. The 55H27 straight mounting tube was used during calibration and a 55H27  $90.0^\circ$  bend mounting tube was used in the wind tunnel. The cable was run through a 17.5 inch guide tube, which was secured to the ISEL lightweight traverse located above the tunnel. The guide tube served to increase the depth that the probe could be positioned within the tunnel, allowing

for a more complete assessment of the cavity flow field. During calibration and wind tunnel testing, three 4.0 meter long BNC cables were used to connect the triple wire mount to the Streamline frame located in the wind tunnel control room.

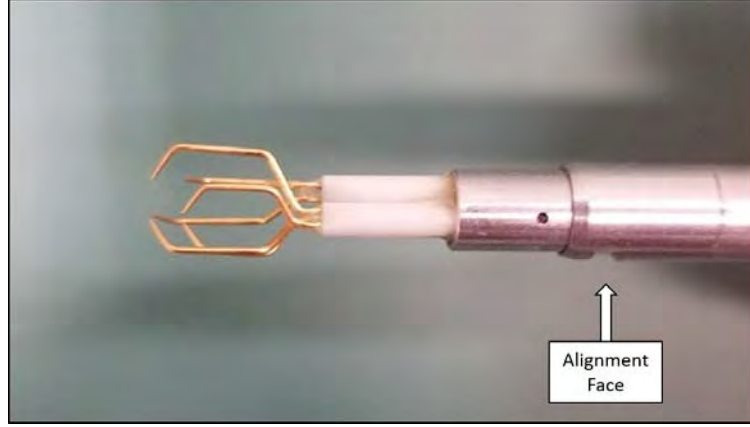


**Figure 25. DANTEC 55P91 Tri-axial probe. The alignment face is used to mount the alignment tool required for velocity and directional calibration**

### **3.3.3.3 Traverse and Tri-axial Probe Control.**

Both the traverse system and the tri-axial probe were controlled from a workstation in the wind tunnel control room using the Streamware-Pro software, Figure 26. The traverse system used an ISEL Schrittmotor C116-4 three axis controller. The C116-4 has 32K of on-board memory and a built in 44.0 Volt/4.3 Amp power supply for each motor with forced air ventilation for continuous duty.

Each of the three BNC cables from the tri-axial probe mount were connected to a 90C10 CTA module installed in a Streamline 90N10 frame. The 90C10 CTA modules each contain two bridge configurations, shaping circuits, cable compensating circuits, and signal conditioner with programmable offset, gain and filters [29]. The two bridge configurations allow for a frequency response of 250.0 - 450.0 kHz [13]. Furthermore, there are two analog outputs from each module that provides for simultaneous sampling of DC and AC values, allowing for small-scale turbulence measurements [29].

The 90N10 Streamline frame has slots for up to six modules and contains a power supply for each potential module. The Streamline frame manages the communication between the 90C10 CTA modules and the PC running the DANTEC Streamware-Pro software. All communication between the computer work station and the ISEL controller and Streamline Frame was accomplished using a National Instruments (NI) USB-6009 multifunction data acquisition (DAQ) device. During the course of the testing, a 10.0 kHz sampling rate with 100,000 samples gathered per point was used.

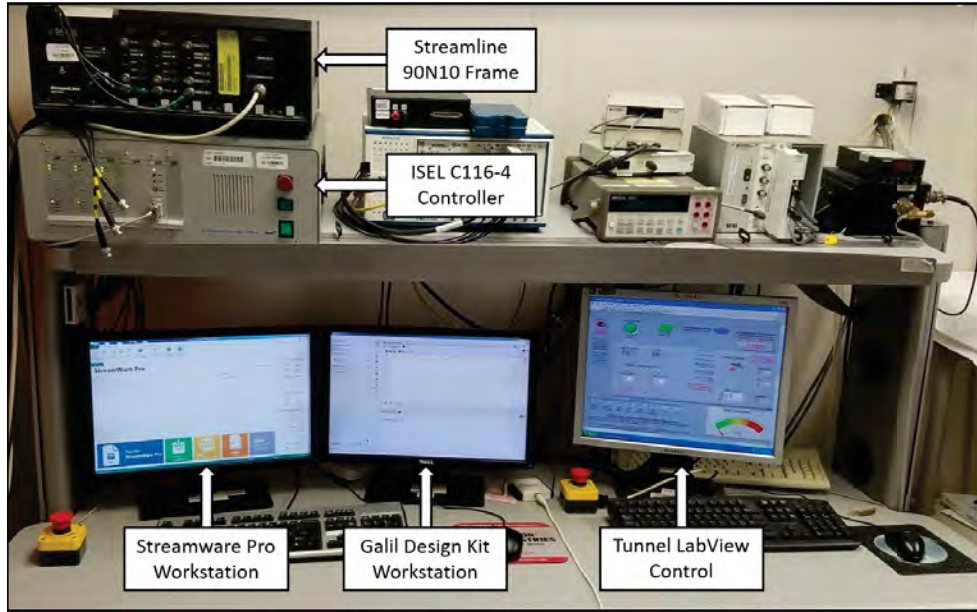


Figure 26. Wind tunnel control room

#### 3.3.3.4 Tri-axial Probe Calibration.

In addition to the CTA modules, a 90H01 calibration module was also installed in the Streamline frame for communication with the Streamline 90H02 calibration unit. The calibration unit, with pitch-yaw manipulator installed for directional calibration, shown in Figure 27, was used to calibrate the tri-axial probe. Using replaceable nozzles, the calibration unit is technically capable of calibrating a probe in a range of airspeeds from  $0.02 \frac{m}{s}$  to greater than  $300 \frac{m}{s}$ , although the 55P91 is limited to

a minimum and maximum velocity of  $0.05 \frac{m}{s}$  and  $200.0 \frac{m}{s}$ . During calibration, the tri-axial probe needs to be oriented with the probe xy-plane parallel with the flow. Shown in Figure 28, is the alignment tool, which is secured to the alignment face on the 55P91 tri-axial probe, shown in Figure 25. Correct use of the alignment tool ensures that the xy-plane is properly oriented during velocity and directional calibration of the probe.



**Figure 27. DANTEC 90H02 Calibration Unit.** The pitch-yaw manipulator allows for calibration of the tri-axial probe.

In general, calibration for a hot-wire exposes the probe to known velocities, creating a relation between CTA voltage output signal and flow velocity [13]. For this experimental study the calibration was completed using the Streamware-Pro software package, which adjusts for temperature correction, overheat adjustment, and generates a polynomial curve fit from sampled data that corrects voltages and calculates the transfer functions [30]. The velocity calibration of the 55P91 tri-axial probe was performed using the #1 nozzle and 15 data points across a range of  $2.0 \frac{m}{s}$  to  $50.0 \frac{m}{s}$ . While wind tunnel testing during Phase I was planned to be conducted at no more than 50.0 mph ( $22.35 \frac{m}{s}$ ) the manual recommends that the velocity calibration of the tri-axial probe be conducted at velocities of at least  $1.6 * U_{max,expected}$  to ensure the curve fit is valid over the full angular acceptance range of the probe [30].

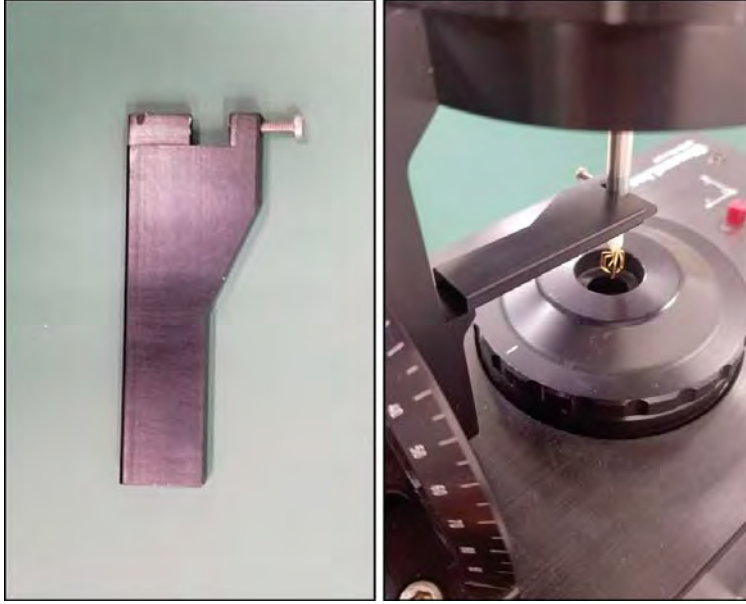


**Figure 28.** Tri-axial wire alignment tool. The left photo shows the alignment tool, and the right photo shows how to line up the probe when it is mounted to the pitch-yaw manipulator

The decomposition of measured velocity components requires the pitch-yaw manipulator shown in Figure 27. The probe was set to a yaw angle of  $10.0^\circ$  and then rotated through 24 angular positions in  $15.0^\circ$  steps. The Streamware Pro software instructs the user step-by-step through the entire process, prompting the movement to each angular position. After the calibration process is complete, sensitivity coefficients are generated for each of the three sensors, which are used to decompose the components of velocity [30]. The accuracy of 55P91 probe, when properly calibrated, was explored by Yeung and Squire [70]. For a flow vector within  $10.0^\circ$  of the probe axis, they found that the flow angularity error was measured at  $\pm 2.0^\circ$  and the velocity magnitude was within a confidence limit of  $\pm 1.0\%$ . As the cone angle increased to  $20.0^\circ$ , the velocity magnitude's confidence limit increased to  $\pm 3.5\%$  and the flow angularity errors increased to  $\pm 4.0^\circ$ .



### 3.3.4 Nano-25 Force/Torque Transducer.

Six-component wind tunnel balances have been used by many researchers to characterize the loads and moments acting on aerodynamic bodies. Traditionally, these balances are used to gather time-averaged values. Recently, however, piezoresistive sensors have shown the potential to provide time-accurate data. The ATI Nano-25, which is 0.984 inches in diameter, 0.85 inches in height, and weighs 0.14 pounds, falls into the latter category.

Each Nano-25 is delivered with a unique signal conditioner box that shares the same serial number as the Nano-25 force balance. The Nano-25 and signal conditioner box used in this study had the label FTI-15790. A Nano-25 senses forces in the x-, y-, and z- axes ( $F_x, F_y, F_z$ ) and torques about the x-, y-, and z-axes ( $T_x, T_y, T_z$ ). The variables  $F_{xy}$  and  $T_{xy}$  denote any combination of forces and torques in the x- and y- directions, respectively. The Nano-25 outputs force and torque data in imperial units. The converted technical specifications are shown in Tables 3 - 4.

|            | Sensing Ranges | Resolution   |
|------------|----------------|--------------|
| $F_x, F_y$ | 25.0 lbf       | 1/224 lbf    |
| $F_z$      | 100.0 lbf      | 3/224 lbf    |
| $T_x, T_y$ | 25.0 lbf-in    | 1/160 lbf-in |
| $T_z$      | 25.0 lbf-in    | 1/320 lbf-in |

**Table 3. Nano-25 Calibration Specifications [50]**

| Single-Axis Overload |                    |
|----------------------|--------------------|
| $F_{xy}$             | $\pm 520.0$ lbf    |
| $F_z$                | $\pm 1600.0$ lbf   |
| $T_{xy}$             | $\pm 380.0$ lbf-in |
| $T_z$                | $\pm 560.0$ lbf-in |

**Table 4. Nano-25 Single-Axis Overload [50]**

Figure 29 depicts the Nano-25's organic reference frame, which is located on the



surface of the Nano-25's model interface plate and follows the right hand rule. The orientation of the Nano-25 during the experimental test is depicted in the image on the left in Figure 30. The Nano-25 coordinate system was transformed to be in accordance with the AIAA Nomenclature and Axis Systems for Aerodynamic Wind Tunnel Testing Guide, as shown in Figure 30. The transformation process used to convert the recorded Nano-25 data to the AIAA standard is depicted in Equation 10. In Equation 10, 'N' is the normal force, 'Y' is the side force, 'A' is the axial force, and 'l', 'm', and 'n' are the rolling moment, pitching moment, and yawing moments, respectively.

$$\begin{bmatrix} F_{x_{Nano25}} \\ F_{y_{Nano25}} \\ F_{z_{Nano25}} \\ T_{x_{Nano25}} \\ T_{y_{Nano25}} \\ T_{z_{Nano25}} \end{bmatrix} = \begin{bmatrix} A_{z_b} \\ A_{y_b} \\ A_{x_b} \\ T_{x_b} \\ T_{y_b} \\ T_{z_b} \end{bmatrix} = \begin{bmatrix} -N \\ Y \\ -A \\ l \\ m \\ n \end{bmatrix} \quad (10)$$

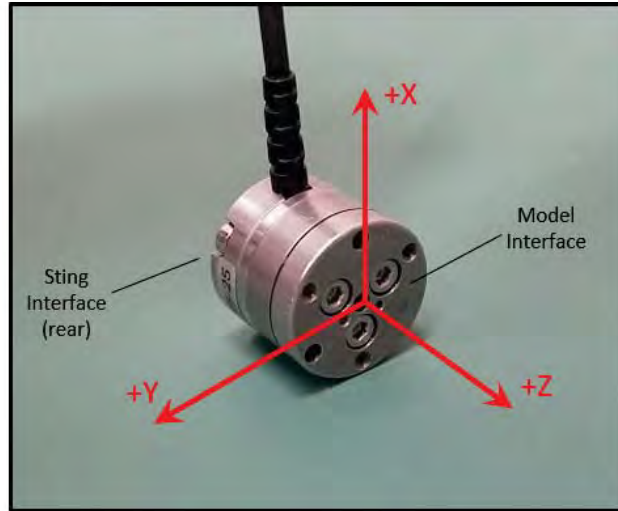
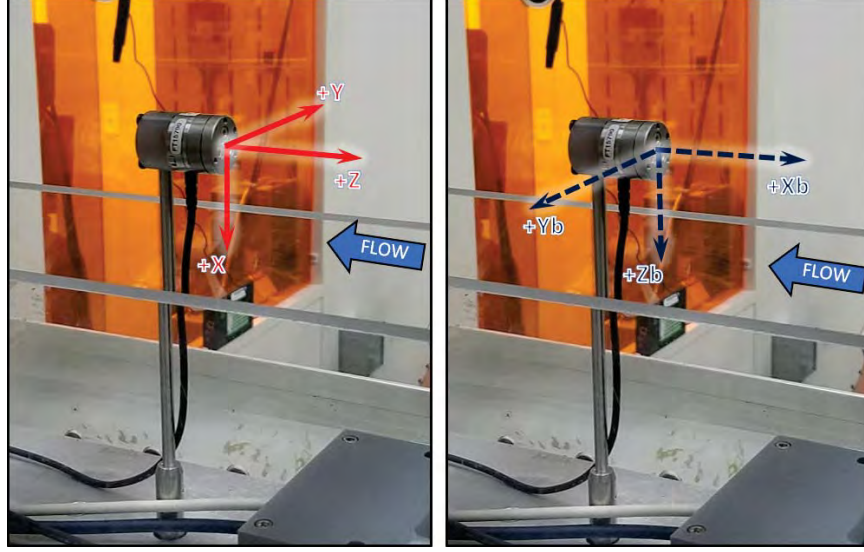


Figure 29. Nano-25's designed reference frame.



**Figure 30.** The left image is the Nano-25 reference frame when mounted to the sting. The right image is the body reference frame in agreement with AIAA standards after post-processing the Nano-25 reference frame.

The Nano-25 produces analog voltages which were recorded using a LabView program and saved as .lvm files. MATLAB was used to post-process the voltages and produce time-accurate forces and torques. Converting the analog voltages required a calibration matrix, which are unique to each Nano-25 and provided by ATI. The calibration matrix used during post-processing is presented in Section 3.10.3.1. This sensor was used by Sellers [51], and Bower [4] to collect data at rates up to 1000.0 Hz for a wing oscillating at 1.5 Hz.

### 3.4 Experimental Models: Piston and Sleeve Design

The mass injection at the leading edge of the cavity was accomplished using a piston driven by an oscillating linear motor. The piston and its corresponding cylinder, seen in Figures 31 and 32 respectively, were designed using CAD software and fabricated using AFIT's Ultimaker 3D printers. The piston's head was designed with two ring grooves, in which two rubber gaskets were placed to ensure a tighter seal and minimize losses in the apparatus. The piston's head was attached to the mount by

two 3.5 inch long arms and the cylinder's depth provided the piston with a maximum travel of 49.5 mm, from fully aft to fully forward. The volume of the cylinder shown in Figure 32 is  $475.7 \text{ cm}^3$ . When the piston from Figure 31 is inserted into the cylinder, the volume is reduced to  $366.6 \text{ cm}^3$

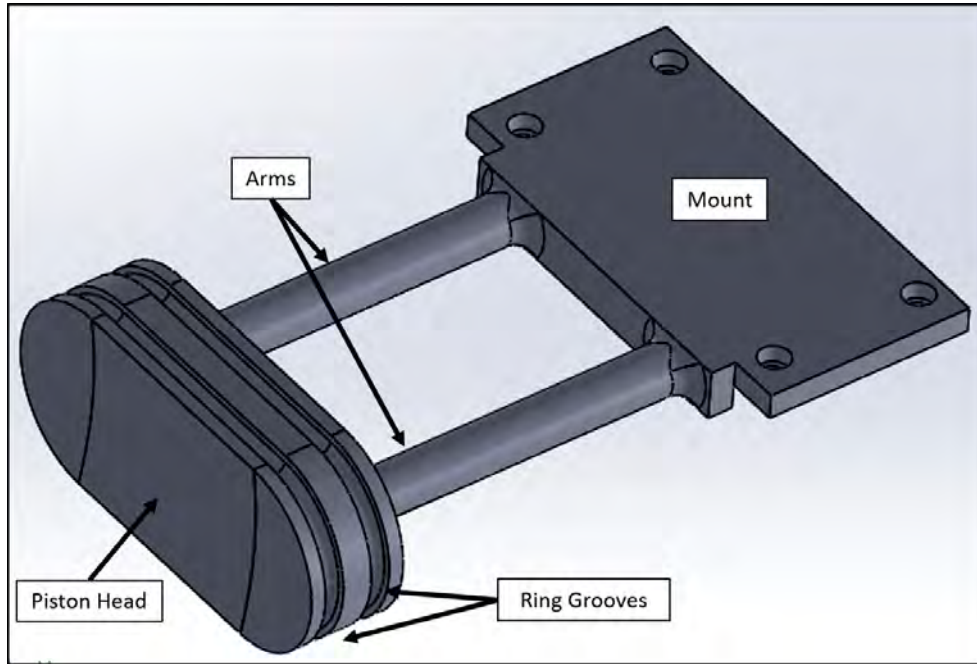


**Figure 31. Piston for the leading edge blower**

The oscillation of the piston-cylinder device during the experimental study was conducted at 5.0 Hz. To mitigate the potential for damage during extended operations, the inside of the cylinder was lined with three inch wide Kapton tape. The Kapton tape improved the performance of the lubricant used in the device. With only a single application of lubricant, the apparatus was run at 5.0 Hz for over 3.5 hours without incident.

To prevent motion of the cylinder during operation, a support structure was fabricated, shown in Figure 33. The support device was secured to the base of the cavity and served to minimize movement of the apparatus during operation and provide proper alignment of the piston and cylinder.

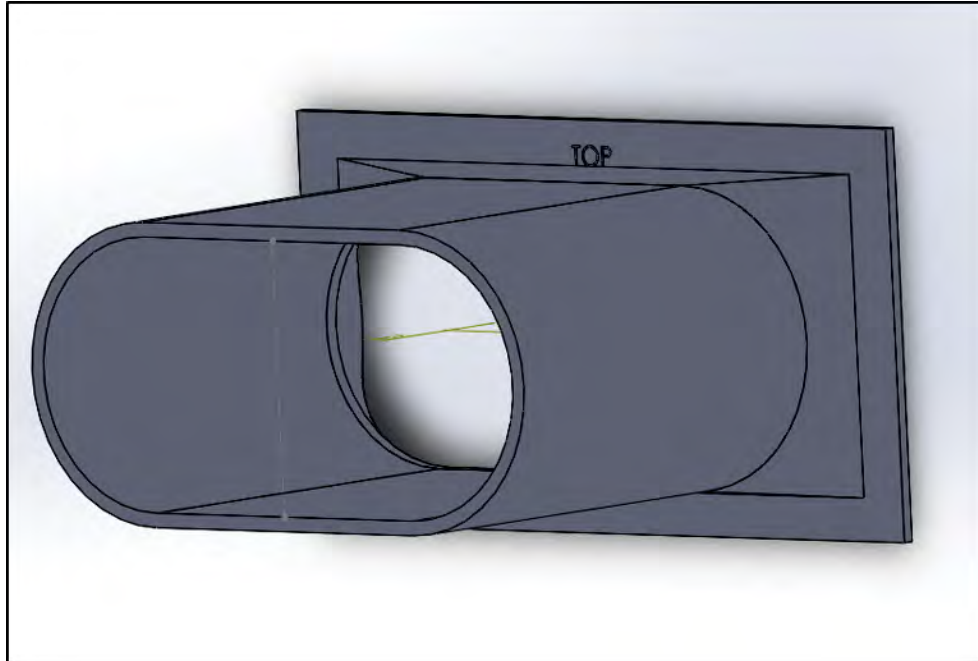


Figure 32. Cylinder for the leading edge blower

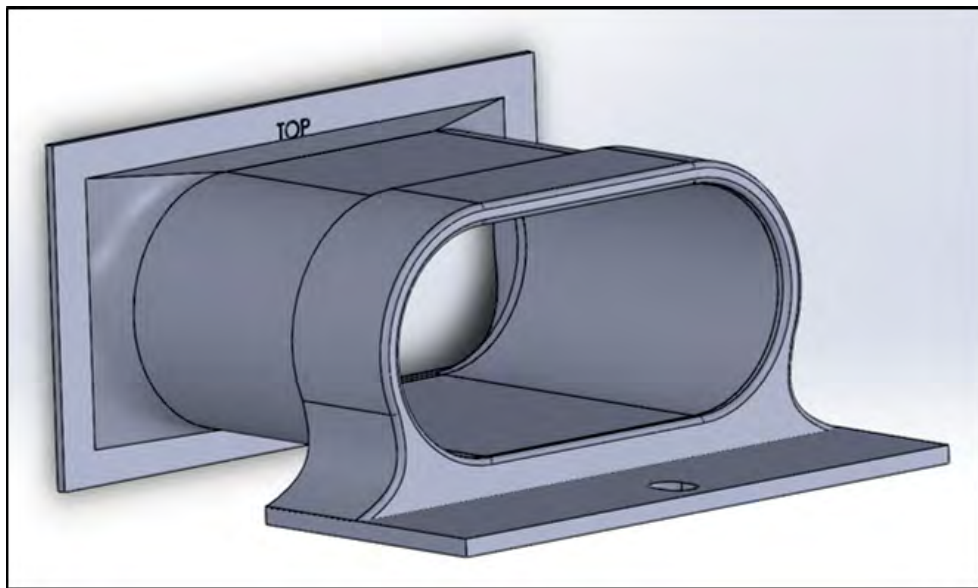
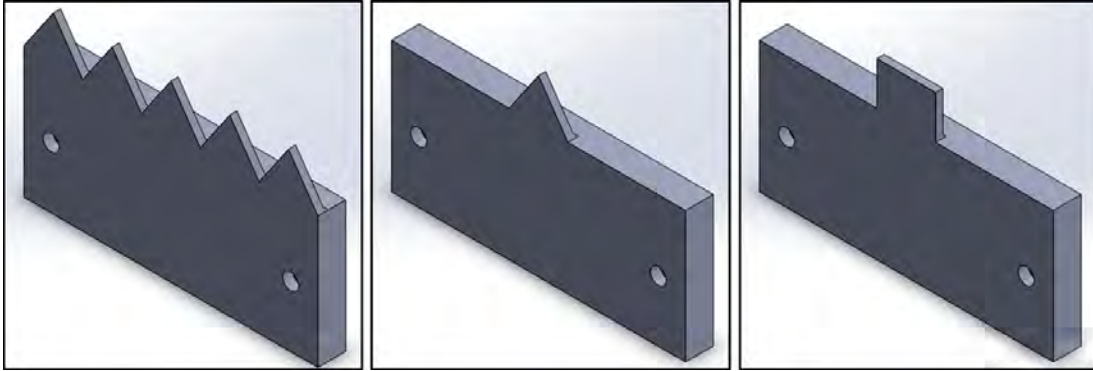


Figure 33. Support mount for the piston-cylinder apparatus.

### 3.5 Experimental Models: Leading Edge Passive Control Devices

The influence of spoilers on the shear layer has been well documented in experimental studies such as those conducted by Heller and Bliss [24], Kaufman and Clark

[26], Schmit et al. [48], as well as Shaw and Bartel [53]. Furthermore, the vorticity induced by streamwise tabs on the leading edge has been studied extensively by Zaman [73], Reeder and Zaman [41], Foss and Zaman [18], as well as Fagan et. al [16]. With this in mind, three passive control devices: a leading edge sawtooth spoiler, triangular tab, and rectangular tab, were fabricated for this experimental study and used as a reference for assessing how effectively our leading edge blowing devices influence the shear layer. All of the leading edge devices, shown in Figure 34, are 134.98 mm wide and span the width of the cavity. The leading edge sawtooth spoiler has five teeth, each of which have a base width of 27.0 mm and a height of 19.71 mm. The triangular tab has a single tab located in the center of the device with a base of 27.0 mm and a height of 19.71 mm. The rectangular tab has the same width and height as the triangular tab.



**Figure 34.** Passive leading edge devices. Left: sawtooth spoiler, Center: triangular tab, Right: rectangular tab.

### 3.6 Experimental Models: Leading Edge Blowing Devices

Multiple leading edge blowing devices were fabricated for this experimental study. While the internal structure of each leading edge device differed from one another, they all had several features in common. Namely, there is a single internal cavity, shown in Figure 37 with dimensions of 128.3 mm x 64.2 mm x 9.5 mm, for a total

volume of 78.5 cm<sup>3</sup>. Furthermore, there are two holes which allow the devices to be secured to the leading edge of the cavity, and also, two guide channels for securing the piston-cylinder assembly to the leading edge device. Figure 35, depicts how the placement of the guide channels allow the leading edge blowing devices to slide onto the cylinder. This allowed for quick removal and replacement of leading edge devices during testing without having to remove the linear motor and piston-cylinder assembly.

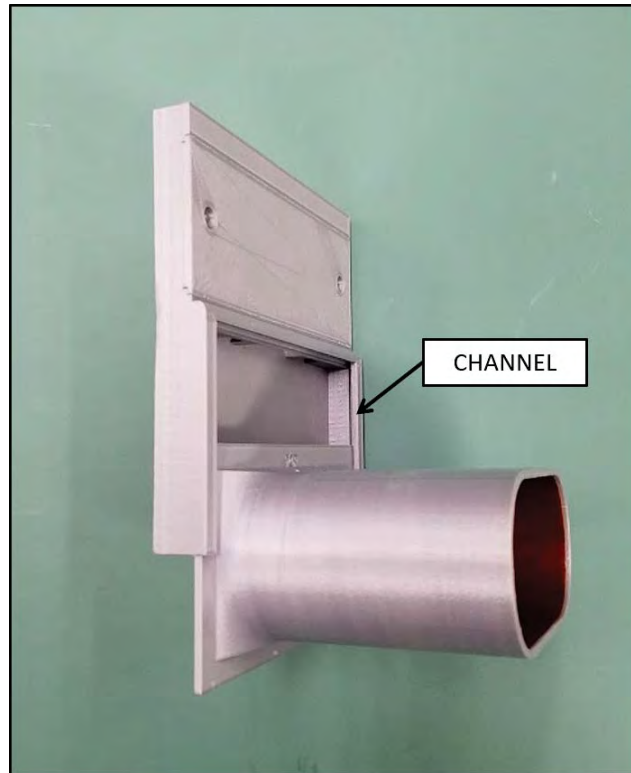


**Figure 35.** Channel to connect the cylinder and leading edge device. The channel opens at the bottom of the leading edge device to simplify process for removal and replacement of leading edge devices during testing.

### **3.6.1 Leading Edge Blowing Device: Single Channel ‘Slot’.**

The leading edge device with a single, straight, internal channel, shown in Figure 36, is referred to as the ‘Slot’ leading edge device. The single internal channel within the Slot device has dimensions of 102.29 mm in width and 6.35 mm in depth, providing



an exit area of  $649.5 \text{ mm}^2$ . A similar approach and geometry was used by George and Ukeiley [21]. The single slot served as comparison to other cases where the internal geometry was varied.

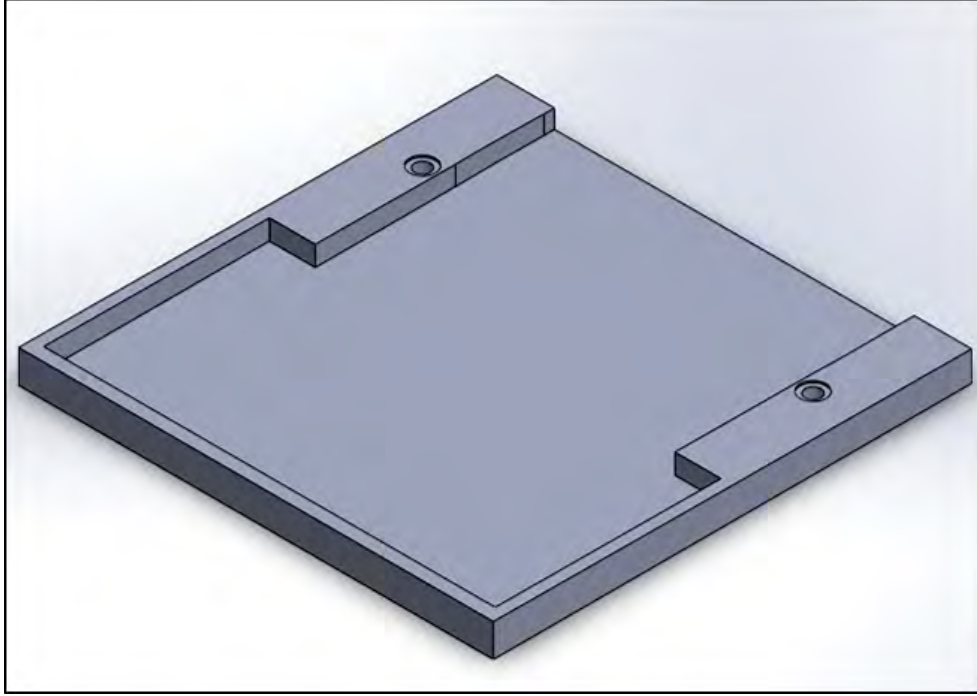


**Figure 36. Slot-Leading Edge Blower**

### **3.6.2 Leading Edge Blowing Device: Fluidic Diodes.**

The design of the leading edge blowing devices referred to as ‘fluidic diodes’ in this research drew inspiration from several of the principles for leading edge devices outlined in section 2.5.2.3. When describing the characteristics of the different fluidic diode designs, the terms ‘top’, ‘middle’, and ‘bottom’ are used to describe location within the channel, shown in Figure 37.

The internal structure was designed using Nikolai Tesla’s principle of the valvular conduit [61], encouraging flow in one direction while offering high resistance to flow in the opposite direction. All of the fluidic diodes designed for this experimental study had three channels: two outer channels and a central channel. The three channels

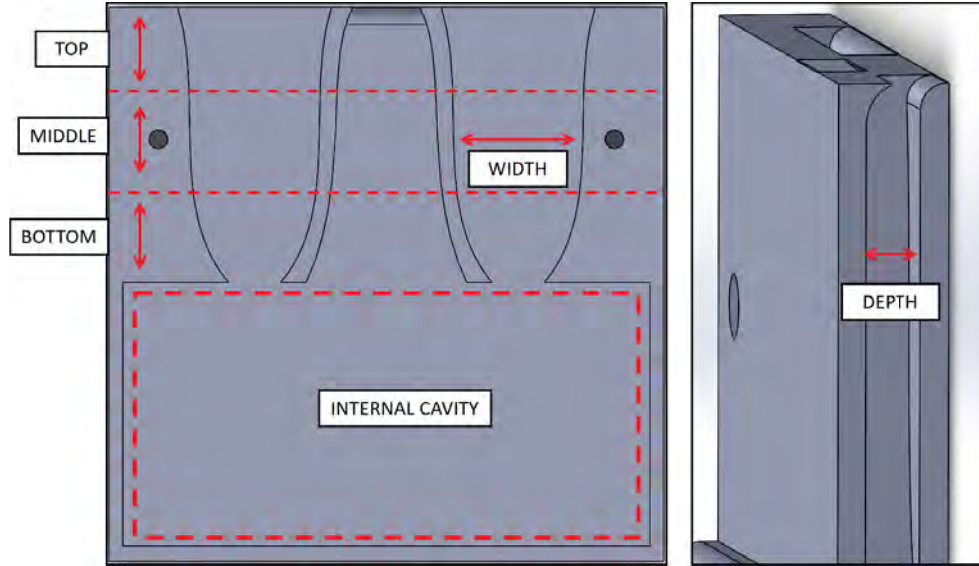


**Figure 37. Reference for terminology used in describing geometry of the Diodes**

were designed to encourage air to be drawn in through the two outer channels as the piston retracts, and preferentially to be blown out through the central channel as the piston drives forward. The width and depth of the two outer channels for all of the fluidic diodes are 12.7 mm by 6.35 mm in at the opening to the internal cavity and 37.44 mm by 6.55 mm the exit to the freestream. Likewise, the center channel for all of the fluidic diodes has dimensions of 39.12 mm by 9.52 mm at the opening to the internal cavity and 16.16 mm by 5.73 mm at the exit to the freestream.

The mass injection out of the central channel was designed to behave as a fluidic-tab, akin to the fluidic spoilers in Bennett et al.'s research [3] and the single-slot leading edge blowing device in George and Ukeiley's research [21]. With each iteration of the fluidic diode, more modifications were made to the channels to encourage flow in a single direction.

While this research primarily focused on influencing the flow over a cavity using leading edge blowing devices, small design features were implemented in an attempt to further suppress the cavity noise. All three of the channels feed into a central cavity. The two outer channels are slanted towards the upstream flow, while the



central channel is slanted downstream, as seen in Figure 38. The orientation of the openings were designed to further encourage air to be drawn in through the outer channels and exhausted through the central channel. Additionally, the shape of the two openings of the outer channels exposed to the flow drew some inspiration from Panton's experiment involving Helmholtz resonators, where he concluded that the orifice sidewall shape has an important effect on the response of the resonator and the orifices slanted towards the upstream flow have increased response [37]. Of note, aside from the curved geometry designed to encourage flow direction at the top exit and bottom interface with the internal cavity for each channels, the depths of the channel are a constant 6.35 mm.

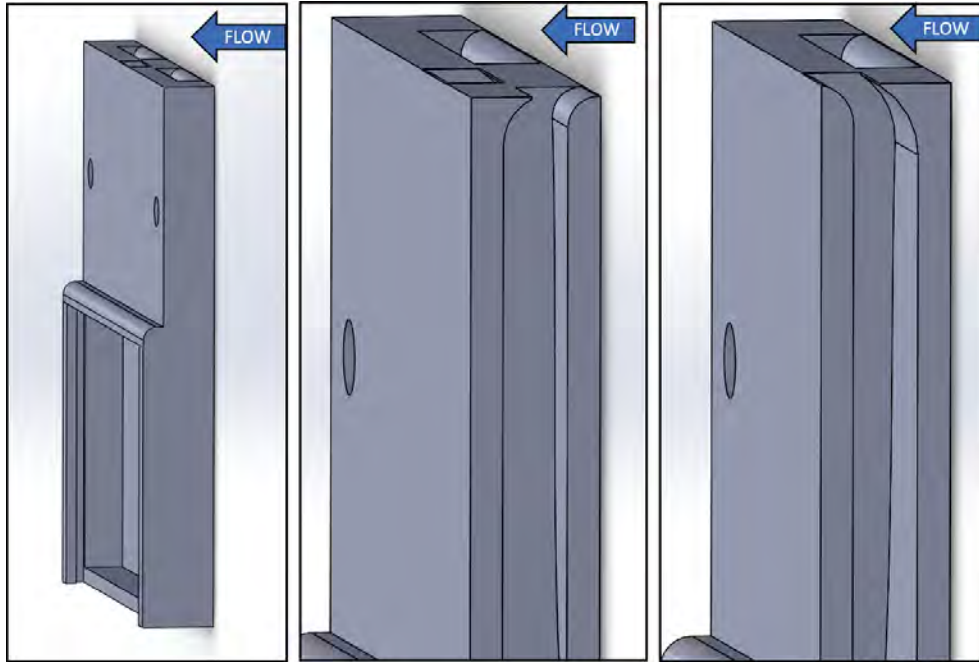


**Figure 38.** Internal view of the fluidic diode openings. The leftmost image is a side view of the entire fluidic diode for orientation. The center image shows the curve of outer channels with respect to flow direction. The right image shows the curve of central channel with respect to the flow direction.

### 3.6.2.1 Fluidic Diode v0.0.

The first iteration of the fluidic diode, Diode 0.0, can be seen in Figure 39. It must be emphasized that, due to a printing error, the openings to the freestream for the outer channel's of Diode 0.0 did not have the designed curvature that all of the other fluidic diodes possessed. Instead, the two outer channel's exit to the free-stream ends abruptly in a flat surface without any curvature. The geometry used for the openings at the top of every other fluidic diode design compared to Diode 0.0 are easily recognizable. As seen in Figures 38 and 40, respectively. Additionally, the edge treatment of the central channel for Diode 0.0 differed from subsequent designs. Specifically, the radius of the fillet curving towards the downstream was smaller than any of the other Diodes. This variation in edge treatment for the central channel can be identified when comparing the far right image of Figure 40, Diode 0.0, and the right image in Figure 38.

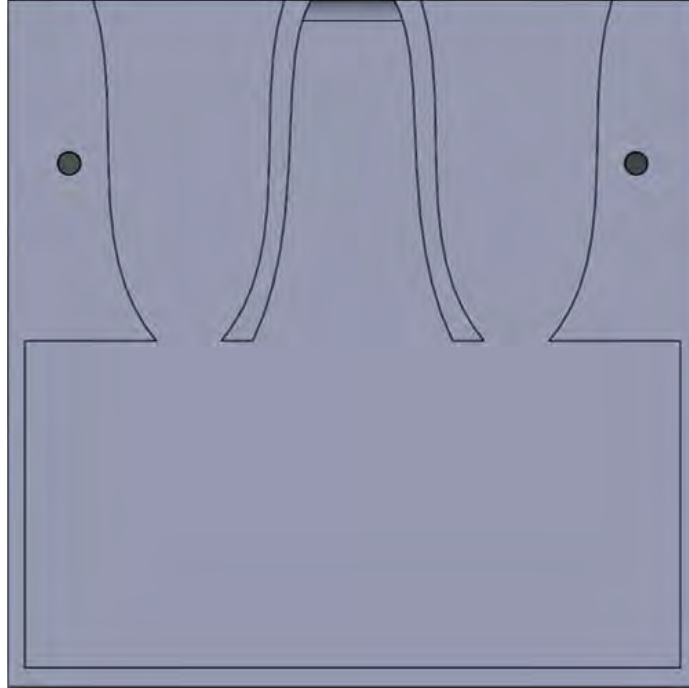


**Figure 39.** Internal view of Diode 0.0. The view presented is from within the cavity looking towards the leading edge.

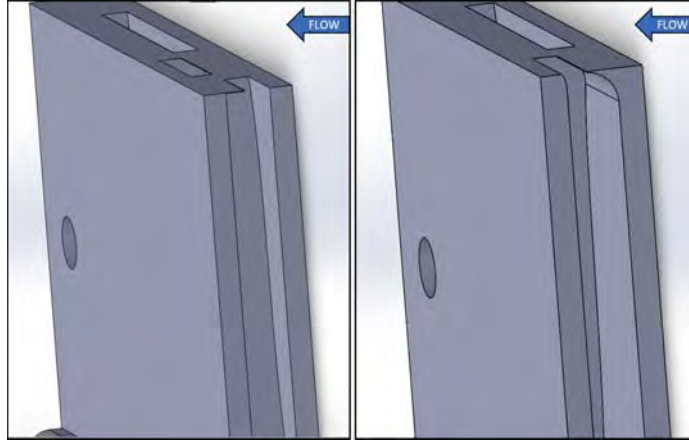


**Figure 40.** Depicting the difference in the geometry of the openings at the top of Diode 0.0. Outer channels coming to an abrupt end (left) and central channel having proper curvature (right).

The exit to the freestream at the top of the outer channels has an area of  $245.2 \text{ mm}^2$ . Moving from the top of fluidic diode down, there is a gradual reduction in the width of the outer channels until the middle third of the channel, where it remains relatively constant. The bottom third of the channel necks down to an area of  $80.6 \text{ mm}^2$  at the interface with the large internal cavity.

The center channel at the top of Diode 0.0 has an exit area of  $49.6 \text{ mm}^2$ . Unlike the outer channels, moving from the top of the channel to the bottom, the width of the center channel increases gradually until the middle third is reached, where it remains relatively constant. The center channel's exit area at the interface with the internal cavity is  $372.42 \text{ mm}^2$ .

### 3.6.2.2 Fluidic Diode v1.0.

The outer channels of Diode 1.0, shown in Figure 41, were changed to be in agreement with that seen in Figure 38, and are the most recognizable change from Diode 0.0. Each outer channel implements a single projection that terminates in a bucket, serving to reduce the channel's area while increasing friction and mass resistance opposite the direction of desired flow. The projections within the outer

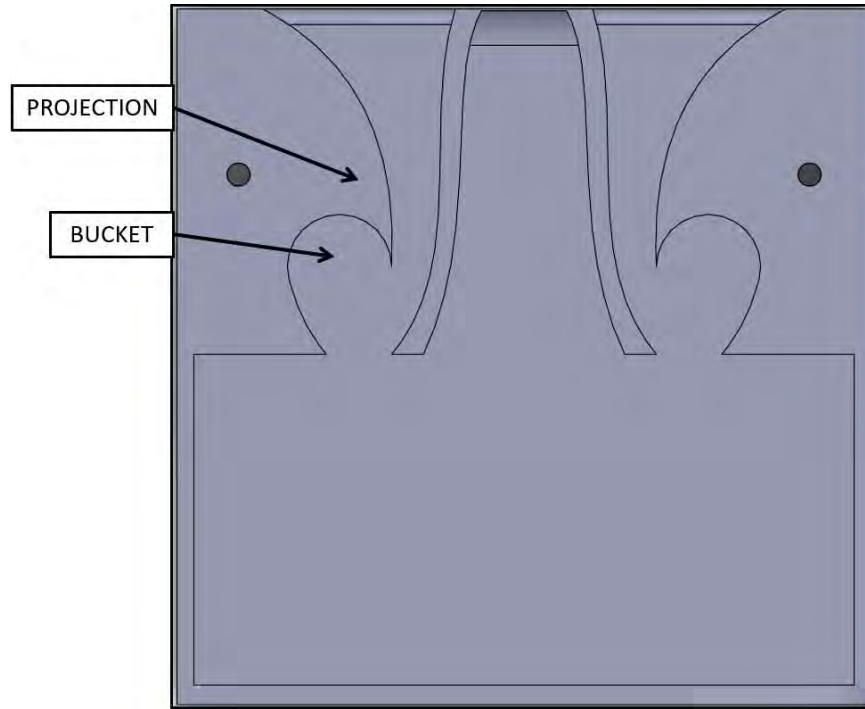


**Figure 41. Internal view of the Diode 1.0. The view presented is from within the cavity looking towards the leading edge.**

channels gradually reduce the channel's area throughout the top and middle portions of the channel until reaching a minimum of  $47.1 \text{ mm}^2$ . After the tip of the projection, the area of the channel jumps to  $175.8 \text{ mm}^2$  before necking down to  $80.6 \text{ mm}^2$  prior to the internal cavity. The bucket has a diameter of 20.26 mm.

### **3.6.2.3 Fluidic Diode v1.0a.**

As previously mentioned, PVA was used as a support material in fluid diode channels because its ability to dissolve in water seemed well suited for the task. However, the imperfections caused during the build process resulted in several of the pieces becoming water-logged. In order to mitigate the need to use PVA, Diode 1.0 was successfully re-designed with a removable face panel. Shown in Figure 42, the face of the panel and diode interlocked for a secure fit. The internal geometry of Diode 1.0a was identical to that of Diode 1.0. Diode 1.0 was chosen for the re-design

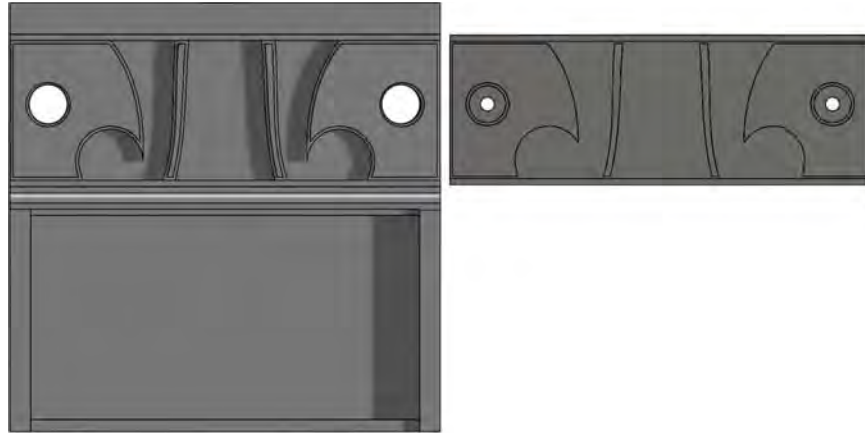


**Figure 42.** Pictures on the left is Diode v1.0a and on the right is the cover plate. The view presented is from within the cavity looking towards the leading edge.

because of its performance during experimental testing.

#### 3.6.2.4 Fluidic Diode v2.0.

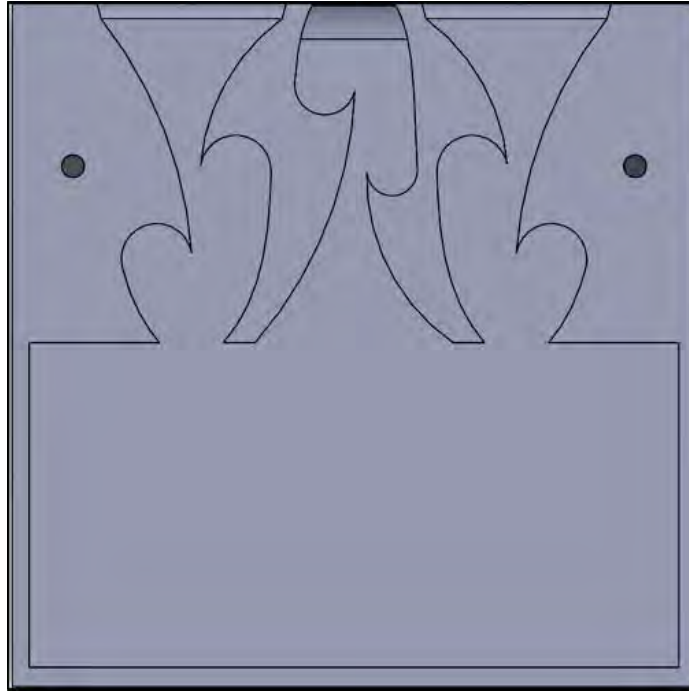


**Figure 43.** Internal view of the Diode 2.0. The view presented is from within the cavity looking towards the leading edge.

Diode 2.0, shown in Figure 43, increased the number of projections and buckets in all of the channels. The exit area at the top and bottom of each channel remains unchanged from Diode 1.0 and 1.0a. Both of the buckets in the outer channels have a diameter of 14.0 mm and the two projections reduce the area of the channel to a minimum of 29.5 mm<sup>2</sup>. The top bucket and the lower bucket in the central channel have diameters of 12.0 mm and 10.0 mm respectively. The two projections in the central channel reduce the channel's area to a minimum of 27.95 mm<sup>2</sup>.

### 3.7 Experimental Model: Mission Store Model and Support Sting

#### 3.7.1 Mission Store Models.

Two mission store models were used for Phase II of the experimental study: a generic store with canards and fins and an ogive-cylinder. The models are a generic design and do not represent any weapons system currently in the United States inventory. The mission stores were previously used for research in the AFIT low speed wind tunnel by A. Bower [4]. Both mission stores are 9.25 inches in length with an outside diameter of 1.29 inches. They were designed to allow an ATI Nano-25 balance to be mounted at the model's  $x/L = 0.5$  plane. The design specifications and drawings of the model are given in the Appendix C. Due to time constraints, only the generic missile store was used during Phase II of this experimental study.

The only modification made to the original mission store model was a redesign of the interface access plate. This was done to accommodate the sting used in Phase II of this experimental study. The models were rebuilt out of plastic with the AFIT Stratasys 3D printer and are pictured alongside their interface access plates in Figure 44.



**Figure 44. Generic Missile (top) and Ogive-cylinder (bottom) models pictured alongside their access panels.**

### **3.7.2 Support Sting.**

A second linear motor was required for use in Phase II of the experiment. The second motor was mounted underneath the cavity and a sting arm was mounted to its travel plate. A 0.5625 inch hole was then drilled into the base of the cavity at  $x/L = 0.52$  to allow a vertical support sting access to the cavity. The support sting was fabricated using hardened steel optical posts. A 6.0 inch by 0.24 inch optical post was affixed to a 6.0 inch by 0.5 inch optical post. Two mounts for the Nano-25 balance, was designed for interface with the 0.24 inch post, providing the mission stores with a fixed  $0.0^\circ$  and  $10^\circ$  angle of attack. Two screws were used to secure the Nano-25 mounts to the support sting and ensure alignment during testing. The sting with the Nano-25 attachment piece is shown in Figure 45. The diameter of the attachment piece is 25.0 mm and the internal diameter of the mission stores is



27.64 mm, ensuring that the model would not come into contact with the missile shell during testing.

A base plate was designed and built using the Ultimaker 3 printer. The base plate elevated the support sting to ensure alignment with the access hole drilled in the base of the cavity. Two holes in the base plate corresponded to two holes tapped into the 0.5 inch post, preventing rotation of the sting arm during wind tunnel testing. Figure 46 shows the fully assembled support sting with ogive-cylinder, access panel, Nano-25, and base plate attached.

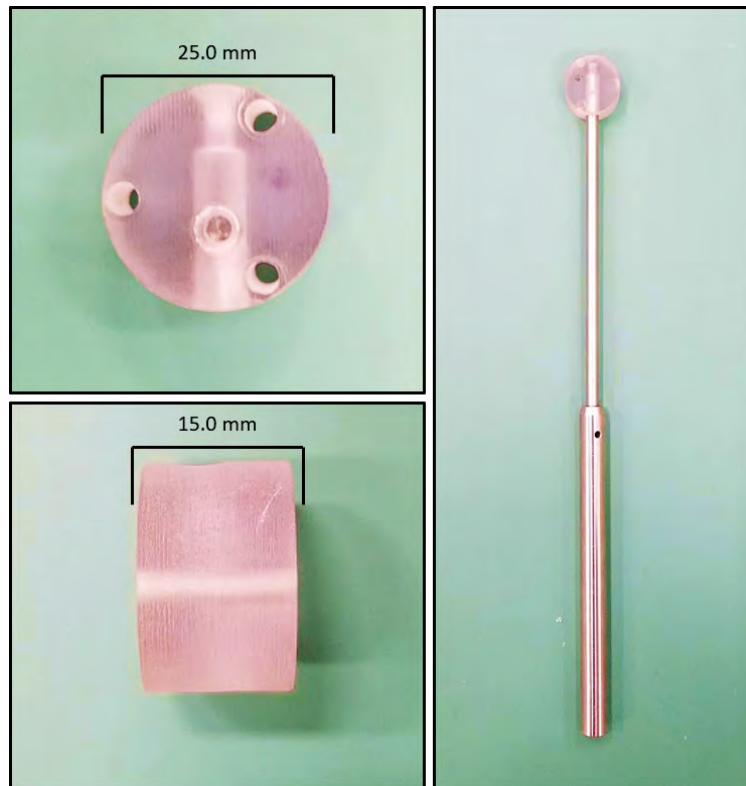


**Figure 45.** The left two images are of the Nano-25 attachment piece and the right image is the sting-arm with the Nano-25 attachment piece mounted.

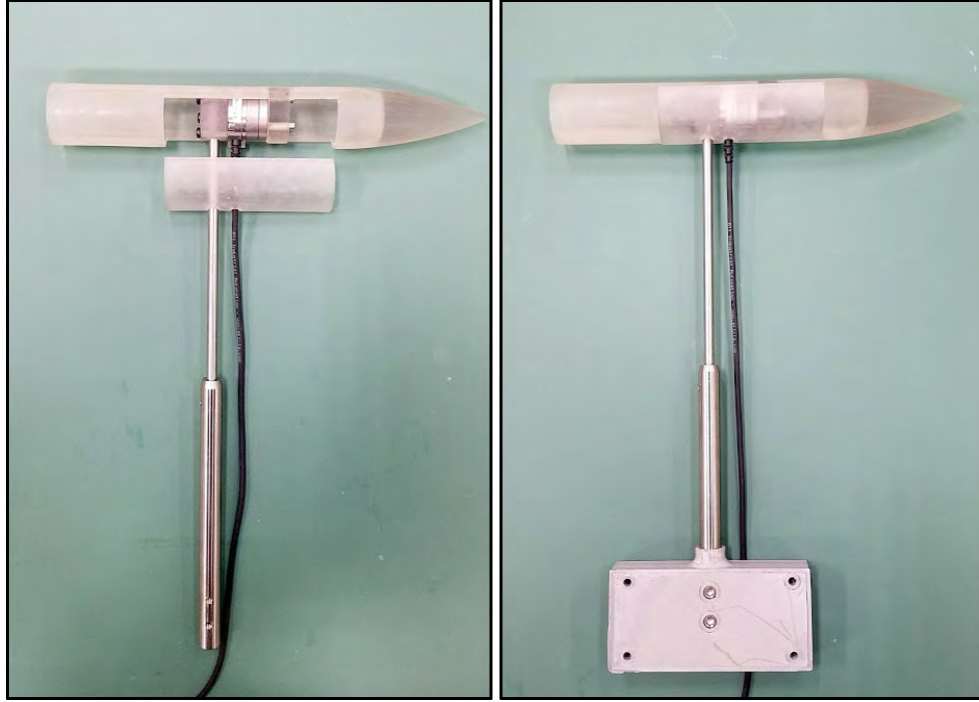


Figure 46. Ogive-cylinder with the access panel open, showing the store and Nano-25 attached to the sting-arm using the  $0.0^\circ$  AoA(left). Cavity store and sting-arm secured to the base plate (right).

### 3.8 Overview of the Experimental Setups

This experimental study can be broken down into two major phases. In the first phase, a tri-axial probe was used to assess an oscillating leading edge blowing device's effect on the shear layer. This phase included the initial verification of the tri-axial probes effectiveness, followed by a series of tests that collected velocity data on numerous leading-edge devices. The second phase explored the collection of force and moment data as a mission store model executed a simulated release trajectory. Store release was successfully synchronized with the linear motor position.

### 3.9 Phase I

#### 3.9.1 Test Profiles: Phase I.

Figure 47 shows the fully assembled cavity used for Phase I in the AFIT wind tunnel, with leading edge device, piston and cylinder, linear motor, and tri-axial probe. The entire oscillatory leading edge blowing apparatus (linear motor, piston, cylinder, and Slot or Diode device) fits within the front half of the cavity. The linear motor is positioned 5.25 inches aft of the cavity leading edge, allowing the piston to achieve the full three inches of travel while leaving ample room for the Slot or fluidic diode devices.

As indicated in Chapter II, the research on passive flow control devices is extensive. Seeking to validate the use of the triple wire, velocity data of an empty cavity, leading edge spoiler, leading edge rectangular tab, and leading edge triangular tab was acquired for comparison to observations in the literature. The principal goal for this part of the study was to determine if the velocity and turbulence intensity profiles indicated the expected alteration and consequential growth of the shear layer [60][46].

To accomplish this task, two types of profiles were used to gather velocity data with the tri-axial probe. The first profile was a simple vertical traverse of the probe from a position in the freestream above the cavity to a position below the cavity lip line, seen in Figure 48. The linear profile was positioned along the cavity center-line at  $x/L = 0.55$  and the step size was set to 5.0 mm in the vertical and lateral directions. The velocity data obtained from the linear profile allowed for assessment of the impact that the leading edge spoiler has on the flow field.

The second type of profile used in the tri-axial probe validation was a raster pattern located at  $x/L = 0.55$ , which enabled analysis of the level of spanwise (wall-normal) uniformity and the characterization of streamwise vorticity. This profile was used to gather all three components of velocity data on a plane oriented perpendicular

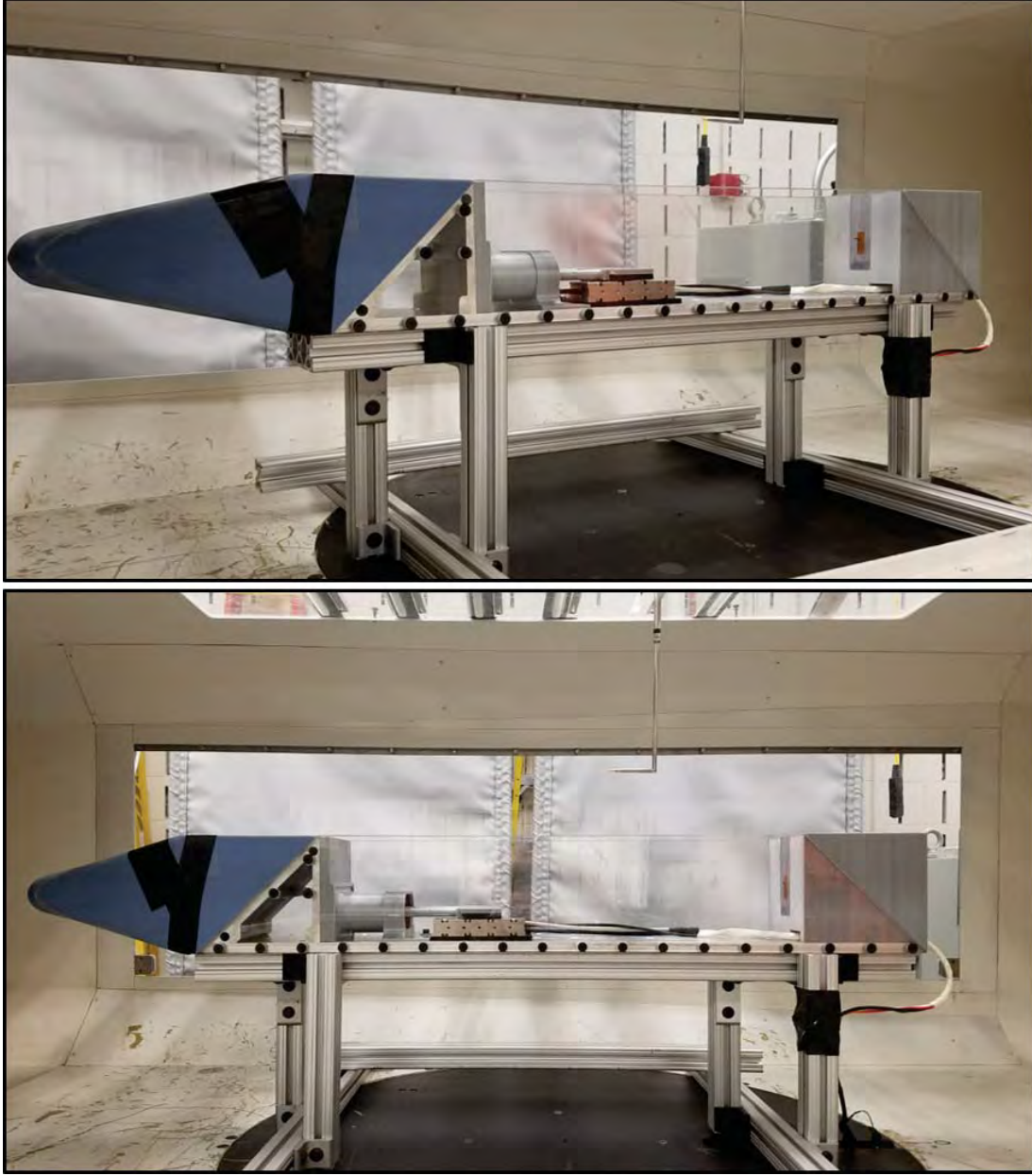


Figure 47. Fully assembled cavity used for Phase I.

to the flow, shown in Figure 49. The  $x/L = 0.55$  position was chosen because its location aft of the leading edge allowed for sufficient growth of the shear layer and development of the turbulence intensity within the shear layer. Additionally, the position of the store during Phase II of the experiment was planned for the middle of the cavity.

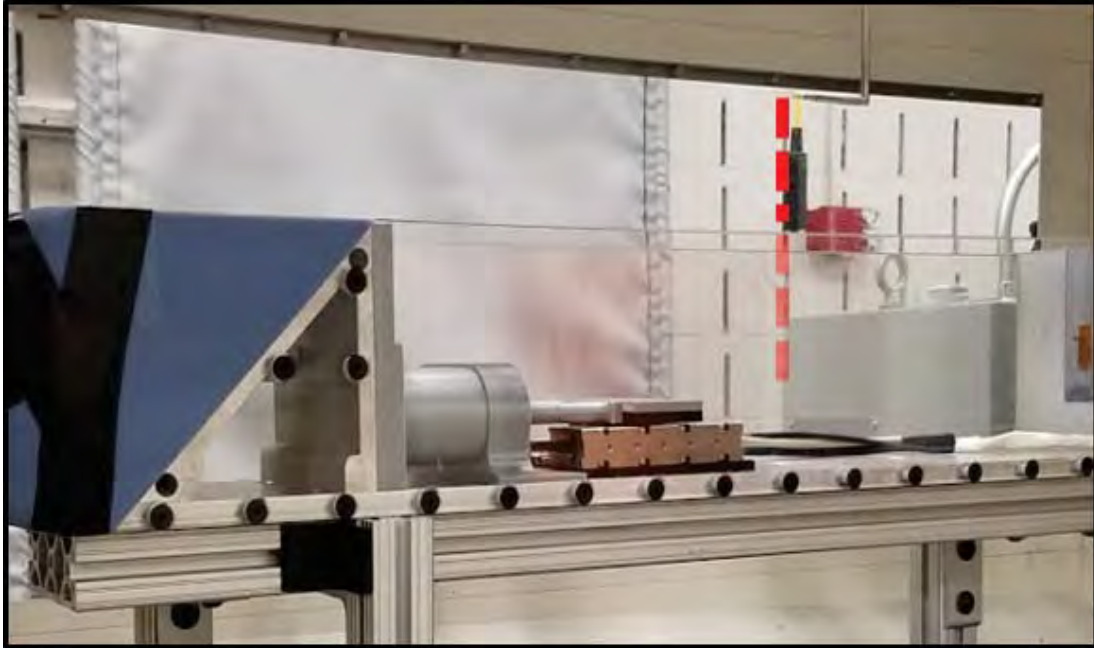


Figure 48. Linear profile used with the tri-axial probe, starting in the freestream and ending within the cavity.

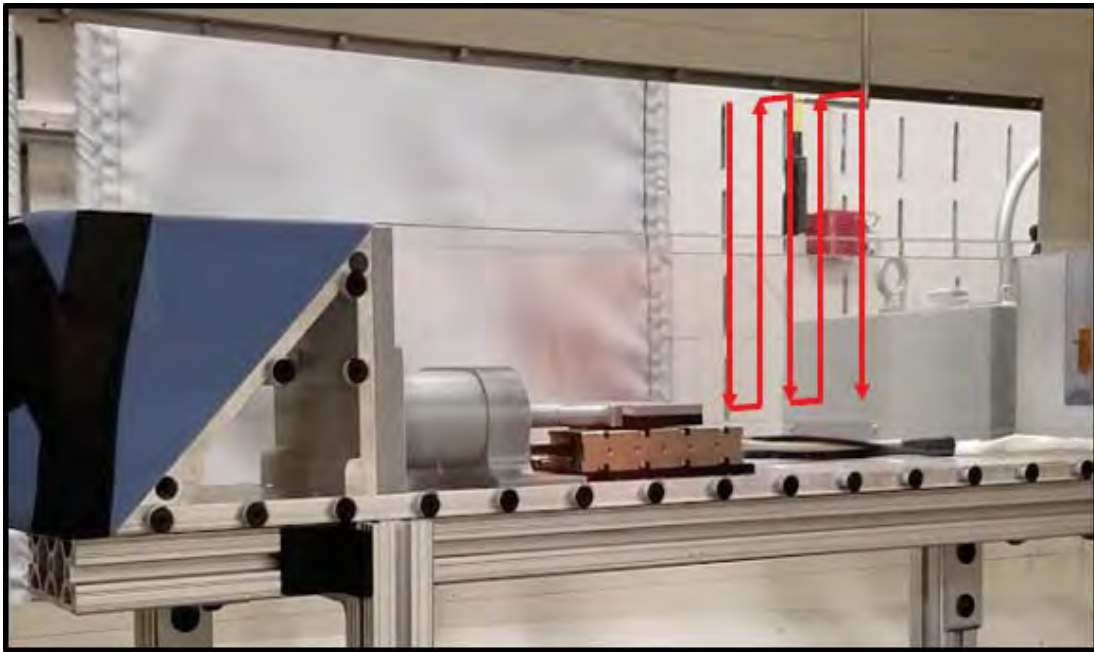


Figure 49. Raster profile used with the tri-axial probe.

Two different raster patterns were run, a high-resolution and a low-resolution. The high-resolution profile consisted of a  $21 \times 36$  grid ( $y \times z$ ) with 5.0 mm spacing



between points in both the y-direction and z-direction. The low-resolution raster pattern was an 11 x 11 grid with 10.0 mm spacing between points in the y-direction and 17.5 mm between points in the z-direction. The low-resolution pattern was chosen for continued use in the experimental study because of the drastically reduced run time, which minimized the potential of damaging the motor and piston-cylinder components. Contour plots that depict the mean and turbulence intensity of all three velocity components were developed using the velocity data from the low-resolution raster patterns. A baseline cavity was utilized for comparison of the contour plots. Within the baseline cavity, the linear motor, piston, cylinder, and a leading edge device without an opening to the freestream were installed; thus ensuring similar internal cavity geometry.

After first verifying the effectiveness of the hot-wire, the leading-edge devices (Slot, and Diodes 0.0, 1.0, 1.0a, and 2.0) were tested and evaluated using the raster pattern at  $x/L = 0.55$  and the linear pattern at three locations within the cavity: forward, middle, and aft at  $x/L = 0.25, 0.55$ , and  $0.85$  respectively. The test scope is included in Tables 5 - 9. After data was gathered from the Slot and Diode 0.0 at all speeds and with the motor both on and off, it was determined that the Diode had little to no effect on the cavity environment with the motor off, which is why the successive iterations of diodes are not assessed with the motor off. Additionally, because Phase II would be conducted at approximately  $x/L = 0.55$  and 50 mph, more emphasis was put on collecting data at those conditions.

| Linear Profile - Passive Actuators |                      |        |                      |        |                      |        |
|------------------------------------|----------------------|--------|----------------------|--------|----------------------|--------|
|                                    | FWD ( $x/L = 0.25$ ) |        | MID ( $x/L = 0.55$ ) |        | AFT ( $x/L = 0.85$ ) |        |
|                                    | 25 MPH               | 50 MPH | 25 MPH               | 50 MPH | 25 MPH               | 50 MPH |
| Sawtooth Spoiler                   |                      |        |                      | x      |                      |        |
| Rectangular Tab                    |                      |        |                      | x      |                      |        |
| Triangular Tab                     |                      |        |                      | x      |                      |        |

**Table 5.** Linear profiles completed with the passive flow control devices for tri-axial probe validation.

| Linear Profile - Motor Off |                      |        |                      |        |                      |        |
|----------------------------|----------------------|--------|----------------------|--------|----------------------|--------|
|                            | FWD ( $x/L = 0.25$ ) |        | MID ( $x/L = 0.55$ ) |        | AFT ( $x/L = 0.85$ ) |        |
|                            | 25 MPH               | 50 MPH | 25 MPH               | 50 MPH | 25 MPH               | 50 MPH |
| Empty                      |                      | x      |                      | x      |                      | x      |
| Slot                       | x                    | x      | x                    | x      | x                    | x      |
| Diode 0.0                  | x                    | x      | x                    | x      | x                    | x      |
| Diode 1.0                  |                      |        |                      |        |                      |        |
| Diode 1.0a                 |                      |        |                      |        |                      |        |
| Diode 2.0                  |                      |        |                      |        |                      |        |

**Table 6.** Linear profiles completed with the oscillating motor inactive.

| Linear Profile - Motor On |                      |        |                      |        |                      |        |
|---------------------------|----------------------|--------|----------------------|--------|----------------------|--------|
|                           | FWD ( $x/L = 0.25$ ) |        | MID ( $x/L = 0.55$ ) |        | AFT ( $x/L = 0.85$ ) |        |
|                           | 25 MPH               | 50 MPH | 25 MPH               | 50 MPH | 25 MPH               | 50 MPH |
| Empty                     | N/A                  | N/A    | N/A                  | N/A    | N/A                  | N/A    |
| Slot                      | x                    | x      | x                    | x      | x                    | x      |
| Diode 0.0                 | x                    | x      | x                    | x      | x                    | x      |
| Diode 1.0                 |                      |        |                      | x      |                      |        |
| Diode 1.0a                |                      |        | x                    | x      |                      |        |
| Diode 2.0                 |                      |        |                      | x      |                      |        |

**Table 7.** Linear profiles completed with the oscillating motor active.

| Raster Profile - Motor Off |                      |        |                 |        |
|----------------------------|----------------------|--------|-----------------|--------|
|                            | MID ( $x/L = 0.55$ ) |        |                 |        |
|                            | Low Resolution       |        | High Resolution |        |
|                            | 25 MPH               | 50 MPH | 25 MPH          | 50 MPH |
| Empty                      |                      | x      |                 |        |
| Baseline                   |                      | x      |                 |        |
| Sawtooth Spoiler           |                      | x      |                 |        |
| Rectangular Tab            |                      | x      |                 |        |
| Triangular Tab             |                      | x      |                 |        |
| Slot                       |                      | x      |                 |        |
| Diode 0.0                  |                      | x      |                 |        |
| Diode 1.0                  |                      |        |                 |        |
| Diode 1.0a                 |                      |        |                 |        |
| Diode 2.0                  |                      |        |                 |        |

**Table 8. Raster patterns completed with the oscillating motor inactive.**

| Raster Profile - Motor On |                      |        |                 |        |
|---------------------------|----------------------|--------|-----------------|--------|
|                           | MID ( $x/L = 0.55$ ) |        |                 |        |
|                           | Low Resolution       |        | High Resolution |        |
|                           | 25 MPH               | 50 MPH | 25 MPH          | 50 MPH |
| Empty                     | N/A                  | N/A    | N/A             | N/A    |
| Baseline                  | N/A                  | N/A    | N/A             | N/A    |
| Sawtooth Spoiler          | N/A                  | N/A    | N/A             | N/A    |
| Rectangular Tab           | N/A                  | N/A    | N/A             | N/A    |
| Triangular Tab            | N/A                  | N/A    | N/A             | N/A    |
| Slot                      |                      | x      |                 | x      |
| Diode 0.0                 |                      | x      |                 | x      |
| Diode 1.0                 |                      | x      |                 |        |
| Diode 1.0a                | x                    | x      |                 |        |
| Diode 2.0                 |                      | x      |                 |        |

**Table 9. Raster patterns completed with the oscillating motor active.**



The difference between the baseline cavity and the empty cavity identified in the tables above is that the empty cavity had no linear motor or leading edge devices installed while the baseline cavity had all test apparatus installed. The leading edge device installed in the baseline cavity was sealed so that there would be no influence upon the shear layer from the openings in the leading edge device.

With the motor installed in the cavity, the linear patterns taken at the middle and front of the cavity were physically limited in the depth they could reach due to the presence of the motor. As a result, the number of points decreases from 36 to 33 to 30 when moving from  $x/L = 0.85$  to 0.55 to 0.25, respectively. When gathering velocity data for the leading edge blowing devices, all patterns started at 100 mm above the cavity lip line. To ensure repeatability, at each location the probe was lowered, and an inclinometer was used to verify that the top of the probe mount was flush with the cavity lip. The maximum error permitted with the inclinometer was 0.1 degrees. Once this position was found, the traverse was raised 100 mm to the starting position.

### **3.9.2 Forcing a Dominant Tone in the Cavity.**

Dominant Rossiter tones and harmonic frequencies are a more predominant occurrence when the cavity is located within a transonic or supersonic flow field. This experimental study was conducted in the AFIT low speed wind tunnel. One of the goals of the research was to determine if the cavity environment in the low speed wind tunnel could be forced to behave in a manner more akin to that found in a supersonic and transonic environment.

The literature has shown that leading-edge devices employ either low frequency forcing or high frequency forcing to reduce the magnitude of the dominant tones [59]. Leveraging this premise, we sought to utilize the leading-edge device to force dominant frequencies that would not normally exist in a subsonic cavity environment. Time-

accurate data obtained with the tri-axial probe permitted assessment of the linear motor's capacity to force a dominant frequency in the cavity environment.

### 3.9.3 Post-Processing:Phase I.

#### 3.9.3.1 Tri-axial Probe Data Conversion.

The tri-axial probe recorded raw analog voltage data. Using the Streamware Pro software, the 100,000 raw data samples at each point can be reduced to the mean and RMS values in the probe coordinate system. Additionally, each of the 100,000 samples from the raw data event can be exported as raw voltage, velocity from calibration curve ( $U_{cal}$ ), velocity in sensor coordinates, velocity in wire coordinates ( $U_1, U_2, U_3$ ), or velocity in the probe coordinate system ( $U, V, W$ ). The reduced data was used to generate all velocity profiles and contour plots and the probe coordinate system, shown in Figure 50, was selected for all raw data exported to complete turbulence calculations. Detailed below is the conversion equations that the Streamware Pro software employs to transform from the wire-coordinate system to the probe-coordinate system.

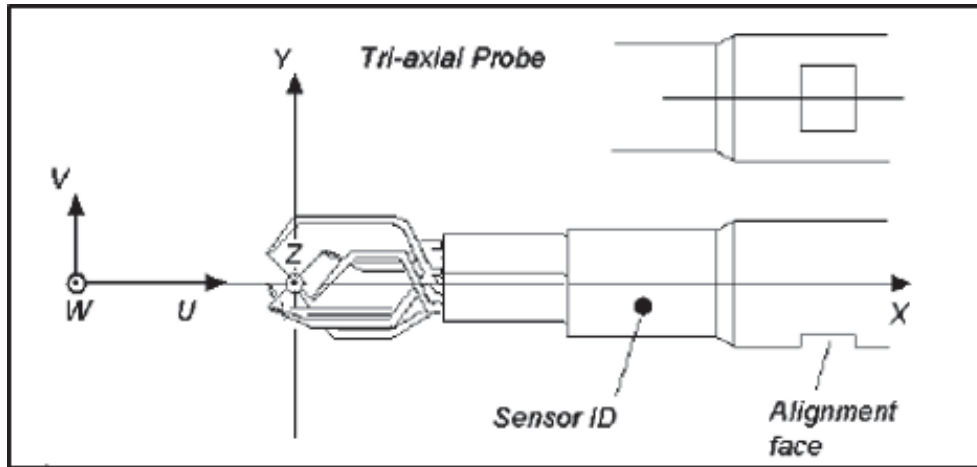


Figure 50. DANTEC 55P91 Tri-axial probe coordinate system [30]

To convert between the wire-coordinate system and the probe coordinate system,

the Streamware software uses pitch and yaw coefficients as well as the calibration velocities ( $U_{cal1}, U_{cal2}, U_{cal3}$ ) gathered during the calibration process. Using the pitch and yaw coefficients of the gold-plated wire sensors, Equations 11 - 13 are used to calculate the velocities  $U_1, U_2, U_3$  in the wire coordinate system [30]. Equations 14 - 16 are then used to convert velocity in the wire-coordinate system to the u-, v-, and w-components of the probe-coordinate system [30].

$$U_1 = \sqrt{-0.3676 * U_{cal1}^2 + 0.3747 * U_{cal2}^2 + 0.3453 * U_{cal3}^2} \quad (11)$$

$$U_2 = \sqrt{0.3453 * U_{cal1}^2 - 0.3676 * U_{cal2}^2 + 0.3747 * U_{cal3}^2} \quad (12)$$

$$U_3 = \sqrt{0.3747 * U_{cal1}^2 + 0.3453 * U_{cal2}^2 - 0.3676 * U_{cal3}^2} \quad (13)$$

$$U = U_1 * \cos(54.74) + U_2 * \cos(54.74) + U_3 * \cos(54.74) \quad (14)$$

$$V = -U_1 * \cos(45) - U_2 * \cos(135) + U_3 * \cos(90) \quad (15)$$

$$W = -U_1 * \cos(114.09) - U_2 * \cos(114.09) - U_3 * \cos(35.26) \quad (16)$$

### 3.9.3.2 Normalizing the Velocity Data and Setting the Reference Frame.

The mean velocity data presented in all velocity profiles and contour plots was normalized using the freestream mean velocity from each test run. The vertical and lateral position of the probe were normalized using the depth of the cavity ( $z/D$

and  $y/D$ ) while the probe location with reference to the leading edge was normalized using the cavity length ( $x/L$ ). When developing the plots, the probe's position within the cavity was transformed from the traverse reference frame to the probe reference frame, aligning the directionality of position and velocity. Additionally, the origin was positioned at the lip line of the cavity and aligned with the cavity centerline. The MATLAB code used to produce the plots is provided in Appendix B.

### 3.9.3.3 Vorticity Calculations.

The streamwise vorticity was calculated using a MATLAB script that incorporated a combination of first order forward, central, and rearward differencing schemes, Equations 17, 18, and 19, respectively. The differencing schemes used were from Anderson's text [1]. The V and W components of velocity data was used in a central differencing scheme, providing second-order accuracy for the interior points of the generated vorticity plot. Forward and rearward differencing schemes were used to generate first-order accurate vorticity data along the edges of the collected data. The resulting values were concatenated to produce a streamwise vorticity plot that incorporated all of the V and W velocity data gathered by the raster pattern. The MATLAB code used to develop the vorticity plots can be found in the Appendix B.

$$\xi(j, k) = \frac{w(j, k+1) - w(j, k)}{\Delta y} - \frac{v(j+1, k) - v(j, k)}{\Delta z} \quad (17)$$

$$\xi(j, k) = \frac{w(j, k+1) - w(j, k-1)}{2\Delta y} - \frac{v(j+1, k) - v(j-1, k)}{2\Delta z} \quad (18)$$

$$\xi(j, k) = \frac{w(j, k) - w(j, k-1)}{\Delta y} - \frac{v(j, k) - v(j-1, k)}{\Delta z} \quad (19)$$

#### 3.9.3.4 Flow Statistics.

The raw data was used to calculate the mean, standard deviation (RMS), fluctuation velocity, and standardized velocity for the u-, v-, and w-components of velocity. Equations 20 and 21 were used for the fluctuating velocity and the standardized velocity, respectively. In Equations 20 and 21,  $\langle U \rangle$  represents the mean velocity and  $\sigma$  represents the standard deviation. The standardized velocity was used to find the Probability Density Functions (PDFs), which were useful in comparing changes in the shear layer's velocity characteristics when the leading-edge device was inactive versus active. Each of the PDFs generated were plotted alongside a Gaussian PDF of the same standardized data set for comparison. The PDFs are included in Appendix A.

$$u(t) = U(t) - \langle U \rangle \quad (20)$$

$$\hat{U}(t) = \frac{U(t) - \langle U \rangle}{\sigma} \quad (21)$$

#### 3.9.3.5 Turbulence Characteristics.

Using a Fourier transform of the U-velocity fluctuations and applying Nyquist's Theorem to the sampling rate, the Energy Frequency Spectrum was obtained. This allowed for identification of dominant frequencies within the cavity. The inverse Fourier transform was used to produce the autocorrelation  $R_{ij}(s)$ , which was normalized using the variance of the fluctuation,  $\langle u(t)^2 \rangle$ , to produce the autocorrelation function,  $\rho(s)$ . Taylor's Hypothesis was applied to switch between the time and space domain, allowing for determination of the autocovariance function  $\rho(r)$ , and consequently the autocovariance,  $R_{ij}(r)$  [39]. The longitudinal integral length scale,  $L_{11}$ , was calculated by taking an integral from the origin to the first zero-crossing of the

autocovariance coefficient. Using Equation 22, the longitudinal integral time-scale ( $\tau_{11}$ ) could be calculated for each data set. The full MATLAB code used to determine the Energy Frequency Spectrum, autocorrelation, autocovariance, and integral length and time-scales can be found in the Appendix B. Only the Energy Spectrum is included in Chapter IV, the results of the remaining turbulence analysis is located in Appendix A.

$$L_{11} = \tau_{11} * < U > \quad (22)$$

### 3.10 Phase II

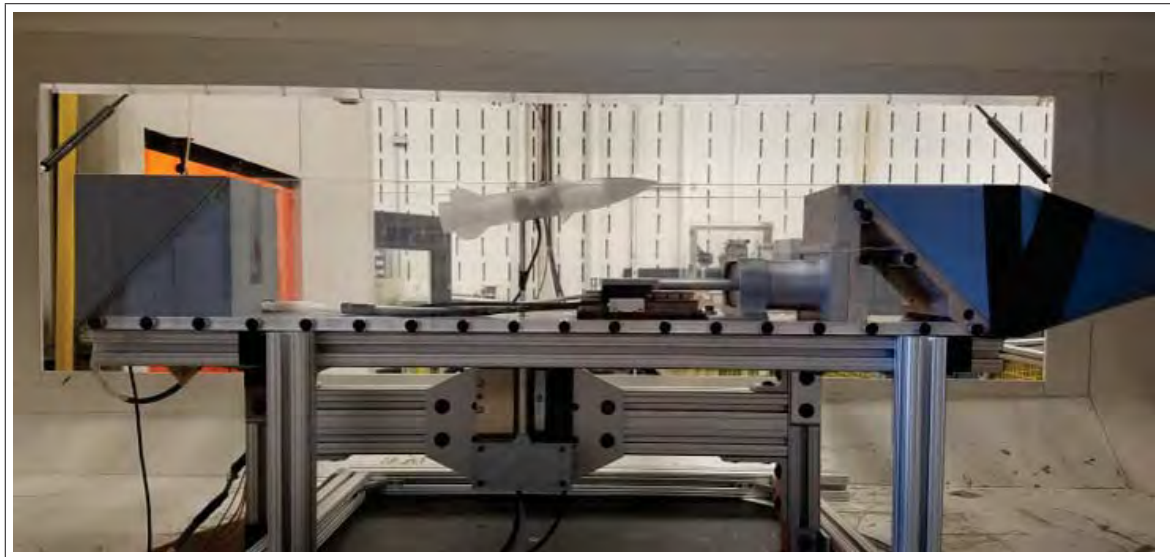
#### 3.10.1 Triggering the Trajectory Motion.

In Phase II, a second motor was used to execute a linear trajectory. This second motor shall be referred to as the trajectory motor. The trajectory motor was attached to the support base underneath the cavity. A sting mounted to the trajectory motor had access to the cavity through a 0.5625 inch hole in the base plate at  $x/L = 0.52$ . Both the Nano-25 balance and the cavity store were affixed to the sting arm using the fabricated Nano-25 mount. The complete setup used in Phase II is shown in Figure 51. The initial position of the mission store, with reference to the store's centerline, is 0.75 inches below the lip line of the cavity. The final position of the mission store is 2.25 inches above lip line.

The oscillating linear motor and the trajectory motor were both controlled using a dual-axis DMC-4020 controller. The original sinusoidal code was modified to contain a conditional 'IF' statement that would trigger actuation of the trajectory motor based upon encoder position of the oscillating motor. Three conditional statements were explored in a bench-top experiment: piston fully retracted, piston at the midpoint of its stroke, and piston at full extension. However, only the fully extended and



(a) Cavity setup for Phase II with  $0^\circ$  Angle of Attack on Mission Store.



(b) Cavity setup for Phase II with  $10^\circ$  Angle of Attack on Mission Store.

**Figure 51.** Fully assembled cavity used for Phase II with second linear motor, sting, and cavity store.

fully retracted positions were evaluated during wind tunnel testing. The conditional statement used to trigger the trajectory motor at the fully retracted position of the stroke is shown below. The remaining codes are included in the Appendix B.

FULLY RETRACTED:

```
i=0
#wait
var1 = _LM; 'Setting the buffer space as a variable
var2 = _LM-var1; 'Defining available buffer space as a variable

'Conditional Statement that anytime buffer space available, add to counter
IF (var2 > 0);
i = i + 1;
ENDIF

'Conditional statement for counter and encoder position
IF (i = 5)
  SB 31 'Sends a digital signal to start data collection for the Nano-25
ENDIF

IF (i = 7)&((_TPA > -400));
  SB 32; XQ #gravity,1; 'When conditions met, execute linear trajectory
ENDIF

IF (@OUT[32] = 0)
JP #LOOP,_LM>1; ' _LM shows how many segments are available in buffer
JP #WAIT,go=1; 'continue adding sine waves until go=0 is entered
ELSE
WT 2000; CB 31; CB 32; WT 5000; JP #homeC;
'Waits 2 sec before sending a digital low to stop data collection

#gravity
SH B
AC ,19620000; '2g acceleration
DC ,10240000; 'deceleration
SP , rate; 'speed
PR ,-77000; 'distance
BGB; 'start the motion
EN

#homeC; 'Home Routine
SH B;
JG ,25000;
```



BG B; 'Begin motion  
AM B; 'After motion  
MO A; MO B;  
EN

A Phantom Mirolab 3a10 high-speed digital camera was used in two benchtop experiments for initial verification of the positional trigger's accuracy. In the first benchtop experiment, neither the oscillating motor or trajectory motor had any components attached. The three different positions of the oscillating motor were observed for validation; all three of which were successful. Additionally, the high-speed camera was used in the first benchtop experiment to refine the acceleration and speed of the store's linear trajectory in order to ensure that the store's motion was complete in one half cycle of the oscillating motor. An acceleration of  $19.62 \frac{m}{s^2}$ , twice the acceleration of gravity, was chosen for the experiment. The store completed the trajectory motion in approximately 0.14 second. In the second benchtop experiment, the cavity setup was fully assembled with loads on the motor, and the trigger at both the minimum and maximum positions was successfully verified.

The Phantom Mirolab was also used to verify the fidelity of the positional trigger during experimental testing in the wind tunnel. To determine if the positional trigger remained reliable under load in the wind tunnel, the mission store was evaluated using both the  $0.0^\circ$  and  $10.0^\circ$  angle of attack mounts in the cavity with tunnel speed set to 50 mph and 100 mph.

### **3.10.2 Test Profiles: Phase II.**

Due to time constraints, only the generic missile store with the leading edge Slot was evaluated. Once the wind tunnel had reached a steady state, the linear motor was activated and allowed to run for a minimum of ten seconds before the conditional trigger activated the trajectory motion. Data was collected at two of the conditional trigger locations: minimum stroke (fully extended) and maximum stroke (fully re-

tracted). Each test configuration was repeated five times. A summary of the wind tunnel tests performed on the mission store models is depicted in Table 10.

| Leading Edge Device: Slot |        |         |         |         |
|---------------------------|--------|---------|---------|---------|
|                           | 0° AoA |         | 10° AoA |         |
| Motor Position            | 50 MPH | 100 MPH | 50 MPH  | 100 MPH |
| Fully Extended            | X      | X       | X       | X       |
| Fully Retracted           | X      | X       | X       | X       |

**Table 10. Summary of Phase II wind tunnel tests performed with the generic missile store model. Each test was repeated five times.**

### 3.10.3 Post-Processing: Phase II.

#### 3.10.3.1 Converting Nano-25 Voltage Signals.

The unique 6 x 6 calibration matrix used to convert raw analog voltages recorded by the Nano-25 is shown in Table 11. The calibration matrix is multiplied by a column vector of voltage data ( $V_i$ ) to produce the forces and torques ( $F_i$  and  $T_i$ ), shown in Equation 23. Using MATLAB, a ‘for’ loop was created to accomplish the matrix multiplication necessary to convert the time-accurate voltage data that was collected. Data from the Nano-25 was sampled at 1000 Hz. The MATLAB code used can be found in Appendix B.

|          |          |          |          |          |          |
|----------|----------|----------|----------|----------|----------|
| 0.01666  | -0.00399 | -0.31744 | 2.98746  | 0.42269  | -3.00593 |
| 0.17884  | -3.47015 | -0.14035 | 1.72288  | -0.31903 | 1.75159  |
| 5.26167  | -0.04467 | 5.59050  | 0.20559  | 5.32144  | -0.10468 |
| 0.07209  | -1.22529 | 2.09820  | 0.72446  | -2.13718 | 0.63742  |
| -2.40927 | 0.01016  | 1.39990  | -1.01331 | 0.98241  | 1.08087  |
| 0.03166  | -1.11580 | 0.14224  | -1.09552 | 0.16628  | -1.10239 |

**Table 11. Calibration matrix for the Nano-25 provided by ATI for converting voltage signals to force and torque measurements.**

$$\begin{bmatrix} F_x \\ F_y \\ F_z \\ T_x \\ T_y \\ T_z \end{bmatrix} = \begin{bmatrix} 0.01666 & \cdots & -3.00593 \\ \vdots & \ddots & \vdots \\ 0.03166 & \cdots & -1.10239 \end{bmatrix} \begin{bmatrix} V_{Fx} \\ V_{Fy} \\ V_{Fz} \\ V_{Tx} \\ V_{Ty} \\ V_{Tz} \end{bmatrix} \quad (23)$$

### 3.10.3.2 Alignment and Taring of the Data.

Aligning the data was accomplished using the DMC-4020 controller and MATLAB. The controller was programmed to output a digital trigger that started data collection prior to trajectory motion, as well as stopped data collection two second after store motion was completed. Unfortunately, the trigger to stop collection of data was not precise for each measurement, and variations of up to 0.15 seconds between data sets were present. In order to ensure accurate alignment of the data, and remove forces sensed by the trajectory motion alone, a tare file was created for generic missile mission store at  $0.0^\circ$  and  $10.0^\circ$  angle of attack with the leading edge actuator active and the wind tunnel at 0.0 mph. Force and torque data collected during each experimental test were plotted alongside the tare file coinciding to the store mount used. The tare data was used as the reference point to align each data set taken with the wind tunnel active. This ensured that all of the test runs for a configuration were aligned with one another. Once aligned, the tare data was subtracted from the cases when the wind tunnel was operating, leaving only the forces that result from the cavity environment and shear layer. Figure 55 shows how data alignment was accomplished in MATLAB. The next step in post-processing was calculating the coefficients.

A filter for the force and moment data was created to improve data presentation

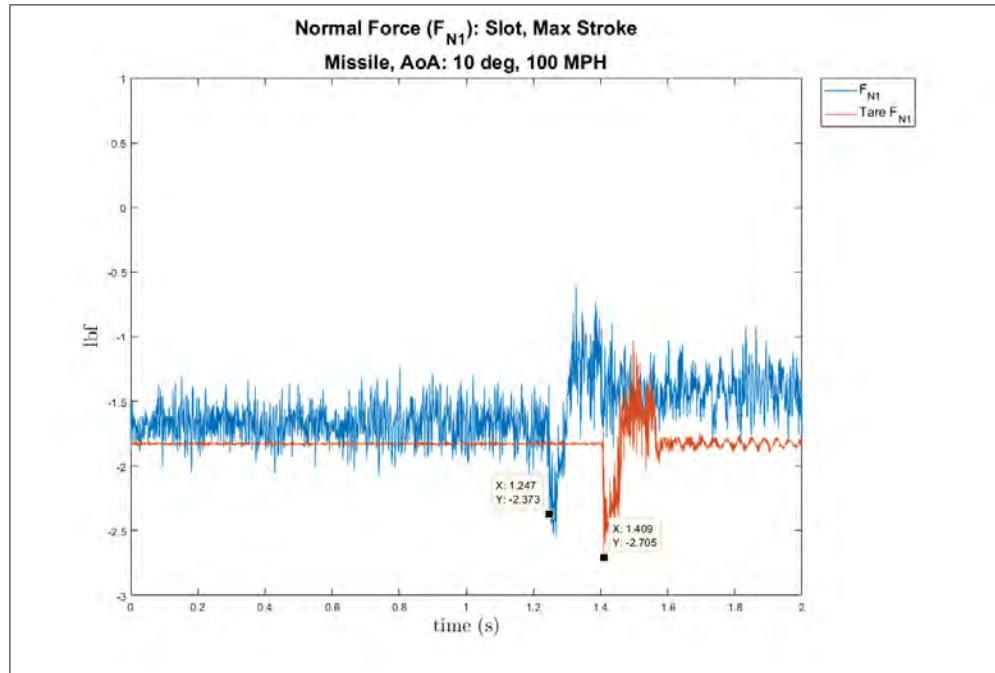
```

%Voltage Import
% Aligning the Tare (0 mph)
VoltageImport_0 = csvread('10deg_0mph.csv'); %Data Imported from .csv
VoltageUse_01 = VoltageImport_0(end-3000:end-1000,:); %Taking the 2 seconds of data around the event

% 50 mph Case Data Imported from .csv
VoltageImport_1 = csvread('10deg_Max_100mph_1.csv');
VoltageUse_1 = VoltageImport_1(end-3000:end-1000,:); %Taking the 2 seconds of data around each event

```

(a) Data Set imported to MATLAB and the 2 second around the event selected.



(b) Tare file and data set prior to alignment

Figure 52. MATLAB code prior to any visual alignment. Distance between the data cursors is used for alignment.

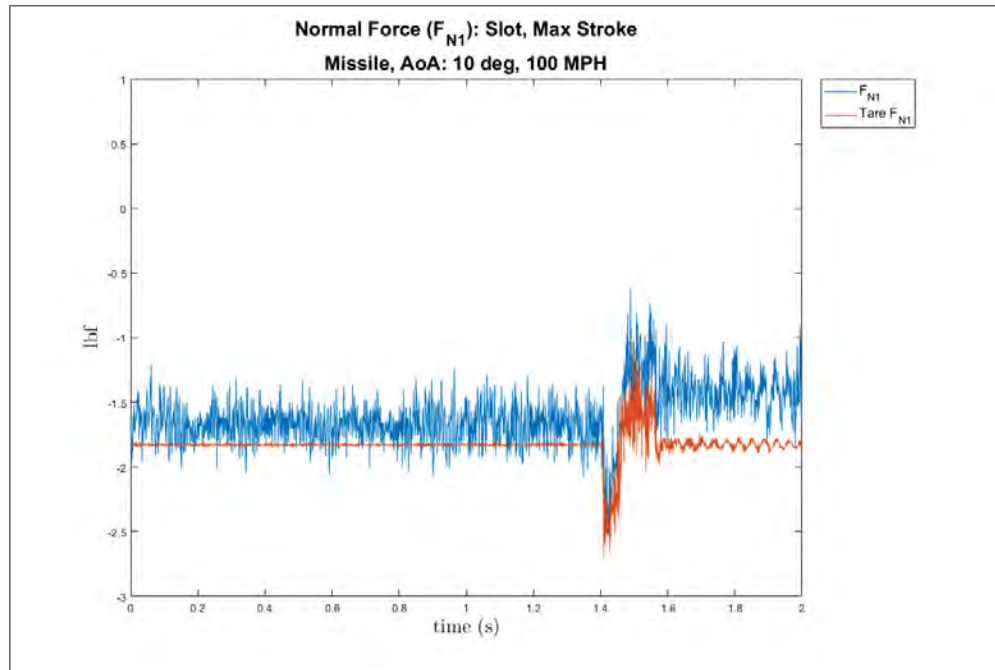
```

%Voltage Import
% Aligning the Tare (0 mph)
VoltageImport_0 = csvread('10deg_0mph.csv'); %Data Imported from .csv
VoltageUse_01 = VoltageImport_0(end-3000:end-1000,:); %Taking the 2 seconds of data around the event

% 50 mph Case Data Imported from .csv
VoltageImport_1 = csvread('10deg_Max_100mph_1.csv');
VoltageUse_1 = VoltageImport_1(end-3162:end-1162,:); %Taking the 2 seconds of data around each event

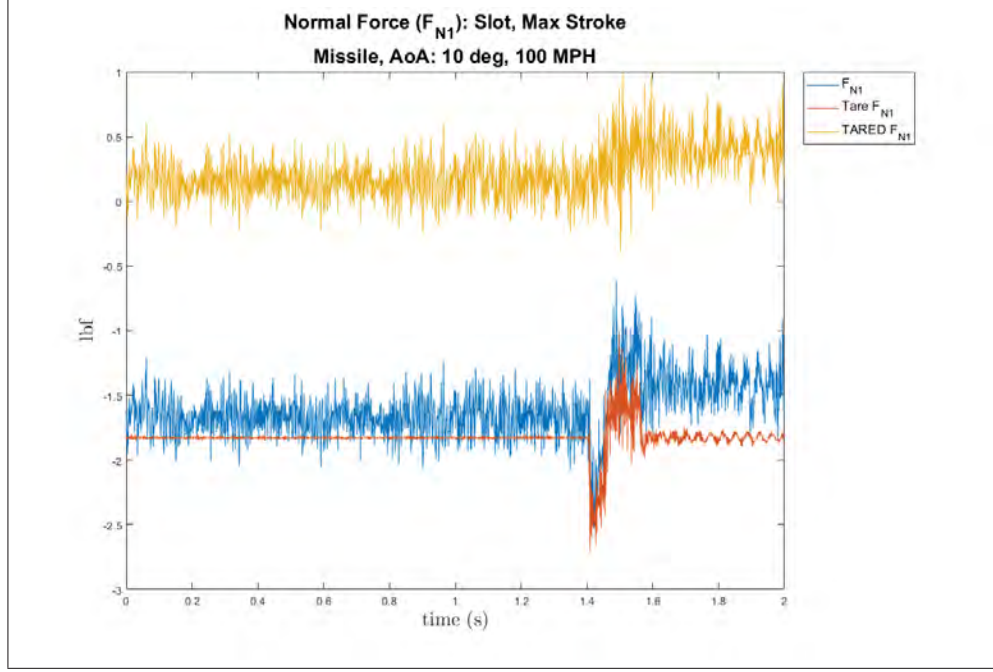
```

(a) Changes made to test data set using the difference between the data cursors identified previously.



(b) Tare file and data set after to alignment

**Figure 53. MATLAB after visual alignment**



(a) TARED data set.

**Figure 54. TARED data set shown after the tared data is subtracted from the test data**

and allow general trend of aerodynamic coefficients to be observed more clearly. Using MATLAB's design digital filter function ('designfilt'), a low-pass filter was created to reduce the jumps in data inherent to time-accurate measurements. Leveraging observations made by A. Bower, the 'cut-off frequency' and 'order' parameters were both varied to produce a filter line that best fits the noisy data based on visual inspection [4]. To normalize the cutoff frequency of 1.0 Hz for use in the MATLAB function, it was divided by half of the sampling rate, in accordance with Nyquist's Theorem. Through iteration, it was found that an 'order' of 60 provided a suitable filter line while maintaining data integrity. Figure 55 shows the code developed by A. Bower [4] for the MATLAB filter as well as an example of the unfiltered normal force data compared to the filtered data collected in this experimental study. The full MATLAB code used for post-processing the force and moment data is in the Appendix B.

```

Fs = 1000;    % sample rate in Hz
cof = 1;      % cufoff frequency in Hz
order = 60;   % -th Order of lowpas filter
Fnorm = cof/(Fs/2); % Normalized frequency

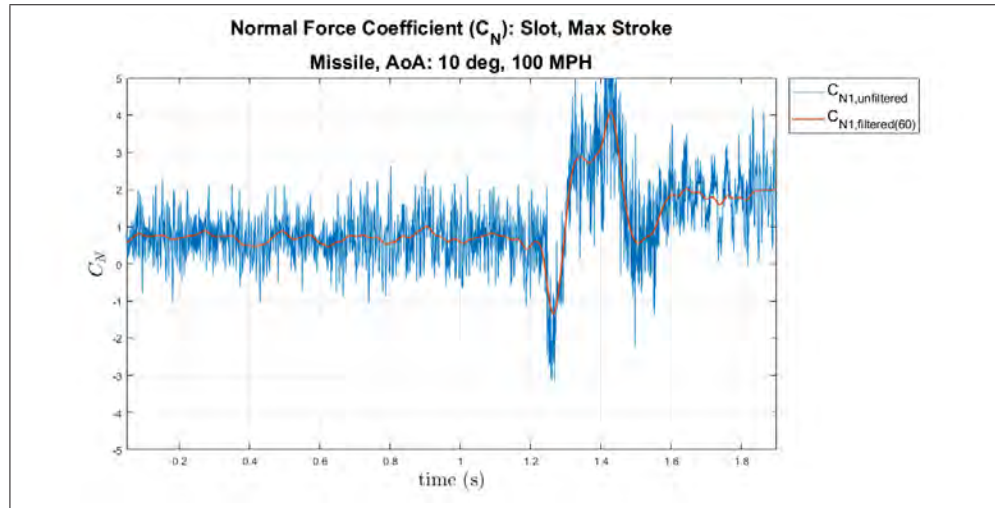
%MATLAB digital filter Function
df_1 = designfilt('lowpassfir','FilterOrder',order,'CutoffFrequency',Fnorm);
Delay_1 = mean(grpdelay(df_1)); % filter delay in samples

% Delay zeros concatenated with the input data
filtered_CN_1 = filter(df_1,[CN_1; zeros(Delay_1,1)]);

% Shift data to compensate for delay
filtered_CN_1 = filtered_CN_1(Delay_1+1:end);

```

(a) Filter developed in MATLAB



(b) Filtered normal force data superimposed on the unfiltered data.

Figure 55. Filter developed in MATLAB for the normal force data. The cut-off frequency and order were chosen based on best visual fit. [4]

The Reynolds number was calculated using air pressure and temperature at the time of collection and the results are shown in Table 12. The characteristic length used for Phase I was the cavity depth, and for Phase II it was the store diameter. The specific gas constant used in both calculations was  $287.05 \frac{J}{kg-K}$ . The MATLAB script is included in the Appendix B.

| Reynolds Number |             |             |             |
|-----------------|-------------|-------------|-------------|
|                 | 25 MPH      | 50 MPH      | 100 MPH     |
| Cavity Depth    | $9.8e^{+4}$ | $1.9e^{+5}$ | $3.9e^{+5}$ |
| Store Diameter  | $2.4e^{+4}$ | $4.7e^{+4}$ | $9.4e^{+4}$ |

**Table 12. Reynolds numbers calculated using the store diameter**

Mach number was calculated using a MATLAB script and the results are shown in Table 13. The adiabatic gas constant,  $\gamma = 1.4$ , was used for the speed of sound calculations. The MATLAB script is included in Appendix B.

| Mach Number |        |         |
|-------------|--------|---------|
| 25 MPH      | 50 MPH | 100 MPH |
| 0.0324      | 0.0647 | 0.1295  |

**Table 13. Machs used in the experimental study.**

### 3.11 Summary

The equipment utilized in the design and execution of the experiment were detailed in Sections 3.1 - 3.7.2. Afterwards, the two phases of the experiments were described. In the first phase, procedures to validate use of the triple wire using passive flow control devices and comparing velocity data with the literature were outlined. The triple wire was then used to characterize the effect that leading edge oscillatory blowing would have on the cavity environment. Five different leading edge devices were tested at both 25 mph and 50 mph: Slot, Diode 0.0, Diode 1.0, Diode



1.0a, and Diode 2.0. Post processing procedures detailed for Phase I included the use of mean and RMS data to develop linear profiles and contour plots of the u-, v-, and w-components. Additionally, the v- and w- components were used to generated vorticity plots. The raw, time-accurate, data was used to analyze the statistical properties and turbulent characteristics at different locations within the shear layer. The scope of Phase I is summarized in Tables 5 - 9.

In the Phase II, initiation of store release was synchronized with position of the oscillating linear motor. Force and torque data during the trajectory were collected using a Nano-25 force balance. During wind-tunnel testing the release was initiated at two different position of the oscillating motors cycle: fully retracted and fully extended. The release trajectory was conducted with the leading edge Slot device. Post processing procedures detailed for Phase II included the conversion of voltage data to force and torque measurements, transformation of force and torque data to the AIAA standard reference frame, determination of force and moment coefficients, as well as taring and filtering methods. The scope of Phase II is summarized in Table 10.

## IV. Analysis and Results

### 4.1 Chapter Overview

Experimental tests were conducted for both Phases, as described in Chapter III. In Phase I, linear and raster patterns were completed with the tri-axial probe and the resultant data was used to verify the effectiveness of the probe and then to characterize the leading edge devices described in Section 3.6. The first data presented from Phase I are linear profiles and contour plots comparing the influence of the passive leading edge device to a baseline cavity at  $x/L = 0.55$ . The velocity profiles, contour plots, and streamwise vorticity are compared with the literature to validate the selection of the tri-axial probe in this experimental study.

Next, a comparison of the leading edge Slot and leading edge Diode 0.0 was completed using linear profiles at  $x/L = 0.25, 0.55, 0.85$  and the with leading edge device active vs. inactive. Data was collected with the wind tunnel operating at both 25 mph and 50 mph. The 25 mph case is shown for these initial linear plots only to demonstrate the increased influence the leading edge devices have at reduced velocities. A comparison of the four fluidic Diode devices to the Slot at  $x/L = 0.55$  followed. The performance comparison of the Slot to the four Fluidic Diode designs is presented to indicate why Diode 1.0 was chosen for modification and further consideration in the study.

The first contour plots presented are a comparison of the velocity data from the Leading Edge Slot and Diode 1.0a at a wind tunnel speed of 50 mph and cavity location  $x/L = 0.55$ . A comparison of the Slot and Diode 1.0a's streamwise vorticity plots at 50 mph and  $x/L = 0.55$  follows. The contour plots of the velocity components, turbulence intensity, and streamwise vorticity focus on further analysis at the  $x/L = 0.55$  position because this closely approximates the location of the mission store's

center of gravity during Phase II.

After analysis of the velocity profiles and contour plots, the capacity to force the shear layer in a subsonic cavity to exhibit properties similar to that of a cavity in a transonic flow field is explored. Analysis of the energy frequency spectrum and velocity vs. time with the motor off and the motor on at  $x/L = 0.55$  and 50 mph is completed for the leading edge Slot at the  $z/D = 0.035$  position. The position at  $z/D = 0.035$  was chosen because it is the location of peak streamwise turbulence intensity and, therefore, where the greatest influence is expected to be seen. In Appendix A, the velocity vs. time plots generated from the raw data collected at  $z/D = 0.7, 0.385$ , and  $-0.14$  are also presented. These additional points were chosen to indicate the effective influence that the leading edge oscillatory devices have throughout the shear layer.

Phase II consists of the verification of synchronization between the oscillating linear motor and the store's trajectory motion using digital encoder position provided by the Galil Software as well as through visual observation with a high speed digital camera operating at 1000 frames per second. Additionally, force and torque data collected at a sample rate of 1000 Hz with a Nano-25 was used to generate axial force, normal force coefficient, and pitch moment coefficient plots for comparison of the completed experimental tests outlined in Table 10. Trends in the normal force data collected during tests with the mission store at  $10.0^\circ$  AoA were more readily identifiable, and will therefore represent the primary focus of Section 4.6.

## 4.2 Verification of Hot-Wire Suitability

Seeking to validate the use of the triple wire, the velocity data of a leading edge sawtooth spoiler, leading edge rectangular tab, and leading edge triangular tab was acquired for comparison to observations in the literature. The principal goal was

to determine if the velocity and turbulence intensity profiles indicated the expected alteration and consequential growth of the shear layer [60][46]. Figure 56 depicts how the mean velocity and turbulence intensity are affected by the sawtooth spoiler. In agreement with the literature, the figures clearly indicate that the leading-edge spoiler lifts the shear layer and causes an increase in thickness. In the mean streamwise velocity profiles for an empty cavity and sawtooth spoiler, looking at the  $u = 0.8U_\infty$  location, the spoiler has lifted the shear layer by an additional 53.0 mm over that observed for the empty cavity at the same location. Notably, the spanwise position of the acquired profile corresponding to a “peak” position in the center of the spoiler. Compared to the mean streamwise velocity components, the plots of the wall normal and floor normal mean components are on a significantly decreased scale, typically ranging from -0.05 to 0.05. The peak turbulence intensity for the streamwise, wall normal, and floor normal components (Figures 56b, 56d, 56f) all serve to reinforce the observation that the spoiler lifts the shear layer, with an increases in the z-direction where the peak magnitudes occur of 64.0 mm, 50.0 mm, and 50.0 mm, respectively. Additionally, the streamwise, wall normal, and floor normal turbulence intensities of the empty cavity and sawtooth spoiler were evaluated at the thickest part of the empty cavity’s shear layer for each plot. The location evaluated for each device corresponds to the  $u$  values of  $0.125U_\infty$ ,  $0.075U_\infty$ , and  $0.075U_\infty$ , respectively. The smallest change in shear layer thickness was the approximate 40.0% increase seen in the streamwise direction. The wall normal and floor normal directions indicated an increase in thickness of the shear layer of 157.0% and 90.0%, respectively. As expected, the sawtooth spoiler generated shear layer instabilities, resulting in the turbulence intensity increasing significantly in the wall normal and floor normal directions.

Of note, the velocity data for the empty cavity in the linear profile depicted in Figure 56 was taken early in the experimental process before the entire model

assembly was raised within the test section to accommodate the probe penetrating deeper into the cavity. As a result, the profile does not begin and end at the same  $z/D$  locations. However, both data sets are referenced to the same origin at the cavity lip line. Furthermore, the linear motor was installed, though not active, when velocity data was collected for the leading edge spoiler.

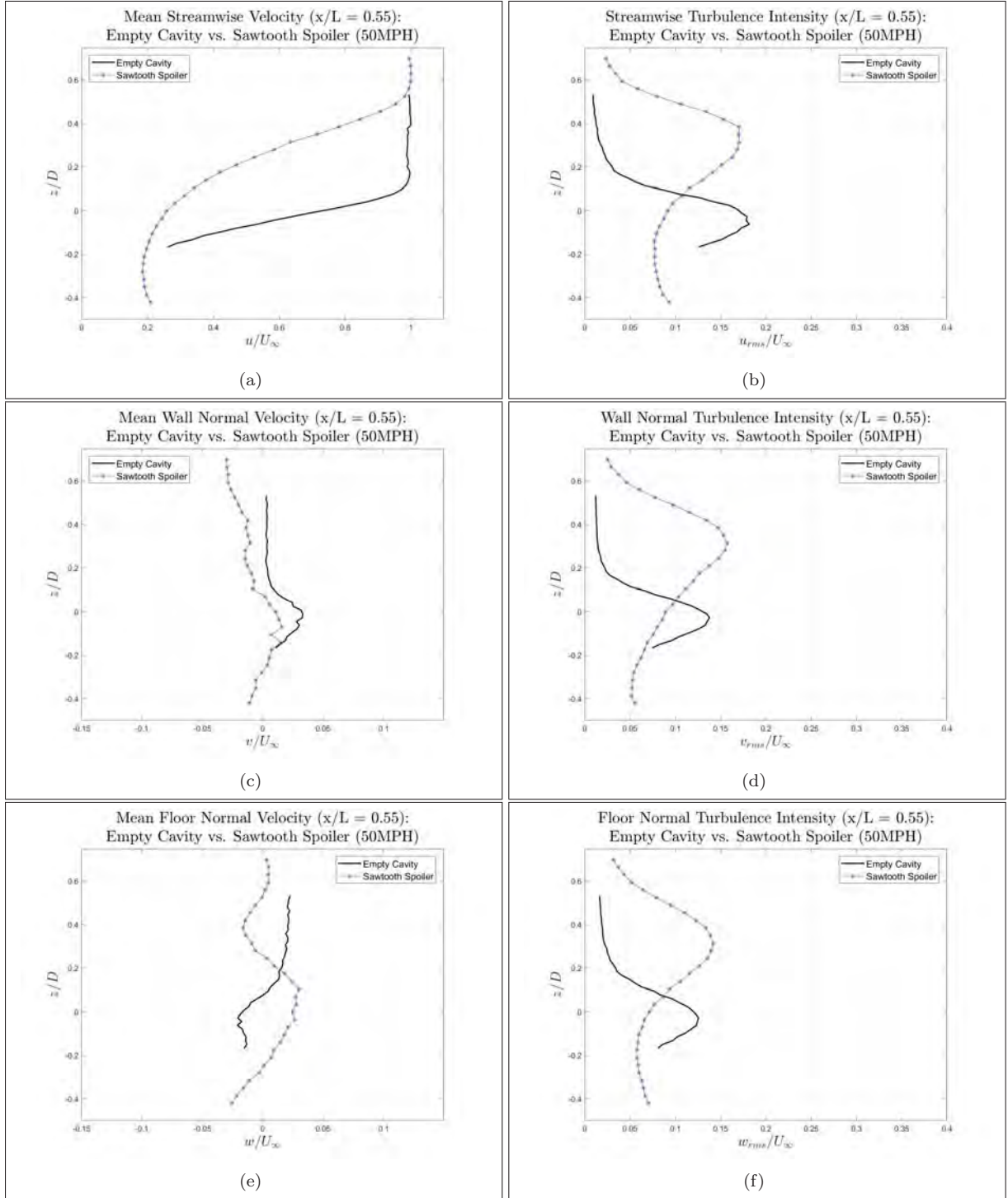


Figure 56. Mean and RMS values of velocity data collected from the linear profile for an empty cavity compared to a cavity with a leading edge sawtooth spoiler

Contour plots that depict the mean and turbulence intensity of all three velocity components were developed using the velocity data from the low-resolution raster patterns. A baseline cavity was utilized for comparison of the contour plots. Within the baseline cavity, the linear motor, piston, cylinder, and a leading edge device without an opening to the freestream were installed; thus ensuring similar internal cavity geometry. The contour plots for the baseline cavity and leading edge Sawtooth spoiler at 50 mph are shown in Figures 57 - 59. In all of the contour plots, the image presented is that of the streamwise flow coming towards the reader, i.e out of the page. For the Baseline mean streamwise case at  $x/L = 0.55$ , shown in Figure 57a, the data shows that the region between  $u = 0.40U_\infty$  and  $0.90U_\infty$  is typically between  $z/D = -0.10$  and  $0.20$ . By contrast, the Sawtooth spoiler leads to the same velocity span covering the region of  $z/D = 0.10$  to  $0.50$ . Some variation can be seen across the span, but overall trends are consistent with linear profiles in Figure 56.

The turbulence intensity in the streamwise direction for the Baseline case, shown in Figure 57c depicts the values that range from  $u = 0.15U_\infty$  to  $0.18U_\infty$  are typically located between  $z/D = -0.10$  and  $0.10$ . Comparatively, the same turbulence intensity values for the Sawtooth spoiler have been lifted to the region between  $z/D = 0.25$  and  $0.45$ . The location of peak turbulence intensities for the wall normal and floor normal components, seen in Figures 58c - 58d and 59c - 59d, are in strong agreement with the lifting of the shear layer indicated in the streamwise turbulence intensity plots. The Baseline cavity in the wall normal and floor normal directions has a region of peak turbulence intensity between values of  $z/D = -0.10$  and  $0.15$ , and the Sawtooth spoiler has peak turbulence intensities at an elevated location of  $z/D = 0.10$  and  $0.45$ .

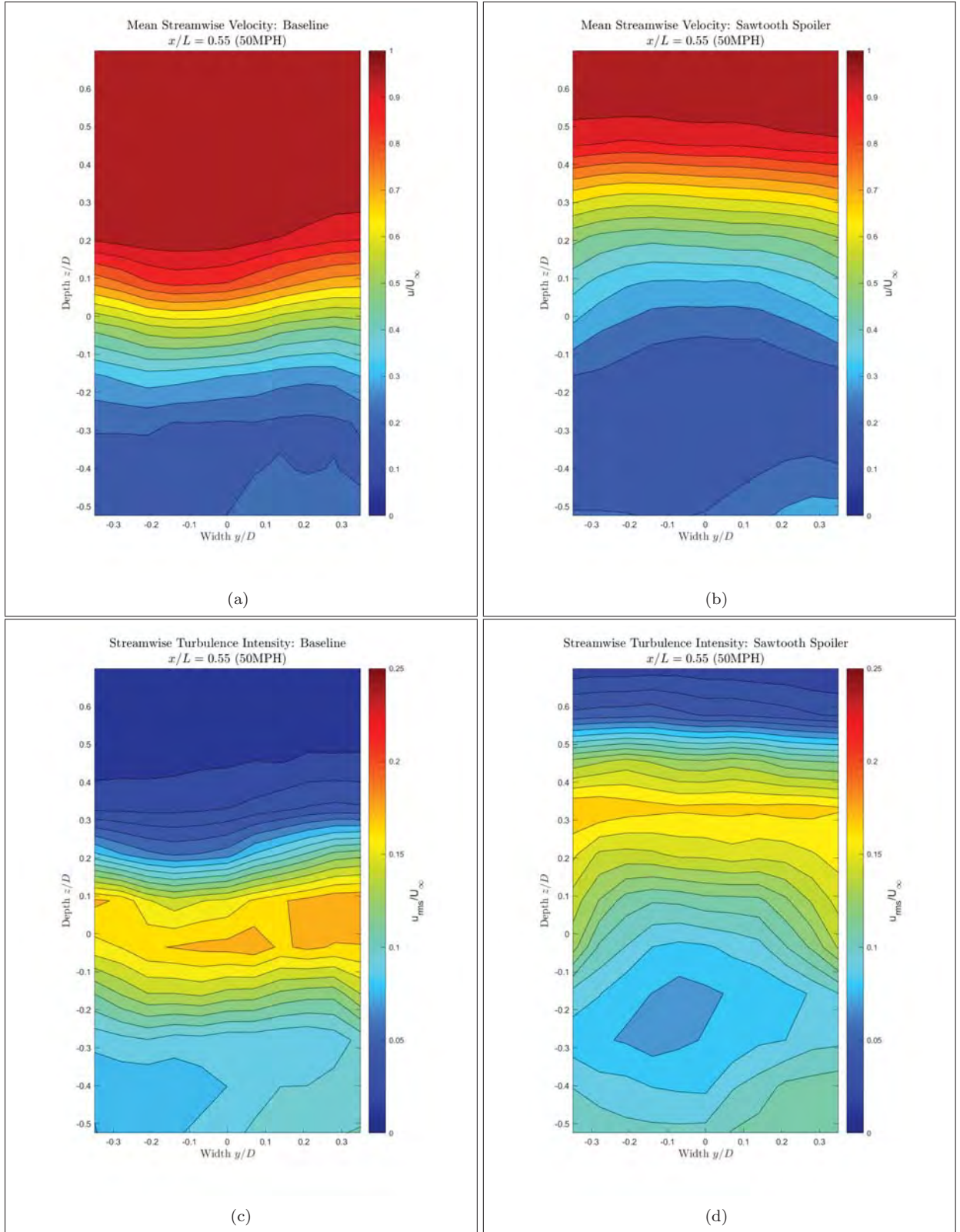


Figure 57. Contour Plots of the streamwise mean velocity and turbulence intensity using data collected from the raster pattern for a baseline cavity compared (left) to a cavity with a leading edge Sawtooth spoiler (right).



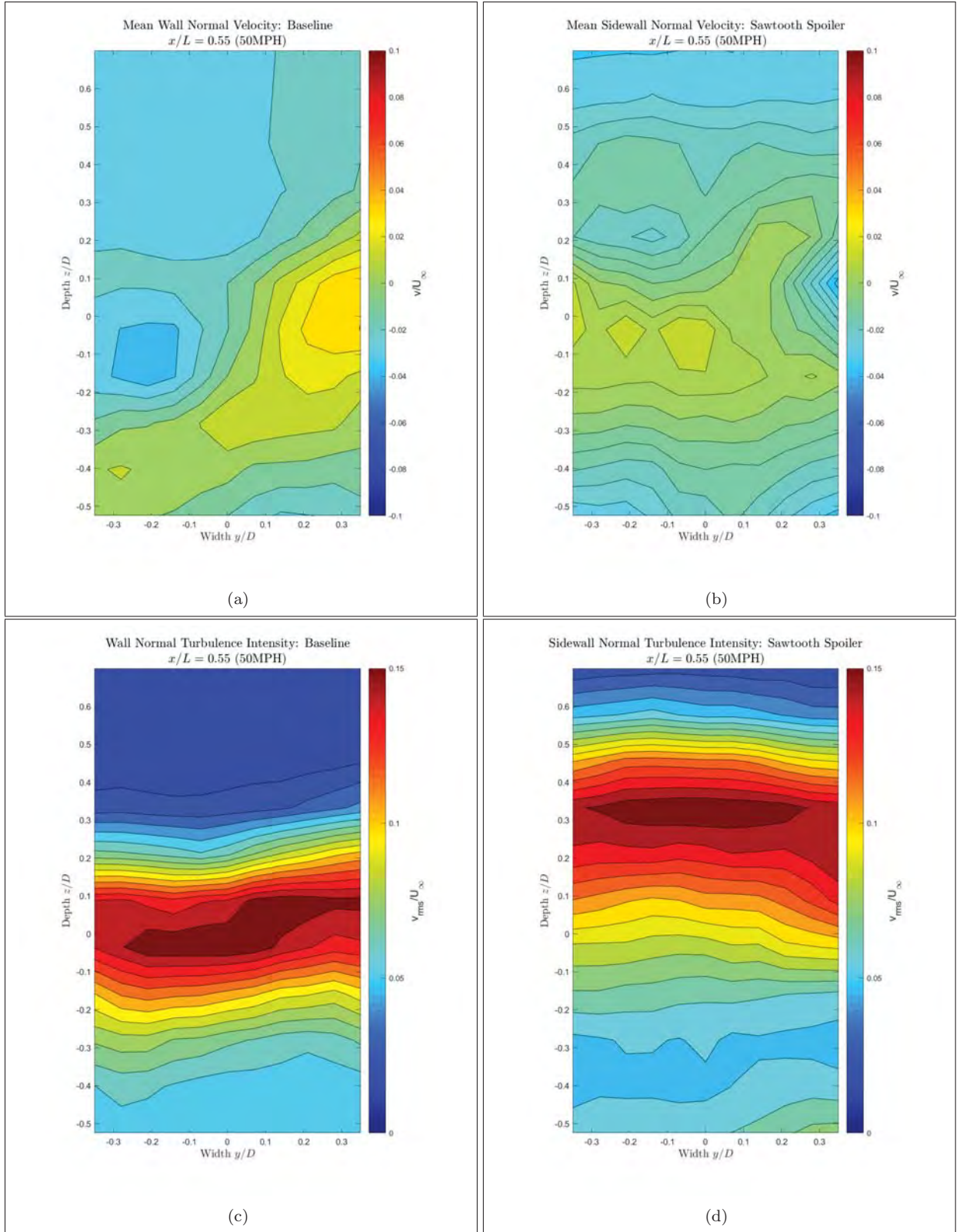


Figure 58. Contour Plots of the wall normal mean velocity and turbulence intensity using data collected from the raster pattern for a baseline cavity compared (left) to a cavity with a leading edge Sawtooth spoiler (right).

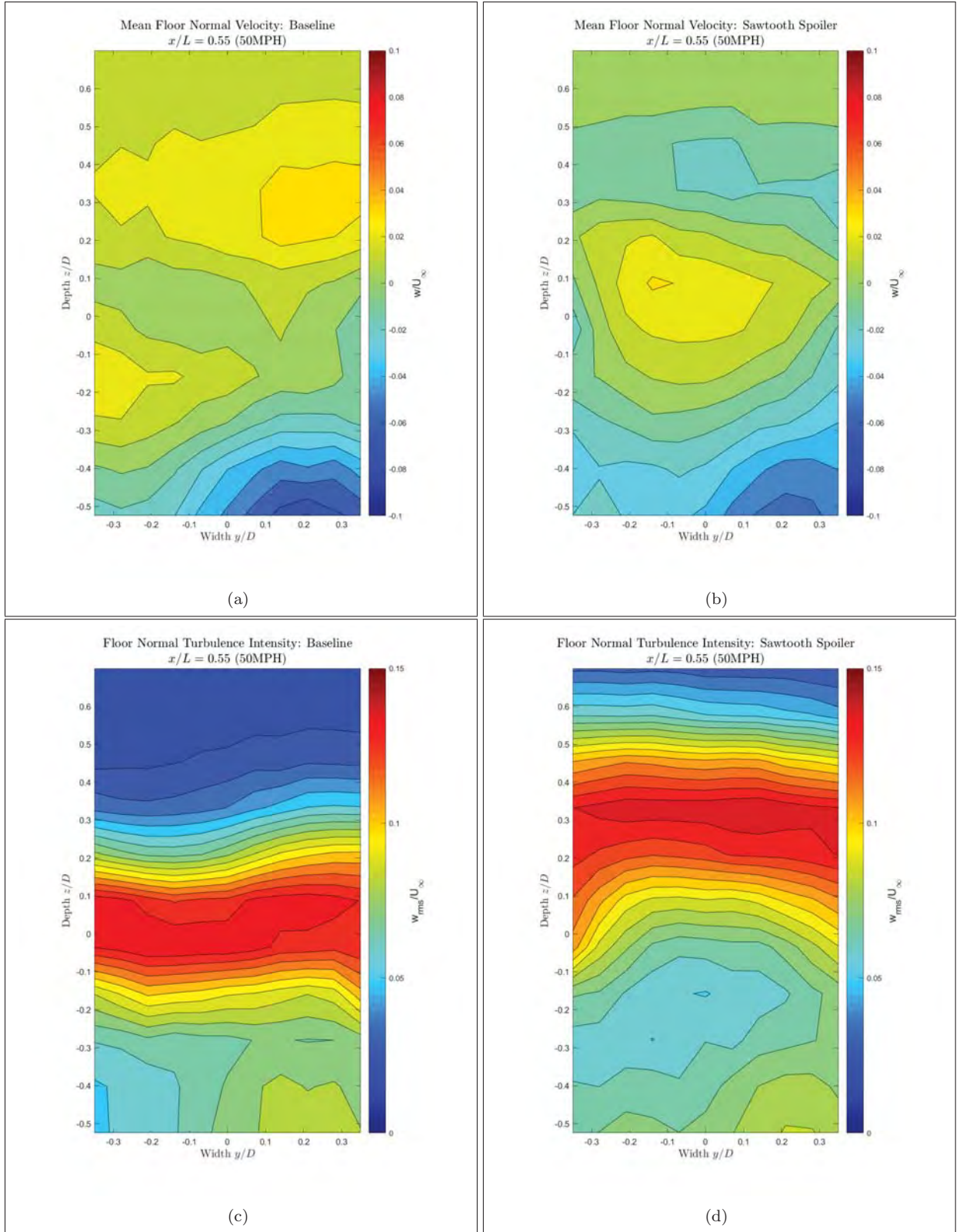


Figure 59. Contour Plots of the floor normal mean velocity and turbulence intensity using data collected from the raster pattern for a baseline cavity compared (left) to a cavity with a leading edge Sawtooth spoiler (right).

The  $v$ - and  $w$ -components of velocity data gathered by the tri-axial velocity probe allowed for the generation of streamwise vorticity plots. In order to verify the accuracy of the vorticity plots generated from hot-wire data, a rectangular tab and triangular tab were installed at the leading edge of the cavity. The resulting vorticity plots for the rectangular tab and triangular tab, generated using velocity data collected at cavity location  $x/L = 0.55$  and a wind tunnel speed of 50 mph, are shown in Figure 60. Both figures clearly indicate the well-developed, counter-rotating, vortical structures that are consistent with the literature [73][41][18][16]. Specifically, for the rectangular tab at  $x/L = 0.55$ , the plot indicates upward flow directly downstream of the tabs with each region of strong vorticity extending to a diameter of approximately  $0.4D$ , or 2 tab widths. For the triangular tab, the region of strong vorticity is somewhat less defined, and appears about 0.15 lower into the cavity. Additional, more comprehensive velocity data for the two tabs are given in Appendix A.

Overall, the velocity data collected for the sawtooth spoiler at  $x/L = 0.55$  corresponded to expectations. In agreement with Saddington et al. [45], the shear layer is vertically displaced, out of the cavity, and the turbulence data showed that the shear layer thickness was increased. The measurement of secondary flows ( $v$  and  $w$ ) did not indicate any clear patterns for the Sawtooth spoiler at this streamwise station. By contrast, the tri-axial velocity probe clearly revealed a strong pair of streamwise vortices for the two single tab cases.

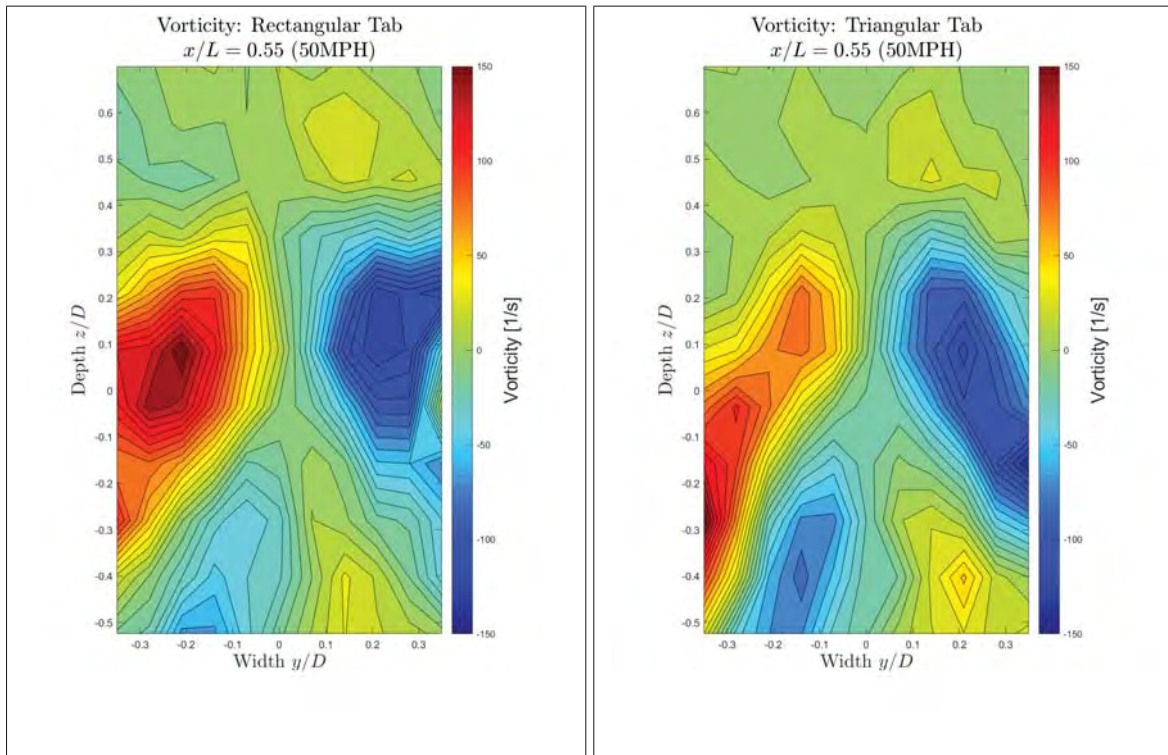


Figure 60. Streamwise vorticity plots using velocity data collected from the raster pattern for a rectangular tab(left) and a triangular tab(right).



### 4.3 Phase I: Linear Plots

#### 4.3.1 Linear Plots: Slot vs. Diode 0.0 (50 mph).

Velocity data of the Slot and Diode 0.0 at  $x/L = 0.25, 0.55$ , and  $0.85$  is presented in Figures 61, 62, 63, and 64. Each figure depicts the change in velocity data when the leading edge actuator is active versus inactive. Figure 61 presents the streamwise mean velocity profiles and Figure 62 contains the streamwise turbulence intensity plots. Figures 63 and 64 depict the wall normal and floor normal turbulence intensities, respectively, for the Slot and Diode 0.0. The wall normal and floor normal mean velocity components are omitted from this section for conciseness but can be found in Appendix A.

The mean streamwise plots shown in Figures 61a and 61b are representative of when the leading edge actuator is active. In each measurement set, operating the motor leads to an increase in the thickness of the shear layer. Furthermore, the shear layer is generally lifted by an approximate value of  $z/D = 0.05$  to  $0.1$  at all three observed positions within the cavity, corresponding to roughly  $5.0$  to  $10.0$  mm. At positions  $x/L = 0.25$  and  $0.55$ , the Slot indicates a slightly greater displacement of the shear layer above the cavity than Diode 0.0, with the slot lifting the shear layer by roughly  $10.0$  mm at these locations and Diode 0.0 only lifting the shear layer by approximately  $5.0$  mm. The influence that each device has on the shear layer is much more apparent in the streamwise turbulence intensity data, shown in Figure 62.

The peak magnitude of streamwise turbulence intensity at  $x/L = 0.25$  for both the Slot and Diode 0.0 more than doubles, from approximately  $u = 0.13U_\infty$  to  $u = 0.30U_\infty$ . The peak magnitude of turbulence intensity At  $x/L = 0.55$ , with the leading edge device active for both devices, increases from approximately  $u = 0.16U_\infty$  to  $u = 0.28U_\infty$ , or roughly  $1.75$  times the value seen with the device inactive. Data collected further aft in the cavity at  $x/L = 0.85$  indicates a greatly reduced influence by

the leading edge devices on peak magnitude of the turbulence intensity, seen by an increase of only 25.0% when the leading edge device is active versus inactive.

When both the Slot and Diode 0.0 are active, the level of increased thickness for the region of turbulence intensity in the streamwise direction at  $x/L = 0.25$  and  $0.55$  is proportional to the degree of increase observed in the peak magnitudes. Assessing the thickness at  $u = 0.05U_\infty$  for inactive and active cases, it can be seen that Diode 0.0 has a slightly larger increase in thickness than the Slot at  $x/L = 0.25$ , with measured increases of 20.0 mm and 15.0 mm, respectively. Conversely, the Slot displayed a slightly greater capacity to increase shear layer thickness at  $x/L = 0.55$ , indicating a marginal increase of 30.0 mm versus 25.0 mm. At the  $z/D = 0.85$  position, the increase in turbulence intensity and thickness is not as great as at the two forward positions, particularly in Diode 0.0 below the cavity lip line,  $z/D = 0.0$ .

Whereas the turbulence intensity in the streamwise direction showed an increase, the plots of turbulence intensity for the wall normal and floor normal components indicate that, with the leading edge devices active, the peak turbulence intensity typically decreases slightly while the thickness of the shear layer increases. The increase in shear layer thickness is comparable to what was observed for the streamwise components. However, the change in turbulence intensity is not. Particularly at  $x/L = 0.25$  and  $x/L = 0.55$ , where the peak turbulence intensity at the two forward positions for both actuators exhibits a decrease of approximately 20%. As in the streamwise measurements, Diode 0.0 has a slightly greater capacity to increase the thickness of the turbulence region at  $x/L = 0.25$  while the Slot has a greater influence at  $x/L = 0.55$ .

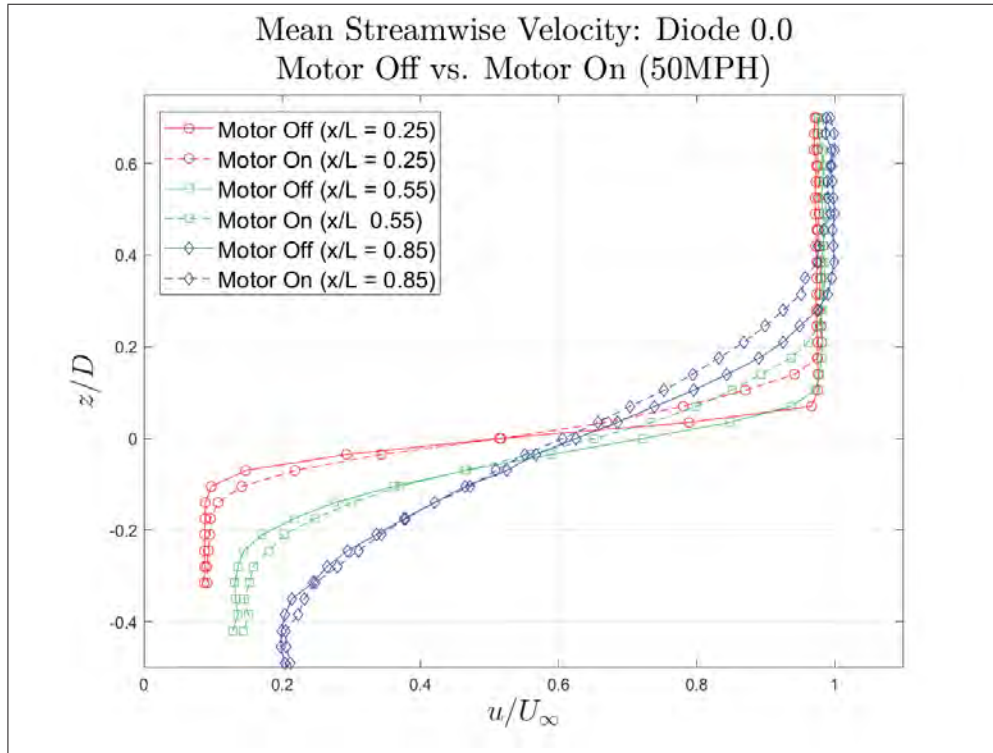
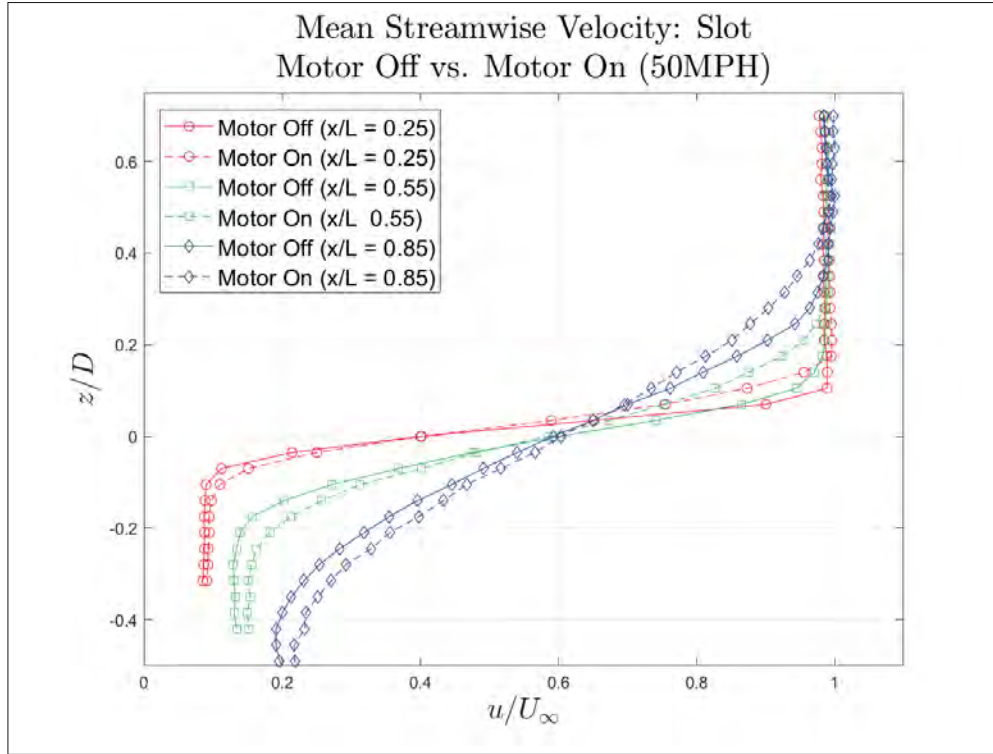
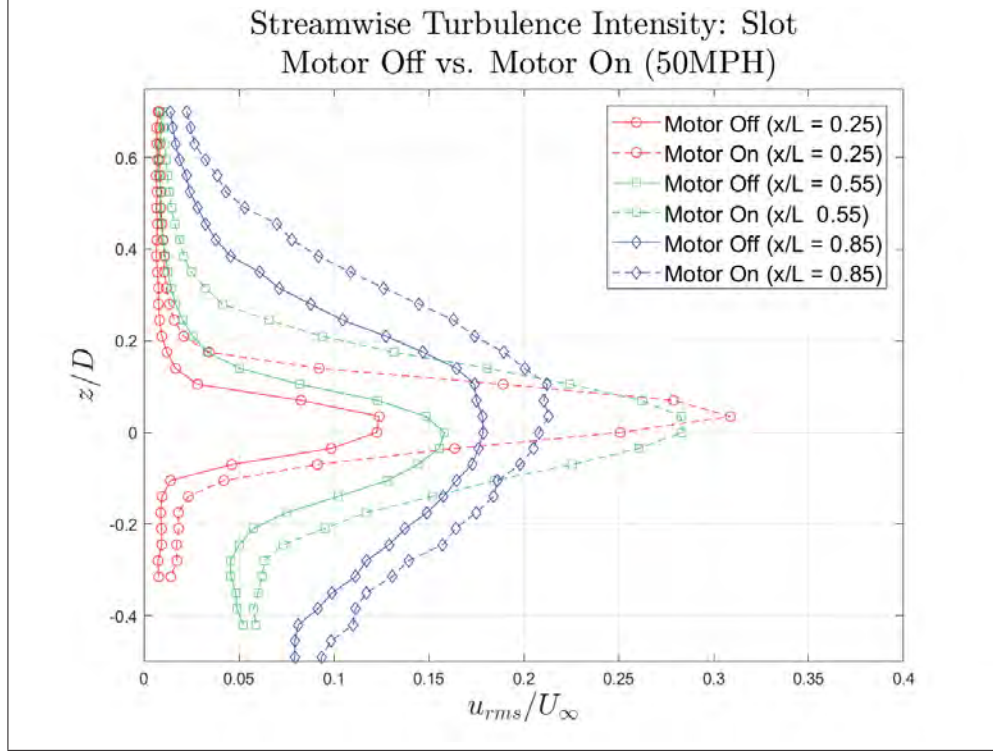
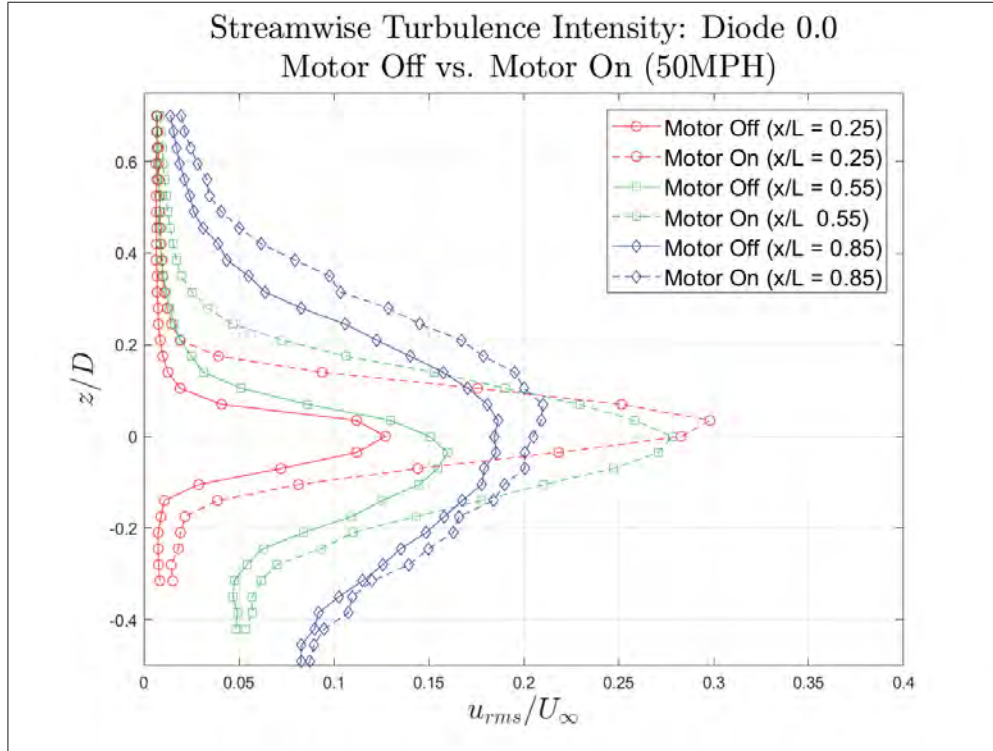


Figure 61. Mean streamwise velocity data collected from linear profiles at  $x/L = 0.25$ ,  $0.55$ , and  $0.85$  of the cavity at 50 mph. The data depicted shows the change at each position when the oscillating linear motor is off and on.



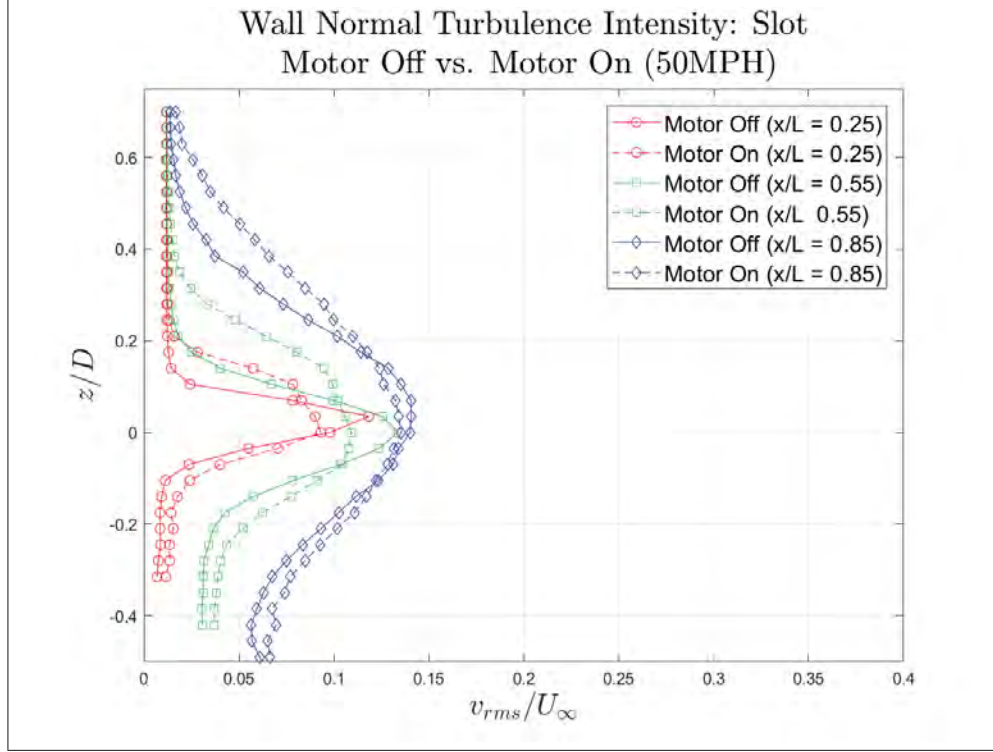
(a) Streamwise Turbulence Intensity: Slot (50mph)



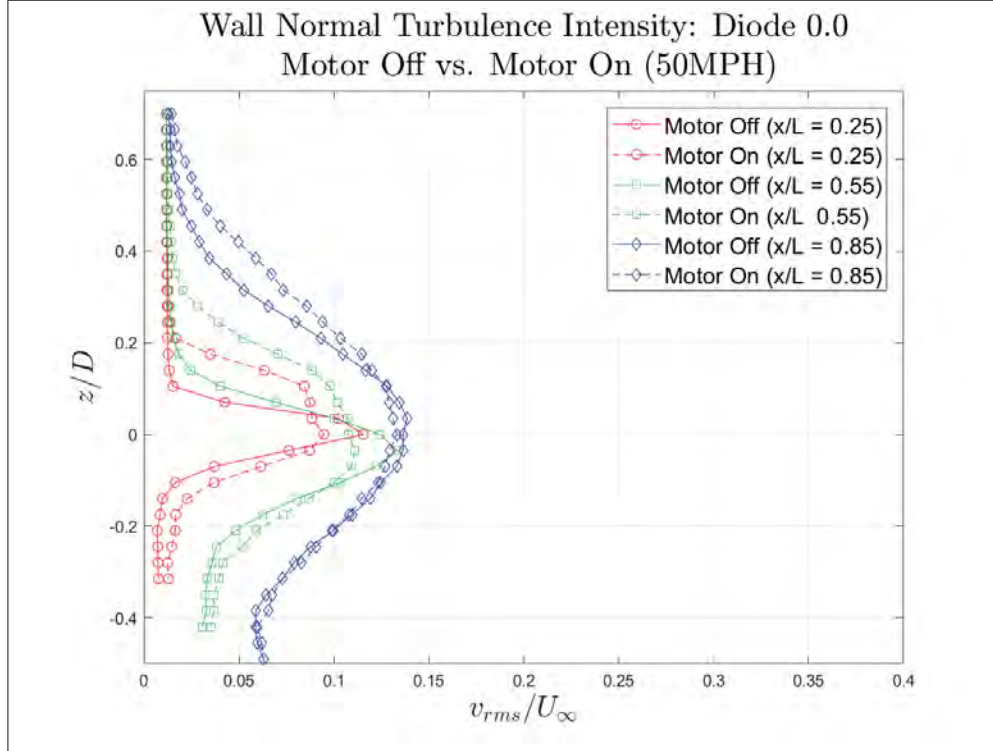
(b) Streamwise Turbulence Intensity: Diode 0.0 (50mph)

**Figure 62.** Turbulence intensity values of the streamwise velocity data collected from linear profiles at  $x/L = 0.25, 0.55$ , and  $0.85$  of the cavity at 50 mph. The data depicted shows the change at each position when the oscillating linear motor is off and on.





(a) Wall Normal Turbulence Intensity: Slot (50mph)



(b) Wall Normal Turbulence Intensity: Diode 0.0 (50mph)

**Figure 63.** Mean and turbulence intensity values of the wall normal velocity data collected from linear profiles at  $x/L = 0.25, 0.55,$  and  $0.85$  of the cavity at 50 mph. The data depicted shows the change at each position when the oscillating linear motor is off and on.

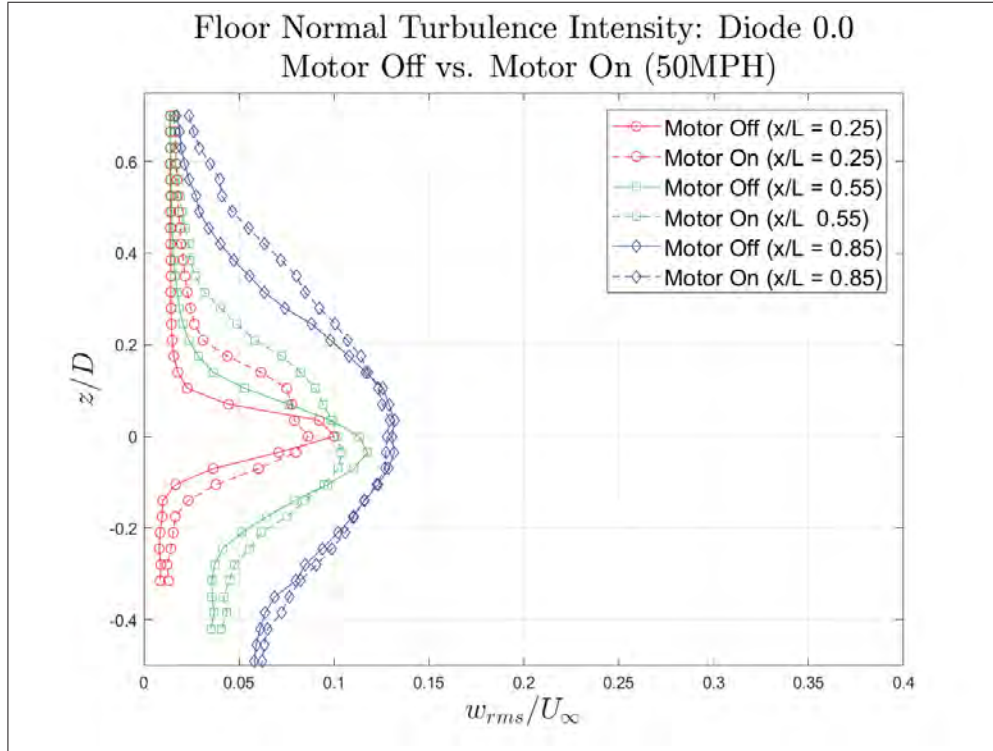
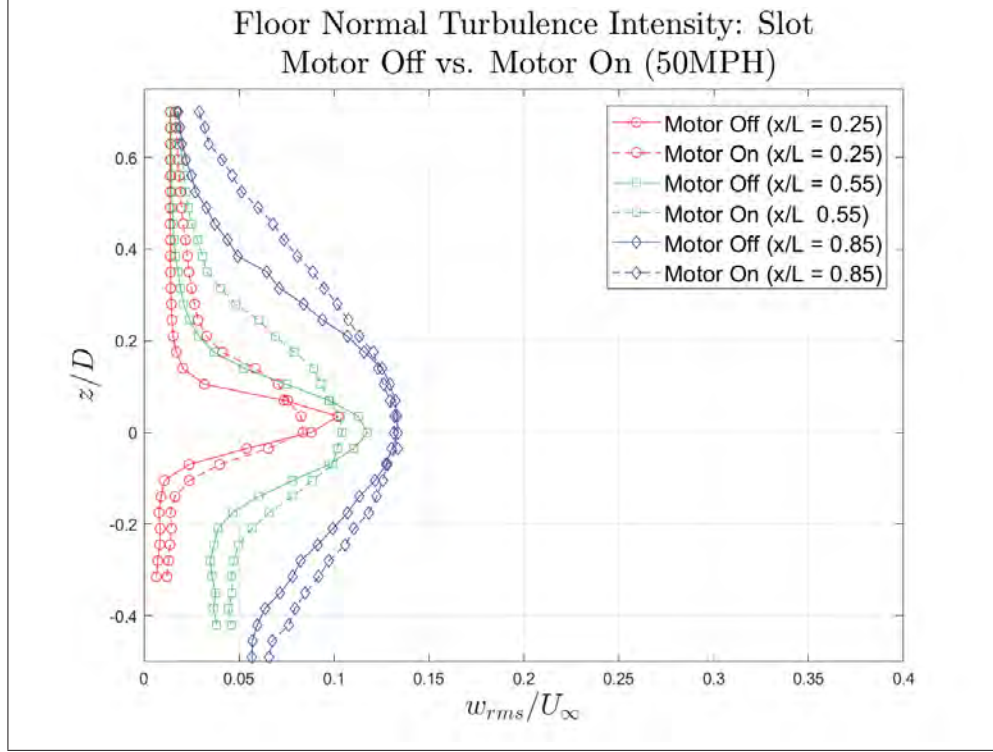


**Figure 64.** Mean and turbulence intensity values of the floor normal velocity data collected from linear profiles at  $x/L = 0.25$ ,  $0.55$ , and  $0.85$  of the cavity at 50 mph. The data depicted shows the change at each position when the oscillating linear motor is off and on.

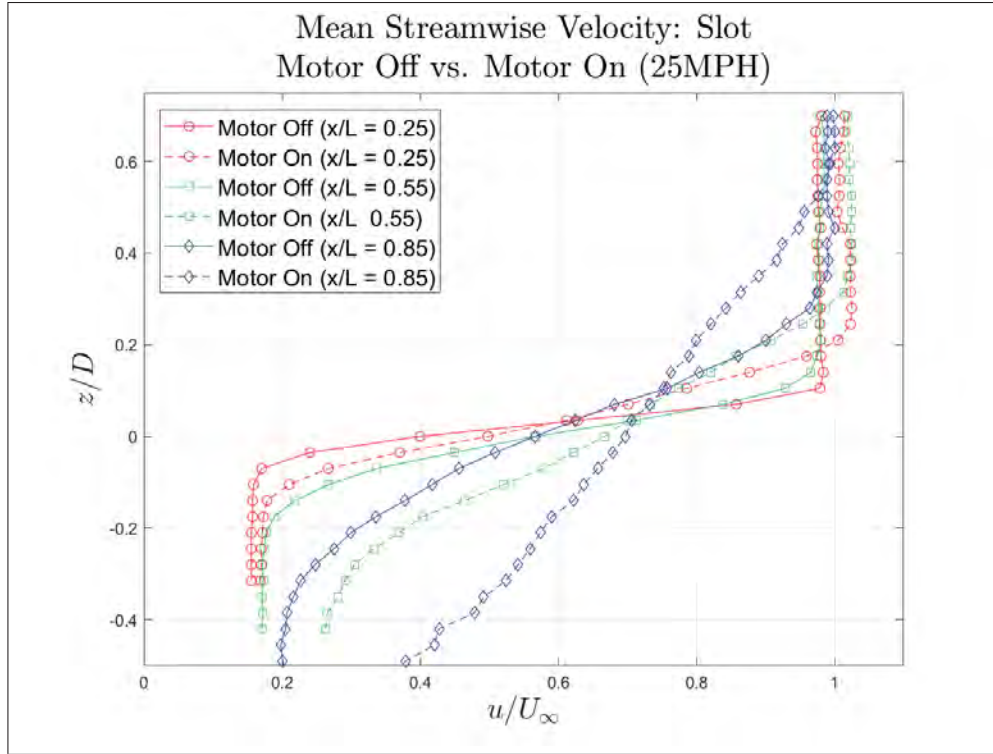
### 4.3.2 Linear Plots: Slot vs. Diode 0.0 (25 mph).

The arrangement of the plots for the 25 mph cases are the same as the 50 mph cases. The 25 mph cases are presented to highlight the increased influence that the leading edge oscillatory devices could have on the cavity shear layer if the relative velocity forced from the leading edge device is increased with respect to the flow field. Because of mechanical limitations and design constraints for this experimental study, the change in ratio between forced air and the flow field velocity was accomplished by reducing wind tunnel speed, as opposed to recreating a device that could force air at a higher velocity. One major differences between the 25 mph case and the 50 mph cases is the increased influence of the leading edge devices visible at the  $x/L = 0.85$  location. This can be seen clearly in the mean streamwise velocity plots of 65a and 65b, where the slope increases and the characteristic flattening near  $z/D = 0.0$  of the  $x/L = 0.25$  and  $x/L = 0.55$  positions is lost.

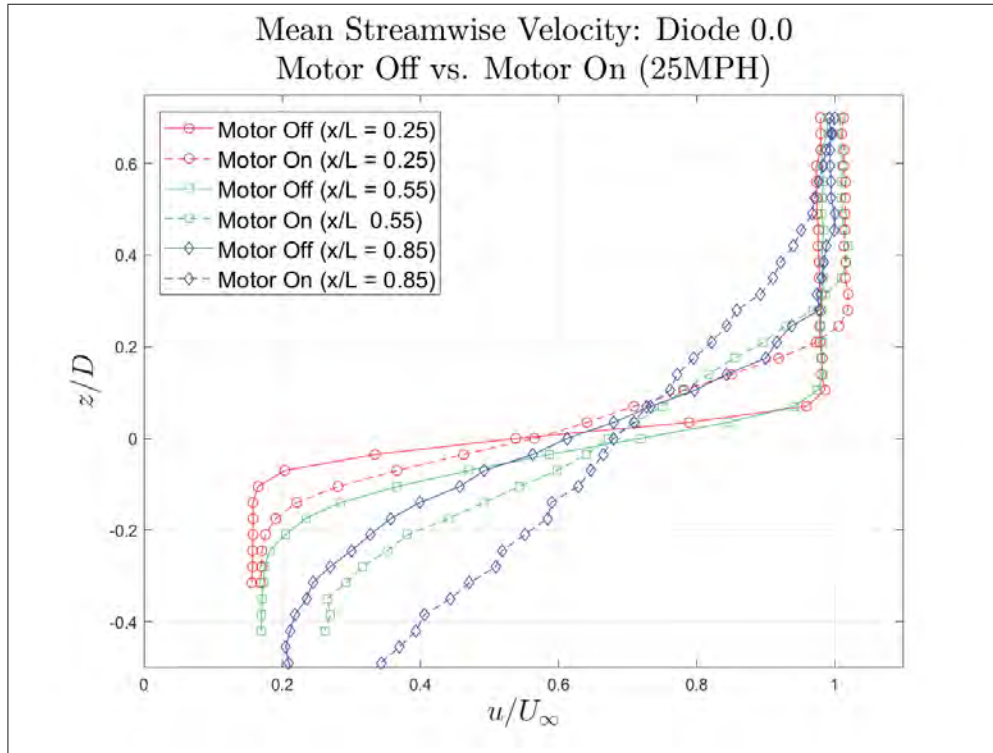
The plots of streamwise turbulence intensity, 66a and 66b, further emphasize the increased influence that the leading edge blowing devices have across the entire length of the cavity. At  $x/L = 0.25$  and  $0.55$ , the peak magnitudes of turbulence intensity with the motor on show an increase of roughly 15% over the 50 mph case. The increase in the thickness of the shear layer from the 25 mph case to the 50 mph case, depicted in the Figures 66a and 66b, is also approximately 15%, similar to the level of increase seen in the peak magnitude of turbulence intensity. Reflective of the mean streamwise plots, the influence seen with the motor on at  $x/L = 0.85$  is significant enough that the depth to which the probe penetrated the cavity was not sufficient to capture velocity data at a turbulence intensity less than  $u = 0.05U_\infty$ . Additionally, unlike the 50 mph case, Diode 0.0 shows a greater increase in thickness than the Slot at both the  $x/L = 0.25$  and  $x/L = 0.55$  positions.

The wall normal and floor normal plots for the Slot and Diode 0.0, seen in Figures

67 and 68, depict a noticeably different profile for turbulence intensity compared to the 50 mph case. Primarily, the presence of two peaks of magnitude at both  $x/L = 0.25$  and  $x/L = 0.55$ . The single peak magnitude of turbulence intensity, observed when the Slot and Diode 0.0 are inactive, occurs at approximately  $z/D = 0.0 \pm 0.035$ . However, once the leading edge device is active, peaks in magnitude can be seen forming above and below the lip line at  $z/D = 0.14$  and  $z/D = -0.035$  for both Diode 0.0 and the Slot. Between the two peaks, a reduction in turbulence intensity of nearly 20% occurs. The cause of this unique profile in the wall normal and floor normal data is currently unknown, further complicated by the strong similarities in the profiles for the two actuators, despite their vastly different blowing patterns and internal geometry.

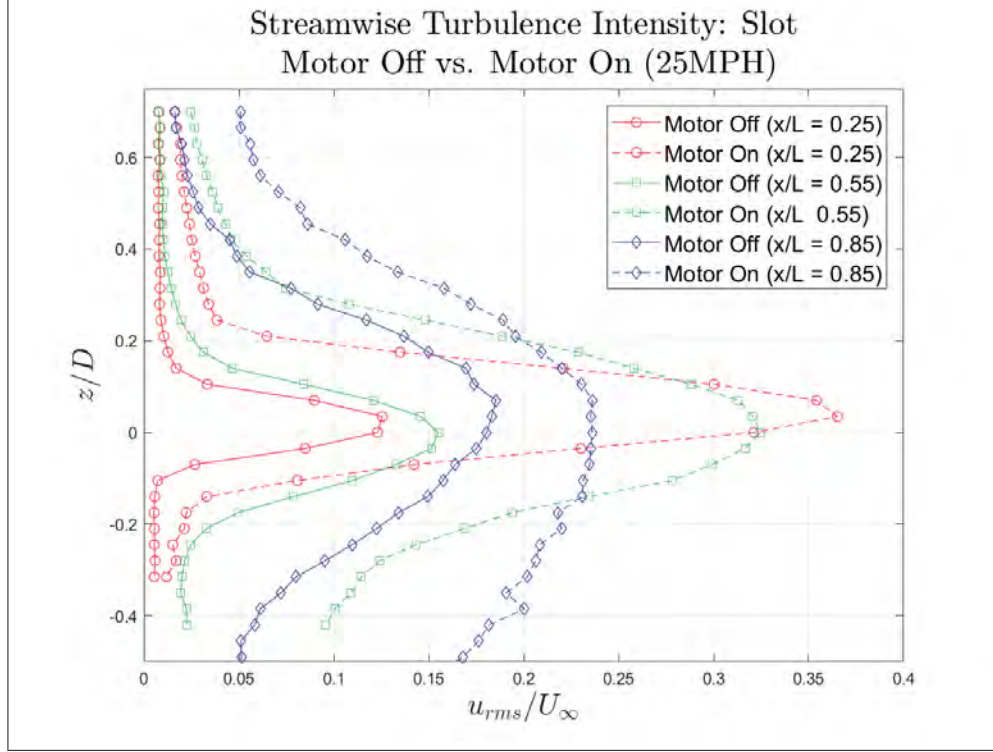


(a) Mean Streamwise Velocity: Slot (25mph)

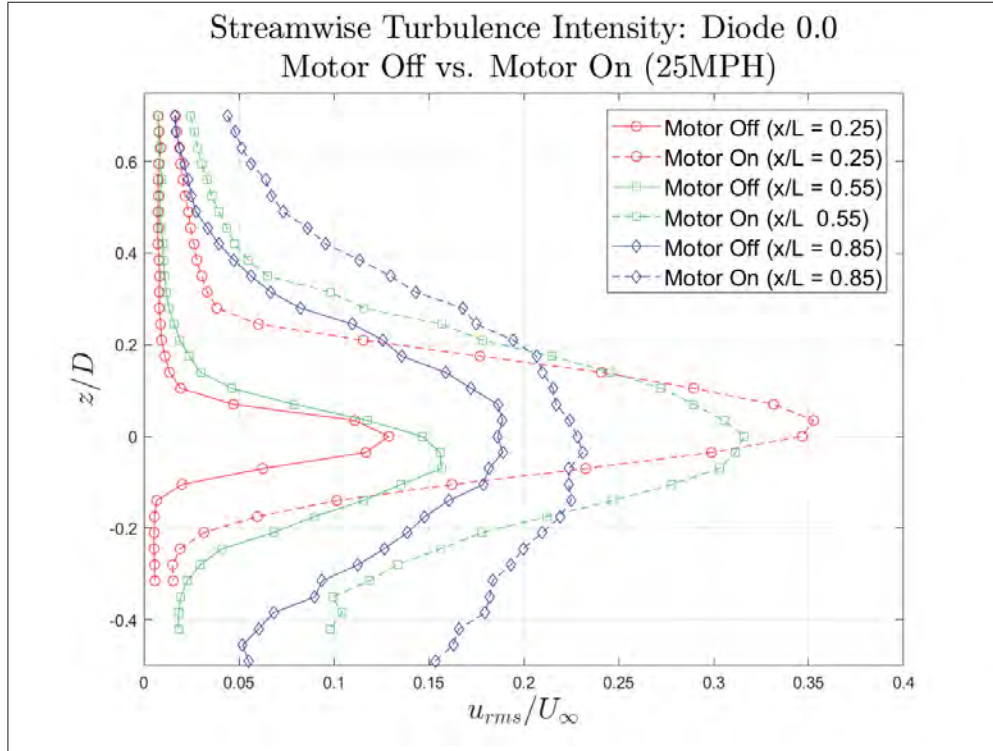


(b) Mean Streamwise Velocity: Diode 0.0 (25mph)

Figure 65. Streamwise mean velocity data collected from linear profiles at  $x/L = 0.25$ ,  $0.55$ , and  $0.85$  of the cavity at 25 mph. The data depicted shows the change at each position when the oscillating linear motor is off and on.



(a) Streamwise Turbulence Intensity: Slot (25mph)



(b) Streamwise Turbulence Intensity: Diode 0.0 (25mph)

**Figure 66.** Turbulence intensity values of the streamwise velocity data collected from linear profiles at  $x/L = 0.25, 0.55$ , and  $0.85$  of the cavity at 25 mph. The data depicted shows the change at each position when the oscillating linear motor is off and on.



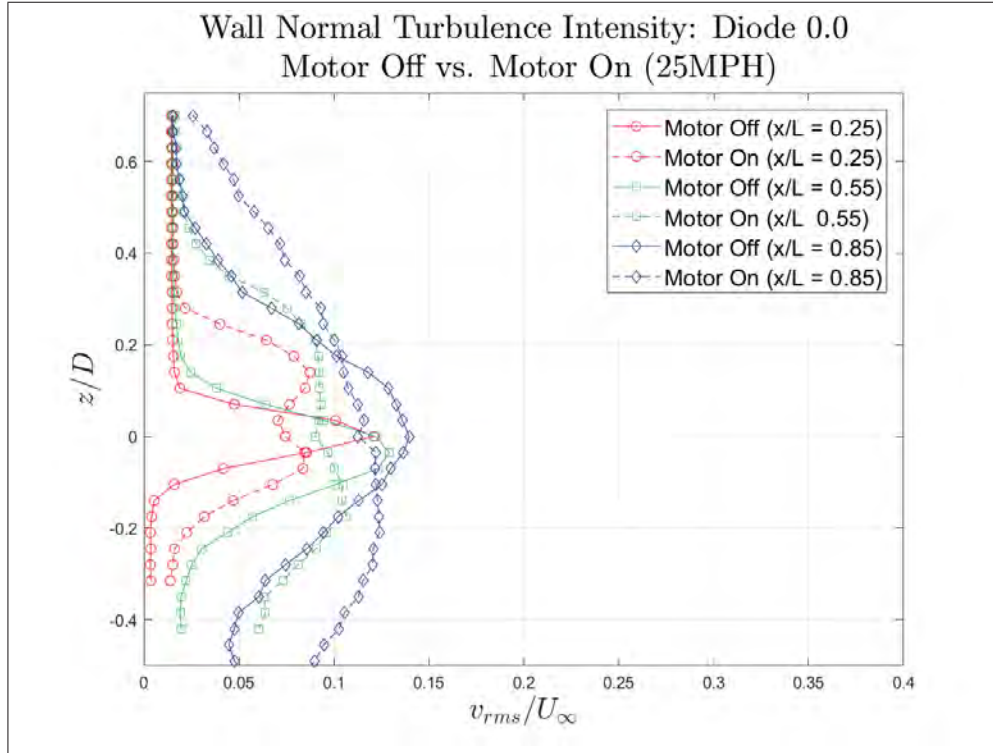
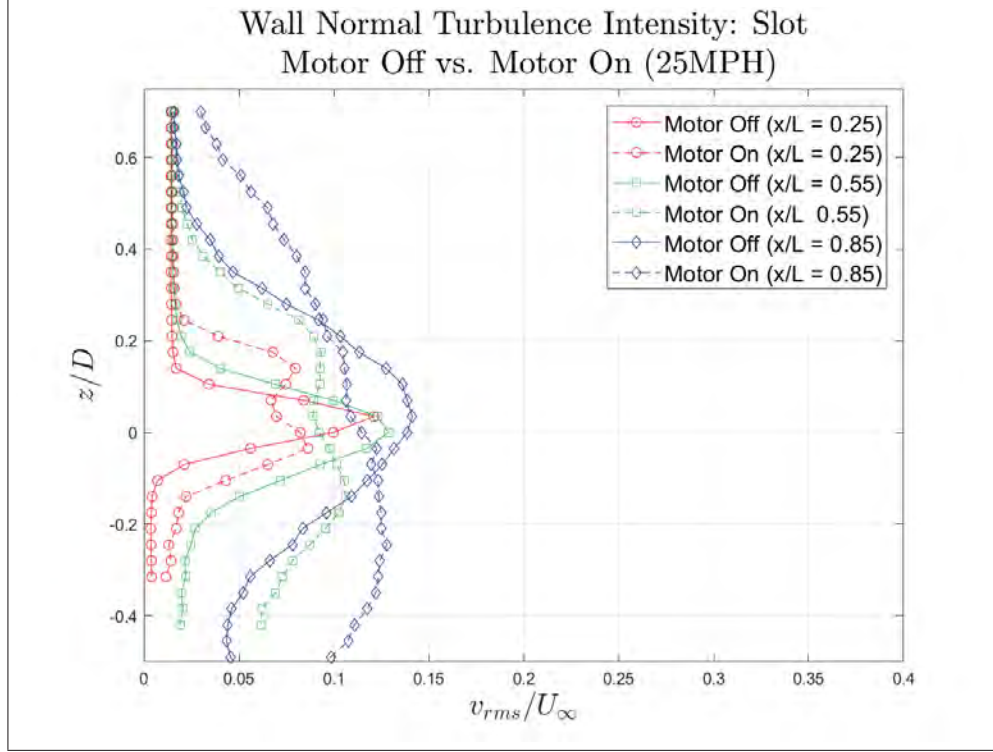
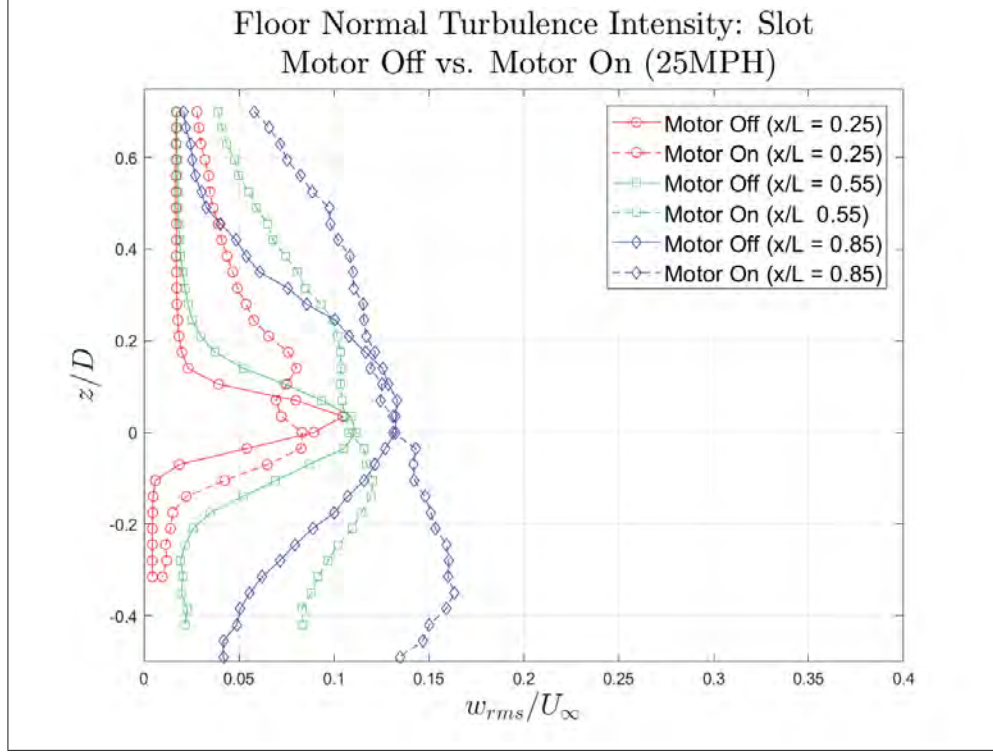
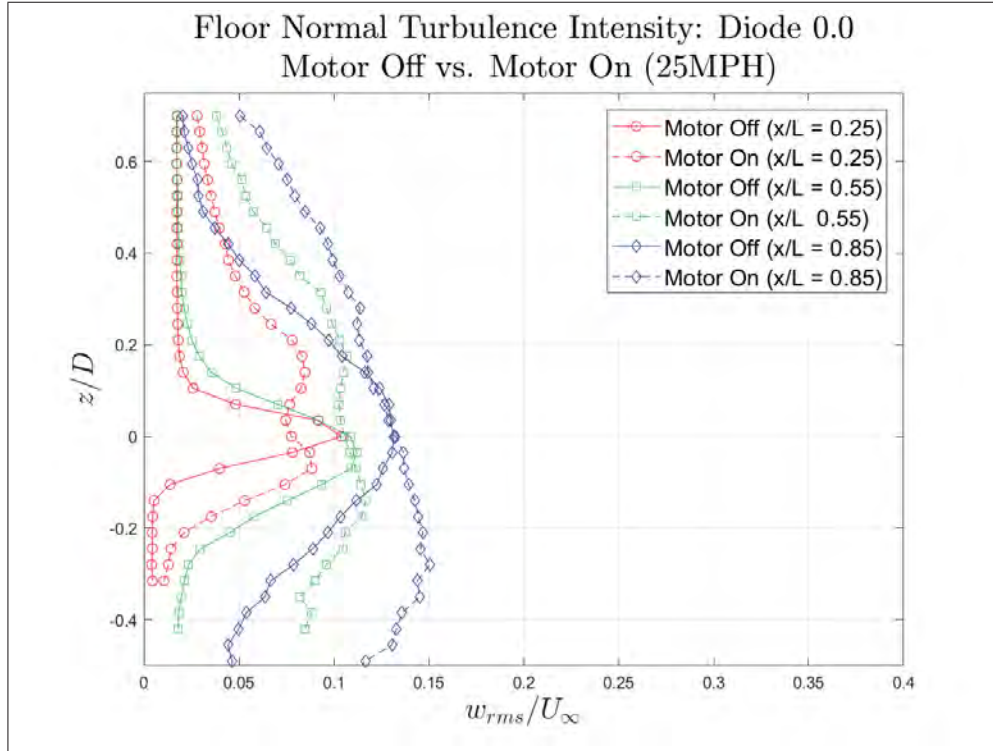


**Figure 67.** Turbulence intensity values of the wall normal velocity data collected from linear profiles at  $x/L = 0.25, 0.55$ , and  $0.85$  of the cavity at 25 mph. The data depicted shows the change at each position when the oscillating linear motor is off and on.



(a) Floor Normal Turbulence Intensity: Slot (25mph)



(b) Floor Normal Turbulence Intensity: Diode 0.0 (25mph)

**Figure 68.** Turbulence intensity values of the floor normal velocity data collected from linear profiles at  $x/L = 0.25, 0.55$ , and  $0.85$  of the cavity at 25 mph. The data depicted shows the change at each position when the oscillating linear motor is off and on.



### 4.3.3 Linear Plots: Slot vs. Diodes 0.0, 1.0, 1.0a, 2.0.

Figures 69, 70, and 71 represent the velocity data at  $x/L = 0.55$  for the Slot and the four fluidic diodes when the leading edge devices are active. Whereas Sections 4.3.1 and 4.3.2 depicted the influence of each device relative to itself when either active or inactive, this section is a pure comparison of the outcome for each device when active. As expected from the previous discussion, Diode 0.0 and the Slot display very similar profiles in the streamwise, wall normal, and floor normal directions. This suggests that the top surface treatments might be critical, since Diode 0.0 did not include this trait for the outer two passageways, as discussed in 3.6.2.1.

Of the leading edge devices evaluated, Diode 1.0 had the greatest influence on both the mean streamwise velocity and streamwise turbulence intensity. The mean streamwise velocity data portrayed in Figure 69a indicates that Diode 1.0 more than doubles the height that the Slot and Diode 0.0 raise the shear layer and is over a 50% increase from Diode 2.0. The peak magnitude of Diode 1.0 is between 3.0% and 5.0% less than the Slot and Diode 0.0. Despite this slight decrease in peak streamwise turbulence intensity, the region of influence is dramatically increased, particularly above  $z/D = 0.0$ . Between  $u$  values of  $0.05U_\infty$  to  $0.25U_\infty$  and above the cavity lip line, the increase in the region of influence for the streamwise turbulence intensity for Diode 1.0 is approximately twice that of both the Slot and Diode 0.0. Likewise, the turbulence intensity of Diode 1.0 is between 30.0 and 50.0% greater than Diode 2.0 in the same region.

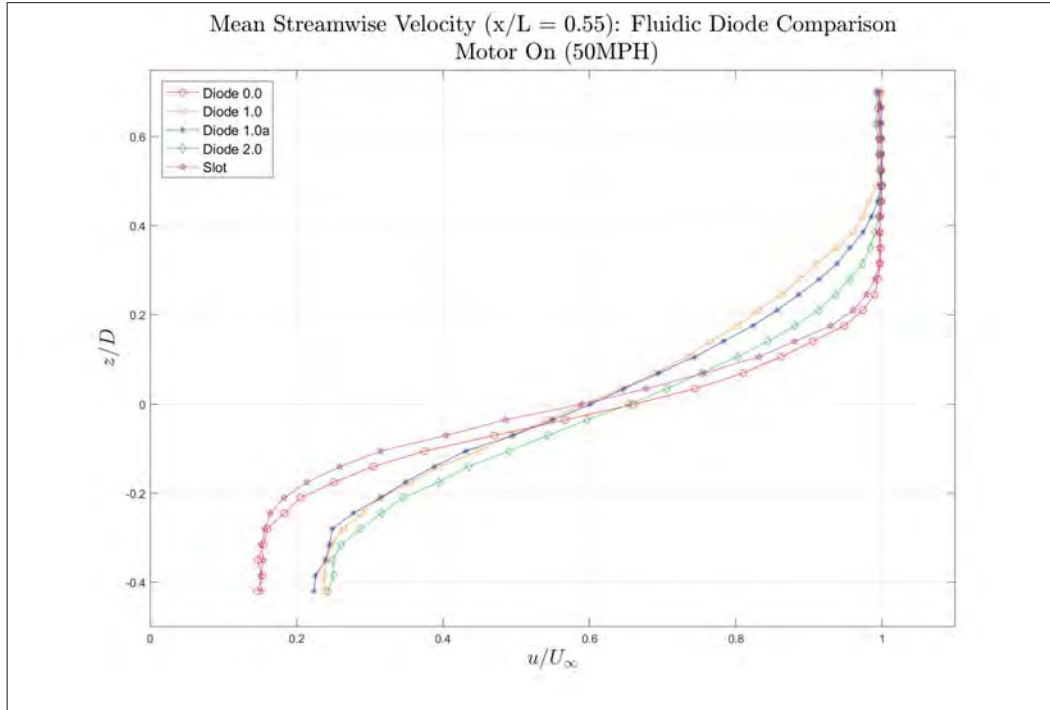
Based upon the observation discussed in this section, Diode 1.0 indicated greater influence on the shear layer. Namely, lifting of the shear layer and thickening the shear layer above the cavity lip line. As a result, and in order to overcome the water intrusion issues discussed in Chapter III, Diode 1.0 was chosen for the modifications and continued testing and evaluation as Diode 1.0a. The profiles of Diode 1.0a are

nearly identical in shape to Diode 1.0 in all regimes. However, the values are consistently 7% to 10% less, indicating losses from the panel used in Diode 1.0a. The use of sealant would be advised for future work to avoid unplanned losses.

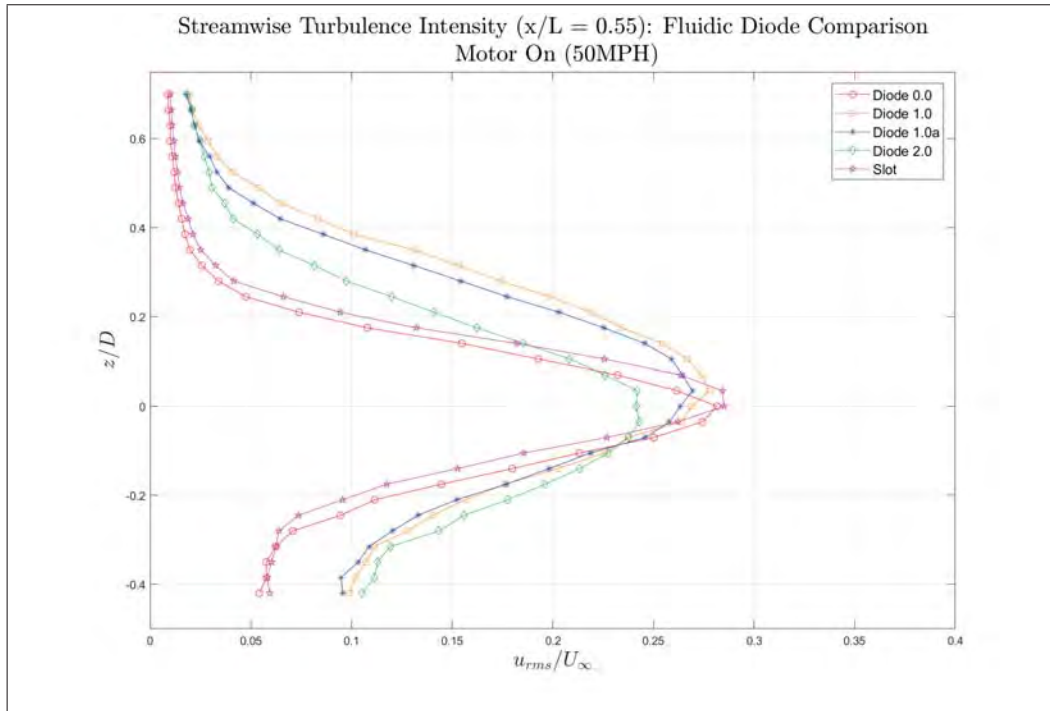
Diode 2.0, shown in Figure 43, was designed with two projections and corresponding buckets in each channel, three times as many as Diode 1.0. The mean streamwise components in Figure 69a indicate that Diode 2.0 possessed a slightly improved capacity to lift the shear layer over that of the Slot and Diode 0.0. Diode 2.0 lifted the shear layer by an additional 15.0 mm compared to Diode 0.0, and 10.0 mm compared to the Slot. The streamwise turbulence intensity plot, Figure 69b, shows that the peak magnitude of Diode 2.0 is 12 – 15% less than all of the other leading edge devices. Despite this reduction in peak magnitude in the streamwise direction, Diode 2.0's has a larger region of increased turbulence intensity than either Diode 0.0 or the Slot. However, Diode 2.0 is apparently outperformed by Diode 1.0 in both the ability to lift the shear layer and increase the thickness above the cavity lip line ( $z/D = 0.0$ ).

With the increased number of projections and buckets, it was anticipated that Diode 2.0 might have the greatest potential to behave as a ‘fluidic tab’, generating coherent vortical structures by strongly encouraging the desired circulatory flow of air drawn in through the outer channels and expelled from the inner channel. The vorticity plot for Diode 0.0, seen in the Appendix A, indicates that the streamwise vorticity generated was not of a magnitude comparable to the leading edge tabs assessed in Section 4.2, Figure 34. However, the peak magnitude of the wall normal turbulence intensity of Diode 2.0 is over 30.0% greater than the Slot and Diode 0.0, as well as 10.0% greater than Diode 1.0. Additionally, the peak magnitude in the floor normal direction is 27.0% greater than both the Slot and Diode 0.0, and 10% greater than Diode 1.0. The region of influence is also notably larger than Diode 0.0 and the Slot. Furthermore, while Diode 1.0 has a stronger influence on the shear layer

above  $z/D = 0.175$ , below this location Diode 2.0 has a bigger influence. Diode 2.0's reduction in peak turbulence intensity in the streamwise direction and corresponding increase in the wall normal and floor normal directions signify that energy from the streamwise direction is being drawn from the streamwise flow and redistributed to the wall and floor normal directions. This is a possible indication that the internal projections and buckets are having the desired effect of producing vortices.

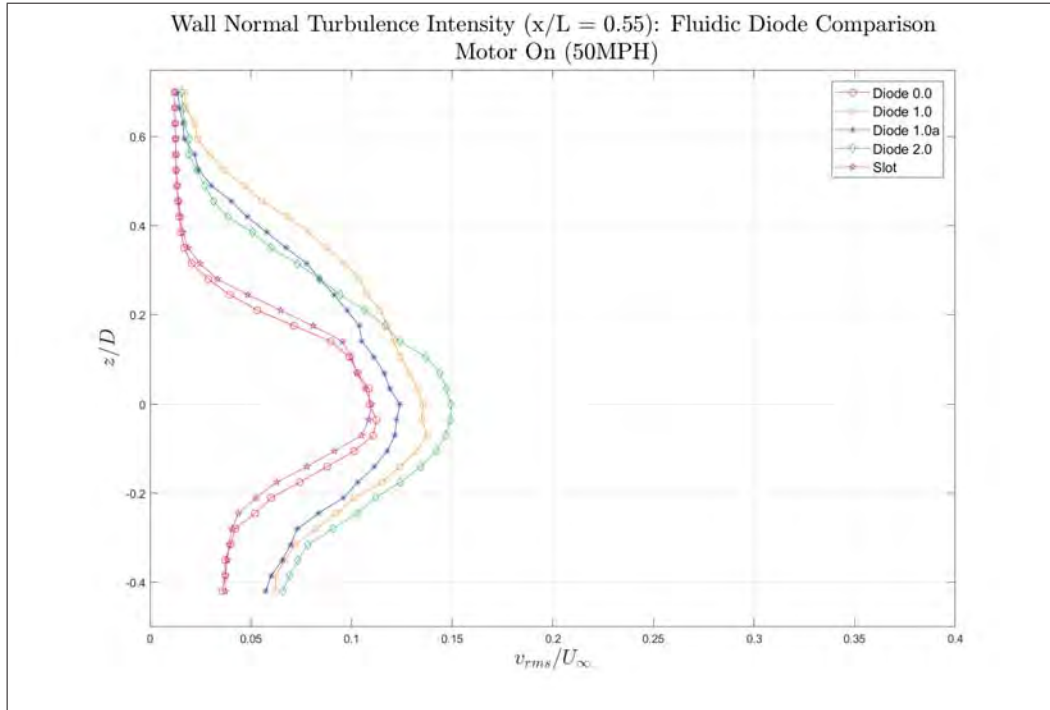


(a) Mean Streamwise Velocity (50mph)



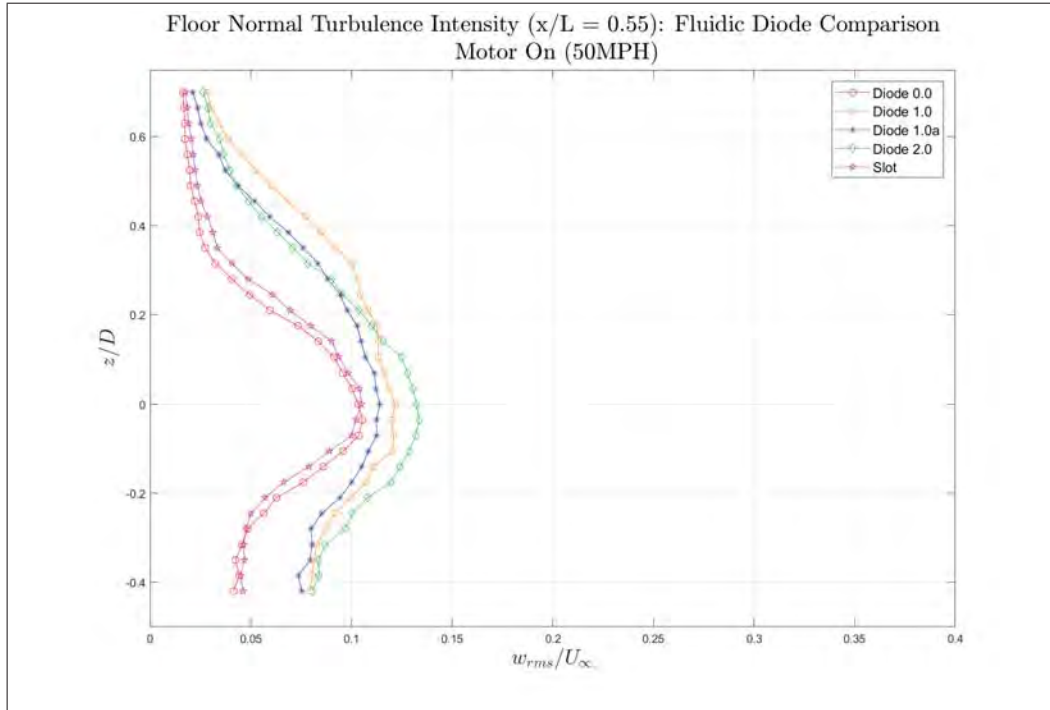
(b) Streamwise Turbulence Intensity (50mph)

**Figure 69.** Mean and turbulence intensity values of the streamwise velocity data collected from linear profiles at  $x/L = 0.55$  of the cavity at 50 mph. The data depicted compares the influence that each diode has on the shear layer.



(a) Wall Normal Turbulence Intensity (50mph)

Figure 70. Turbulence intensity values of the wall normal velocity data collected from linear profiles at  $x/L = 0.55$  of the cavity at 50 mph. The data depicted compares the influence that each diode has on the shear layer.



(a) Floor Normal Turbulence Intensity (50mph)

**Figure 71.** Turbulence intensity values of the floor normal velocity data collected from linear profiles at  $x/L = 0.55$  of the cavity at 50 mph. The data depicted compares the influence that each diode has on the shear layer.

## 4.4 Phase I: Raster Plots

### 4.4.1 Contour Plots: Baseline vs. Slot vs. Diode 1.0a .

While linear profiles provide detailed, and useful, comparisons at a single spanwise station, it is important to understand whether there are variations across the span. Hence, contour plots depicting the mean and turbulence intensity of all three velocity components were developed using the velocity data from the low-resolution raster patterns. Contour plots of the Baseline cavity, Slot, and Diode 1.0a at  $x/L = 0.55$  and 50 mph are presented for comparison in Figures 72 - 75. Within the Baseline cavity, the linear motor, piston, cylinder, and a leading edge device without an opening to the freestream were installed; thus ensuring similar internal cavity geometry for all tests. Figure 72 presents contour plots of the streamwise mean velocity for the Baseline, Slot, and Diode 1.0a. Similar to the linear plots, the mean velocity data for the wall normal and floor normal components are presented in Appendix A. Figures 74 and 75 depict the wall normal and floor normal turbulence intensity data for the three configurations.

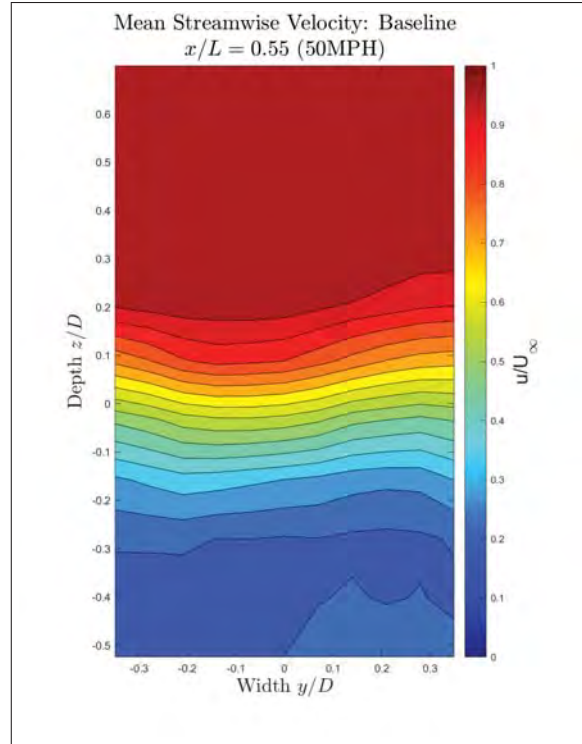
The mean streamwise velocity of the Baseline cavity, shown in Figure 72a, indicates that the region between  $u = 0.40U_\infty$  and  $0.90U_\infty$  is typically between  $z/D = -0.10$  and  $0.20$ . By contrast, the same velocity range for the Slot and Diode 1.0a spans the region of  $z/D = -0.15$  to  $0.35$ . Some variation can be seen across the span, particularly in the Diode 1.0a near  $y/D > 0.15$ , but overall trends are consistent with linear profiles in Figure 69.

The turbulence intensity in the streamwise direction for the Baseline case, shown in Figure 73a depicts that the region between  $u_{rms} = 0.15U_\infty$  and  $0.18U_\infty$  is typically between  $z/D = -0.10$  and  $0.10$ . Comparatively, the same turbulence intensity values for the Slot and Diode 1.0a have expanded substantially to the region between  $z/D = -0.20$  and  $0.25$ .

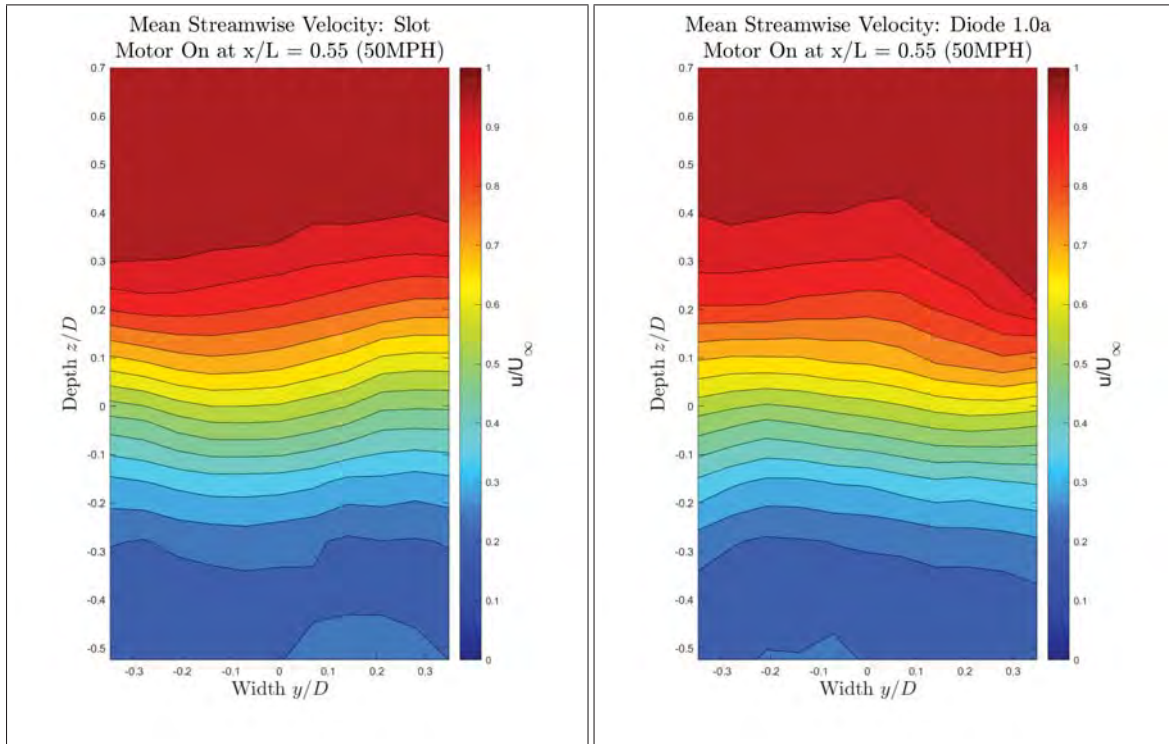
For the wall normal and floor normal components of the Baseline cavity, the region between  $u_{rms} = 0.10U_\infty$  and  $0.15U_\infty$  falls within the range of  $z/D = -0.20$  and  $0.15$ . The same turbulence intensity range for the wall normal component of the Slot falls within the range of  $z/D = -0.20$  and  $0.25$ , with an average increase in the region of turbulence intensity above  $z/D = 0.0$ . The same turbulence intensity range in the floor normal direction lies between  $z/D = -0.15$  and  $0.25$ . Compared to the Baseline cavity, this indicates significant growth in the region of turbulence intensity above  $z/D = 0.0$  and slight reduction in the region below  $z/D = 0.0$ . For Diode 1.0a, the  $u_{rms} = 0.10U_\infty$  and  $0.15U_\infty$  turbulence intensity range for the wall normal direction lies between  $z/D = -0.20$  and  $0.20$ , indicating a slight growth above  $z/D = 0.0$  compared to the Baseline cavity. Likewise, the floor normal direction falls between  $z/D = -0.25$  to  $0.25$ , displaying larger growth above and below  $z/D = 0.0$  compared to both the Baseline cavity and leading edge Slot.

The overall increase in thickness and reduction in turbulence intensity when comparing the Baseline cavity to the Slot and Diode 1.0a was expected. However, the two regions of peak intensity at approximately  $y/D = -0.30$  and  $0.30$  was not anticipated. Particularly the strong similarities in the floor normal turbulence intensities shown in Figures 75b and 75c. The vastly different geometries, especially the planned circulatory intake and expulsion of air in Diode 1.0a, would be expected to produce a more varied outcome than the Slot. Further investigation at  $x/L = 0.25$ , and under different wind tunnel velocities, would be necessary to determine if wall and floor normal turbulence intensities for the various devices display similar results across the length of the cavity, or if  $x/L = 0.55$  is far enough aft that the unique flow influence for each device has been lost. Overall, these raster plots showed only modest changes across the spanwise region measured. Thus, they did not change general conclusions reached via analysis of the linear plots.





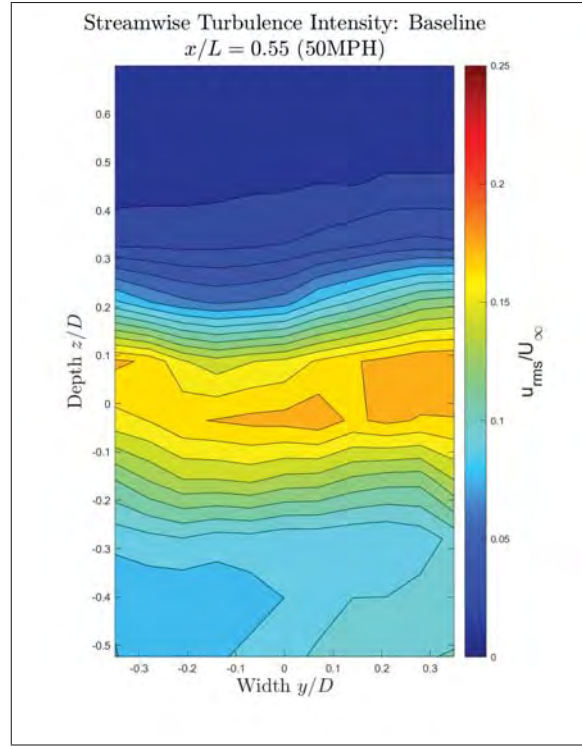
(a)



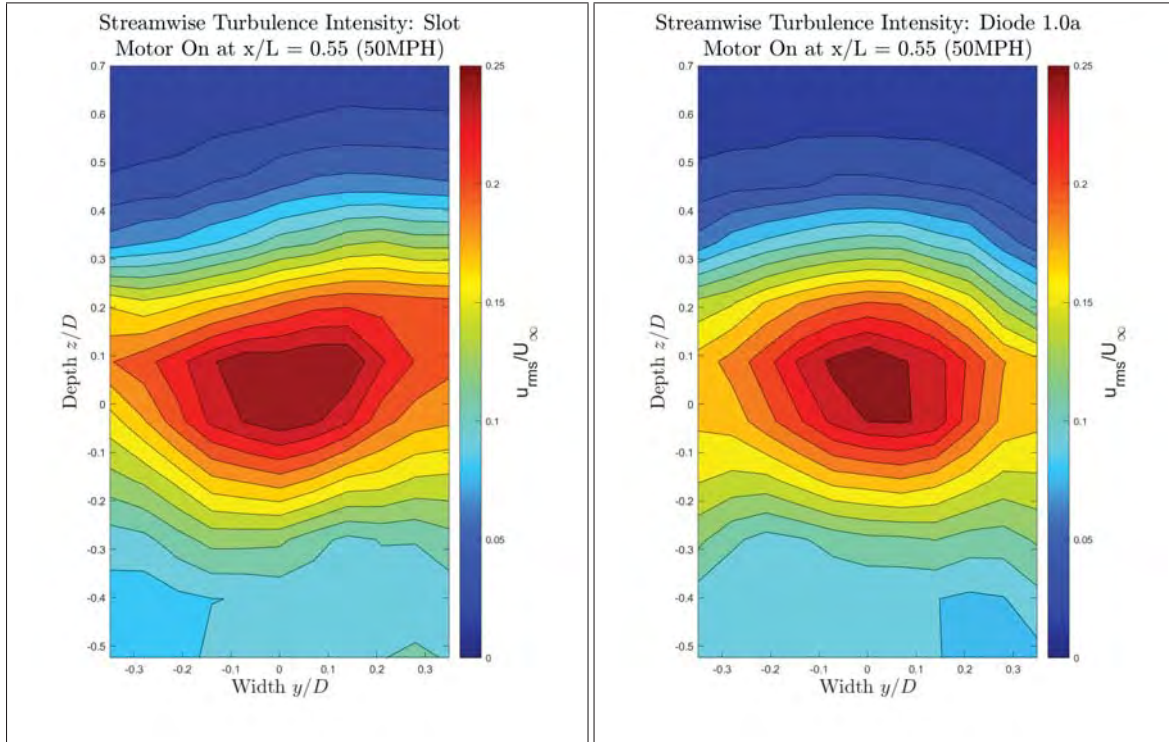
(b)

(c)

Figure 72. Streamwise mean velocity data collected from raster profiles at  $x/L = 0.55$  of the cavity at 50 mph. The data depicted shows the change at each position when the oscillating linear motor is on.



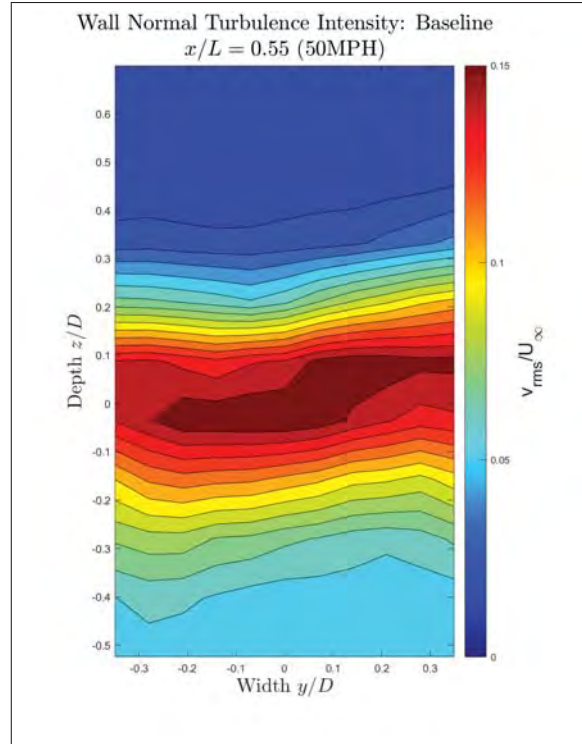
(a)



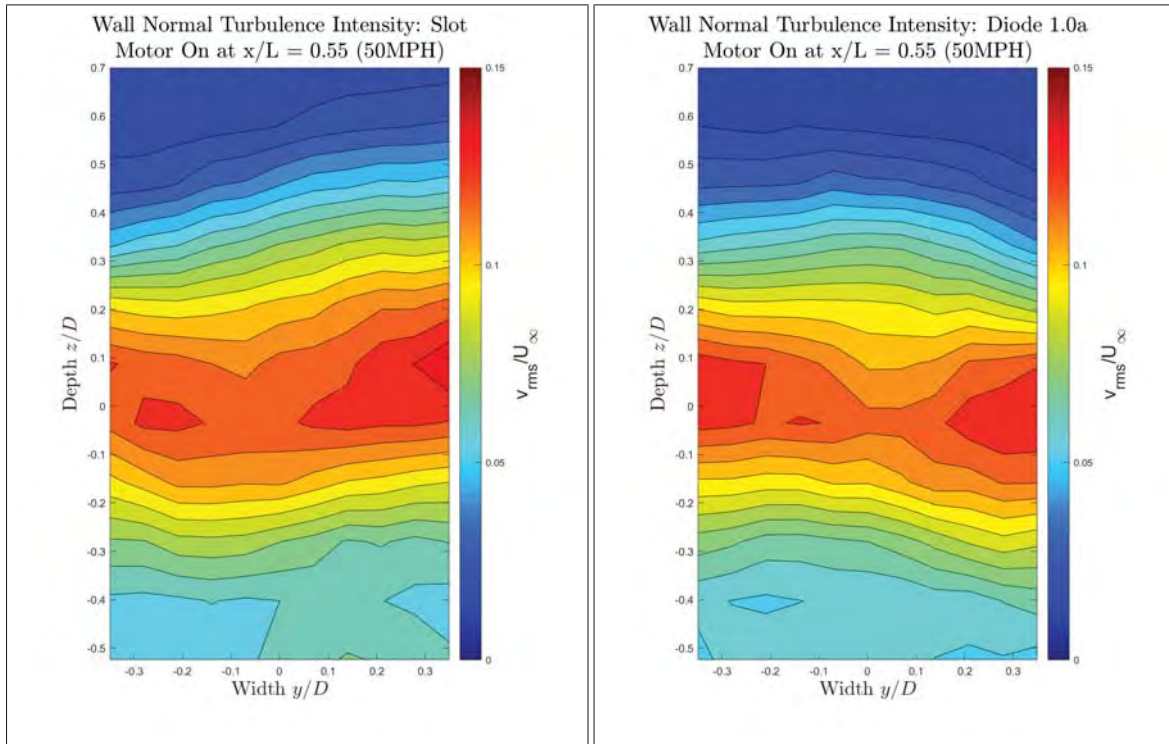
(b)

(c)

Figure 73. Turbulence intensity values of the streamwise velocity data collected from raster profiles at  $x/L = 0.55$  of the cavity at 50 mph. The data depicted shows the change at each position when the oscillating linear motor is on.



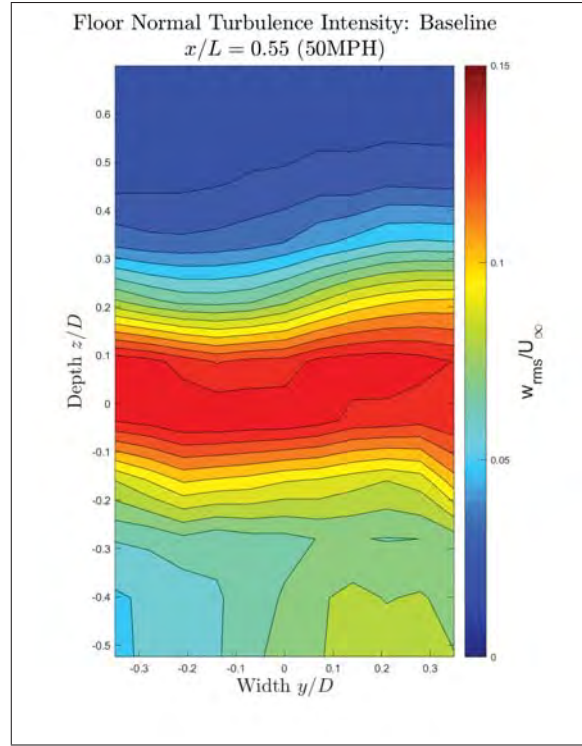
(a)



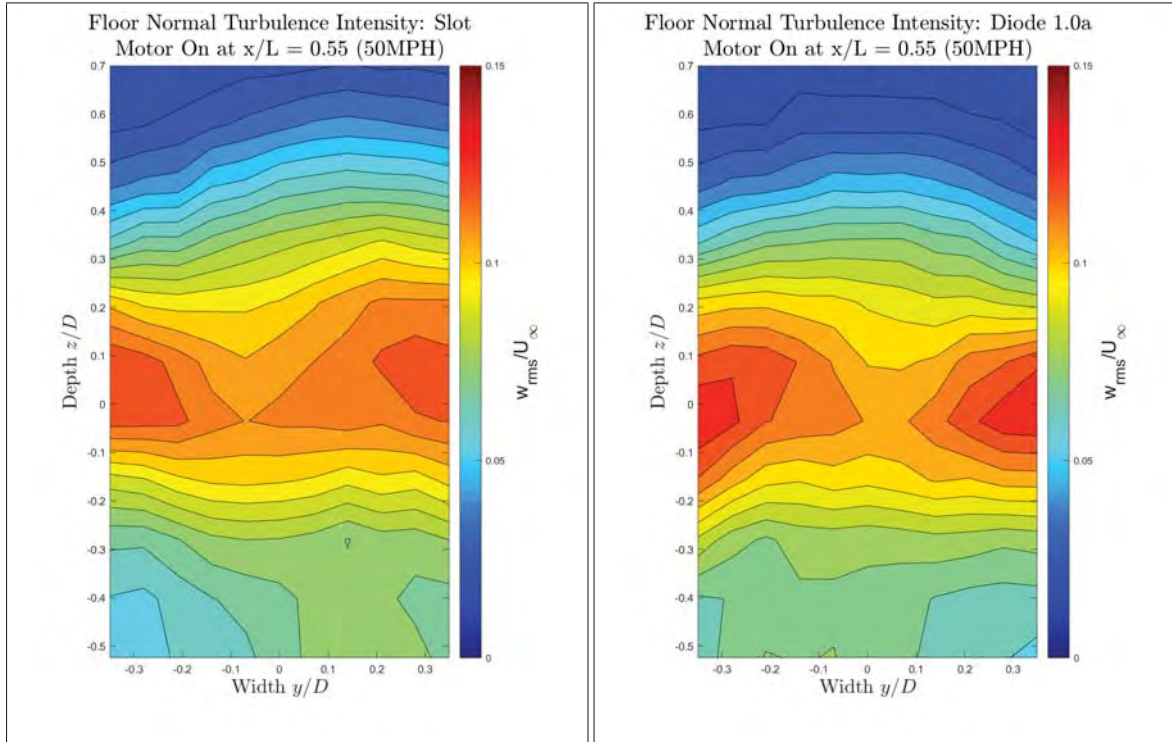
(b)

(c)

Figure 74. Turbulence intensity values of the wall normal velocity data collected from raster profiles at  $x/L = 0.55$  of the cavity at 50 mph. The data depicted shows the change at each position when the oscillating linear motor is on.



(a)



(b)

(c)

Figure 75. Turbulence intensity values of the floor normal velocity data collected from raster profiles at  $x/L = 0.55$  of the cavity at 50 mph. The data depicted shows the change at each position when the oscillating linear motor is on.



#### 4.4.2 Vorticity: Slot vs. Diode 1.0a.

The vorticity plots for the Baseline cavity, Slot, and Diode 1.0a taken at  $x/L = 0.55$  and with the wind tunnel at 50 mph are presented in Figure 76. The scale used for the vorticity contours, -150.0 to 150.0, correspond to the scale used for the leading edge tabs in Figure 60; wherein the vorticity plot generated by the leading edge tabs displayed two readily identifiable, counter-rotating, vortical structures. None of the devices evaluated produced spatially stationary coherent vortical structures of a magnitude comparable to those produced by the leading edge tabs. If anything, the strongest evidence for the presence of vortical structures was found in the Baseline cavity, shown in Figure 76a, which indicates three negative regions (clockwise rotation) at the sidewalls and bottom of the cavity, and one positive region (counter-clockwise rotation) centered on  $z/D = 0.2$  and  $y/D = 0.15$ . The only leading edge device with regions of detectable vorticity as strong as the Baseline cavity is Diode 2.0, shown in Figure 76d.

There are two potential explanations for the lack of coherent vortical structures present in the streamwise vorticity plots. First, the vortical structures might be occurring outside of the range  $-0.3 < y/D < 0.3$  and are therefore not present in the velocity data collected. Alternatively, the vortical structures might be present, but because the vortical structures in the shear layer are being vertically displaced from instant-to-instant by the dominant 5.0 Hz oscillation being forced in the shear layer, the time-averaged data fails to indicate their presence.

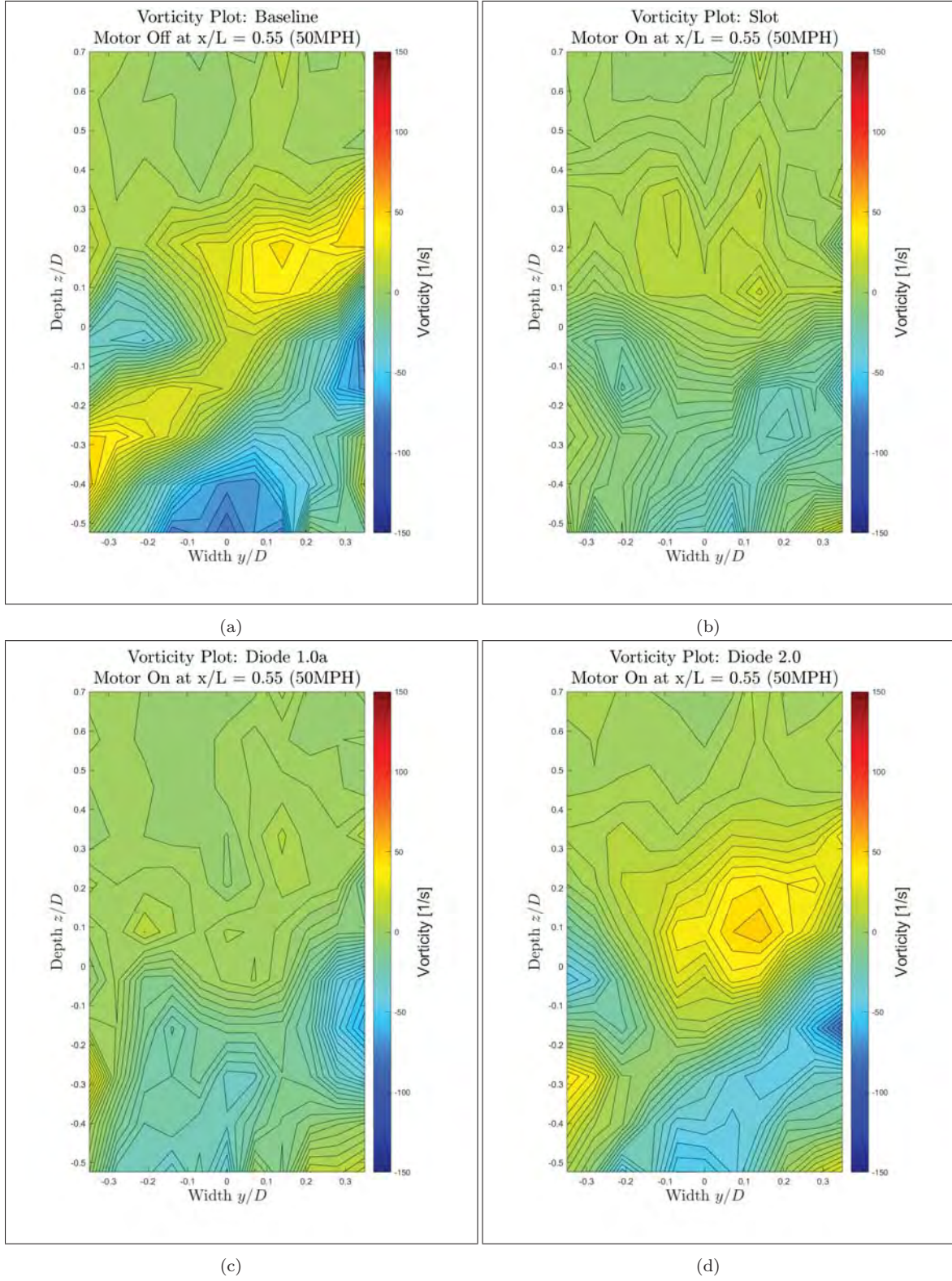
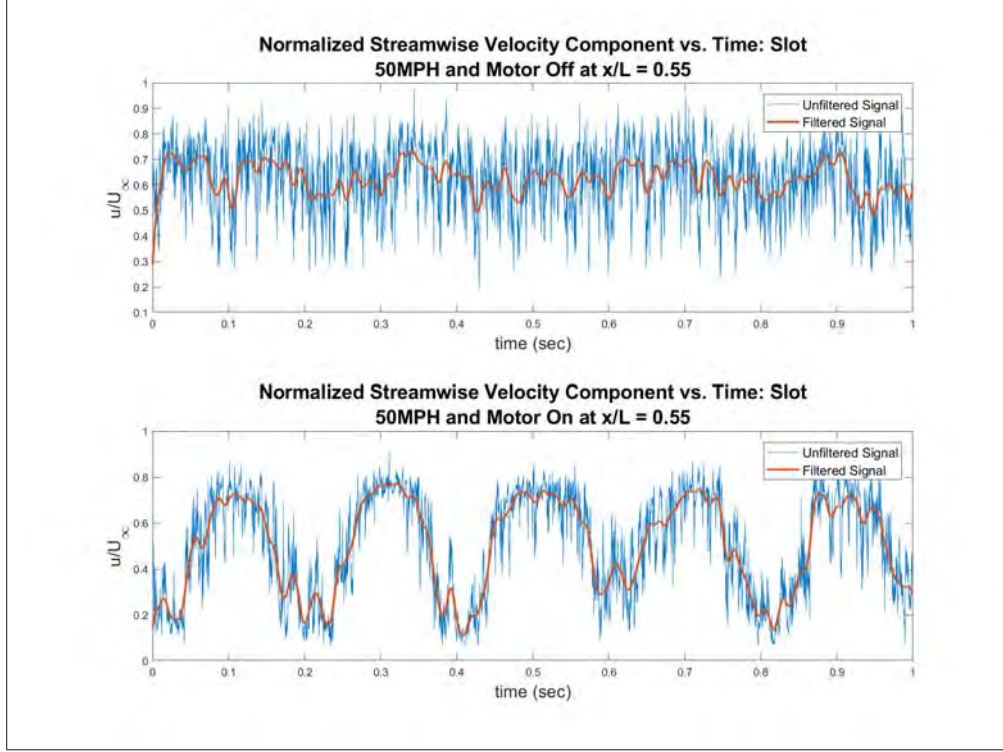


Figure 76. Vorticity plots generated from the  $v$ - and  $w$ - components of velocity data collected using a raster profiles at  $x/L = 0.55$  with the motor on at 50 MPH

## 4.5 Forcing a Dominant Tone in the Cavity

The ability to force a low-speed cavity environment to exhibit the dominant frequencies within the shear layer that are prevalent in a transonic and supersonic cavity environment was explored. Figure 77 depicts the velocity data gathered at a sample rate of 10.0 kHz using a tri-axial velocity probe at  $z/D = 0.035$  when the leading edge Slot is both active and inactive. The  $z/D = 0.035$  location in the shear layer was chosen because it corresponds to the point of peak streamwise turbulence intensity for the Slot at wind tunnel speeds of 50 mph. The same low-pass digital filter technique described in Chapter 3.10.3.2 was applied to the velocity data with an ‘order’ of 200 used to account for the higher sampling rate of the tri-axial probe. Both the top and bottom images of Figure 77 cover a time period of 1.0 second, indicated on the x-axis; the y-axis is the normalized streamwise component of velocity.

The upper plot in Figure 77 depicts the velocity data collected when the actuator was inactive and the lower plot is representative of the data collected when the leading edge Slot was operating at 5.0 Hz. In agreement with expectations for a cavity in a low speed flow field, the streamwise velocity data collected with the leading edge device inactive indicates a lack of coherent structure in the velocity fluctuations. Comparatively, the data collected when the leading edge device is active definitively indicates how the leading edge actuator forces a velocity fluctuation in the shear layer that matches the rate of oscillatory blowing. Indications of the velocity being forced at the same rate as the Slot leading edge actuator is most apparent at the region of peak turbulence intensity, and becomes less so at locations further from  $z/D = 0.035$ . This can be seen in the velocity vs. time plots for  $z/D = 0.7, 0.385$ , and  $-0.14$ , included in Appendix A. The influence of the leading edge device on the shear layer is further reinforced by examining differences in the energy frequency spectrum for the forced and unforced conditions.



**Figure 77. Velocity vs. Time comparison with the Leading Edge Slot off and on at  $z/D = 0.035$ .**

Figure 78 depicts the energy-frequency spectrum calculated for the leading edge Slot at  $z/D = 0.035$  with the leading edge actuator inactive (left) and active (right). The energy-frequency spectrum with the leading edge device active depicts a significant increase in energy at 5.0 Hz, corresponding to the frequency at which the actuator is oscillating. The energy level at 5.0 Hz with the leading edge device active has a magnitude of  $13.23 \frac{m^2}{s^2}$ , while the peaks at the harmonic frequencies of 10.0 and 15.0 Hz indicate a magnitude of 0.303 and  $0.054 \frac{m^2}{s^2}$ , respectively. This is a dramatic increase compared to the approximate magnitude of  $0.0025 \frac{m^2}{s^2}$ , measured at the 5.0, 10.0, and 15.0 Hz with the leading edge device inactive. The energy present at the forcing frequency of 5.0 Hz has a direct impact on the normal forces present in the shear layer, the measurement of which is presented in Section 4.6.2.



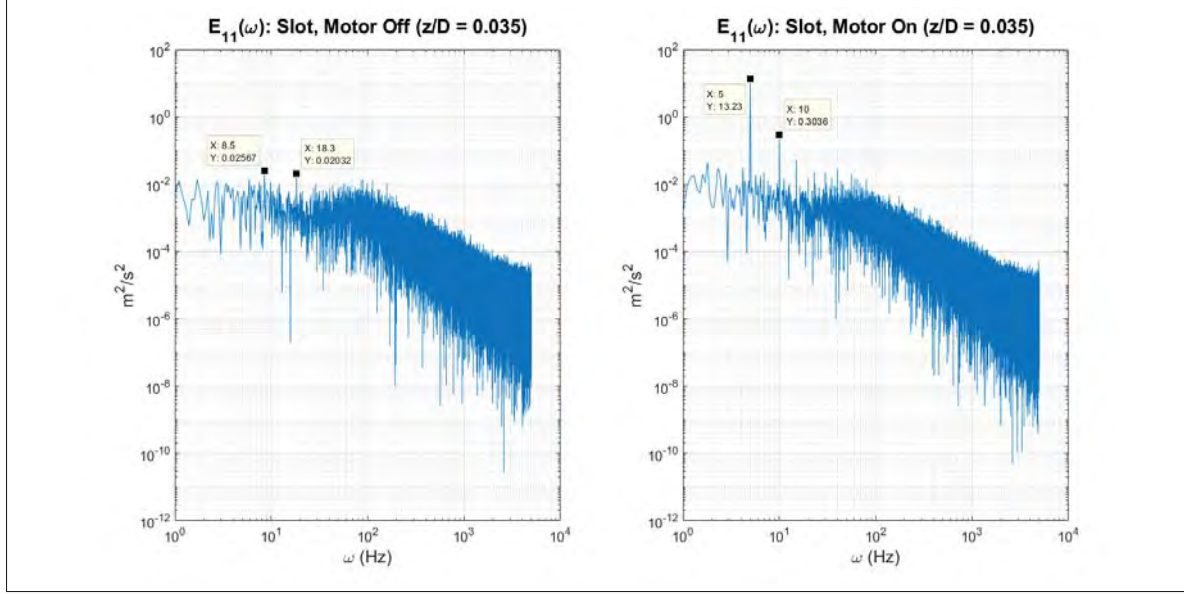


**Figure 78. Energy Frequency Spectrum for the leading edge Slot at  $x/L = 0.55$  and  $z/D = 0.035$  with the motor off and motor on.**

Of note, initial estimations for the dominant vortex shedding frequency ( $n=1$ ) were made using Equation 2 from Chapter II. An assumed Strouhal number of 0.2 [34], a freestream velocity of 50 mph ( $22.352 \frac{m}{s}$ ), and a cavity length of 24 inches (0.61 m) were used to predict a vortex shedding frequency of 7.33 Hz. Observing the energy frequency spectrum with the leading edge device inactive, two distinct peaks occur at 8.5 Hz and 18.3 Hz, respectively. At 8.5 Hz, the energy indicates a magnitude of  $0.0257 \frac{m^2}{s^2}$ , while at 18.3 Hz, the energy has a magnitude of  $0.0203 \frac{m^2}{s^2}$ . The increased energy present at 8.5 Hz indicates it is the dominant Rossiter mode ( $n=1$ ). In order to achieve a vortex shedding frequency of 8.5 Hz at the established freestream velocity, a Strouhal number of 0.23 would be required, very much in agreement with the assumed Strouhal number of 0.2. Using the assumed Strouhal number of 0.2, The vortex shedding frequency predicted at 25 mph and 100 mph are 3.66 Hz and 14.66 Hz respectively. While not an exact match with any of the wind tunnel conditions, the 5.0 Hz dominant frequency being forced in the cavity is of the same order of magnitude as the cavity's natural vortex shedding frequencies.

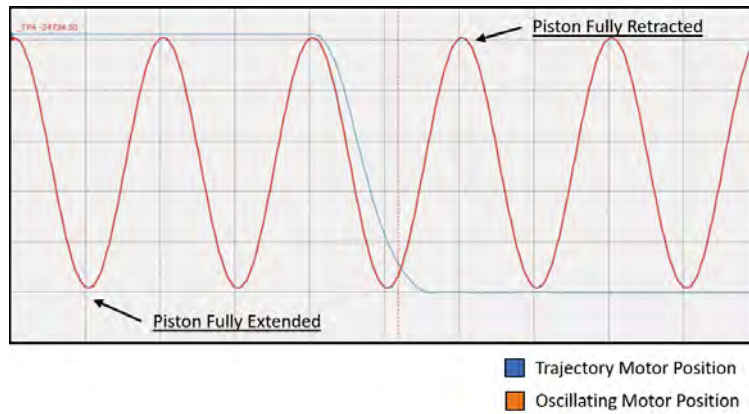
## 4.6 Phase II

### 4.6.1 Verification of Store Release Timing.

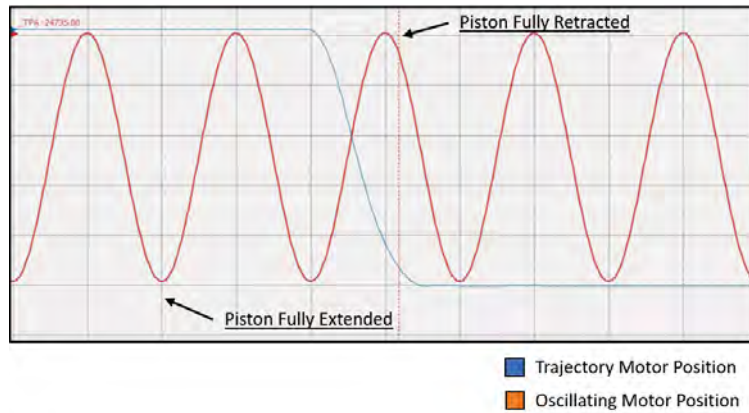
Validating the synchronization between the oscillating linear motor and the store's trajectory motion was paramount to this experimental study and planned follow-on research. While synchronization of the motors was assessed in a benchtop test, it was deemed necessary to determine if the loading of the mission store with the wind tunnel active would impact motor response. The Galil Design Kit includes a scope that allows for real time observation of digital encoder position. Figure 80 presents two screen captures of the Galil scope that were taken for the two cases studied: trajectory motion of the store triggered with the piston fully retracted (Figure 79a) and trajectory motion triggered with the piston fully extended (Figure 79b). The wind tunnel was operating at 100 mph when each image was captured. The sinusoidal orange line represents the oscillating motor position and the blue line represents the trajectory motor position. The crest of the sine wave corresponds to when the piston is fully retracted. Likewise, the trough corresponds to when the piston is in the fully extended position. As indicated in both cases, the trajectory motor initiates motion at the desired oscillatory motor position.

The Phantom MiroLab 3a10 used in the benchtop experiments, described in Chapter 3.10.1, was also used to obtain visual verification that release timing remains synchronized with an operational wind tunnel. The initiation of trajectory motion can be visually detected within 3.0 milliseconds of the piston reaching the desired location. However, a uniform time-step of 22.0 milliseconds was chosen purely for presentation purposes. Figures 80a and 80b present a series of images taken at 22.0 millisecond intervals with the wind tunnel operating at 100 mph. Each image has a time-step in the top right corner, with zero indicating when the oscillating motor has reached either full extension or retraction and that store motion has been initiated.

The verification was successfully completed with the store at both a  $0.0^\circ$  and  $10.0^\circ$  angle of attack.



(a) Fully retracted.

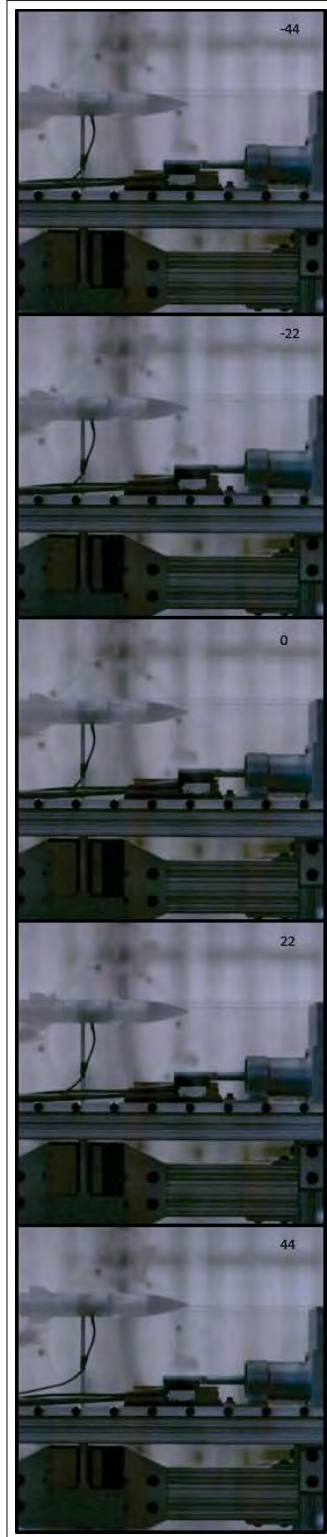


(b) Fully extended.

**Figure 79.** Encoder position taken from the Galil Software for trajectory release in a 100 mph test when piston is fully retracted or fully extended.



(a) Piston fully retracted,  $0.0^\circ$   
AoA, 100 mph



(b) Piston fully extended,  $0.0^\circ$   
AoA, 100 mph

Figure 80. Images from high speed camera footage demonstrating motor synchronization. Timing between each image is 22 milliseconds, time-stamp is in the top right of each frame. Zero indicates when fully retracted or extended position has been reached and initiates motion of the store.

#### 4.6.2 Trajectory Analysis.

Tests were completed for multiple iterations of store AoA and initialization parameters, the scope of which is outlined in Table 10. The Nano-25 collected time-accurate force and moment data at a sample rate of 1000 Hertz. The focus of the following sections is on the normal force coefficient data ( $C_N$ ) which was detected by the Nano-25 and calculated using Equation 24. Each of the plots presented in Figures 81, 82, 83, 84, and 85 contain the filtered normal force coefficient data collected from all five runs at a specified AoA and tunnel speed. Figure 86 compares the filtered averages of the five data sets collected when the trajectory was initialized at the fully extended position with the five data sets collected at the fully retracted position. The store was mounted at  $10^\circ$  AoA and the wind tunnel speed set to 100 mph for the data presented in Figure 86. Provided for reference in Appendix A is the data collected for the axial force ( $F_A$ ) and pitch moment coefficient ( $C_m$ ) for each test.

$$C_N = \frac{N}{\frac{1}{2}\rho V_\infty^2 (\frac{\pi}{4}D^2)} \quad (24)$$

Figure 81 presents the normal force coefficient data collected with the mission store at a  $0.0^\circ$  and  $10.0^\circ$  AoA. Furthermore, for the cases shown in Figure 81, the wind tunnel was set at 50 mph and trajectory motion was initiated when the piston was in the fully retracted position. It should be noted, that because the tare files used for the  $0.0^\circ$  and  $10.0^\circ$  AoA were not the same, the indications of trajectory motion do not occur at the exact same time for the two different store configurations. Additionally, in every 50 mph case there was one data set collected from a single trajectory that mirrored the shape of the other four data sets, but whose average value differed by  $\pm 0.8$ . This is commonly labeled as the first test run ( $C_{N1}$ ) in Figures 81, 82, and 83. It is unclear why this abnormality occurred in the 50 mph cases only, as it does not present itself in the 100 mph data sets collected with the Nano-25.

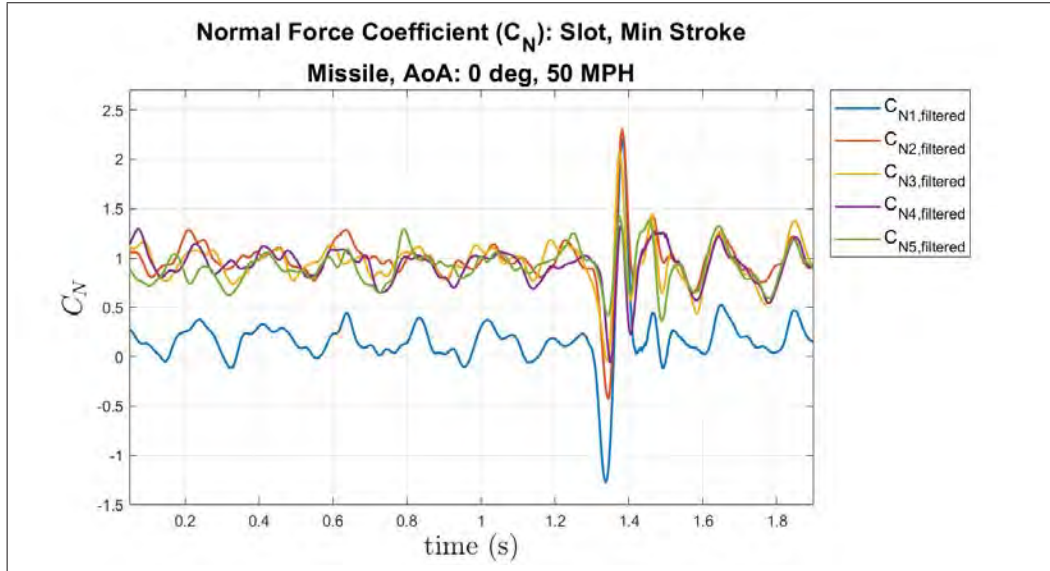
In both Figure 81a and 81b, the influence on the store generated by the 5.0 Hz oscillations of the leading edge blowing device is apparent in the normal force coefficient, with a visually identifiable repeating pattern over each 0.2 second interval. The 5.0 Hz oscillation forced in the shear layer by the leading edge device are also evidenced in the axial force coefficient and pitch moment coefficient plots shown in Appendix A.

As is expected, for all data sets there is a sharp increase in magnitude of the oscillating normal force that indicates the store's trajectory motion. However, the difference between the values of the  $C_N$  before and after trajectory motion for the  $0.0^\circ$  and  $10.0^\circ$  AoA is significant. For the  $0.0^\circ$  AoA data, the value of  $C_N$  before and after trajectory motion store are within 10% of each other, which makes detecting trends in the forces imparted on the store during trajectory motion difficult. Comparatively, for the  $10.0^\circ$  AoA data, the value of  $C_N$  after motion is approximately five times what was measured before motion. For this reason alone, the remainder of this chapter will focus on normal force coefficient data collected with the mission store at  $10.0^\circ$  AoA.

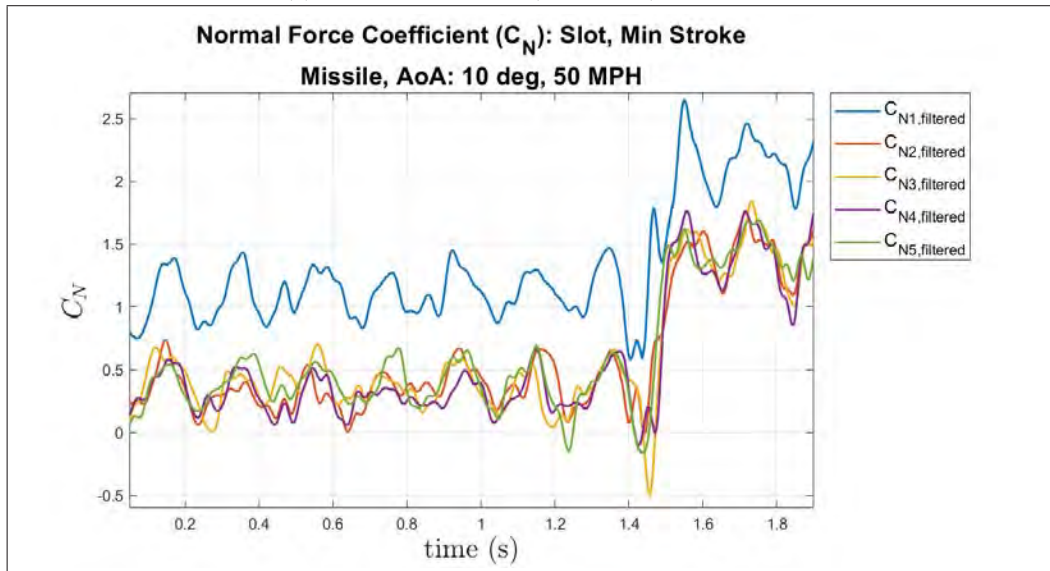
#### **4.6.3 Trajectory Analysis: $C_N$ for $10.0^\circ$ AoA, 50 mph.**

Figures 82 and 83 represent the data collected with a mission store at  $10.0^\circ$  AoA and the wind tunnel operating at 50 mph for the fully retracted and fully extended triggers. The data presented in Figures 84 and 85 were taken under the same conditions, with the exception that the wind tunnel was operated at 100 mph. For each of the aforementioned figures, the upper plot is representative of 1.85 seconds of data including the trajectory motion, allowing for analysis of trends prior to, and following, trajectory motion of the store. The lower plot covers a time period of 0.4 seconds, emphasizing a focus on the trajectory motion event. Since each figure represents the data collected from the  $10.0^\circ$  AoA mission store, all of the data sets were aligned





(a)  $C_N$ , Fully Retracted (Min Stroke),  $0.0^\circ$  AoA



(b)  $C_N$ , Fully Retracted (Min Stroke),  $10.0^\circ$  AoA

**Figure 81. Comparison of the difference in detecting trends for the  $0.0^\circ$  AoA and  $10.0^\circ$ , with  $V_\infty = 50\text{mph}$ .**



using the same tare file and an 'order' of 60 was used for the digital filter with a cutoff frequency of 1.0 Hz.

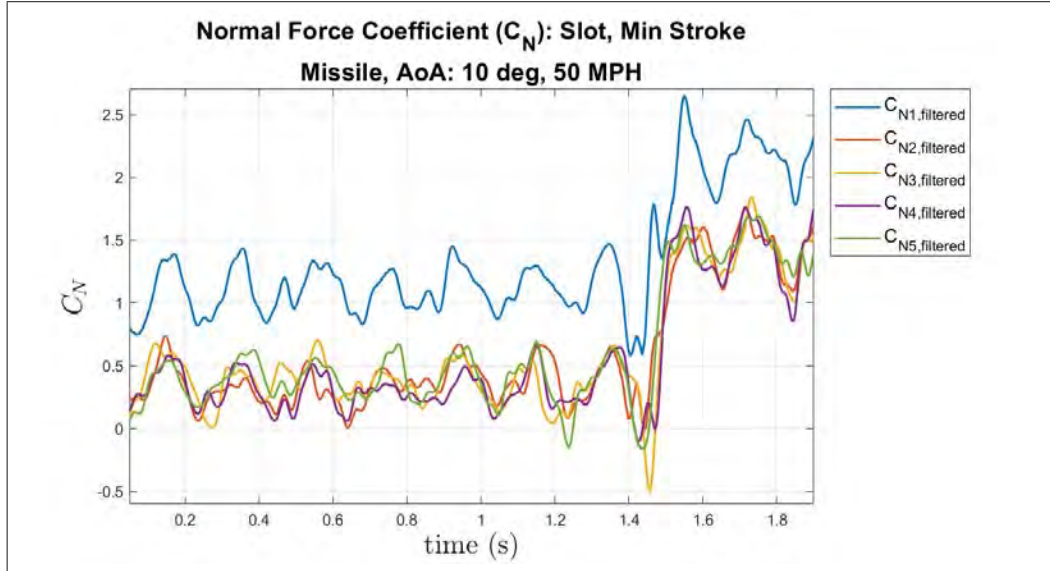
The previously identified 5.0 Hz oscillations present in the shear layer for the 50 mph case were also detected by the Nano-25 in the 100 mph cases. For the 50 mph cases, neglecting the outlying data set from  $C_{N1}$ , the oscillations occur around an average  $C_N$  value of 0.25 prior to trajectory motion, and roughly 1.3 after the motion. Comparatively, the 100 mph cases oscillate around an average  $C_N$  value of 0.75 prior to motion, and 1.8 afterwards.

Shown in Figure 83b, just prior to when trajectory motion is initiated at the piston's fully retracted position, and neglecting  $C_{N1}$ , the normal force coefficients reach a trough in the sinusoidal wave at  $t = 1.45$ , with an approximate value of  $C_N = -0.15$ . This is followed by a relatively constant increase to a  $C_N$  value of nearly 1.75. After the peak  $C_N$  value of 1.75, the next trough is reached by  $t = 1.65$  with a  $C_N$  value of roughly 1.25. When motion is initialized at the fully extended position, shown in Figure 83b, the  $C_N$  values observed in the troughs before, during, and after motion are nearly identical to the case when the trajectory motion is initiated at the piston's fully retracted position. Despite the similar  $C_N$  values, there are several notable differences in the trends observed between the two cases.

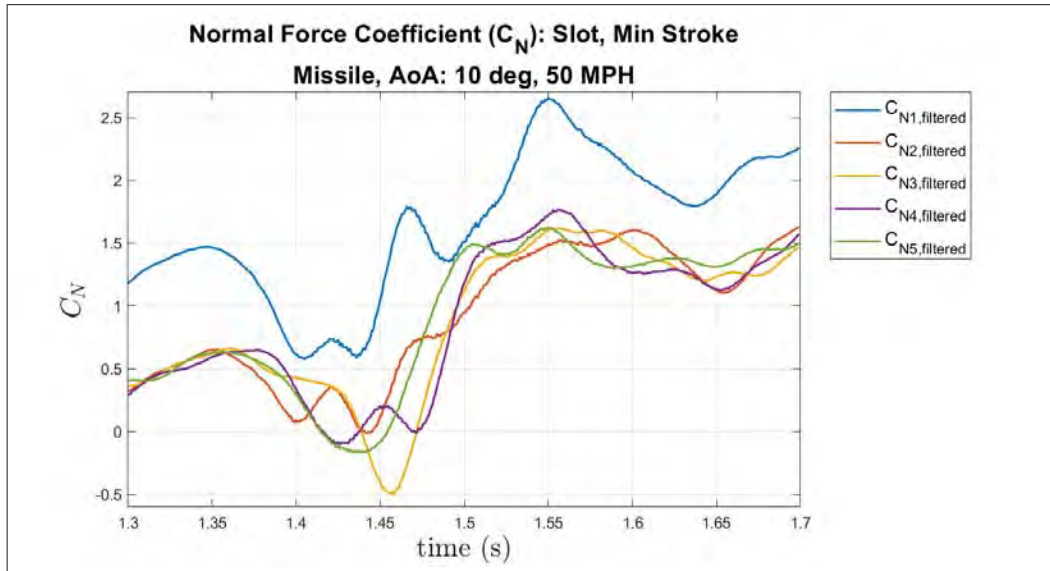
When motion is initiated from the fully retracted position, there is a fairly constant increase in  $C_N$ , with only minor fluctuations observed. Conversely, the store motion in the fully extended case does not display a smooth increase in value during the store motion. Instead, a sharp decrease of approximately  $C_N = 0.5$  at roughly  $t = 1.47$  is observed during store trajectory. After the sharp decrease the trend of increasing  $C_N$  resumes. This sharp decrease is observed during store motion in four of the five data sets collected when motion was initiated from the fully extended position. Only one data set does not follow this trend, and that is the previously mentioned outlier that

presented itself in each 50 mph test configuration  $C_{N1}$ . While the magnitude of the  $C_{N1}$  values differ for the fully retracted case, the period of the troughs and peaks is in agreement with the other four data sets.

Another key differences between the two initialization cases was observed in their ability to adhere to the forced 5.0 Hz period during store motion. Following the 5.0 Hz pattern for the fully retracted case in Figure 82a, the trough just prior to store motion should occur at a time of approximately  $t = 1.45$  and the next trough should occur at approximately  $t = 1.65$ ; this expectation is met. In contrast, when store motion is initiated at the fully extended position, show in in Figure 83b, the final trough prior to store motion should have occurred at approximately  $t = 1.35$ , however, it occurs roughly 0.06 seconds later at  $t = 1.41$ . Furthermore, the next trough does not occur in the normal force data until around  $t = 1.75$ , a deviation of nearly one full period. This deviation in the established period of oscillations that presented itself when store motion is triggered at the fully extended position is potentially responsible for the sharp changes in the value of  $C_N$  during store motion.

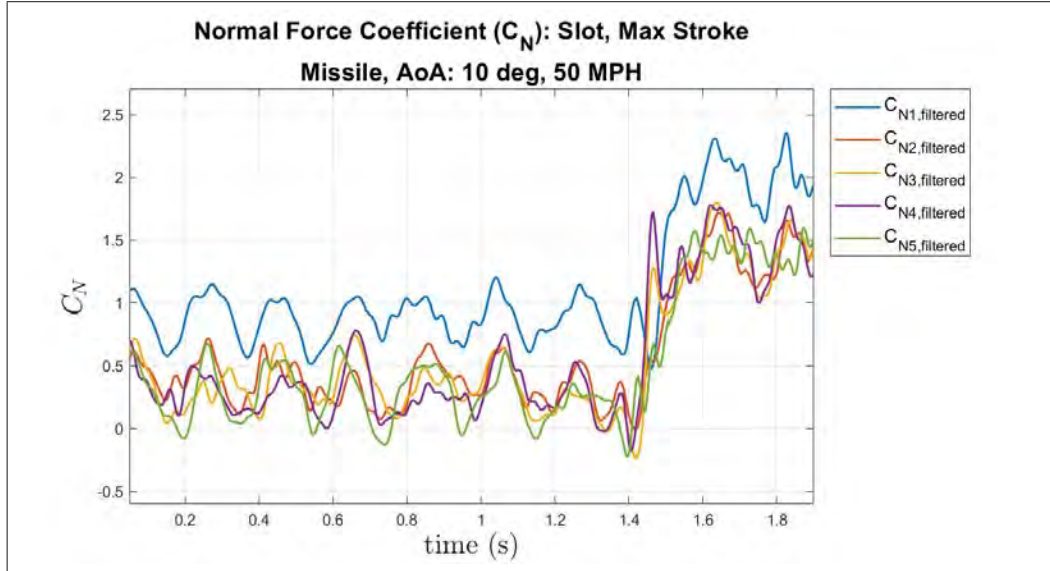


(a) Large Window: 1.85 seconds

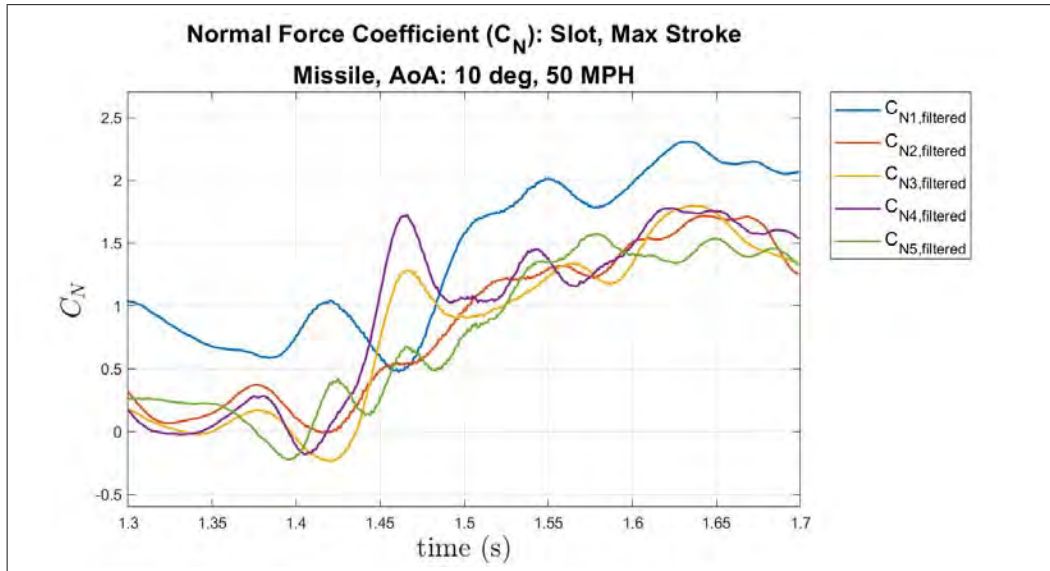


(b) Narrow Window: 0.4 seconds

**Figure 82.**  $C_N$ , Fully Retracted (Min Stroke),  $10.0^\circ$  AoA,  $V_\infty = 50\text{mph}$ .



(a) Large Window: 1.85 seconds



(b) Narrow Window: 0.4 seconds

**Figure 83.**  $C_N$ , Fully Extended (Max Stroke),  $10.0^\circ$  AoA,  $V_\infty = 50\text{mph}$ .

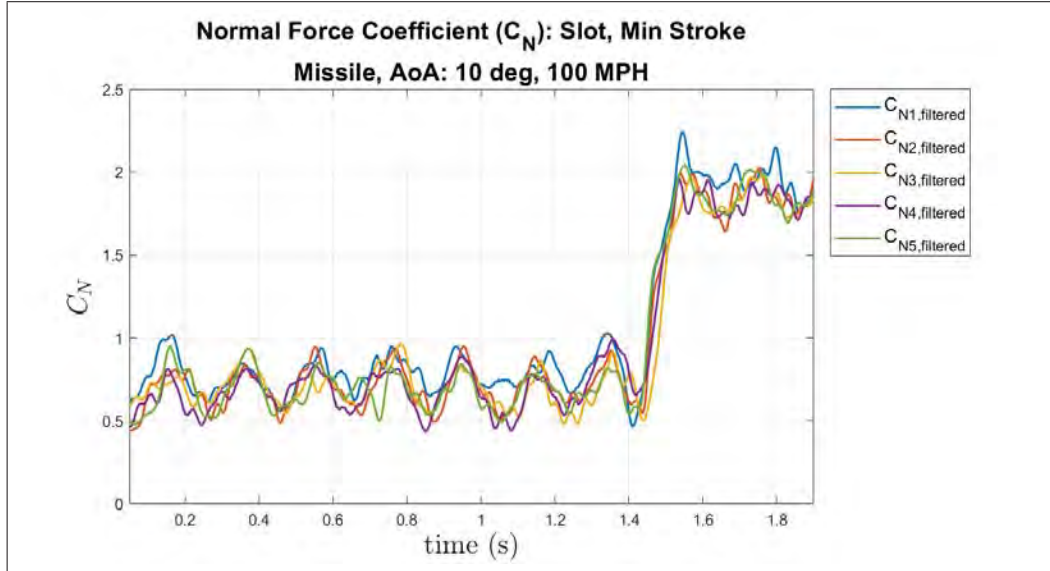
#### 4.6.4 Trajectory Analysis: $C_N$ for 10.0° AoA, 100 mph.

For the cases where the wind tunnel was operated at 100 mph, shown in Figures 84 and 85, the trends previously identified in the 50 mph case remain and are easier to identify, presumably due to an increase in signal-to-noise ratio. Also, the single outlying data set,  $C_{N1}$ , is no longer present. Additionally, when the test were conducted at wind tunnel speeds of 100 mph, the 5.0 Hz oscillation in the normal force coefficient is more evident between the five data sets for both the fully retracted and fully extended cases. Close examination of the fully retracted case in Figure 84 reveals that each of the five trajectory have a monotonic increase in  $C_N$  between  $t = 1.45$ s and  $t = 1.53$ s. By contrast, four of the five trajectories for the fully extended case in Figure 85 show a local minimum in  $C_N$  between  $t = 1.45$ s and  $t = 1.53$ s; and even the fifth trajectory,  $C_{N2}$ , came close to a local minimum near  $t = 1.51$ s.

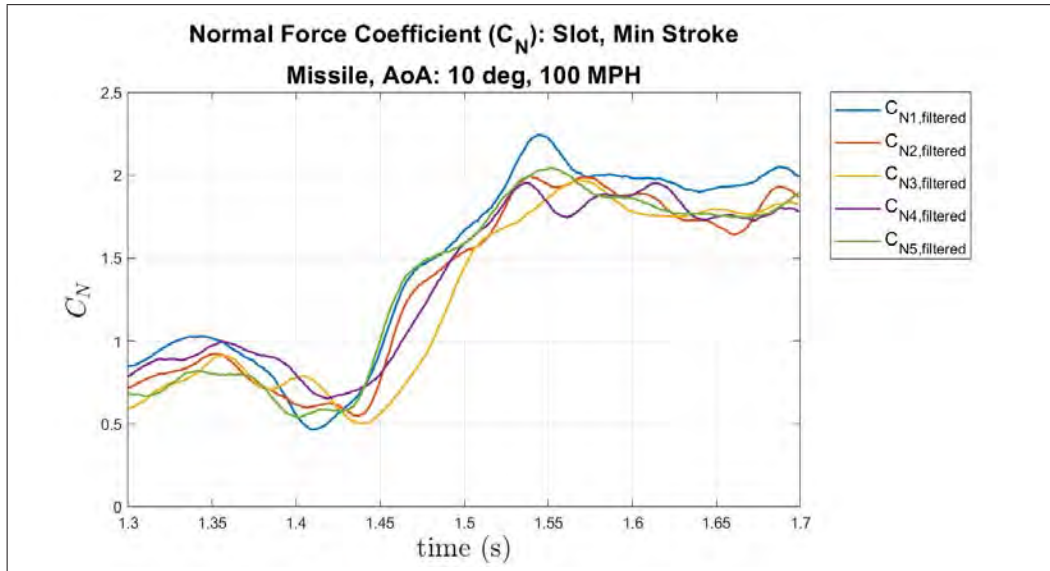
The higher signal-to-noise ratio makes identification of trends in the time prior to trajectory motion more apparent. During store motion initialized from the fully retracted position, the final trough prior to store motion occurs at the anticipated time of roughly  $t = 1.43$ , and the trough after store motion adheres to the 0.2 second period, and occurs at approximately  $t = 1.63$ . When trajectory motion is initialized at the fully extended position for the 100 mph case, the trough immediately preceding store motion appears to follow the period of 0.2 seconds, occurring at  $t = 1.35$ . However, after the trough at  $t = 1.35$ , another small oscillation lasting 0.07 seconds is observed prior to the large increase in  $C_N$  associated with store motion. This small oscillation lasts nearly one third of the 5.0 Hz time period. The sharp decrease in  $C_N$  during store motion is present in all five of the the max extension data sets, and occurs at roughly  $t = 1.50$ . After reaching a peak  $C_N$  value of approximately 2.1, the next major identifiable trough in the normal force coefficient values does not occur until approximately  $t = 1.75$ , nearly two time periods later. This deviation from the

established time period in the normal forces was present in both the 50 mph and 100 mph cases where motion was initialized at the fully extended position, although it is easier to identify in the 100 mph case than the 50 mph case. Based on the behavior of the normal force data, it appears that when store motion is initiated from the fully extended position, there is a stronger interaction with the normal forces acting on the store during trajectory motion.

It is notable that by the end of the stroke, the  $C_N$  values were comparable for both the 50 mph and 100 mph cases. Due to the relatively short stroke distance, mandated by the constraints in the wind tunnel, the influence of the cavity structure remains after  $t = 1.8s$ . Thus, the values at the end of the stroke do not correspond to the freestream values, which according to Bower [4], would be approximately  $1.9V_\infty$  for the  $10.0^\circ$  case.

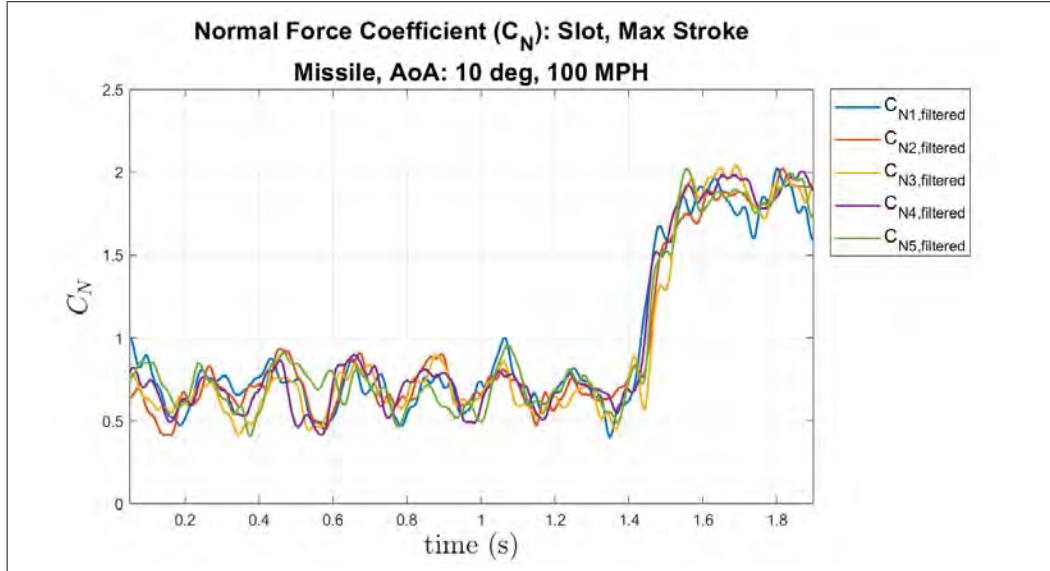


(a) Large Window: 1.85 seconds

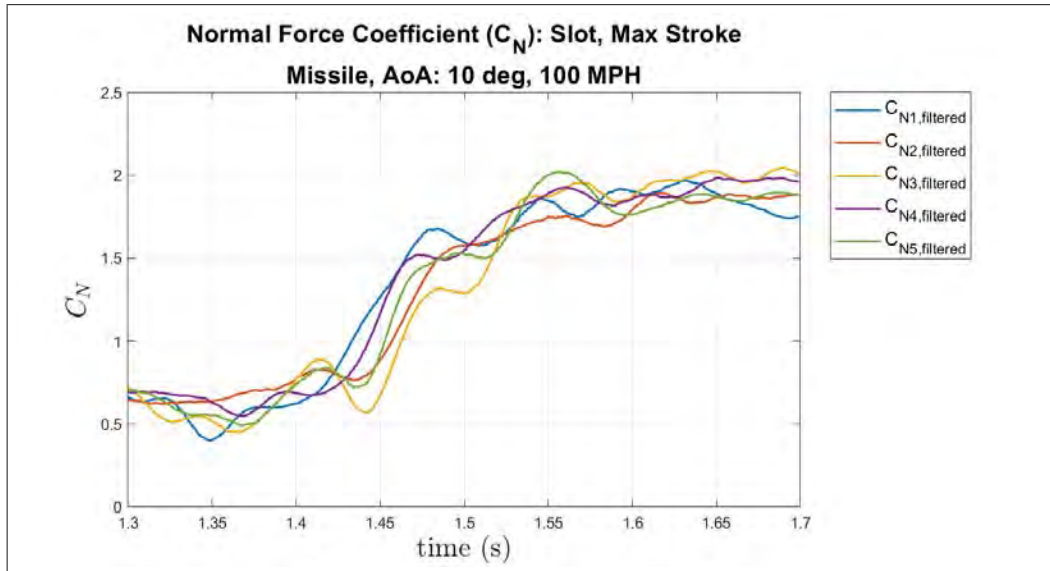


(b) Narrow Window: 0.4 seconds

Figure 84.  $C_N$ , Fully Retracted (Min Stroke),  $10.0^\circ$  AoA,  $V_\infty = 100\text{mph}$ .



(a) Large Window: 1.85 seconds



(b) Narrow Window: 0.4 seconds

Figure 85.  $C_N$ , Fully Extended (Max Stroke),  $10.0^\circ$  AoA,  $V_\infty = 100\text{mph}$ .



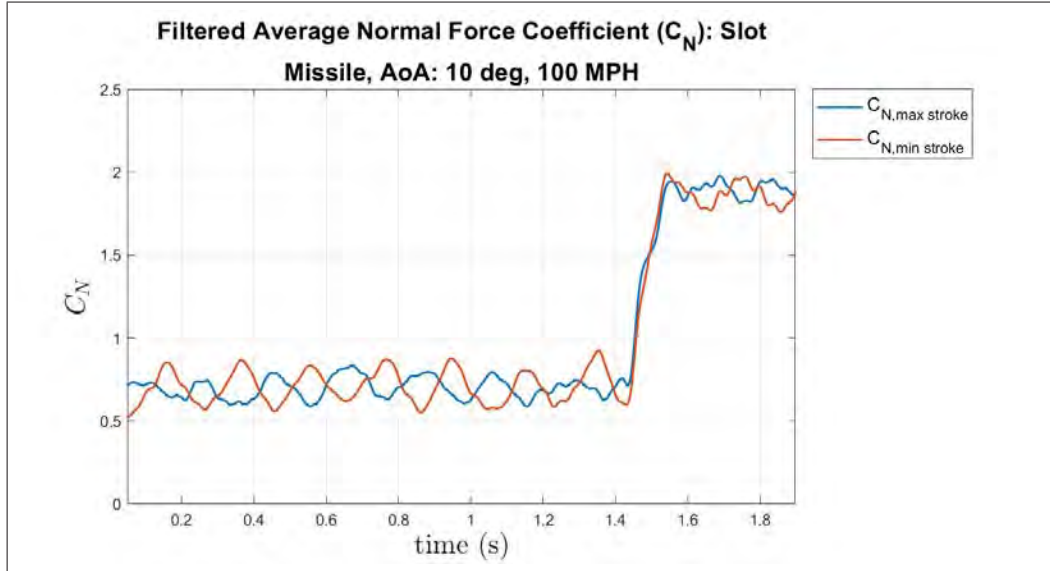
#### 4.6.5 Trajectory Analysis: Average $C_N$ Values for $10.0^\circ$ AoA, 100 mph.

The average values of the data sets collected when trajectory was initialized at either the fully extended position or the fully retracted position are presented for further analysis in Figure 86. For the data shown in Figure 86, the mission store was set to  $10^\circ$  AoA and the wind tunnel operated at 100 mph. It was anticipated that the 5.0 Hz oscillations seen in the normal forces of the two initialization positions would be out of phase due to the two triggers chosen for trajectory initialization being  $180^\circ$  out of phase with one another as well as the alignment of all data sets being accomplished using store motion. Figure 86a presents clear confirmation of the  $180^\circ$  offset expected between the normal forces in the fully extended case and the fully retracted case. Additionally, when analyzing the averaged data prior to store motion, the fully retracted case indicates a standard deviation of 0.0972 while the fully extended case has a standard deviation of 0.0620.

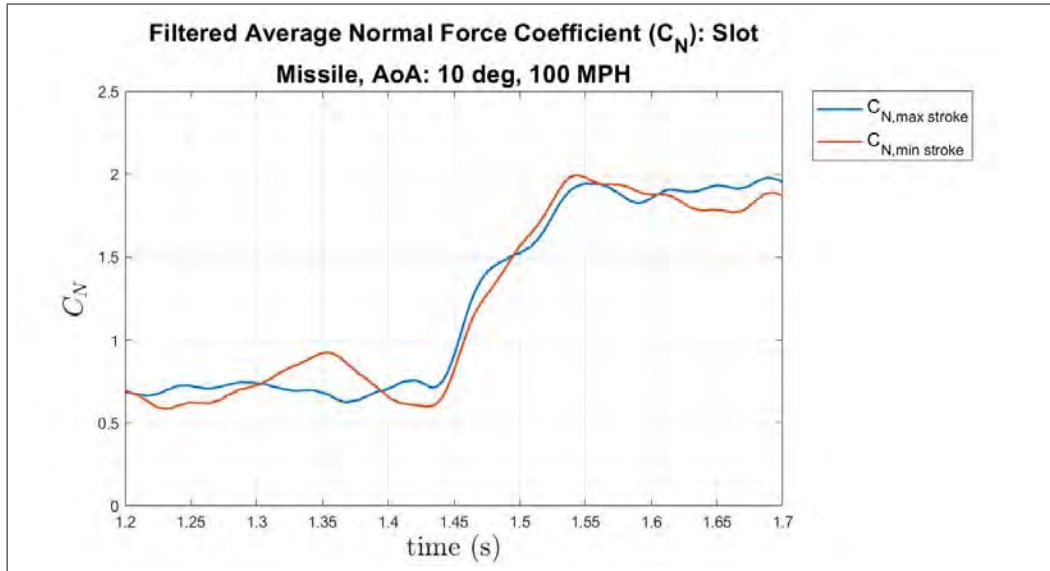
The average  $C_N$  values of the data sets also allow for identification of general differences in the slope during the trajectory motion for each initialization case. The monotonic increase observed in each of the five cases when store motion is initialized from the fully retracted position remains present when the values are averaged. Compared to the fully retracted case, the slope of the average  $C_N$  values in the fully extended case is steeper between  $t = 1.44\text{s}$  and  $t = 1.46\text{s}$ . At  $t = 1.46\text{s}$  the slope begins to decrease in magnitude until roughly  $t = 1.51$ , at which point the slope increases, resuming its upward trend until  $t = 1.54$ . The slope of the  $C_N$  values between  $t = 1.51\text{s}$  and  $1.54\text{s}$  for the fully extended case is not as steep as the initial rise between  $t = 1.44\text{s}$  and  $1.46\text{s}$ . Additionally, the concavity in the fully extended case changes from an initial negative value to positive at roughly  $t = 1.49$ .

The time at which the slope changes from positive to negative is not the same in each of the five individual data sets collected for the fully extended case, shown

in Figure 85b. As a result, a negative slope is not observed when the average values are plotted. However, the average values serve to reinforce the previously identified differences in the nearly constant slope of the fully retracted case and the variation in slope, and resultant change in concavity, for the fully extended case.



(a) Large Window: 1.85 seconds



(b) Narrow Window: 0.4 seconds

**Figure 86.**  $C_N$  Averages, Fully Retracted vs Fully Extended,  $10.0^\circ$  AoA,  $V_\infty = 100\text{mph}$ .

## 4.7 Summary

In this chapter the experimental data from Phase I was presented first. Verification of hot-wire suitability for the experimental study was accomplished by comparing velocity data collected from passive leading edge devices to the literature. Linear and contour plots of the velocity data, as well as streamwise vorticity, were presented for analysis. Following probe verification, the velocity data collected from the leading edge Slot and Diode 0.0 devices using a linear profile at  $x/L = 0.25, 0.55, 0.85$  with the motor off vs. on and the wind tunnel operating at 25 mph and 50 mph was presented. Growth of the shear layer with increasing  $x/L$  was reported and the effect of the pumping motor was to stimulate higher turbulence and shear layer growth.

Next, a comparison of the four fluidic Diode devices with the Slot at  $x/L = 0.55$  was completed to indicate why Diode 1.0 was the design chosen for modification and further consideration in the study. The data from the raster patterns were presented.

After analysis of the velocity profiles and contour plots, the capacity to force the cavity to behave in a manner more akin to a cavity in a transonic flow field is explored. A comparison of the energy frequency spectrum and velocity vs. time with the motor off and the motor on at  $x/L = 0.55$  and 50 mph was completed for the Leading Edge Slot. It was observed that the shear layer of a cavity in a subsonic environment could be directly influenced to oscillate at the same frequency as the leading edge oscillatory blowing device.

The first data presented from Phase II was the verification of synchronization between the oscillating linear motor and the store's trajectory motion. Digital encoder position collected using the Galil Software was presented, followed by images from a high-speed digital camera used for visual confirmation. Finally, force and torque data collected with a Nano-25 was used to generate plots of the filtered normal force coefficients collected at 50 and 100 mph with the mission store fixed at a  $10.0^\circ$  AoA.

## V. Conclusions and Recommendations

The primary purpose of this research was two-fold. The first goal was to explore the capacity of various leading edge oscillatory blowing devices to influence cavity flow using time-accurate velocity data collected for all three components of velocity by a tri-axial velocity probe. The second goal was to develop a method to synchronize initialization of trajectory motion with position of an oscillating linear motor and measure the effect on the store. Time-accurate force and moment measurements of the mission store were collected by a Nano-25 6-DOF sensor and analyzed for identifiable trends. Both aspects serve as an important step toward understanding and overcoming the problem of time-dependent store release from a cavity in a flow field. The following sections discuss the summary of results and the significance of the research. Additionally, recommendation for future research are discussed.

### 5.1 Summary of Results

The tri-axial velocity probe proved to be highly versatile, collecting time-accurate data for all three velocity components, which could in turn be used to analyze the cavity environment in a variety of ways. The linear profiles and contour plots of the mean streamwise velocity, as well as the turbulence intensity for the  $u$ -,  $v$ -, and  $w$ -components, proved to be the most helpful in determining the ability of the leading edge device to displace and grow the shear layer. The time vs. velocity plots and energy frequency spectrum provided insight into the capacity for the leading edge devices to force a dominant frequency in the shear layer.

The oscillatory leading edge devices evaluated in this experimental study included a single channel ‘Slot’ as well as four experimental devices referred to as ‘fluidic diodes’. The Slot was similar to that used by George and Ukeiley [21] and led to per-

formance comparisons with other leading edge devices. By design, the fluidic diodes encourage flow in one direction while offering resistance in the opposite, allowing for a desired circulation of the flow to be established within the leading edge device. In this study, leading edge devices employing the fluidic diode concept were designed with three internal channels. The changes between the initial design, Diode 0.0, and the subsequent designs include an increase in internal structures and a modification to the edge treatment at the inlet and exhaust openings. The modification to the edge treatment at the openings included curving the exhaust openings toward the direction of the flow and the inlet openings toward the upstream direction. Compared to Diode 0.0, Diode 1.0 lifted and increased the thickness of the shear layer by a factor of two at  $y/D = 0$ . Because there were two major modifications made between Diode 0.0 and Diode 1.0, determining whether the increased complexity of the internal geometry or the curvature at the inlet and exhaust openings played a greater factor is not definitive.

Of all the active leading edge devices observed, Diode 1.0 and 1.0a had the greatest capacity to lift, and increase thickness of, the shear layer. Additionally, Diode 2.0, which had the most complex internal geometry, was observed as having increased the wall-normal and floor-normal components of turbulence intensity (by nearly 30%) over Diode 1.0. This is a possible indicator that the ability to encourage flow in the desired direction within Diode 2.0 was in fact more pronounced.

The ability to force a dominant frequency within the shear layer and detect its influence on the store was highly successful, as evidenced by the time-accurate velocity vs. time and energy frequency spectrum completed in this study. The frequency at which the leading edge blowing device operates correlates directly with the velocity vs. time fluctuations detected in the shear layer.

The synchronization of the oscillatory leading edge device and initialization of the

store trajectory with the wind tunnel operating was successfully verified using two different methods. First, the time-accurate position of the two motors, provided by the high-resolution (1.0 micron) digital encoder, was collected using the Galil Software. Second, a high-speed digital camera was used to provide visual confirmation. Only two locations in the oscillating cycle were assessed in the wind tunnel experiment: piston fully retracted and piston fully extended. However, a bench-top experiment proved that the conditional loop in the Galil program could be modified so that store motion trajectory can be initiated at any point during the oscillatory motion, allowing for flexibility in future studies.

The time-accurate data collected at 1000 Hz using the Nano-25 showed distinct evidence that the frequency of the oscillatory blowing influences the normal force component within the shear layer to oscillate at the same frequency. Furthermore, when evaluating the normal forces during store trajectory motion, there were distinct differences observed when motion was initiated at the fully extended and fully retracted locations. However, the extent of the experimental study evaluating the force and moment data was not sufficiently thorough to determine if a pitch bifurcation can be reliably predicted.

## **5.2 Significance of Research**

The major significance of the research conducted in Phase I is proof that forcing flow through the fluidic diode leads to different flow characteristics compared to the leading edge Slot. While further design refinement is necessary, the fluidic diodes in this experimental study demonstrated a definite capacity to influence the thickness and height of the shear layer that spans a cavity in a flow field. The simplicity of the fluidic diode and the lack of internal moving parts make them a strong candidate for further research. Additionally, it was found that leading edge devices in a low speed

wind tunnel have the capability to force the shear layer at a desired frequency, with the potential to replicate the vortex shedding and dominant frequencies present in a transonic and supersonic flow field.

The major significance of the research conducted in Phase II is the successful proof of concept that mission store release can be synchronized with an oscillatory leading edge blowing device. Additionally, the time-accurate force and moment data collected by the Nano-25 indicated that the 5.0 Hz oscillatory blowing from the leading edge device forces a clear, 5.0 Hz oscillation in the normal forces of the shear layer. Furthermore, identifiable patterns were observed in the data collected when the store was released at different times in the oscillating motor's cycle.

### **5.3 Recommendations for Future Testing**

The fluidic diodes were primarily developed as a proof-of-concept for leading edge oscillatory blowing and when compared to the leading edge Slot, indicated a very strong capacity to influence the shear layer at the span-wise center. Given the store's position at span-wise center during trajectory analysis, it could be anticipated that an even greater normal force would be imparted on the store by the fluidic diode. Using the experimental setup and store motion triggers detailed in this document, a suggested starting point for future trajectory analysis would be to collect force and moment data imparted on the store by Diode 1.0a. Additionally, the design of the fluidic diode has room for significant refinement, particularly in exploring their capacity to encourage flow in a desired direction or how increasing the number of channels might influence the cavity shear layer.

While it was found that the leading edge oscillatory blowing can force a dominant frequency in the cavity flow field, as currently configured the linear motor is not capable of attaining the oscillatory rates found in a transonic cavity. Alternate methods

capable of achieving the required frequency of oscillation to accurately mimic the cavity environment found at higher Mach numbers should be explored. A modified version of the actuator used by Lamp and Chokani [32], capable of delivering oscillatory blowing at frequencies up to 750.0 Hz using pressurized air, would be preferable. However, concurrently running the setup used in this experimental study along with the pressurized air device has the potential to become exceedingly complicated.

The linear motors were selected for their ability to be synchronized using a DMC-4020 multi-axis controller. Working to incorporate synchronized trajectory motion with the the developments made by Sellers [50] and Bower [4] on the Motion Test Apparatus would allow for investigation of more complex store separation trajectories.



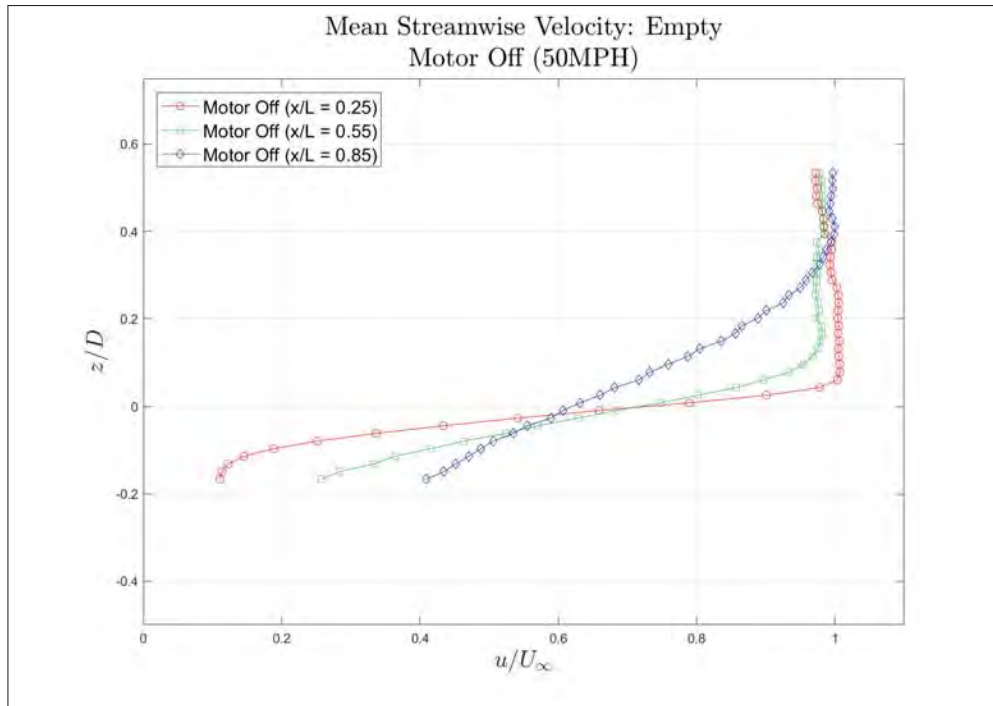
## Appendix A. Additional Experimental Data

### Index of Figures in Appendix A

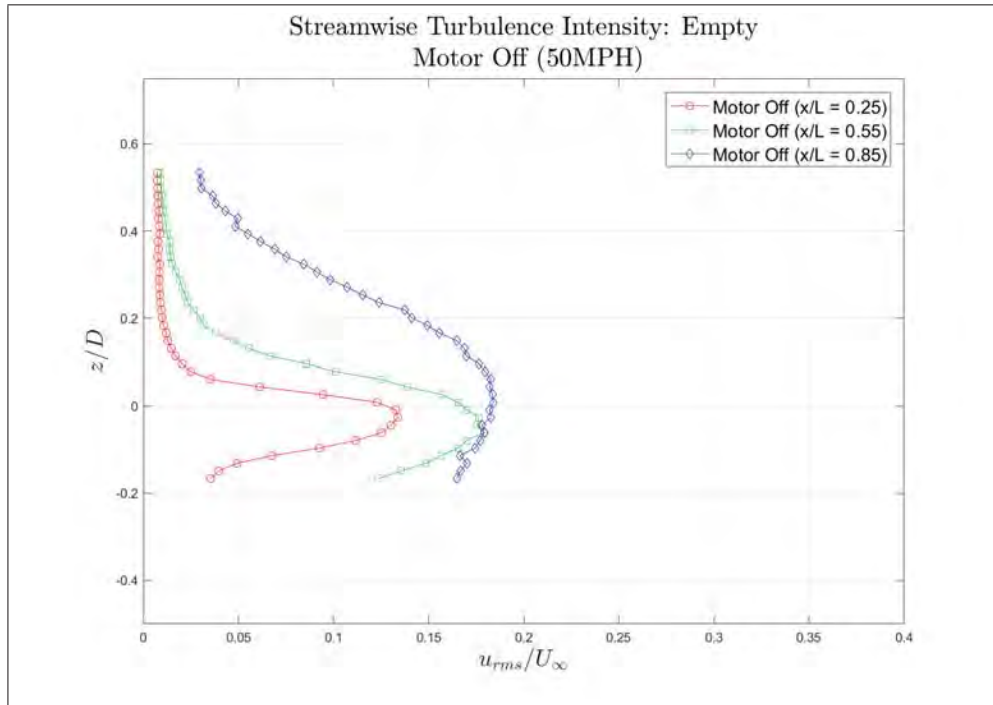
|   |          |
|---|----------|
| Linear Patterns - Empty Cavity  | (pg 162) |
| Linear Patterns - Passive Devices                                     | (pg 165) |
| Linear Patterns - Slot: 50 and 25mph at $x/L = 0.25, 0.55, 0.85$      | (pg 168) |
| Linear Patterns - Diode 0.0: 50 and 25mph at $x/L = 0.25, 0.55, 0.85$ | (pg 174) |
| Linear Patterns - Slot vs. Diodes at $x/L = 0.55$                     | (pg 180) |
| Raster Patterns - Passive Devices: Sawtooth Spoiler                   | (pg 183) |
| Raster Patterns - Passive Devices: Rectangular Tab                    | (pg 185) |
| Raster Patterns - Passive Devices: Triangular Tab                     | (pg 187) |
| Raster Patterns - Baseline Cavity: 50mph at $x/L = 0.55$              | (pg 189) |
| Raster Patterns - Slot: 50mph at $x/L = 0.55$                         | (pg 191) |
| Raster Patterns - Diode 0.0: 50mph at $x/L = 0.55$                    | (pg 193) |
| Raster Patterns - Diode 1.0: 50mph at $x/L = 0.55$                    | (pg 195) |
| Raster Patterns - Diode 1.0a: 50mph at $x/L = 0.55$                   | (pg 197) |
| Raster Patterns - Diode 2.0: 50mph at $x/L = 0.55$                    | (pg 199) |
| Streamwise Vorticity Plots - 50mph at $x/L = 0.55$                    | (pg 201) |
| Velocity vs. Time Plots - Slot: 50 mph at $x/L = 0.55$                | (pg 207) |
| Energy Frequency Spectrum - Slot: 50 mph at $x/L = 0.55$              | (pg 209) |
| Autocovariance Plots - Slot: 50mph at $x/L = 0.55$                    | (pg 211) |
| Probabily Distribution Functions - Slot: 50mph at $x/L = 0.55$        | (pg 215) |
| Force and Moment Plots - 0.0 degree AoA                               | (pg 219) |
| Force and Moment Plots - 10.0 degree AoA                              | (pg 231) |

# Linear Patterns

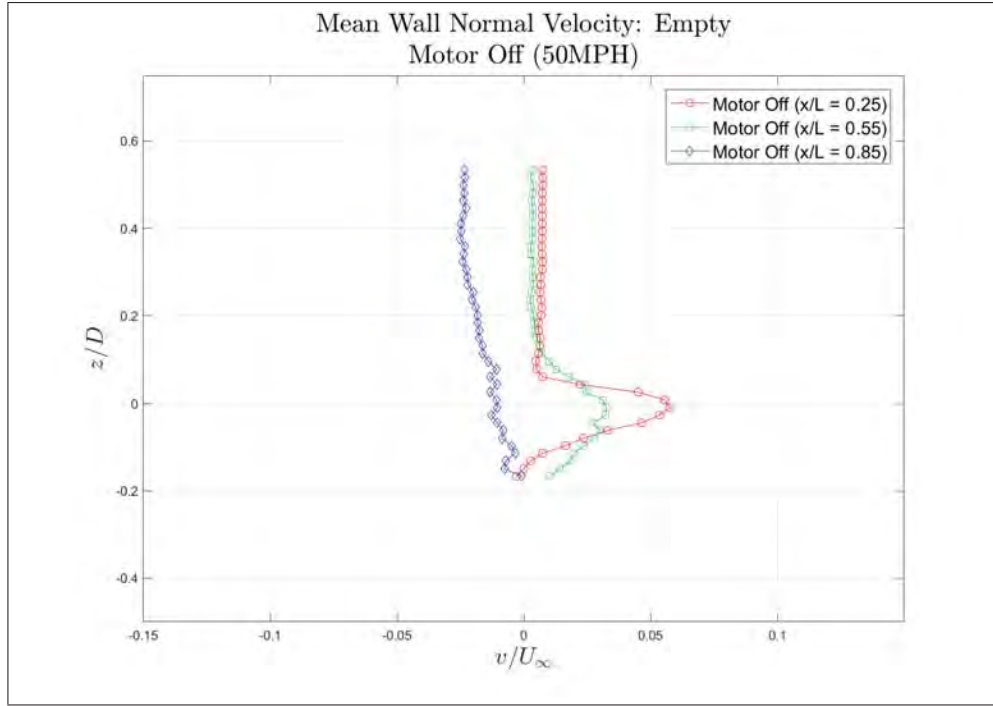
## Empty Cavity



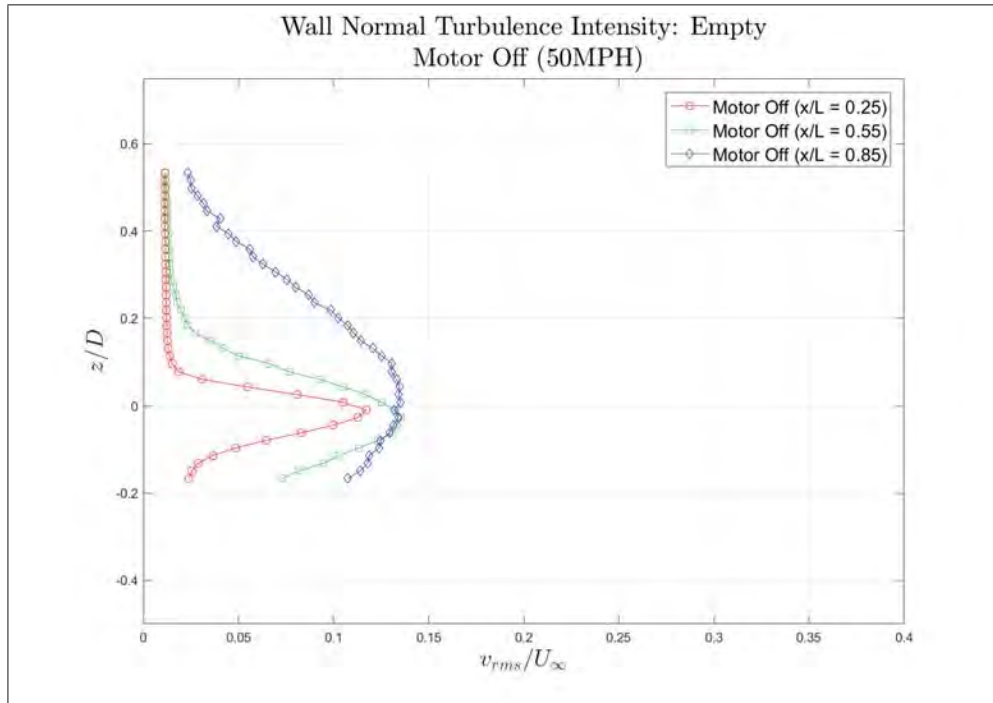
(a) Mean Streamwise Velocity: Empty (50mph)



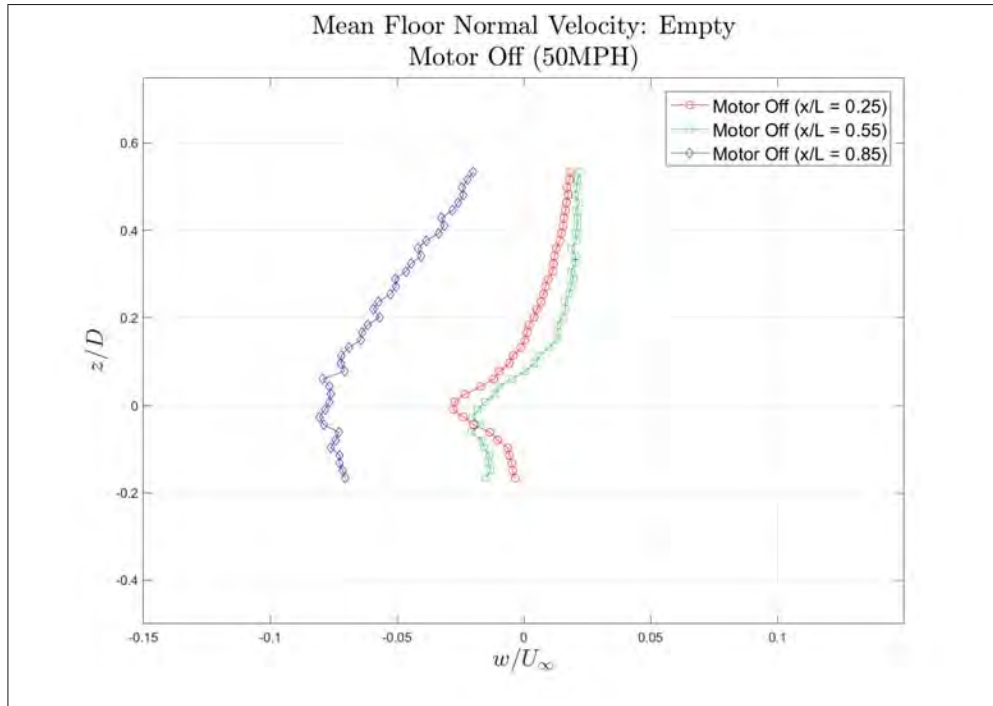
(b) Streamwise Turbulence Intensity: Empty (50mph)



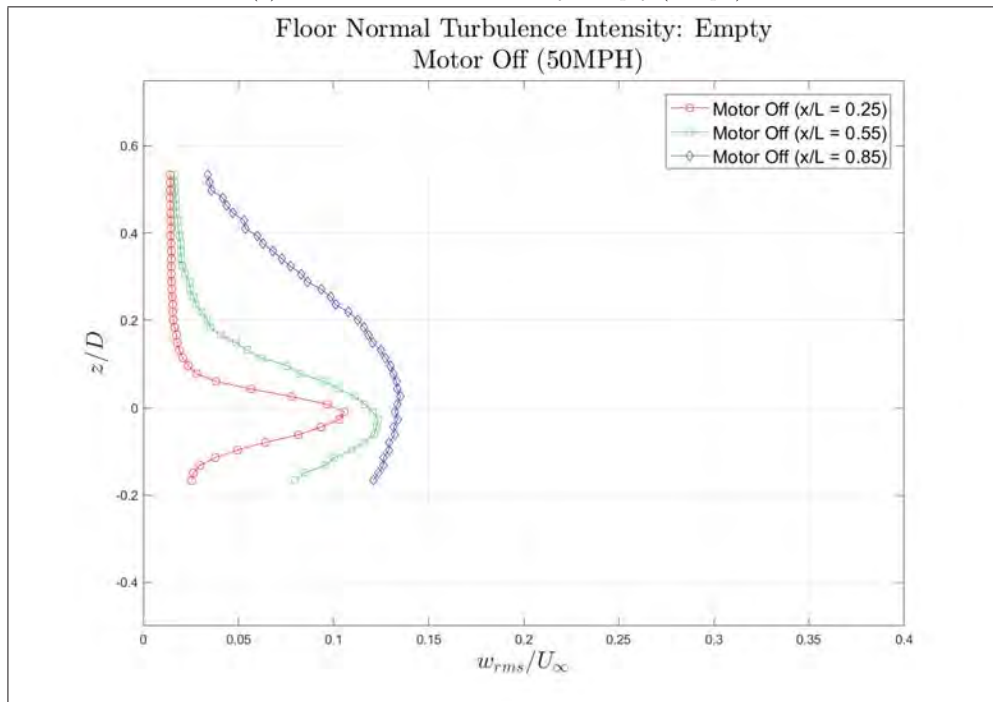
(a) Mean Wall Normal Velocity: Empty (50mph)



(b) Wall Normal Turbulence Intensity: Empty (50mph)

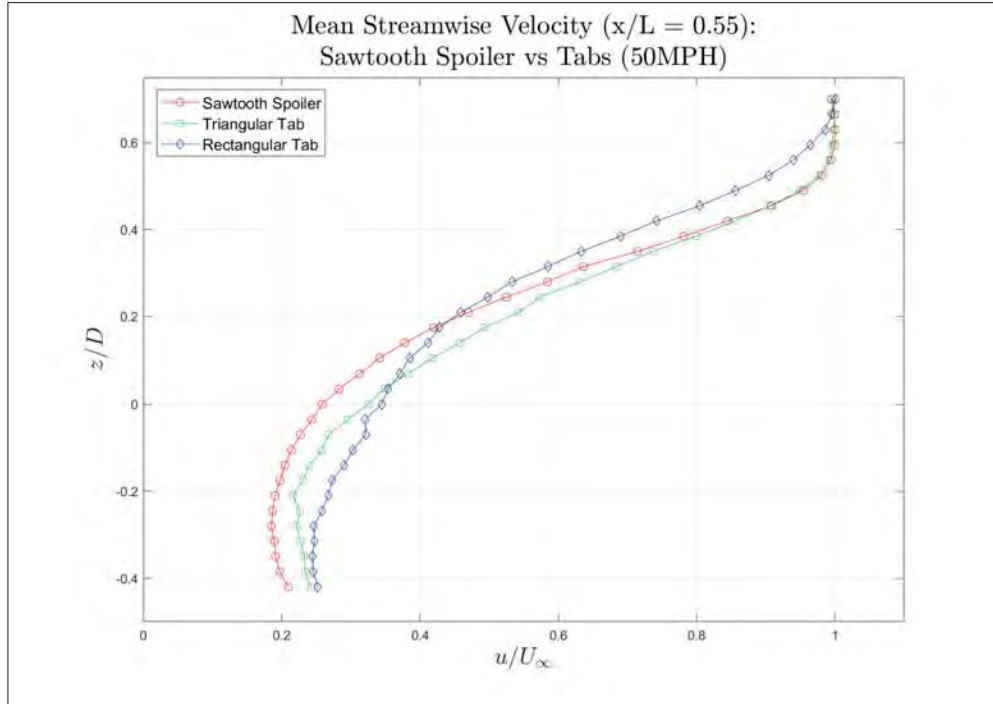


(a) Mean Floor Normal Velocity: Empty (50mph)

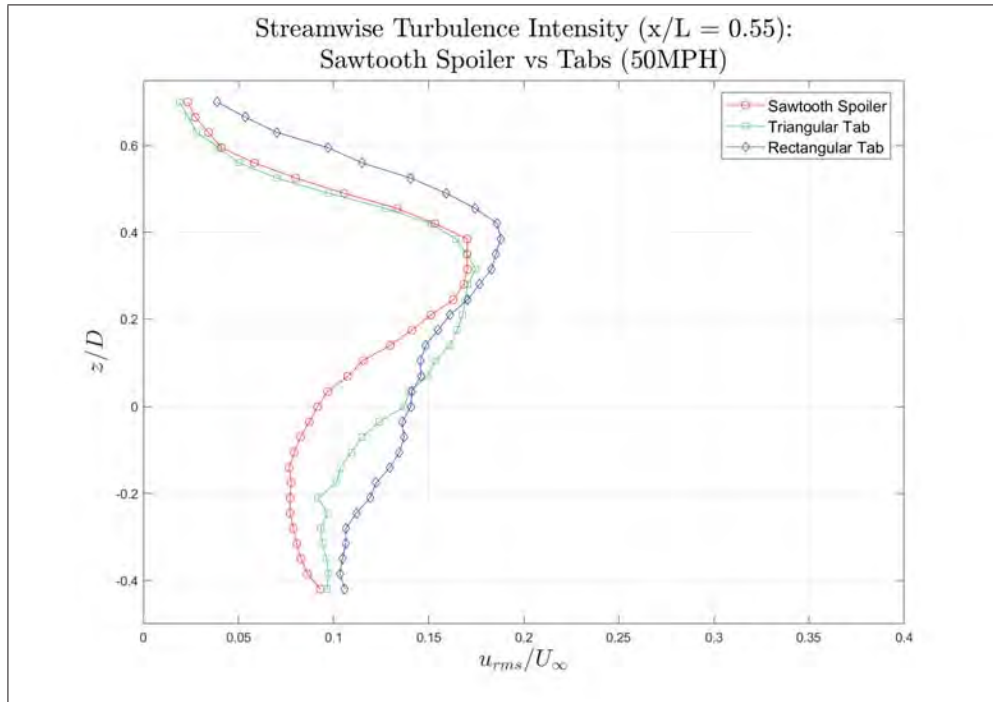


(b) Floor Normal Turbulence Intensity: Empty (50mph)

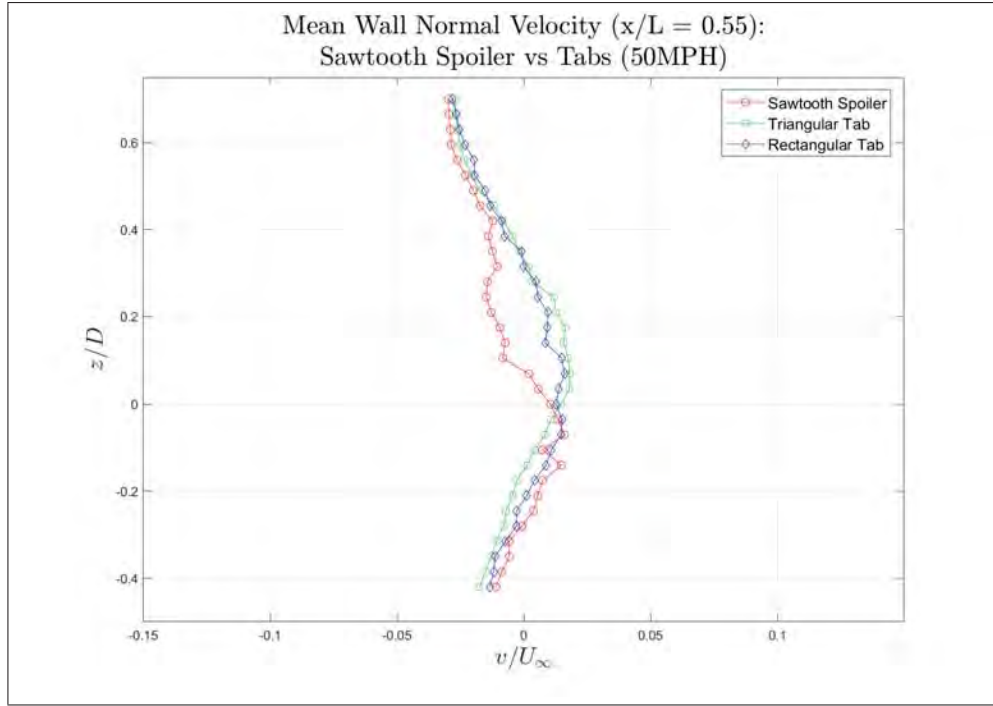
## Passive Devices



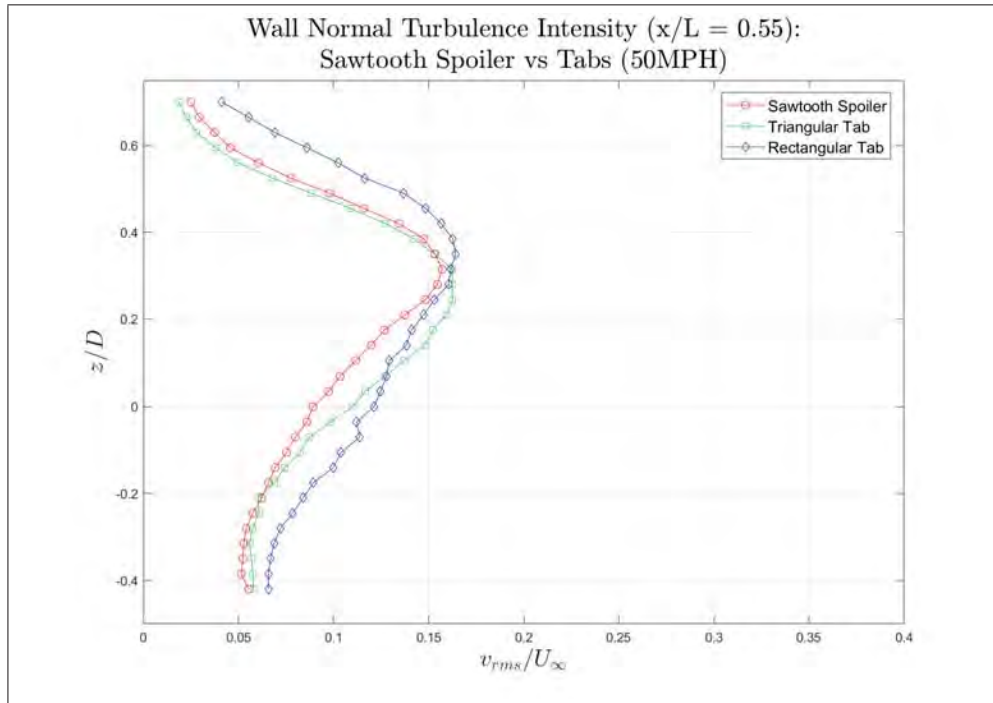
(a) Mean Streamwise Velocity: Passive Devices (50mph)



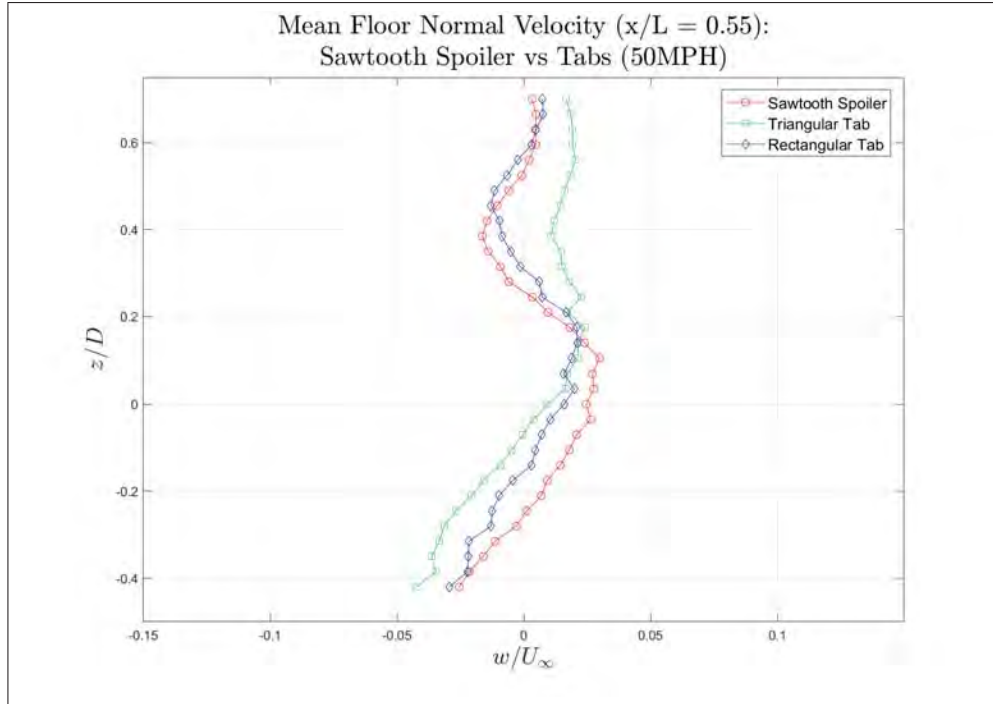
(b) Streamwise Turbulence Intensity: Passive Devices (50mph)



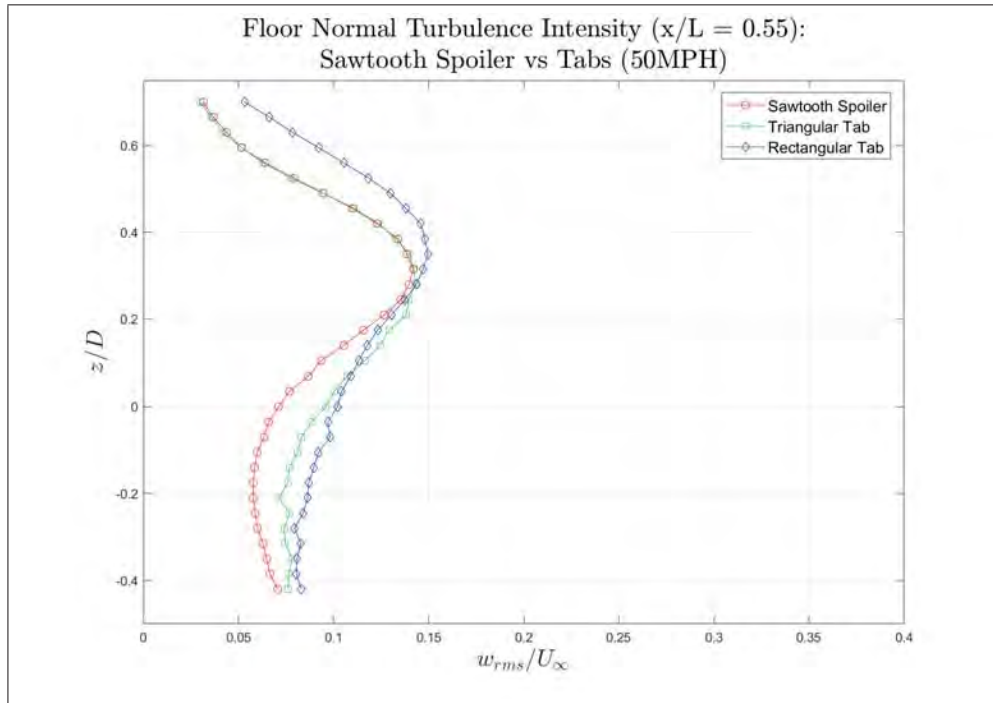
(a) Mean Wall Normal Velocity: Passive Devices (50mph)



(b) Wall Normal Turbulence Intensity: Passive Devices (50mph)

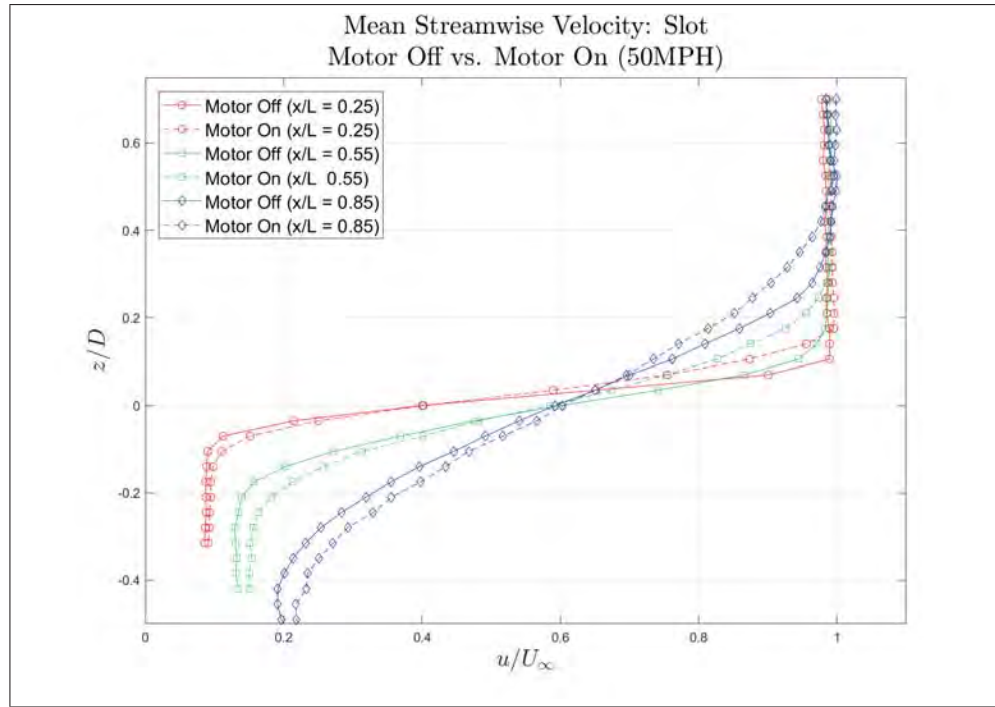


(a) Mean Floor Normal Velocity: Passive Devices (50mph)

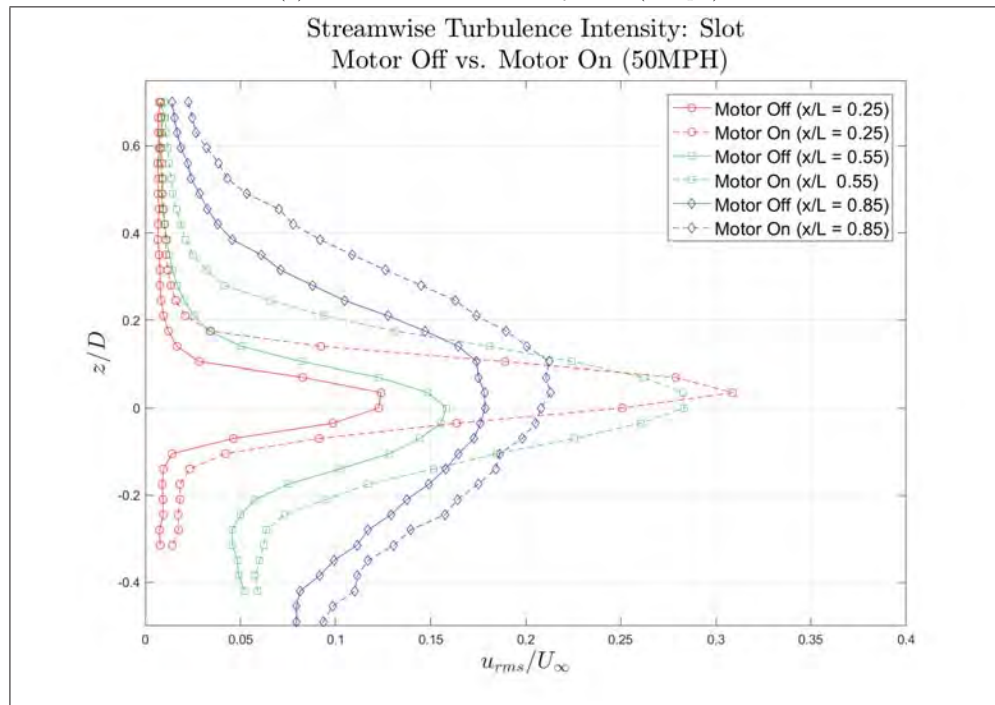


(b) Floor Normal Turbulence Intensity: Passive Devices (50mph)

Slot: 50mph and 25mph ( $x/L = 0.25, 0.55, 0.85$ )

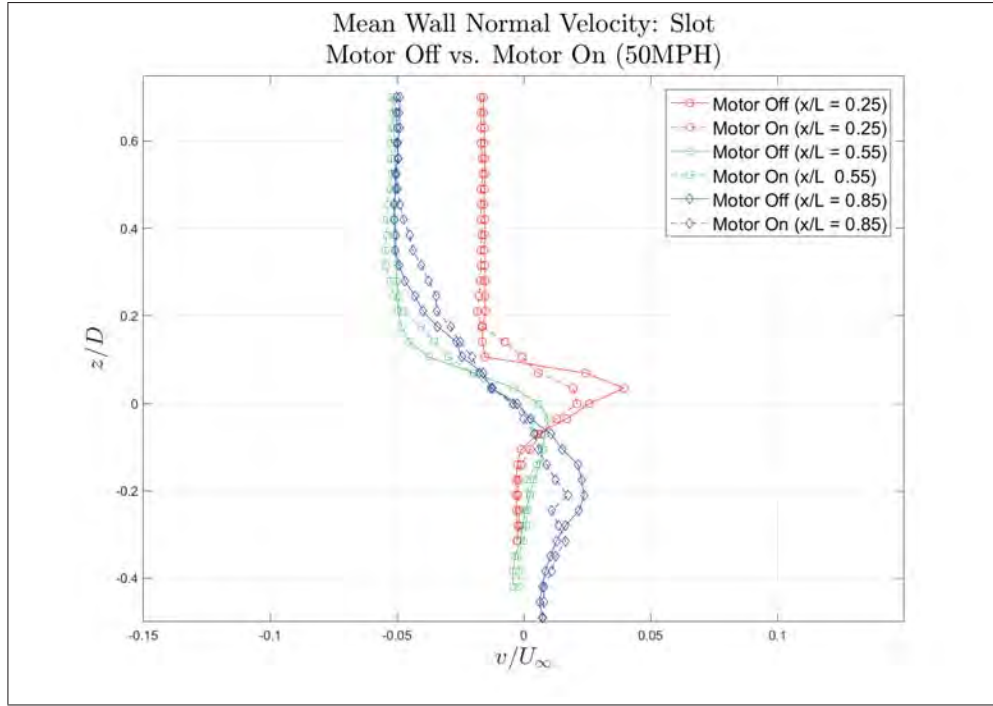


(a) Mean Streamwise Velocity: Slot (50mph)

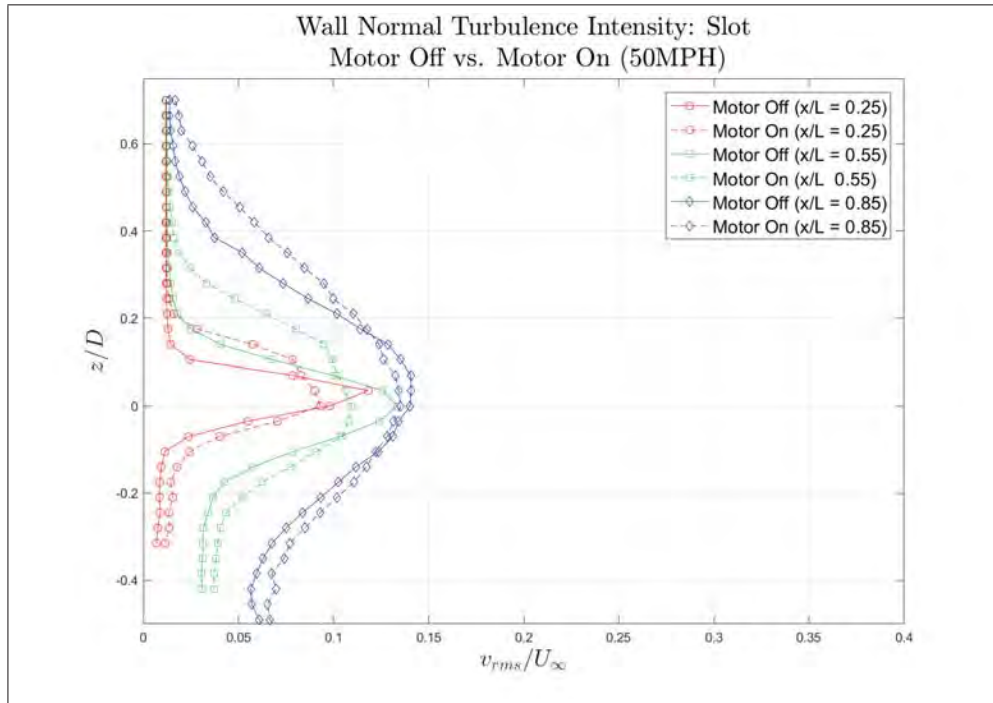


(b) Streamwise Turbulence Intensity: Slot (50mph)

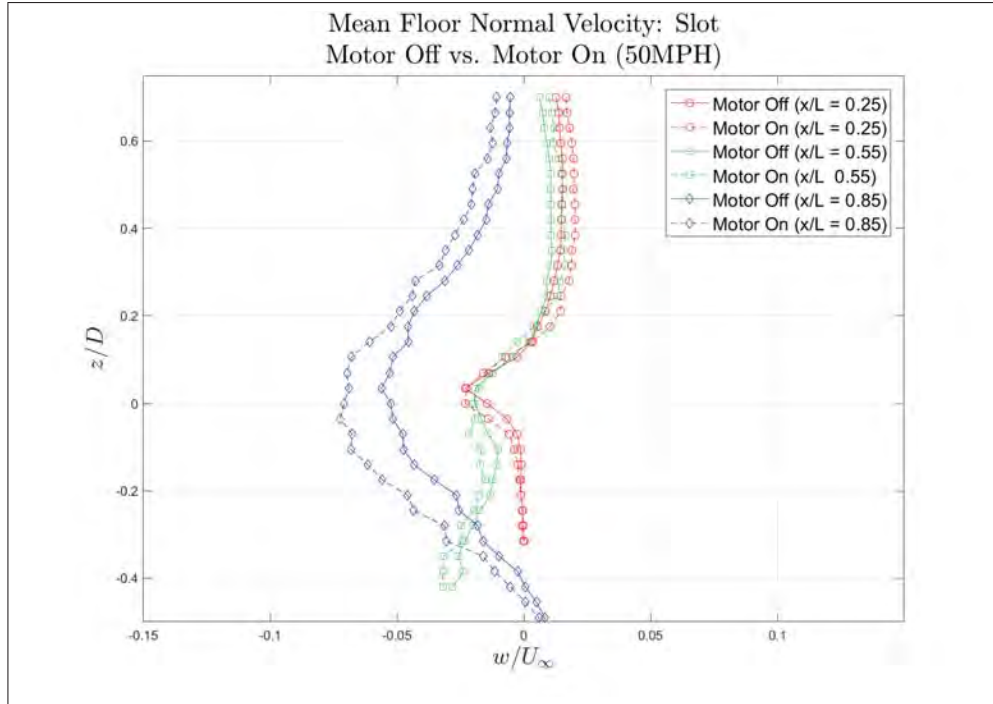




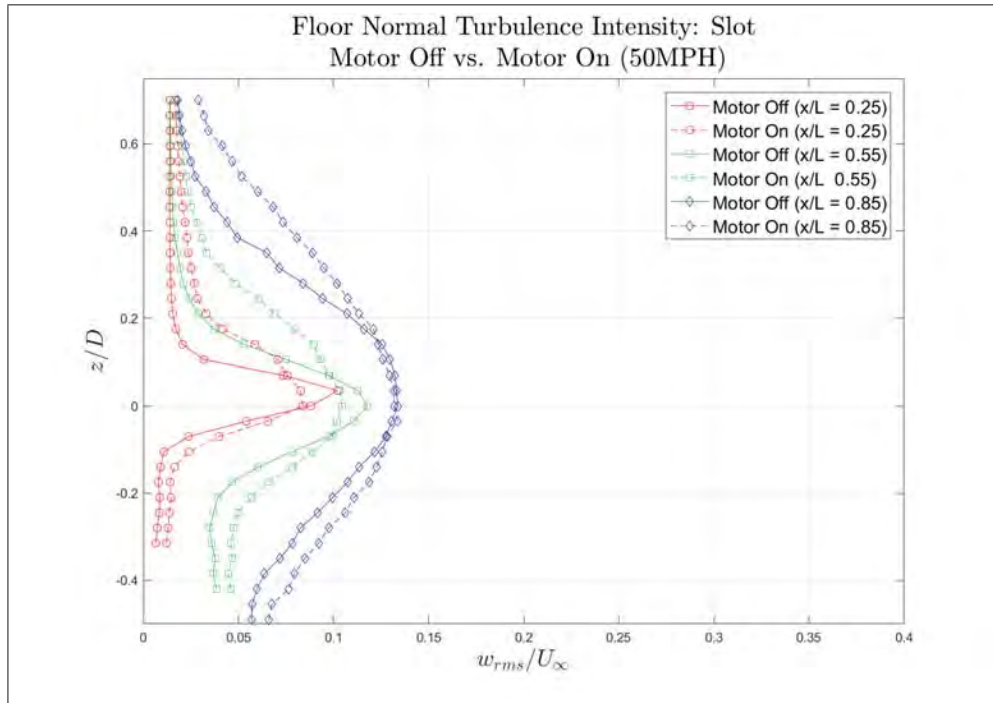
(a) Mean Wall Normal Velocity: Slot (50mph)



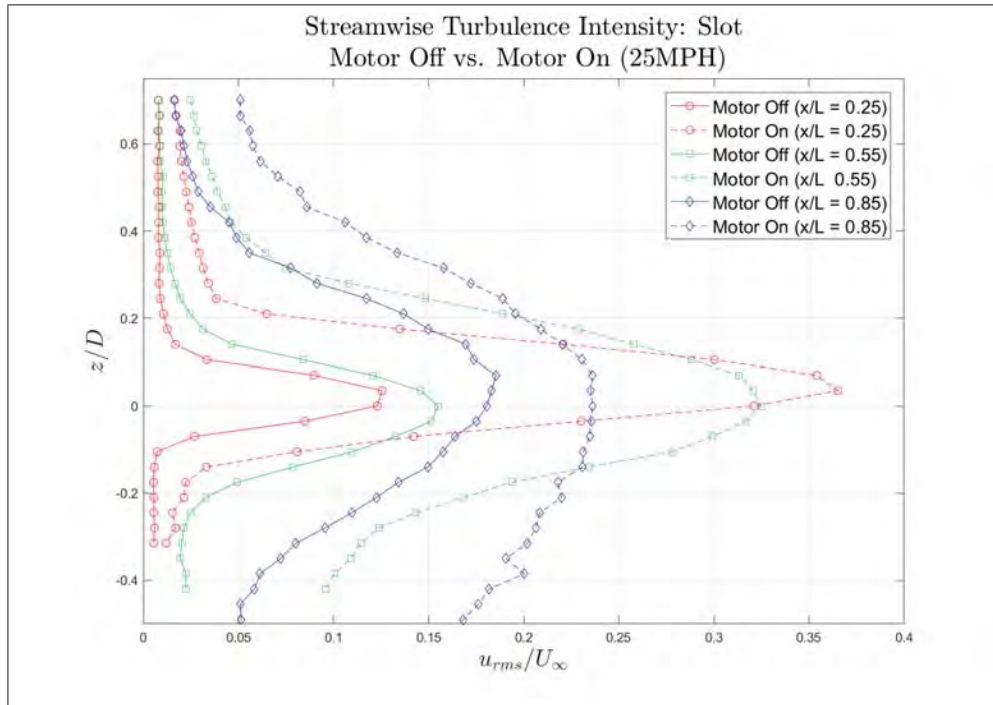
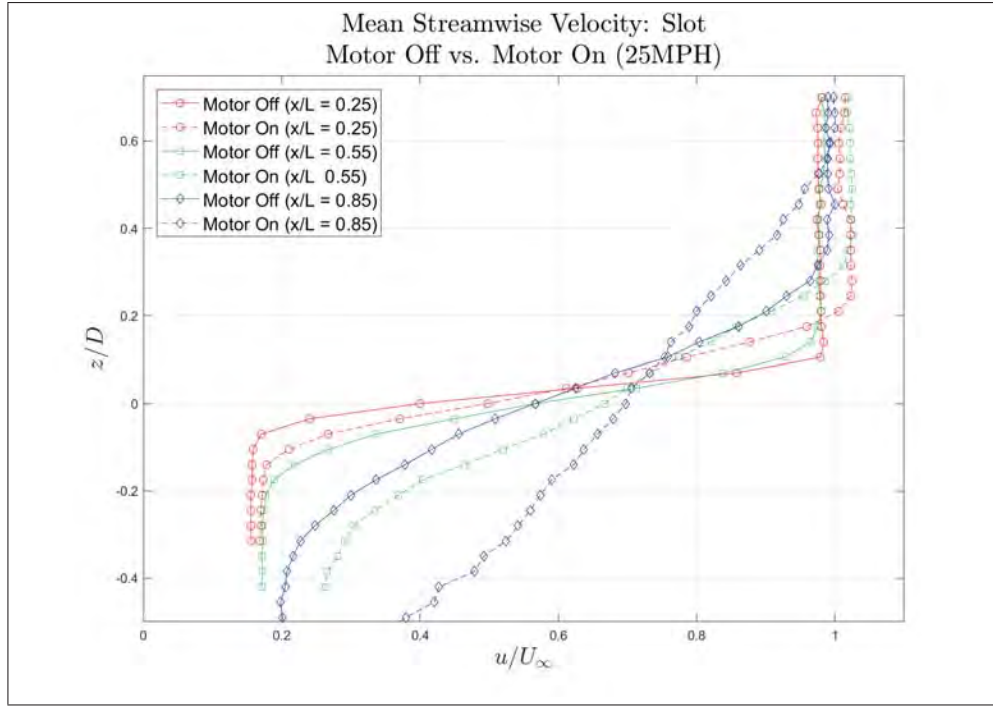
(b) Wall Normal Turbulence Intensity: Slot (50mph)

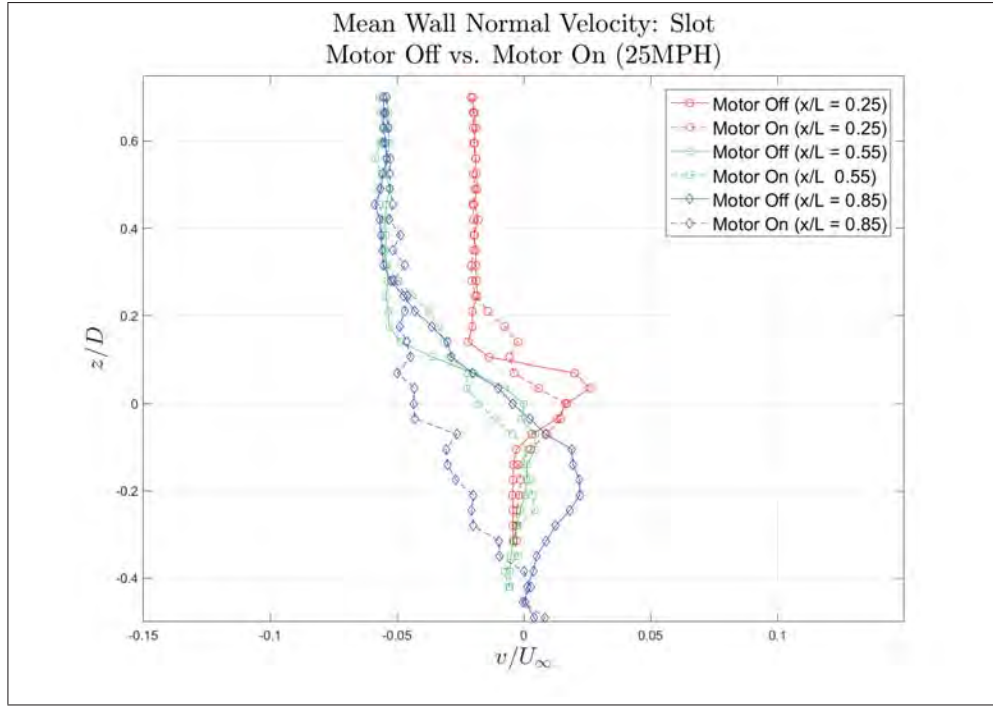


(a) Mean Floor Normal Velocity: Slot (50mph)

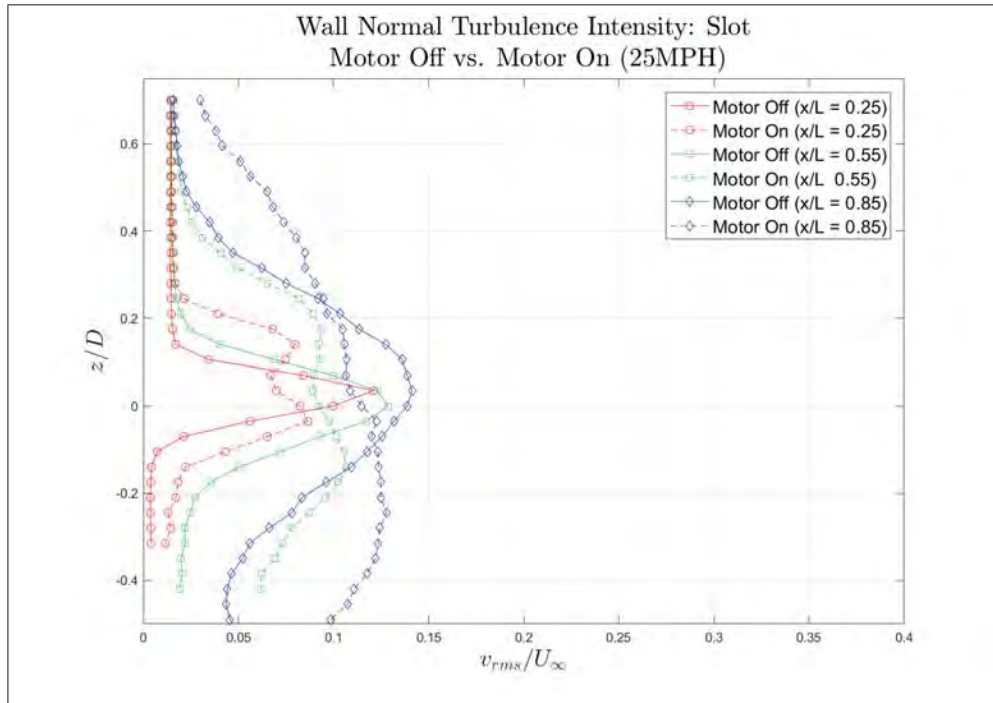


(b) Floor Normal Turbulence Intensity: Slot (50mph)

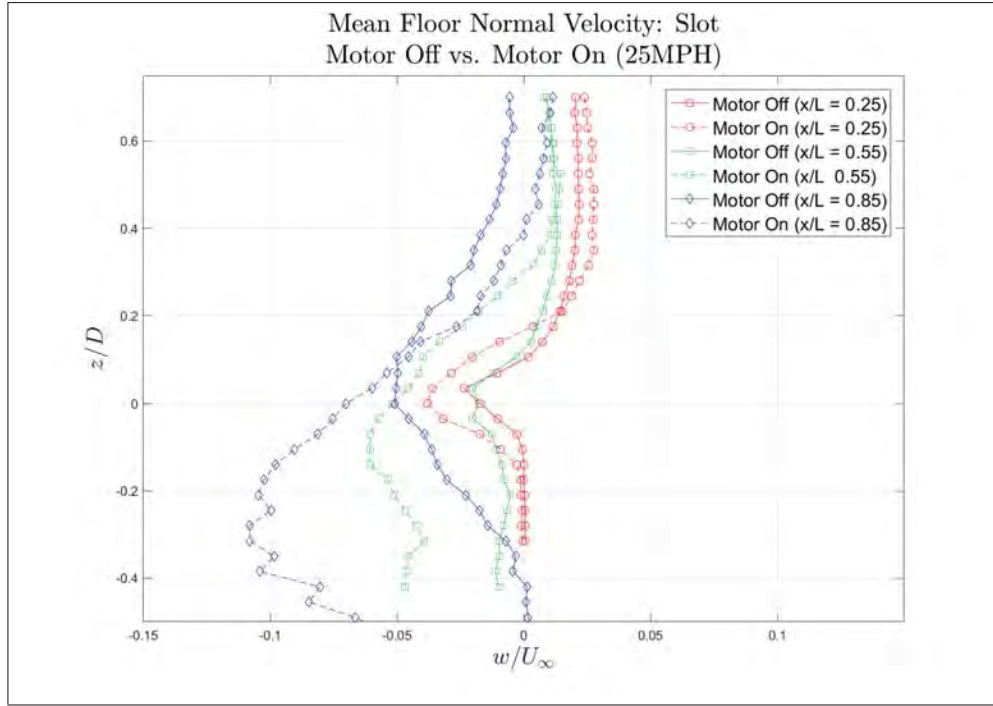




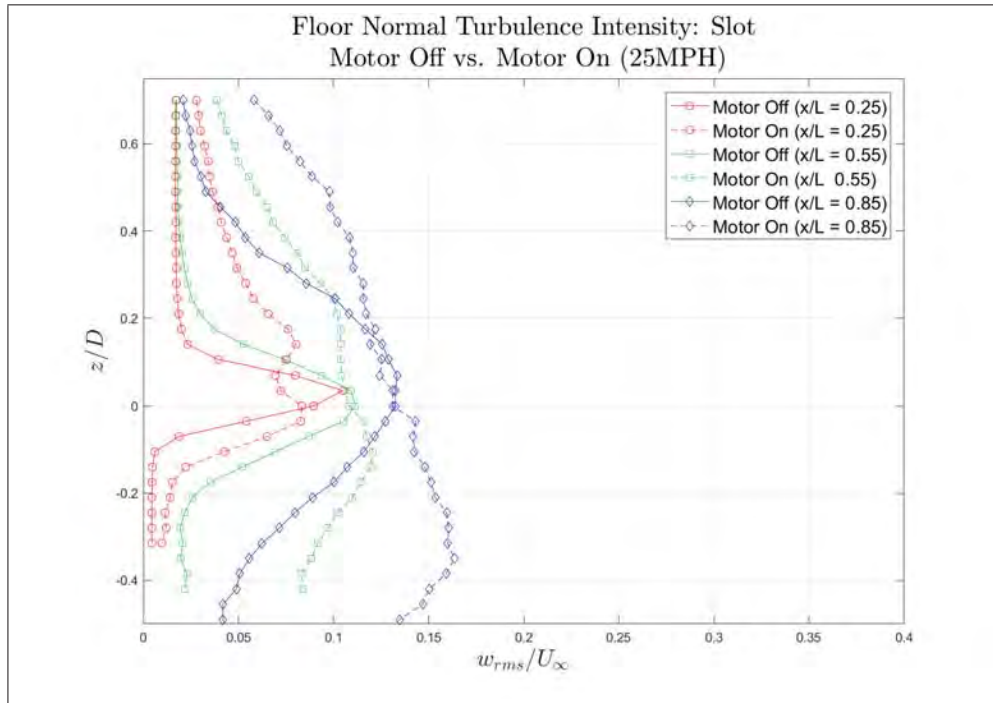
(a) Mean Wall Normal Velocity: Slot (25mph)



(b) Wall Normal Turbulence Intensity: Slot (25mph)

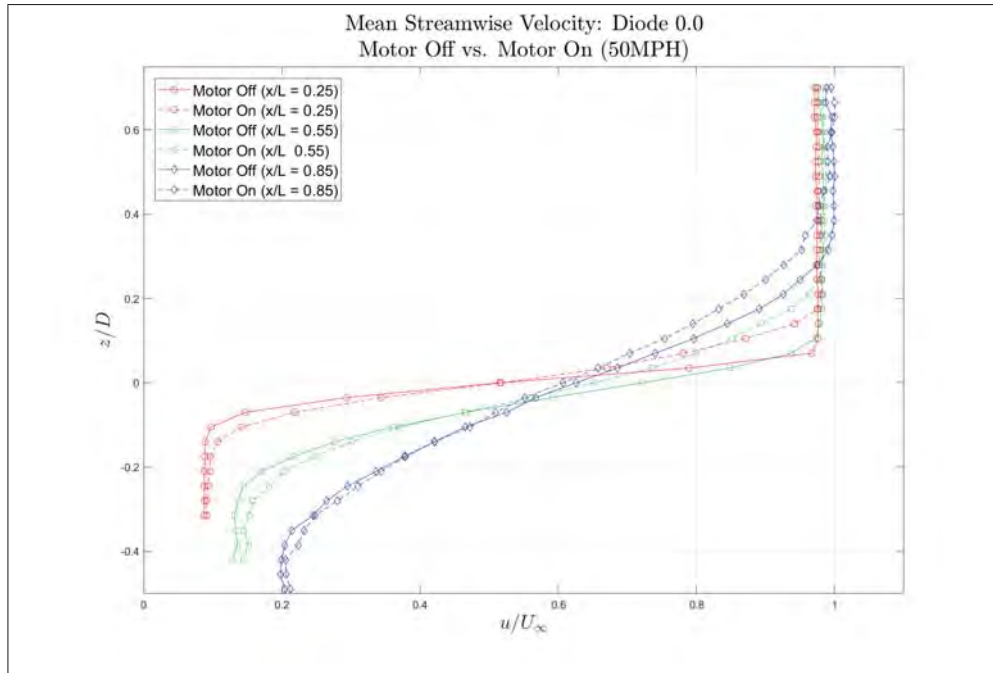


(a) Mean Floor Normal Velocity: Slot (25mph)

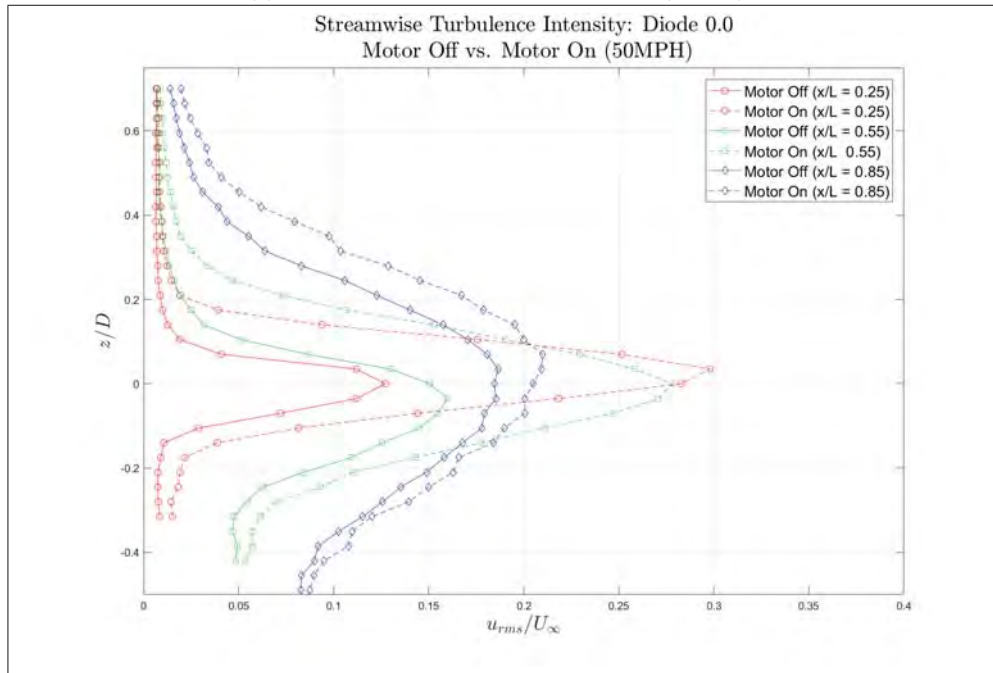


(b) Floor Normal Turbulence Intensity: Slot (25mph)

Diode 0.0: 50mph and 25mph ( $x/L = 0.25, 0.55, 0.85$ )

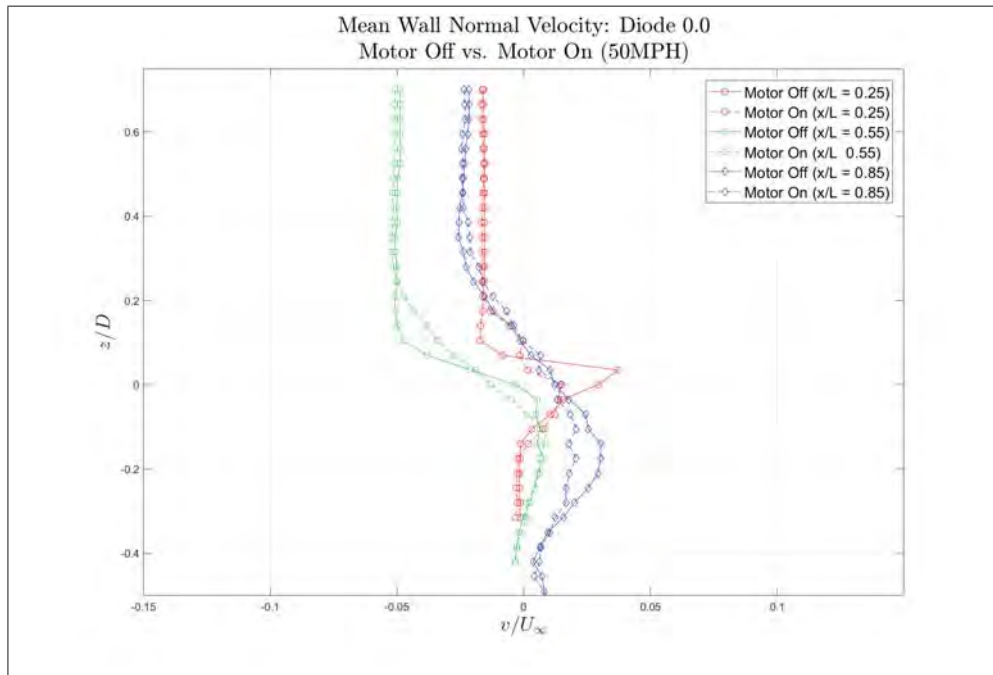


(a) Mean Streamwise Velocity: Diode 0.0 (50mph)

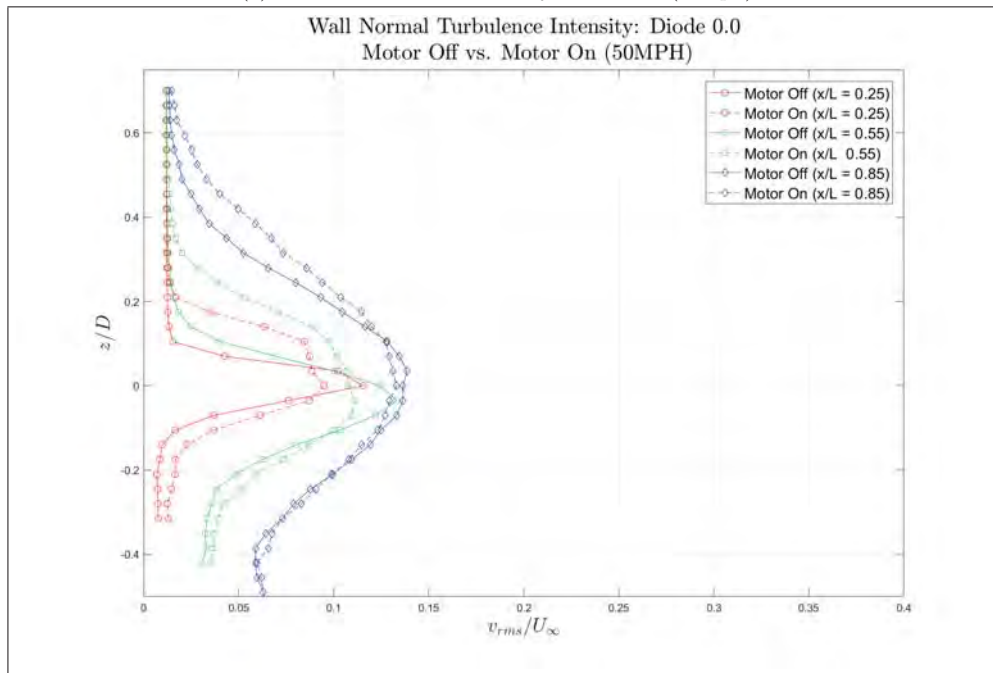


(b) Streamwise Turbulence Intensity: Diode 0.0 (50mph)

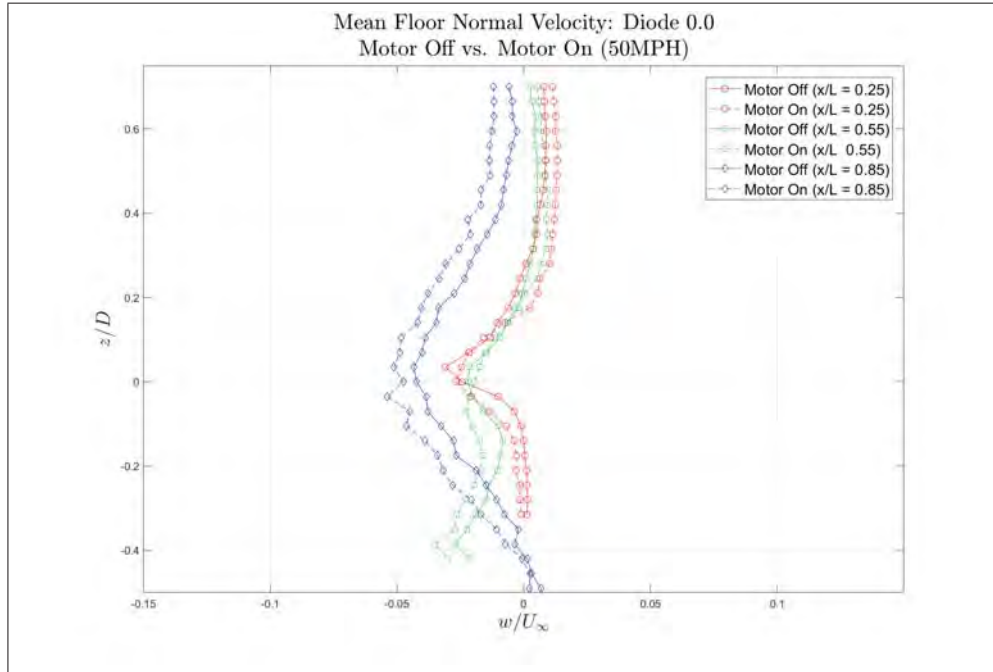




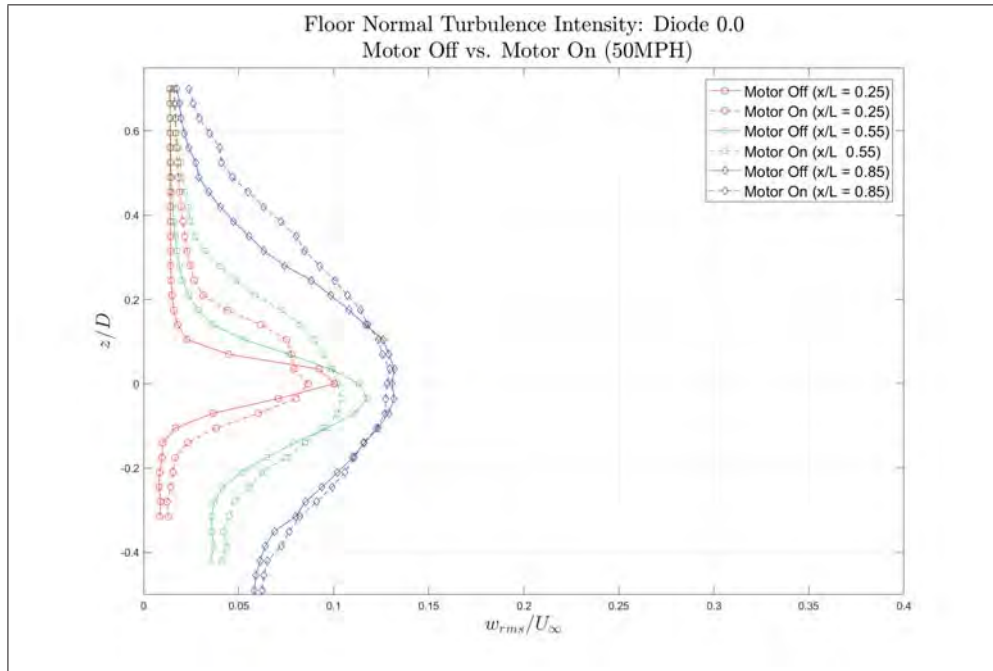
(a) Mean Wall Normal Velocity: Diode 0.0 (50mph)



(b) Wall Normal Turbulence Intensity: Diode 0.0 (50mph)

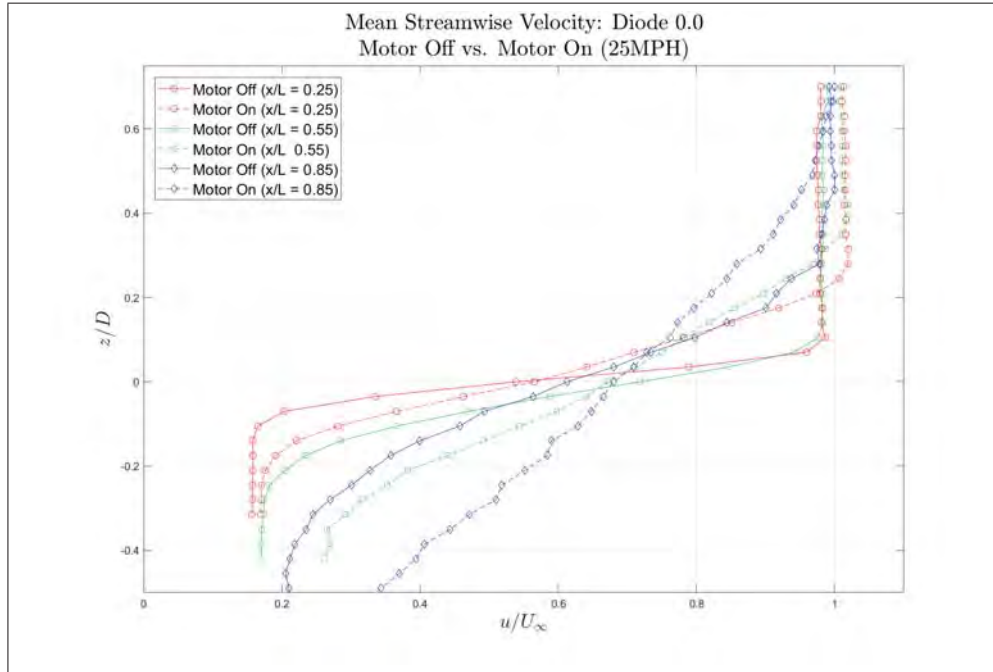


(a) Mean Floor Normal Velocity: Diode 0.0 (50mph)

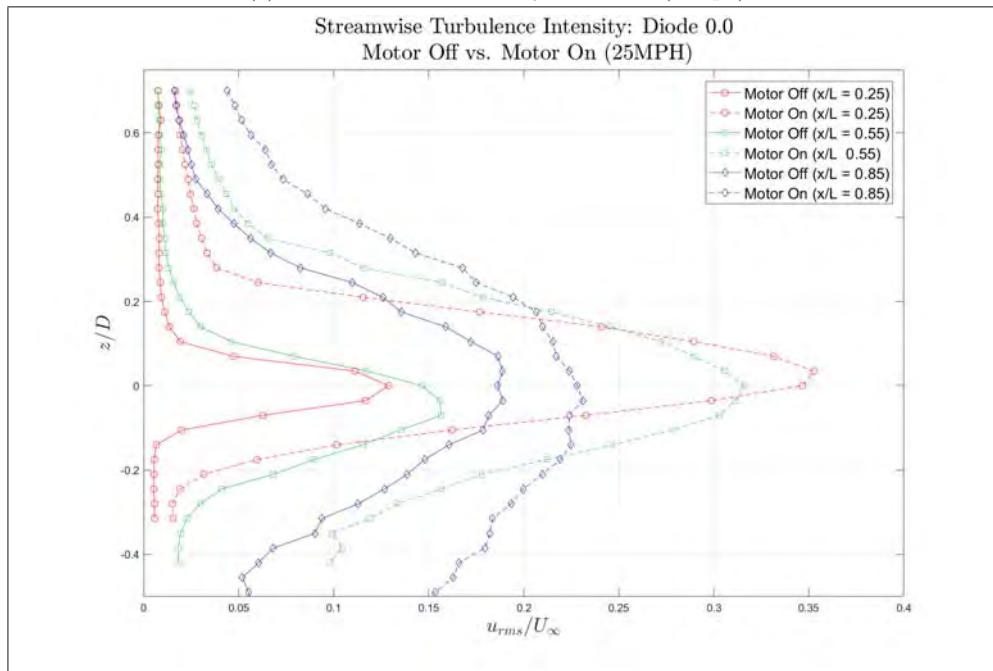


(b) Floor Normal Turbulence Intensity: Diode 0.0 (50mph)

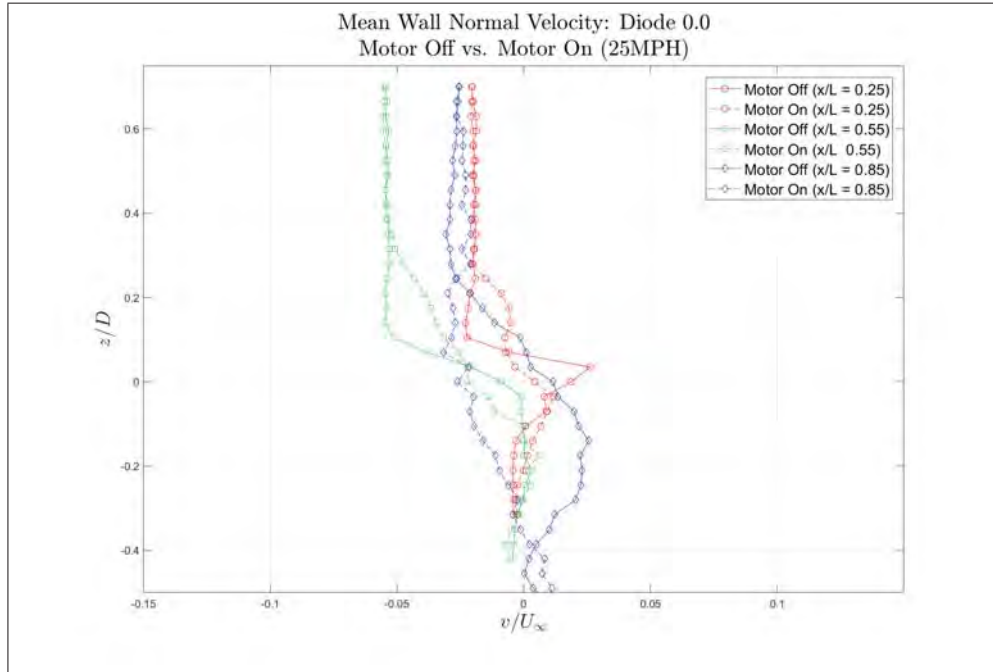




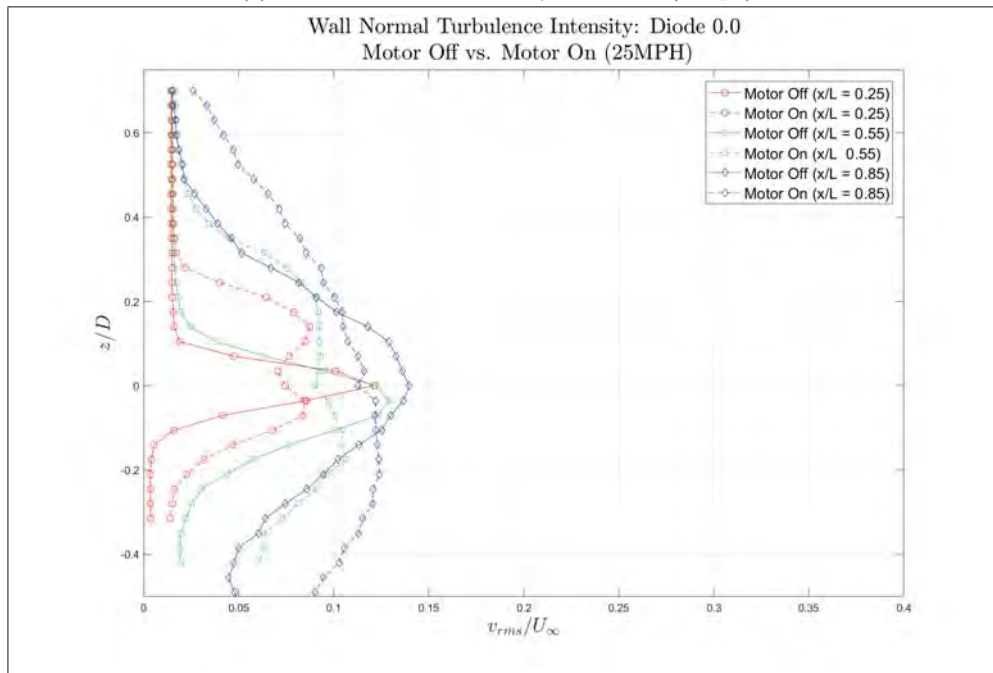
(a) Mean Streamwise Velocity: Diode 0.0 (25mph)



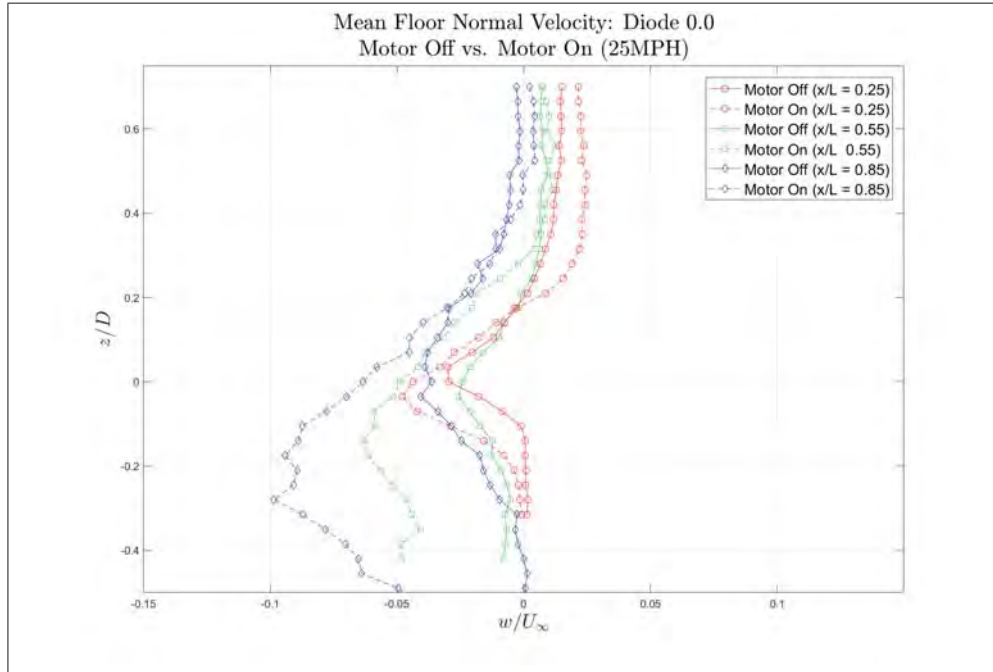
(b) Streamwise Turbulence Intensity: Diode 0.0 (25mph)



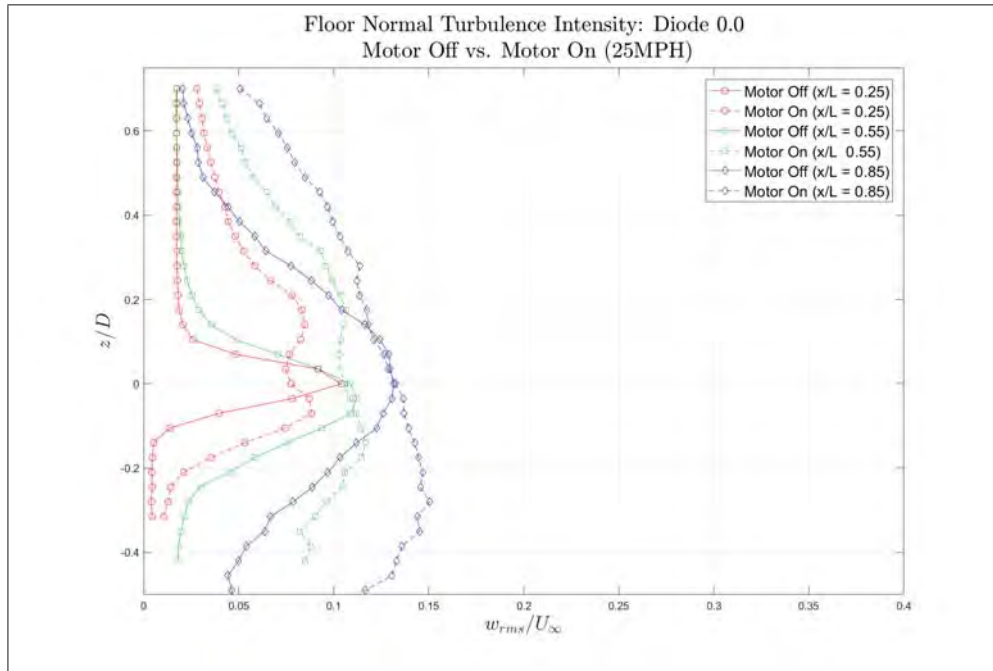
(a) Mean Wall Normal Velocity: Diode 0.0 (25mph)



(b) Wall Normal Turbulence Intensity: Diode 0.0 (25mph)

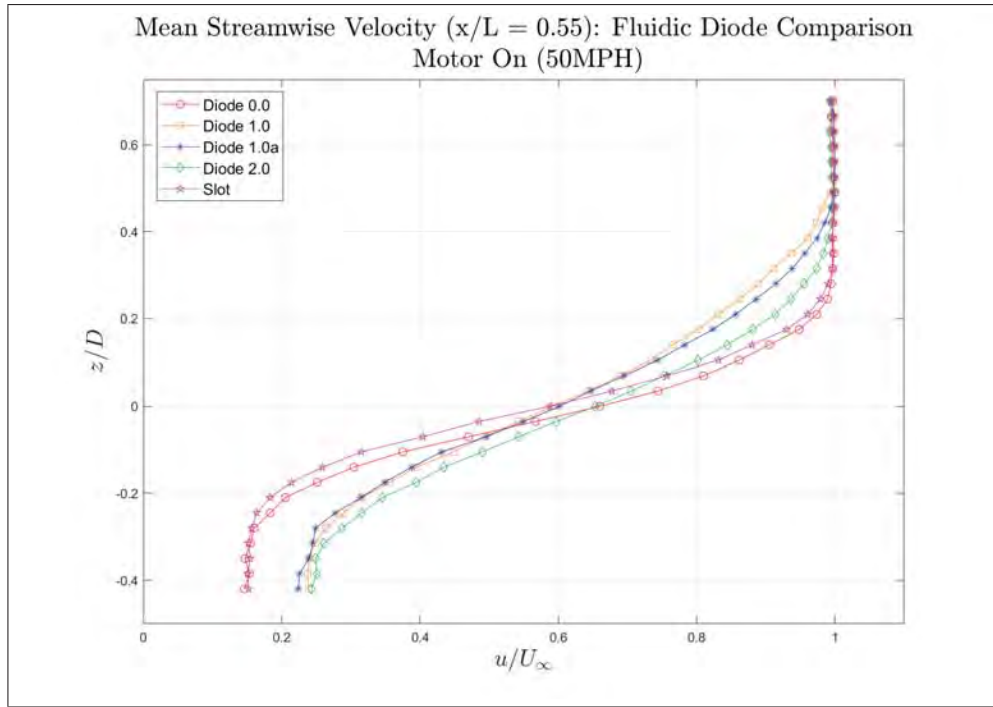


(a) Mean Floor Normal Velocity: Diode 0.0 (25mph)

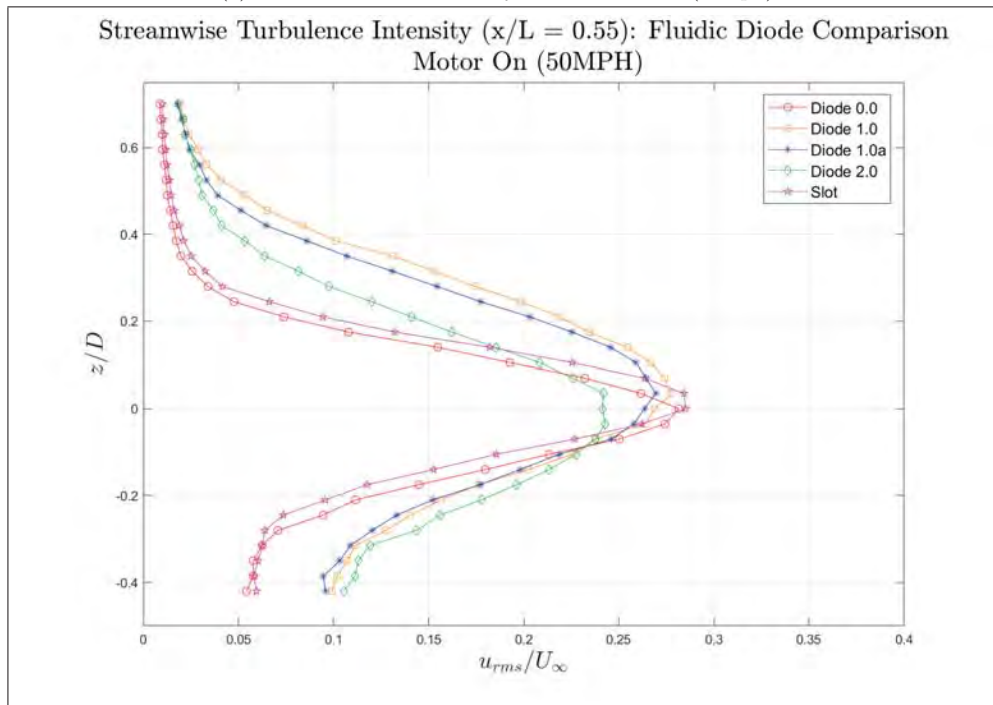


(b) Floor Normal Turbulence Intensity: Diode 0.0 (25mph)

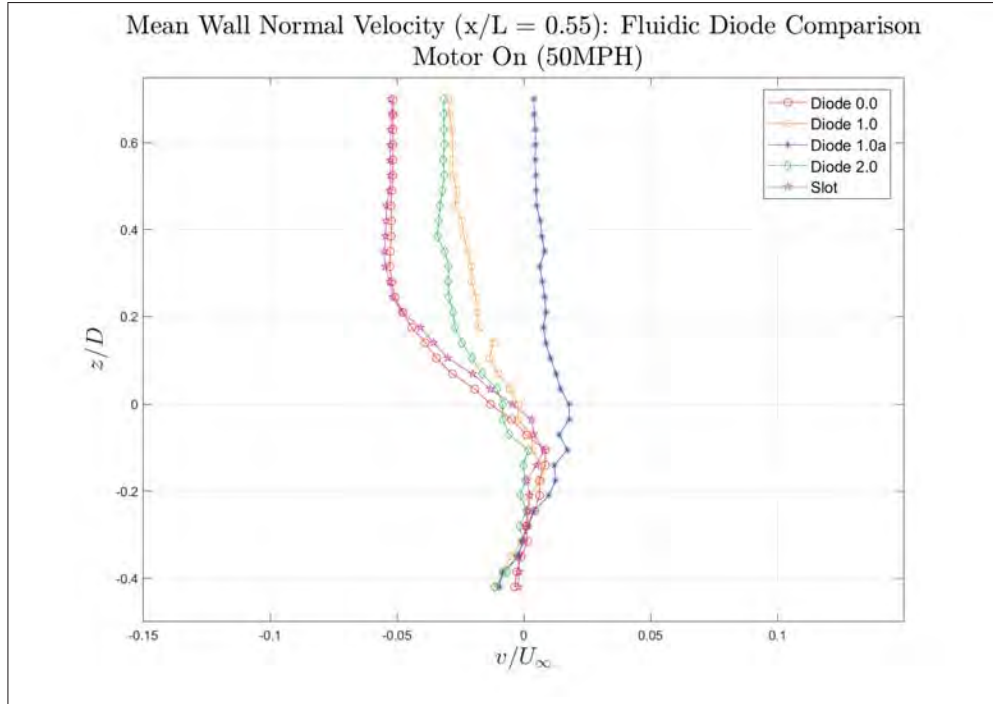
# Slot vs. Diodes: 50mph ( $x/L = 0.55$ )



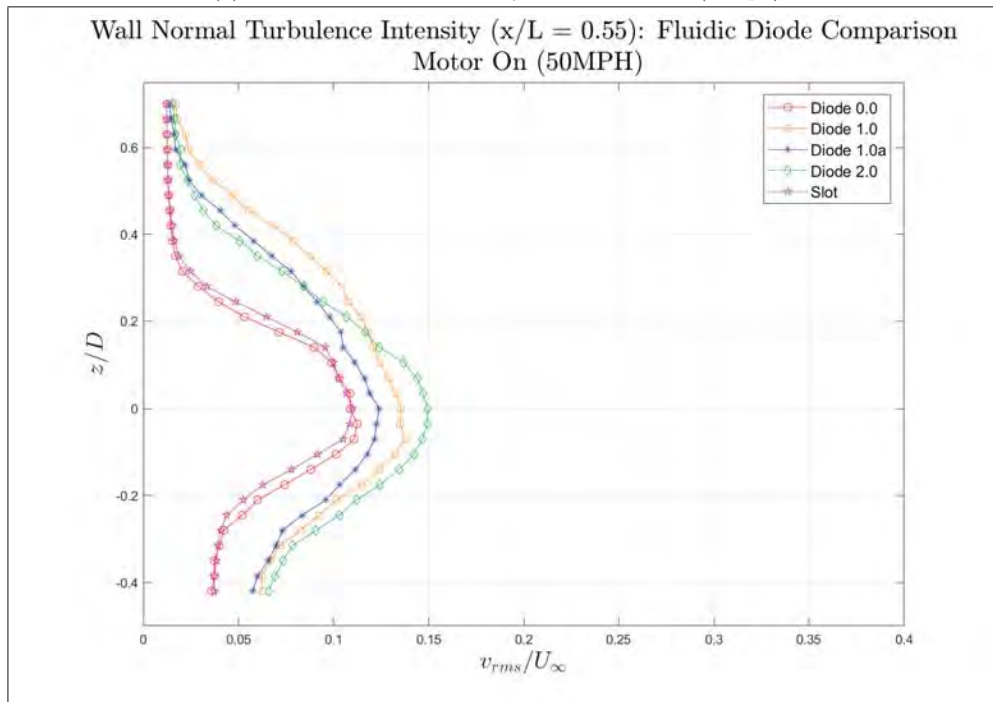
(a) Mean Streamwise Velocity: Slot vs. Diodes (50mph)



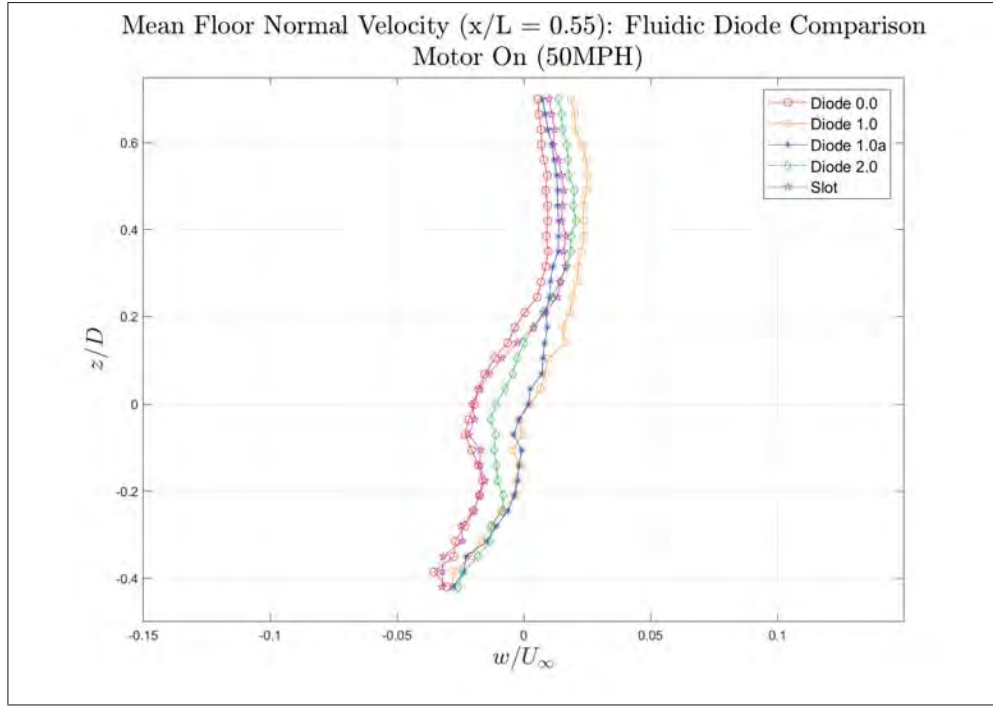
(b) Streamwise Turbulence Intensity: Slot vs. Diodes (50mph)



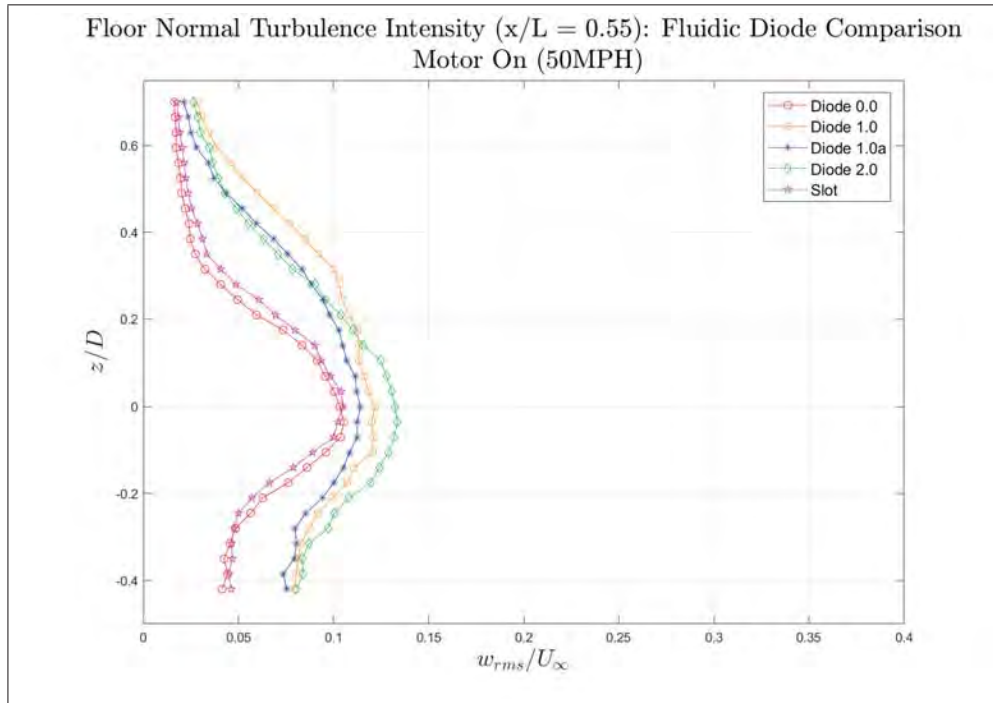
(a) Mean Wall Normal Velocity: Slot vs. Diodes (50mph)



(b) Wall Normal Turbulence Intensity: Slot vs. Diodes (50mph)



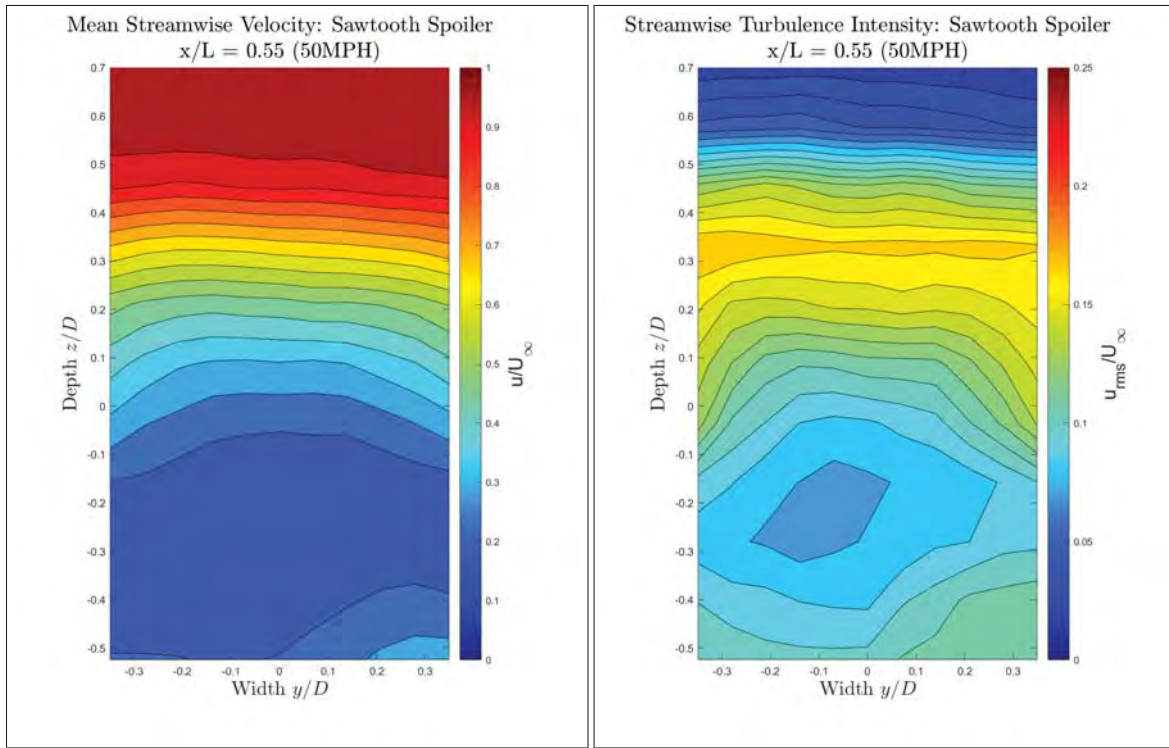
(a) Mean Floor Normal Velocity: Slot vs. Diodes (50mph)



(b) Floor Normal Turbulence Intensity: Slot vs. Diodes (50mph)

# Raster Patterns

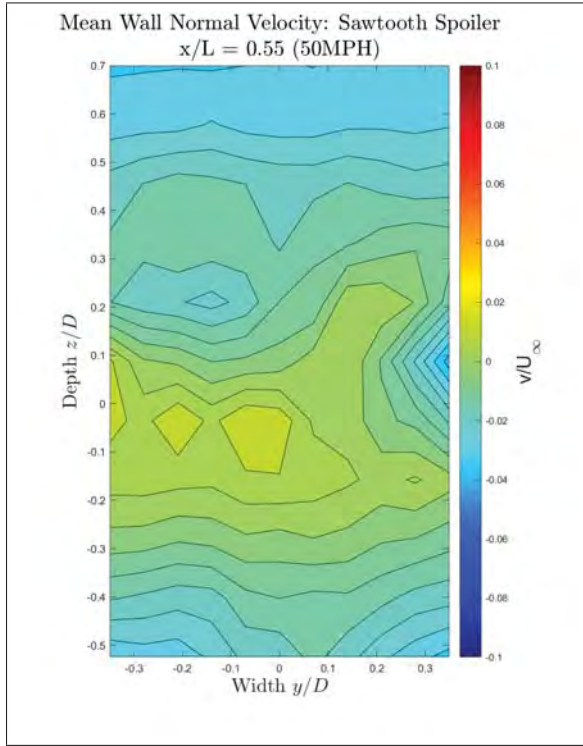
## Passive Devices: Sawtooth Spoiler



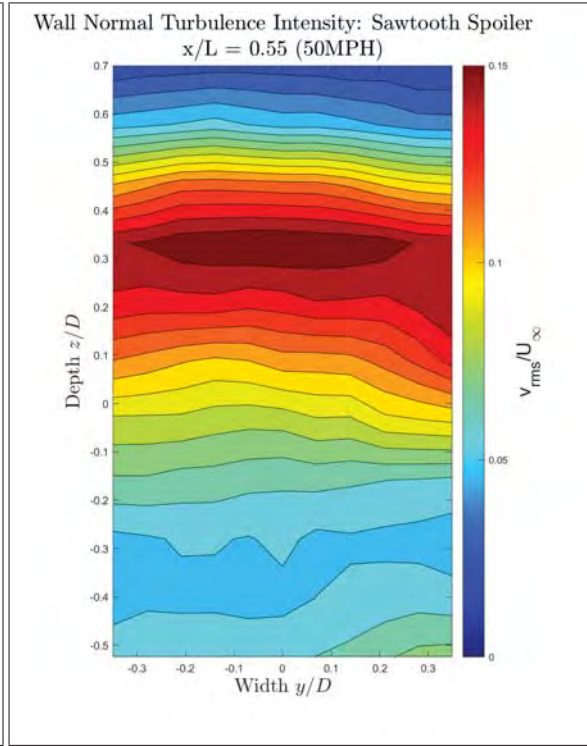
(a) Mean Streamwise Velocity: Sawtooth Spoiler (50mph)

(b) Streamwise Turbulence Intensity: Sawtooth Spoiler (50mph)

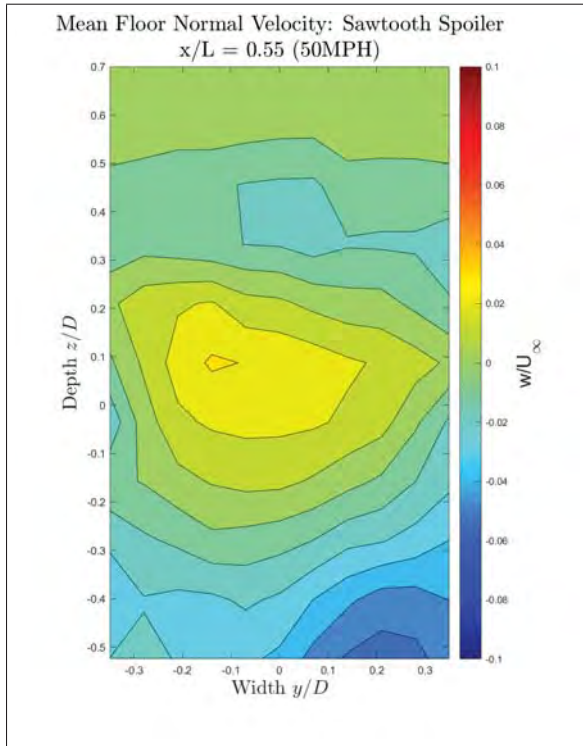




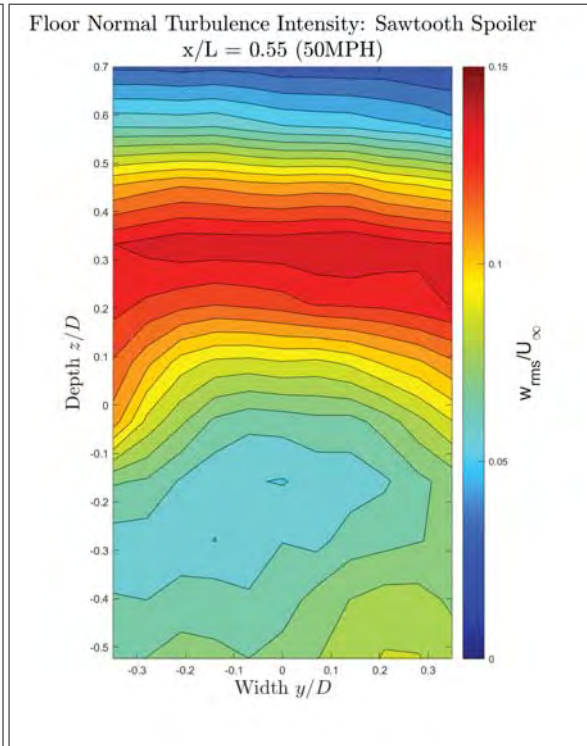
(a) Mean Wall Normal Velocity: Sawtooth Spoiler (50mph)



(b) Wall Normal Turbulence Intensity: Sawtooth Spoiler (50mph)



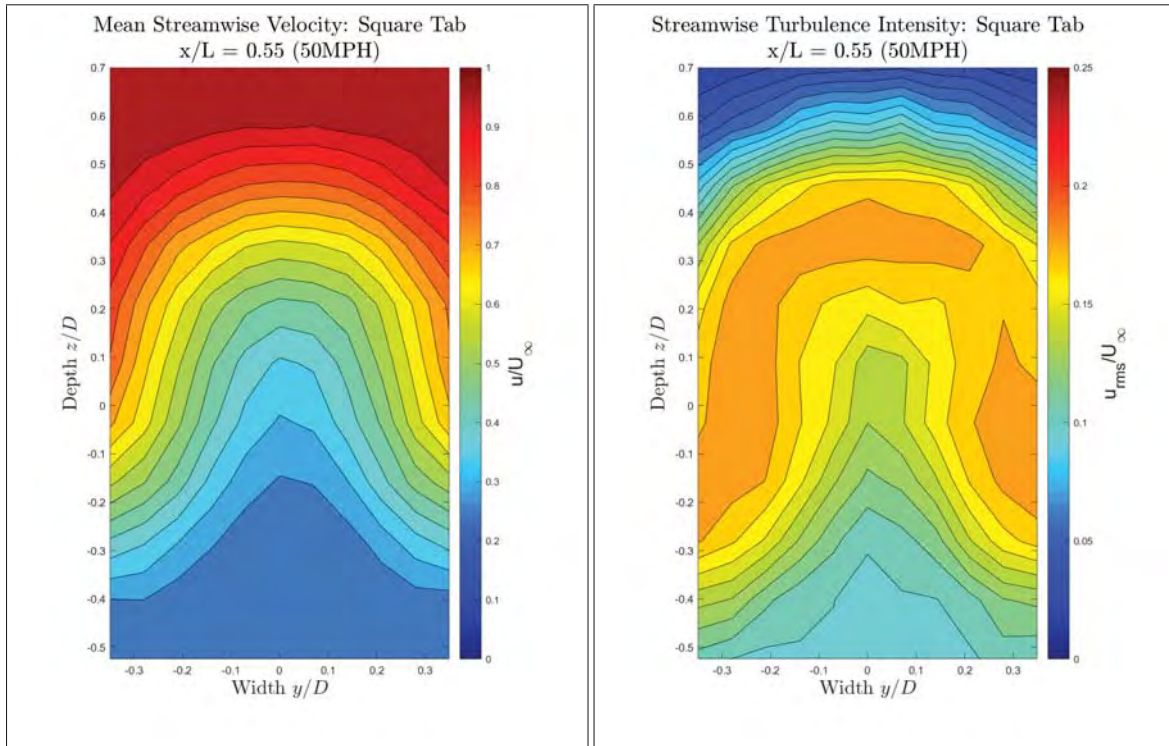
(a) Mean Floor Normal Velocity: Sawtooth Spoiler (50mph)



(b) Floor Normal Turbulence Intensity: Sawtooth Spoiler (50mph)

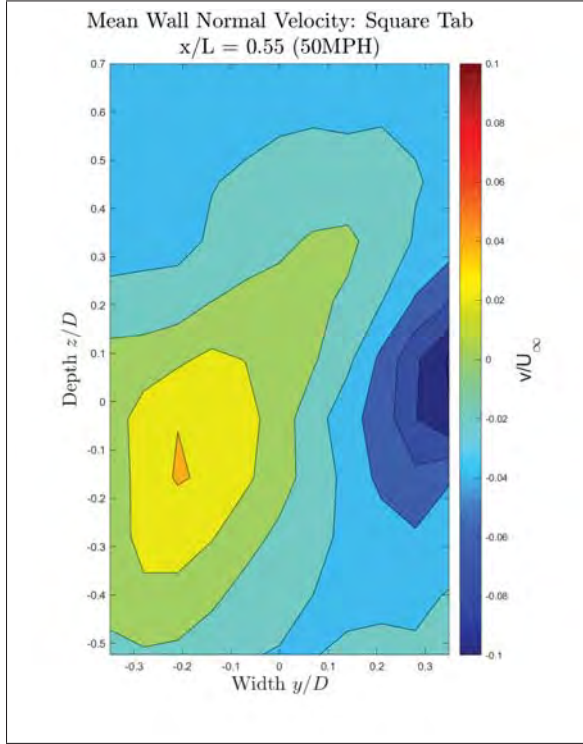


## Passive Devices: Rectangular Tab

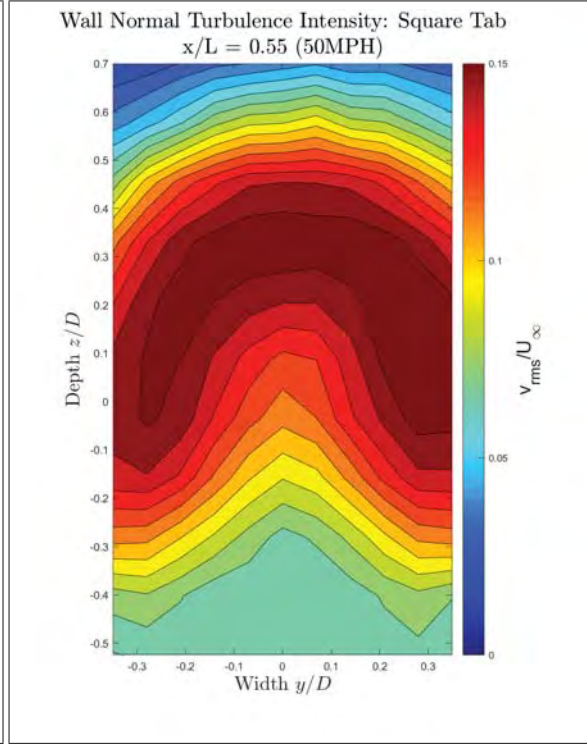


(a) Mean Streamwise Velocity: Square Tab (50mph)

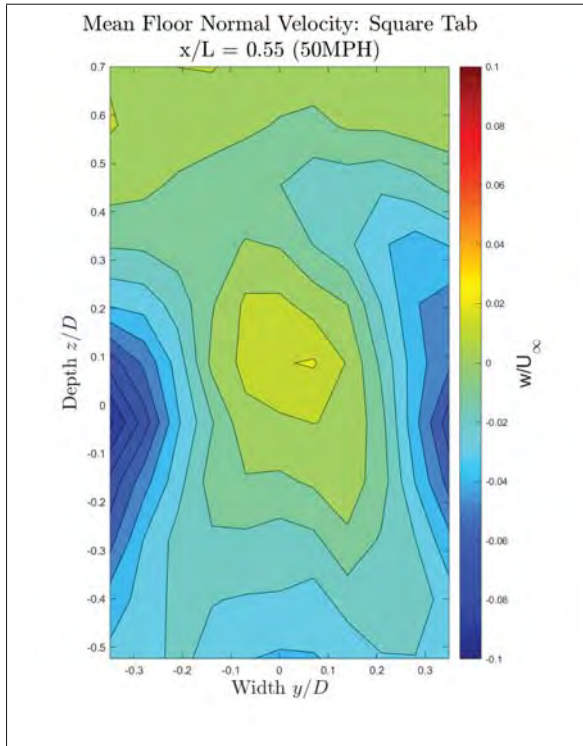
(b) Streamwise Turbulence Intensity: Square Tab (50mph)



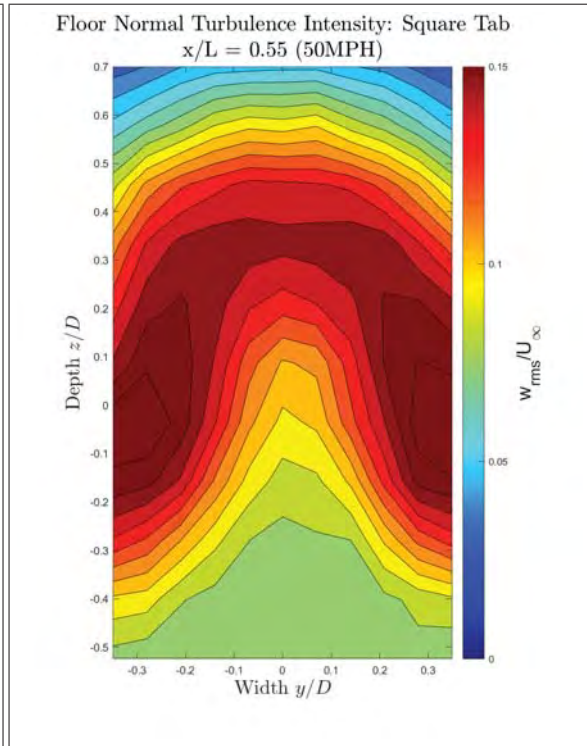
(a) Mean Wall Normal Velocity: Square Tab (50mph)



(b) Wall Normal Turbulence Intensity: Square Tab (50mph)

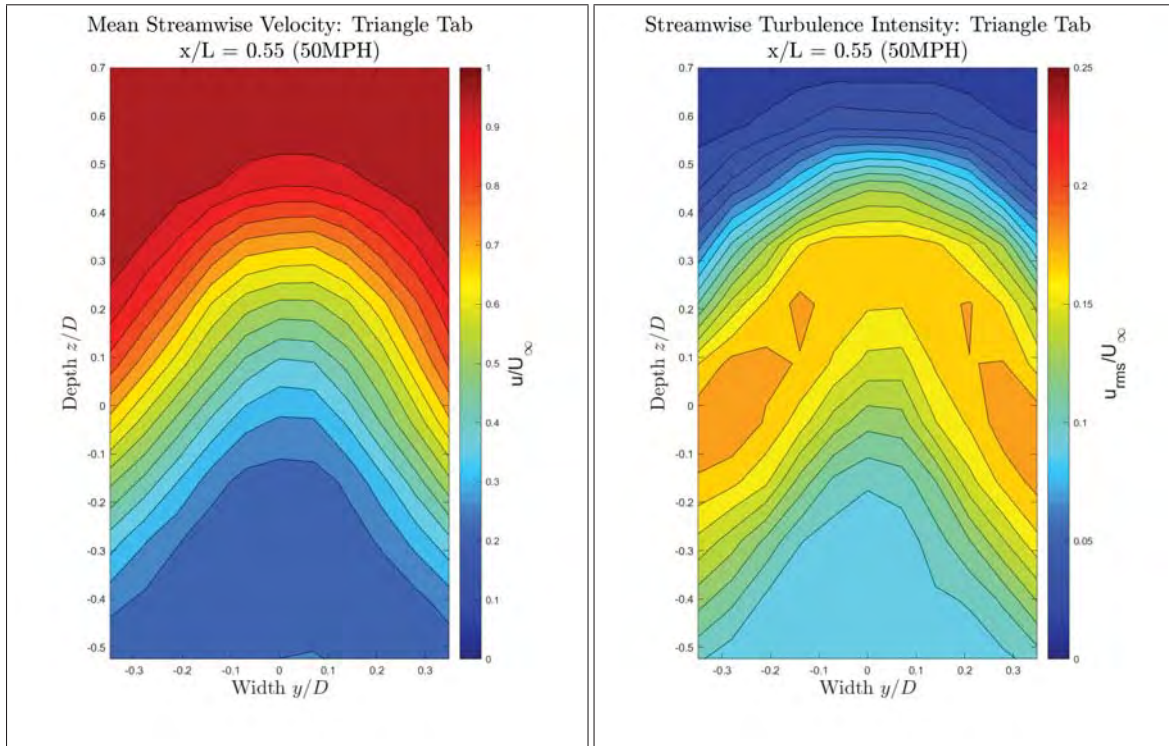


(a) Mean Floor Normal Velocity: Square Tab (50mph)



(b) Floor Normal Turbulence Intensity: Square Tab (50mph)

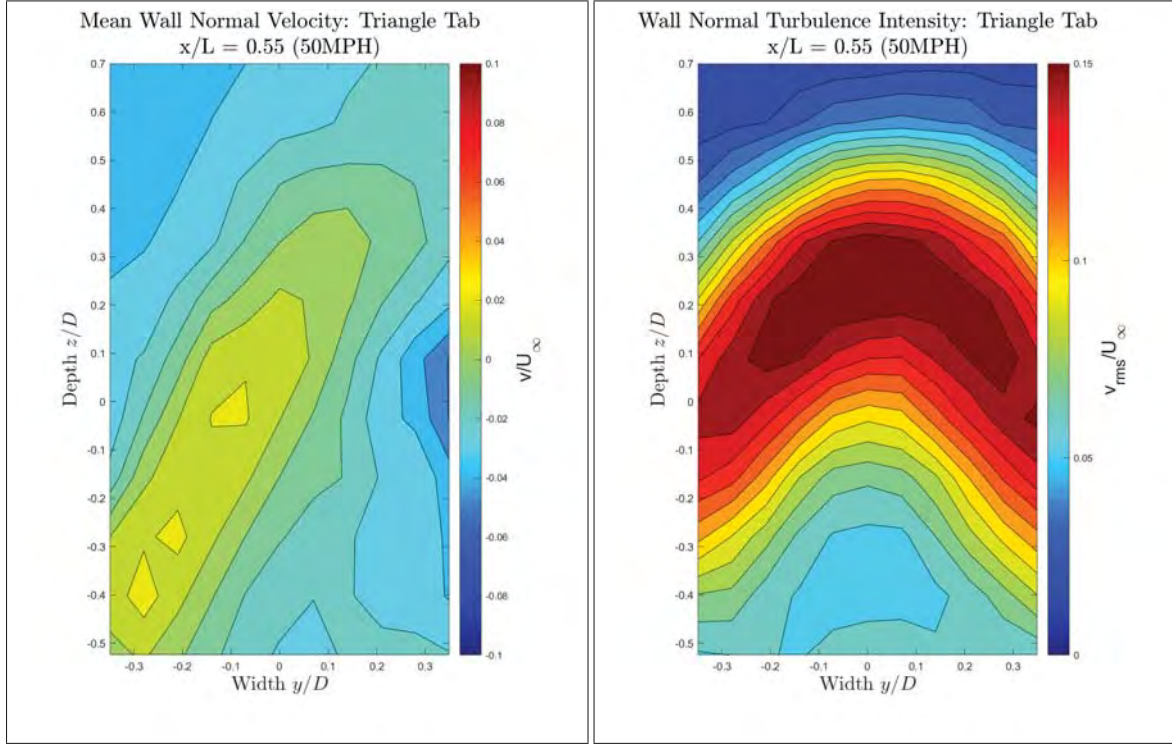
## Passive Devices: Triangular Tab



(a) Mean Streamwise Velocity: Triangle Tab (50mph)

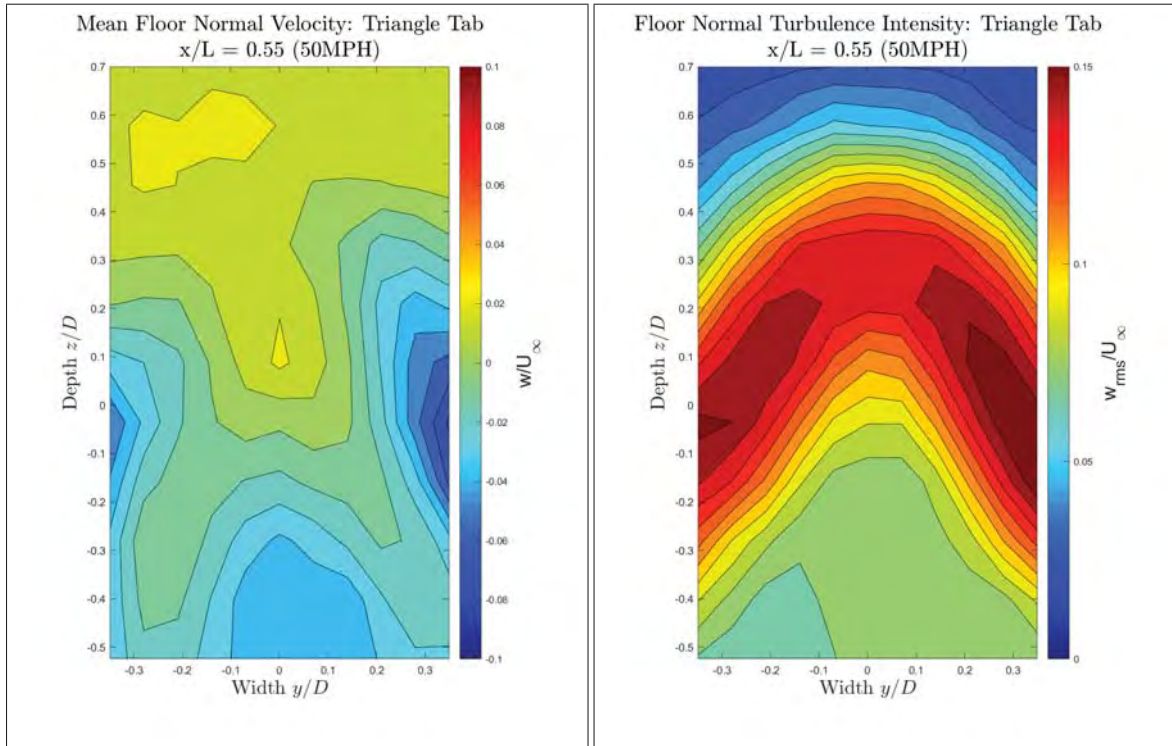
(b) Streamwise Turbulence Intensity: Triangle Tab (50mph)





(a) Mean Wall Normal Velocity: Triangle Tab (50mph)

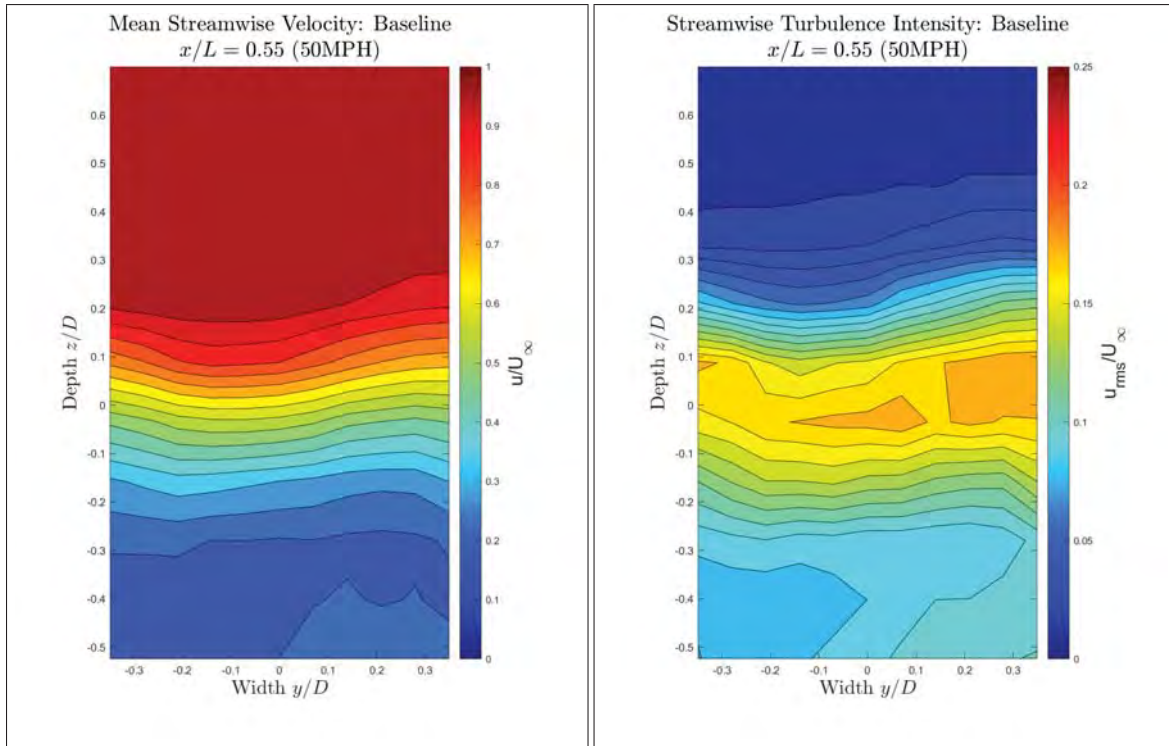
(b) Wall Normal Turbulence Intensity: Triangle Tab (50mph)



(a) Mean Floor Normal Velocity: Triangle Tab (50mph)

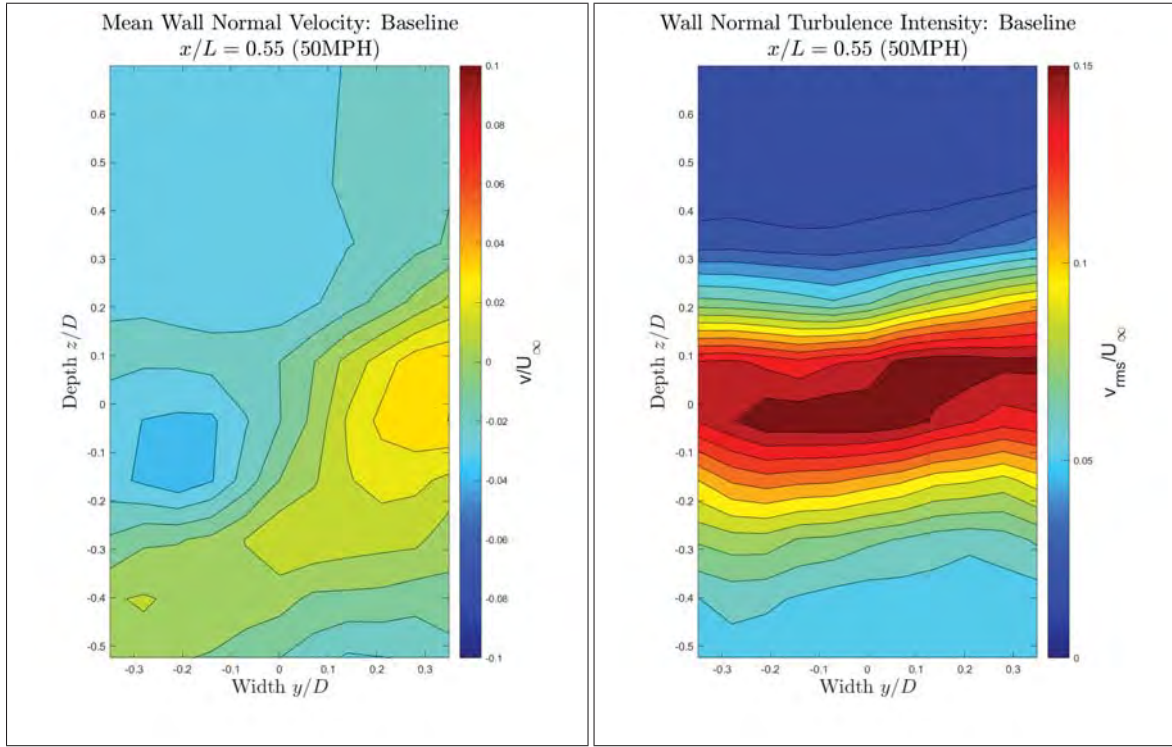
(b) Floor Normal Turbulence Intensity: Triangle Tab (50mph)

Baseline Cavity: 50mph ( $x/L = 0.55$ )



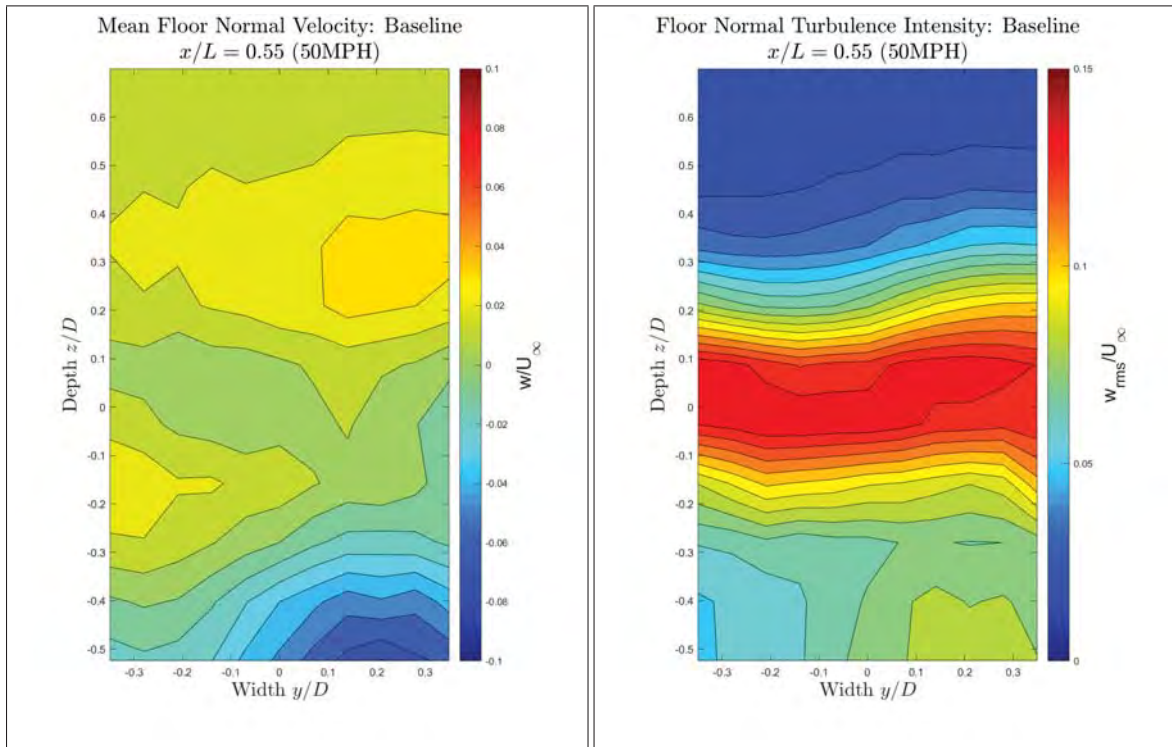
(a) Mean Streamwise Velocity: Baseline (50mph)

(b) Streamwise Turbulence Intensity: Baseline (50mph)



(a) Mean Wall Normal Velocity: Baseline (50mph)

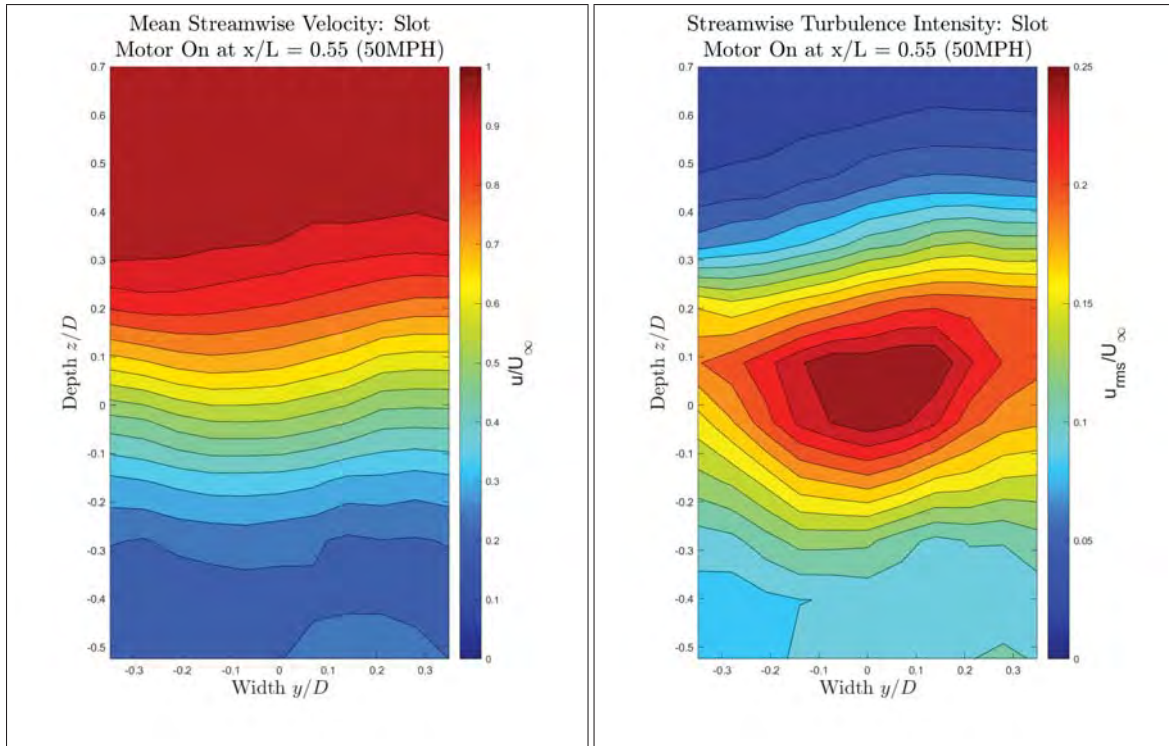
(b) Wall Normal Turbulence Intensity: Baseline (50mph)



(a) Mean Floor Normal Velocity: Baseline (50mph)

(b) Floor Normal Turbulence Intensity: Baseline (50mph)

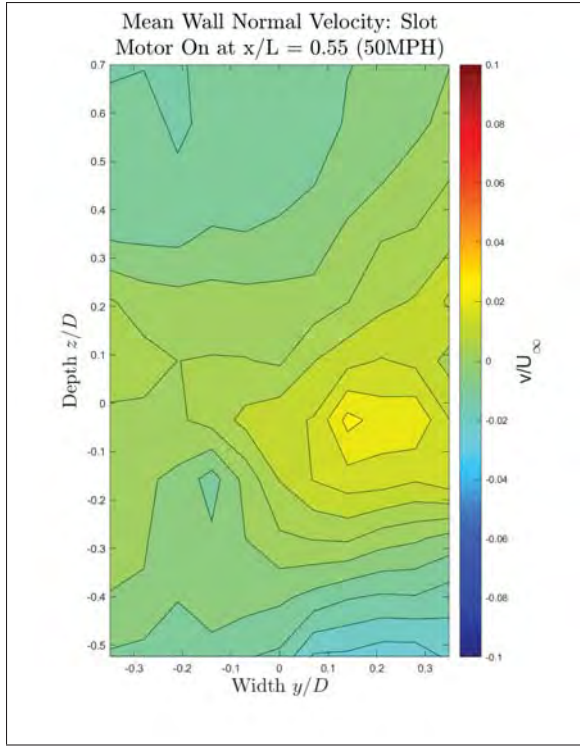
Slot: 50mph ( $x/L = 0.55$ )



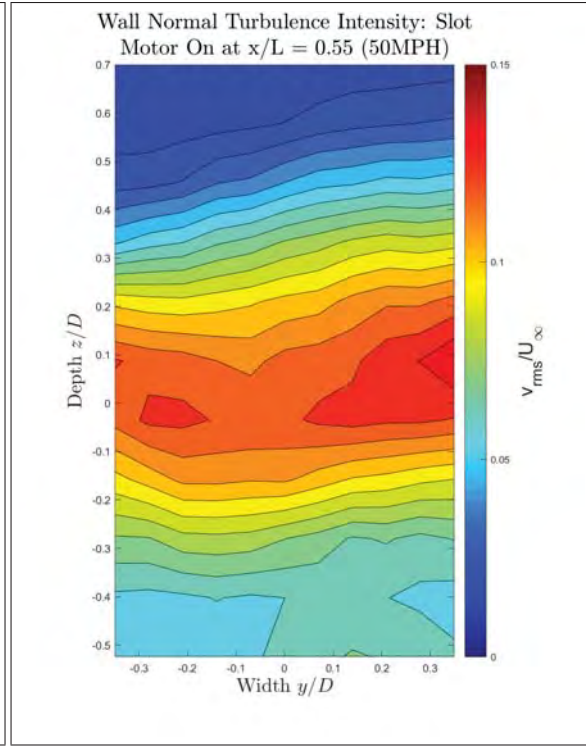
(a) Mean Streamwise Velocity: Slot (50mph)

(b) Streamwise Turbulence Intensity: Slot (50mph)

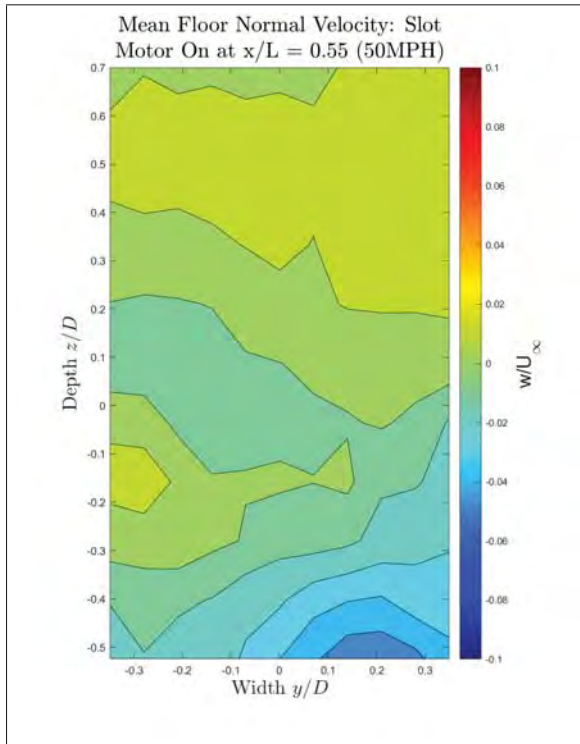




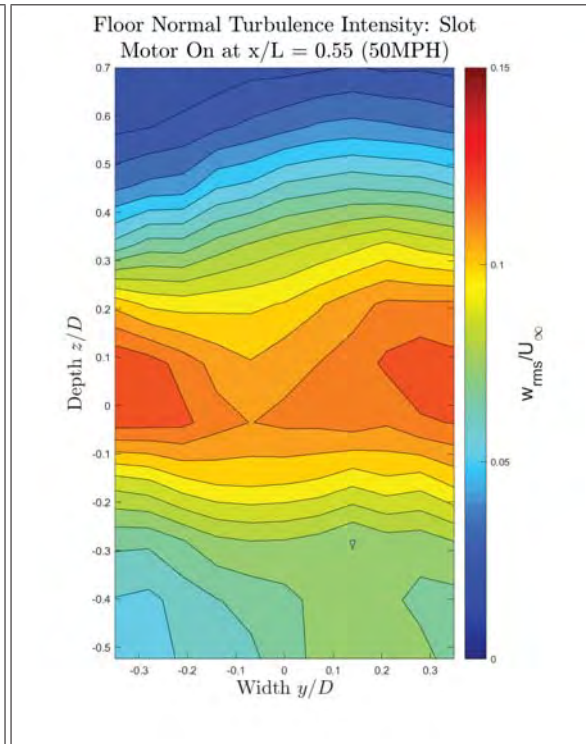
(a) Mean Wall Normal Velocity: Slot (50mph)



(b) Wall Normal Turbulence Intensity: Slot (50mph)

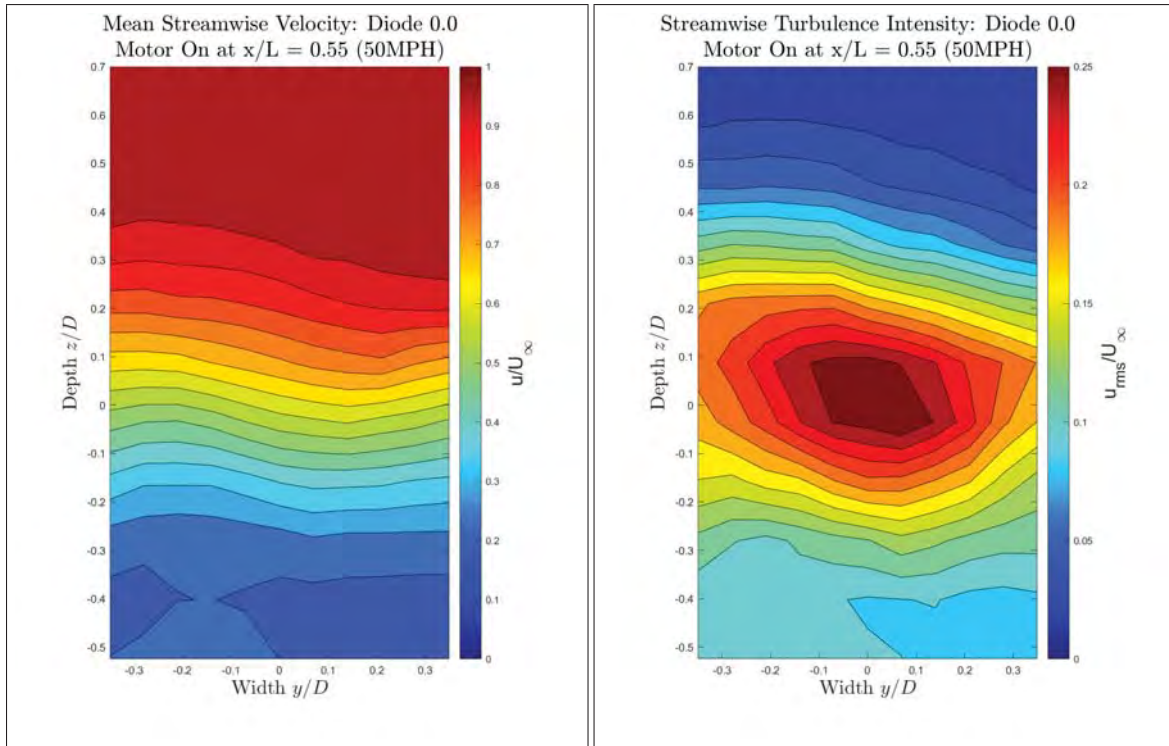


(a) Mean Floor Normal Velocity: Slot (50mph)



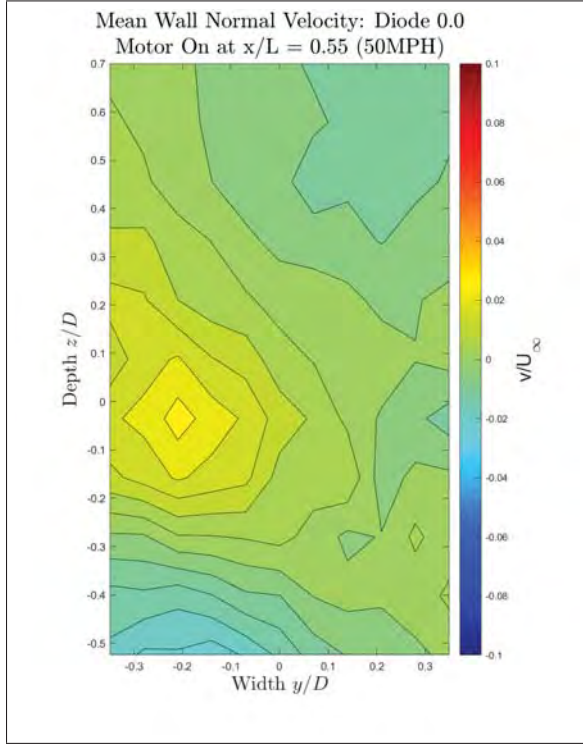
(b) Floor Normal Turbulence Intensity: Slot (50mph)

Diode 0.0: 50mph ( $x/L = 0.55$ )

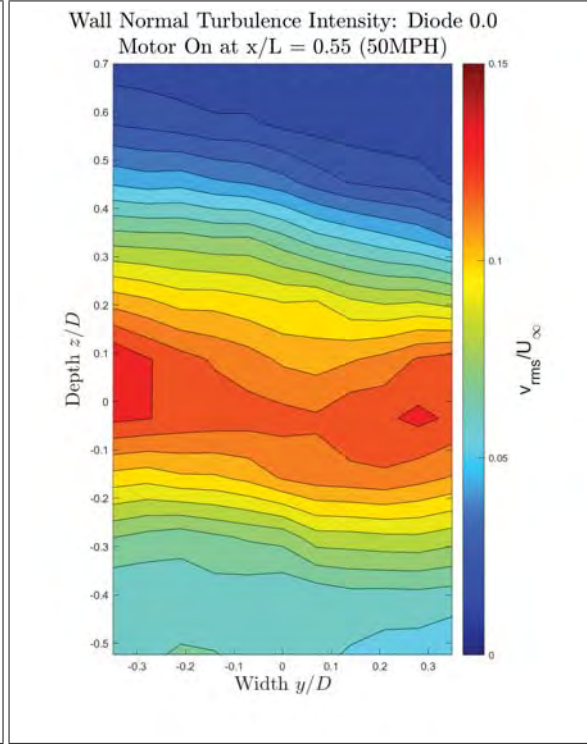


(a) Mean Streamwise Velocity: Diode 0.0 (50mph)

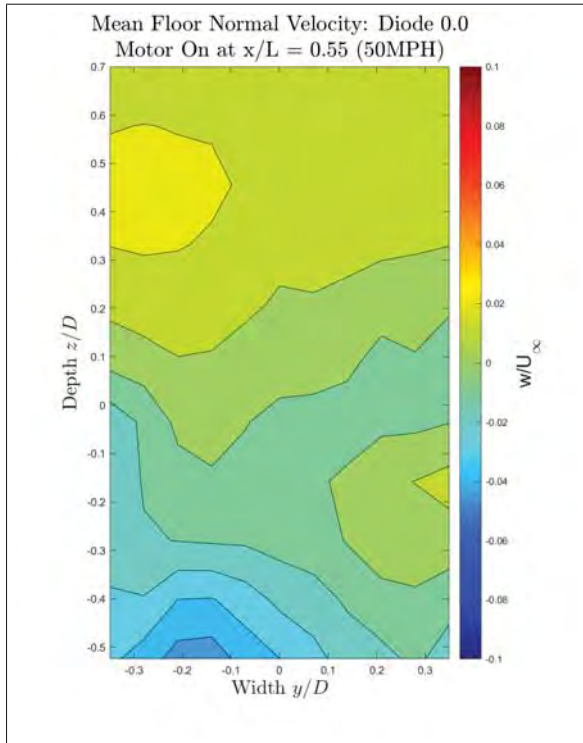
(b) Streamwise Turbulence Intensity: Diode 0.0 (50mph)



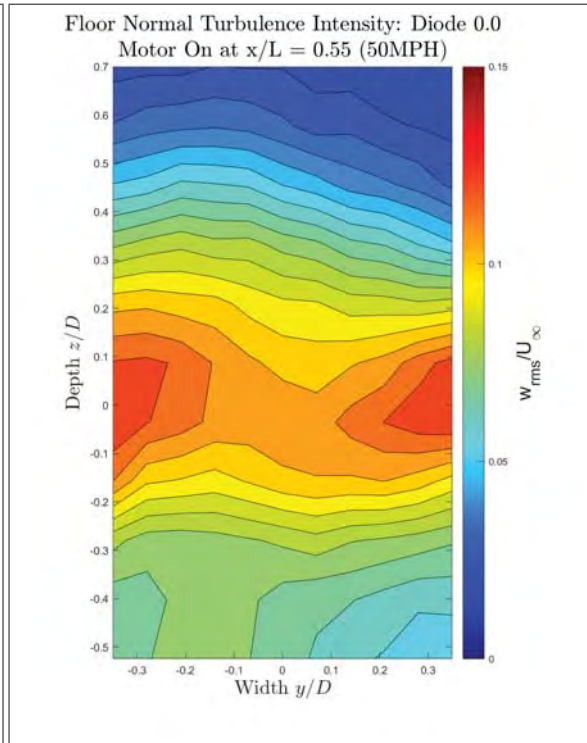
(a) Mean Wall Normal Velocity: Diode 0.0 (50mph)



(b) Wall Normal Turbulence Intensity: Diode 0.0 (50mph)

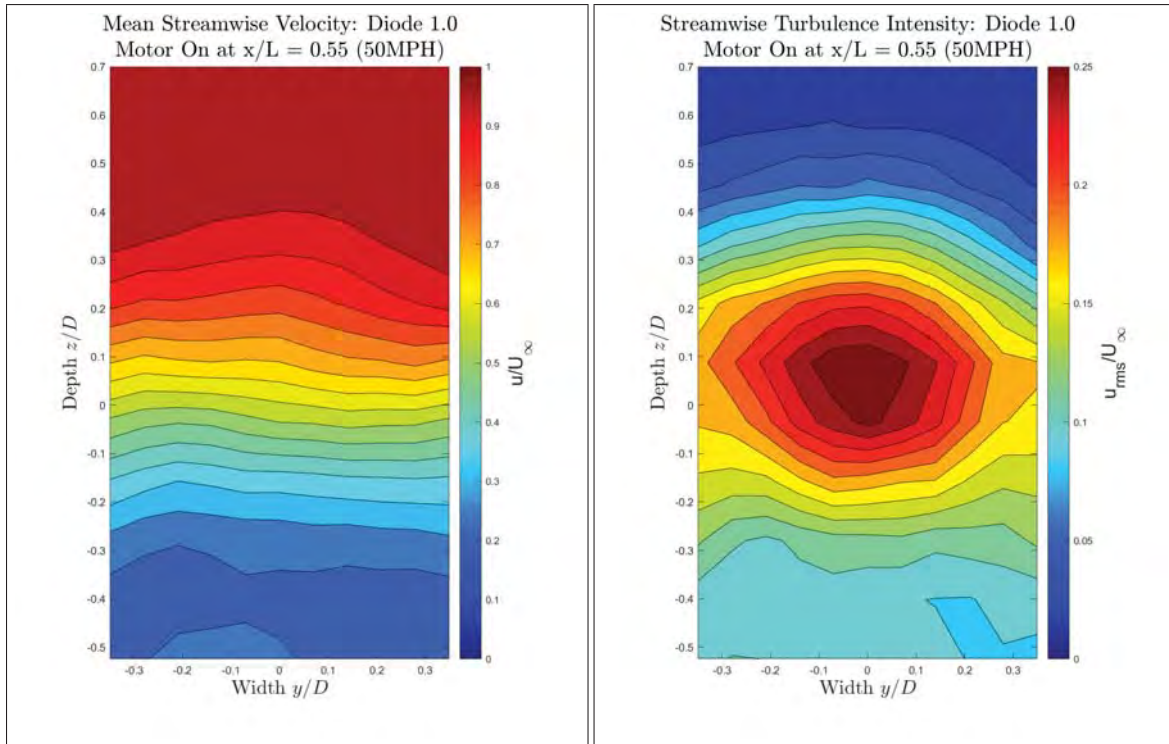


(a) Mean Floor Normal Velocity: Diode 0.0 (50mph)



(b) Floor Normal Turbulence Intensity: Diode 0.0 (50mph)

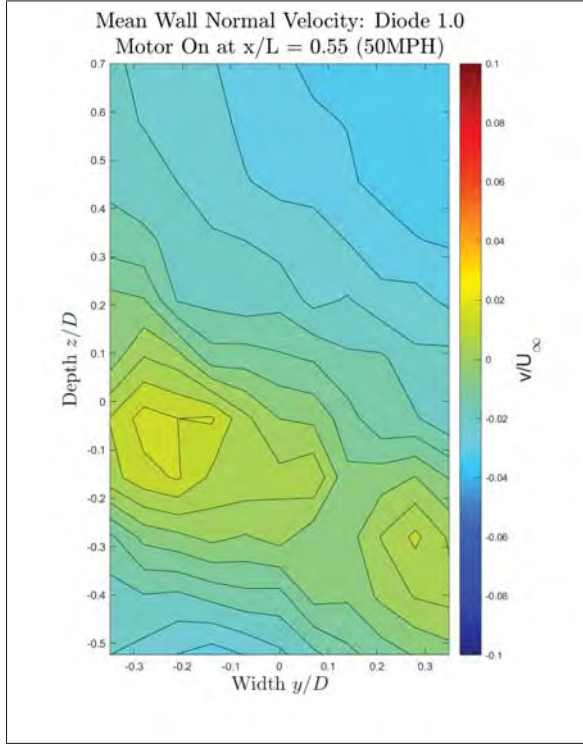
Diode 1.0: 50mph ( $x/L = 0.55$ )



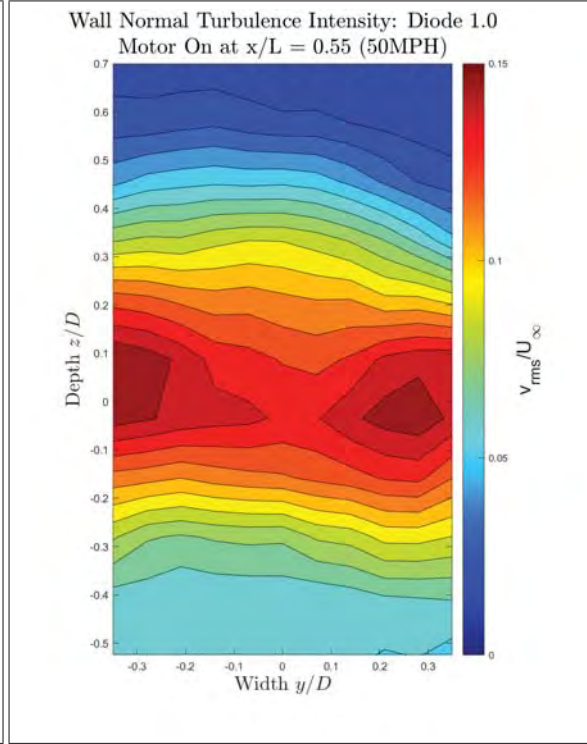
(a) Mean Streamwise Velocity: Diode 1.0 (50mph)

(b) Streamwise Turbulence Intensity: Diode 1.0 (50mph)

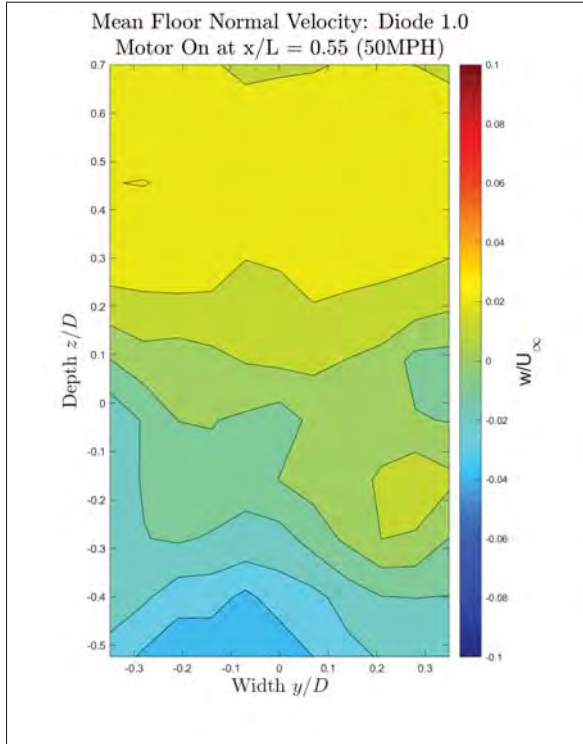




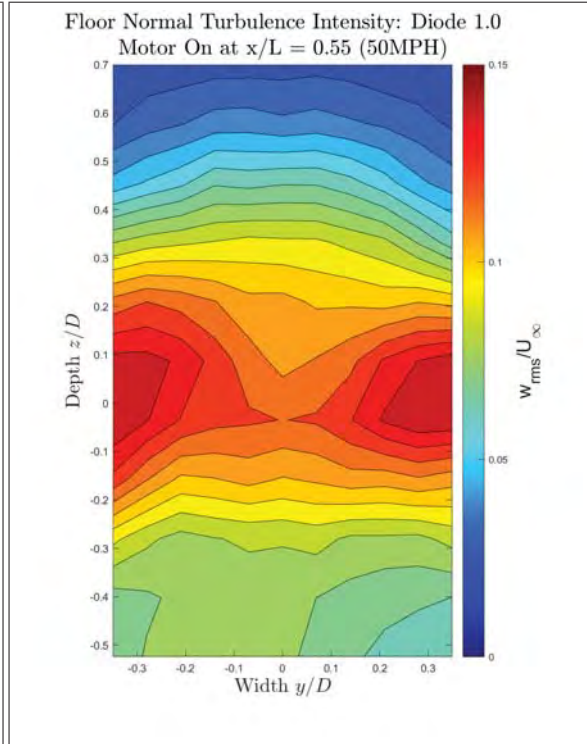
(a) Mean Wall Normal Velocity: Diode 1.0 (50mph)



(b) Wall Normal Turbulence Intensity: Diode 1.0 (50mph)

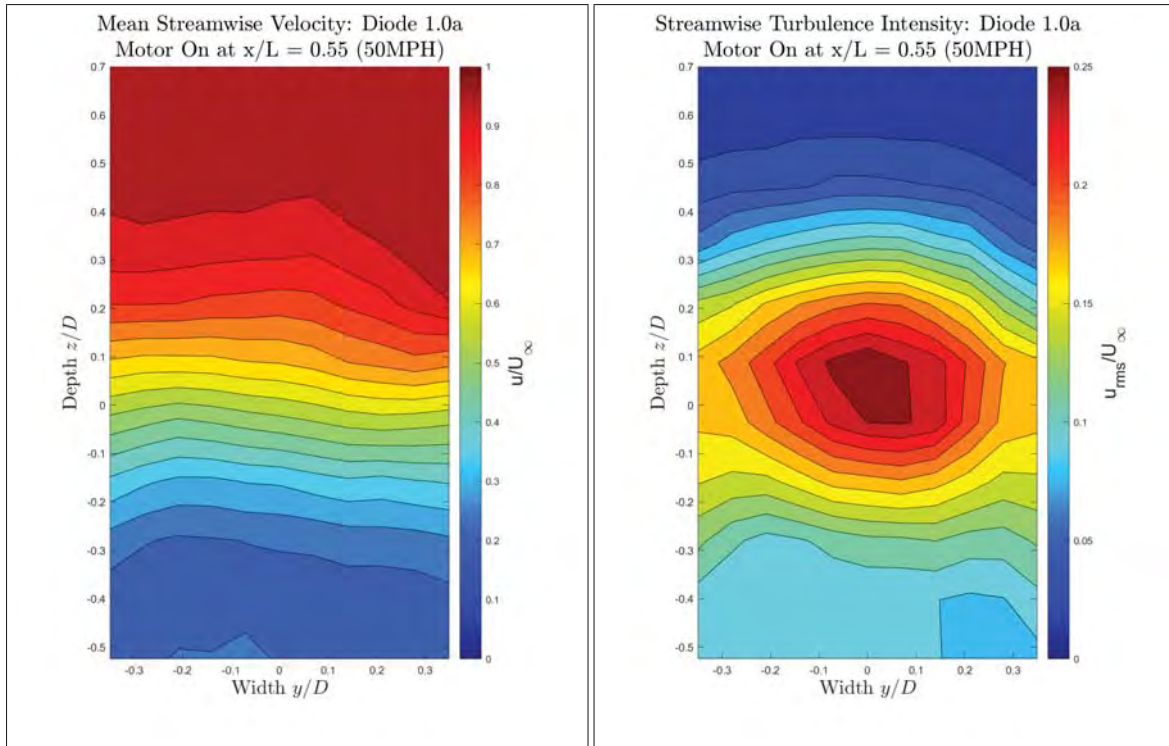


(a) Mean Floor Normal Velocity: Diode 1.0 (50mph)



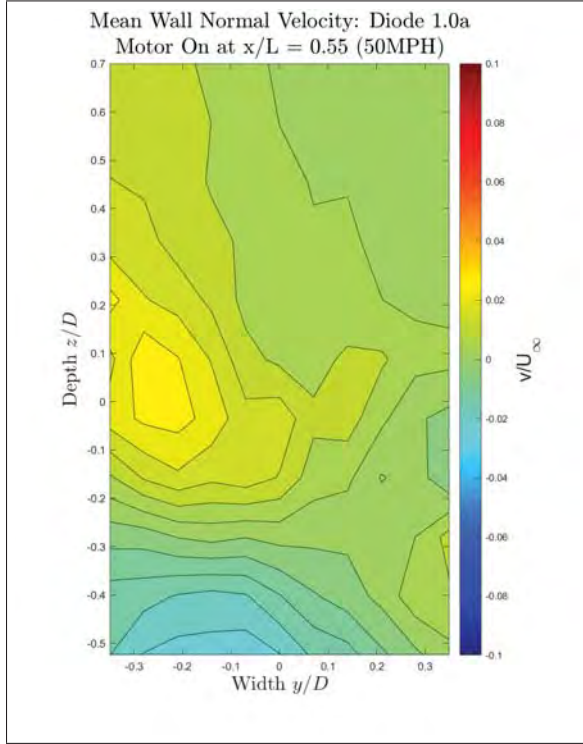
(b) Floor Normal Turbulence Intensity: Diode 1.0 (50mph)

Diode 1.0a: 50mph ( $x/L = 0.55$ )

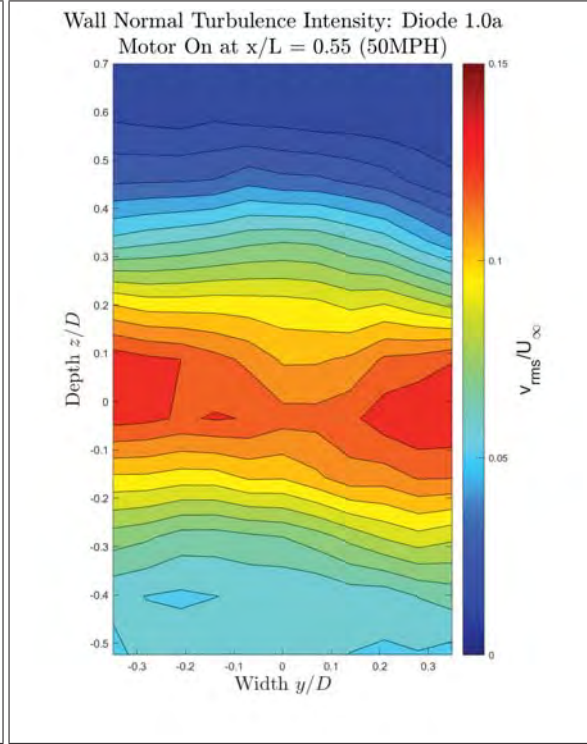


(a) Mean Streamwise Velocity: Diode 1.0a (50mph)

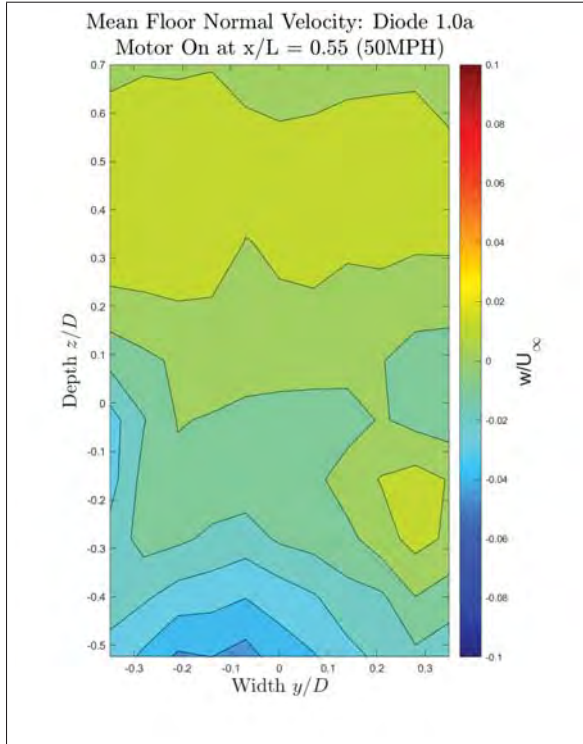
(b) Streamwise Turbulence Intensity: Diode 1.0a (50mph)



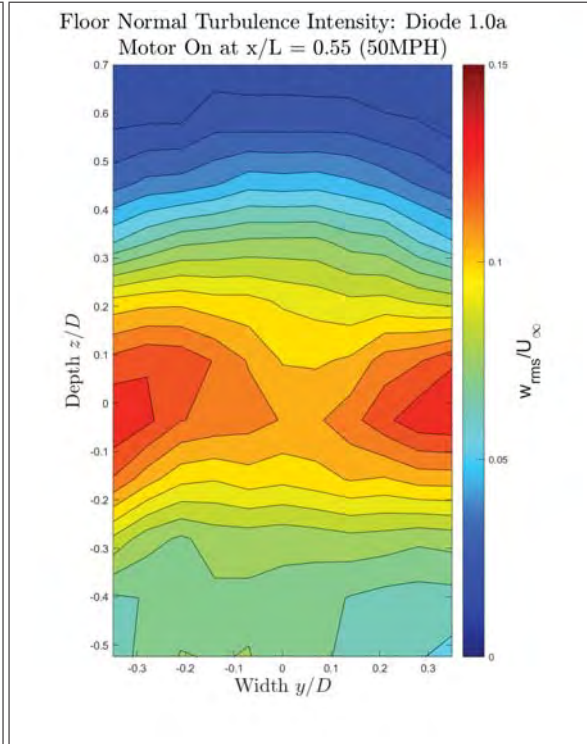
(a) Mean Wall Normal Velocity: Diode 1.0a (50mph)



(b) Wall Normal Turbulence Intensity: Diode 1.0a (50mph)



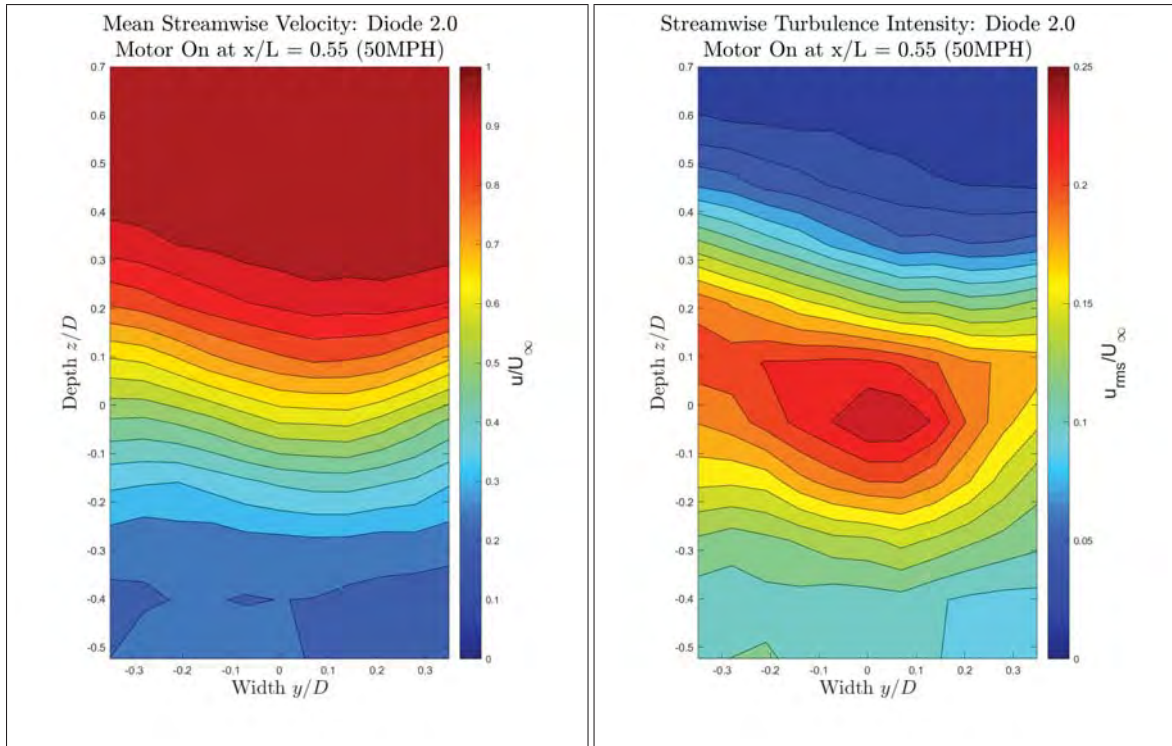
(a) Mean Floor Normal Velocity: Diode 1.0a (50mph)



(b) Floor Normal Turbulence Intensity: Diode 1.0a (50mph)

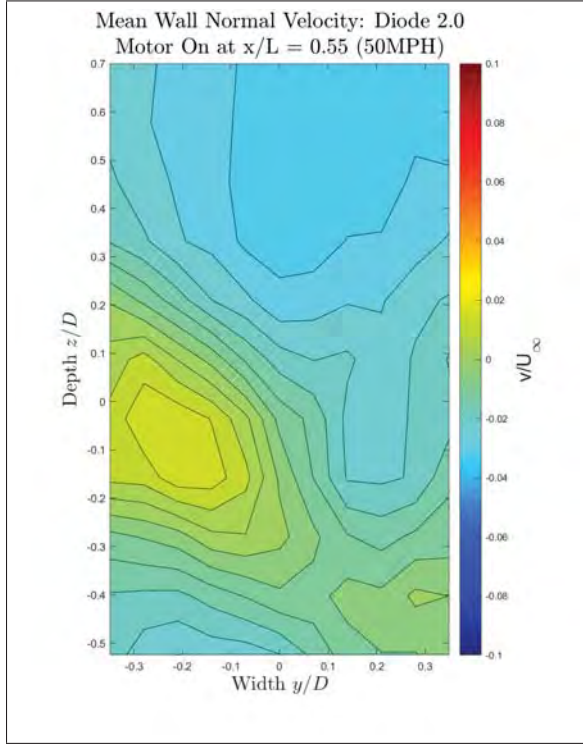


Diode 2.0: 50mph ( $x/L = 0.55$ )

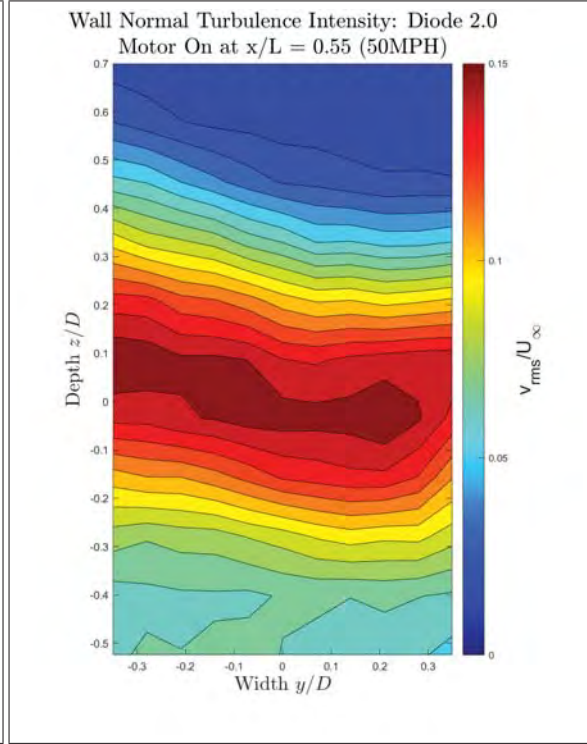


(a) Mean Streamwise Velocity: Diode 2.0 (50mph)

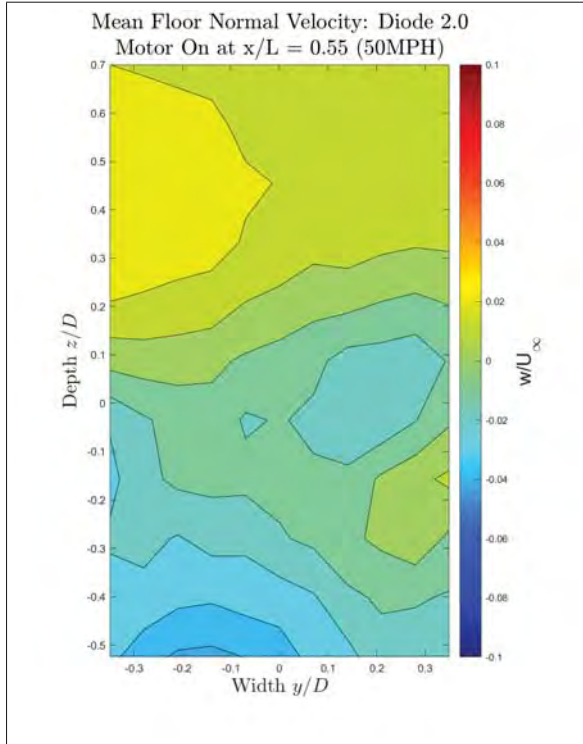
(b) Streamwise Turbulence Intensity: Diode 2.0 (50mph)



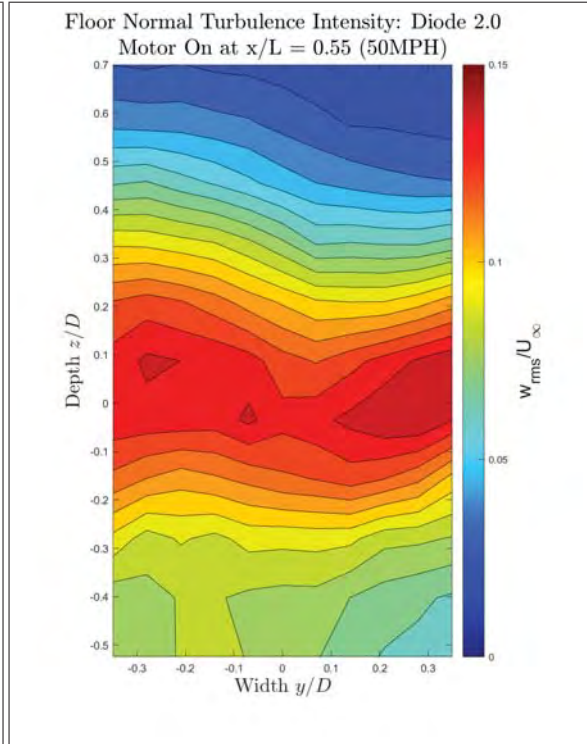
(a) Mean Wall Normal Velocity: Diode 2.0 (50mph)



(b) Wall Normal Turbulence Intensity: Diode 2.0 (50mph)



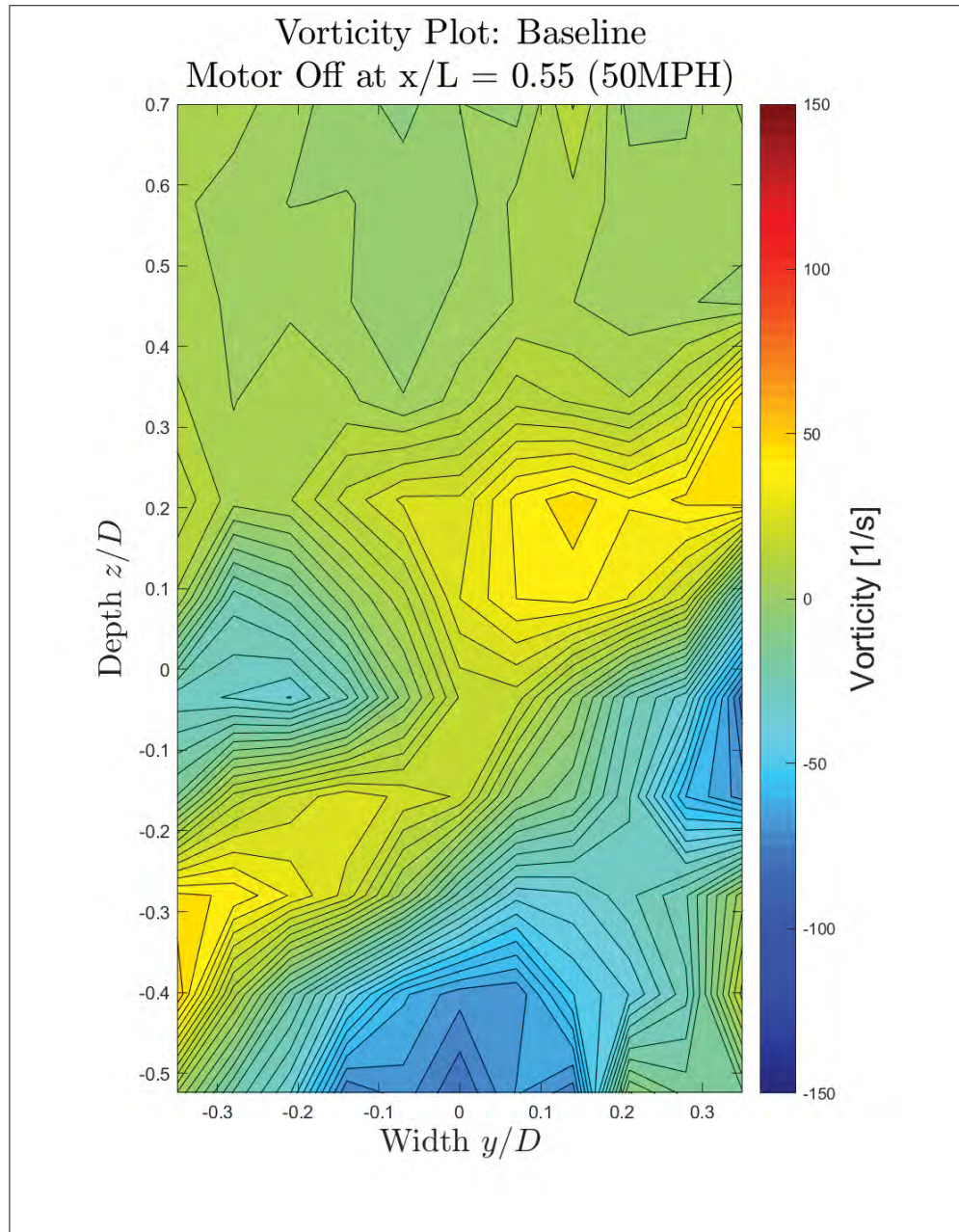
(a) Mean Floor Normal Velocity: Diode 2.0 (50mph)



(b) Floor Normal Turbulence Intensity: Diode 2.0 (50mph)

# Streamwise Vorticity Plots

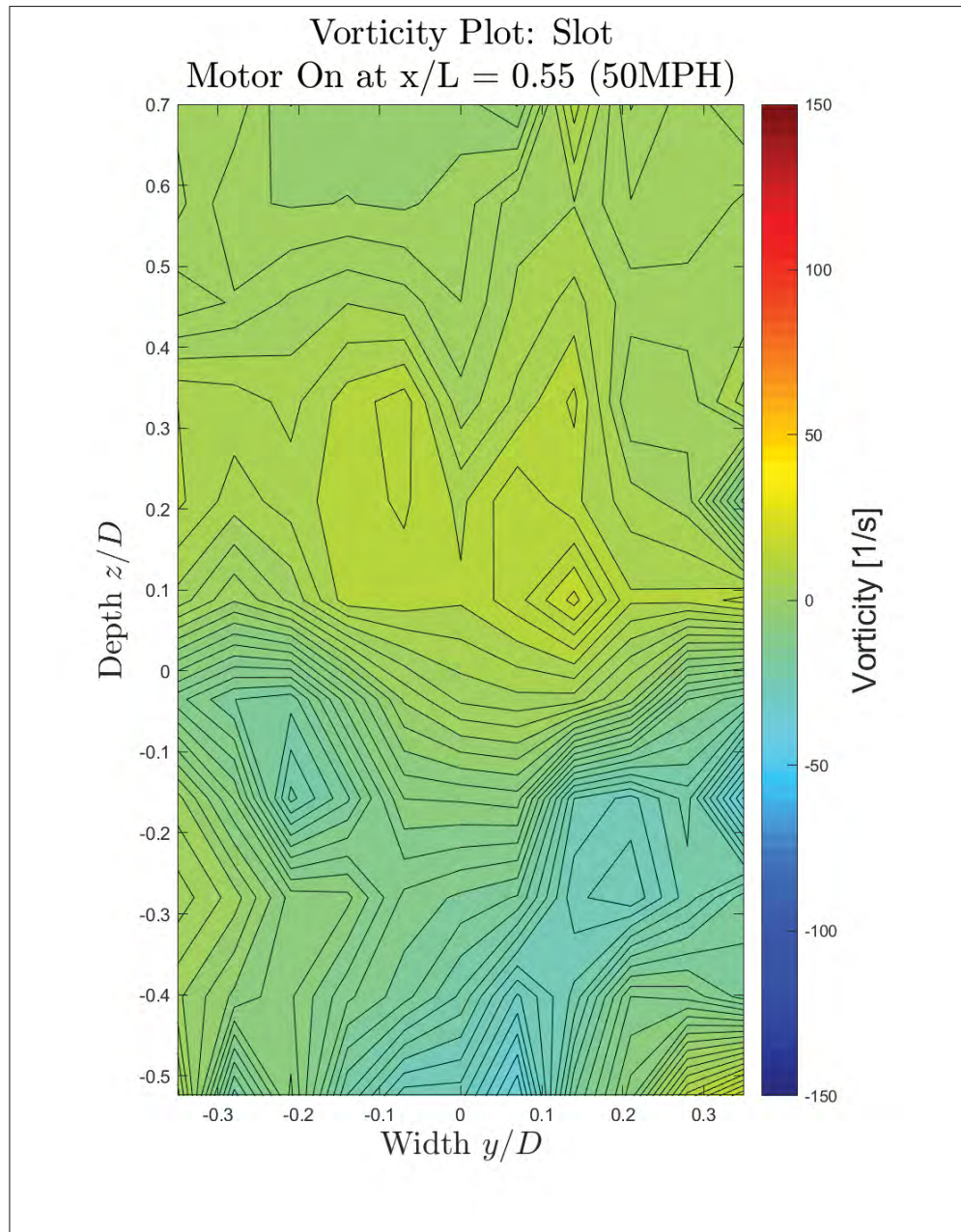
Baseline Cavity: 50mph ( $x/L = 0.55$ )



(a) Streamwise Vorticity: Baseline Cavity (50mph)

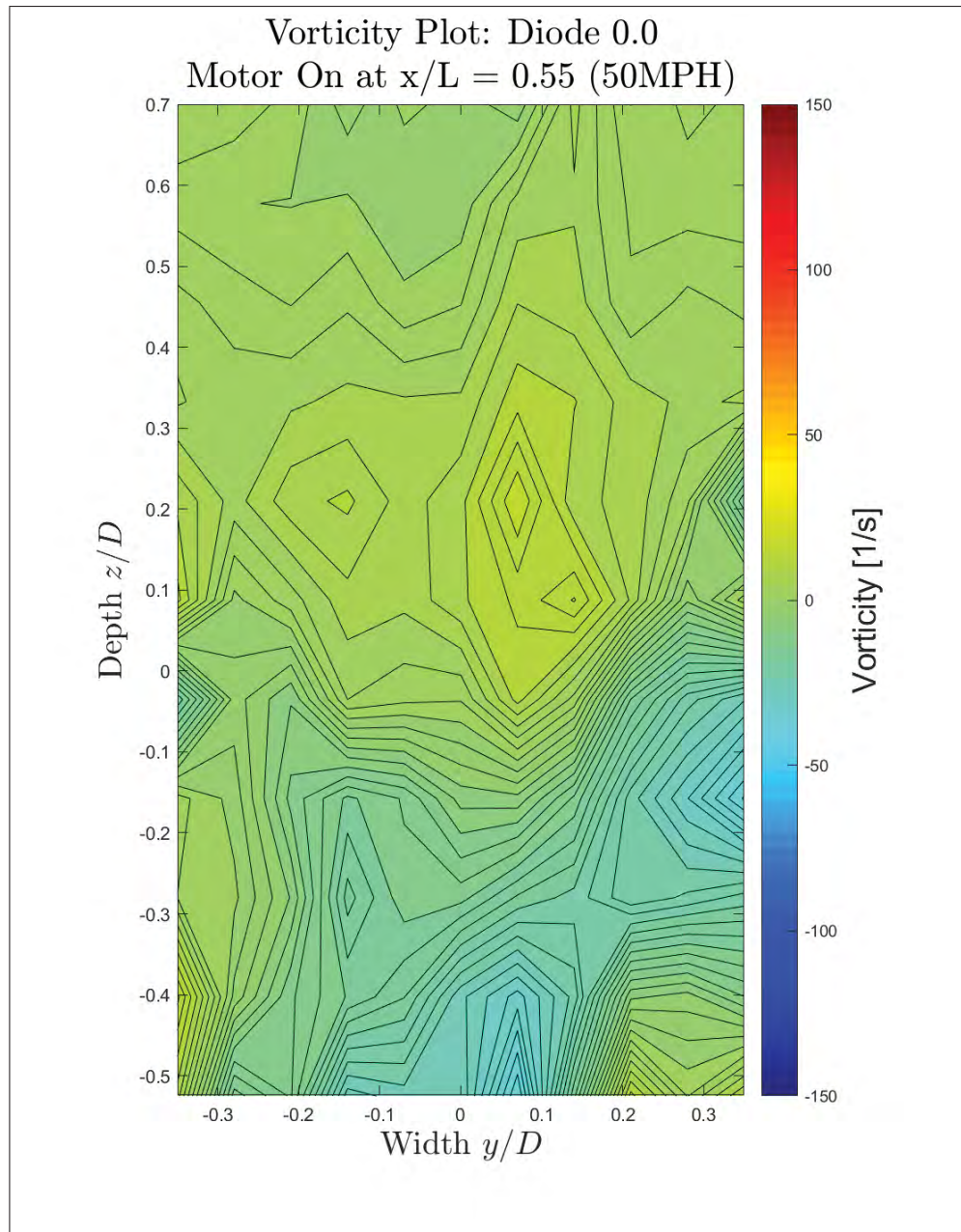


Slot: 50mph ( $x/L = 0.55$ )



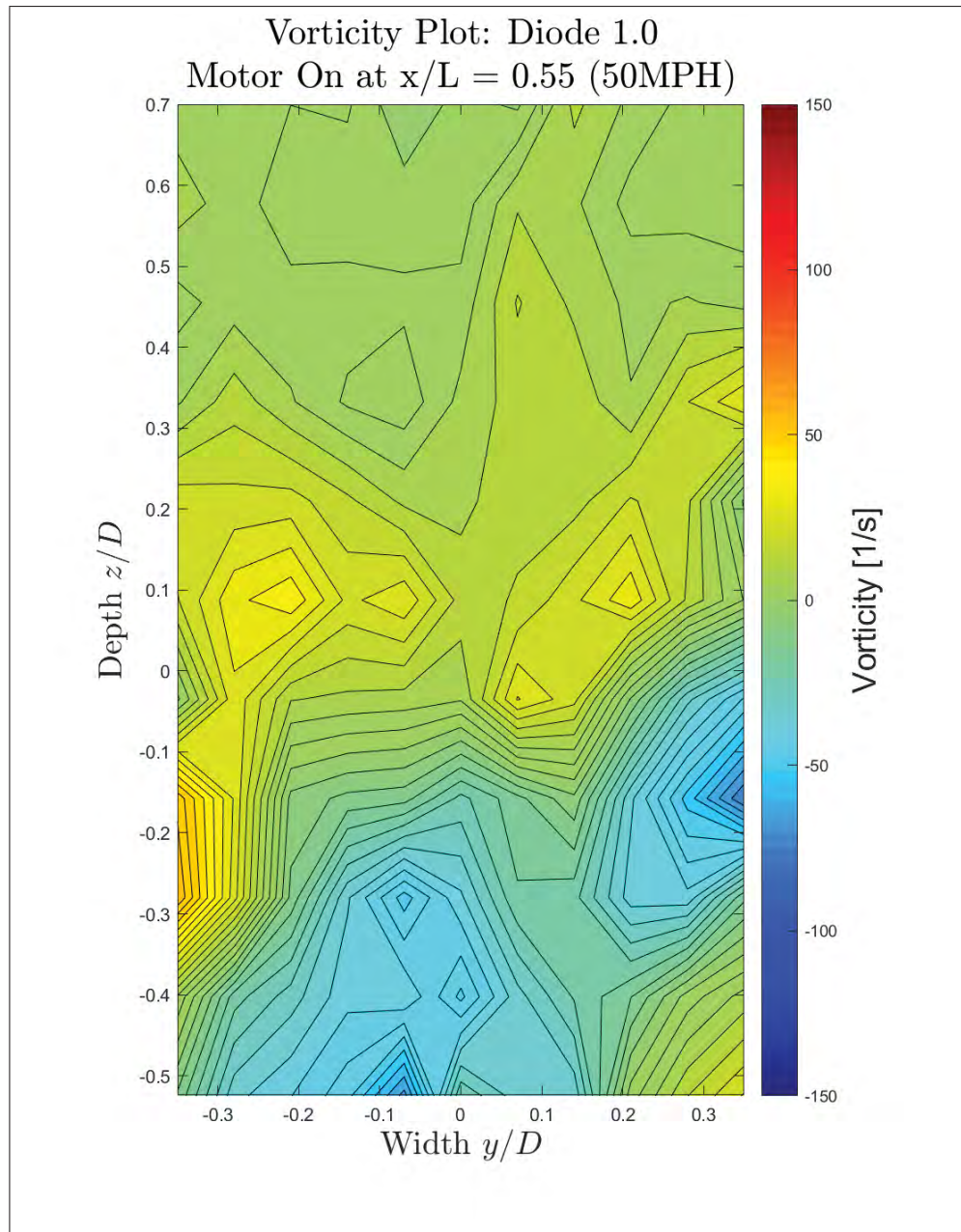
(a) Streamwise Vorticity: Slot (50mph)

Diode 0.0: 50mph ( $x/L = 0.55$ )



(a) Streamwise Vorticity: Diode 0.0 (50mph)

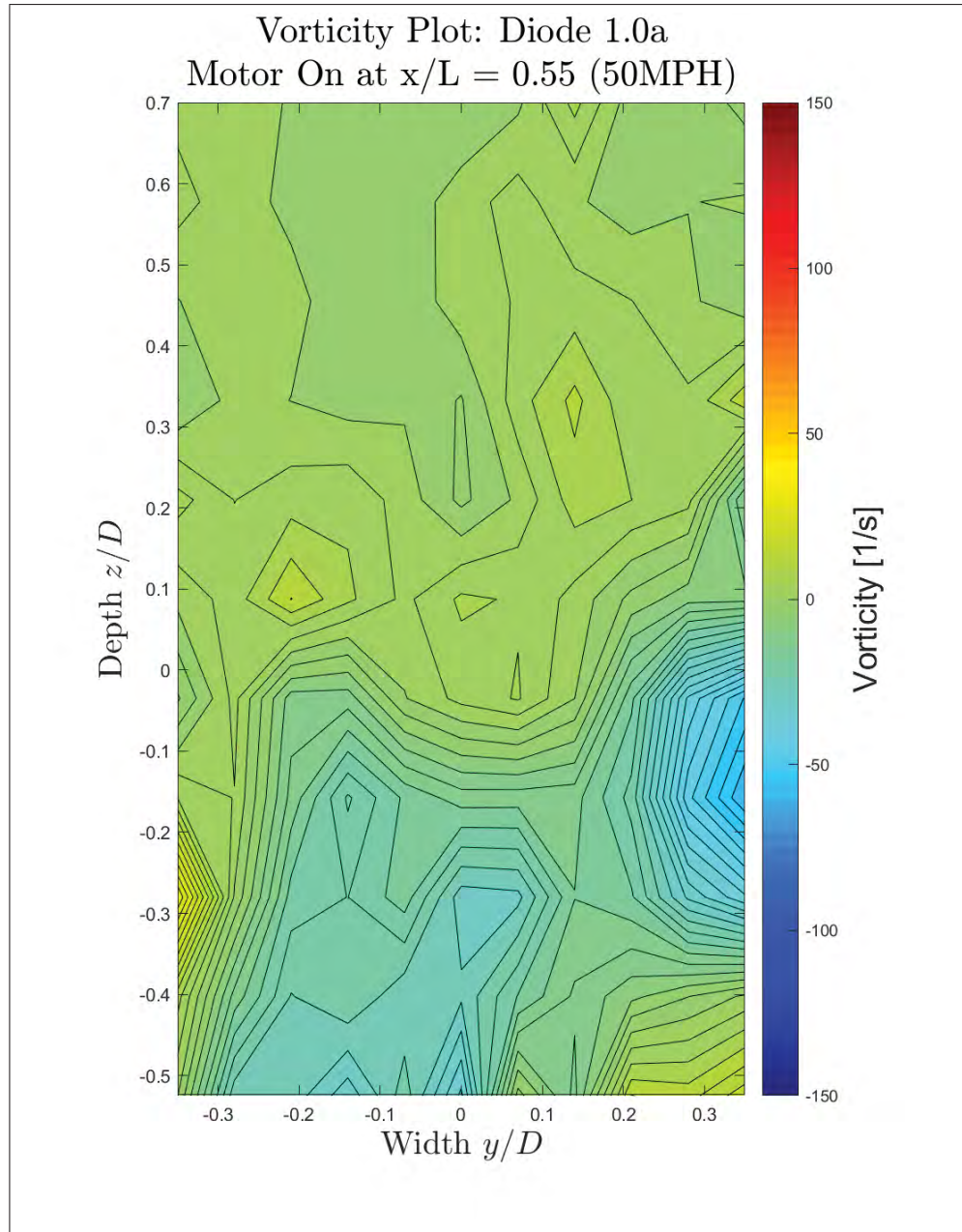
Diode 1.0: 50mph ( $x/L = 0.55$ )



(a) Streamwise Vorticity: Diode 1.0 (50mph)



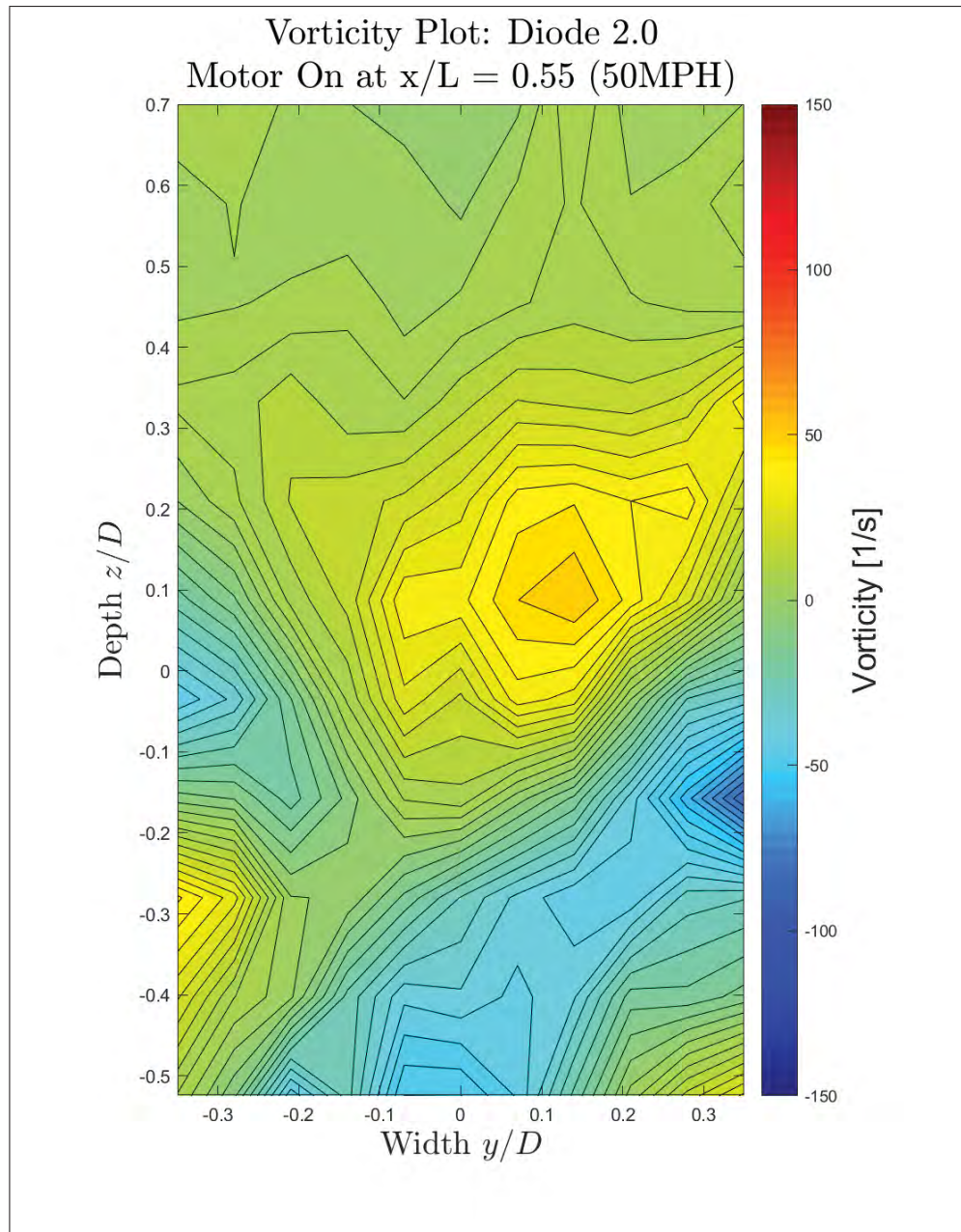
Diode 1.0a: 50mph ( $x/L = 0.55$ )



(a) Streamwise Vorticity: Diode 1.0a (50mph)



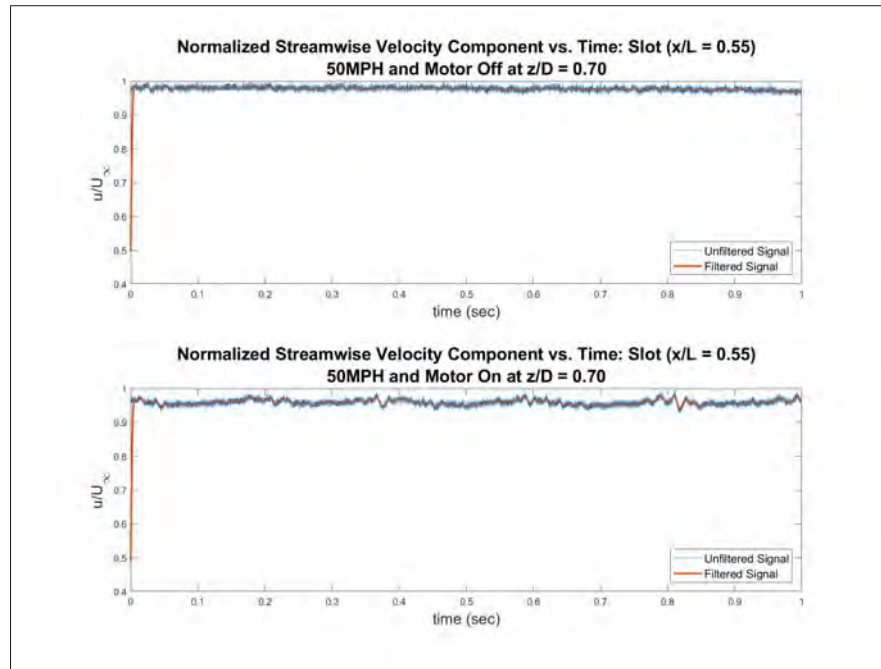
Diode 2.0: 50mph ( $x/L = 0.55$ )



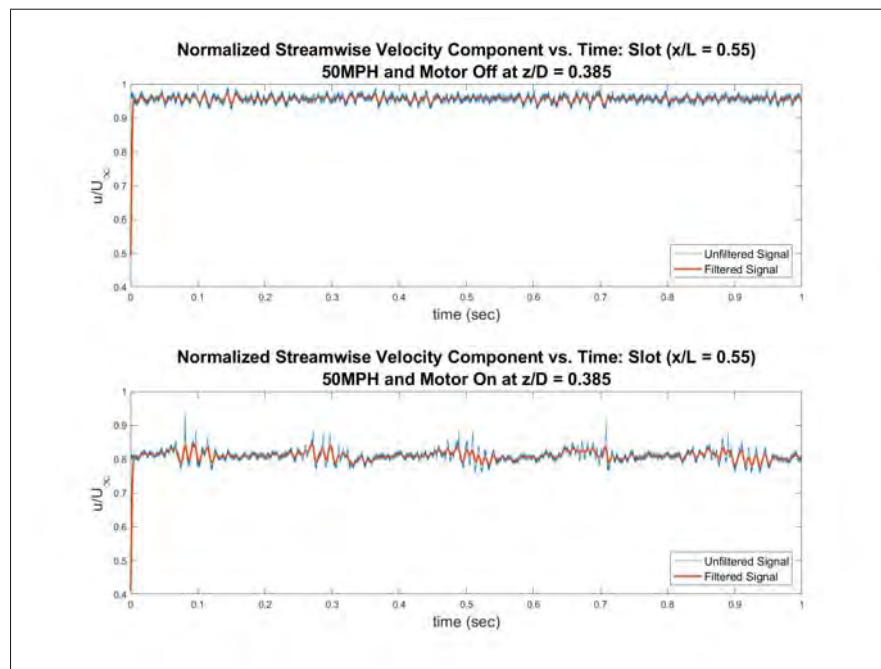
(a) Streamwise Vorticity: Diode 2.0 (50mph)

# Velocity vs. Time Plots

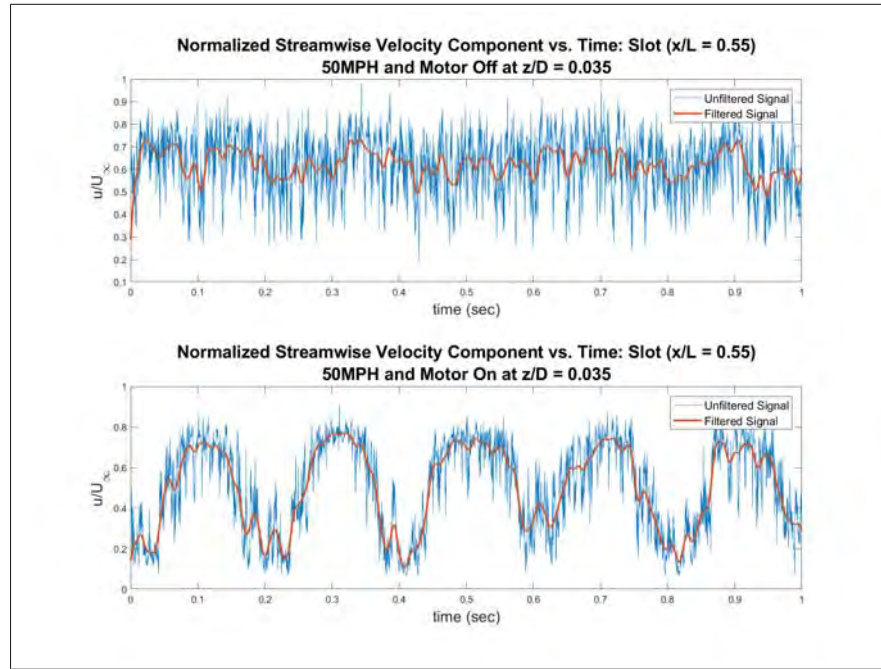
Slot: 50mph ( $x/L = 0.55$ )



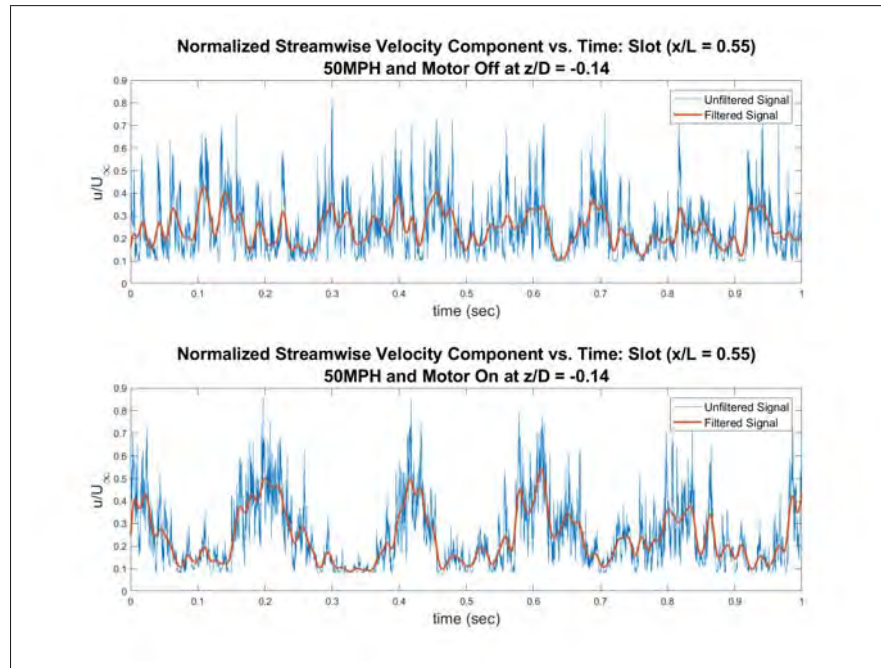
(a) Velocity vs. Time for the leading edge Slot ( $z/D = 0.7$ ) (50mph)



(a) Velocity vs. Time for the leading edge Slot ( $z/D = 0.385$ ) (50mph)



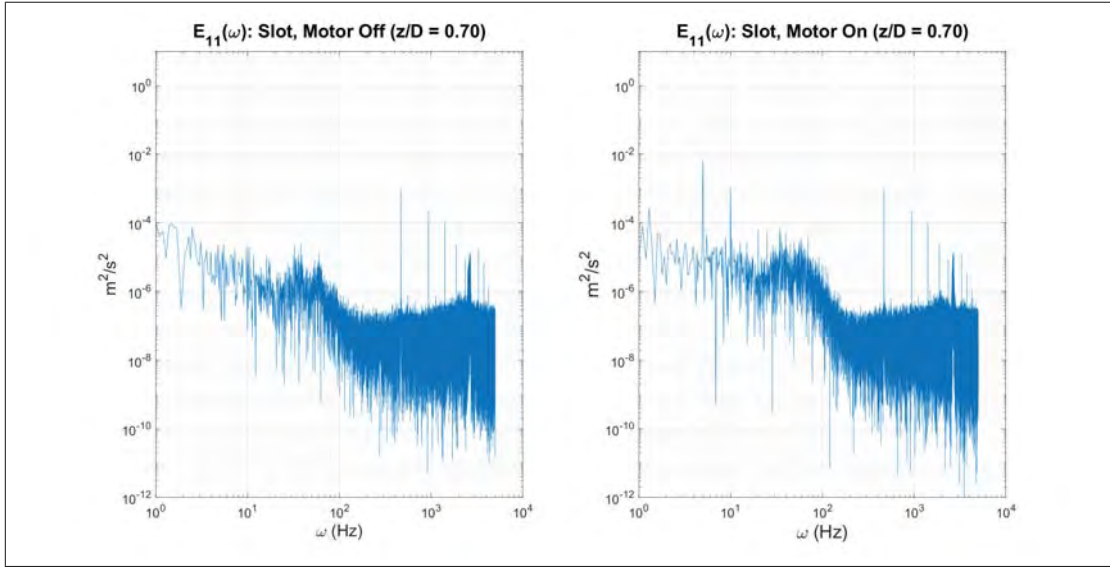
(a) Velocity vs. Time for the leading edge Slot ( $z/D = 0.035$ ) (50mph)



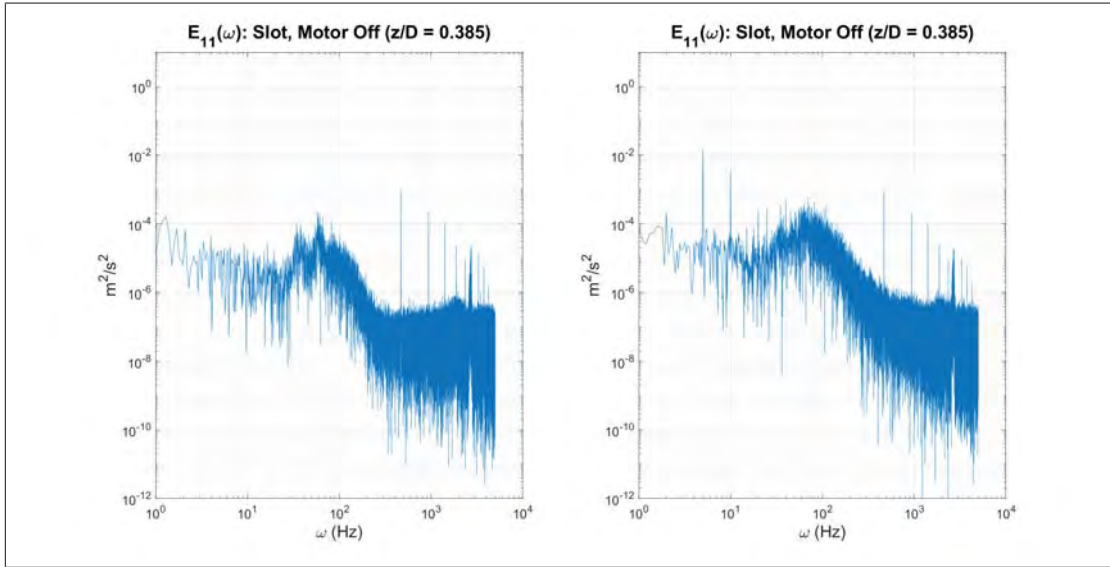
(a) Velocity vs. Time for the leading edge Slot ( $z/D = -0.14$ ) (50mph)

# Energy Frequency Spectrum

Slot: 50mph ( $x/L = 0.55$ )

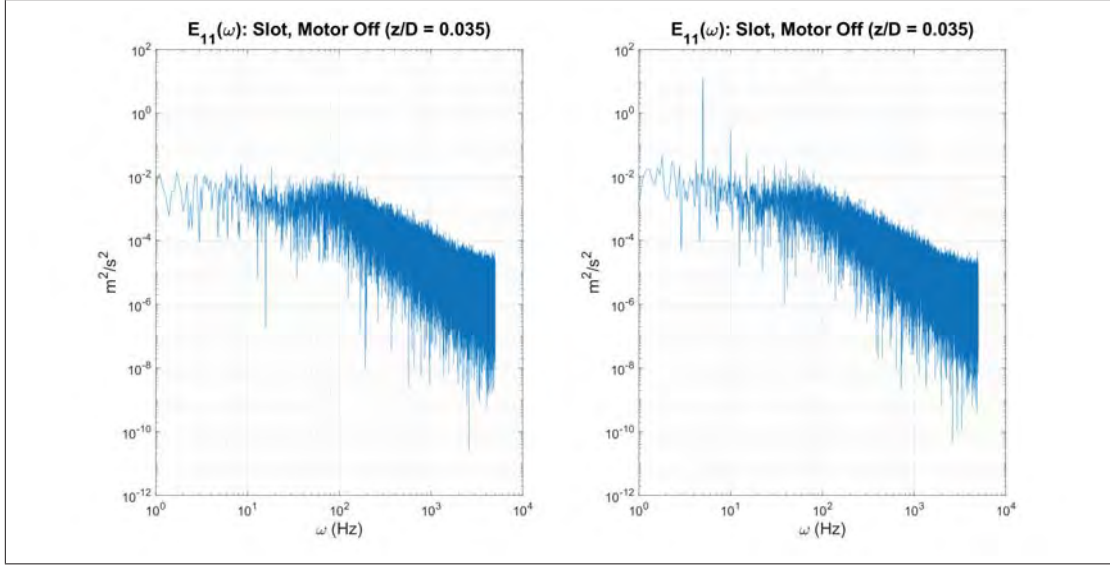


(a) Energy Frequency Spectrum for the leading edge Slot ( $z/D = 0.7$ ) (50mph)

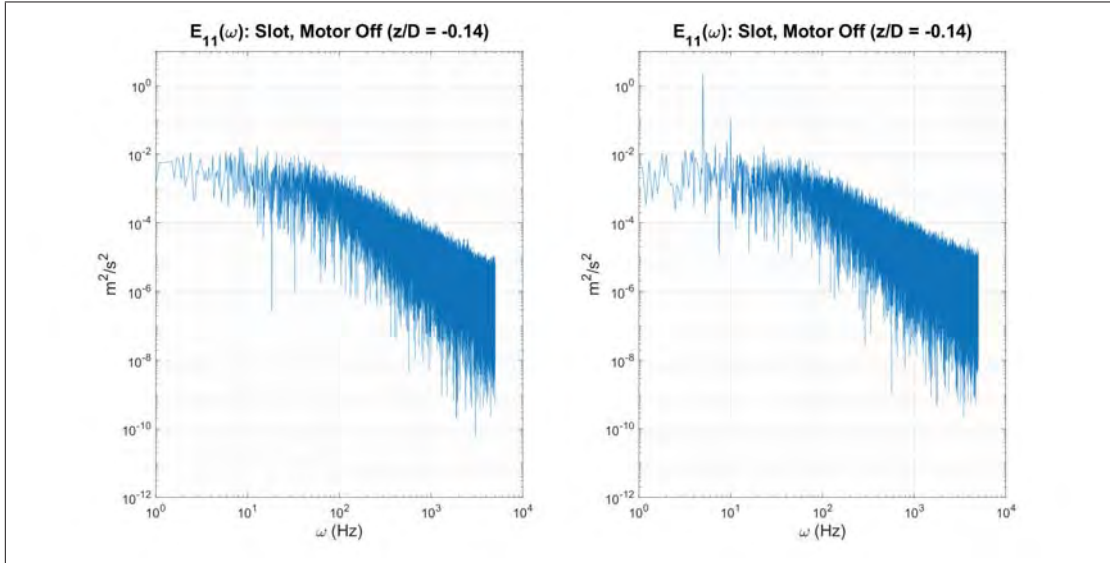


(a) Energy Frequency Spectrum for the leading edge Slot ( $z/D = 0.385$ ) (50mph)





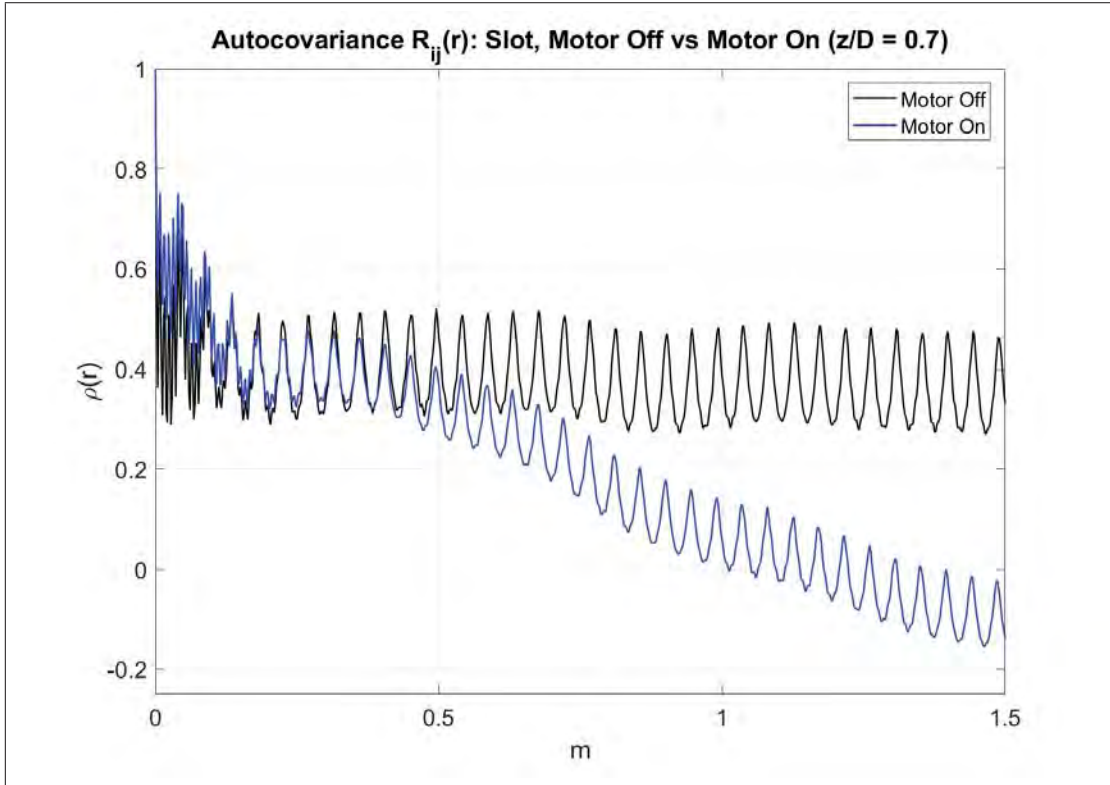
(a) Energy Frequency Spectrum for the leading edge Slot ( $z/D = 0.035$ ) (50mph)



(a) Energy Frequency Spectrum for the leading edge Slot ( $z/D = -0.14$ ) (50mph)

# Autocovariance Plots

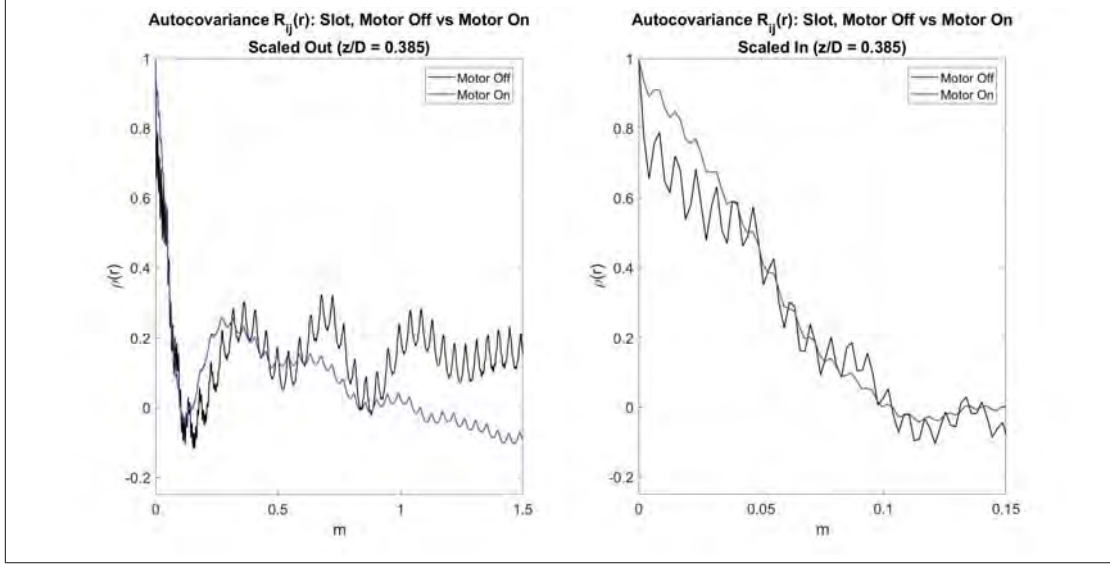
Slot: 50mph ( $x/L = 0.55$ )



(a) Autocovariance comparison for the leading edge Slot ( $z/D = 0.70$ ) (50mph)

| Turbulence Data: Slot ( $z/D = 0.70$ ) |           |          |
|--|-----------|----------|
|  | Motor Off | Motor On |
| Integral Length Scale ( $L_{11}$ )     | 0.0 m     | 0.307 m  |
| Integral Time Scale ( $\tau_{11}$ )    | 0.0 s     | 0.015 s  |

Table 14. Integral length and time scales in the streamwise direction at  $z/D = 0.70$

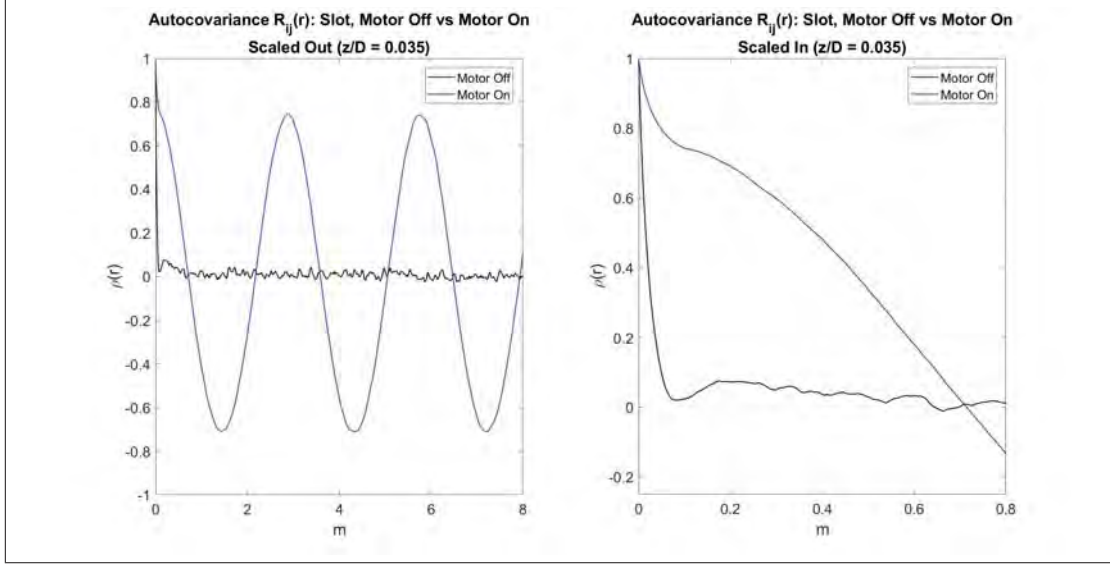


(a) Autocovariance comparison for the leading edge Slot ( $z/D = 0.385$ ) (50mph)

| Turbulence Data: Slot ( $z/D = 0.385$ ) |           |          |
|---|-----------|----------|
|   | Motor Off | Motor On |
| Integral Length Scale ( $L_{11}$ )      | 0.040 m   | 0.045 m  |
| Integral Time Scale ( $\tau_{11}$ )     | 0.002 s   | 0.002 s  |

Table 15. Integral length and time scales in the streamwise direction at  $z/D = 0.385$

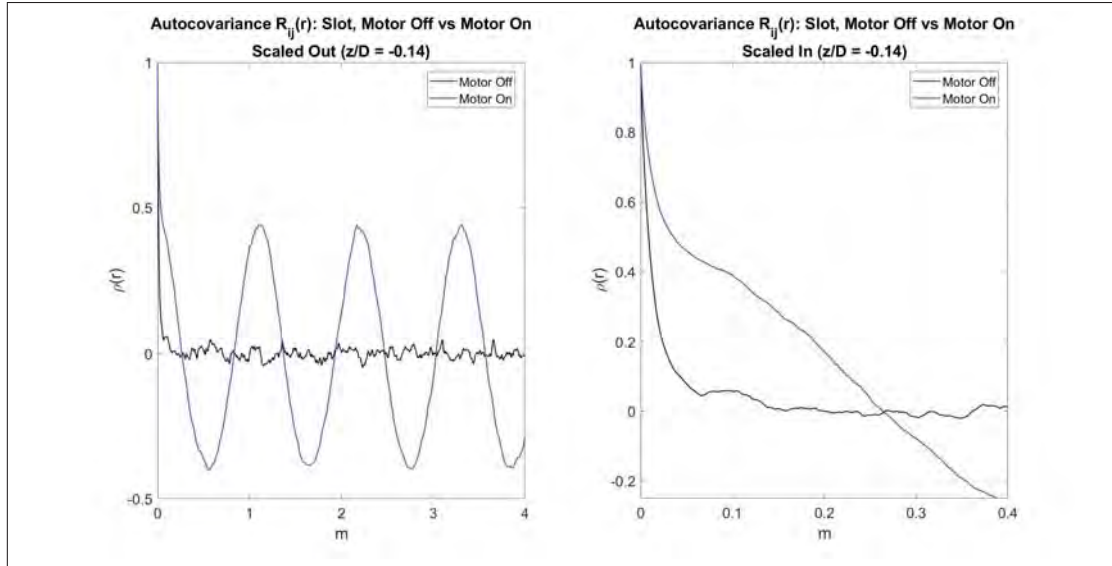




(a) Autocovariance comparison for the leading edge Slot ( $z/D = 0.035$ ) (50mph)

| Turbulence Data: Slot ( $z/D = 0.035$ ) |           |          |
|---|-----------|----------|
|   | Motor Off | Motor On |
| Integral Length Scale ( $L_{11}$ )      | 0.046 m   | 0.349 m  |
| Integral Time Scale ( $\tau_{11}$ )     | 0.003 s   | 0.024 s  |

Table 16. Integral length and time scales in the streamwise direction at  $z/D = 0.035$



(a) Autocovariance comparison for the leading edge Slot ( $z/D = -0.14$ ) (50mph)

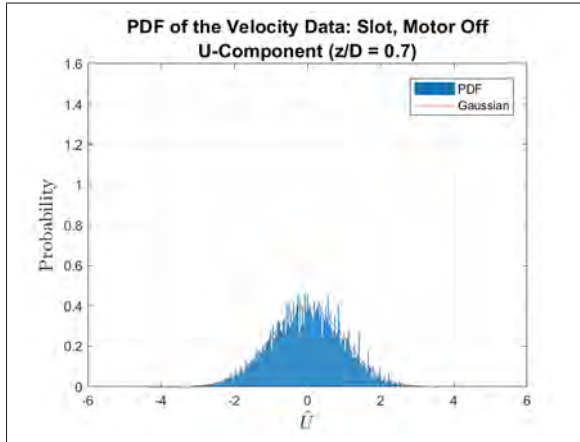
| Turbulence Data: Slot ( $z/D = -0.14$ ) |           |          |
|---|-----------|----------|
|   | Motor Off | Motor On |
| Integral Length Scale ( $L_{11}$ )      | 0.019 m   | 0.085 m  |
| Integral Time Scale ( $\tau_{11}$ )     | 0.004 s   | 0.015 s  |

Table 17. Integral length and time scales in the streamwise direction at  $z/D = -0.14$

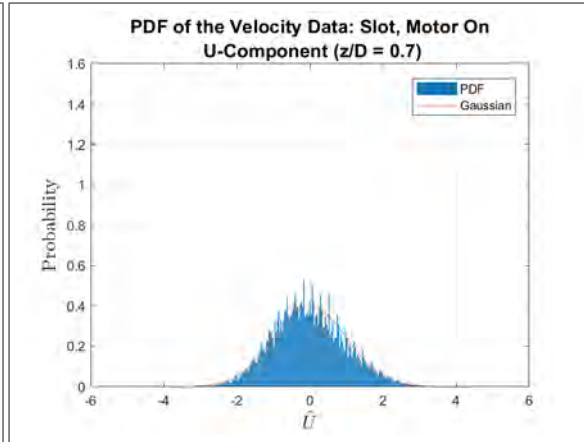
# Probability Distribution Functions

Slot: 50mph ( $x/L = 0.55$ )

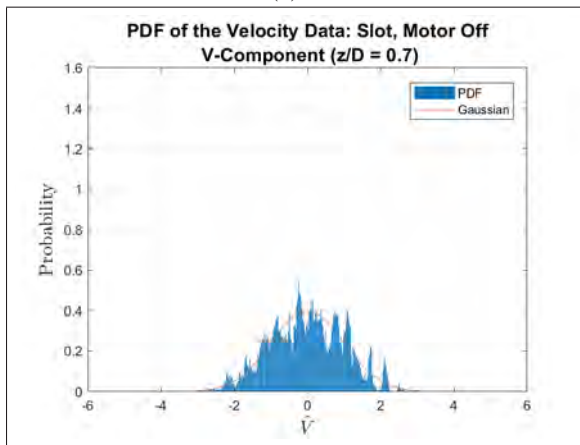
Slot: Motor Off vs. Motor On at  $z/D = 0.70$  and 50 mph



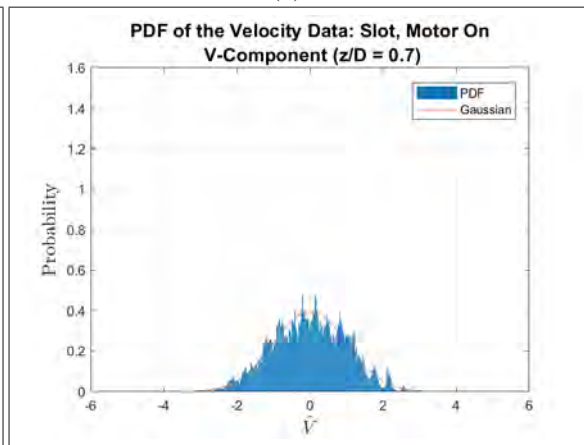
(a)



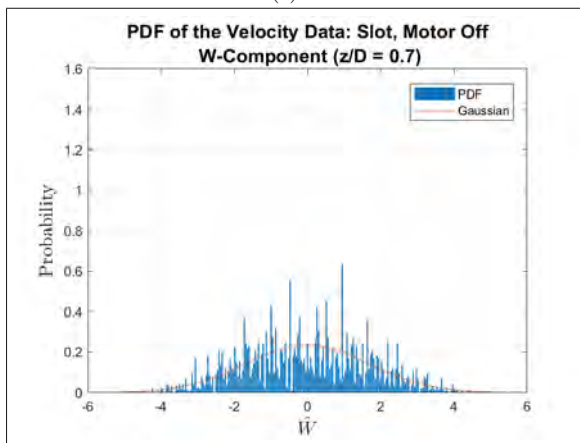
(b)



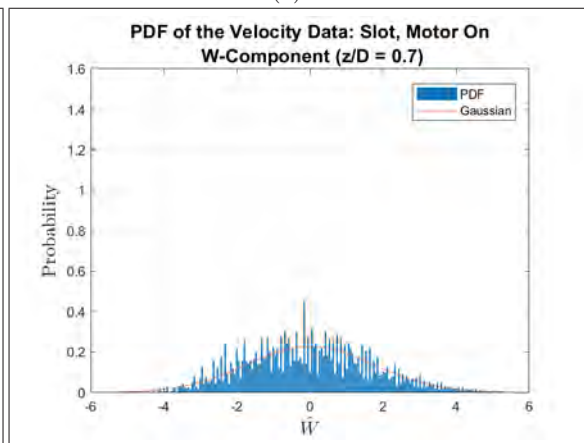
(c)



(d)

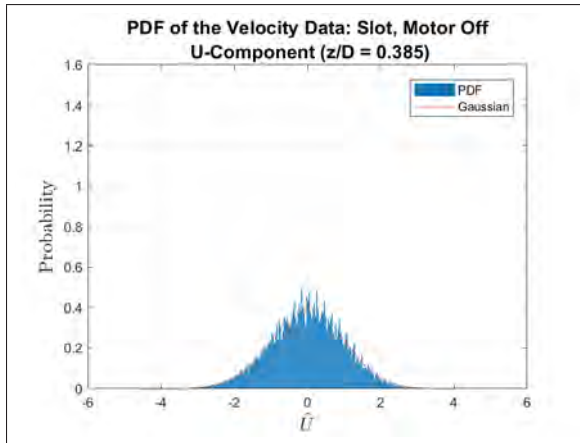


(e)

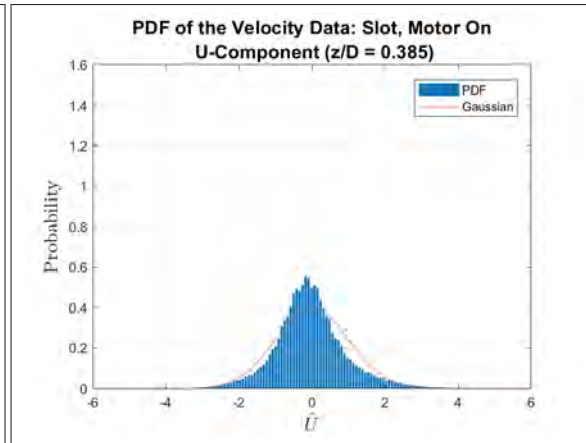


(f)

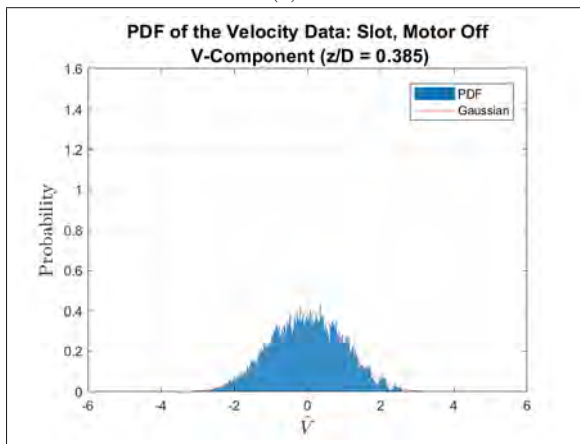
Slot: Motor Off vs. Motor On at  $z/D = 0.385$  and 50 mph



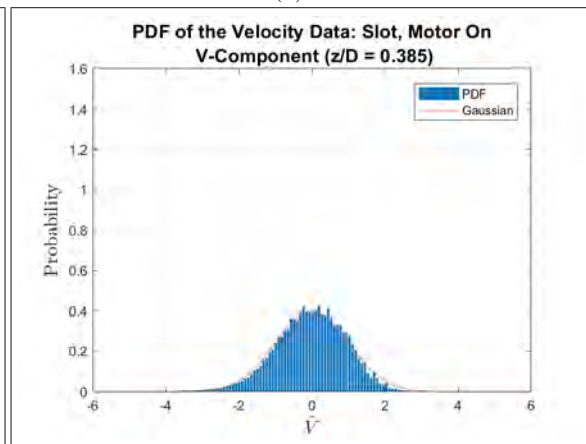
(a)



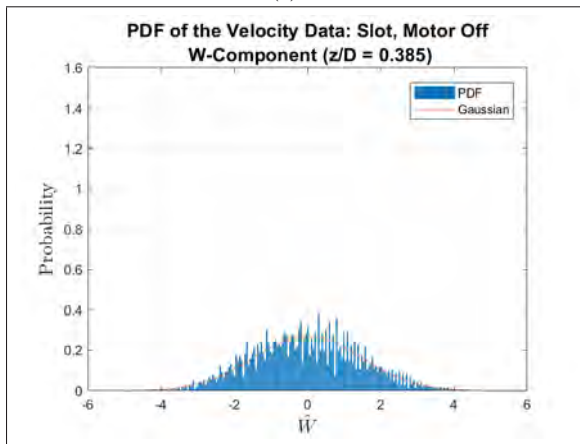
(b)



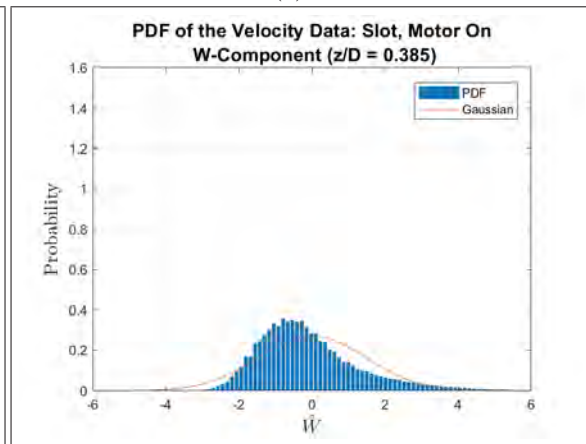
(c)



(d)

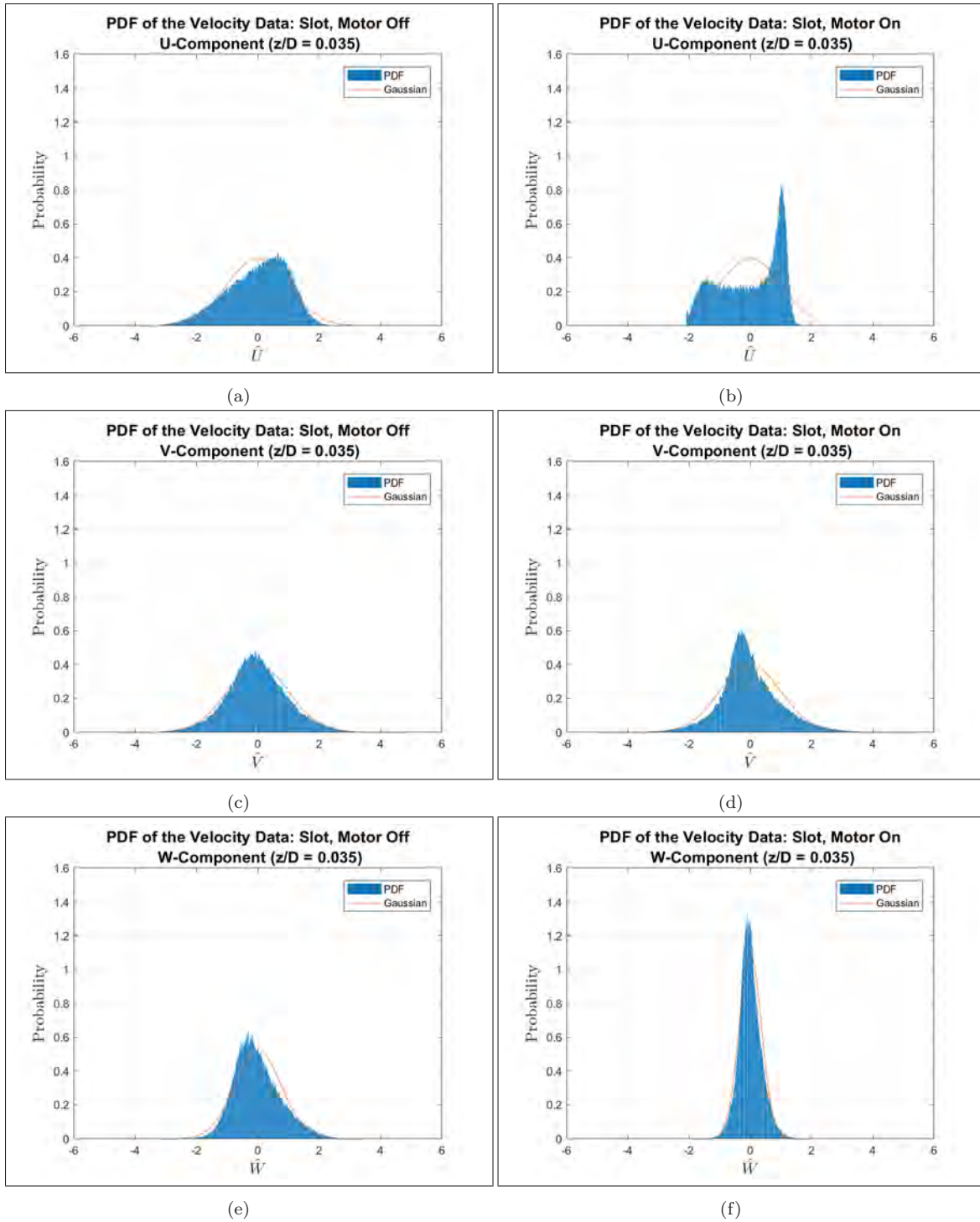


(e)

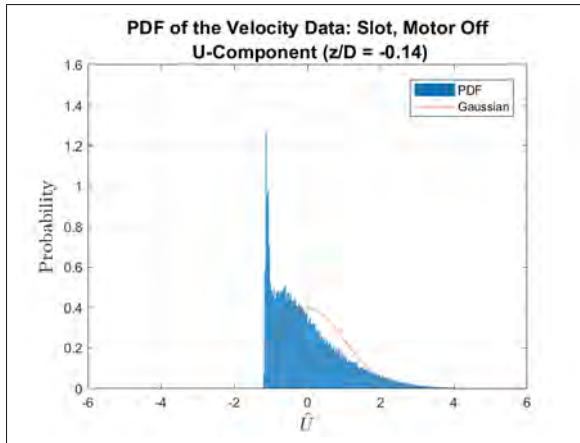


(f)

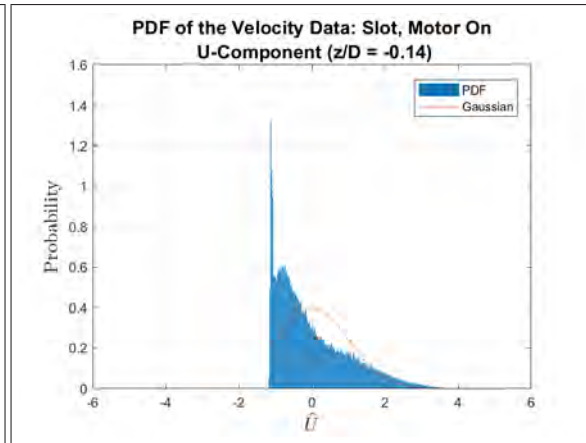
Slot: Motor Off vs. Motor On at  $z/D = 0.035$  and 50 mph



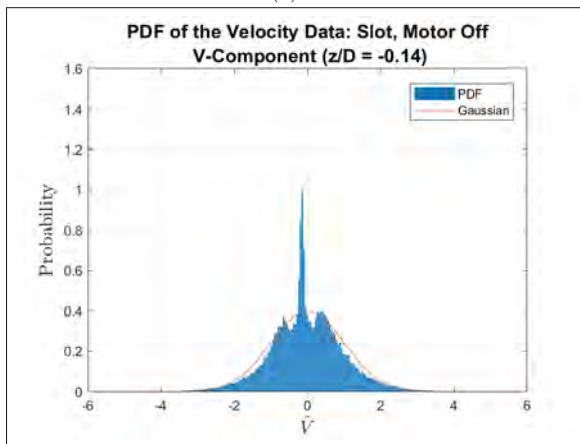
Slot: Motor Off vs. Motor On at  $z/D = -0.14$  and 50 mph



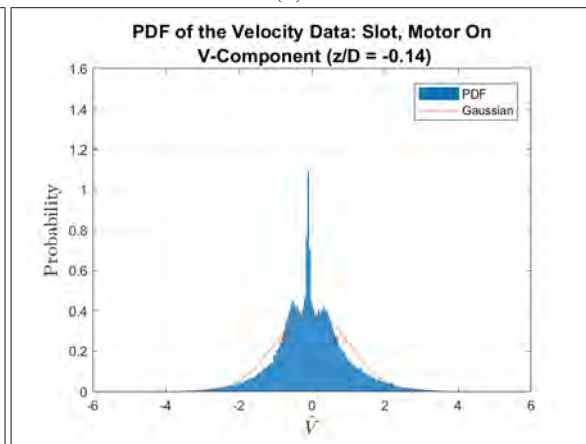
(a)



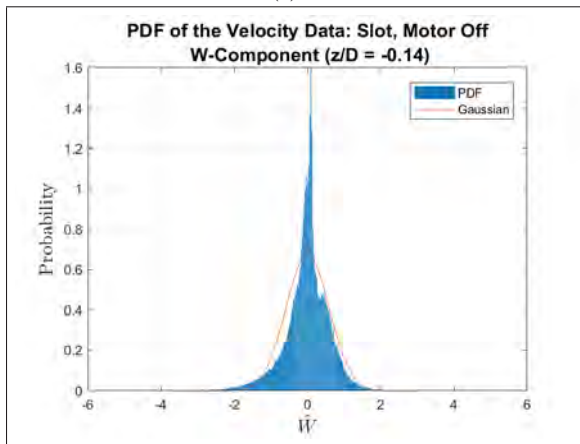
(b)



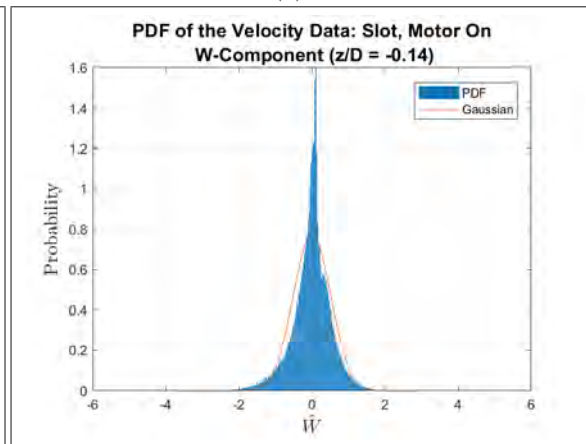
(c)



(d)



(e)



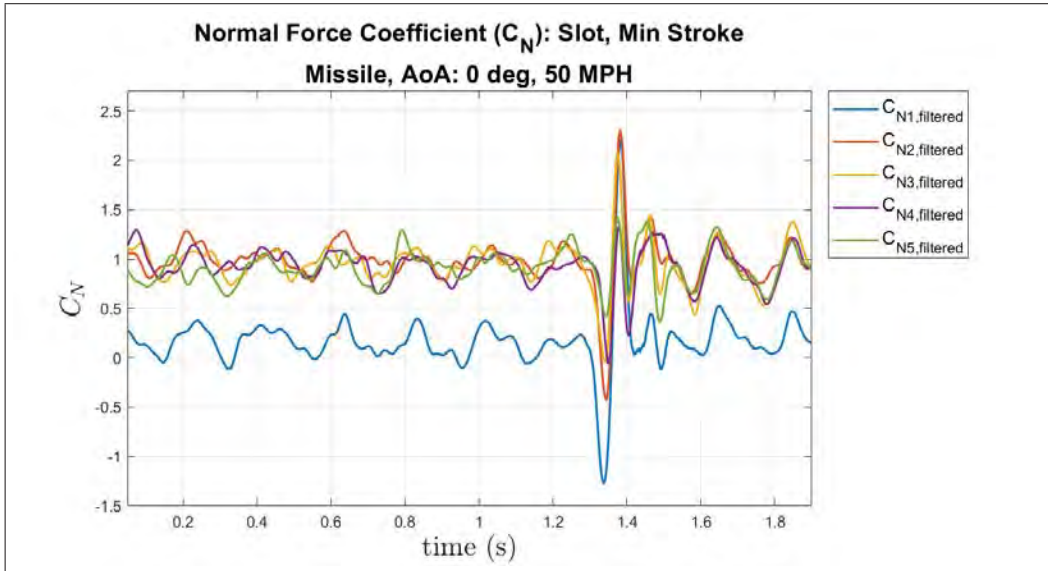
(f)



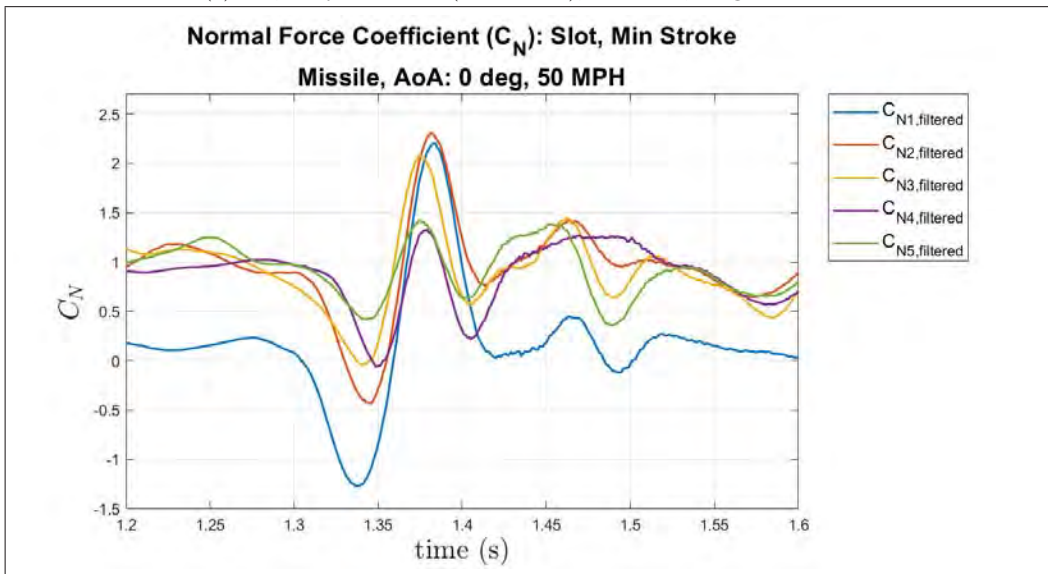
## Phase II

### 0.0° Angle of Attack

Fully Retracted Initialization: 50 mph

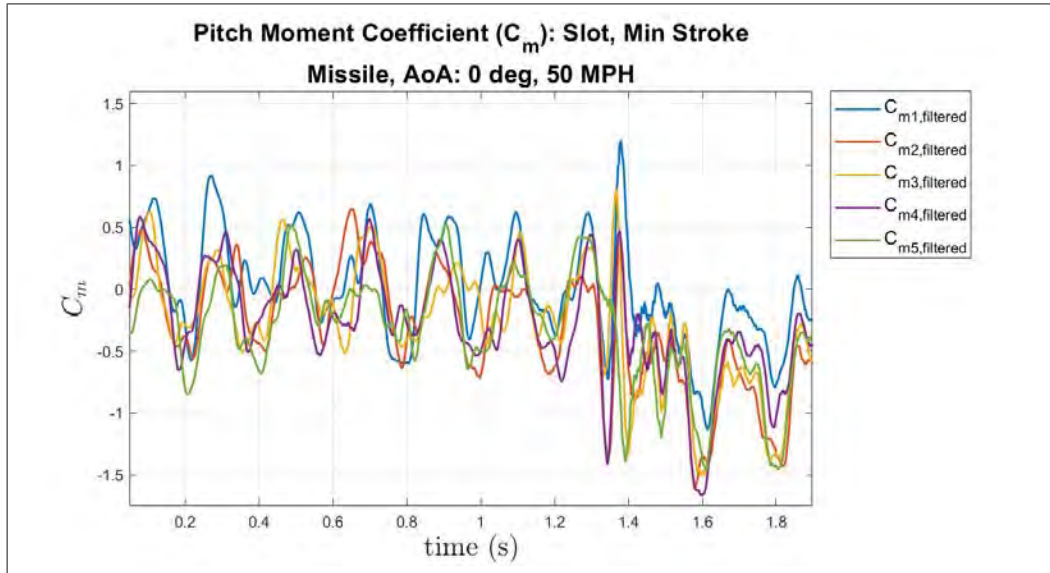


(a)  $C_N$ , Fully Retracted (Min Stroke), 0.0° AoA, Large Window

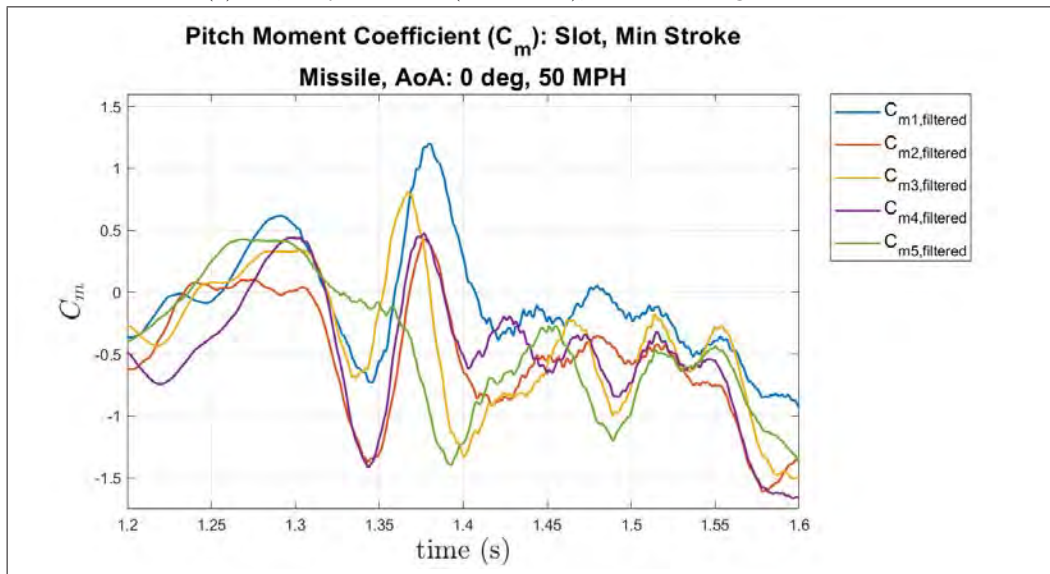


(b)  $C_N$ , Fully Retracted (Min Stroke), 0.0° AoA, Small Window

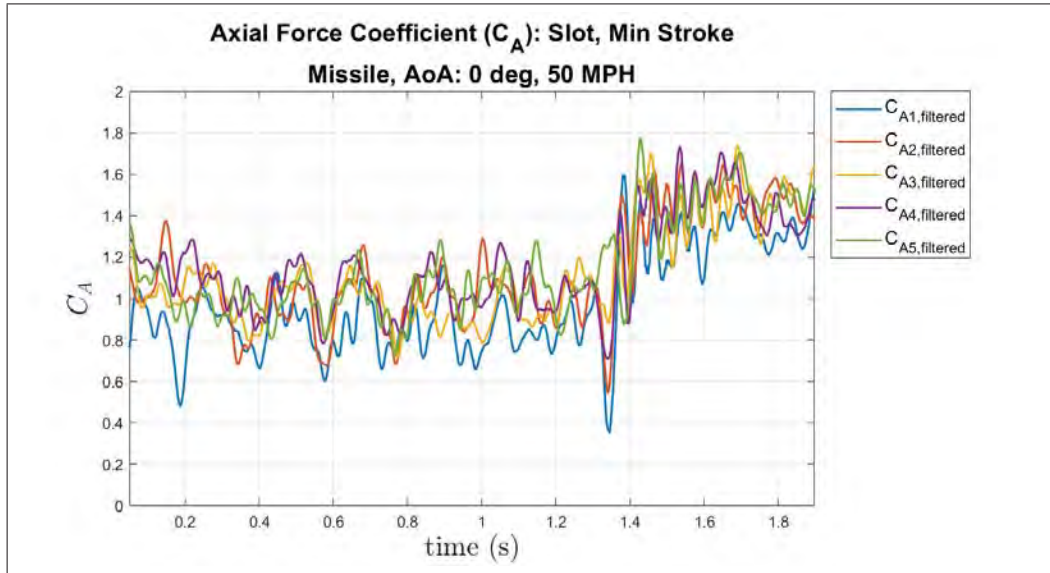




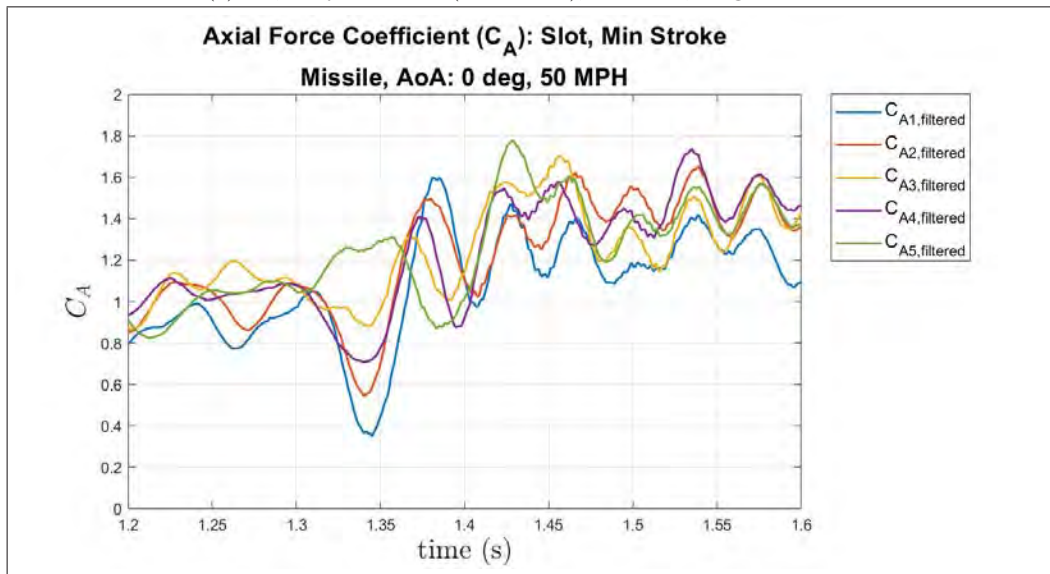
(a)  $C_m$ , Fully Retracted (Min Stroke),  $0.0^\circ$  AoA, Large Window



(b)  $C_m$ , Fully Retracted (Min Stroke),  $0.0^\circ$  AoA, Small Window

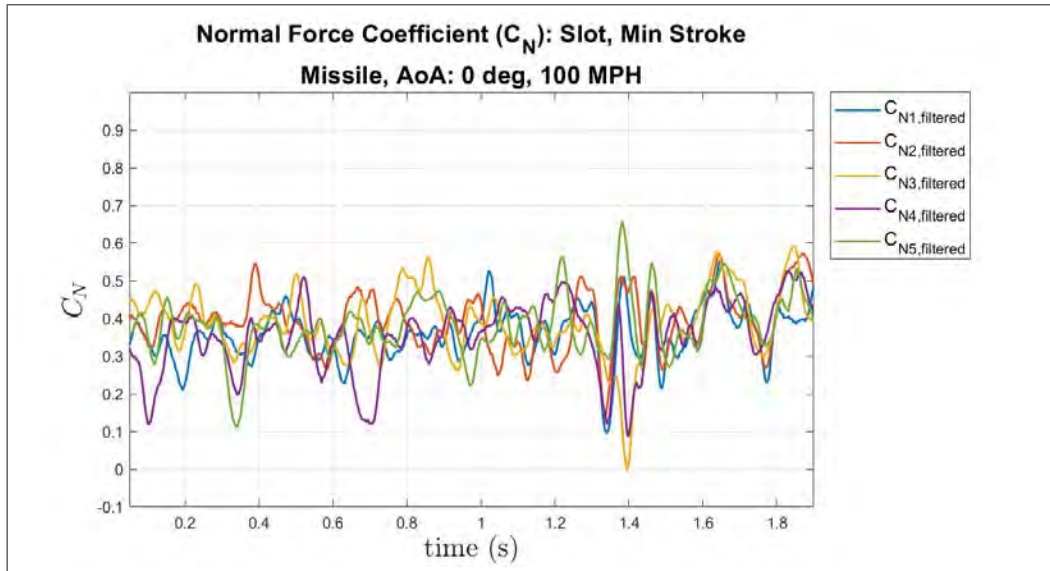


(a)  $C_A$ , Fully Retracted (Min Stroke),  $0.0^\circ$  AoA, Large Window

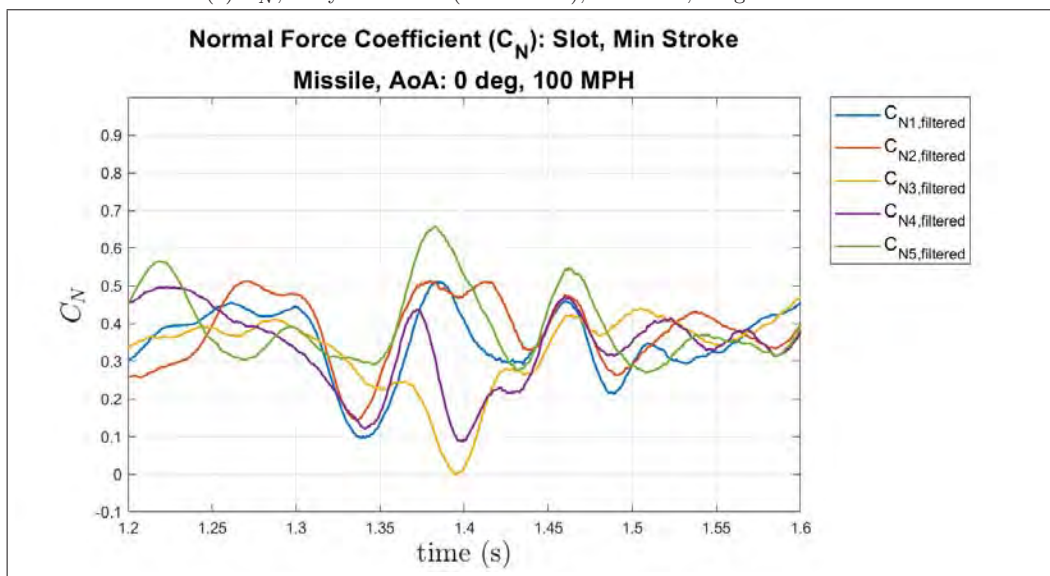


(b)  $C_A$ , Fully Retracted (Min Stroke),  $0.0^\circ$  AoA, Small Window

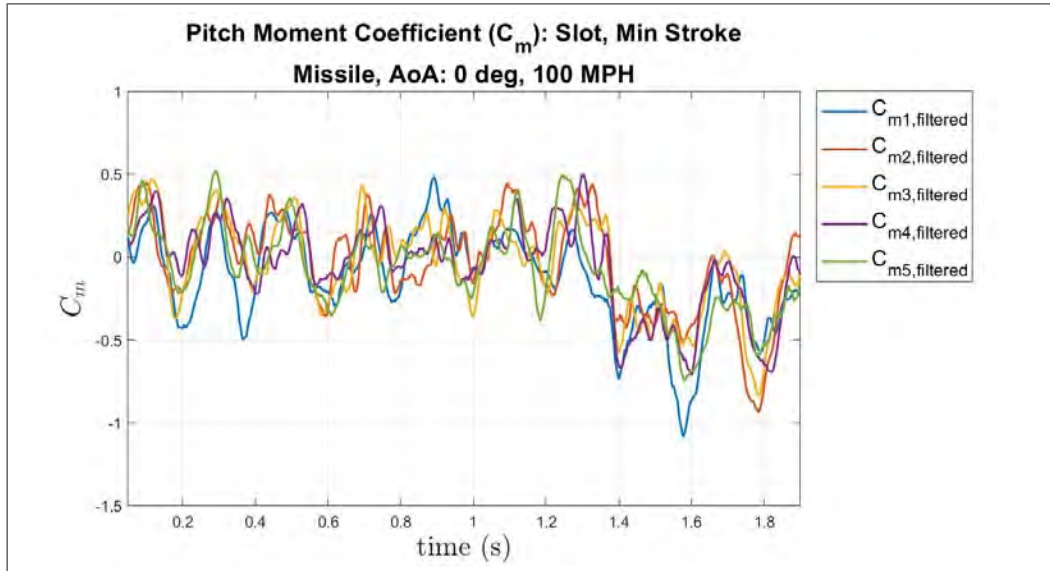
## Fully Retracted Initialization: 100 mph



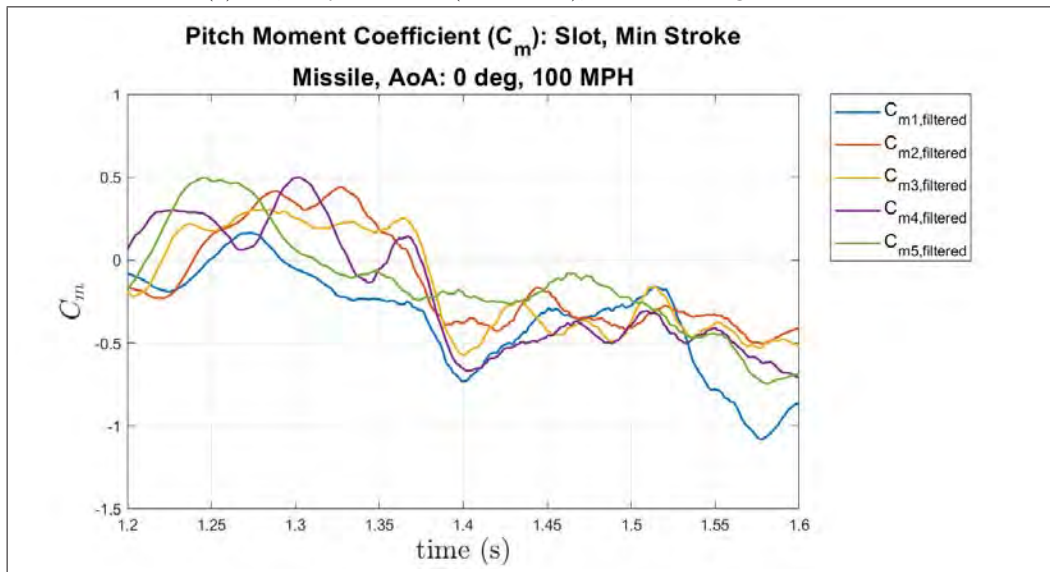
(a)  $C_N$ , Fully Retracted (Min Stroke),  $0.0^\circ$  AoA, Large Window



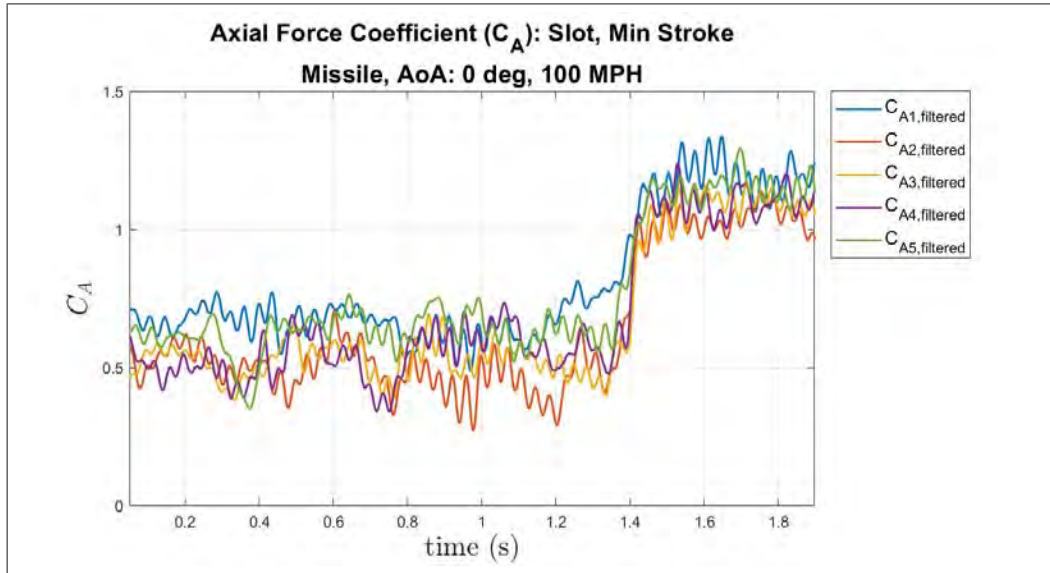
(b)  $C_N$ , Fully Retracted (Min Stroke),  $0.0^\circ$  AoA, Small Window



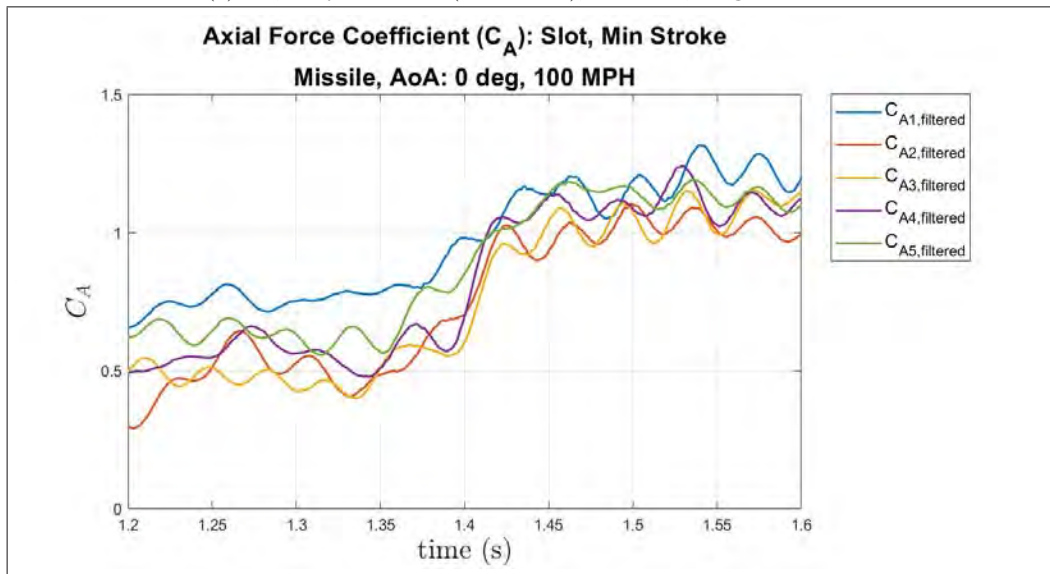
(a)  $C_m$ , Fully Retracted (Min Stroke),  $0.0^\circ$  AoA, Large Window



(b)  $C_m$ , Fully Retracted (Min Stroke),  $0.0^\circ$  AoA, Small Window



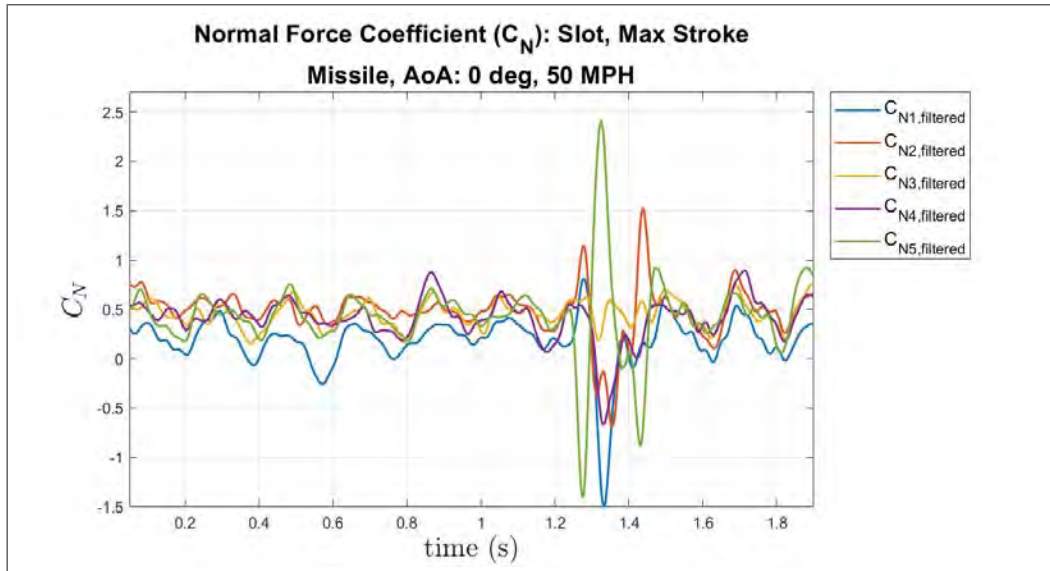
(a)  $C_A$ , Fully Retracted (Min Stroke),  $0.0^\circ$  AoA, Large Window



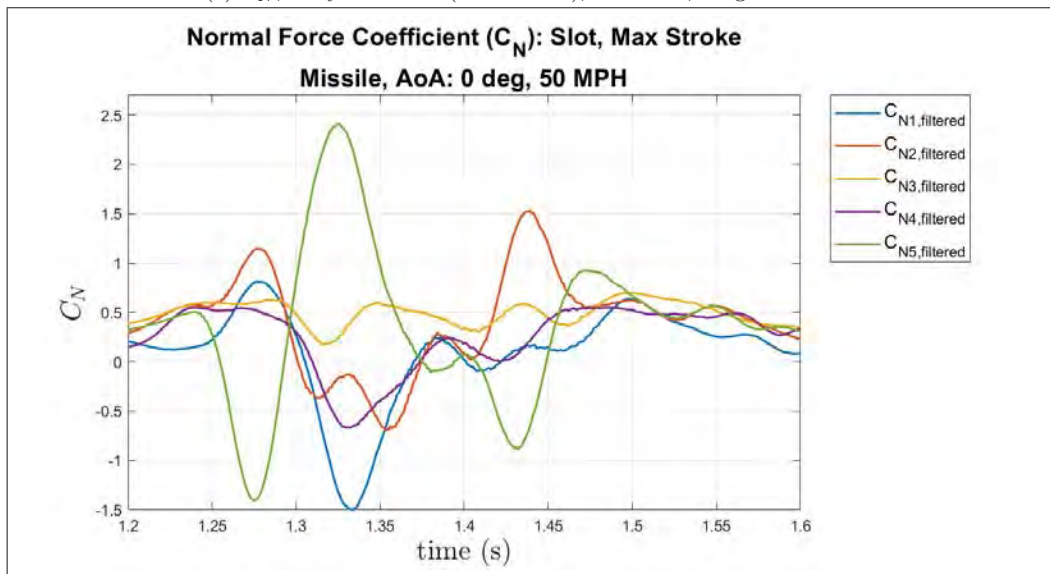
(b)  $C_A$ , Fully Retracted (Min Stroke),  $0.0^\circ$  AoA, Small Window



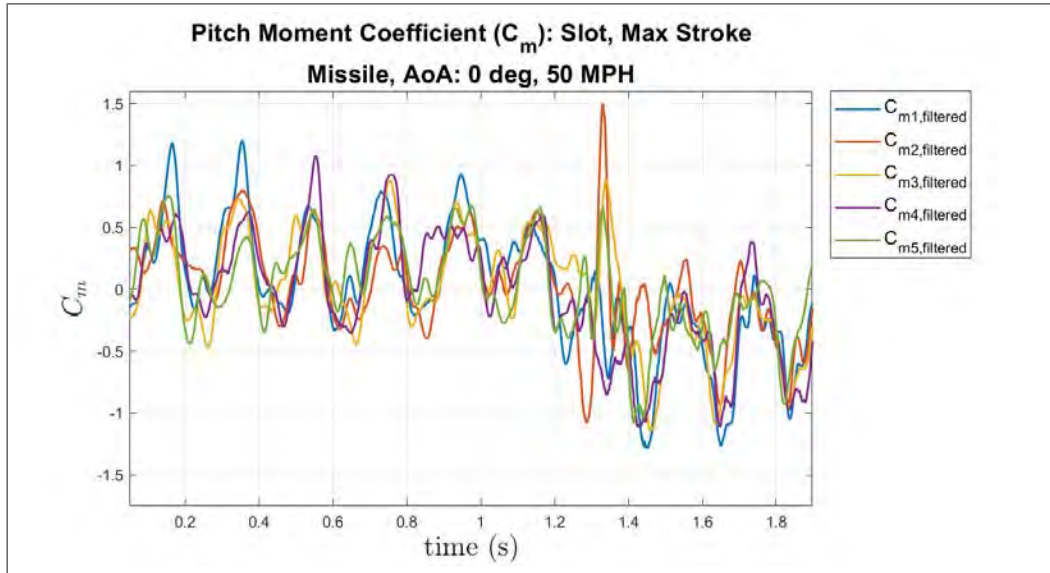
## Fully Extended Initialization: 50 mph



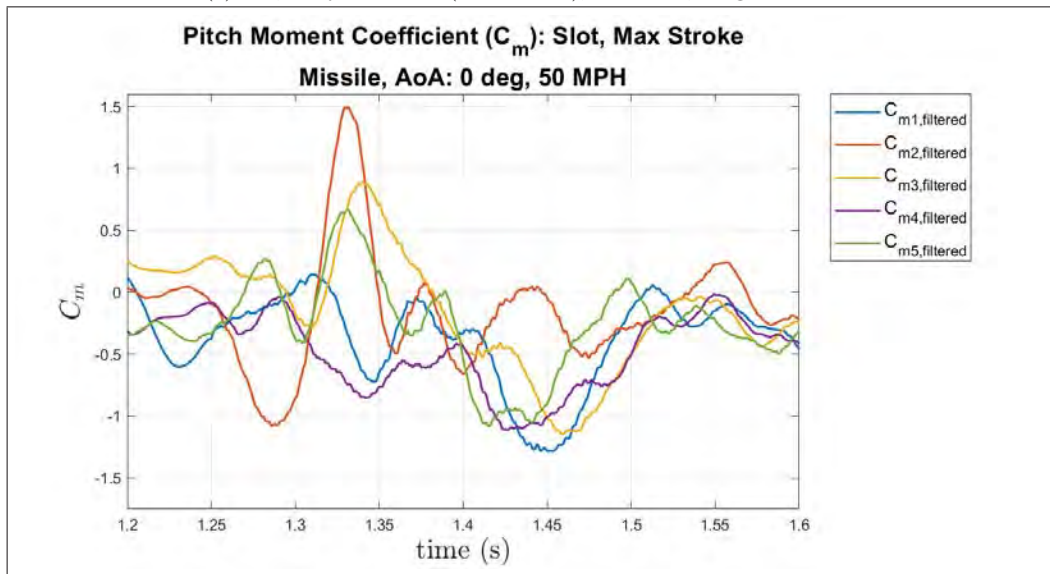
(a)  $C_N$ , Fully Extended (Max Stroke),  $0.0^\circ$  AoA, Large Window



(b)  $C_N$ , Fully Extended (Max Stroke),  $0.0^\circ$  AoA, Small Window

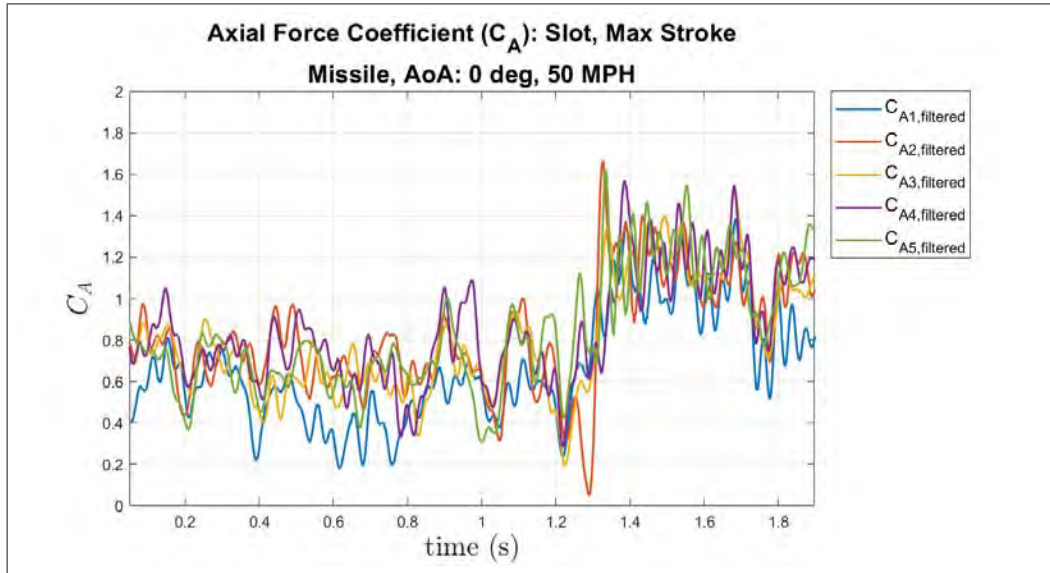


(a)  $C_m$ , Fully Extended (Max Stroke),  $0.0^\circ$  AoA, Large Window

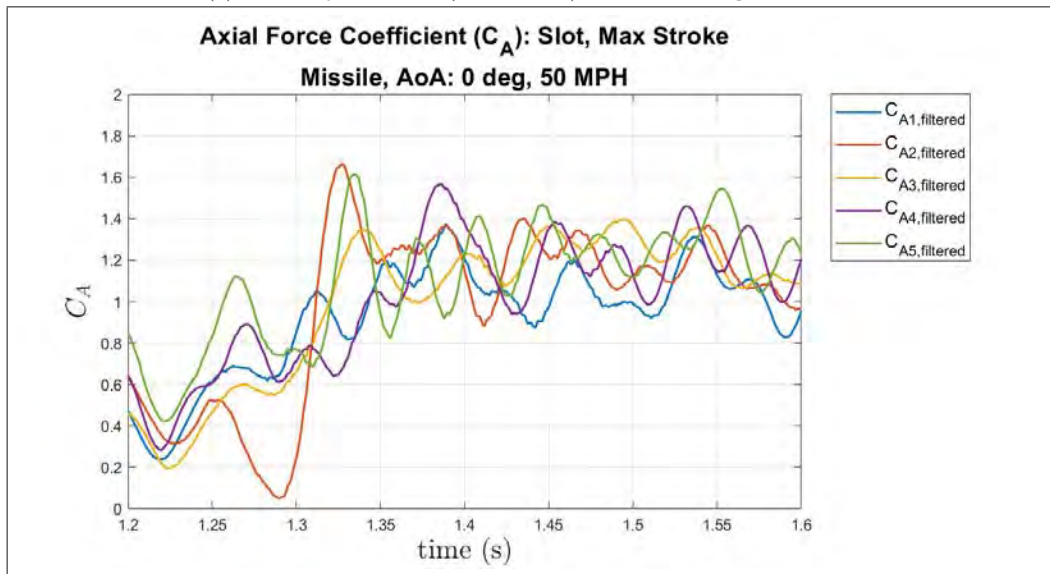


(b)  $C_m$ , Fully Extended (Max Stroke),  $0.0^\circ$  AoA, Small Window



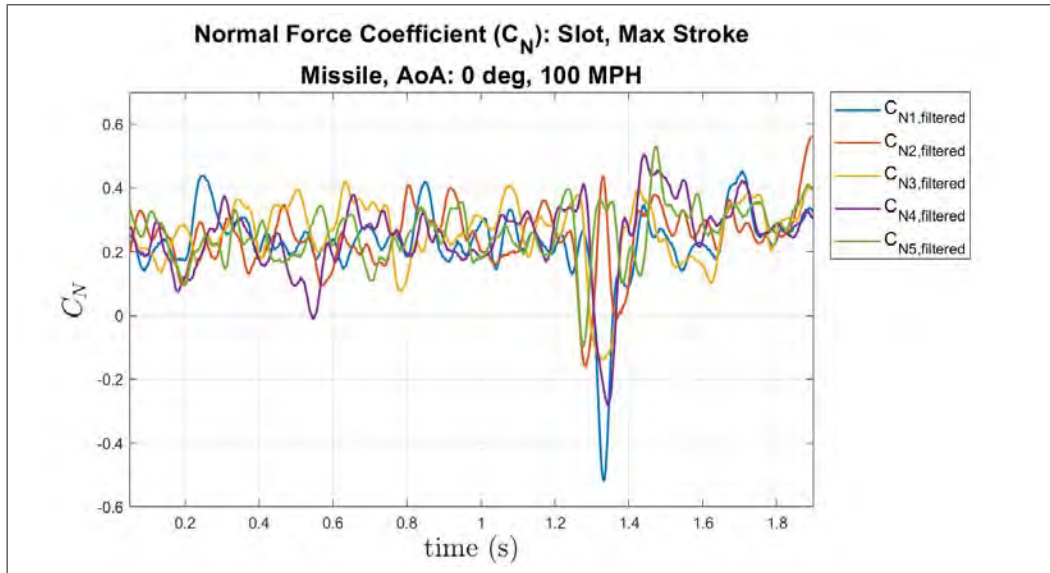


(a)  $C_A$ , Fully Extended (Max Stroke),  $0.0^\circ$  AoA, Large Window

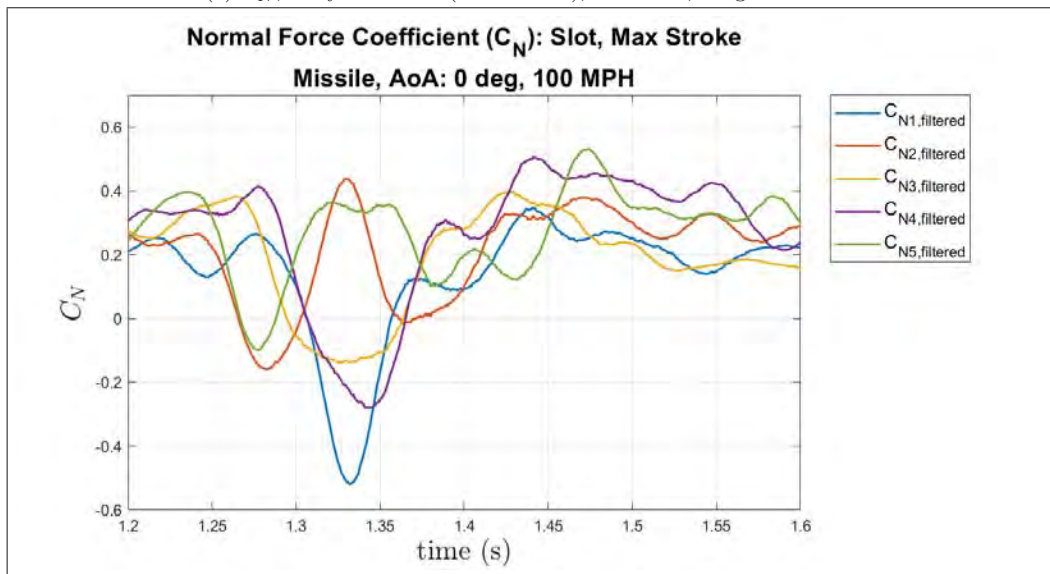


(b)  $C_A$ , Fully Extended (Max Stroke),  $0.0^\circ$  AoA, Small Window

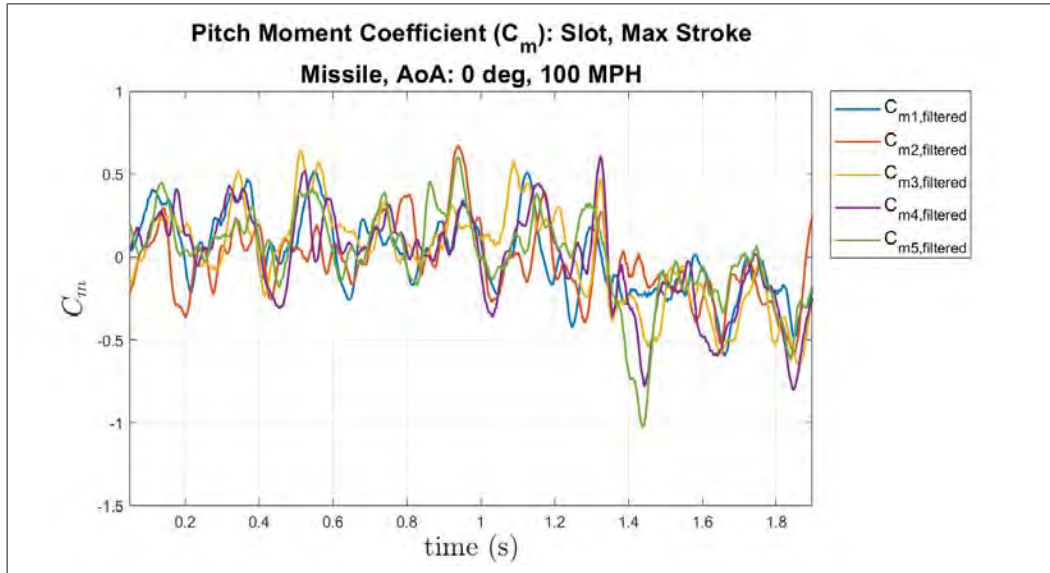
Fully Extended Initialization: 100 mph



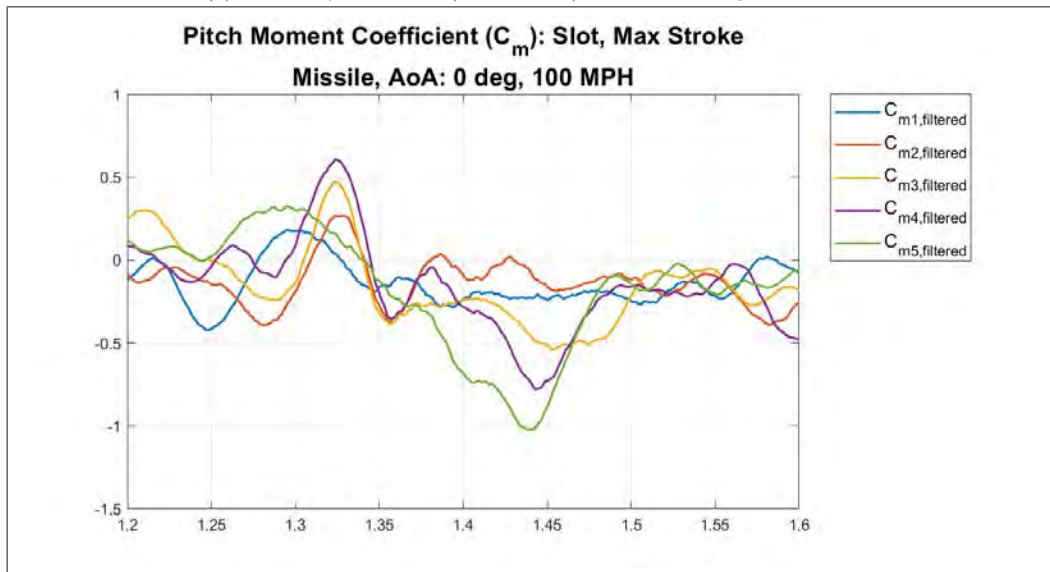
(a)  $C_N$ , Fully Extended (Max Stroke),  $0.0^\circ$  AoA, Large Window



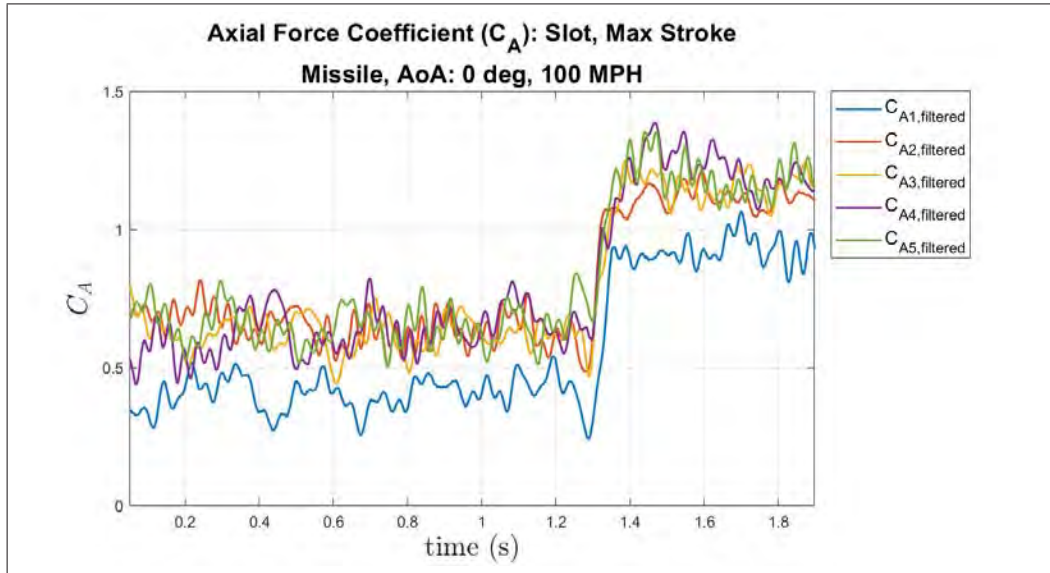
(b)  $C_N$ , Fully Extended (Max Stroke),  $0.0^\circ$  AoA, Small Window



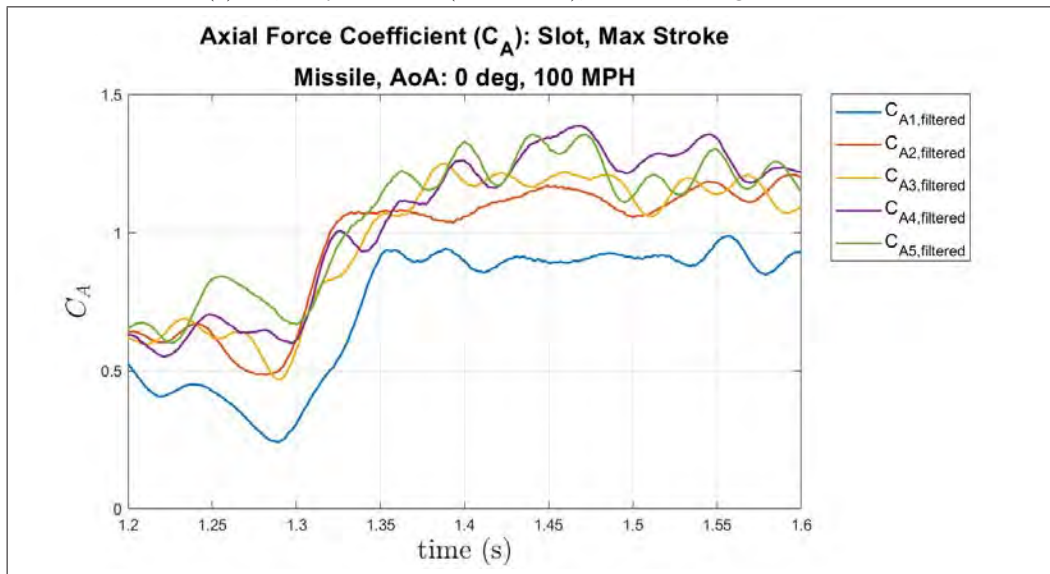
(a)  $C_m$ , Fully Extended (Max Stroke),  $0.0^\circ$  AoA, Large Window



(b)  $C_m$ , Fully Extended (Max Stroke),  $0.0^\circ$  AoA, Small Window



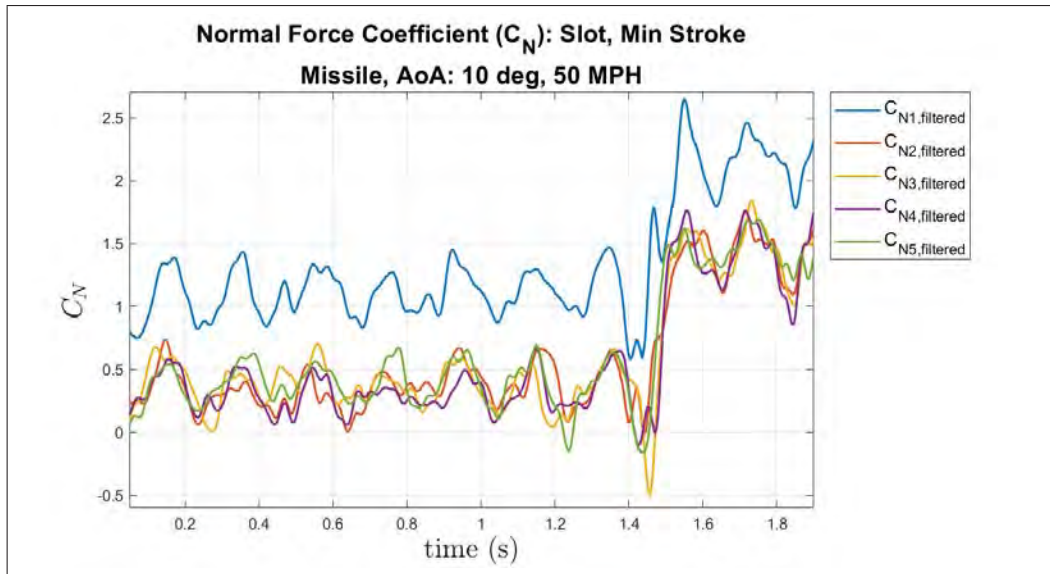
(a)  $C_A$ , Fully Extended (Max Stroke),  $0.0^\circ$  AoA, Large Window



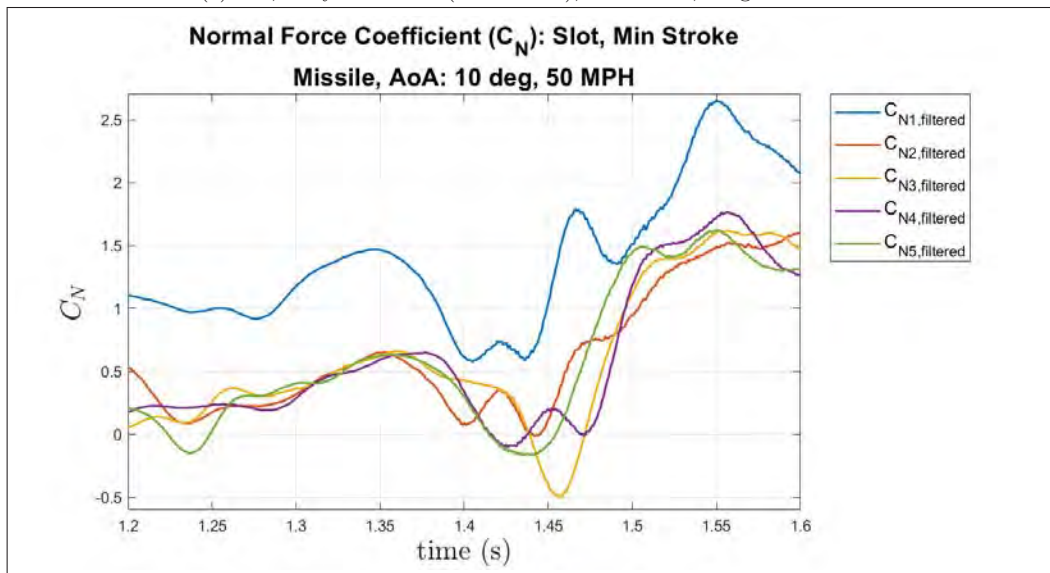
(b)  $C_A$ , Fully Extended (Max Stroke),  $0.0^\circ$  AoA, Small Window

## 10.0° Angle of Attack

Fully Retracted Initialization: 50 mph

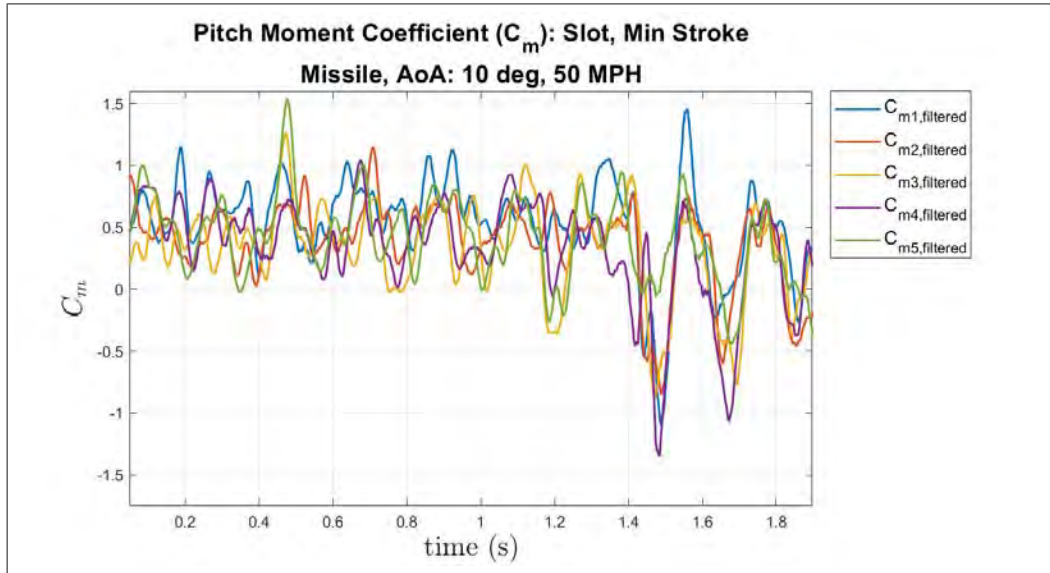


(a)  $C_N$ , Fully Retracted (Min Stroke), 10.0° AoA, Large Window

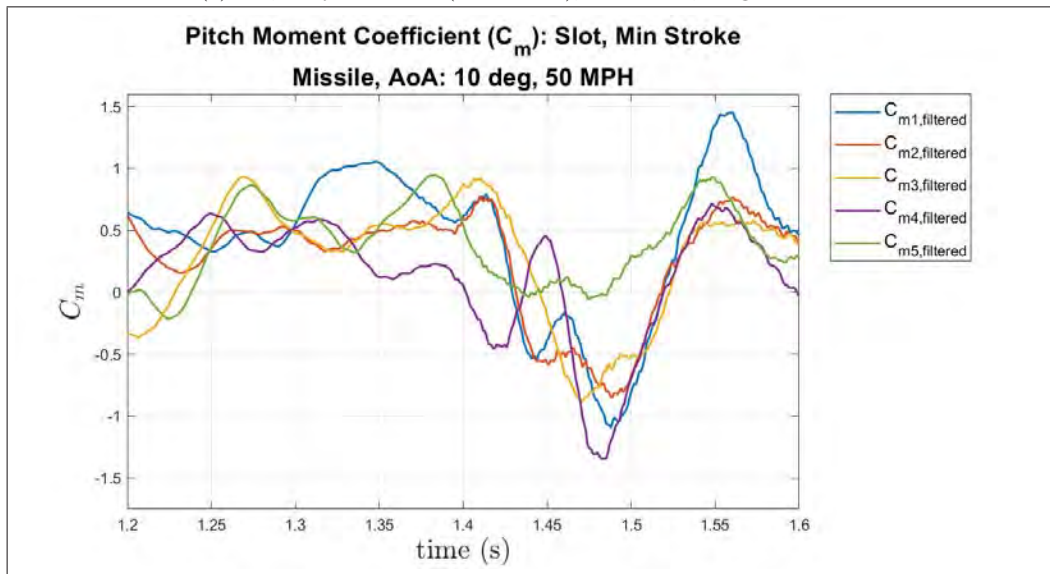


(b)  $C_N$ , Fully Retracted (Min Stroke), 10.0° AoA, Small Window

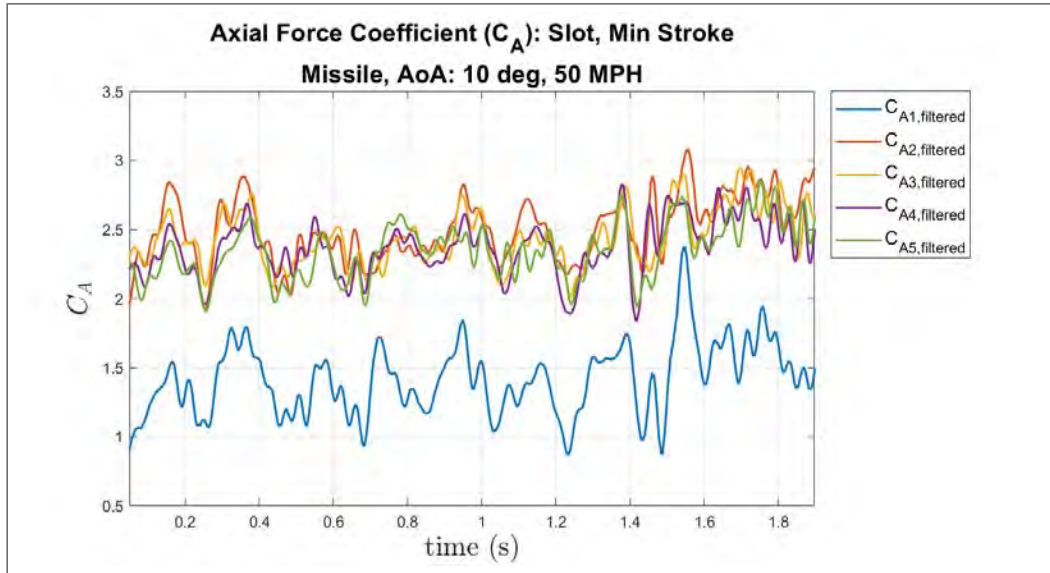




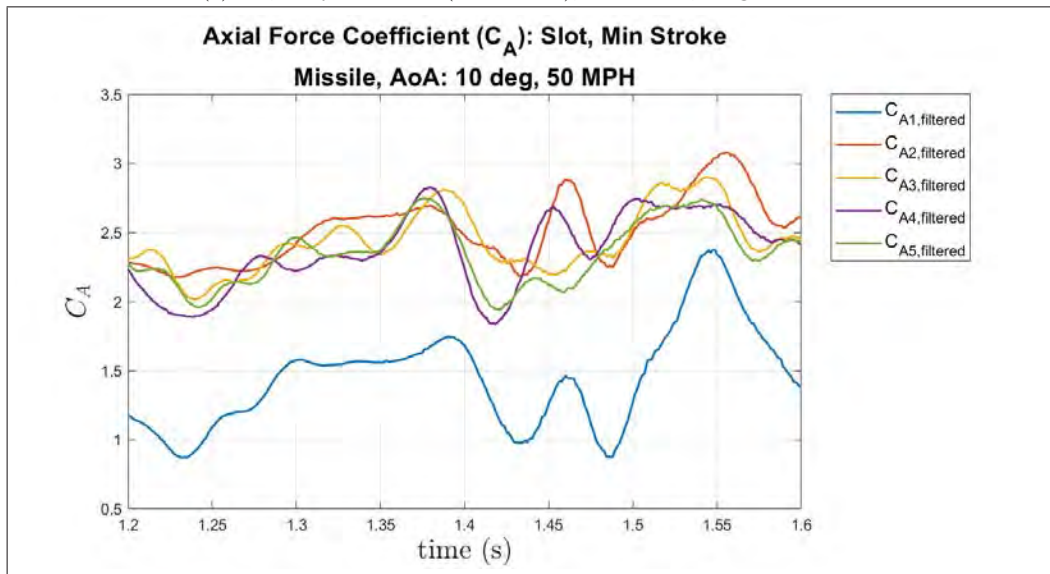
(a)  $C_m$ , Fully Retracted (Min Stroke),  $10.0^\circ$  AoA, Large Window



(b)  $C_m$ , Fully Retracted (Min Stroke),  $10.0^\circ$  AoA, Small Window



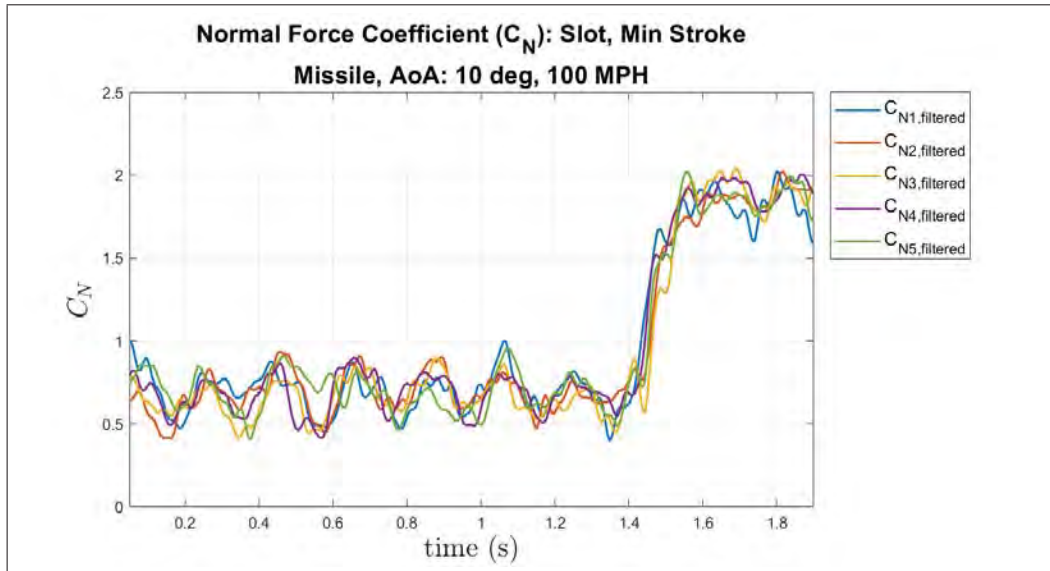
(a)  $C_A$ , Fully Retracted (Min Stroke),  $10.0^\circ$  AoA, Large Window



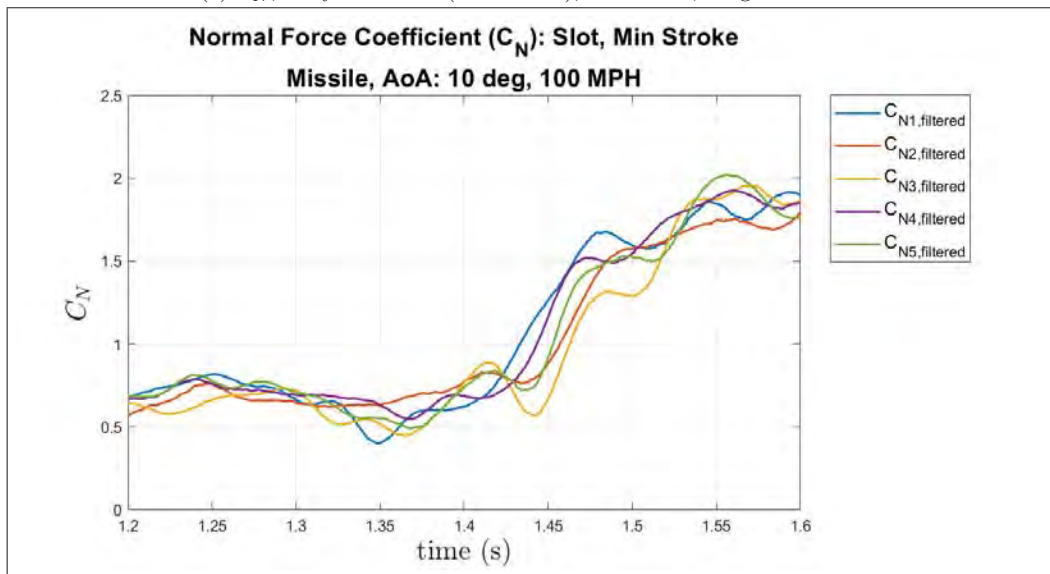
(b)  $C_A$ , Fully Retracted (Min Stroke),  $10.0^\circ$  AoA, Small Window



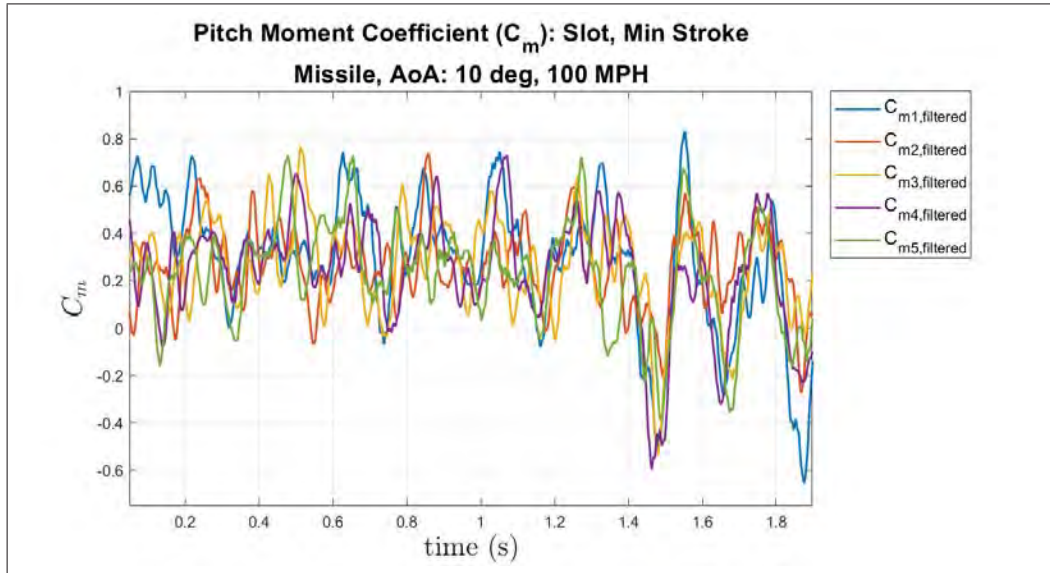
## Fully Retracted Initialization: 100 mph



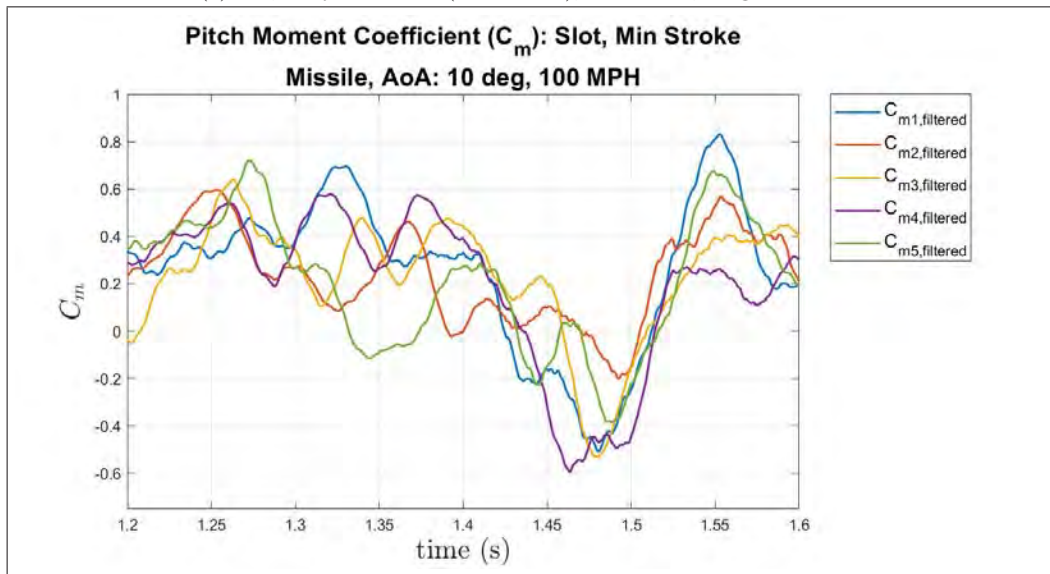
(a)  $C_N$ , Fully Retracted (Min Stroke),  $10.0^\circ$  AoA, Large Window



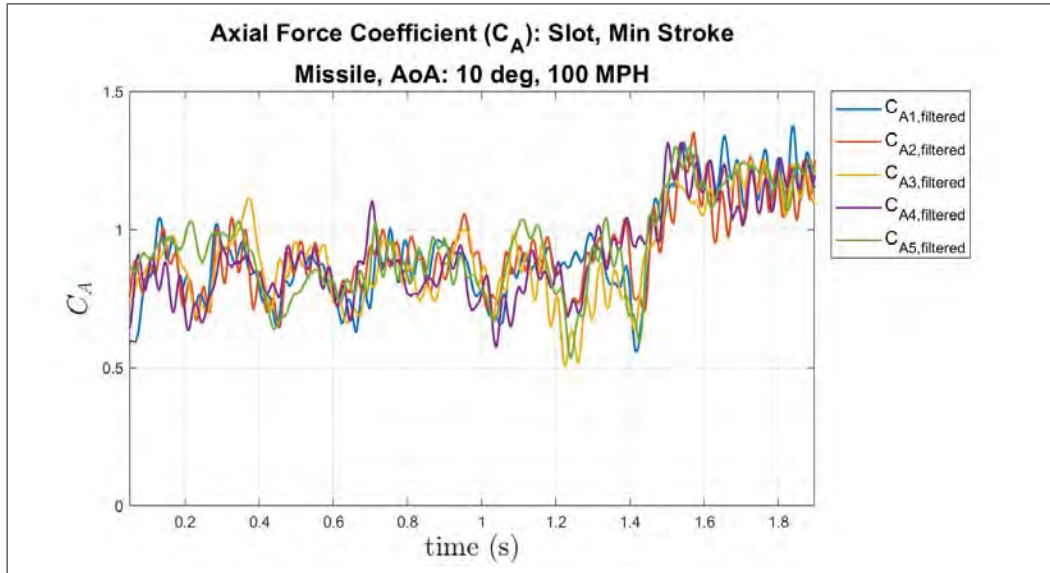
(b)  $C_N$ , Fully Retracted (Min Stroke),  $10.0^\circ$  AoA, Small Window



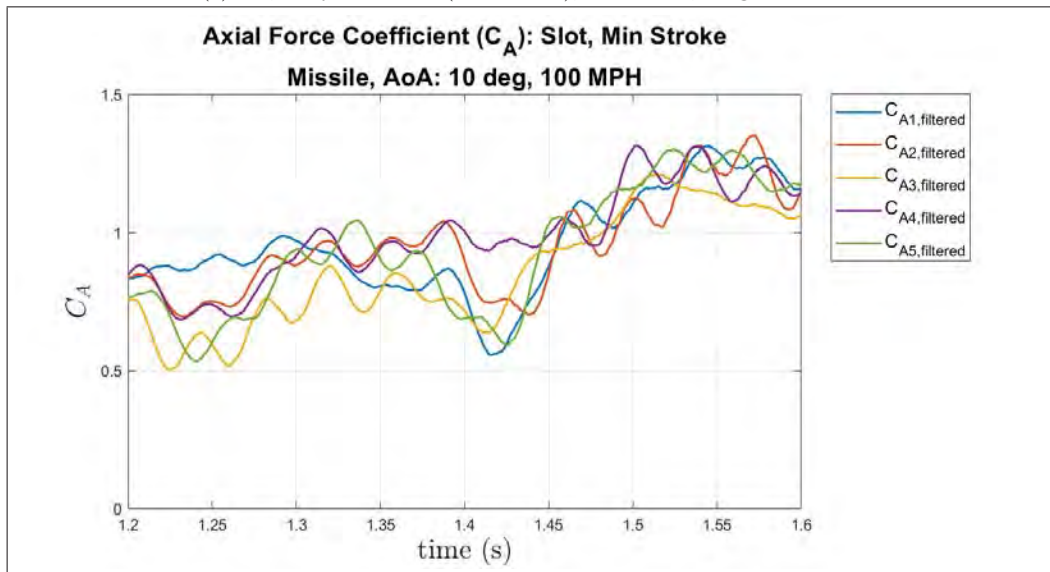
(a)  $C_m$ , Fully Retracted (Min Stroke),  $10.0^\circ$  AoA, Large Window



(b)  $C_m$ , Fully Retracted (Min Stroke),  $10.0^\circ$  AoA, Small Window

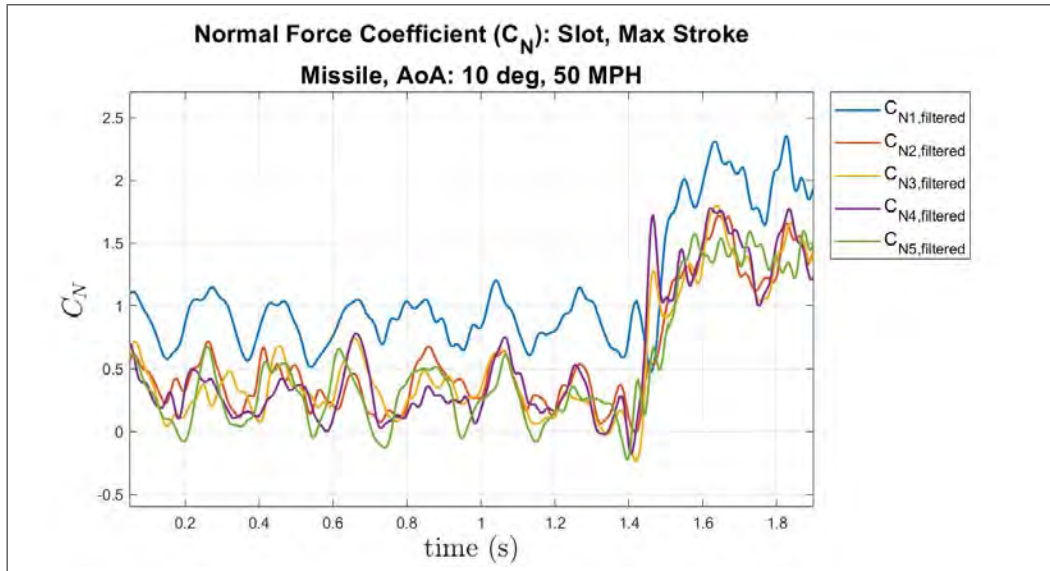


(a)  $C_A$ , Fully Retracted (Min Stroke), 10.0° AoA, Large Window

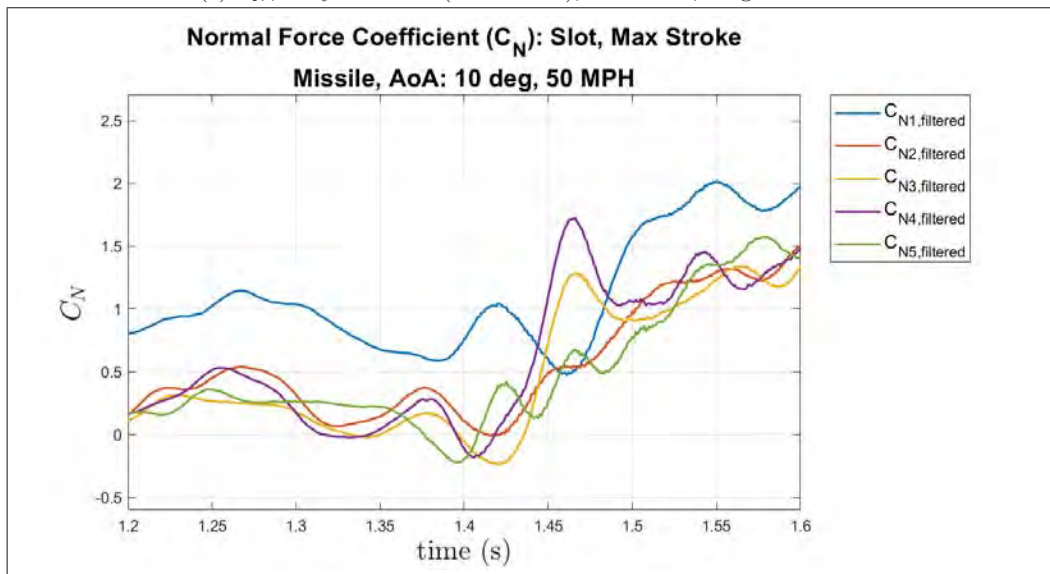


(b)  $C_A$ , Fully Retracted (Min Stroke), 10.0° AoA, Small Window

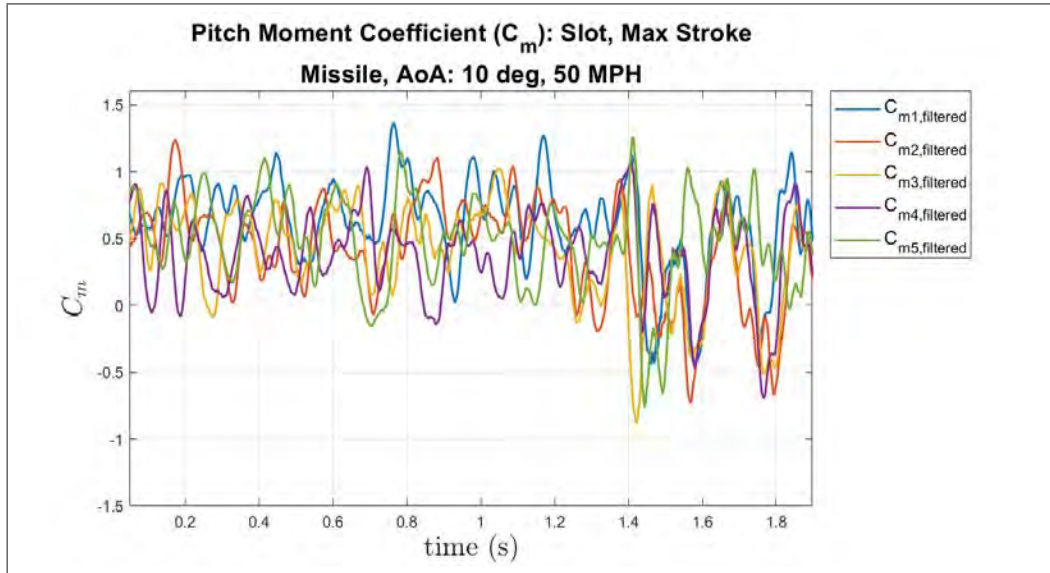
Fully Extended Initialization: 50 mph



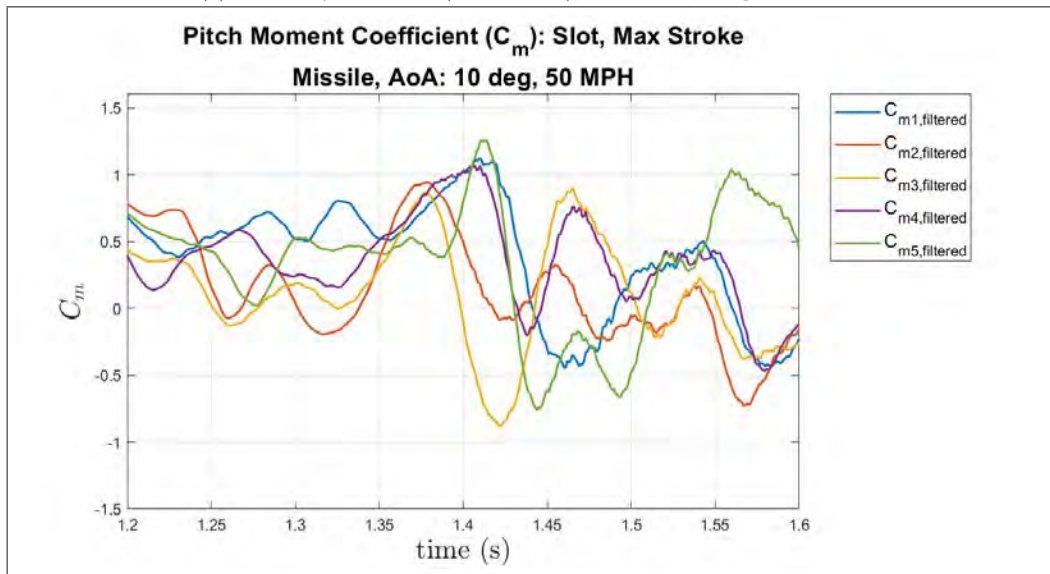
(a)  $C_N$ , Fully Extended (Max Stroke),  $10.0^\circ$  AoA, Large Window



(b)  $C_N$ , Fully Extended (Max Stroke),  $10.0^\circ$  AoA, Small Window

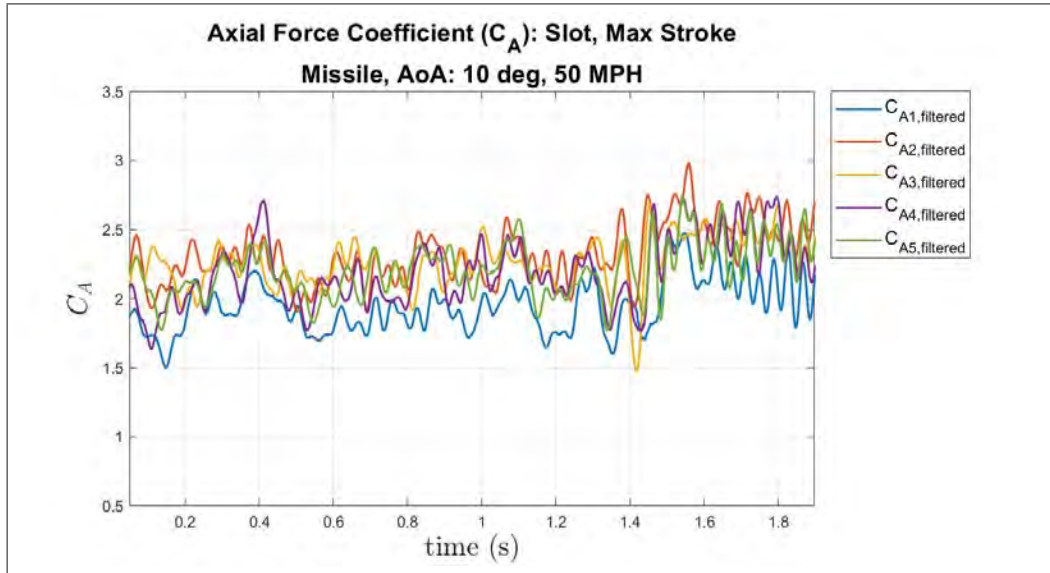


(a)  $C_m$ , Fully Extended (Max Stroke), 10.0° AoA, Large Window

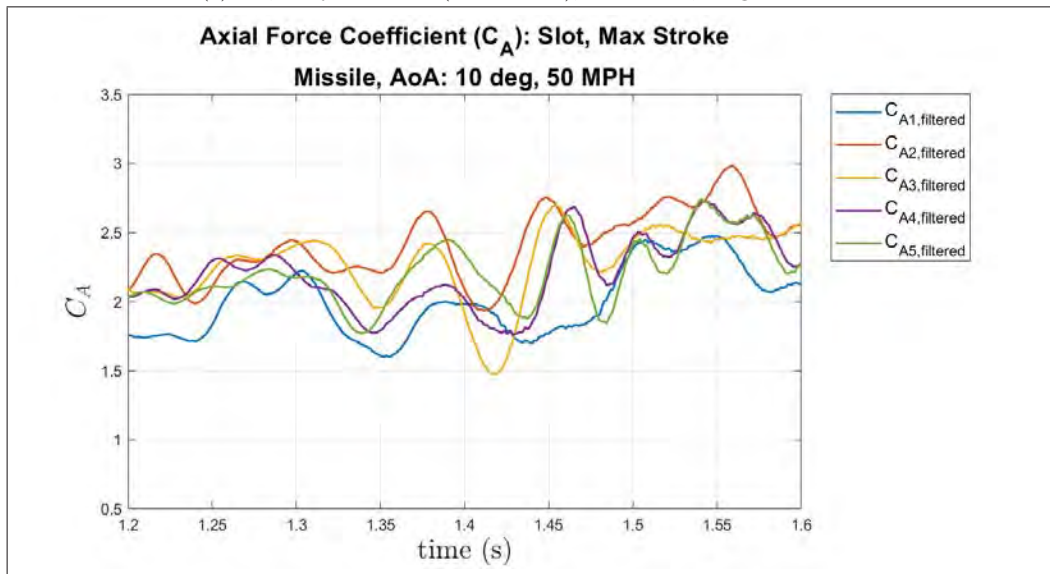


(b)  $C_m$ , Fully Extended (Max Stroke), 10.0° AoA, Small Window



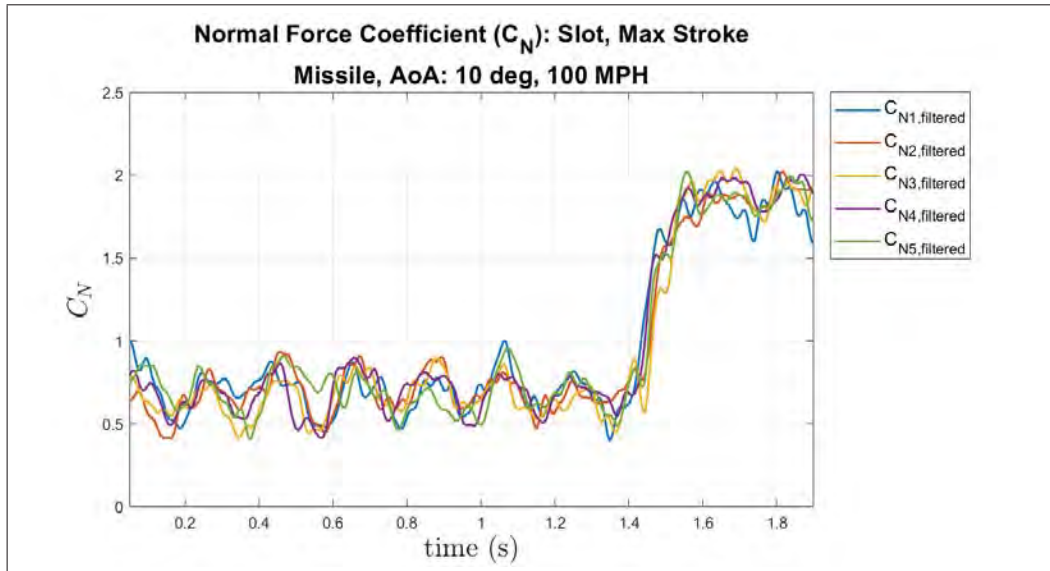


(a)  $C_A$ , Fully Extended (Max Stroke),  $10.0^\circ$  AoA, Large Window

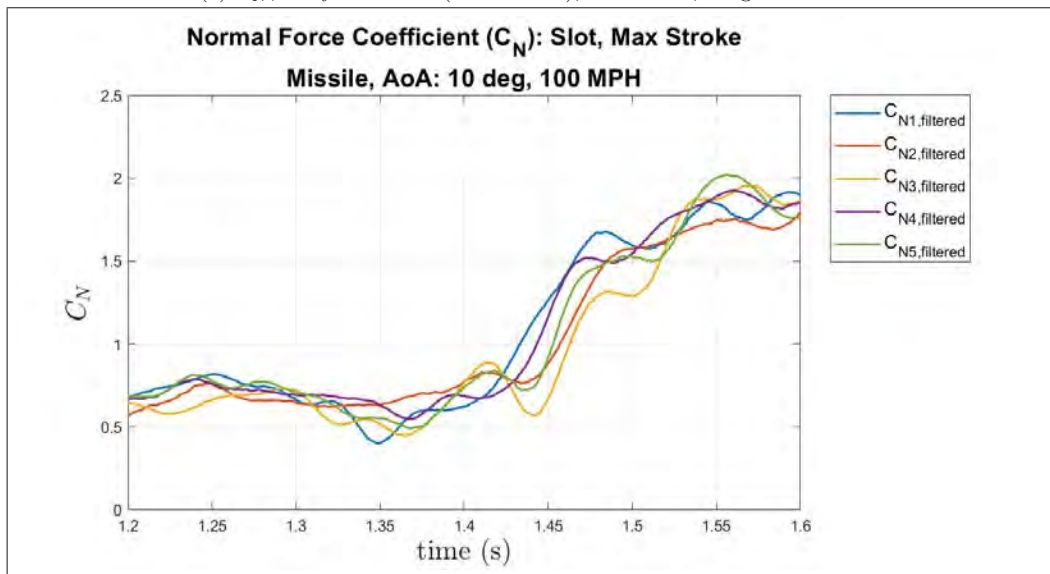


(b)  $C_A$ , Fully Extended (Max Stroke),  $10.0^\circ$  AoA, Small Window

Fully Extended Initialization: 100 mph

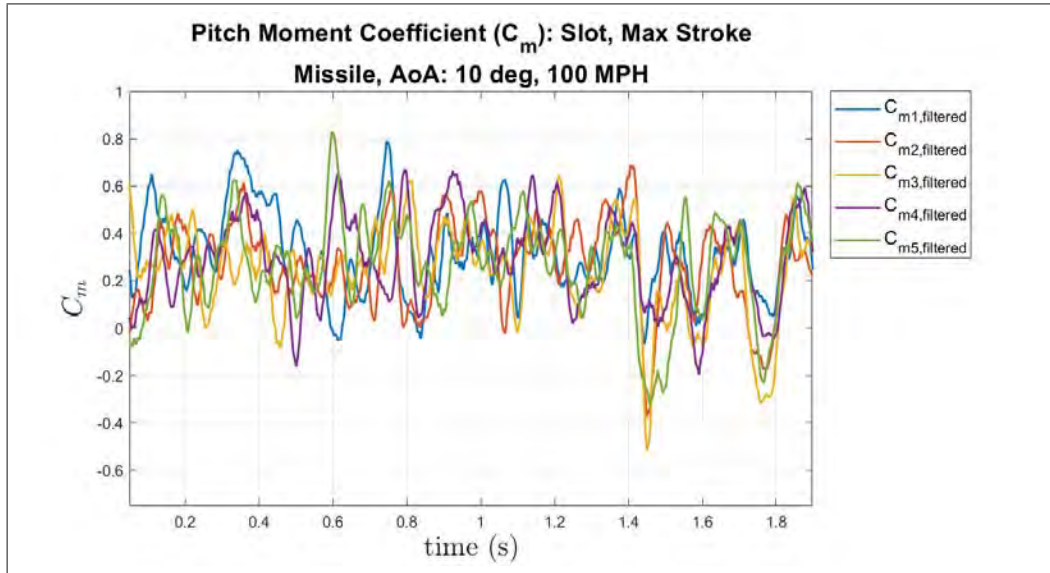


(a)  $C_N$ , Fully Extended (Max Stroke),  $10.0^\circ$  AoA, Large Window

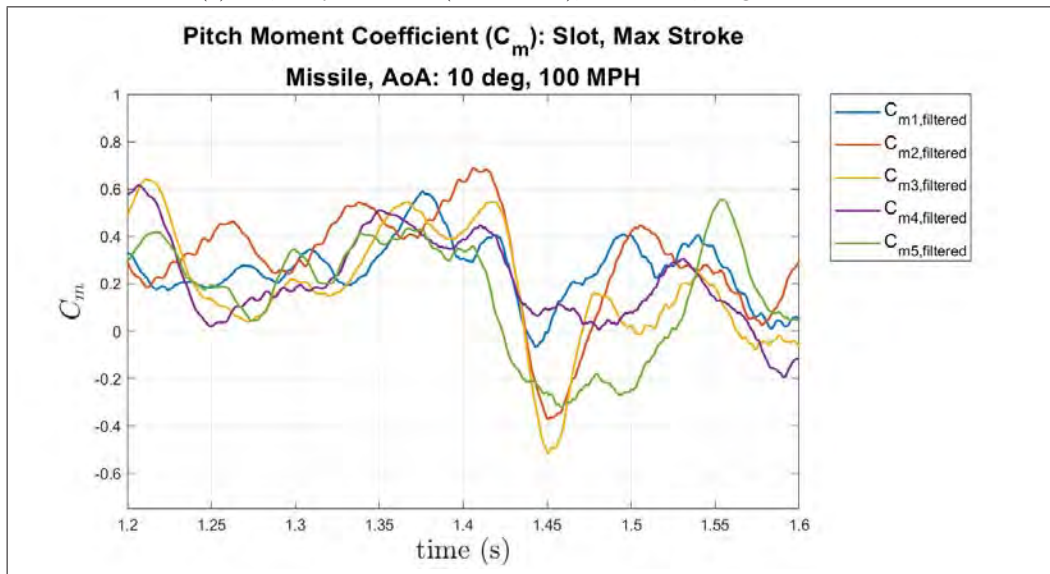


(b)  $C_N$ , Fully Extended (Max Stroke),  $10.0^\circ$  AoA, Small Window

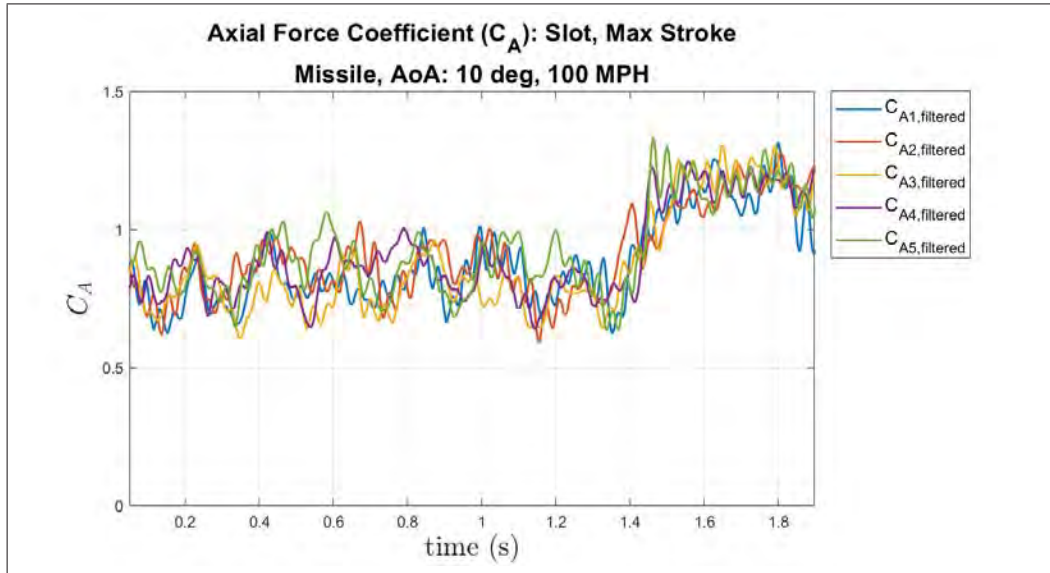




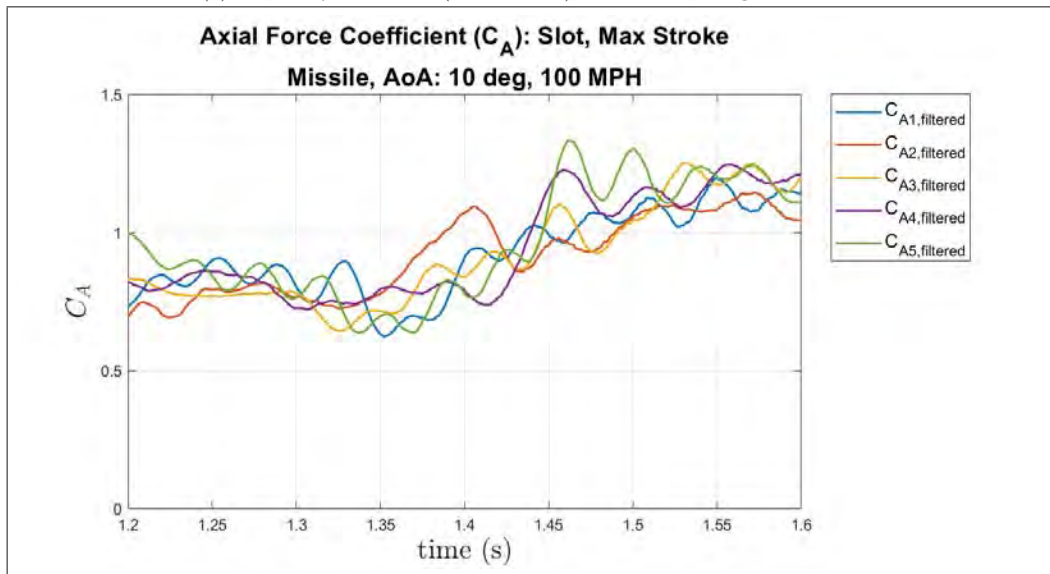
(a)  $C_m$ , Fully Extended (Max Stroke), 10.0° AoA, Large Window



(b)  $C_m$ , Fully Extended (Max Stroke), 10.0° AoA, Small Window



(a)  $C_A$ , Fully Extended (Max Stroke),  $10.0^\circ$  AoA, Large Window



(b)  $C_A$ , Fully Extended (Max Stroke),  $10.0^\circ$  AoA, Small Window

## Appendix B. Galil and MATLAB Code

### Index of Figures in Appendix B

|   |          |
|---|----------|
| MATLAB Sample Code - Linear Plots                           | (pg 244) |
| MATLAB Sample Code - Velocity Contour Plots                 | (pg 248) |
| MATLAB Sample Code - Streamwise Vorticity Plots             | (pg 252) |
| MATLAB Sample Code - Velocity vs. Time Plots                | (pg 255) |
| MATLAB Sample Code - Turbulent Statistics                   | (pg 257) |
| MATLAB Sample Code - Probability Distribution Functions     | (pg 262) |
| MATLAB Sample Code - Post-Processing Nano25 Data            | (pg 267) |
| Galil Sample Code - Initializing Motor A                    | (pg 272) |
| Galil Sample Code - Initializing Motor B                    | (pg 272) |
| Galil Sample Code - Sinewave Code for Oscillating Motor     | (pg 273) |
| Galil Sample Code - Initialization Trigger: Fully Retracted | (pg 275) |
| Galil Sample Code - Initialization Trigger: Mid-Stroke      | (pg 278) |
| Galil Sample Code - Initialization Trigger: Fully Extended  | (pg 281) |

## Phase I

Linear Plot Example: Slot at  $x/L = 0.25, 0.55, 0.85$

(Motor Off vs. Motor On)

### Linear Profile\_Combo\_Slot\_50MPH

```
clear all;close all;clc

%Importing the Data
%The columns of original data are arranged as such
%[X pos.,Y pos.,Z pos.,U Mean,U RMS,V Mean,V RMS,W Mean,W RMS,0]

%Motor Off
StraightRear_MOff = csvread('LinearRear_Straight_MotorOff_50MPH.csv');
StraightMid_MOff = csvread('LinearMid_Straight_MotorOff_50MPH.csv');
StraightFront_MOff = csvread('LinearFront_Straight_MotorOff_50MPH.csv');
%Motor On
StraightRear_MOn = csvread('LinearRear_Straight_MotorOn_50MPH.csv');
StraightMid_MOn = csvread('LinearMid_Straight_MotorOn_50MPH.csv');
StraightFront_MOn = csvread('LinearFront_Straight_MotorOn_50MPH.csv');

Depth = 142.86; %[mm];
Length = 609.6; %[mm];

%The columns for the normalized data are arranged as such
%[Z pos.,U Mean,U RMS,V Mean,V RMS,W Mean,W RMS]

StraightRear_MOff_Normal = [(StraightRear_MOff(:,3)*-1+100)/Depth,...
    StraightRear_MOff(:,4:9)/max(StraightRear_MOff(:,4))];
StraightMid_MOff_Normal = [(StraightMid_MOff(:,3)*-1+100)/Depth,...
    StraightMid_MOff(:,4:9)/max(StraightRear_MOff(:,4))];
StraightFront_MOff_Normal = [(StraightFront_MOff(:,3)*-1+100)/Depth,...
    StraightFront_MOff(:,4:9)/max(StraightRear_MOff(:,4))];

StraightRear_MOn_Normal = [(StraightRear_MOn(:,3)*-1+100)/Depth,...
    StraightRear_MOn(:,4:9)/max(StraightRear_MOn(:,4))];
StraightMid_MOn_Normal = [(StraightMid_MOn(:,3)*-1+100)/Depth,...
    StraightMid_MOn(:,4:9)/max(StraightRear_MOn(:,4))];
StraightFront_MOn_Normal = [(StraightFront_MOn(:,3)*-1+100)/Depth,...
    StraightFront_MOn(:,4:9)/max(StraightRear_MOn(:,4))];
```



## U-COMPONENT

```
%plots of the Normalized U-Mean
figure('Position',[100 100 800 600]);
plot(StraightFront_MOff_Normal(:,2),StraightFront_MOff_Normal(:,1),'-or')
hold on
plot(StraightFront_MOn_Normal(:,2),StraightFront_MOn_Normal(:,1),'--or')
plot(StraightMid_MOff_Normal(:,2),StraightMid_MOff_Normal(:,1),'-s',...
     'color',[.1 .7 .3])
plot(StraightMid_MOn_Normal(:,2),StraightMid_MOn_Normal(:,1),'--s',...
     'color',[.1 .7 .3])
plot(StraightRear_MOff_Normal(:,2),StraightRear_MOff_Normal(:,1),'-db')
plot(StraightRear_MOn_Normal(:,2),StraightRear_MOn_Normal(:,1),'--db')
hold off;grid on
title({'Mean Streamwise Velocity: Slot','Motor Off vs. Motor On (50MPH)'},...
      'Interpreter','latex','fontweight','bold','fontsize',20)
xlabel('$u/U_{\infty}$','Interpreter','latex','fontsize',18) % x-axis
ylabel('$z/D$', 'Interpreter','latex','fontsize',18) % y-axis
legend({'Motor Off (x/L = 0.25)','Motor On (x/L = 0.25)',...
       'Motor Off (x/L = 0.55)', ...
       'Motor On (x/L = 0.55)','Motor Off (x/L = 0.85)',...
       'Motor On (x/L = 0.85)'},'FontSize',14,'Location','northwest')
axis([0 1.1 -0.5 0.75])

%plots of the U-Turbulent Intensity
figure('Position',[100 100 800 600]);
plot(StraightFront_MOff_Normal(:,3),StraightFront_MOff_Normal(:,1),'-or')
hold on
plot(StraightFront_MOn_Normal(:,3),StraightFront_MOn_Normal(:,1),'--or')
plot(StraightMid_MOff_Normal(:,3),StraightMid_MOff_Normal(:,1),'-s',...
     'color',[.1 .7 .3])
plot(StraightMid_MOn_Normal(:,3),StraightMid_MOn_Normal(:,1),'--s',...
     'color',[.1 .7 .3])
plot(StraightRear_MOff_Normal(:,3),StraightRear_MOff_Normal(:,1),'-db')
plot(StraightRear_MOn_Normal(:,3),StraightRear_MOn_Normal(:,1),'--db')
hold off;grid on
title({'Streamwise Turbulent Intensity: Slot',...
      'Motor Off vs. Motor On (50MPH)'},'Interpreter','latex',...
      'fontweight','bold','fontsize',20)
xlabel('$u_{rms}/U_{\infty}$','Interpreter','latex','fontsize',18) % x-axis
ylabel('$z/D$', 'Interpreter','latex','fontsize',18) % y-axis
legend({'Motor Off (x/L = 0.25)','Motor On (x/L = 0.25)',...
       'Motor Off (x/L = 0.55)', 'Motor On (x/L = 0.55)',...
       'Motor Off (x/L = 0.85)', 'Motor On (x/L = 0.85)'},...
       'FontSize',14,'Location','northeast'); axis([0 0.4 -0.5 0.75])
```

## V-COMPONENT

```
%plots of the Normalized V-Mean
figure('Position',[100 100 800 600]);
plot(StraightFront_MOff_Normal(:,4),StraightFront_MOff_Normal(:,1),'-or')
hold on
plot(StraightFront_MOn_Normal(:,4),StraightFront_MOn_Normal(:,1),'--or')
plot(StraightMid_MOff_Normal(:,4),StraightMid_MOff_Normal(:,1),'-s',...
     'color',[.1 .7 .3])
plot(StraightMid_MOn_Normal(:,4),StraightMid_MOn_Normal(:,1),'--s',...
     'color',[.1 .7 .3])
plot(StraightRear_MOff_Normal(:,4),StraightRear_MOff_Normal(:,1),'-db')
plot(StraightRear_MOn_Normal(:,4),StraightRear_MOn_Normal(:,1),'--db')
hold off;grid on
title({'Mean Wall Normal Velocity: Slot','Motor Off vs. Motor On (50MPH)'},...
     'Interpreter','latex','fontweight','bold','fontsize',20)
xlabel('$v/U_{\infty}$','Interpreter','latex','fontsize',18) % x-axis
ylabel('$z/D$', 'Interpreter','latex','fontsize',18) % y-axis
legend({'Motor Off (x/L = 0.25)','Motor On (x/L = 0.25)',...
       'Motor Off (x/L = 0.55)', 'Motor On (x/L = 0.55)',...
       'Motor Off (x/L = 0.85)', 'Motor On (x/L = 0.85)'},...
       'FontSize',14,'Location','northeast'); axis([-0.15 0.15 -0.5 0.75])

%plots of the V-Turbulent Intensity
figure('Position',[100 100 800 600]);
plot(StraightFront_MOff_Normal(:,5),StraightFront_MOff_Normal(:,1),'-or')
hold on
plot(StraightFront_MOn_Normal(:,5),StraightFront_MOn_Normal(:,1),'--or')
plot(StraightMid_MOff_Normal(:,5),StraightMid_MOff_Normal(:,1),'-s',...
     'color',[.1 .7 .3])
plot(StraightMid_MOn_Normal(:,5),StraightMid_MOn_Normal(:,1),'--s',...
     'color',[.1 .7 .3])
plot(StraightRear_MOff_Normal(:,5),StraightRear_MOff_Normal(:,1),'-db')
plot(StraightRear_MOn_Normal(:,5),StraightRear_MOn_Normal(:,1),'--db')
hold off;grid on
title({'Wall Normal Turbulent Intensity: Slot',...
     'Motor Off vs. Motor On (50MPH)'},...
     'Interpreter','latex','fontweight','bold','fontsize',20)
xlabel('$v_{rms}/U_{\infty}$','Interpreter','latex','fontsize',18) % x-axis
ylabel('$z/D$', 'Interpreter','latex','fontsize',18) % y-axis
legend({'Motor Off (x/L = 0.25)','Motor On (x/L = 0.25)',...
       'Motor Off (x/L = 0.55)', 'Motor On (x/L = 0.55)',...
       'Motor Off (x/L = 0.85)', 'Motor On (x/L = 0.85)'},...
       'FontSize',14,'Location','northeast'); axis([0 0.4 -0.5 0.75])
```



## W-COMPONENT

```
%plots of the Normalized W-Mean
figure('Position',[100 100 800 600]);
plot(StraightFront_MOff_Normal(:,6),StraightFront_MOff_Normal(:,1),'-or')
hold on
plot(StraightFront_MOn_Normal(:,6),StraightFront_MOn_Normal(:,1),'--or')
plot(StraightMid_MOff_Normal(:,6),StraightMid_MOff_Normal(:,1),'-s',...
     'color',[.1 .7 .3])
plot(StraightMid_MOn_Normal(:,6),StraightMid_MOn_Normal(:,1),'--s',...
     'color',[.1 .7 .3])
plot(StraightRear_MOff_Normal(:,6),StraightRear_MOff_Normal(:,1),'-db')
plot(StraightRear_MOn_Normal(:,6),StraightRear_MOn_Normal(:,1),'--db')
hold off;grid on
title({'Mean Floor Normal Velocity: Slot','Motor Off vs. Motor On (50MPH)'},...
      'Interpreter','latex','fontweight','bold','fontsize',20)
xlabel('$w/U_{\infty}$','Interpreter','latex','fontsize',18) % x-axis
ylabel('$z/D$','Interpreter','latex','fontsize',18) % y-axis
legend({'Motor Off (x/L = 0.25)','Motor On (x/L = 0.25)',...
       'Motor Off (x/L = 0.55)', 'Motor On (x/L = 0.55)',...
       'Motor Off (x/L = 0.85)', 'Motor On (x/L = 0.85)'},...
       'FontSize',14,'Location','northeast'); axis([-0.15 0.15 -0.5 0.75])

%plots of the W-Turbulent Intensity
figure('Position',[100 100 800 600]);
plot(StraightFront_MOff_Normal(:,7),StraightFront_MOff_Normal(:,1),'-or')
hold on
plot(StraightFront_MOn_Normal(:,7),StraightFront_MOn_Normal(:,1),'--or')
plot(StraightMid_MOff_Normal(:,7),StraightMid_MOff_Normal(:,1),'-s',...
     'color',[.1 .7 .3])
plot(StraightMid_MOn_Normal(:,7),StraightMid_MOn_Normal(:,1),'--s',...
     'color',[.1 .7 .3])
plot(StraightRear_MOff_Normal(:,7),StraightRear_MOff_Normal(:,1),'-db')
plot(StraightRear_MOn_Normal(:,7),StraightRear_MOn_Normal(:,1),'--db')
hold off;grid on
title({'Floor Normal Turbulent Intensity: Slot',...
      'Motor Off vs. Motor On (50MPH)'},...
      'Interpreter','latex','fontweight','bold','fontsize',20)
xlabel('$w_{rms}/U_{\infty}$','Interpreter','latex','fontsize',18) % x-axis
ylabel('$z/D$','Interpreter','latex','fontsize',18) % y-axis
legend({'Motor Off (x/L = 0.25)','Motor On (x/L = 0.25)',...
       'Motor Off (x/L = 0.55)', 'Motor On (x/L = 0.55)',...
       'Motor Off (x/L = 0.85)', 'Motor On (x/L = 0.85)'},...
       'FontSize',14,'Location','northeast'); axis([0 0.4 -0.5 0.75])
```



## Velocity Contour Plots Example: Slot at $x/L = 0.55$ (Motor On)

### RasterMid\_Slot\_50mph\_LowRes\_MOn

```
clear all;close all;clc

%Importing the Data
%The columns of original data are arranged as such
%[X pos.,Y pos.,Z pos.,U Mean,U RMS,V Mean,V RMS,W Mean,W RMS,0]
Depth = 142.86; %[mm];

%Motor Off
RasterMid_MOn = csvread('RasMid_Slot_50mph_MOn.csv');

y = (RasterMid_MOn(:,2)*-1+50)/Depth;
z = (RasterMid_MOn(:,3)*-1+100)/Depth;
```

## U-Component

```
% U-Mean Component
umean_array = [y,z,RasterMid_MOn(:,4)/max(RasterMid_MOn(:,4));];
umean_array_sorted = sortrows(umean_array);
umean_column = umean_array_sorted(:,3);
UMEAN_reshape = reshape(umean_column,[11,11]);

figure('Position',[100 100 700 900]);
a = linspace(-0.35,0.35,11); b = linspace(-.525,.7,11);
[A,B] = meshgrid(a,b);
contourf(A,B,UMEAN_reshape,15)
caxis([0 1]); colorbar; colormap('jet')
hC = colorbar('eastoutside');
LabelText = 'u/U_{\infty}'; 'Interpreter','latex';
ylabel(hC,LabelText,'FontSize',18)
title(['Mean Streamwise Velocity: Slot',...
      'Motor On at x/L = 0.55 (50MPH)'],...
      'Interpreter','latex','fontweight','bold','fontsize',20)
xlabel('Width $y/D$', 'Interpreter','latex','fontsize',18) % x-axis label
ylabel('Depth $z/D$', 'Interpreter','latex','fontsize',18) % y-axis label
daspect([1 1 1]); set(gca,'XTick',(-0.3:0.1:0.3));
set(gca,'YTick',(-0.5:0.1:0.7))

%U-RMS Component
urms_array = [y,z,RasterMid_MOn(:,5)/max(RasterMid_MOn(:,4));];
urms_array_sorted = sortrows(urms_array);
urms_column = urms_array_sorted(:,3);
URMS_reshape = reshape(urms_column,[11,11]);

figure('Position',[100 100 700 900]);
a = linspace(-0.35,0.35,11); b = linspace(-.525,.7,11);
[A,B] = meshgrid(a,b);
contourf(A,B,URMS_reshape,15)
caxis([0 0.25]); colorbar; colormap('jet')
hC = colorbar('eastoutside');
LabelText = 'u_{rms}/U_{\infty}'; 'Interpreter','latex';
ylabel(hC,LabelText,'FontSize',18)
title(['Streamwise Turbulent Intensity: Slot',...
      'Motor On at x/L = 0.55 (50MPH)'],...
      'Interpreter','latex','fontweight','bold','fontsize',20)
xlabel('Width $y/D$', 'Interpreter','latex','fontsize',18) % x-axis label
ylabel('Depth $z/D$', 'Interpreter','latex','fontsize',18) % y-axis label
daspect([1 1 1]); set(gca,'XTick',(-0.3:0.1:0.3));
set(gca,'YTick',(-0.5:0.1:0.7))
```

## V-Component

```
% V-Mean Component
vmean_array = [y,z,RasterMid_MOn(:,6)/max(RasterMid_MOn(:,4))];
vmean_array_sorted = sortrows(vmean_array);
vmean_column = vmean_array_sorted(:,3);
VMEAN_reshape = reshape(vmean_column,[11,11]);

figure('Position',[700 100 700 900]);
a = linspace(-0.35,0.35,11); b = linspace(-.525,.7,11);
[A,B] = meshgrid(a,b);
contourf(A,B,VMEAN_reshape)
caxis([-0.1 0.1]); colorbar; colormap('jet')
hC = colorbar('eastoutside');
LabelText = 'v/U_{\infty}'; 'Interpreter','latex';
ylabel(hC,LabelText,'FontSize',18)
title({'Mean Wall Normal Velocity: Slot',...
      'Motor On at x/L = 0.55 (50MPH)'},...
      'Interpreter','latex','fontweight','bold','fontsize',20)
xlabel('Width $y/D\$', 'Interpreter','latex','fontsize',18) % x-axis label
ylabel('Depth $z/D\$', 'Interpreter','latex','fontsize',18) % y-axis label
daspect([1 1 1]); set(gca,'XTick',(-0.3:0.1:0.3))
set(gca,'YTick',(-0.5:0.1:0.7))

% V-RMS Component
vrms_array = [y,z,RasterMid_MOn(:,7)/max(RasterMid_MOn(:,4))];
vrms_array_sorted = sortrows(vrms_array);
vrms_column = vrms_array_sorted(:,3);
VRMS_reshape = reshape(vrms_column,[11,11]);

figure('Position',[700 100 700 900]);
a = linspace(-0.35,0.35,11); b = linspace(-.525,.7,11);
[A,B] = meshgrid(a,b);
contourf(A,B,VRMS_reshape,15)
caxis([0 0.15]); colorbar; colormap('jet'); hC = colorbar('eastoutside');
LabelText = 'v_{rms}/U_{\infty}'; 'Interpreter','latex';
ylabel(hC,LabelText,'FontSize',18)
title({'Wall Normal Turbulent Intensity: Slot',...
      'Motor On at x/L = 0.55 (50MPH)'},...
      'Interpreter','latex','fontweight','bold','fontsize',20)
xlabel('Width $y/D\$', 'Interpreter','latex','fontsize',18) % x-axis label
ylabel('Depth $z/D\$', 'Interpreter','latex','fontsize',18) % y-axis label
daspect([1 1 1]); set(gca,'XTick',(-0.3:0.1:0.3))
set(gca,'YTick',(-0.5:0.1:0.7))
```



## W-Component

```
% W-Mean Component
wmean_array = [y,z,RasterMid_MON(:,8)/max(RasterMid_MON(:,4))];
wmean_array_sorted = sortrows(wmean_array);
wmean_column = wmean_array_sorted(:,3);
WMEAN_reshape = reshape(wmean_column,[11,11]);

figure('Position',[1100 100 700 900]);
a = linspace(-0.35,0.35,11); b = linspace(-.525,.7,11);
[A,B] = meshgrid(a,b);
contourf(A,B,WMEAN_reshape)
caxis([-0.1 0.1]); colorbar; colormap('jet')
hC = colorbar('eastoutside');
LabelText = 'w/U_{\infty}'; 'Interpreter','latex';
ylabel(hC,LabelText,'FontSize',18)
title(['Mean Floor Normal Velocity: Slot',...
      'Motor On at x/L = 0.55 (50MPH)'],...
      'Interpreter','latex','fontweight','bold','fontsize',20)
xlabel('Width $y/D$', 'Interpreter','latex','fontsize',18) % x-axis label
ylabel('Depth $z/D$', 'Interpreter','latex','fontsize',18) % y-axis label
daspect([1 1 1]); set(gca,'XTick',(-0.3:0.1:0.3))
set(gca,'YTick',(-0.5:0.1:0.7))

% W-RMS Component
wrms_array = [y,z,RasterMid_MON(:,9)/max(RasterMid_MON(:,4))];
wrms_array_sorted = sortrows(wrms_array);
wrms_column = wrms_array_sorted(:,3);
WRMS_reshape = reshape(wrms_column,[11,11]);

figure('Position',[1100 100 700 900]);
a = linspace(-0.35,0.35,11); b = linspace(-.525,.7,11);
[A,B] = meshgrid(a,b);
contourf(A,B,WRMS_reshape,15)
caxis([0 0.15]); colorbar; colormap('jet')
hC = colorbar('eastoutside');
LabelText = 'w_{rms}/U_{\infty}'; 'Interpreter','latex';
ylabel(hC,LabelText,'FontSize',18)
title(['Floor Normal Turbulent Intensity: Slot',...
      'Motor On at x/L = 0.55 (50MPH)'],...
      'Interpreter','latex','fontweight','bold','fontsize',20)
xlabel('Width $y/D$', 'Interpreter','latex','fontsize',18) % x-axis label
ylabel('Depth $z/D$', 'Interpreter','latex','fontsize',18) % y-axis label
daspect([1 1 1]); set(gca,'XTick',(-0.3:0.1:0.3))
set(gca,'YTick',(-0.5:0.1:0.7))
```

## Vorticity Plot Example: Slot at $x/L = 0.55$ (Motor On)

### Vorticity\_Slot\_Mid Cavity\_50mph\_MOn

```
clear all;close all;clc

%Importing the Data
%The columns of original data are arranged as such
%[X pos.,Y pos.,Z pos.,U Mean,U RMS,V Mean,V RMS,W Mean,W RMS,0]
Depth = 142.86; %[mm];

%Motor On
RasterMid_MOn = csvread('RasMid_Slot_50mph_MOn.csv');

y = (RasterMid_MOn(:,2)*-1+50)/Depth;
z = (RasterMid_MOn(:,3)*-1+100)/Depth;
```

### Velocity Components

```
umean_array = [(RasterMid_MOn(:,2)*-1+50)/Depth,...
               (RasterMid_MOn(:,3)*-1+100)/Depth,...
               RasterMid_MOn(:,4)/max(RasterMid_MOn(:,4))];
vmean_array = [(RasterMid_MOn(:,2)*-1+50)/Depth,...
               (RasterMid_MOn(:,3)*-1+100)/Depth, RasterMid_MOn(:,6)];
wmean_array = [(RasterMid_MOn(:,2)*-1+50)/Depth,...
               (RasterMid_MOn(:,3)*-1+100)/Depth,RasterMid_MOn(:,8)];

umean_array_sorted = sortrows(umean_array);
umean_column = umean_array_sorted(:,3);
UMEAN_reshape = reshape(umean_column,[11,11]);

vmean_array_sorted = sortrows(vmean_array);
vmean_column = vmean_array_sorted(:,3);
VMEAN_reshape = reshape(vmean_column,[11,11]);

wmean_array_sorted = sortrows(wmean_array);
wmean_column = wmean_array_sorted(:,3);
WMEAN_reshape = reshape(wmean_column,[11,11]);

[m,n] = size(VMEAN_reshape);
delta_y = 0.01;
delta_z = 0.0175;
```

## Differencing Schemes

```
%Central Differencing
for i = 2:m-1
    for j = 2:n-1
        VorticityCent(i-1,j-1)= ...
            ((WMEAN_reshape(i,j+1)-WMEAN_reshape(i,j-1))/(2*delta_y))-...
            ((VMEAN_reshape(i+1,j)-VMEAN_reshape(i-1,j))/(2*delta_z));
    end
end

%Forward Differencing
for i = 1:m-1
    for j = 1:n-1
        VorticityFwd(i,j)=...
            ((WMEAN_reshape(i,j+1)-WMEAN_reshape(i,j))/(delta_y))-...
            ((VMEAN_reshape(i+1,j)-VMEAN_reshape(i,j))/(delta_z));
    end
end

%Rearward Differencing
for i = 2:m
    for j = 2:n
        VorticityRwd(i,j)=...
            ((WMEAN_reshape(i,j)-WMEAN_reshape(i,j-1))/(delta_y))-...
            ((VMEAN_reshape(i,j)-VMEAN_reshape(i-1,j))/(delta_z));
    end
end

%Corner Vorticities
VorticityTR = ((WMEAN_reshape(1,length(WMEAN_reshape))-...
    WMEAN_reshape(1,length(WMEAN_reshape)-1))/(delta_y))-...
    ((VMEAN_reshape(2,length(VMEAN_reshape))-...
    VMEAN_reshape(1,length(VMEAN_reshape)))/(delta_z));

VorticityBL = ((WMEAN_reshape(length(WMEAN_reshape),2))-...
    WMEAN_reshape(length(WMEAN_reshape),1))/(delta_y))-...
    ((VMEAN_reshape(length(VMEAN_reshape),1))-...
    VMEAN_reshape(length(VMEAN_reshape)-1,1))/(delta_z));
```



## Concatenation: Rebuilding the Matrix

```
KSI = [VorticityFwd(1,1:n-1),VorticityTR;...  
      VorticityFwd(2:m-1,1),VorticityCent(1:m-2,1:n-2),...  
      VorticityRwd(2:m-1,n); VorticityBL, VorticityRwd(m,2:n)];
```

## Vorticity Plots

```
figure('position', [0, 0, 700, 900])  
a1 = linspace(-0.35,0.35,11); b1 = linspace(-.525,.7,11);  
[A1,B1] = meshgrid(a1,b1);  
contourf(A1,B1,KSI,30); caxis([-150 150]); colorbar; colormap('jet')  
hC = colorbar('eastoutside');  
LabelText = 'Vorticity [1/s]'; 'Interpreter':'latex';  
ylabel(hC,LabelText, 'FontSize',18)  
title({'Vorticity Plot: Slot','Motor On at x/L = 0.55 (50MPH)'},...  
      'Interpreter','latex','fontweight','bold','fontsize',20)  
xlabel('Width $y/D$', 'Interpreter','latex','fontsize',18) % x-axis label  
ylabel('Depth $z/D$', 'Interpreter','latex','fontsize',18) % y-axis label  
daspect([1 1 1])  
set(gca,'XTick',(-0.3:0.1:0.3))  
set(gca,'YTick',(-0.5:0.1:0.7))
```

Velocity vs. Time Example: Slot at  $x/L = 0.55$

(Motor On vs. Motor Off)

#### Velocity vs. Time\_Middle Cavity\_Slot\_50MPH\_pt20 (z/D = 0.035)

```
clear all;close all;clc

%Importing the Data
%The columns of original data are arranged as such
%[X pos.,Y pos.,Z pos.,U Mean,U RMS,V Mean,V RMS,W Mean,W RMS,0]

MotorOn = csvread('LinMid_50_MOn_Slot_pt20_probecoord.csv');
MotorOff = csvread('LinMid_50_MOff_Slot_pt20_probecoord.csv');

Depth = 142.86; %[mm];
Length = 609.6; %[mm];

%Time and U-variables with the Motor Off
time_MOff = MotorOff(:,1);
U_MOff = MotorOff(:,2);
U_MOff_Normal = U_MOff/max(U_MOff);

%Time and U-variables with the Motor On
time_MOn = MotorOn(:,1);
U_MOn = MotorOn(:,2);
U_MOn_Normal = U_MOn/max(U_MOn);
```

### Filter for Coefficient Data Sets\_Slot

```
Fs = 10000; % sample rate in Hz
cof = 1; % cutoff frequency in Hz
order = 200; % -th Order of lowpas filter

% Design a -th order lowpass FIR filter with cutoff frequency of (Hz)
Fnorm = cof/(Fs/2); % Normalized frequency

df = ...
designfilt('lowpassfir','FilterOrder',order,'CutoffFrequency',Fnorm);
Delay = mean(grpdelay(df)); % filter delay in samples

% Append Delay zeros to the input data
filtered_MOn = filter(df,[U_MOn_Normal; zeros(Delay,1)]);
filtered_MOn = filtered_MOn(Delay+1:end); %Shift to compensate for delay

% Repeat Steps for MOff
filtered_MOff = filter(df,[U_MOff_Normal; zeros(Delay,1)]);
filtered_MOff = filtered_MOff(Delay+1:end);
```

### Plotting the Velocity vs. Time with the Motor Off and On

```
figure('Position',[10 10 1200 900]);
subplot(2,1,1); grid on;
plot(time_MOff(1:10000,1),U_MOff_Normal(1:10000,1)); hold on
plot(time_MOff(1:10000,1),filtered_MOff(1:10000,1),'LineWidth',2);
title({'Normalized Streamwise Velocity Component vs. Time: Slot',...
      '50MPH and Motor Off at x/L = 0.55'},'fontweight','bold','fontsize',18)
xlabel('time (sec)','fontsize',16) % x-axis label
ylabel('u/U_{\infty}','fontsize',16) % y-axis label
legend({'Unfiltered Signal','Filtered Signal'},...
      'FontSize',12,'Location','northeast');hold off

subplot(2,1,2);grid on;
plot(time_MOn(1:10000,1),U_MOn_Normal(1:10000,1)); hold on
plot(time_MOn(1:10000,1),filtered_MOn(1:10000,1),'LineWidth',2);
title({'Normalized Streamwise Velocity Component vs. Time: Slot',...
      '50MPH and Motor On at x/L = 0.55'},'fontweight','bold','fontsize',18)
xlabel('time (sec)','fontsize',16) % x-axis label
ylabel('u/U_{\infty}','fontsize',16) % y-axis label
legend({'Unfiltered Signal','Filtered Signal'},...
      'FontSize',12,'Location','northeast'); hold off
```

Turbulent Calculations Example: Slot at  $x/L = 0.55$   
(Motor On vs. Motor Off)

**Turbulence Calculations\_Slot\_MOff vs. MOn\_50MPH\_pt20 (z/D = 0.035)**

```
clear all;close all;clc

%Importing the Data
MotorOff = csvread('LinMid_50_MOff_Slot_pt20_probecoord.csv');
MotorOn = csvread('LinMid_50_MOn_Slot_pt20_probecoord.csv');
sampletime = 10; %seconds
samplerate = 10000; %kHz
N = length(MotorOff(:,1));

%Time and U-variables with the Motor Off
time = MotorOff(:,1);
UOff = MotorOff(:,2);
VOff = MotorOff(:,3);
WOff = MotorOff(:,4);

%Time and U-variables with the Motor On
time = MotorOn(:,1);
UOn = MotorOn(:,2);
VOn = MotorOn(:,3);
WOn = MotorOn(:,4);
```



### Mean and Standard Deviation for each velocity component

```
% Motor Off
UmOff = mean(UOff); %Mean
UsOff = std(UOff); %Standard Deviation
uOff = UOff - UmOff; % Fluctuation

VmOff = mean(VOff); %Mean
VsOff = std(VOff); %Standard Deviation
vOff = VOff - VmOff; % Fluctuation

WmOff = mean(WOff); %Mean
WsOff = std(WOff); %Standard Deviation
wOff = WOff - WmOff; % Fluctuation

% Motor On
UmOn = mean(UOn); %Mean
UsOn = std(UOn); %Standard Deviation
uOn = UOn - UmOn; % Fluctuation

VmOn = mean(VOn); %Mean
VsOn = std(VOn); %Standard Deviation
vOn = VOn - VmOn; % Fluctuation

WmOn = mean(WOn); %Mean
WsOn = std(WOn); %Standard Deviation
wOn = WOn - WmOn; % Fluctuation
```

### Calculate Energy Spectrum E(w)

```
%Motor Off
E11Off = fft(uOff)./N.*conj(fft(uOff)./N);
xe = [linspace(0,10000,100000)]';
figure('Position',[100 100 1600 800]); subplot(1,2,1);
loglog(xe(1:length(UOff)/2),E11Off(1:length(UOff)/2)); grid on;
set(gca, 'FontName', 'Arial', 'FontSize', 14)
axis([10^0 10^4 10^-12 10^2]);
title('E_{11}(\omega): Slot, Motor Off (z/D = 0.035)',...
      'fontweight','bold','fontsize',20);
xlabel('\omega','fontsize',18); % x-axis label
ylabel('m^2/s^2','fontsize',18); % y-axis label
hold on

%Motor On
E11On = fft(uOn)./N.*conj(fft(uOn)./N);
xe = [linspace(0,10000,100000)]';
subplot(1,2,2)
loglog(xe(1:length(UOn)/2),E11On(1:length(UOn)/2)); grid on;
set(gca, 'FontName', 'Arial', 'FontSize', 14)
axis([10^0 10^4 10^-12 10^2]);
title('E_{11}(\omega): Slot, Motor Off (z/D = 0.035)',...
      'fontweight','bold','fontsize',20);
xlabel('\omega','fontsize',18); % x-axis label
ylabel('m^2/s^2','fontsize',18); % y-axis label
hold off
```



### Use Taylor's Hypothesis to convert from time to space

```
%Motor Off
% Change time vector to space
rOff = time.*UmOff;

% Autocorrelation Rij(s) is calculated here:
R11Off = ifft(E11Off).*N;
f11Off = R11Off./UsOff^2; %Longitudinal Function

%Motor On
% Change time vector to space
rOn = time.*UmOn;

% Autocorrelation Rij(s) is calculated here:
R11On = ifft(E11On).*N;
f11On = R11On./UsOn^2; %Longitudinal Function
```

### Plot the Autocorrelation Rij(s)

```
%Motor Off
figure;
plot(time(1:10000),f11Off(1:10000),'k'); grid on; hold on;

%Motor On
plot(time(1:1000),f11On(1:1000),'b'); grid on;
title('Autocorrelation R_{ij}(s)');
xlabel('s'); ylabel('\rho(s)');axis([0 .06 -.1 1]);
legend('Motor Off','Motor On'); hold off;

%Autocorrelation Rij(s) = Autocovariance Rij(r) per Taylors Hypothesis
```

## Plot the Autocovariance $R_{ij}(r)$

```
%Scaled Out
%Motor Off
figure('Position',[100 100 1600 800]);subplot(1,2,1);
plot(rOff(1:10000),f11Off(1:10000),'k'); grid on; hold on;
%Motor On
plot(rOn(1:10000),f11On(1:10000),'b'); grid on;
title({'Autocovariance  $R_{ij}(r)$ : Slot, Motor Off vs Motor On',...
      'Scaled Out ( $z/D = 0.035$ )'},'fontweight','bold','fontsize',13);
xlabel('m','fontsize',13); % x-axis label
ylabel('\rho(r)','fontsize',13); % y-axis label
legend('Motor Off','Motor On');
axis([0 8 -1.0 1.0]);

%Scaled In
%Motor Off
subplot(1,2,2);
plot(rOff(1:10000),f11Off(1:10000),'k'); grid on; hold on;
%Motor On
plot(rOn(1:10000),f11On(1:10000),'b'); grid on;
title({'Autocovariance  $R_{ij}(r)$ : Slot, Motor Off vs Motor On',...
      'Scaled In ( $z/D = 0.035$ )'},'fontweight','bold','fontsize',13);
xlabel('m','fontsize',13); % x-axis label
ylabel('\rho(r)','fontsize',13); % y-axis label
legend('Motor Off','Motor On'); hold off;
axis([0 0.8 -0.25 1.0]);
```

## Calculating the Integral Length and Time Scales

```
%X-axis crossings
xcrossOff = 405;
xcrossOn = 496;

% Integral Length Scales
L11Off = trapz(f11Off(1:xcrossOff)).*UmOff./samplerate
L11On = trapz(f11On(1:xcrossOn)).*UmOn./samplerate

%Integral Time Scales
TauOff = L11Off/UmOff
TauOn = L11On/UmOn
```

### PDF Calculations\_Slot\_MOn\_point 20 (z/D = 0.035)

```
clear all;close all;clc

%Importing the Data
MotorOn = csvread('LinMid_50_MOn_Slot_pt20_probecoord.csv');
sampletime = 10; %seconds
samplerate = 10000; %kHz

%Time and U-variables with the Motor Off
time = MotorOn(:,1);
U = MotorOn(:,2);
V = MotorOn(:,3);
W = MotorOn(:,4);
NU = length(U);
NV = length(V);
NW = length(W);
```

### Finding the mean, fluctuating component and max/min of U,V, and W

```
%Mean of the U, V, and W velocity components
Um = mean(U); Vm = mean(V); Wm = mean(W);

%Fluctuation components of the U, V, and W velocity components
uf = U - Um; uf_std = std(uf);
vf = V - Vm; vf_std = std(vf);
wf = W - Wm; wf_std = std(wf);

%Maximum and Minimum values of the U and V velocity components
Umax = max(U); Umin = min(U);
Vmax = max(V); Vmin = min(V);
Wmax = max(W); Wmin = min(W);
```



## Determining if this time record is stationary

%First thing done is to reshape the data in order to make it easier to  
%build a for loop that cycles through each desired data block. In this  
%case I sorted the data into 40 columns with 100 rows

```
columns_N = 1000; %number of columns
rows_N = NU/columns_N; %number of data points in each bin
Usorted = reshape(U,[rows_N,columns_N]);
Vsorted = reshape(V,[rows_N,columns_N]);
Wsorted = reshape(W,[rows_N,columns_N]);

for i = 1:columns_N
    Usorted_mean(i) = mean(Usorted(:,i));
    uf_stationary(:,i) = Usorted(:,i)-Usorted_mean(i);
    uf_stationary_std(i) = std(uf_stationary(:,i));

    Vsorted_mean(i) = mean(Vsorted(:,i));
    vf_stationary(:,i) = Vsorted(:,i)-Vsorted_mean(i);
    vf_stationary_std(i) = std(vf_stationary(:,i));

    Wsorted_mean(i) = mean(Wsorted(:,i));
    wf_stationary(:,i) = Wsorted(:,i)-Wsorted_mean(i);
    wf_stationary_std(i) = std(wf_stationary(:,i));
end
Bin_u_std = std(Usorted_mean);
Bin_v_std = std(Vsorted_mean);
Bin_w_std = std(Wsorted_mean);

count = 1:i;
figure; plot(count,Usorted_mean,count,uf_stationary_std)
title('Mean and Standard Deviation: U-component')
xlabel('Sample','Interpreter','latex') % x-axis label
ylabel('$U$', 'Interpreter','latex') % y-axis label
legend('U_{mean}', 'u_{flux std}', 'location', 'east')

figure; plot(count,Vsorted_mean,count,vf_stationary_std)
title('Mean and Standard Deviation: V-component')
xlabel('Sample','Interpreter','latex') % x-axis label
ylabel('$V$', 'Interpreter','latex') % y-axis label
legend('V_{mean}', 'v_{flux std}', 'location', 'east')

figure; plot(count,Wsorted_mean,count,wf_stationary_std)
title('Mean and Standard Deviation: W-component')
xlabel('Sample','Interpreter','latex') % x-axis label
ylabel('$W$', 'Interpreter','latex') % y-axis label
legend('W_{mean}', 'w_{flux std}', 'location', 'east')
```

## Developing the PDF for the U-velocity component

```
%Standardizing the data
U_stand = (U - Um)/uf_std;
Ustand_mean = mean(U_stand);
Ustand_std = std(U_stand);
Ustand_max = max(U_stand);
Ustand_min = min(U_stand);

num_bins = 250;
F = zeros(num_bins,1);
ub = F;
binwth = (Ustand_max-Ustand_min)/(num_bins);

%Building the CDF for the Data Set
for i = 1:num_bins+2
    ub(i) = Ustand_min + binwth*(i-1);
    A = U_stand(U_stand<ub(i));
    F(i) = length(A)/NU; %Building the CDF
    clear A
end
ub1 = ub(1:length(ub)-1); %making the matrix dimensions agree

%Calculating the PDF by taking the derivative of the CDF and dividing by
%the binwidth. This is our delta y over delta x.
f_u = diff(F); %function of U_standardized
f_ul = f_u/binwth; %function of U_standardized

%Building a plot of the PDF data and comparing it to a Gaussian curve
figure; bar(ub(1:length(ub)-1),f_ul); hold on; grid on;

% Gaussian Plot
U_stand_sort = sort(U_stand); %sorting the data for a cleaner Gaussian plot
norm = normpdf(U_stand_sort,Ustand_mean,Ustand_std);
plot(U_stand_sort,norm)
title({'PDF of the Velocity Data: Slot, Motor On',...
    ' U-Component (z/D = 0.035)'},'fontweight','bold','fontsize',14);
xlabel('$\hat{U}$','Interpreter','latex','fontsize',14); % x-axis label
ylabel('Probability','Interpreter','latex','fontsize',14); % y-axis label
legend('PDF','Gaussian','location','northeast'); hold off;
axis([-6 6 0 1.6]);
xticks([-6 -4 -2 0 2 4 6]);
yticks([0 0.2 0.4 0.6 0.8 1.0 1.2 1.4 1.6]);
```



## Developing the PDF for the V-velocity component

```
%Standardizing the data
V_stand = (V - Vm)/vf_std;
Vstand_mean = mean(V_stand);
Vstand_std = std(V_stand);
Vstand_max = max(V_stand);
Vstand_min = min(V_stand);

num_bins = 250;
F = zeros(num_bins,1);
vb = F;
binwth = (Vstand_max-Vstand_min)/(num_bins);

%Building the CDF for the Data Set
for i = 1:num_bins+2
    vb(i) = Vstand_min + binwth*(i-1);
    A = V_stand(V_stand<vb(i));
    F(i) = length(A)/NU; %Building the CDF
    clear A
end
vb1 = vb(1:length(vb)-1); %making the matrix dimensions agree

%Calculating the PDF by taking the diff of the CDF and dividing by the
%binwidth. This is our delta y over delta x.
f_v = diff(F); %function of U_standardized
f_v1 = f_v/binwth; %function of U_standardized

%Building a plot of the PDF data and comparing it to a Gaussian curve
figure; bar(vb(1:length(vb)-1),f_v1); hold on; grid on;

% Gaussian Plot
V_stand_sort = sort(V_stand); %sorting the data for a cleaner Gaussian plot
norm = normpdf(V_stand_sort,Vstand_mean,Vstand_std);
plot(V_stand_sort,norm)
title(['PDF of the Velocity Data: Slot, Motor On',...
    ' V-Component (z/D = 0.035)'], 'fontweight','bold','fontsize',14);
xlabel('$\hat{V}$','Interpreter','latex','fontsize',14); % x-axis label
ylabel('Probability','Interpreter','latex','fontsize',14); % y-axis label
legend('PDF','Gaussian','location','northeast'); hold off;
axis([-6 6 0 1.6]);
xticks([-6 -4 -2 0 2 4 6]);
yticks([0 0.2 0.4 0.6 0.8 1.0 1.2 1.4 1.6]);
```



## Developing the PDF for the W-velocity component

```
%Standardizing the data
W_stand = (W - Wm)/wf_std;
Wstand_mean = mean(W_stand);
Wstand_std = std(W_stand);
Wstand_max = max(W_stand);
Wstand_min = min(W_stand);

num_bins = 250;
F = zeros(num_bins,1);
wb = F;
binwth = (Wstand_max-Wstand_min)/(num_bins);

%Building the CDF for the Data Set
for i = 1:num_bins+2
    wb(i) = Wstand_min + binwth*(i-1);
    A = W_stand(W_stand<wb(i));
    F(i) = length(A)/NU; %Building the CDF
    clear A
end
wb1 = wb(1:length(wb)-1); %making the matrix dimensions agree

%Calculating the PDF by taking the derivative of the CDF and dividing by the
%binwidth. This is our delta y over delta x.
f_w = diff(F); %function of U_standardized
f_w1 = f_w/binwth; %function of U_standardized

%Building a plot of the PDF data and comparing it to a Gaussian curve
figure; bar(wb(1:length(wb)-1),f_w1); hold on; grid on;

% Gaussian Plot
W_stand_sort = sort(W_stand); %sorting the data for a cleaner Gaussian plot
norm = normpdf(W_stand_sort,Wstand_mean,Wstand_std);
plot(W_stand_sort,norm)
title({'PDF of the Velocity Data: Slot, Motor On',...
    ' W-Component (z/D = 0.035)'},'fontweight','bold','fontsize',14);
xlabel('$\hat{W}$','Interpreter','latex','fontsize',14); % x-axis label
ylabel('Probability','Interpreter','latex','fontsize',14); % y-axis label
legend('PDF','Gaussian','location','northeast'); hold off;
axis([-6 6 0 1.6]);
xticks([-6 -4 -2 0 2 4 6]);
yticks([0 0.2 0.4 0.6 0.8 1.0 1.2 1.4 1.6]);
```

## Phase II

Post-Processing Nano-25 Data: Slot at  $x/L = 0.55$

(Motor On vs. Motor Off)

### Missile and Wind Tunnel Properties

```
clear all;close all;clc

V_inf = 50*(1/3600)*(5280); % MPH freestream velocity converted to (ft/s)
Fahrenheit = 74.3;
Inches_Hg = 29.6660;
    L = 2.0; % weapon bay length (ft)
    Dia = 1.29/12; % missile diameter converted to (ft)
    Ref_Area = (pi/4)*Dia^2; % Model reference Area (ft^2)
    P_psi = Inches_Hg*0.49115420057253 ;% Inches Hg converted to psi
    P_psf = P_psi*12^2; %psi to psf
    T = Fahrenheit + 459.67;% temp deg F converted to Rankine
    R = 1716; % (lb-ft)/(slug-R) Imperial Gas constant for Dry Air
    rho = P_psf/(R*T); % density from ideal gas law [slug/ft^3]
```

### Importing the Data and Calibration Matrix

```
%Voltage Import
% Aligning the Tare (0 mph)
VoltageImport_0 = csvread('Min_0mph.csv'); %Data Imported from .csv
%Taking the 2 seconds of data around the event
VoltageUse_01 = VoltageImport_0(end-3000:end-1000,:);

% 50 mph Case Data Imported from .csv
VoltageImport_1 = csvread('Min_50mph_1.csv');
%Taking the 2 seconds of data around the event
VoltageUse_1 = VoltageImport_1(end-3046:end-1046,:);

%Calibration Matrix Nano-25
CalMat = [ 0.01666, -0.00399, -0.31744, 2.98746, 0.42269, -3.00593;...
           0.17884, -3.47015, -0.14035, 1.72288, -0.31903, 1.75159;...
           5.26167, -0.04467, 5.59050, 0.20559, 5.32144, -0.10468;...
           0.07209, -1.22529, 2.09820, 0.72446, -2.13718, 0.63742;...
           -2.40927, 0.01016, 1.39990, -1.01331, 0.98241, 1.08087;...
           0.03166, -1.11580, 0.14224, -1.09552, 0.16628, -1.10239];
```

### Calculating the Force and Moment Tare Data at 0 mph

```
time_01 = VoltageUse_01(:,1) - (VoltageUse_01(1,1));
VFX_01 = VoltageUse_01(:,2);
VFY_01 = VoltageUse_01(:,3);
VFZ_01 = VoltageUse_01(:,4);
VTX_01 = VoltageUse_01(:,5);
VTY_01 = VoltageUse_01(:,6);
VTZ_01 = VoltageUse_01(:,7);

for i = 1:length(time_01)

Voltages_01=[VFX_01(i);VFY_01(i);VFZ_01(i);VTX_01(i);VTY_01(i);VTZ_01(i)];
Forces_01(:,i) = CalMat*Voltages_01;

end

%Converting the Nano-25 Coordinate System to conform with AIAA standard
Tare_N_01 = (-1)*Forces_01(1,:); % AIAA Normal Force N --> Nano25 Fx(lbf)
Tare_Y_01 = (-1)*Forces_01(2,:); % AIAA Side Force Y --> Nano25 Fy(lbf)
Tare_A_01 = (-1)*Forces_01(3,:); % AIAA Axial Force A --> Nano25 Fz(lbf)
Tare_n_01 = Forces_01(4,:)*(1/12); % AIAA yaw moment n --> Nano25 Tx (ft-lbs)
Tare_m_01 = Forces_01(5,:)*(1/12); % AIAA pitch moment m --> Nano25 Ty (ft-lbs)
Tare_l_01 = Forces_01(6,:)*(1/12); % AIAA roll moment l --> Nano25 Tz (ft-lbs)
```

### Calculating the Force and Moments

```
%Case 1
time_1 = VoltageUse_1(:,1) - (VoltageUse_1(1,1));
VFX_1 = VoltageUse_1(:,2); VFY_1 = VoltageUse_1(:,3);
VFZ_1 = VoltageUse_1(:,4); VTX_1 = VoltageUse_1(:,5);
VTY_1 = VoltageUse_1(:,6); VTZ_1 = VoltageUse_1(:,7);

for i = 1:length(time_01)

Voltages_1=[VFX_1(i);VFY_1(i);VFZ_1(i);VTX_1(i);VTY_1(i);VTZ_1(i)];
Forces_1(:,i) = CalMat*Voltages_1;

end
```



### Force and Moments converted to AIAA convention

```
% (-1) is for AIAA convention
%F_ corresponds to Nano25(lbf)
%T_ Corresponds to Nano25converted to ft-lb
% Case 1
N_1 = (-1)*Forces_1(1,:);
Y_1 = (-1)*Forces_1(2,:);
A_1 = (-1)*Forces_1(3,:);
n_1 = Forces_1(4,:)*(1/12);
m_1 = Forces_1(5,:)*(1/12);
l_1 = Forces_1(6,:)*(1/12);
```

### Calculating the TARED Data by subtracting the Tare Values

```
%Case 1
TARED_N_1 = (N_1 - Tare_N_01);
TARED_Y_1 = (Y_1 - Tare_Y_01);
TARED_A_1 = (A_1 - Tare_A_01);
TARED_n_1 = (n_1 - Tare_n_01);
TARED_m_1 = (m_1 - Tare_m_01);
TARED_l_1 = (l_1 - Tare_l_01);
```

### Plots of the Normal Force Data at Wind Tunnel Velocity vs. Tared

```
figure('Position',[100 100 1200 800]);
plot(time_1,N_1); hold on; plot(time_01,Tare_N_01); plot(time_1,TARED_N_1);
title({'Normal Force (F_{N1}): Slot, Min Stroke',...
      'Missile, AoA: 0 deg, 50 MPH'},'fontweight','bold','fontsize',18)
xlabel('time (s)','Interpreter','latex','fontsize',18) % x-axis label
ylabel('lbf','Interpreter','latex','fontsize',18) % y-axis label
legend({'F_{N1}','Tare F_{N1}','TARED F_{N1}'},...
      'FontSize',12,'Location','bestoutside');hold off
axis([0 2 -3.0 1.0])
```

### Calculate Coefficients (Case 1)

```
q = (1/2)*rho*V_inf^2; %Dynamic Pressure
% Case 1
CN_1 = (TARED_N_1) / (q*Ref_Area); %Normal Force Coeff
CY_1 = (TARED_Y_1) / (q*Ref_Area); %Side Force Coeff
CA_1 = (TARED_A_1) / (q*Ref_Area); %Axial Force Coeff
Cl_1 = (TARED_l_1) / (q*Ref_Area*Dia); %Roll Moment Coeff
Cm_1 = (TARED_m_1) / (q*Ref_Area*Dia); %Pitch Moment Coeff
Cn_1 = (TARED_n_1) / (q*Ref_Area*Dia); %Yaw Moment Coeff
```

### Filter for Coefficient Data Sets\_Slot (Case 1)

```
Fs = 1000; % sample rate in Hz
cof = 1; % cutoff frequency in Hz
order = 60; % -th Order of lowpas filter

%Transforming the noisy data array from a row into a column
%Case 1
CN_1 = CN_1';
CY_1 = CY_1';
CA_1 = CA_1';
Cn_1 = Cn_1';
Cm_1 = Cm_1';
Cl_1 = Cl_1';
```

### Design a -th order lowpass FIR filter with cutoff frequency of (Hz)

```
Fnorm = cof/(Fs/2); % Normalized frequency

%CASE 1
df_1 = designfilt('lowpassfir','FilterOrder',order,'CutoffFrequency',Fnorm);
Delay_1 = mean(grpdelay(df_1)); % filter delay in samples
filtered_CN_1 = filter(df_1,[CN_1; zeros(Delay_1,1)]); % Append Delay zeros to the input data
filtered_CN_1 = filtered_CN_1(Delay_1+1:end); % Shift data to compensate for delay
filtered_CY_1 = filter(df_1,[CY_1; zeros(Delay_1,1)]);
filtered_CY_1 = filtered_CY_1(Delay_1+1:end);
filtered_CA_1 = filter(df_1,[CA_1; zeros(Delay_1,1)]);
filtered_CA_1 = filtered_CA_1(Delay_1+1:end);
filtered_Cn_1 = filter(df_1,[Cn_1; zeros(Delay_1,1)]);
filtered_Cn_1 = filtered_Cn_1(Delay_1+1:end);
filtered_Cm_1 = filter(df_1,[Cm_1; zeros(Delay_1,1)]);
filtered_Cm_1 = filtered_Cm_1(Delay_1+1:end);
filtered_Cl_1 = filter(df_1,[Cl_1; zeros(Delay_1,1)]);
filtered_Cl_1 = filtered_Cl_1(Delay_1+1:end);
```

## Plotting Normal Force Coefficients

```
%Normal Force Coeff

figure('Position',[100 100 900 480]);
plot(time_1(50:1900),filtered_CN_1(50:1900)); grid on;
    title({'Normal Force Coefficient (C_{N}): Slot, Min Stroke',...
        'Missile, AoA: 0 deg, 50 MPH'},'fontweight','bold','fontsize',16);
    legend({'C_{N1},filtered'},'FontSize',12,'Location','bestoutside');
    xlabel('time (s)','Interpreter','latex','fontsize',18) % x-axis label
    ylabel('$C_{N}$','Interpreter','latex','fontsize',18) % y-axis label
    axis([.05 1.9 -1.5 2.7]); hold off;
    set(findall(gca, 'Type', 'Line'),'LineWidth',1.5);
```

## Plotting Pitch Moment Coefficients

```
%Pitch Moment Coeff

figure('Position',[100 100 900 480]);
plot(time_1(50:1900),filtered_Cm_1(50:1900)); grid on;
    title({'Pitch Moment Coefficient (C_{m}): Slot, Min Stroke',...
        'Missile, AoA: 0 deg, 50 MPH'},'fontweight','bold','fontsize',16);
    legend({'C_{m1},filtered'},'FontSize',12,'Location','bestoutside');
    xlabel('time (s)','Interpreter','latex','fontsize',18) % x-axis label
    ylabel('$C_{m}$','Interpreter','latex','fontsize',18) % y-axis label
    axis([.05 1.9 -1.75 1.6]); hold off;
    set(findall(gca, 'Type', 'Line'),'LineWidth',1.5);
```

## Axial Force Coefficients

```
%Axial Force Coeff

figure('Position',[100 100 900 480]);
plot(time_1(50:1900),filtered_CA_1(50:1900)); hold on
    title({'Axial Force Coefficient (C_{A}): Slot, Min Stroke',...
        'Missile, AoA: 0 deg, 50 MPH'},'fontweight','bold','fontsize',16);
    legend({'C_{A1},filtered'},'FontSize',12,'Location','bestoutside');
    xlabel('time (s)','Interpreter','latex','fontsize',18) % x-axis label
    ylabel('$C_{A}$','Interpreter','latex','fontsize',18) % y-axis label
    axis([.05 1.9 0.0 2.0]); hold off;
    set(findall(gca, 'Type', 'Line'),'LineWidth',1.5);
```



# Galil Codes

## Initializing Motor A

BA A  
BMA = 30720  
TLA = 6.75  
TKA = 9  
ERA = -1  
AUA = 1  
OEA = 1  
BZA = 4  
MTA = 1  
KPA = 53.6250  
KDA = 400.625  
KIA = 2.5801

## Initializing Motor B

BA B  
BMB = 30720  
TLB = 6.75  
TKB = 9  
ERB = -1  
AUB = 1  
OEB = 1  
BZB = 4  
MTB = 1  
KPB = 53.6250  
KDB = 400.625  
KIB = 2.5801

## SineWave for Oscillating Motor

```
#home; 'Home Routine
SH A
JG 25000
FI A; 'Find index
BG A; 'Begin motion
AM A; 'After motion
DP 0; 'set current position to 0
MG "Found Index"
WT 500

#reposit; 'Reposition to center
SH A
PR -19532 ; 'move to position
BG A; 'Begin Motion
AM A; 'After Motion
DP 0; 'Set current position to 0
MG "New Zero - Start NI Motion Controller"
WT 3000

#sine;'Sine Wave Motion
SH A;      'turns on motor A
amp= 24736; 'amplitude in counts
freq= 5;   'frequency in Hz
rate= freq*amp*6.2832; 'calculates correct speed
VS rate
'set VA and VD if non-standard accel and decel are needed

#init
go= 1
' sine wave on "A" axis
VM AN
  CR amp,0,360; '1 sine wave to get started
  BG S;        'starts motion

#1
CR amp,0,360; 'add 1 sine wave continuously

#wait
  JP #1,_LM>1; '_LM shows how many segments in buffer
  JP #wait,go=1; 'continue adding sine waves until go=0 is entered
```

```
#stop
ST ;    'stops motion
AM S;   'waits for motion to complete
VE;     'ends vector mode
CS S;   'clears all sine waves out of vector buffer
MG "FINISHED"
EN
```

## Fully Retracted Initialization

```
i = 0
#homeA; 'Home Routine
SH A
JG 25000
FI A; 'Find index
BG A; 'Begin motion
AM A; 'After motion
DP 0; 'set current position to 0
MG "Found Index"
WT 1000

#set
CO 2
CB 31;CB 32;

#homeB; 'Home Routine
SH B
JG ,25000
FI B; 'Find index
BG B; 'Begin motion
AM B; 'After motion
DP ,0; 'set current position to 0
MG "Found Index"

#reposit; 'Reposition to center
SH A
PR -19532 ; 'move to position
BG A; 'Begin Motion
AM A; 'After Motion
DP 0; 'Set current position to 0
MG "New Zero"

#sin;'Sine Wave Motion
SH A;      'turns on motor A
amp= 24736; 'amplitude in counts
freq= 5.0;  'frequency in Hz
rate= freq*amp*6.2832;    'calculates correct speed
VS rate
'set VA and VD if non-standard accel and decel are needed
```

```

#init
GO = 1
' sine wave on "A" axis
VM AN
CR amp,0,360; '1 sine wave to get started
BG S; 'starts motion

#loop
CR amp,0,360; 'add 1 sine wave continuously
VE

#wait
var1 = _LM;
var2 = _LM-var1;

IF (var2 > 0)
i = i + 1;
ENDIF

IF (i = 5)
SB 31
ENDIF

IF ((i = 7)&(_TPA > -400))
SB 32; XQ #gravity,1;
ENDIF

IF @OUT[32]=0
JP #loop,_LM>1; '_LM shows how many segments are available in buffer
JP #wait,GO=1; 'continue adding sine waves until GO=0 is entered
ELSE
WT 2000; CB 32; CB 31; WT 5000; ST; JP #homeC;
ENDIF

#gravity
SH B
AC ,19620000 ;'acceleration
DC ,10240000 ;'deceleration
SP , rate ;'speed
PR ,-77000 ;'distance
BG B;' Begin the move
AM B;' After the move is over
EN

```

```
#homeC; 'Home Routine
SH B
JG ,25000
BG B; 'Begin motion
AM B; 'After motion
MO A; MO B;
EN
```



## Mid-Range Initialization

```
i = 0
#homeA; 'Home Routine
SH A
JG 25000
FI A; 'Find index
BG A; 'Begin motion
AM A; 'After motion
DP 0; 'set current position to 0
MG "Found Index"
WT 1000

#set
CO 2
CB 31;CB 32;

#homeB; 'Home Routine
SH B
JG ,25000
FI B; 'Find index
BG B; 'Begin motion
AM B; 'After motion
DP ,0; 'set current position to 0
MG "Found Index"

#reposit; 'Reposition to center
SH A
PR -19532 ; 'move to position
BG A; 'Begin Motion
AM A; 'After Motion
DP 0; 'Set current position to 0
MG "New Zero"

#sin;'Sine Wave Motion
SH A;      'turns on motor A
amp= 24736; 'amplitude in counts
freq= 5.0;  'frequency in Hz
rate= freq*amp*6.2832;  'calculates correct speed
VS rate
'set VA and VD if non-standard accel and decel are needed
```

```

#init
go A= 1
' sine wave on "A" axis
VM AN
CR amp,0,360; '1 sine wave to get started
BG S; 'starts motion

#loop
CR amp,0,360; 'add 1 sine wave continuously
VE

#wait
var1 = _LM;
var2 = _LM-var1;

IF (var2 > 0)
i = i + 1;
ENDIF

IF (i = 5)
SB 31
ENDIF

IF (i=7)&((_TPA<-24500)&(_TPA>-25000))
SB 32; XQ #GRAVITY,1
ENDIF

IF @OUT[32]=0
JP #loop,_LM>1; '_LM shows how many segments are available in buffer
JP #wait,go=1; 'continue adding sine waves until G0=0 is entered
ELSE
WT 2000; CB 32; CB 31; WT 5000; ST; JP #homeC;
ENDIF

#gravity
SH B
AC ,19620000 ;'acceleration
DC ,10240000 ;'deceleration
SP , rate ;'speed
PR ,-77000 ;'distance
BG B;' Begin the move
AM B;' After the move is over
EN

```

```
#homeC; 'Home Routine
SH B
JG ,25000
BG B; 'Begin motion
AM B; 'After motion
MO A; MO B;
EN
```

## Fully Extended Initialization

```
i = 0
#homeA; 'Home Routine
SH A
JG 25000
FI A; 'Find index
BG A; 'Begin motion
AM A; 'After motion
DP 0; 'set current position to 0
MG "Found Index"
WT 1000

#set
CO 2
CB 31;CB 32;

#homeB; 'Home Routine
SH B
JG ,25000
FI B; 'Find index
BG B; 'Begin motion
AM B; 'After motion
DP ,0; 'set current position to 0
MG "Found Index"

#reposit; 'Reposition to center
SH A
PR -19532 ; 'move to position
BG A; 'Begin Motion
AM A; 'After Motion
DP 0; 'Set current position to 0
MG "New Zero"

#sin;'Sine Wave Motion
SH A;      'turns on motor A
amp= 24736; 'amplitude in counts
freq= 5.0;  'frequency in Hz
rate= freq*amp*6.2832;  'calculates correct speed
VS rate
'set VA and VD if non-standard accel and decel are needed
```

```

#init
GO = 1
' sine wave on "A" axis
VM AN
CR amp,0,360; '1 sine wave to get started
BG S; 'starts motion

#loop
CR amp,0,360; 'add 1 sine wave continuously
VE

#wait
var1 = _LM;
var2 = _LM-var1;

IF (var2 > 0)
i = i + 1;
ENDIF

IF (i = 5)
SB 32
ENDIF

IF (i = 7)
SB 31
ENDIF

IF (i=7)&(_TPA<-49000)
SB 31; XQ #GRAVITY,1
ENDIF

IF @OUT[31]=0
JP #loop,_LM>1; '_LM shows how many segments are available in buffer
JP #wait,G0=1; 'continue adding sine waves until G0=0 is entered
ELSE
WT 2000; CB 32; CB 31; WT 5000; ST; JP #homeC;
ENDIF

#gravity
SH B
AC ,19620000 ;'acceleration
DC ,10240000 ;'deceleration
SP , rate ;'speed

```

```
PR ,-77000    ;'distance
BG B;' Begin the move
AM B;' After the move is over
EN
```

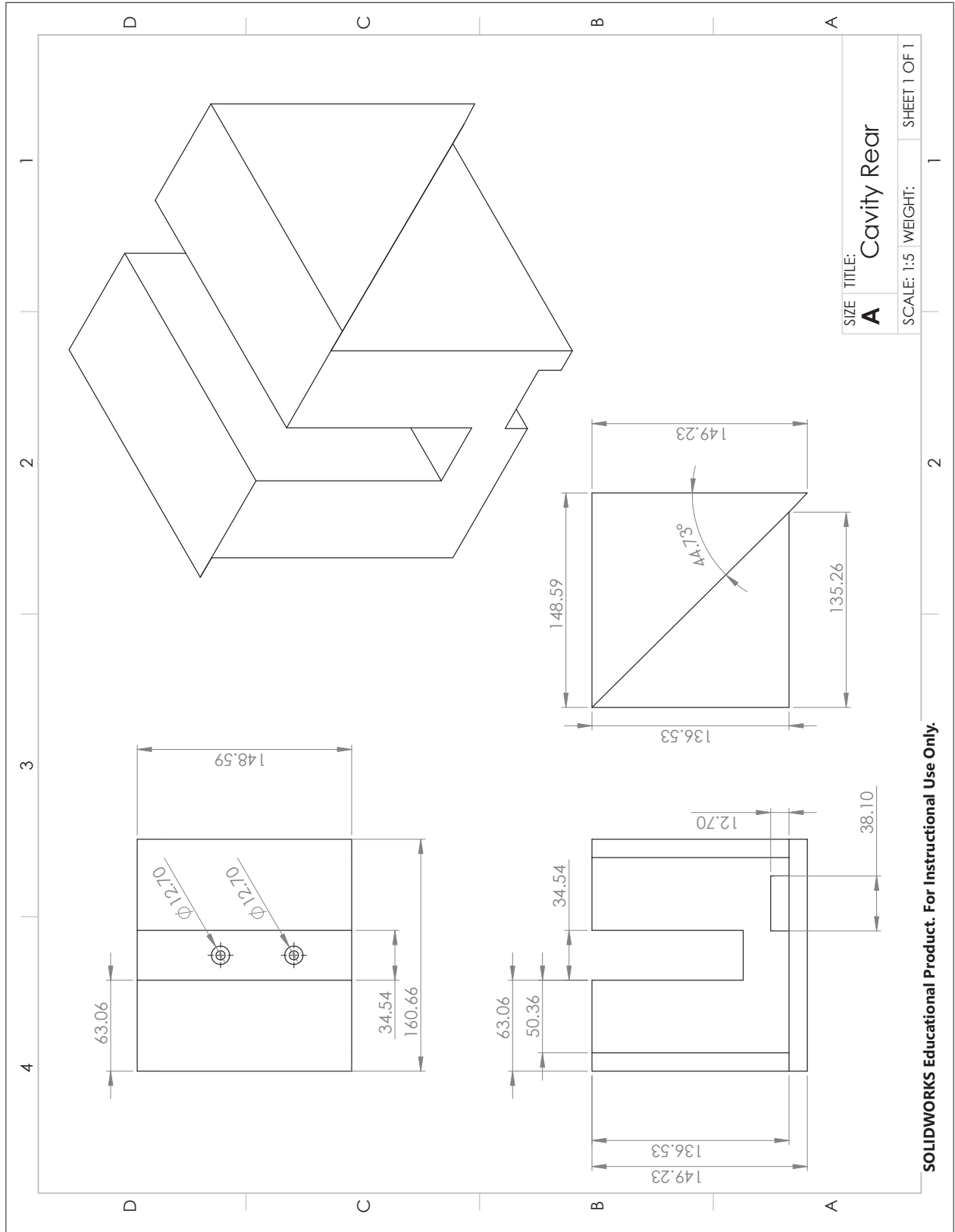
```
#homeC; 'Home Routine
SH B
JG ,25000
BG B; 'Begin motion
AM B; 'After motion
MO A; MO B;
EN
```

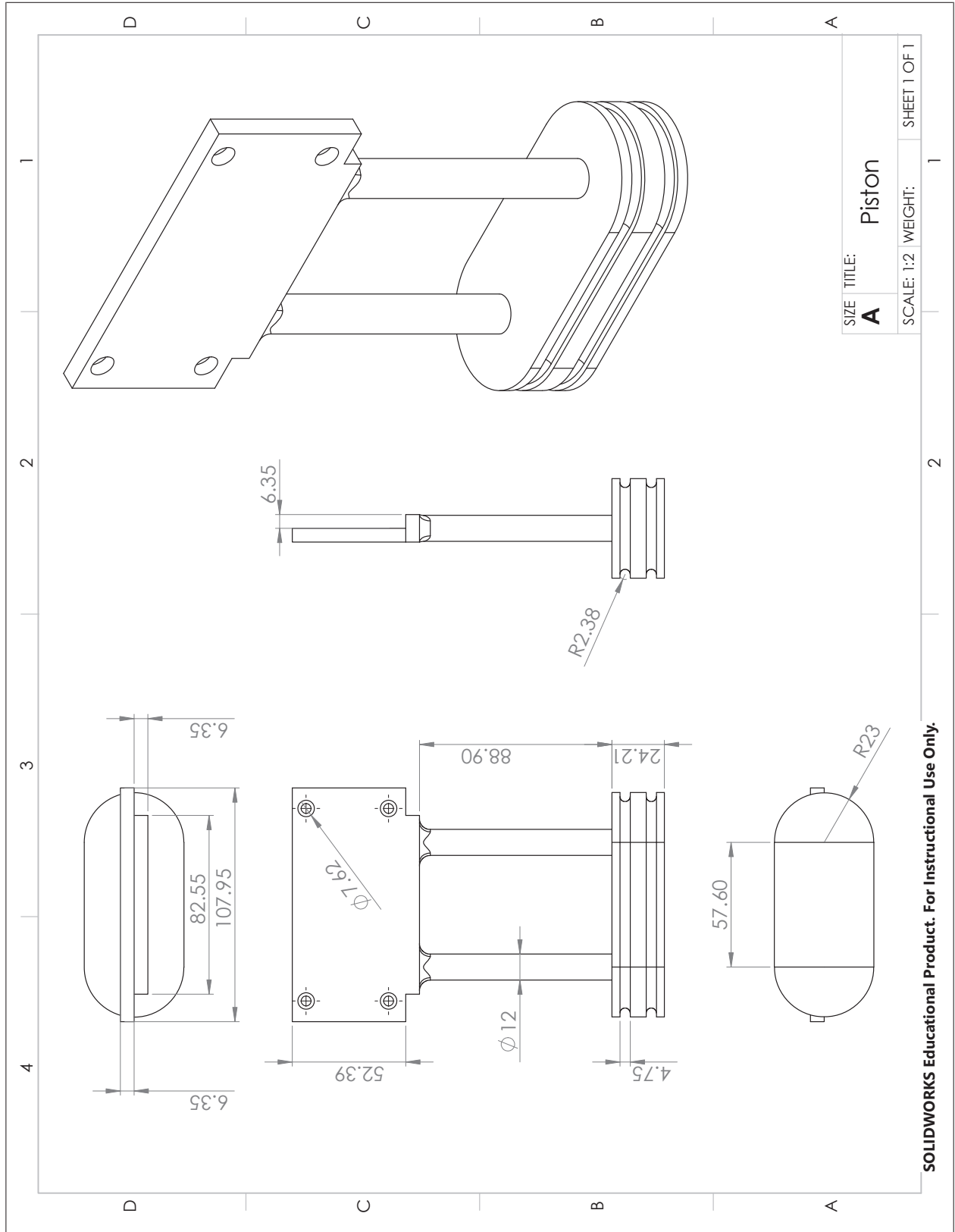


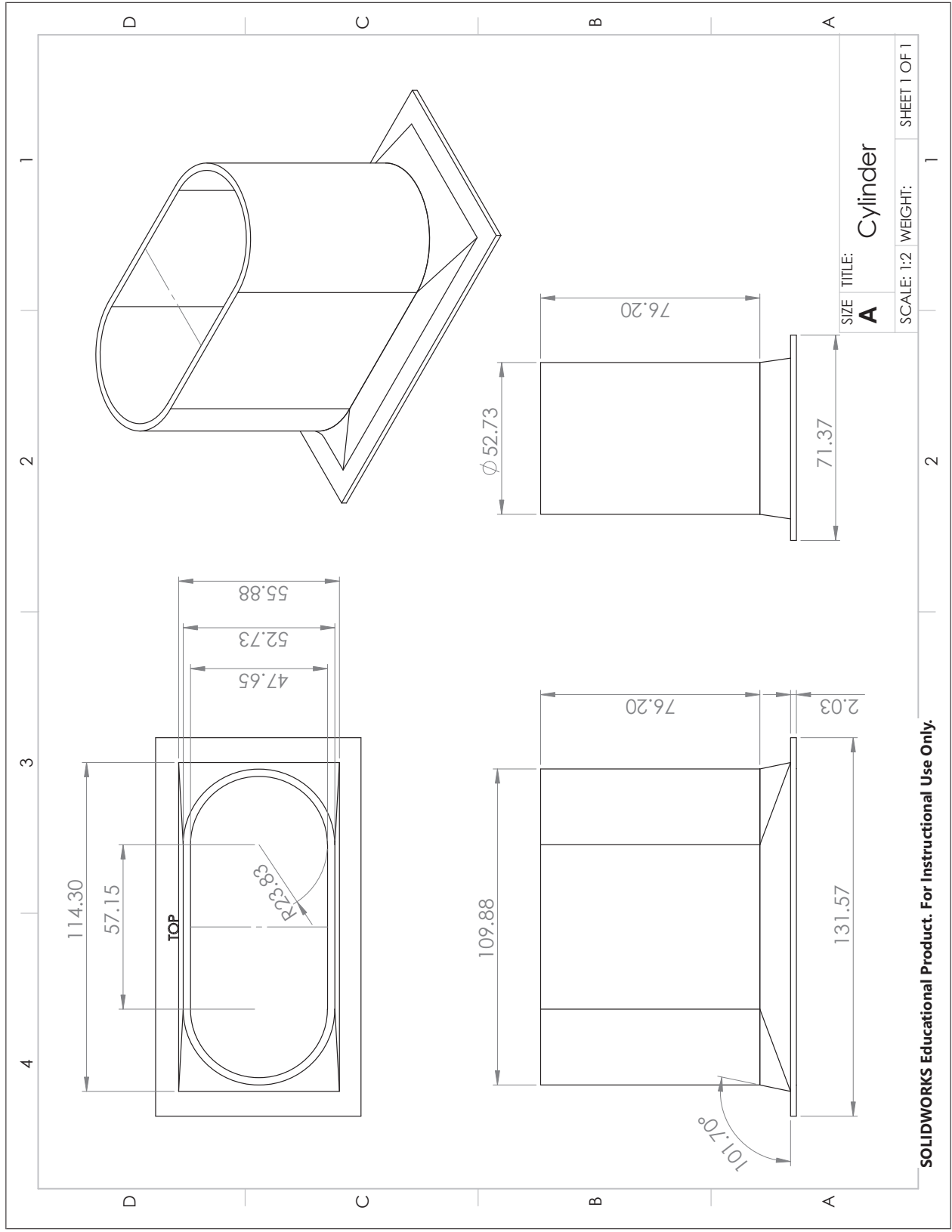
## Appendix C. Drawings of Models

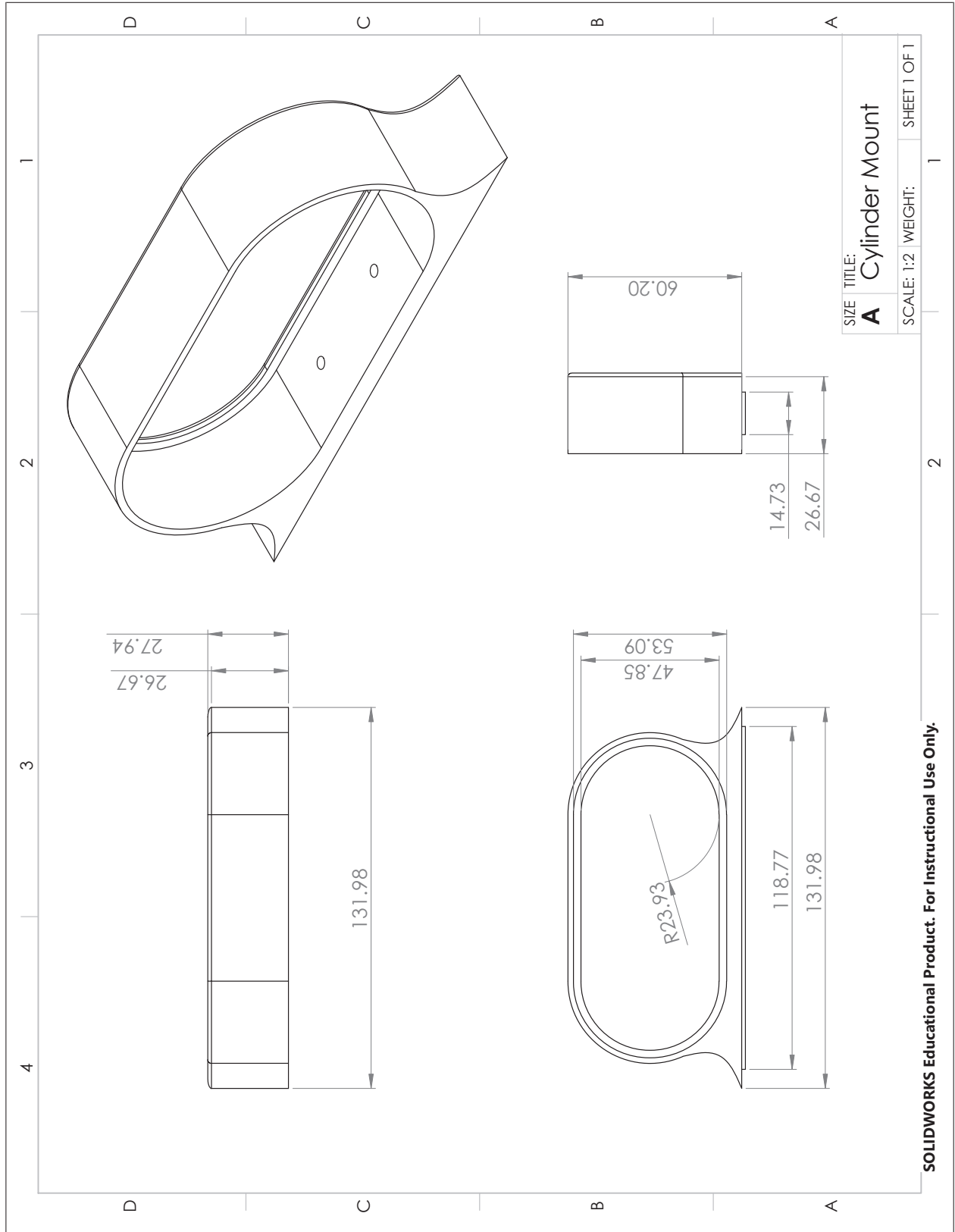
### Index of Figures in Appendix C

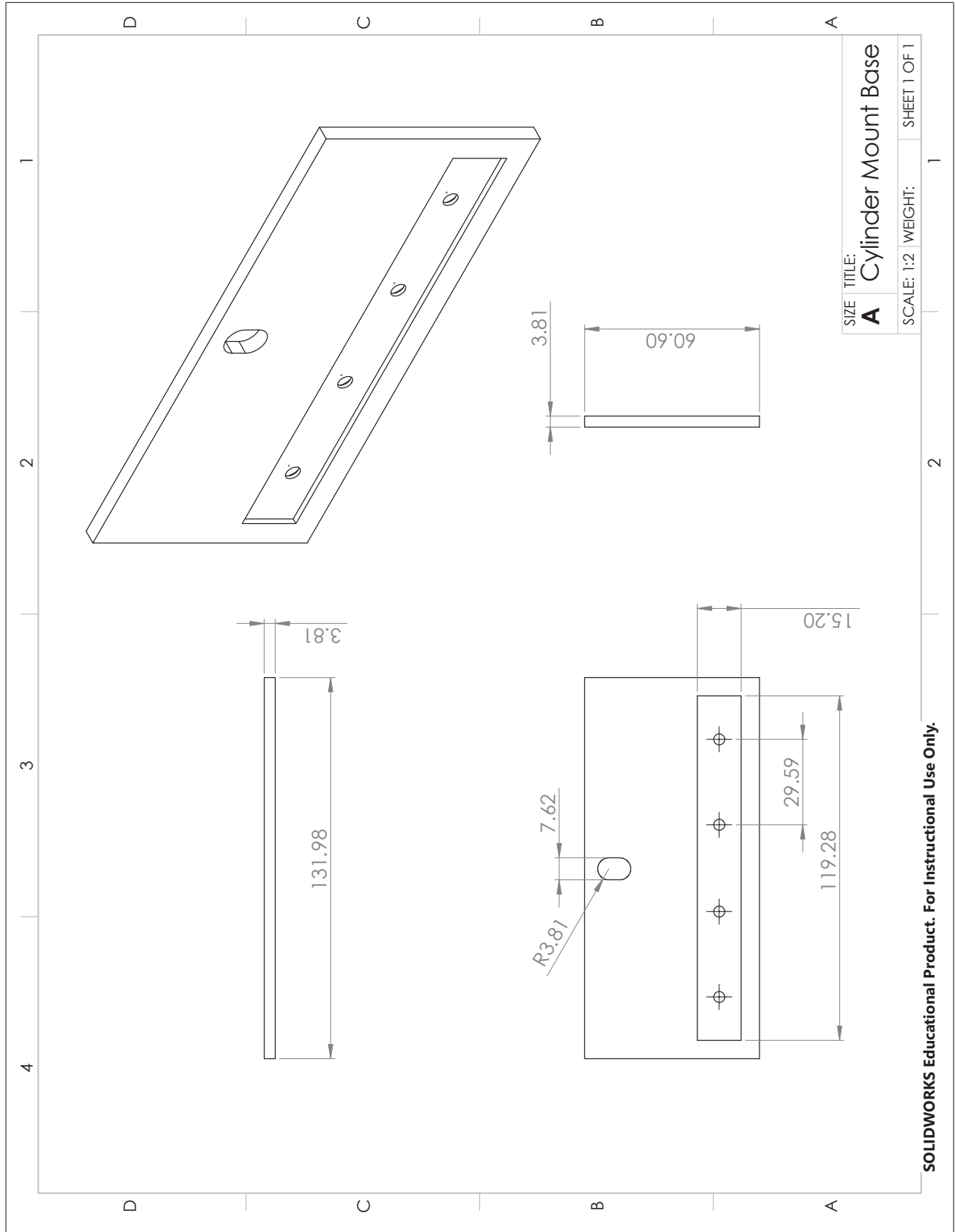
|   |          |
|---|----------|
| Cavity Components - Cavity Rear               | (pg 285) |
| Linear Motor Components - Piston              | (pg 286) |
| Linear Motor Components - Cylinder            | (pg 287) |
| Linear Motor Components - Cylinder Mount      | (pg 288) |
| Linear Motor Components - Cylinder Mount Base | (pg 289) |
| Leading Edge Device - Sawtooth Spoiler        | (pg 290) |
| Leading Edge Device - Square Tab              | (pg 291) |
| Leading Edge Device - Triangular Tab          | (pg 292) |
| Mission Store - Generic Store                 | (pg 293) |
| Mission Store - Ogive Cylinder                | (pg 294) |
| Nano 25 Mount: 0 degree AoA                   | (pg 295) |
| Nano 25 Mount: 10 degree AoA                  | (pg 296) |





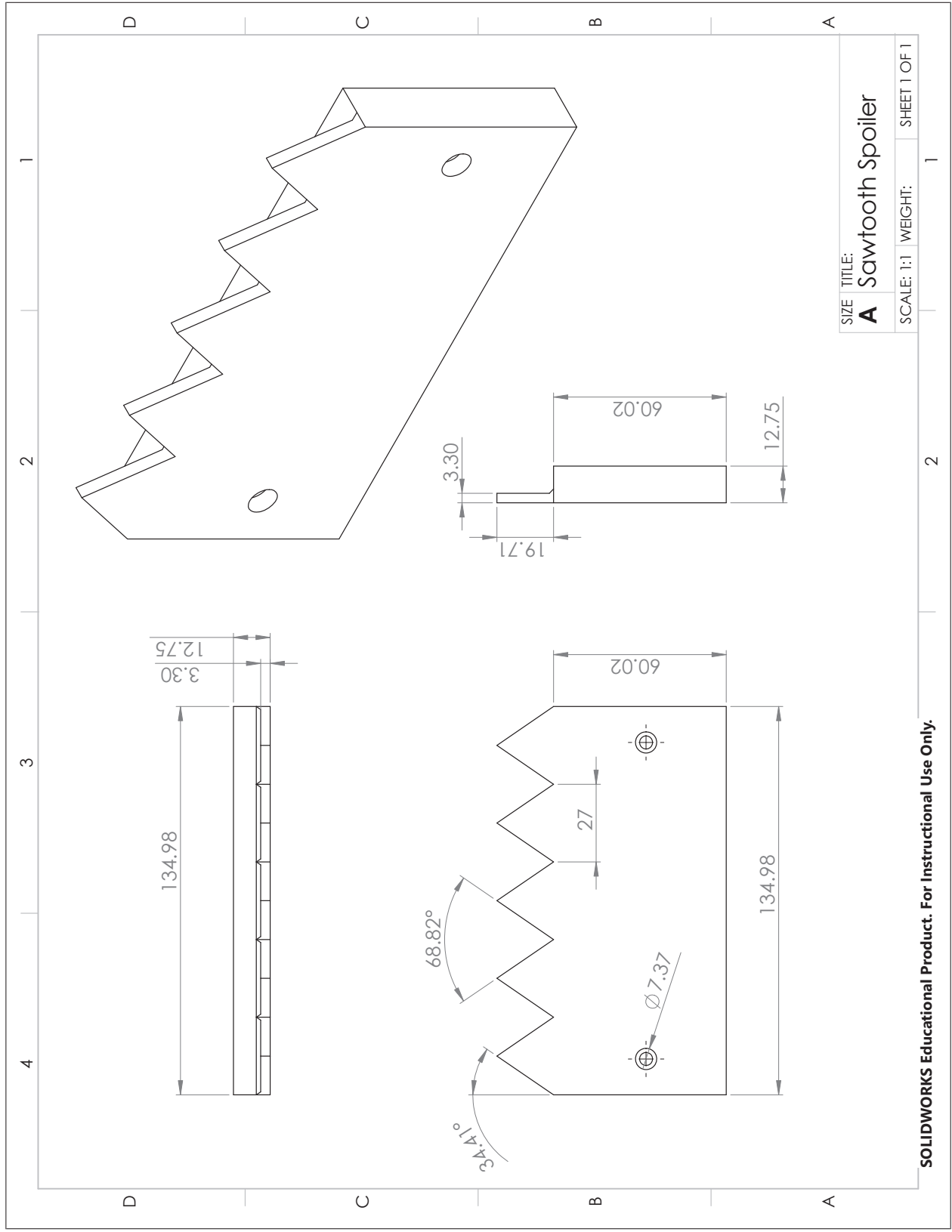


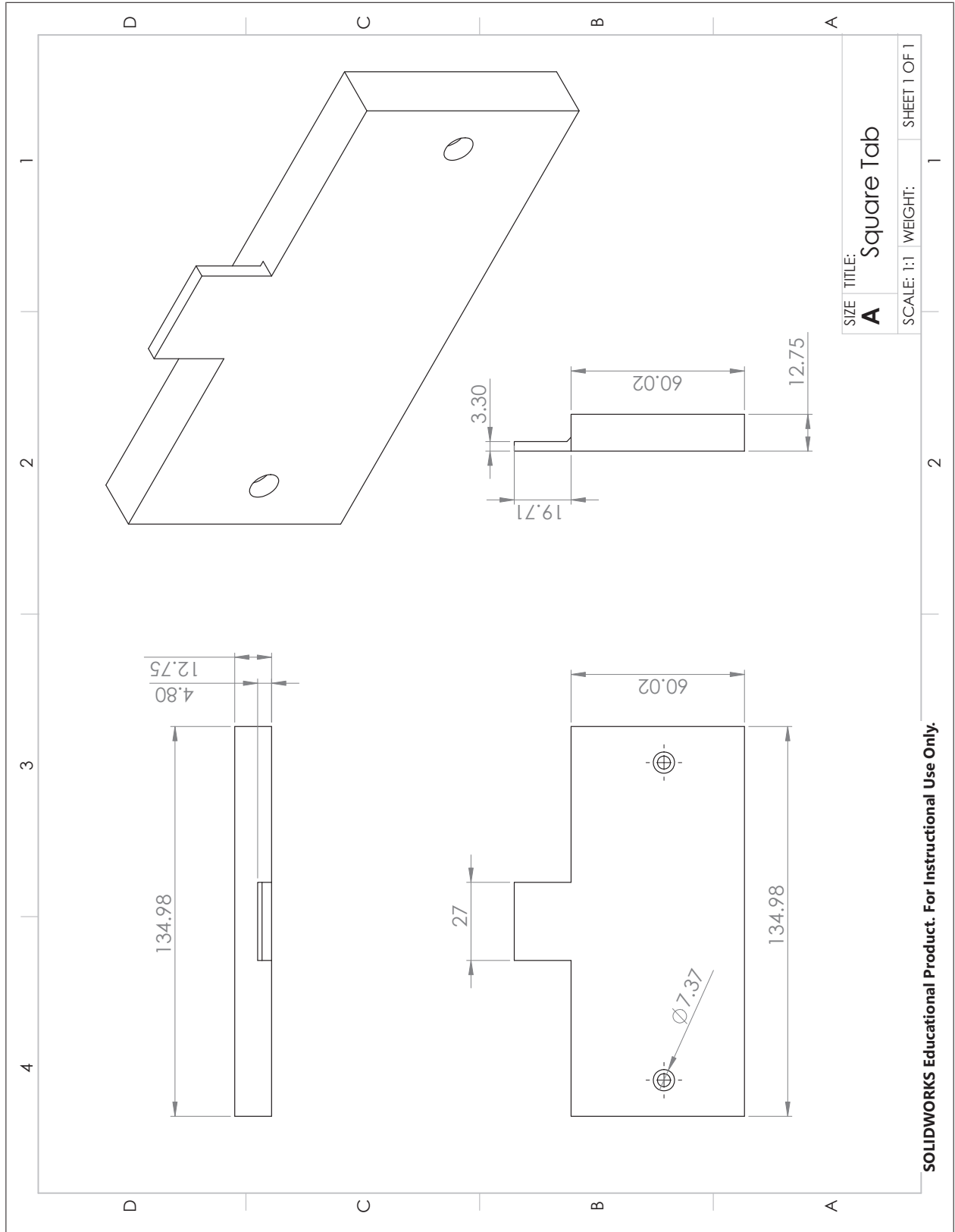


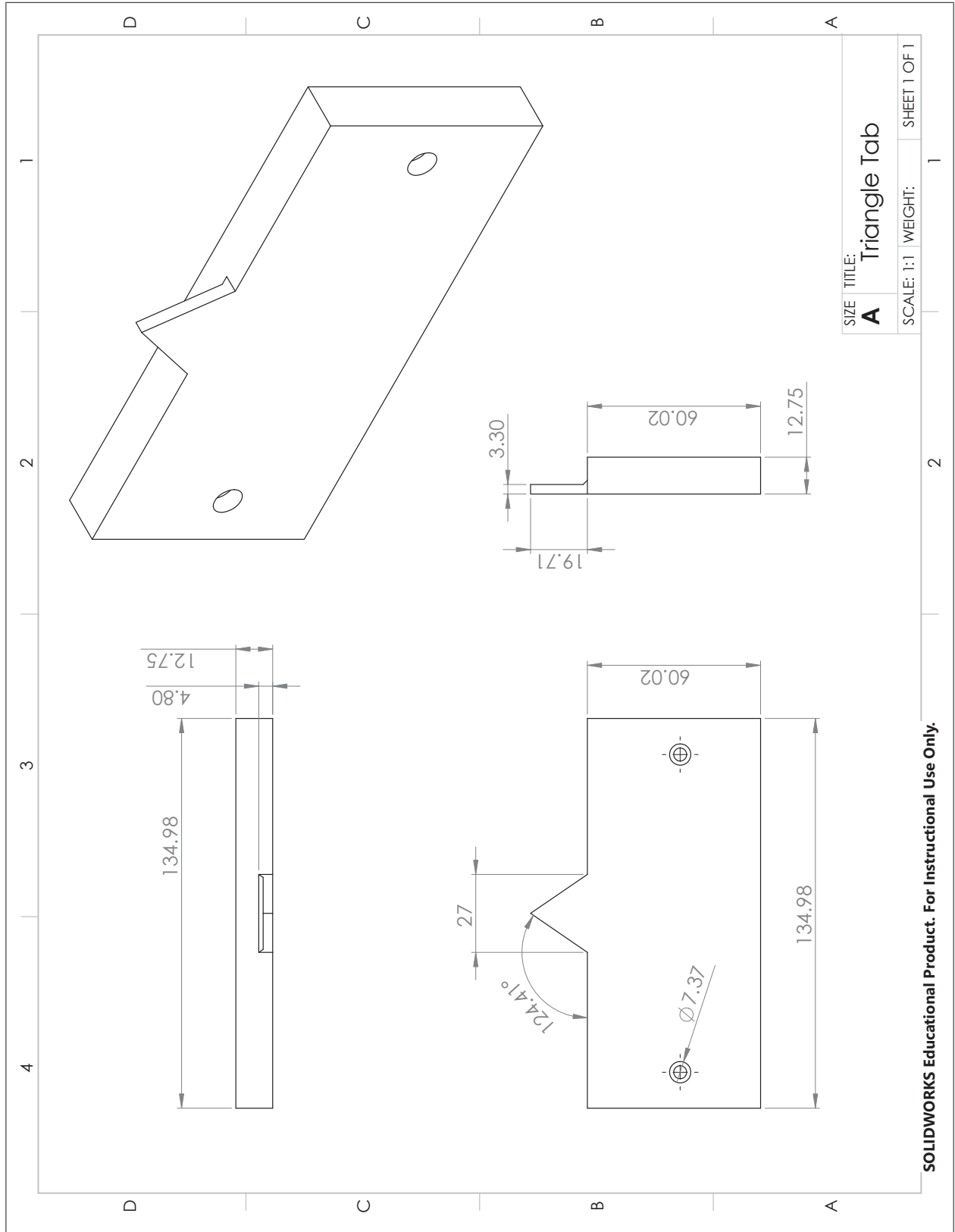


SOLIDWORKS Educational Product. For Instructional Use Only.

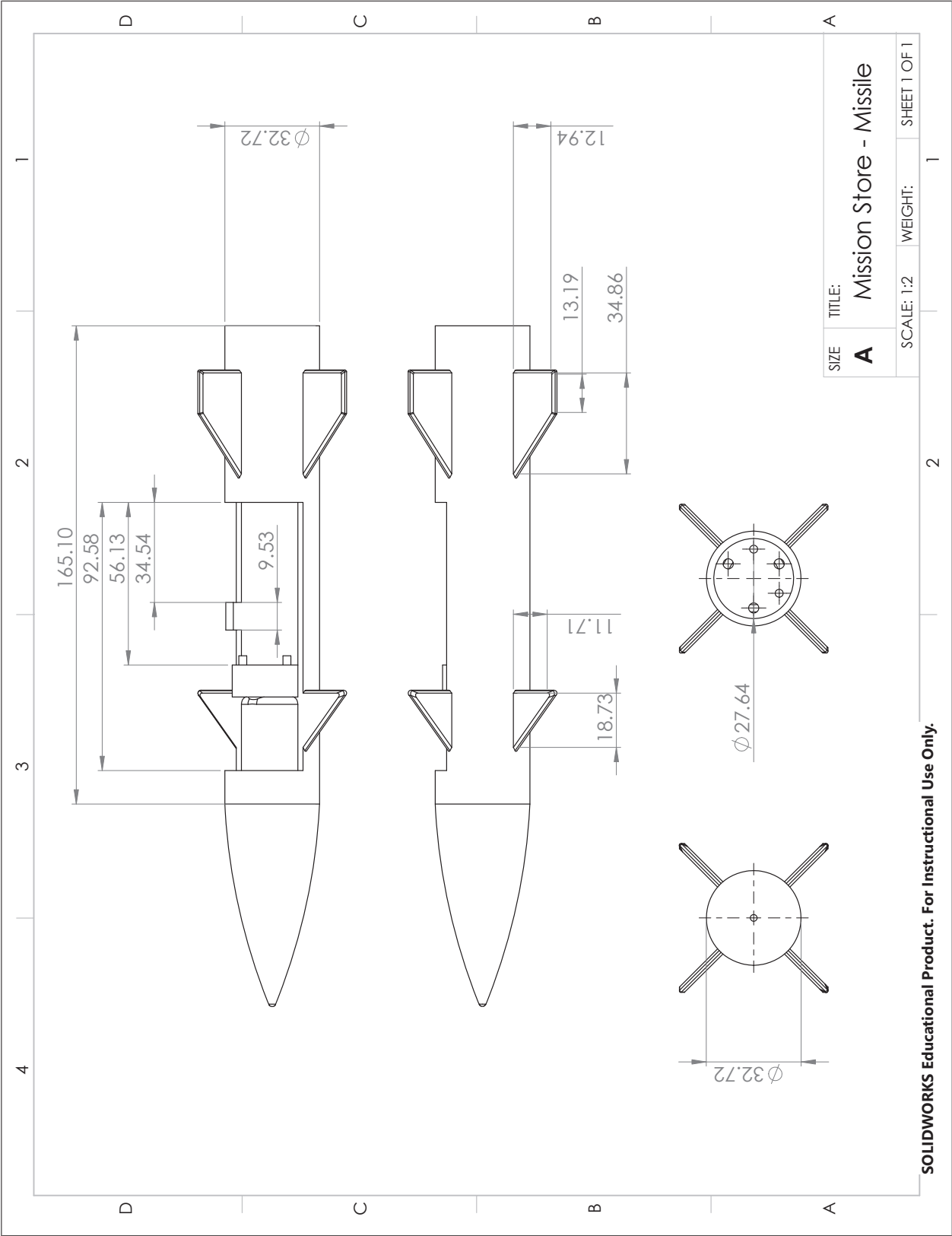


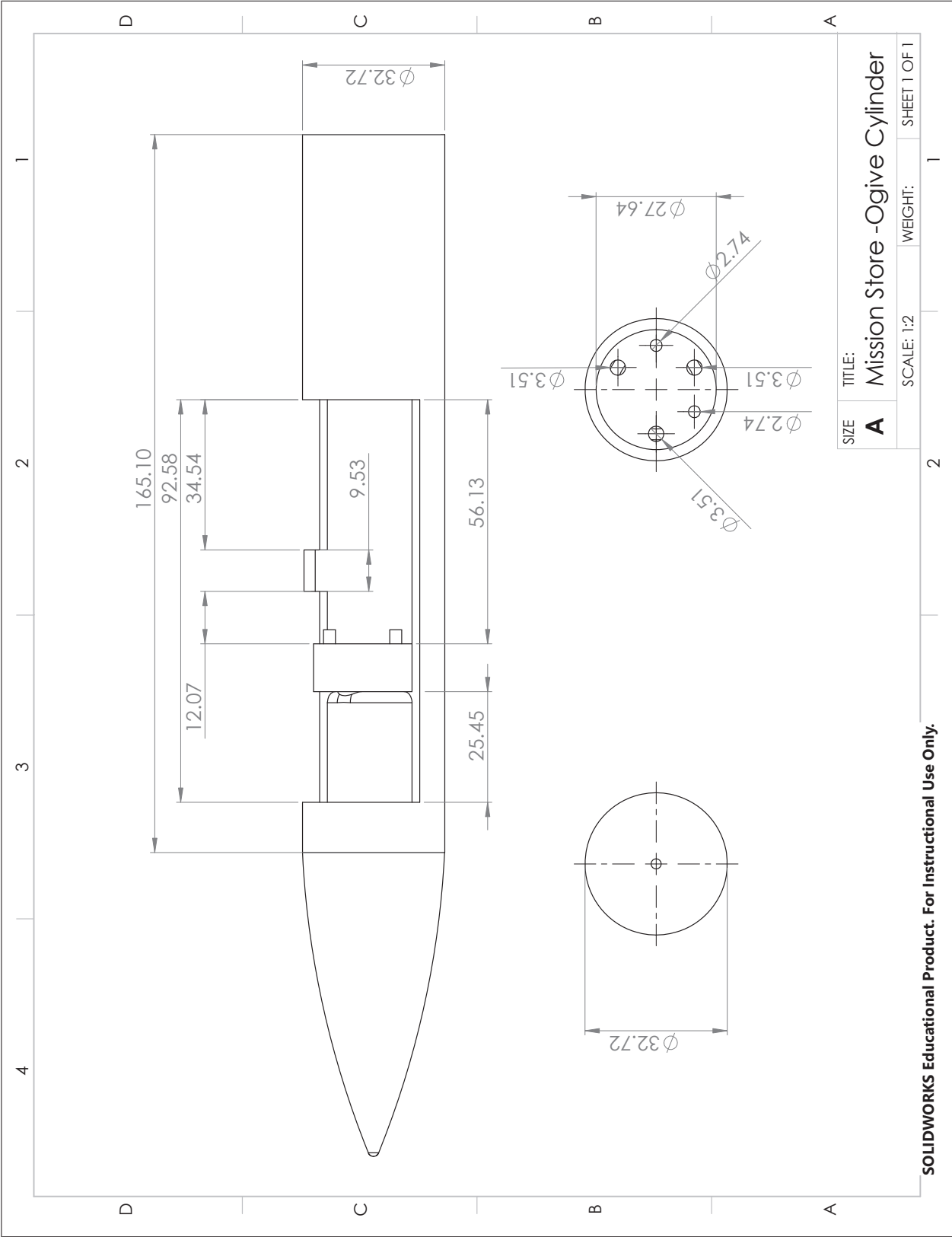


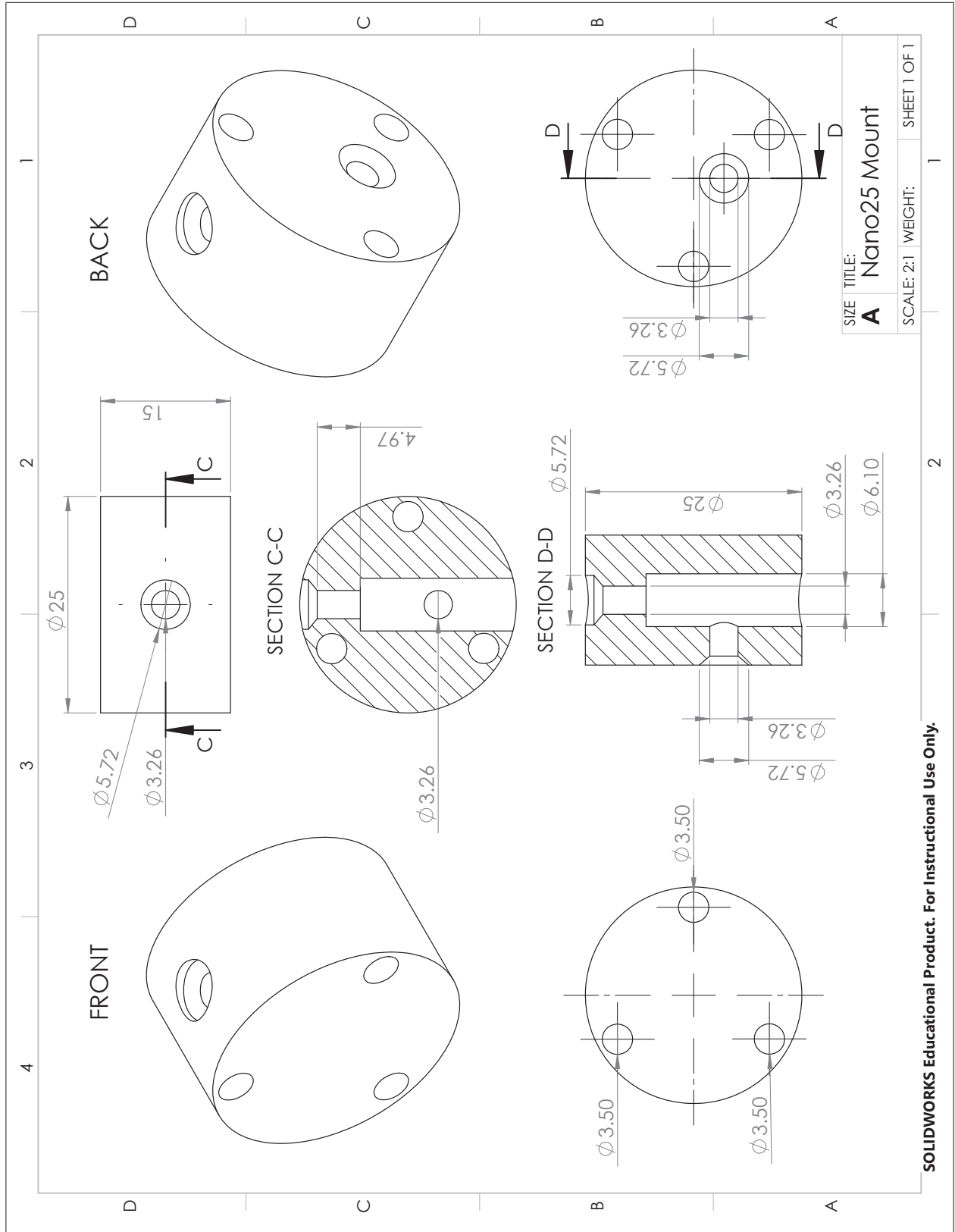




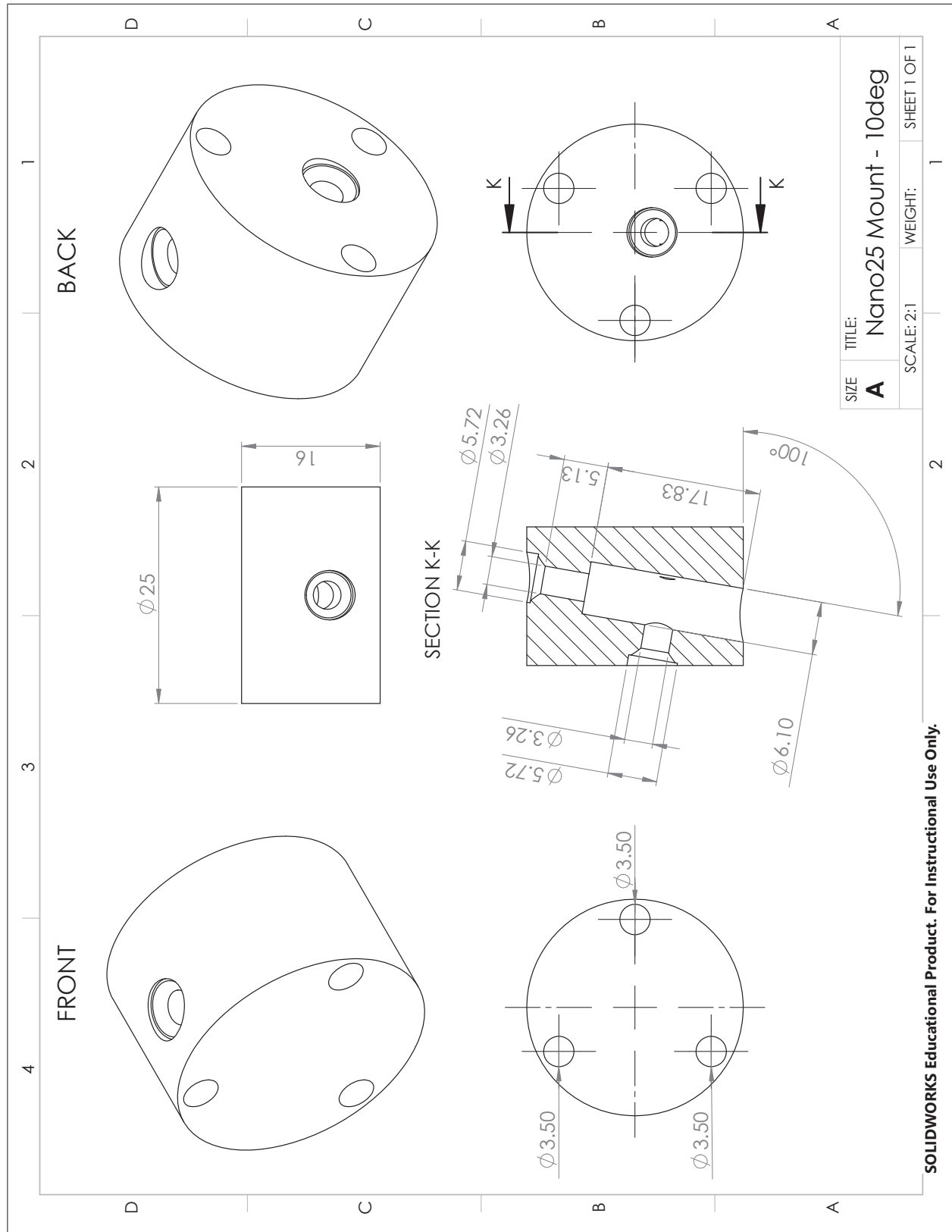
SOLIDWORKS Educational Product. For Instructional Use Only.











## Bibliography

1. J. Anderson. *Fundamentals of Aerodynamics*. McGraw-Hill Education, 5th edition, 2010.
2. Srinivasan Arunajatesan, Chandrasekhar Kannepalli, Neeraj Sinha, Michael Sheehan, Farrukh Alvi, A Florida, George Shumway, and Lawrence Ukeiley. Suppression of Cavity Loads Using Leading-Edge Blowing. 47(5), 2009.
3. Gareth J. Bennett, Kun Zhao, John Philo, Yaoyi Guan, and Scott C. Morris. Cavity Noise Suppression Using Fluidic Spoilers. *22nd AIAA/CEAS Aeroacoustics Conference*, pages 1–17, 2016.
4. Andrew D Bower. INVESTIGATION OF DYNAMIC STORE SEPARATION OUT OF A WEAPONS BAY CAVITY UTILIZING A LOW SPEED WIND TUNNEL.
5. G. Burniston Brown. The vortex motion causing edge tones. *Proceedings of the Physical Society*, 49(5):493–507, 1937.
6. Tiffany A. Camp. EVALUATION OF FLUID DIODES FOR USE A PULMONARY HEART VALVE REPLACEMENTS A Dissertation Presented to the Graduate School of Clemson University In Partial Fulfillment of the Requirements for the Degree Doctor of Philosophy Mechanical Engineering by Tiffany. (December), 2009.
7. Lou Cattafesta, Farrukh Alvi, David Williams, and Clancy Rowley. Review of Active Control of Flow-Induced Cavity Oscillations (Invited). *33rd AIAA Fluid Dynamics Conference and Exhibit*, (June):1–21, 2003.
8. Louis N. Cattafesta III, David R. Williams, Clarence W. Rowley, and Farrukh S. Alvi. Review of Active Control of Flow-Induced Cavity Resonance. *33rd AIAA Fluid Dynamics Conference*, (June):0–20, 2003.
9. A Cenko and Pax River. Unsteady Weapon Bay Aerodynamics - Urban Legend or Flight Clearance Nightmare. *Sciences-New York*, (January):1–13, 2008.
10. Christopher J Coley and Andrew J Lofthouse. Correlation of Weapon Bay Resonance and Store Unsteady Force and Moment Loading.
11. Galil Motion Control. GALIL Manual:DMC-30000, 2016.
12. Galil Motion Control. Galil Motion Control: Command Reference. 2017.
13. Dantec Dynamics. StreamLine ® / StreamWare ® Installation and User’s guide. 3, 2000.

14. Dantec Dynamics. Probes for Hot wire Anemometry. 2012.
15. Jonathan G. Dudley. The Mechanisms for Passive Suppression of Fluctuating Surface Pressure in a Supersonic Cavity Flow. *Dissertaion UF*, (July):1–225, 2010.
16. Amy Fagan, Michelle Clem, Khairul Zaman, and Kristie Elam. Application of Spectroscopic Doppler Velocimetry for Measurement of Streamwise Vorticity. *51st AIAA Aerospace Sciences Meeting including the New Horizons Forum and Aerospace Exposition*, (January), 2013.
17. FL Fernandez and EE Zukoski. Experiments in supersonic turbulent flow with large distributed surface injection. *AIAA Journal*, (68):0–9, 1968.
18. J K Foss. Optimal configuration of an array of tabs for mixing enhancement in a shear layer OPTIMAL CONFIGURATION OF AN ARRAY OF TABS FOR MIXING ENHANCEMENT IN A SHEAR LAYER. (January), 1997.
19. Freeman J., Keen J., and Jolly B. Quick-Reaction Computational Fluid Dynamics Support of Aircraft Store Compatibility. *ITEA Aircraft Store Compatibility Symposium*, pages 19–24, 2006.
20. Galil. Controllers: DMC - 40x0. pages 0–7.
21. Benjamin George and Lawrence Ukeiley. Control of Three-Dimensional Cavity Flow Using Leading-Edge Slot Blowing. *AIAA SciTech*, (January):1–14, 2015.
22. J Grove, L Shaw, J Leugers, and G Akroyd. USAF/RAAF F-111 flight test with active separation control. *AIAA paper*, (January), 2003.
23. H. H. Heller, D. G. Holmes, and E. E. Covert. Flow-induced pressure oscillations in shallow cavities. *Journal of Sound and Vibration*, 18(4):545–553, 1971.
24. Hanno H Heller and Donald B Bliss. The physical mechanism of flow-induced pressure fluctuations in cavities and concepts for their suppression. *AIAA paper*, 491:1975, 1975.
25. J S Hsu and K. K. Ahuja. Cavity noise control using Helmholtz resonators. *AIAA Conference*, (May), 1996.
26. G Kaufman Ii and Rodney L Clark. Mach 0.6 to 3.0 Flows Over Rectangular Cavities. 1983.
27. Rudy A Johnson, Michael J Stanek, and James E Grove. Store Separation Trajectory Deviations Due to Unsteady Weapons Bay Aerodynamics. *46th AIAA Aerospace Sciences Meeting and Exhibit*, (January):1–15, 2008.

28. J. Jordan, A. Denny, J. Jordan, and A. Denny. Approximation methods for computational trajectory predictions of a store released from a bay. *15th Applied Aerodynamics Conference*, 1997.
29. Finn E. Jorgensen. A new concept for an automated hot-wire anemometer with fully integrated experiment manager, 1994.
30. Finn E. Jorgensen. How to measure turbulence with hot-wire anemometers a practical guide. *Dantec Dynamics*, page 3244, 2002.
31. K Krishnamurty. Acoustic Radiation from Two-dimensional Rectangular Cutouts in Aerodynamic Surfaces.
32. A M Lamp and N Chokani. Control of cavity resonance using steady and oscillatory blowing. *AIAA Stud. J.*, 37(c):99–999, 1999.
33. James V Leggett and Baker Hughes Incorporated. United States Patent. 1(12), 1998.
34. Stephen F Mcgrath, Leonard L Shaw, Lt Stephen, and F Mcgrath. Active control of shallow cavity acoustic resonance. *AIAA Meeting Papers on Disc*, pages 96–1949, 1996.
35. Myonghyon Han. Sound reduction by a Helmholtz resonator. page 110, 2008.
36. Praveen Panickar and Ganesh Raman. Understanding the Mechanism of Cavity Resonance Suppression Using a Cylindrical Rod in Crossflow. *46th AIAA Aerospace Sciences Meeting and Exhibit*, (January), 2008.
37. Ronald L Panton. Effect of Orifice Geometry on Helmholtz Resonator Excitation by Grazing Flow. *AIAA Journal*, 28(1):60–65, 1989.
38. Ronald L. Panton. *Incompressible Flow*. Wiley, 4th edition, 2013.
39. Stephen B. Pope. *Turbulent Flows*. Cambridge University Press, 2000.
40. Zachary A Probst. PROJECT HAVE WASSP. 2015.
41. Mark F. Reeder and K. B. M. Q. Zaman. Impact of tab location relative to the nozzle exit on jet distortion. *AIAA Journal*, 34(1):197–199, 1996.
42. RLS. LM13 linear magnetic encoder system. (11):10, 2011.
43. D. Rockwell and E. Naudascher. Review - Self-Sustaining Oscillations of Flow Past Cavities. *Journal of Fluids Engineering*, 100(June):14, 1978.
44. J Rossiter. Wind-tunnel experiments on the flow over rectangular cavities at subsonic and transonic speeds, 1966.

45. A. J. Saddington, K. Knowles, and V. Thangamani. Scale effects on the performance of sawtooth spoilers in transonic rectangular cavity flow. *Experiments in Fluids*, 57(1):1–12, 2016.
46. A. J. Saddington, V. Thangamani, and Kevin Knowles. Comparison of Passive Flow Control Methods for a Cavity in Transonic Flow. *Journal of Aircraft*, 53(5):1439–1447, 2016.
47. R. L. Sarno and M. E. Franke. Suppression of flow-induced pressure oscillations in cavities. *Journal of Aircraft*, 31(1):90–96, 1994.
48. Ryan Schmit, Christopher McGaha, John Tekell, James Grove, and Michael Stanek. Performance Results for the Optical Turbulence Reduction Cavity. *47th AIAA Aerospace Sciences Meeting including The New Horizons Forum and Aerospace Exposition*, (January), 2009.
49. Ryan F Schmit, Frank Semmelmayr, Mitchell Haverkamp, and James E Grove. Analysis of Cavity Passive Flow Control using High Speed Shadowgraph Images. *Fluid Dynamics*, (January):1–17, 2012.
50. James B. A. Sellers. Force and Moment Measurements Applicable to a Flexible Weapons System. page 128, 2016.
51. James B A Sellers, Andrew Bower, Ian Maatz, and Mark F Reeder. Dynamic Measurement of Forces and Moments with the Motion Test Apparatus.
52. V. Shalaev, A. Fedorov, and N. Malmuth. Dynamics of slender bodies separating from rectangular cavities. *15th AIAA Computational Fluid Dynamics Conference*, (June), 2001.
53. L. Shaw, H. Bartel, and J. McAvoy. Acoustic environment in large enclosures with a small opening exposed to flow. *Journal of Aircraft*, 20(3):250–256, 1983.
54. Leonard Shaw. Active control for cavity acoustics. *Aiaa*, (4):AIAA 1998–2347, 1998.
55. B. Smith, T. Welterlen, B. Maines, L. Shaw, M. Stanek, and J. Grove. Weapons bay acoustic suppression from rod spoilers. *40th AIAA Aerospace Sciences Meeting & Exhibit*, (January), 2002.
56. P C Stainback and K A Nagabushana. Review of Hot-Wire Anemometry Techniques and the Range of their Applicability for Various Flows.
57. R Stallings and F Wilcox. Experimental Cavity Pressure Distributions at Supersonic Speeds. *NASA*, 40(4), 1987.

58. Michael Stanek, Ganesh Raman, Valdis Kibens, John Ross, Jessaji Odedra, and James Peto. Control of cavity resonance through very high frequency forcing. *6th Aeroacoustics Conference and Exhibit*, 2000.
59. Michael J Stanek, Ganesh Raman, John A Ross, Jessaji Odedra, James Peto, Farouk Alvi, and Valdis Kibens. AIAA 2002-2404 High Frequency Acoustic Suppression - The Role of Mass Flow, The Notion of Superposition, And The Role of Inviscid Instability A New Model (Part II) High Frequency Acoustic Suppression - The Role of Mass Flow, The Notion of Superposition,.
60. MJ Stanek, JA Ross, Jessaji Odedra, and James Peto. High frequency acoustic suppression- The mystery of the rod-in-crossflow revealed. *AIAA Conference*, (January), 2003.
61. Nikolai Tesla. Patented Feb. 3, 1920. 1920.
62. Carolyn Leigh Thiemann. An Experimental Study of Supersonic Cavity Flow Control with Vertical Rods. pages 1–13, 2013.
63. Maureen B. Tracy, E. B. Plentovich, and Robert Jr. Stallings. Experimental cavity pressure measurements at subsonic and transonic speeds. *Nasa Technical Paper*, 3358:132, 1993.
64. Lawrence S. Ukeiley, Michael K Ponton, John M Seiner, and Bernard J. Jansen. Suppression of Pressure Loads in Resonating Cavities Through Blowing. *41st AIAA Aerospace Sciences Meeting and Exhibit*, (January):1–11, 2003.
65. Ultimaker. Technical data sheet PLA. pages 1–3, 2008.
66. Ultimaker. Ultimaker 3 Specification Sheet. pages 1–4, 2009.
67. Ultimaker. Ultimaker 2+ Specifactions Sheet. (December), 2012.
68. Ultimaker. PVA Data Sheet. pages 2–7, 2014.
69. Ahmad D. Vakili and Christian Gauthier. Control of cavity flow by upstream mass-injection. *Journal of Aircraft*, 31(1):169–174, 1994.
70. C. P. Yeung and L. C. Squire. Numerical calibration and verification tests of an orthogonal triple-hot-wire probe. *Measurement Science and Technology*, 4(12):1446–1456, 1993.
71. Graydon L Yoder Jr, Yousri M. Elkassabgi, Gerardo I. De Leon, Caitlin N. Fetterly, Jorge A. Ramos, and Richard Burns Cunningham. *Vortex Diode Analysis and Testing for Fluoride Salt-Cooled High-Temperature Reactors*. Number September. 2012.



72. K. Yugulis, S. Hansford, J. W. Gregory, and M. Samimy. Control of High Subsonic Cavity Flow Using Plasma Actuators. *AIAA Journal*, 52(7):1542–1554, 2014.
73. K.B.M.Q. Zaman. Streamwise Vorticity Generation and Mixing Enhancement in Free Jets by Delta Tabs. *AIAA Shear Flow Conference, Orlando, Florida*, pages 1–13, 1993.
74. Ning Zhuang. Experimental Investigation of Supersonic Cavity Flows and Their Control. 2007.

|   |                         |  |  |  |  |
|---|-------------------------|--|--|--|--|
| <b>REPORT DOCUMENTATION PAGE</b>  |                         |  |  | <i>Form Approved</i><br>OMB No. 0704-0188                                  |  |
| Public reporting burden for this collection of information is estimated to average 1 hour per response, including the time for reviewing instructions, searching existing data sources, gathering and maintaining the data needed, and completing and reviewing this collection of information. Send comments regarding this burden estimate or any other aspect of this collection of information, including suggestions for reducing this burden to Department of Defense, Washington Headquarters Services, Directorate for Information Operations and Reports (0704-0188), 1215 Jefferson Davis Highway, Suite 1204, Arlington, VA 22202-4302. Respondents should be aware that notwithstanding any other provision of law, no person shall be subject to any penalty for failing to comply with a collection of information if it does not display a currently valid OMB control number. <b>PLEASE DO NOT RETURN YOUR FORM TO THE ABOVE ADDRESS.</b>   |                         |  |  |  |  |
| <b>1. REPORT DATE (DD-MM-YYYY)</b><br>24-06-2018  |                         | <b>2. REPORT TYPE</b><br>Master's Thesis |  | <b>3. DATES COVERED (From - To)</b><br>Sept 2016 - May 2018                |  |
| <b>4. TITLE AND SUBTITLE</b><br><br><b>LEADING EDGE OSCILLATORY BLOWING: INFLUENCE ON SUBSONIC CAVITY FLOW AND APPLICATION IN SYNCHRONIZED DYNAMIC STORE RELEASE</b>  |                         |  |  | <b>5a. CONTRACT NUMBER</b>   |  |
|   |                         |  |  | <b>5b. GRANT NUMBER</b>  |  |
|   |                         |  |  | <b>5c. PROGRAM ELEMENT NUMBER</b>  |  |
| <b>6. AUTHOR(S)</b><br><br>Wood, Matthew L. Captain (USMC)  |                         |  |  | <b>5d. PROJECT NUMBER</b>  |  |
|   |                         |  |  | <b>5e. TASK NUMBER</b>   |  |
|   |                         |  |  | <b>5f. WORK UNIT NUMBER</b>  |  |
| <b>7. PERFORMING ORGANIZATION NAME(S) AND ADDRESS(ES)</b><br><br>Air Force Institute of Technology<br>Graduate School of Engineering and Management (AFIT/EN)<br>2950 Hobson Way, Building 640<br>WPAFB OH 45433-8865   |                         |  |  | <b>8. PERFORMING ORGANIZATION REPORT NUMBER</b><br><br>AFIT-ENY-MS-18-J083 |  |
| <b>9. SPONSORING / MONITORING AGENCY NAME(S) AND ADDRESS(ES)</b>  |                         |  |  | <b>10. SPONSOR/MONITOR'S ACRONYM(S)</b><br>AFRL RQ/ AFRL RW/ AFOSR         |  |
|   |                         |  |  | <b>11. SPONSOR/MONITOR'S REPORT NUMBER(S)</b>                              |  |
| <b>12. DISTRIBUTION / AVAILABILITY STATEMENT</b><br><br>DISTRIBUTION STATEMENT A: APPROVED FOR PUBLIC RELEASE; DISTRIBUTION UNLIMITED.  |                         |  |  |  |  |
| <b>13. SUPPLEMENTARY NOTES</b><br>This material is declared a work of the U.S. Government and is not subject to copyright protection in the United States.  |                         |  |  |  |  |
| <b>14. ABSTRACT</b><br>The objective of the research was twofold: first, investigate the effect of leading-edge flow control on subsonic (Mach < 0.13) flow fields over a rectangular cavity (L/D = 4.465), and second, develop the capability to synchronize store release with an oscillatory leading edge blowing device's position and identify any trends in forces and moments imparted on the store. The active flow control method utilized a linear motor oscillating at 5.0 Hz to provide leading edge blowing. Five different leading-edge devices were designed and characterized: a single channel 'Slot' and four fluidic diodes. The study used the AFIT low-speed wind tunnel in combination with a tri-axial velocity probe to gather time-accurate data for all three velocity components. Flow control methods were compared using measurements of growth in the shear layer, turbulence intensity, and spatial representation of secondary flows. Compared to the 'Slot', the fluidic diode designs increased shear layer thickness and displaced it toward the freestream. A second linear motor was used to move the store from 0.75 inches below the cavity lip line to 2.25 inches above the lip line. Two initialization positions were tested: the oscillatory linear motor either fully retracted or fully extended. Synchronization between the motors was successfully accomplished using in-situ position readouts from the high-resolution digital encoders in each linear motor and visually with a high-speed digital camera. A dedicated data acquisition system incorporating a Nano-25 balance, collecting data at 1000 Hz, provided time-accurate measurements of the forces and moments acting on the store before, during, and after trajectory motion. The oscillatory blowing was observed to influence the normal force component within the shear layer prior to store motion. During trajectory motion, distinct and generally repeatable patterns in the normal forces during the store motion were observed for the two different initialization positions. |                         |  |  |  |  |
| <b>15. SUBJECT TERMS</b><br>Wind Tunnel; Weapons Bay Cavity; Leading Edge Oscillatory Blowing; Fluidic Diodes; Synchronized Dynamic Store Release; Time-accurate measurements; Thesis   |                         |  |  |  |  |
| <b>16. SECURITY CLASSIFICATION OF:</b>  |                         |  | <b>17. LIMITATION OF ABSTRACT</b><br><br>U | <b>18. NUMBER OF PAGES</b><br><br>304                                      | <b>19a. NAME OF RESPONSIBLE PERSON</b><br>Dr. Mark F. Reeder, AFIT/ENY                             |
| <b>a. REPORT</b><br>U   | <b>b. ABSTRACT</b><br>U | <b>c. THIS PAGE</b><br>U                 |  |  | <b>19b. TELEPHONE NUMBER (include area code)</b><br>(937) 255-3636, x4555;<br>Mark.reeder@afit.edu |